AGARD CP No. 19

AGARD CONFERENCE PROCEEDINGS No. 19

AGARD

ADVISORY GROUP FOR AEROSPACE RESEARCH & DEVELOPMENT

64 RUE DE VARENNE PARIS 7E FRANCE

Fluid Physics of Hypersonic Wakes

VOLUME 1

★

MAY 1967

NORTH ATLANTIC TREATY ORGANIZATION

CONFERENCE PROCEEDINGS No. 19

NORTH ATLANTIC TREATY ORGANIZATION

ADVISORY GROUP FOR AEROSPACE RESEARCH AND DEVELOPMENT

(ORGANISATION DU TRAITE DE L'ATLANTIQUE NORD)

FLUID PHYSICS OF HYPERSONIC WAKES

Published in Two Volumes

VOLUME 1

Papers presented at a Specialists' Meeting of the
Fluid Dynamics Panel of AGARD held at the
Colorado State University, Fort Collins, Colorado, U.S.A.,
10-12 May 1967

The material in this publication has been reproduced directly from copy supplied by each author.

Printed by Technical Editing and Reproduction Ltd
Harford House, 7-9 Charlotte St. London. W. 1.

SUMMARY

The proceedings contain a collection of the papers presented at the AGARD Specialists' Meeting on "Fluid Physics of Hypersonic Wakes", held at Fort Collins, Colorado, 10-12 May 1967 under the sponsorship of the AGARD Fluid Dynamics Panel.

The purpose of the meeting was to review and discuss recent developments in the study of the complex phenomena taking place in the high temperature hypersonic wakes, to present a good cross-section of the state-of-the-art, to point out major problems and to provide guidance for further research and development.

The collection of papers emphasizes the areas: flow over bodies, inviscid and viscous wakes, near and far wakes characteristics, stability and transition, equilibrium and non-equilibrium wake profiles, ablating and non-ablating bodies. Contributions have come from five NATO countries.

RESUME

Ce volume rassemble la plupart des mémoires présentés lors de la réunion de Spécialistes de l'AGARD sur "La Physique des Sillages Hypersoniques" qui fut tenue à Fort Collins, Colorado, du 10 au 12 Mai 1967, sous le patronage du Groupe de la Dynamique des Fluides de l'AGARD.

L'objet de la réunion était de présenter et discuter les progrès récents de l'étude des phénomènes complexes qui se manifestent dans les sillages hypersoniques à haute température, de donner un bon aperçu de l'état de l'art, de mettre en évidence les principaux problèmes et enfin de diriger les recherches ultérieures.

L'ensemble des mémoires explore les domaines ci-après: - écoulement autour des corps, sillages non visqueux et visqueux, caractéristiques des sillages proches et lointains, stabilité et transition, équilibre ou défaut d'équilibre de la distribution dans les sillages, corps soumis ou non à l'ablation. Des contributions ont été reçues de cinq pays de l'OTAN.

061.3:533.6.048.3:533.6.011.55

FOREWORD

The study of wakes has not been overlooked by the AGARD Fluid Dynamics Panel; their formation process has to be fully comprehended for the proper design of aircraft afterbodies and projectile bases. The Panel devoted several meetings to discussions on boundary layers and separation phenomena, the re-attachment of two separated flows, and in general all the aspects of fluid mechanics problems which have to be solved to arrive at a good understanding of the formation of wakes.

However, this is the first time the Panel ventures to discuss the physics of the plasma appearing in a hypersonic wake, and it decides to do so with self-explanatory carefulness, keeping for the discussion of the papers which will not be published, interpretations which fall outside the scope of scientific research. By thus acting, the Panel follows the example of several big nations which would jeopardize the access to information of their own researchers if they did not provide all the experts in the physics of plasmas with their views and the outcome of their experience. The Panel hopes, primarily, to bring into touch the researchers of various NATO countries in favour of faster advances.

The discussions are based on forms completed by the authors and questioners during the meeting.

PREFACE

Le Groupe de la Dynamique des Fluides de l'AGARD n'a pas négligé l'étude des sillages dont il faut dominer les mécanismes de formation pour concevoir correctement les arrières-corps des avions et les culots des projectiles. Il a consacré plusieurs réunions à des discussions sur les couches limites et les phénomènes de séparation qui s'y manifestent, sur le recollement de deux écoulements séparés et d'une manière générale de tous les aspects des problèmes de mécanique des fluides qu'il faut résoudre pour comprendre la formation des sillages.

C'est cependant la première fois qu'il se hasarde à discuter la physique du plasma qui se forme dans un sillage hypersonique et il s'y décide avec une prudence bien compréhensible en réservant pour la discussion des mémoires qui ne seront pas publiés, les interprétations qui sortent du cadre de la recherche scientifique. Il suit ainsi l'exemple déjà donné dans plusieurs grands pays qui compromettraient l'information de leur propres chercheurs s'ils ne donnaient pas à tous les spécialistes de la physique des plasmas l'occasion d'échanger des fruits de leurs expériences et de leurs réflexions. Il espère surtout établir des contacts entre les chercheurs des divers pays de l'OTAN, favorables à une progression plus rapide des études.

Les discussions se basent sur les fiches remplies par les auteurs en réponse aux questions écrites posées au cours de la réunion.

CONTENTS

VOLUME 1

---

* This paper will not be published

VOLUME 2

FLUID MECHANICS OF WAKES*

by

Lester Lees

* This paper will not be published.

BLANK PAGE

KINETIC PROCESSES IN HYPERSONIC WAKES*

by

Alan Q. Eschenroeder

Head, Aerophysics Section

General Motors Corporation

AC Electronics Defense Research Laboratories

Santa Barbara, California

* This work was sponsored by the Advanced Research Projects Agency and monitored by U. S. Army Missile Command under contract No. DA-01-021-AMC-11359(z) as part of Project Defender.

NOTATION

D_B, d	Maximum Body Diameter
D_p	Wake Plasma Diameter
K	Coefficient in Eddy Viscosity Expression
N_e	Mean Electron Density
P_∞	Ambient Pressure
R_N	Nose Radius of Cone
R_B	Base Radius of Cone
Re_d	Body Reynolds Number Based on Free Stream Conditions
U_∞	Flight Speed
X	Axial Distance from Nose
δ	Physical Plane Wake Width
θ_c	Cone Half Angle
μ	Microns
μ_ε	Eddy Viscosity
Ω	Steradians

SUBSCRIPTS

c	Wake Axis
e	Wake Edge
i	Incipient Laminar Instability
T	Fully Developed Turbulence
∞	Free Stream

SUMMARY

The roles played by chemistry, ionization, and energy transfer processes are discussed in the context of hypersonic wake flows. Of primary interest is the influence of the microscopic gas phase behavior on the observable features of the wake. Emphasis is placed on pure air processes for both blunt and slender body shapes. Essential differences between the two cases exist in the deposition of energy in the flow field and in the subsequent appearance of active species.

Atom recombination and exchange processes are the classes of neutral particle reactions which are most significant in determining the bulk energetics of the flow. Moreover, certain classes of neutral reactions seem to control the major part of the radiant energy emitted by the far wake. Charged particle processes are directly involved in establishing levels of free electrons which, in turn, control the appearance of a wake to ground based radars.

Because of the numerous possibilities offered by electron-ion, ion-ion, and ion-molecule interactions, it is desirable to simplify the kinetic representations of charged particle interactions. Examples of specific wake flow field calculations are cited in light of experimental measurements from ballistic ranges in order to illustrate an operational approach to theoretical models.

Following the reviews of current work, some areas of future interest are identified. Residual lags of internal excitation can affect greatly the species production rates. Vibrational-electronic exchanges, however, could constitute rapid equilibration paths which suppress the influence. Ablation kinetics are discussed briefly in light of wake ionization effects. Organic and metallic materials in air are considered. Finally, the role of turbulent inhomogeneity is described as a possible determinant of mean chemical rates for portions of the wake having highly nonuniform edge conditions.

1. INTRODUCTION

Microscopic kinetic activity is the intermediary between fluid motion and those effects which we see or measure in the wake behind an object entering the atmosphere at hypersonic speeds. Excitation of the gas marks the trail by radiant emission and free electron production. The latter renders the wake effective as a scatterer of radar signals. If we wish to learn something of the object or its flight-characteristics, it is generally necessary to trace back through the aerophysical aspects of the interaction between the object and its environment.

In the absence of a reliable empirical "transfer function" connecting object and observables, we are obliged to seek an operational understanding of the physics controlling those effects which we may sense. With regard to the microscopic processes, a fruitful approach has arisen from the combination of laboratory findings and theoretical analyses. The experimental results can be categorized either as fundamental kinetic data (e.g., rate constants from shock tube measurements) or as laboratory flight information (e.g., wake radiation decay rates from free flight range tests). The theoretical analyses have sought to synthesize a physical model incorporating the pieces of fundamental data to predict measurable wake phenomena. An iterative process between measurements and calculations has begun to identify the kinetic building blocks which are essential features in describing the observed behavior of hypersonic wakes.

The objective here is to report on our progress in determining the roles played by the elementary phenomena. It is beyond the scope of this paper to collect and assess the pertinent kinetic rate data. Motivated by studies in aeronomy, reentry phenomena, and late fireball phenomena, numerous efforts in this direction have been made in past years. (1, 2, 3, 4, 5, 6, 7, 8, 9, 10)* Great care has been exerted in some cases, and sheer

---

* The references given above cite other compilations which predated them. Note added in proof: A recent compilation is given in J. Heicklen, AIAA J., Vol. 5, No. 1 (January 1967) pp 4-15.

quantity has been achieved in others. Because of our compelling needs to predict kinetic behavior in wakes, the hasty application of numbers from rate compilations has sometimes misled us. Information thus obtained is sometimes second or third hand at the source cited.

Under the auspices of U.S. Department of Defense agencies, M. H. Bortner and M. H. Bloom have instituted an informal effort to collect and update kinetic information for flow calculations. An attempt is being made to involve directly those investigators who are the primary sources of the data. The compilation effort was initiated at an informal conference held at the Institute for Defense Analyses January 5, 1966, which was organized by R. Zirkind. Since the meeting, Dr. Ernest Bauer (Chairman of the Atomic and Molecular Panel at IDA, 400 Army-Navy Drive, Arlington, Va. 22202) has been the recipient of current comments and new rate data.

Returning to the present purposes, we are concerned with making an optimum choice in the kinetic description of wake phenomena. The result of such a choice may be termed a kinetic model and consists of a list of reaction steps with corresponding rate data. Identification of significant steps depends both on expected concentration levels and collision efficiencies. The complicated nonlinearity of reaction coupling often renders the selection process more an art than a science. Short, trial, computer solutions are almost essential in this decision-making procedure. While extreme truncation of the kinetic specifications can be instructive, it sometimes removes the problem from what is observed in nature in order to place it in the realm of analytic solutions. On the other extreme, the availability of vast computer resources has sometimes given rise to the "all-inclusive" kinetic model. The extensive compilations of rate estimates have in no small way contributed to premature and unjustified complexities in flow field calculations. The optimum choice, then, is the smallest model containing the crucial determinants of that

observable one wishes to predict. The final test of the choice is clearly its general utility in predicting observed phenomena over a wide range of flight conditions.

The discussions of wake kinetics will begin with a reexamination of neutral particle chemistry in air. We then move on to examine in some detail some of the current notions on ion kinetic processes influencing electron removal in wakes. Three areas of possible future research will then be briefly reviewed: (1) Influence of internal mode energy transfer processes on reaction rates and, (2) Ablative contaminant kinetics in wakes, and (3) Influences of turbulent fluctuations on reaction rates. Evidently, these areas are presently neglected either because they are poorly understood or because they are believed to be unimportant.

2. AIR NEUTRAL CHEMISTRY

2.1 Active Coupling with Flow

Energetic interaction with the wake flow is practically confined to the neutral chemistry for flight speeds of 15 to 25 kfps. We shall consider the chemistry of air alone although most natural and man-made entry bodies ablate to some extent. The paths for storage and release of latent chemical energy involve either molecular dissociation (and recombination) or metathetical exchange (shuffle) reactions. Species present are largely limited to monatomic and diatomic particles in the $3000^{\circ}K$ to $8000^{\circ}K$ temperature range. Rates of the principal reaction steps as suggested by Wray (4) in his review are essentially those presently used in flow field calculations. Wake measurements which are presently available give no basis for revising those values. In the range from ambient air temperature up to $3000^{\circ}K$, equilibrium calculations (11) suggest that triatomic species such as O_3, NO_2, and N_2O may be significant. The kinetic matrix including the additional species

is also far richer in possibilities for reaction steps (2, 11).

Active coupling between energetic chemistry and the wake flow is largely characterized by a constant pressure dilution process of gas which has experienced a dissipative heating pulse in a shock wave and/or boundary layer. Chemical energy and viscous dissipation compete with molecular or turbulent transport to determine the temperature and density fields. Few, if any, of the significant reaction steps have large activation requirements so that the temperature coupling is of a lower order than that in the near-body flow field. Oxygen atom concentration is probably the key species in controlling the far wake observables because of its participation in chemiluminescent radiation reactions and in low temperature electron removal processes. Vacuum ultraviolet absorption is under evaluation at the AC Electronics Defense Research Laboratories (AC-DRL) as a direct means for measuring O-atom levels in wakes (12). The application is contemplated for use in free flight range facilities.

Oxygen atoms persist because three-body recombination is the energetically favored removal path and tertiary collisions are relatively rare at typical flight conditions. Nitrogen atoms react rapidly with nitric oxide and with oxygen molecules to produce N_2 and NO respectively. Each of these exchange steps produces O-atoms. In the final stages of wake decay, stabilization of the triatomic oxygen bearing species opens fast two-body paths for O_2 formation by the abstraction of an oxygen atom from these species in the far wake.

2.2 Blunt Body Wake Kinetics

Blunt body wakes are dominated by the reactions following the strong portions of the bow shock wave. Schlieren photographs, (13) radiation measurements (14) and ionization measurements (15) support the notion that there is a distinctive, hot entropy wake formed by the nose portion of the shock set up by a sphere in hypersonic flight. Evidently this region is bounded by sharp radial density gradients and is the order of a sphere

diameter wide. Nearly all of the electrons and oxygen atoms are contained in this region initially. If the viscous core (originating from the body boundary layer) is stabilized by viscous stresses, no flow disturbances grow until the entropy wake breaks up thousands of diameters downstream. For supercritical Reynolds numbers, the core undergoes transition and grows outward gradually until it reaches the "entropy edge". At this point the core receives a large injection of velocity defect and it explodes into the colder surroundings. Wilson (13) has called this phenomenon "breakthrough".

Although the present discussion primarily deals with kinetics, it could not proceed without considering the fluid dynamic observations outlined above. During the breakthrough process, nitric oxide, which has its peak concentration near the "entropy edge", * is rapidly mixed with oxygen atoms from the wake interior. Also, any residual nitrogen atoms may react rapidly with nitric oxide and oxygen molecules. Energy release from the N-atom cleanup could occur rapidly enough to produce a heating pulse (16). Experimental observations of seeded wakes at AC-DRL tend to support this finding. Nitric oxide level is probably further enhanced, as a net result, by the suffle reactions. Following breakthrough, nitric oxide reacting with oxygen atoms produces excited NO_2 which subsequently emits chemiluminescent radiation. As shown in Fig. 1, such radiation intensifies greatly after the turbulent front traverses the entropy edge (14). The local temperatures are too low to support much O-atom abstraction from NO to form O_2 + N. The spectral distribution strongly suggests that the NO_2 chemiluminescent reaction is operative since it compares favorably with low temperature experimental results (17) for the $NO + O - NO_2 + h$ reaction as shown in Fig. 2.

---

* The familiar NO-overshoot behind the bow shock is completed in a short distance for the stagnation streamlines, but persists well behind the body for the outer streamlines of the entropy wake.

Far back in the sphere wake, oxygen atoms are the most abundant of the free radical species remaining. Subsequent cooling of the gas by mixing promotes their removal by three-body formation of ozone, nitrous oxide and nitrogen dioxide. E. Sutton and M. Camac (18) have further suggested that oxygen abstraction reactions with low activation energy like $O + NO_2 \rightarrow O_2 + NO$ may also remove oxygen atoms. Also, nitric oxide or N-atoms may abstract an oxygen atom; however, it is unlikely that any but a trace of free nitrogen atom will survive into the far wake.

2.3 Slender Body Wake Kinetics

Low temperature levels and short residence times characterize the "heating-pulse" produced by the flight of a slender body through the air. In the absence of ablation these factors combine to suppress markedly the net production of active species. The small fraction of the flow that is exposed to sites of high temperature and low velocity is diluted by molecular or turbulent transport of species and energy. The relative size of the "hot-fraction" is measured by the bluntness, which is largely determined by tip geometry and, for slender cones, to a lesser extent by the angle of flow deflection. Incubation sites for free radicals include forward stagnation, boundary layer, base recirculation zone, and rear stagnation region, (roughly in descending order of relative importance). Preliminary calculations assuming inviscid nose shock layer flow (19, 20) indicate an extremely sensitive dependence of reactions upon nose blunting. Inclusion of transport effects in the nose flow will markedly decrease the sensitivity for small tip Reynolds numbers. Estimates of limiting behavior in the base recirculation zone also show some potential for active species production. (21, 22) Both cases are somewhat exaggerated because they are upper bound calculations compared with the sharp cone boundary layer calculations. Radial spatial distributions of the reaction products will depend on the outcome

of near-wake flow field studies discussed in the preceding review paper in this conference. Evidently the supersonic portion of the boundary layer rapidly expands to occupy an extensive transverse portion of the near wake and probably quenches any chemical activity incubated in the boundary layer. Shock systems associated with the expanded region are probably weak.

Transition from laminar to turbulent flow is observed to be a very gradual process because of a lack of driving energy in the inner viscous core. A weak entropy edge emanates from the changes in cone shock strength aft of the body, and breakthrough is observed as in the sphere case. At subcritical Reynolds numbers the cuter wake goes unstable because of viscous suppression of inner core transition.

Evidence of air chemistry in slender body wakes is less extensive than that for blunt body wakes because of far lower levels energy of dissipation in the flow. Inferential evidence may be surmised from line reversal temperature measurements behind cones of 6% bluntness for velocities exceeding 20 kfps. (23) Although the results are complicated by ablation and vibrational lags, they are consistent with the notion that the gas at the beginning of the wake is nearer a local equilibrium than it is a near-frozen condition which would be expected for sharp cones. Reduction of data from a Twyman-Green interferometer instrument recently applied to the AC-DRL free flight range holds out the possibility of obtaining more definitive information on pure air translational temperatures in slender body wakes.

The fragmentary evidence available from experiments and calculations indicates that oxygen atoms must be initially abundant at the axis of slender body wakes; however, other radical species have rather lower concentrations. Formation of the oxygen bearing triatomic species which are stable at low temperatures is likely to be controlled by diffusion following break up of the sluggish laminar instability waves.

2.4 Remarks on Kinetic Models for Neutral Air Species

The fate of free radicals in the far wake has become a subject of great interest in recent years. Although some new information has come to light for high temperature kinetics, the dominant flow processes in the near wake have received greater attention. Electron wake lengths (which are discussed in the next section) depend intimately on the final disposition of free radical species at moderate temperatures.

The IDA kinetics conference held in early 1966 revealed that a great majority of flow field models still essentially employ the model suggested by Wray (4) in 1961 for high temperature neutral air kinetics. It was reported at that conference, however, that investigators at the Avco Laboratories have found that the reaction rate previously ascribed to $2NO \rightarrow N_2 + O_2$ in reality applies to the same colliders producing $N_2O + O$. Specifically, the rates reported by Freedman and Daiber (24) and by Wray and Teare (25) apply to the latter set of products. This helps explain the tenfold discrepancy noted by Wray (4) in attempting to reconcile the high and low temperature findings. The current compilation of rate data referred to previously lists the rates to be employed for each set of products. A possible meaning of this finding in wake predictions enters the ionization predictions via the reverse reaction. It is probable that the sharp cone boundary layer chemistry follows the low temperature NO chain scheme.

$$N_2 + O_2 \rightarrow 2\,NO \qquad (1)$$

$$NO + O \rightarrow O_2 + N \qquad (2)$$

$$N + O \rightarrow NO^+ + e^- \qquad (3)$$

in which reaction (2) is the primary source of nitrogen atoms for reaction (3). Preferential production of N_2O in reaction 1 blocks this chain and may therefore lower the predicted ionization because reverse rates are related

to forward rates through the equilibrium constant. The $N_2 + O_2$ reaction is usually omitted in high temperature shock layer calculations because it has little effect.

For the moderate temperature far wake processes, two reaction chains for oxygen atom removal may be significant in addition to atom-atom recombination. The principal one involves ozone as a chain carrier by way of the steps

$$O + O_2 + M \rightarrow O_3 + M \qquad (4)$$

$$O + O_3 \rightarrow 2O_2 \qquad (5)$$

and the other depends on the survival of nitric oxide via

$$O + NO + M \rightarrow NO_2 + M \qquad (6)$$

$$O + NO_2 \rightarrow O_2 + NO \qquad (7)$$

The chemiluminescent reaction

$$O + NO \rightarrow NO_2 + h\nu \qquad (8)$$

could be another source of NO_2 and is certainly a significant source of wake radiation.

Although one-way arrows are shown above, it is imperative that reverse reactions be carried along in wake calculations for the collisional processes. Reactions (4) and (6), in particular, will follow partial equilibrium when they first become important. In practice, these equilibria drive strongly leftward in all but the far wake and will lead to drastic inefficiencies in practical computations if included prematurely. Proper introduction of the reactions may be effected either by periodic trial calculations or some kind of by-pass logic in a computing program. Oxygen abstraction reactions of the types (5) and (7) have modest activation requirements; however, since they are binary, they must probably be included in the scheme.

3. AIR ION KINETICS

3.1 Electron Decay Mechanisms

Recent advances in applying microwave (26, 27) and uhf (28) diagnostics to free flight range measurements have resulted in a comparatively large body of data on one species in the wake: the free electron. The production and removal of electrons have been the main subject of kinetics investigations for hypersonic wakes in recent years. Ion kinetics are discussed separately here because they are passively coupled (29) with the flow which acts as a kind of heat bath. Ion measurements in wakes are presently under experimental evaluation for the free flight range using two approaches. The first involves the use of a flash lamp to photodetach electrons from negative ions. Choice of the appropriate spectral interval limits the release to low threshold processes. Liberated electrons would then be detected using focused millimeter wave resonator techniques. (27) The second approach will employ insertion of a time-of-flight-mass spectrometer to analyze the ions.

As with the neutral species, mechanisms can be conveniently categorized as high or low temperature in nature. High temperature processes dominate at small axial or radial distances in the wake. What is meant by "small" depends greatly upon body shape and flight conditions. At high temperatures (thousands of Kelvin degrees) the wake deionization proceeds primarily via dissociative recombination of molecular ions with electrons. Any atomic ions which may be present feed the reaction efficiently via charge transfers with neutral molecules. Thus, the entire process may effectively be represented by a single dissociative recombination step since the rates of all dissociative recombinations have closely grouped values of rate constants (30). In reality, $NO^+ + e^- \rightarrow N + O$ alone removes most of the electrons in the high temperature wake regions (31) for sub-meteoric reentry speeds.

As temperatures decrease from outward energy transport, electron population decreases, and oxygen molecule population increases. Since recombination is effectively second order in electron density, its rate is suddenly exceeded by that of three-body attachment to $e^- + O_2 + M \rightarrow O_2^- + M$ at some station in the wake (32, 33). Taken as the only electron reaction in addition to recombination, this process can lead to precipitous extinction of the electron wake because of its exponential character. Its influence intensifies with decreasing altitude.

Competing reactions include attachment to other electronegative species coupled with negative ion charge transfers. Collisional and associative detachment oppose the electron removal processes tending to prolong electron decay. Attachment and mutual neutralization must be the paths of final removal of charged particles. Specific consideration of reaction steps is deferred to the last part of the present section.

3.2 Blunt Body Wake Ionization

As described in §2.2, the hot entropy wake in the near field and mixing phenomena in the far field are the predominant features of the fluid dynamics forming a background for our ionization study. Depending upon Reynolds number, the mixing may be due to a turbulent front which has outgrown the entropy edge or laminar diffusion of the entropy wake followed by its eventual unstable breakdown.

For a nonablating sphere in hypersonic flight, electron density within the first hundred body diameters is describable by means of a relatively simple theoretical model (16). The air kinetic scheme includes only the $N + O \rightleftarrows NO^+ + e^-$ reaction for electrons with the usual set of neutral particle steps, and only the inviscid flow field is considered on the body. The inverse method is used for the inviscid flow in the stagnation region (34). Streamtube calculations (35) begin at the final ray in the inverse net, and are employed to continue the flow field behind the

body. Inviscid convection (16) is retained to describe the near wake ionization. By the use of microwave wake measurements (which are described elsewhere in some detail (16, 36) it has been demonstrated that this simple approach adequately represents observed results (37). Specifically, it has been tested for wake ionization behind spheres over a range of (pressure) x (diameter) product of 45 to 1500 torr-mm and a range of flight speeds from 18 to 22 kfps. Figures 3 and 4 illustrate the results of the analysis showing that the essential features of reaction order and temperature dependence are described adequately by the model. The range of conditions includes both laminar and turbulent viscous core conditions. Evidently the integrated electron densities are insensitive to mixing model in the near field.

For the purpose of obtaining initial conditions for far-wake calculations, J. P. Appleton and C. C. Yang have used equilibrium characteristics solutions for near field pressure distribution instead of the patched Newtonian-blast wave-constant pressure variation assumed in ref. 37. The characteristics solutions were carried out by E. Lieberman of the General Applied Science Laboratories. Nonequilibrium streamtubes were employed throughout so that the inverse method for nonequilibrium initial conditions was not needed. Interpolations in the curves from ref. 37 were carried out to obtain an ionization decay curve for comparable conditions of (pressure) x (diameter) product, velocity, and recombination rate constant.

Figure 5 illustrates that the approximate approach is probably adequate for describing transverse integral effects in the near wake. Since radial pressure variation is omitted, the approximation will not reproduce details of the flow very near the body or the shock system. The more precise calculations have also included the homogeneous mixing limit for experimentally observed turbulent front growth. The integrated electron density appears to be insensitive to the degree of mixing until some distance approaching fifty diameters. This finding is consistent

with the earlier observation that the validity of the near wake ionization approximation was unaffected by the existence of turbulent core flow in the flight experiments.

At low Reynolds numbers ($Re_d \gtrsim 5 \times 10^4$ based on sphere size and free stream conditions) the entropy wake persists unperturbed for a few thousand body diameters and before breakup occurs (13). The viscous core becomes indistinct, and molecular transport smears the rather sharp edges of the species profiles. Using the simple random convection method to obtain initial profiles at 40 body diameters, an axisymmetric laminar nonequilibrium calculation has shown good agreement with observations for a (pressure) x (diameter) product of 150 torr-mm out to wake breakup at a few thousand diameters. This calculation was performed using the analysis (38) and code (39) developed by Wen and Chen.

Fig. 6 shows the axial ionization decay reported in ref. 40. The displacement between the experimental and theoretical curves is a systematic deviation arising from the slight difference in velocities. Referring to Figure 3 we may note that the velocity correction indicated would bring the two curves together. Omission of the transport terms gives a minimum in the curve at a few hundred diameters followed by monotonic growth.

Because of its prominence in reentry observables, the ionization in the turbulent far wake has been studied for a longer time than in the near wake and laminar far wake. The integral treatment used in the Lees and Hromas diffusion analysis (41) was applied to extensive wake kinetics investigations (42). In this work, Webb and Hromas pioneered the use of a complex ion kinetic model in the far wakes of spheres. Electron attachment to oxygen atoms was recognized as an important feature in sphere wakes and the role of negative ion charge transfer was brought out. The existence of an activation energy for the $O_2^- + O \rightarrow O^- + O_2$ reaction is very doubtful, and it has been considered

zero in the current IDA rate list. Thus, the Webb and Hromas result for rapid electron decay is more consistent with current ideas than the result which is based on a 1/2 eV activation requirement. The comparisons of the far wake calculation with the Lincoln Laboratory sphere measurements showed too rapid a decay was predicted at 1000 diameters and too slow at 10,000 diameters. According to the tabular rate data in reference 42 the activation energy for charge transfer was retained. If it were omitted, it is likely that the decay rate would be overpredicted throughout the wake. Comparisons of the General Applied Science Laboratories finite difference calculations (44) with similar data shows the same trends (45).

Under the assumptions of the homogeneous mixing and random convection limits (16), J. P. Appleton and C. C. Yang have carried out quasi-one-dimensional calculations of wake ionization for the far wake using initial conditions obtained as described above. Their results and experimental data (which are described in another paper in this conference (15)) are shown in Fig. 7. Curves A and B represent the mixing limits with the experimentally observed wake envelope as an input for Curve B, the homogeneous mixing case. Only attachment to molecular oxygen is considered in this case; however, more recent calculations include attachment to oxygen atoms, charge transfer, rapid associative detachment (46) and ozone formation following some of the suggestions of Sutton and Camac (18). Addition of the latter results in higher electron levels for 100 to 1000 diameters, but the final observed decay is not predicted without some chain breaking reactions added to the scheme. Axisymmetric finite difference calculations utilizing the analysis of Wen and Chen (38) give essentially the same decay as curve B, if the same kinetic model is used.

The significant feature of Fig. 7 is the wide variance between either limiting theory and the experimental data. Curves D and C

represent pure recombination and a reduced effective wake width respectively. In order to represent the mean position of the front, the wake width in curve C was chosen empirically to be 25% less wake width than the formula of Lin and Hayes (16) calls for. Neglecting attachment (as shown in Curve D) reverses the sign of the curvature and reducing the wake width only postpones the downward departure of the calculated curve from the data.

Variable "K" eddy viscosity laws are being studied by K. S. Wen as possible representations of partial mixing. Other approaches already proposed for the intermediate mixing model are the bimodal, (47) delayed mixing (48) and stochastic analyses (49) which are all in various stages of development. The influence of turbulence on chemical kinetics will be discussed in a later portion of the paper.

A significant experimental finding reported here by Hayami and Primich (36) is binary reaction scaling of sphere wake ionization for nearly 2000 diameters or over a four decade range of integrated electron density in a turbulent flow. The apparent inability of dissociative recombination to explain this suggests an attachment-detachment reaction chain consisting of two body reactions. Dissociative attachment to oxygen is energetically disfavored, unless there is a substantial excited state population among the oxygen molecules. Modest excitation can lower the dissociative attachment threshold drastically according to the experiments of Fite and Brackman. (50) The proper accounting for this rate enhancement in flow field calculations must be regarded as problematical at this time because of the difficulty in representing the excitation mechanics with an accurate mathematical model. This reaction and its reverse are likely to be important factors in the final deionization in wakes.

Ionization in the blunt body turbulent wake seems to be described in three rather distinct regions: (1) Near Wake (10 to 100 diameters)

dominated by electron-ion recombination, (2) Intermediate Wake (100 to 1000 diameters) controlled by post-breakthrough mixing processes which initiate attachment, and (3) Far Wake (greater than 1000 diameters characterized by complex charge transfer and attachment chains involving triatomic negative ions.

3.3 Slender Body Wake Ionization

Accurate specification of initial conditions continues to be a central problem in slender body wake ionization calculations. Some early estimates for a cone at 22 kfps put the near wake neck temperature at 9000°K with the oxygen fully dissociated. This enthalpy corresponds to the full stagnation state for flight in excess of 30 kfps. Initial electron densities for this condition reached $10^{12} cm^{-3}$. Other more conservative estimates froze the nonequilibrium boundary layer conditions at the cone base giving initial electron levels near $10^{7} cm^{-3}$ for approximately the same flight conditions. This five orders of magnitude variance of opinion left a broad field open for future research, and, as we see from the previous paper by Prof. Lees, it has progressed a great deal since then. Shock tunnel and free flight range experiments in recent years have provided us with important benchmarks from which to begin the hypersonic wake kinetics calculations.

The reacting wake calculations of Webb and Hromas represent some of the significant original efforts in the field. (51) Their 12° cone calculations displayed binary similitude over a large extent of the wake because of the extremely hot initial conditions which were believed to exist. The sensitivity to the negative ion charge transfer activation energy was studied in conjunction with the tertiary scaling of the far wake. In the work which followed (42) the ion kinetic model was studied further and the first considerations of bluntness-induced ionization appeared.

In the same period other reacting wake programs were developed for slender body calculations. A multi-strip integral technique was

reported by Lien, Erdos and Pallone (52). Finite difference techniques follow the methods presented by Zeiberg and Bleich (44) and more recently by Wen and Chen (38, 39). Comparison calculations were made between the methods in references 44, 51 and 52. In addition, the General Electric Company participated in the comparison using a finite difference code. The results of this comparison,which are summarized in ref. 51, were compromised somewhat by possible ambiguity in specification of conditions. Ionization levels scattered by factors of five. These difficulties were eliminated in a more recent computational comparison which includes the method of reference 38 in addition to the four named above. Scatter in the ionization results has been greatly reduced. The outcome will be published soon by J. Menkes of IDA under the CALCOM project.

Another type of comparison was also suggested by J. Menkes a few years ago. Its objective was to assess the ability of the various codes to predict the ionization measured in the wakes of slender conical bodies in the AC-DRL free flight range. In this case each investigator developed his own initial conditions based on the flight variables of the test. The experimentally observed decay is far more rapid than any of the predictions regardless of where laminar to fully turbulent transition was assumed. The initial levels are also observed to be considerably lower than any of the calculations in the study. Reference 53 summarizes the results of the comparisons.

Intensive studies have been recently conducted (53) for the purpose of understanding the rapid ionization decay observed behind slender cones (15). The analysis uses a finite difference scheme in the physical plane (38) and is implemented in the form of a FORTRAN IV computer program (39). Initial conditions for the calculation are based on scaling shock tunnel measurements of the near wake total enthalpy profiles (54). Boundary-layer-type Crocco relations are invoked to relate static

enthalpy to velocity and local equilibrium is assumed to obtain species profiles. Such a procedure yields approximately the ionization (15) and temperature (23) levels observed in the free flight range experiments. Approximate base flow mixing calculations using non-equilibrium sharp cone boundary layer inputs underestimate initial ionization levels (22). It is found, however, that allowing equilibration of the recirculatory flow has a threefold upward influence on the ionization. Proper accounting for this effect and bluntness effects (19, 20) probably holds the key to this problem. The apparent success of the local equilibrium assumption, therefore, may be fortuitous. Figure 8 shows the effect of different trade-offs between axis velocity and static enthalpy in the initial conditions. Levels are influenced, but decay rates all becomes the same after 40 diameters of laminar wake without attachment. Addition of O_2^- and O^- followed by NO_2 and NO_2^- has practically no effect as shown on Fig. 9 because the high temperature persists.

Isolation of kinetics effects from mixing is difficult for the 75 torr pressure case shown in Figs. 8 and 9. Schlieren pictures show the incipient instability of the laminar wake beginning around 30 diameters and the full development of turbulence in the vicinity of 60 diameters. The effect of assuming transition to fully developed turbulence and including attachment at 30 diameters is shown in Fig. 9 as the curve labeled turbulent. The decay is clearly too rapid.

Reduction of the ambient pressure to 20 torr extends the laminar run to about 100 diameters. Calculations of ionization for the 20 torr conditions then are useful to test the high temperature kinetic assumptions and the procedure for determining initial conditions. Fig. 10 shows that the computed decay even without negative ions falls within the experimental uncertainties of the measured values. The final decay rate at 80 to 100 diameters does not track the data precisely because attachment was excluded.

Now considering the converse case, Wen, et al (53), have examined the turbulent mixing for a wake flow with simple kinetics. Ionization measurements for nonablating cones flying through a nitrogen atmosphere are the basis of this study. At a pressure of 150 torr the laminar instabilities begin near 10 diameters behind the body. As shown by Kornegay for spheres in nitrogen (43) and by Hayami and Primich (15) for cones, the electron wake in nitrogen is more extensive than that in air. Nitrogen has a much greater chemical bond energy than oxygen. Consequently, it gets hotter than air before dissociation begins to absorb any sizable portion of the energy. Despite its higher effective ionization potential, nitrogen ionizes nearly as much as air in the initial region of the wake (15). The absence of attachment confines the electron concentration decay to the recombination regime.

Figure 11 shows the data with various predicted ionization histories. The kinetic model includes atom recombination, electron ion recombination, and charge transfers between atomic and molecular ions. As usual, all reverse steps are also allowed. The laminar transport calculation does surprisingly well in approximating the observations. Initiation of fully turbulent diffusion at 10 diameters, however, leads to far too fast a predicted decay. Noting the possibility that the wake was not nearly self-preserving yet, Wen has suggested that the eddy diffusion process develops gradually over a considerable axial extent of the wake. One way of describing this feature in conventional wake calculations is to give the eddy viscosity constant (which is applied to a width times a momentum defect) a streamwise variation from a level which provides a match with laminar transport to one which is appropriate for fully developed turbulence. The curve designated "transitional" on Fig. 11 shows the result of such a description. While its level is too low, its decay approaches the experimental rate rather closely. Thus, Figs. 10 and 11 tend to indicate that the conventional turbulent transport model is in more serious difficulty than are either the initial profiles or

the hot air chemistry in the example considered in Fig. 9.

Returning to the wake ionization behind cones in air at 75 torr, we note on Fig. 12 that the application of the transitional eddy diffusion representation brings the prediction into far better agreement with observations than either laminar or turbulent calculations. This is true even if all attachment is omitted. The transition from laminar to turbulent mixing was assumed to occur between 30 and 60 diameters to correspond with schlieren observations. Consideration of attachment improves the model still further. It is evident, then, that the most likely cause for the initial discrepancies between calculations and observations is the eddy diffusion model. Wake growth comparisons also confirm such a conclusion. (53)

Improved instrumental sensitivity has yielded preliminary results for ionization in the next decade below the range shown in Fig. 12. The turbulent wake predictions with O_2^- and O^- included begin to fall below the data as in the case of sphere wakes. Investigations are now underway to extend the kinetic model as in the case of the spheres. Associative detachment and its reverse involving excited O_2 may both be actively involved in modifying the ionization level.

Fluid dynamic studies of the details of the turbulent diffusion processes, which have been shown to influence wake ionization, are underway both at Avco Missile Systems Division and at the General Applied Science Laboratories (GASL). In the former, H. Gold is extending his earlier work on wake stability to the growth of disturbances in the nonlinear regime. (55) An objective of the study is the description of the transitional region mixing mechanisms. In the GASL work, H. Lien and G. Widhopf have instituted a research program on turbulent momentum diffusion. (56) The objective of the program is an examination of the universality of the eddy Reynolds number (or Townsend Reynolds Number) on which most mixing models are based. Experimental velocity and density data from the Canadian Armament Research and Development

Establishment (CARDE) ballistic ranges will be "inverted" to obtain detailed distributions of eddy viscosity. The analytical formulation of the problem is now complete.

3.4 Kinetic Models for Wake Ionization

The findings discussed above for air and its component gases illustrate the recent progress in refining the kinetic descriptions of wake ionization. Experimental observations using instrumentation of ever increased sensitivity and resolution have paced the developments. As in the cases of neutral chemistry, the stability of complex species at lower temperatures enlarges the kinetic problem tremendously.

The presence of O_3 leads to the fast exothermic dissociative attachment reaction (18) to the right

$$e^- + O_3 \rightleftharpoons O^- + O_2 \qquad (9)$$

and O_3^- formed by three body attachment may be attacked by O-atoms to return electrons to the system via

$$O + O_3^- \rightleftharpoons 2O_2 + e^- \qquad (10)$$

Likewise, associative detachment may occur earlier in the wake by means of

$$O + O^- \rightleftharpoons O_2 + e^- \qquad (11)$$

It was mentioned earlier that a great enhancement of the reverse of reaction (11) is observed for hot oxygen. (50) Fehsenfeld and co-workers (46) now report three orders of magnitude higher rate values for forward reaction (11) than was previously suspected. The significant role of these two-body binary steps in the far wake must be assessed in the interpretation of the long extents of binary scaling found for the sphere wakes. (15) After extensive calculations, Sutton and Camac (18) suggest a correspondence between O-atom levels and electron levels.

The role of NO_2 in atmospheric deionization processes has been considered by Whitten and Poppoff. (7) They favor the processes

$$e^- + NO_2 \rightarrow O^- + NO \tag{12}$$

and

$$O^- + NO_2 \rightarrow O + NO_2^-$$

or (13)

$$O_2^- + NO_2 \rightarrow O_2 + NO_2^-$$

because other possibilities would require unrealistically high rates. Reactions (13) probably constitute chain breaking steps in electron removal. Because of its large electron affinity NO_2^- is relatively invulnerable to attack by any species which may compete for the attached electron. Final cleanup of ions must proceed by mutual neutralization or recombination steps like

$$A^+ + B^- (+M) \rightarrow A + B (+M) \tag{14}$$

which, either require a third body or excited states of A and B. Most of these processes have been reviewed by Branscomb (6) for atmospheric deionization following polar cap absorption events. Experimental advances in wake temperature measurements and ion identification analyses are essential for a detailed understanding of these additional complications at moderate to low temperatures.

4.0 WAKE KINETICS PROBLEM AREAS

Considerable emphasis has been laid on the studies of air chemistry and ionization described above, and, we find that much remains to be done in those fields. Yet, there are some aspects of wake kinetics which are still farther from a satisfactory state of understanding. Three of them are: (1) the role of energy transfer processes, (2) the kinetics of ablative species in air and, (3) the influence of turbulent fluctuations on kinetic rates. Some workers believe that (1) and (3) simply are not problems, but all will agree that item (2) is.

4.1 Energy Transfer Processes

The partitioning of internal energy among the various species and their various quantum states influences the net species production rates. It remains to be seen, however, how significant these effects could be in hypersonic wake flows. In expanding nozzle flows, vibrational deactivation has been observed to occur at anomalously high rates (57). Free electrons have been considered as a possible energy carrier, but their low population rules them out despite their close coupling to vibrational excitation (58). Hurle and Russo then studied electron temperature freezing in the nozzle (59) and observed very large non-equilibrium lags. Although energy transfer from the electron gas via space charge fields (60) precludes the mechanism proposed in Ref. 59, the fact remains that electron removal processes will be sensitive to the freezing phenomenon leading to hot residual electrons.

Another consequence of vibrational nonequilibrium in expanding flows could be reduction of atom recombination rates. Bray and Pratt (61) have hypothesized that an overcrowding of upper vibrational quantum states result in a "bottleneck" for recombining flows. Efficient vibration-vibration exchange, (62, 63) however, could act to relieve the congestion by depopulation of upper states. Experimental techniques such as that employed recently by Appleton (64) could resolve the vibrational energy distribution sufficiently well to probe further the details of such processes.

The significance of the internal energy distributions to wakes may lie in ion kinetics as well as neutral chemistry. Atom recombination delays could support high electron levels through fast associative detachment unless some mechanism exists for efficient vibrational depopulation. Electron temperature lags coupled with negative ion screening effects (65) would maintain high levels of electron Lewis numbers in the far wake as well as delay the attachment rate. Space charge coupling or inelastic collision processes might effectively

eliminate these departures from present notions of deionization. It is clear that further study is necessary to resolve some of these questions. For argon wakes Hoffert and Lien (66) have begun two-fluid considerations of electron temperature lags. The objective is to limit the study initially to a system which is kinetically simple relative to air. Extension of the findings to air must be regarded with caution for several reasons: Fewer possibilities exist for inelastic collisions, the Ramsauer effect reduces elastic collision probabilities markedly, and impurities present a larger threat to experimental interpretation in argon compared with air because argon has a high ionization potential.

4.2 Ablation Effects

Despite the existence of many calculations and measurements, the effects of ablation is only considered briefly here. Our incomplete understanding of even pure air somewhat compromises our confidence in detailed analyses of ablation products plus air.

Hydrocarbon substances present a technically important class of ablation problem. Heavily charring ablators provide a carbonaceous skeleton structure which can provide an environment for the virgin products to react to H_2 and CO. Other possibilities certainly include CN, OH, C_2 and similar free radicals (67, 68). Oxidation and chemi-ionization represent the significant classes of neutral and charged processes, respectively, which are probable in the near-body flow field. Chemiluminescence of CO with oxygen atoms is seen in flames as is band emission from CH, C_2 and OH. These are likely to occur in wakes. Oxidative attack of CH radicals produces CHO^+ which can charge transfer with H_2O to form H_3O^+ and an electron. The reverse of the chemiionization chains are dissociative recombinations which have rates comparable to their counterparts in pure air (69). A four

center ionization can evolve from N_2 colliding with CO to form $NO^+ + CN^-$ (70). Although threshold for this reaction with ground state nitrogen and CO is 11.9 eV, the abundance of excited states in the flow field may lower this substantially. Electron removal processes at moderate temperatures may be aided by formation of C_2^- or CN^-, which have relatively large binding energies for the extra electron. In addition, the oxygen atoms could be removed in the chain suggested by Sutton and Camac (18):

$$H + O_2 (+M) \rightarrow HO_2 (+M) \qquad (15)$$

$$O + HO_2 \rightarrow O_2 + OH \qquad (16)$$

$$O + OH \rightarrow O_2 + H \qquad (17)$$

By the mechanisms given in the previous section, the O-atom removal would be accompanied by electron removal leading to another binary deionization path.

A few years ago, the CHNO-system was computed for wake flows by Langan, Cresswell and Browne (71) using some of the kinetic schemes suggested by Kaskan and Browne (10). Significant ionization enhancements were noted, but the results must be considered as preliminary ones in light of more recent findings both in the areas of fluid dynamics and kinetics.

The fluorocarbon system is also significant because polytetrafluoroethylene is a candidate ablation material. Pyrolysis of the plastic occurs cleanly to yield primarily monomer, C_2F_4. The breakdown of the monomer in gas phase and its subsequent oxidation have been studied by Modica and La Graff (72). Adding to these results, they have suggested an extensive list of reaction steps including dissociation of C_2F_4 and CF_2, oxygen-atom attack of C_2F_4, CF_2 and CF_3 and some exchange reactions. These reactions and their rates are included in the compilation by Heicklen referred to earlier. The electronegative character of

fluorine in the various possible species is believed to be significant in the electron removal process (73).

Metallic impurities both alkali and otherwise are also effective in modifying electron concentrations in wake flows. In general, the most prominent class is the alkali metals and, in particular, sodium is the most common element to be found as a trace contaminant. The role of sodium is considered extensively in a report by M. H. Bortner (74). He concludes that impact ionization is probably overshadowed by other mechanisms despite the low ionization potential (5.14 eV). O-atom collisions will produce O^- and Na^+ with a net endothermicity of 3.68 eV which is still somewhat higher than that of the $N + O \rightarrow NO^+ + e^-$ reaction. Charge transfer of any positive air ion with neutral sodium is likely to sustain electron levels in wakes because the ionization potential is low for sodium. This is borne out by Cesium seeded air calculations for nozzle flows by Boyer (75) which show that the charge transfer quickly breaks the dissociative recombination chain by draining off molecular ions. Dissociative recombination with diatomic alkali metal ions, which was suggested earlier (76), was found to be unimportant because such ions are unstable at high temperature. At some point, cooling will lead to attachment to oxygen and mutual neutralization will clean up the sodium ions.

Wake calculations by Webb and Hromas (42) indicate that the phenomena described above are operative with sodium. Measurements of seeded wakes also confirm this behavior with the interesting additional finding that electron wake lengths are almost unaffected despite the higher levels. Attachment to oxygen bearing species evidently controls the length (in the absence of fluorine). Other calculations (71) already referred to have dealt with the enhancement due to sodium with hydrogenic impurities.

4.3 Interactions Between Turbulence and Chemistry

Considering the combined effects of species production and fluctuating flow, we find it convenient to isolate the influence of each process on the other. First, we shall examine the effect that chemical energy release might have on the turbulent motion of the gas. It can be shown (77) that the coupling is confined to the "divergence field" component of turbulence rather than the "curl field"; that is, it only arises by virtue of dilatational motion of the gas and not by solenoidal motion. Hence, it is highly Mach number sensitive. Statistical treatment based on analyses of the inertial range of large eddies (78) shows that the energy feeds into the central spectral band where most of the energy is concentrated. (79) Although boundary layer measurements indicate that the spectral selectivity is correctly predicted (80), it is likely that the turbulence Mach number and heat release are low enough in a wake to suppress the effect of chemistry on turbulence (81). Thus, what we might term "active coupling" (29) is not very effective in the fluctuating component of hypersonic wake flows of interest, even in the upper limit of coupling efficiency.

The significance of the reverse effect (the influence of concentration fluctuations on mean reaction rates) is unresolved, however. It was shown by Corrsin (82) several years ago that the reactant conversion rates depend explicitly upon concentration fluctuations for all but first order reactions. In a recent paper (83). Lykoudis suggests that quasi-steady state chemistry should be modified by fluctuations only where strong temperature dependence appears in the rates; i.e., only in the very near wake where endothermic reactions may still be important. On the other hand, reactants in the far wake are principally cold molecular oxygen mixed in from the outside with hot core gas which contains the electrons. One might expect the larger scale (convective) concentration eddies to be anticorrelated between these

two reactants. The anti-correlation is by-passed if the reactants are "fully mixed" as soon as outside gas is engulfed by the turbulent edge; i.e., only the minor effects of edge intermittency will enter the mean rate calculation. The physics of the instantaneous-mixing case would require zero time for the inertial cascade process connecting Fourier regions of main eddy-size with those of Kolmogoroff size. Thus, the turbulent edge would be required to act on the spectral density function somewhat the way a shock wave does on a molecular distribution function, but even more so. It is likely that mixedness influences chemistry in the near wake where nonuniformity in edge conditions prevails. For the far wake, the edge conditions are relatively uniform over a mixing-length and fluctuation coupling with chemistry probably becomes negligible (especially at low turbulence Reynolds numbers).

Several approaches have been devised to describe the concentration fluctuations arising from turbulent wake entrainment. Among them are the models of Proudian and Feldman (48), Lin (47), and Gibson (49), In Reference 48 the wake is assumed to be composed of mixed and unmixed regions of gas. The delineation between the two is prescribed by a mixing lag time referred to a Lagrangian frame of reference. Lin's "bi-modal approximation" (47) allows continuous dissipation of an inhomegeneity arising from the swallowing of a portion of cold gas by the wake edge. Both of these approaches depend upon some prescription of a statistically determined quantity. Presumably such a quantity would be found from analyzing the cospectrum of cold and hot gas or from experimental measurement. Gibson (49) supplies the statistical information in the form of prescribed stochastic functions describing the velocity and enthalpy fields in the wake. Proceeding from these, he obtains the particle histories governed by exact solutions of the continuity and species rate equations. Mean and fluctuating concentration fields emerge from the analysis as well as correlation functions. None of these theories is based on instantaneous mixing. It remains for experiments on turbulent

concentration fields to demonstrate the validity of one or the other approaches. The interaction between reaction kinetics and the evolution of far wake observables will depend intimately upon the mechanism governing mixing.

5. CONCLUDING REMARKS

While the chemical kinetics of wakes in uncontaminated air hold out unanswered questions, the problems have become circumscribed more distinctly in the past few years. Because of their lengths and levels of observability, the blunt body wakes have provided much of the detailed data on which new theoretical models are based. There is often a temptation to put the blunt body wake in the class of solved problems. The details of ion kinetics and swallowing mechanisms, however, continue to pose challenging problems. The near wake observables are largely described by considering the excited gas in the hot entropy wake. Beyond a few hundred diameters turbulence breaks through the outer edge of this wake for Reynolds numbers much in excess of 5×10^4 and the rate of mixing becomes crucial in determining the kinetics. Back in the range of thousands of diameters, the gas is cooled enough to promote a host of kinetic processes involving triatomic formation, associative detachment, negative ion charge transfer and others. Free flight range measurements of oxygen atom levels, electron densities,and temperatures show great promise in unravelling some of the mysteries.

The kinetics situation with slender bodies still suffers from its chronic deficiencies in the near body flow field, but signs of improvement are imminent. Intensive work in fluid dynamics as described in the previous paper by Prof. Lees is leading to firmer predictions of the gasdynamic profile quantities. The laminar wake kinetics are within the scope of analytical description beyond a few body diameters downstream from

the body. Transition is such a gradual process that the mixing model becomes a problem in predicting kinetically dominated observables. After degradation to turbulence, the wake reaction mechanism may be nearly as complex as that in the sphere far wake. Because all measurement levels are very low in this region we are only at the threshold of obtaining experimental information with highly refined sensitivities.

The outstanding problems of excited state effects, ablation product kinetics, and turbulence effects on kinetics are in the early stages of investigation. Even in pure air, residual vibrational or electronic excitation in the wake could seriously alter reaction rates. Progress has been made in reducing the number of possible reaction steps in wake kinetic models for ablation products in air, and identification of species levels in flight experiments appears to be the next important step. Finally, turbulence problems continue to appear in ever more complicated forms when kinetics enter in. It is probable that semi-empirical approaches are the most hopeful routes to their solutions.

REFERENCES*

1. Bortner, M. H., "Chemical Kinetics in a Reentry Flow Field", General Electric Report R63SD63 (August 1963)
2. Bortner, M. H., "The Chemical Kinetics of Atmospheric Deionization", General Electric Report R63SD34 (September 1963)
3. Nawrocki, P. G., "Reaction Rates", Geophysics Corporation of America Technical Report 61-2-A (January 1961)
4. Wray, K., "Chemical Kinetics of High Temperature Air", Hypersonic Flow Research, Academic Press (1962), p. 181
5. Anon, "Reaction Rates", DASA Special Bibliography No. 5, DASA 1832 (August 1966)
6. Branscomb, L. M., Annales de Geophysique, 20, (January thru March 1964), p. 88
7. Whitten, R. C., and Poppoff, I. G., Physics of the Lower Ionosphere, Englewood Cliffs, New Jersey, Prentice Hall, (1965)
8. Danilov, A. D., and Ivanov-Kholodynyi, G. S., Soviet Physics Uspekhi, 8, (July-August 1965), p. 92
9. Dunn, M. G., "Reaction Rate Constants for Ionized Air", Cornell Aeronautical Laboratory Report No. AI-2187-A-1 (April 1966)
10. Kaskan, W. E., and Browne, W. G., "Kinetics of the $H_2/CO/O_2$ System", General Electric Report R64SD37 (July 1964)
11. Clifton, D. G., "Equilibrium Compositions of Ionized Air Including the Negative Ions NO_2^-, NO^-, O_2^-, C_2^-, and CN^- Over A Range of Temperatures and Pressures", GM Defense Research Laboratories TR66-01N (August 1966)
12. Steinberg, M., Private Communication (November 1966)
13. Wilson, L., "The Far Wake Behavior of Hypersonic Spheres", GM Defense Research Laboratories TR66-19 (June 1966). To be published in AIAA J.

* In an effort to credit recent work, unpublished company reports are cited extensively.

14. Reis, V. H., "Chemiluminescent Radiation from the Far Wake of Hypersonic Spheres", GM Defense Research Laboratories, TR66-01J (June 1966)

15. Hayami, R. A., and Primich, R. I., "Wake Electron Density Measurements Behind Hypersonic Spheres and Cones", AGARD Specialists' Meeting on "Fluid Physics of Hypersonic Wakes" (10-12 May 1967)

16. Lin, S. C., and Hayes, J. E., AIAA J., 2, (July 1964), p. 1214

17. Fontijn, A., Meyers, C. B., and Schiff, H. I., J. Chem. Phys. 40, (1964), p. 64-70

18. Sutton, E., and Camac, M., IDA Reentry Kinetics Meeting, Washington (5 January 1966)

19. Zeiberg, S. L., and Fields, A. K., "Boundary Layer and Wake Calculations for Slender Cones with Slight Nose Blunting", General Applied Science Laboratories Report No. 556 (September 1965)

20. Webb, W. H., RAND Wake Conference, Santa Monica (6 October 1966)

21. King, H. H., "Laminar Mixing with Arbitrary Initial Species Profile Shapes", GM Defense Research Laboratories TR66-01D (April 1966)

22. King, H. H., "Initial Profiles for Wake Calculations", GM Defense Research Laboratories, TR66-51 (October 1966)

23. Rockman, C. M., "Line Reversal Measurements of Hypersonic Wake Temperatures", GM Defense Research Laboratories, TR66-01B (March 1966)

24. Freedman, E., and Daiber, J. W., J. Chem. Phys., 34, (1961), p. 1271

25. Wray, K. L., and Teare, J. D., "A Shock Tube Study of the Kinetics of Nitric Oxide at High Temperatures", Avco-Everett Research Laboratory RR95 (June 1961)

26. Hayami, R. A., and Primich, R. I., "Ionization in Hypersonic Wakes", GM Defense Research Laboratories TR62-209D (December 1962)

27. Primich, R. I., and Hayami, R. A., "Millimeter Wavelength Focused Probes and Focused, Resonant Probes for Use in Studying Ionized Wakes Behind Hypersonic-Velocity Projectiles", GM Defense Research Laboratories TR63-217C (July 1963)

28. Kornegay, W. M., "Decay of Electron Density in the Wakes of Hypervelocity Spheres", Lincoln Laboratory Technical Report 370 (23 December 1964)

29. Eschenroeder, A. Q., "Reaction Kinetics in Hypersonic Flow", Advances in Chemical Physics, New York, John Wiley and Son, (in press)

30. Eschenroeder, A. Q., Daiber, J. W., Golian, T. C., and Hertzberg, A., "Shock Tunnel Studies of High Enthalpy-Ionized Airflows", The High Temperature Effects of Hypersonic Flow, Oxford, Pergamon Press (1964) Ch. 11

31. Lin, S. C., "Ionized Wakes of Hypersonic Objects", Avco-Everett Research Laboratory, RR151 (June 1959)

32. Greenhow, J. S., and Hall, J. E., Journal of Atmospheric and Terrestial Physics, 21, (1961) p. 261

33. Lees, L, Hypersonic Wakes and Trails, AIAA J. 2, (March 1964)p. 417

34. Hall, J. G., Eschenroeder, A. Q., and Marrone, P., V. Aerospace Sciences 29, (September 1962), 1. 1038

35. Chen, T., and Eschenroeder, A. Q., "A Fortran Computer Code for Inviscid Nonequilibrium Streamtube Flow", GM Defense Research Laboratories, TR65-01P (December 1965)

36. Hayami, R. A., and Primich, R. I., "Integrated Electron Density in the Near Wakes of Hypersonic Velocity Spheres", GM Defense Research Laboratories, TR65-01F (May 1965)

37. Eschenroeder, A. Q., and Chen, T., AIAA J., 4 (1966), p. 2149

38. Wen, K. S., and Chen , T., "Axisymmetric Viscous Wake Analysis for a Hypersonic Reentry Body", GM Defense Research Laboratories TR66-12A (April 1966)

39. Chen, T., and Wen, K. S., "Fortran Computer Code for Axisymmetric Viscous Wake Analysis for a Hypersonic Reentry Body", GM Defense Research Laboratories TR66-66 (November 1966)

40. Wen, K. S., and Chen, T., "Preliminary Theoretical Results of Laminar Wake Ionization Behind Hypersonic Spheres and Cones", GM Defense Research Laboratories, TR66-22 (June 1966)

41. Lees, L., and Hromas, L. A., J. Aerospace Sci., 29, (August 1962), p. 976

42. Webb, W. H., Hromas, L. A., AIAA J., 3, (1965), p. 826

43. Kornegay, W. M., AIAA J., 3, (October 1965), p. 1819

44. Zeiberg, S. L., and Bleich, G. D., AIAA J., 2, (August 1964) p. 1396

45. Zeiberg, S. L., and Daskin W., "Comparison of Theoretical Predictions of Wake Electron Density with Ballistic Range Measurements", General Applied Science Laboratories Technical Report No. 477 (November 1964)

46. Fehsenfeld, F. C., Ferguson, F. E., and Schmeltekopf, A. L., J. Chem. Phys., 45, (September 1966), p. 1844

47. Lin, S. C., AIAA J., 4, (February 1966), p. 202

48. Proudian, A. P., and Feldman, S., AIAA J., 3, (April 1965) p. 602

49. Gibson, W. E., AIAA J., 4, (November 1966), p. 2001

50. Fite, W. L., and Brackman, R. T., Proc. 3rd International Conference on Physics of Electronic and Atomic Collisions in London, North-Holland Publ. Co., Amsterdam (1963).

51. Webb, W. H., and Hromas, L. A., "Turbulent Diffusion of a Reacting Gas in the Wake of a Sharp Nosed Body at Hypersonic Speeds", Space Technology Laboratories Report 6130-3262-RU-000 (April 1963)

52. Lien, H., Erdos, J. I., and Pallone, A. J.,"Nonequilibrium Wakes with Laminar and Turbulent Transport", AIAA Paper No. 63-447, Conference on Physics of Entry Into Planetary Atmospheres (August 1963)

53. Wen, K. S., and Chen, T., Hayami, R. A., and Primich, R. I., "An Eddy Diffusion Model for Predicting Rapid Wake Ionization Decay Behind Hypersonic Cones", AIAA Paper 67-21, Fifth Aerospace Sciences Meeting (January 1967)

54. Todisco, A., and Pallone, A. J., AIAA J. 3, (November 1965) p. 2075

55. Gold, H., RAND Wake Conference, Santa Monica (6 October 1966)

56. Lien, H., Private Communication (November 1966)

57. Hurle, I. R., Russo, A. L., and Hall, J. G., J. Chem. Phys., 40, (15 April 1964) p. 2076

58. Hurle, I. R., J. Chem. Phys. 41, (1 December 1964) p. 3592

59. Hurle, I. R., and Russo, A. L., J. Chem. Phys. 43, (15 December 1965) p. 4434

60. Appleton, J. P., and Bray, K. N. C., J. Fluid Mech. 20, (April 1964) p. 659

61. Bray, K. N. C., and Pratt, N. H., "Effect of Certain Energy Transfer Processes on Population Distribution in Expanding Gas Flows", AGARD Colloquium, "Recent Advances in Aerothermochemistry", Oslo, Norway (May 1966)

62. Taylor, R. L., Camac, M., and Feinberg, R. M., "Measurements of Vibration-Vibration Coupling in Gas Mixture", Avco-Everett Research Laboratory RR250 (May 1966)

63. Treanor, C. E., "Molecular Vibrational Energy Distributions During Exchange Dominated Relaxation", Cornell Aeronautical Laboratory Report No. AF-2184-A-1 (October 1966)

64. Appleton, J. P. and Steinberg, M., "The Vacuum Ultraviolet Absorption of Shock-Heated Vibrationally Excited Nitrogen", GM Defense Research Laboratories, TR66-01N (July 1966) J. Chem. Phys. (in press)

65. Oskam, H. J., Phillips Research Reports 13, (1958) p. 335

66. Hoffert, M. I., and Lien, H., "Correlation of Theoretical and Experimental Results with Nonequilibrium Argon Wakes - Part I: Two-Temperature Stream Tube Analysis and Ionization Behind Normal Shock Waves", General Applied Science Laboratories Technical Report No. 610 (April 1966)

67. Wray, K. L., Rose, P. H., and Kortz, H. E., "Measurements of the Radiation from an Ablation Contaminated Boundary Layer under Simulated Flight Conditions", Avco-Everett Research Laboratories, RR226 (August 1965)

68. Clifton, D. G., "Equilibrium Compositions for Carbon-Air Systems at High Temperatures and Several Pressures", GM Defense Research Laboratories TR65-11E (September 1965)

69. Wilson, L. N., and Evans, E. W., "Electron Ion Recombination in Hydrocarbon-Oxygen Reactions Behind a Shock Wave", J. Chem. Phys. (in press)

70. Utterback, N. G., J. Chem. Phys., 44 (15 March 1966) p. 2540

71. Langan, T., Cresswell, J. D. and Browne, W. G., AIAA J. 3, (December 1965), p. 2211

72. Modica, A. P., and La Graff, J. E., J. Chem. Phys. 43, (1965) p. 3383

73. Clifton, D. G., "A Study of Equilibrium Compositions of Carbon-Fluorine, Carbon-Fluorine-Oxygen, Air Fluorine, and Air-C_2F_4, GM Defense Research Laboratories TR65-11A (March 1965)

74. Bortner, M. H., "The Chemical Kinetics of Sodium in Reentry", General Electric Report R64SD33 (April 1964)

75. Boyer, D. W., "Ionization Nonequilibrium Effects on the Magneto-gasdynamic Interaction in the Stagnation Region of an Axisymmetric Blunt Body", Cornell Aeronautical Laboratory, Report No. ASD-TDR-62-1078 (June 1963)

76. Eschenroeder, A. Q., ARS Journal 32, 2, (February 1962) p. 196

77. Eschenroeder, A. Q., Physics of Fluids 7, (November 1964) p. 1735

78. Eschenroeder, A. Q., Physics of Fluids 8, (April 1965) p. 598

79. Eschenroeder, A. Q., AIAA J. 3, (October 1965) p. 1839

80. Wooldridge, C. E., and Muzzy, R. J., AIAA J., 4, 2009 (November 1966) p. 2009

81. Eschenroeder, A. Q., Pyrodynamics (in press)

82. Corrsin, S., Physics of Fluids, 1, (January - February 1958) p. 42

83. Lykoudis, P. S., AIAA J., 4, (April 1966) p. 577

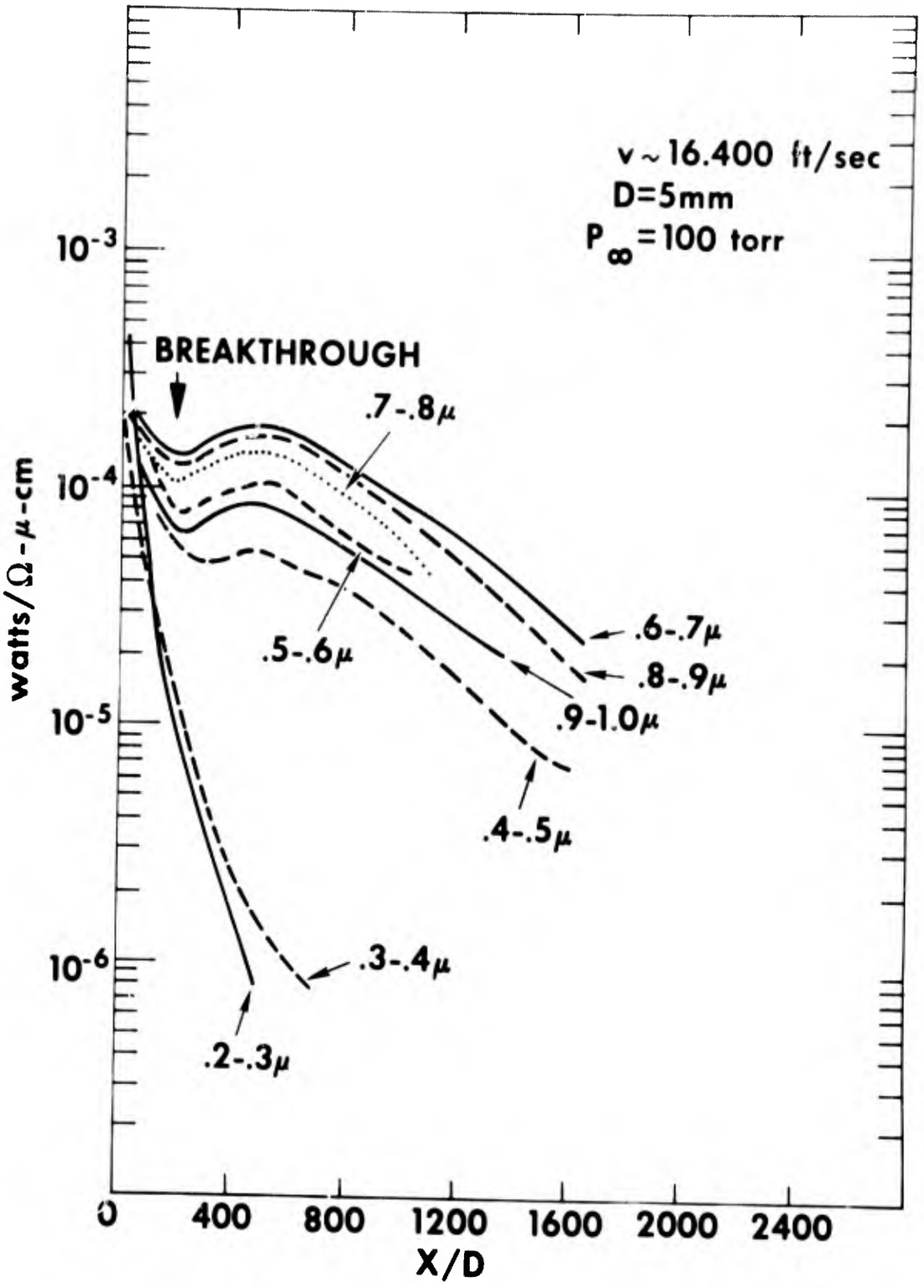

FIG. 1 WAKE RADIATION MEASUREMENTS

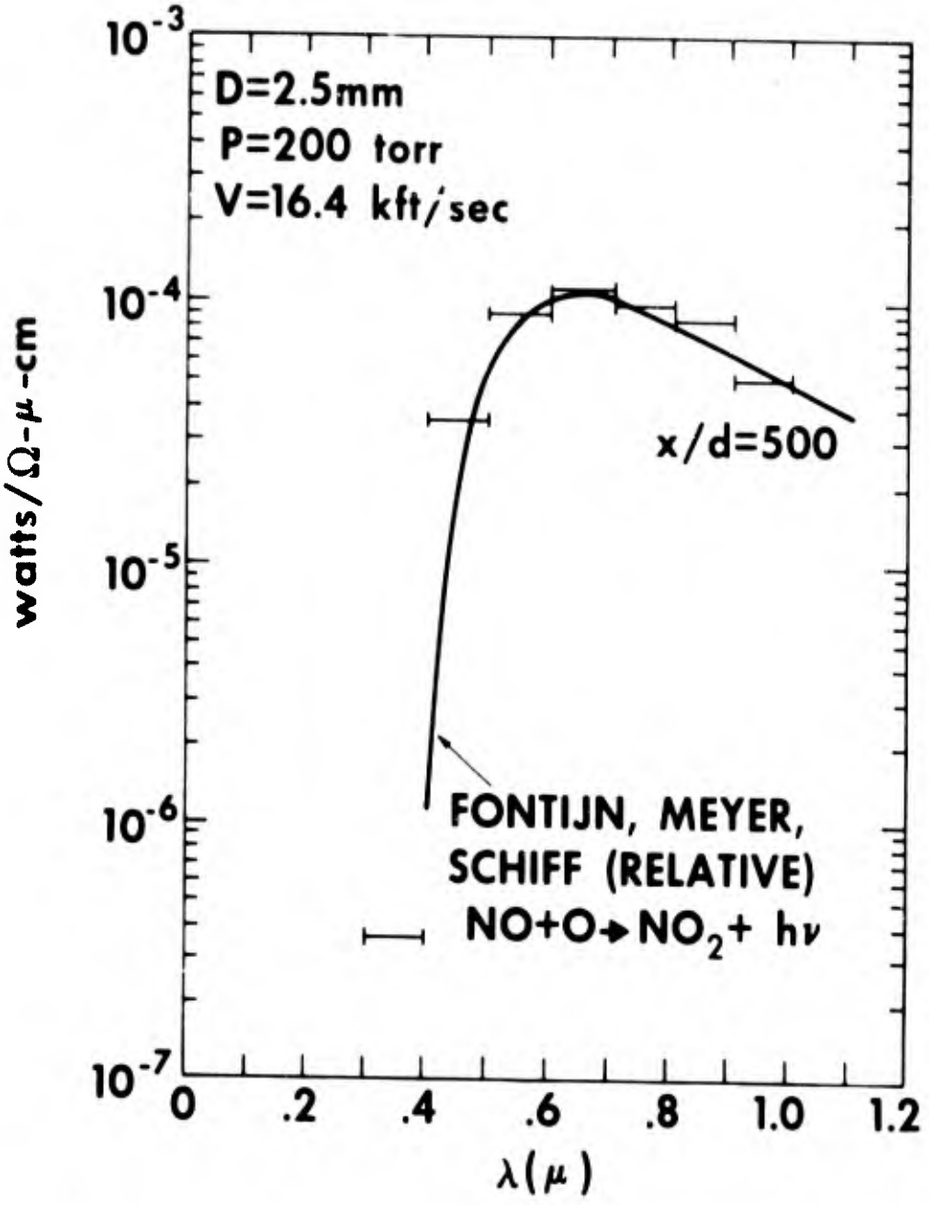

FIG. 2 WAKE RADIATION SPECTRAL DISTRIBUTION

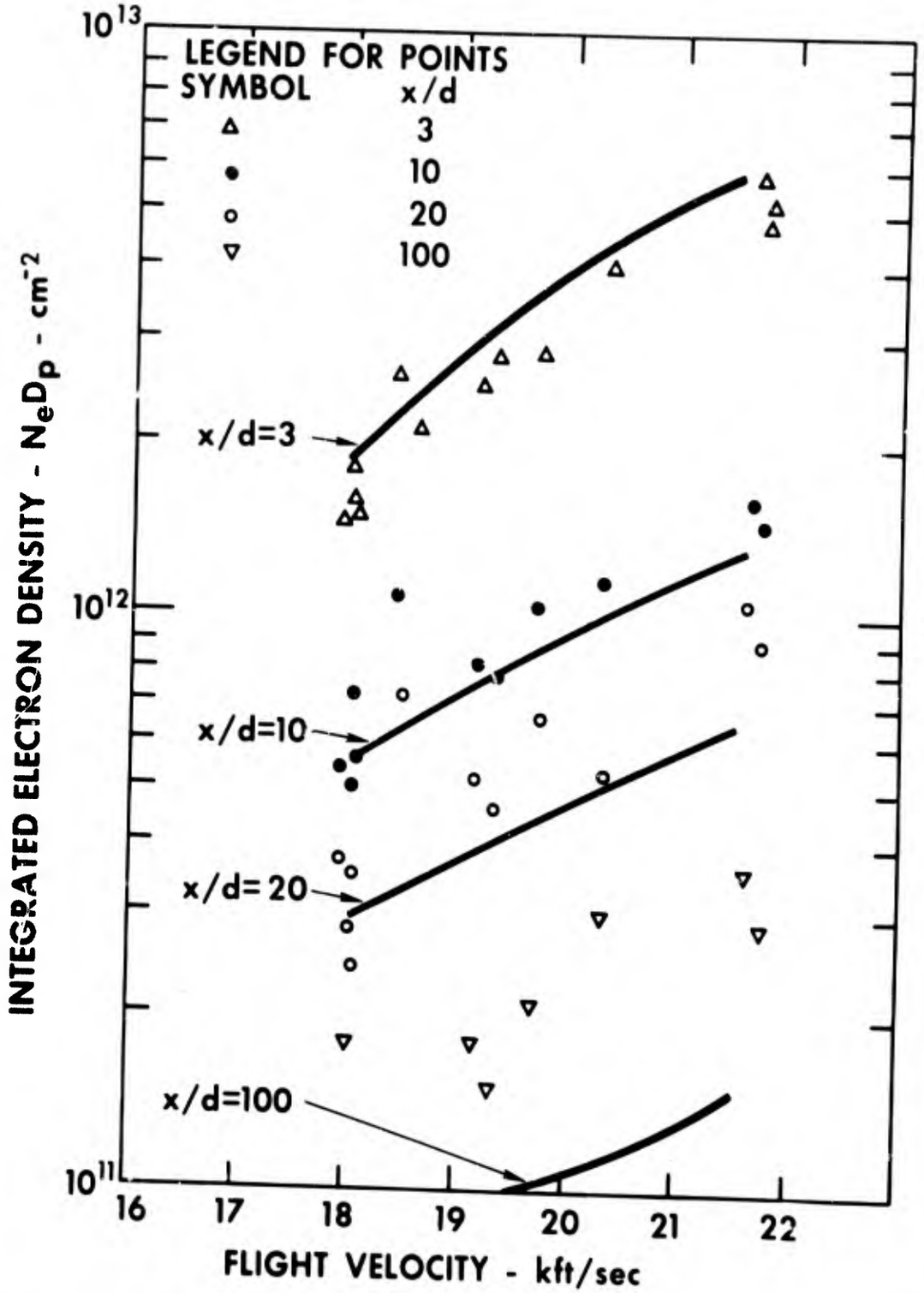

FIG. 3 NEAR WAKE IONIZATION - EFFECT OF VELOCITY AT 10 torr AMBIENT PRESSURE

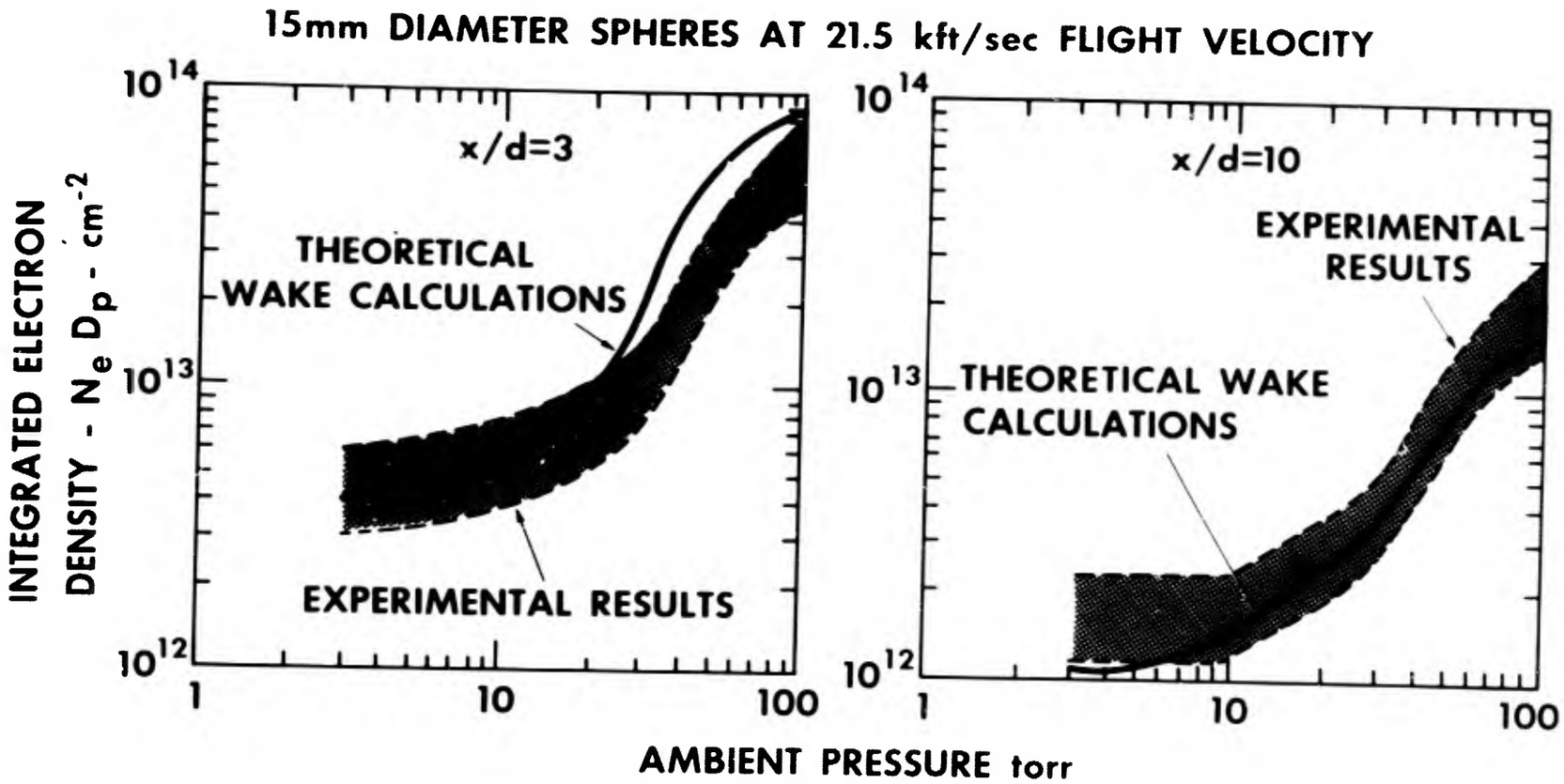

FIG. 4 NEAR WAKE IONIZATION - EFFECT OF PRESSURE AT 21.5 kft/sec VELOCITY

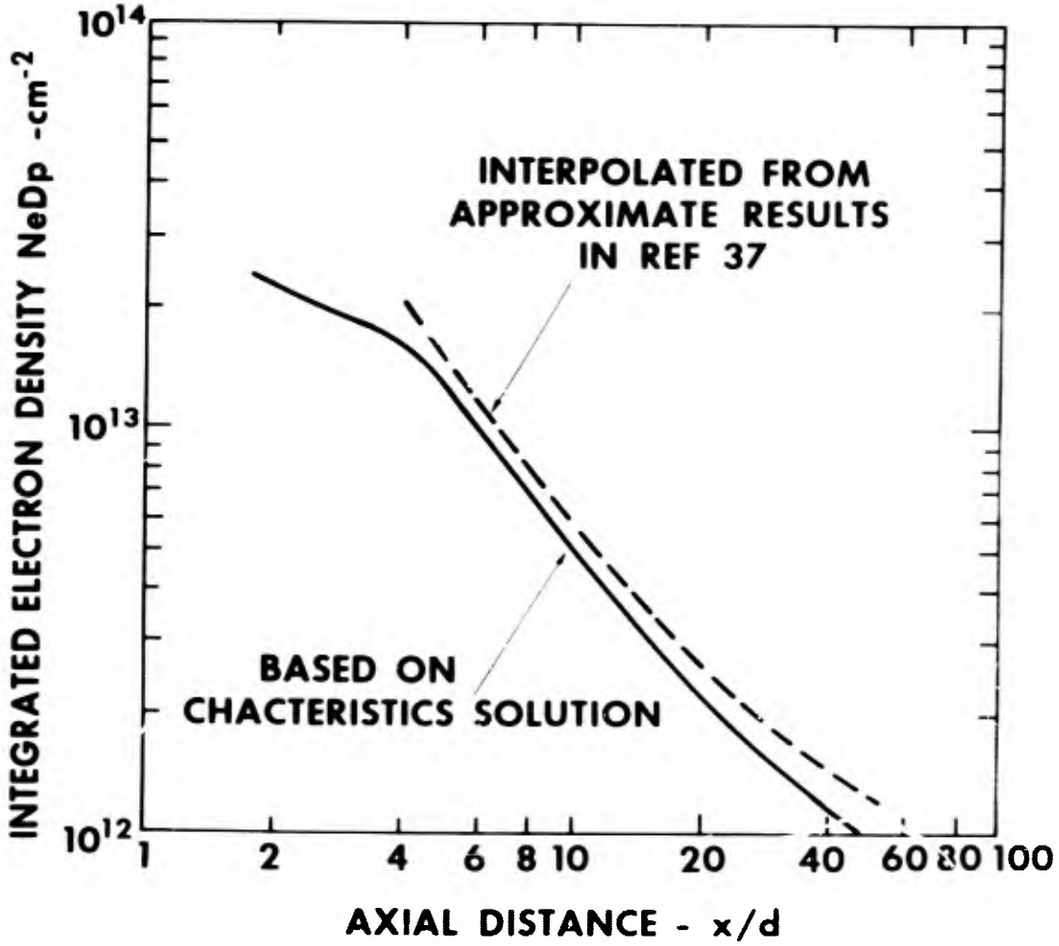

FIG. 5 COMPARISON BETWEEN CHARACTERISTICS AND APPROXIMATE RESULTS FOR NEAR WAKE IONIZATION BEHIND A SPHERE - 5mm diam., 75 torr PRESSURE 20.5 kfps VELOCITY

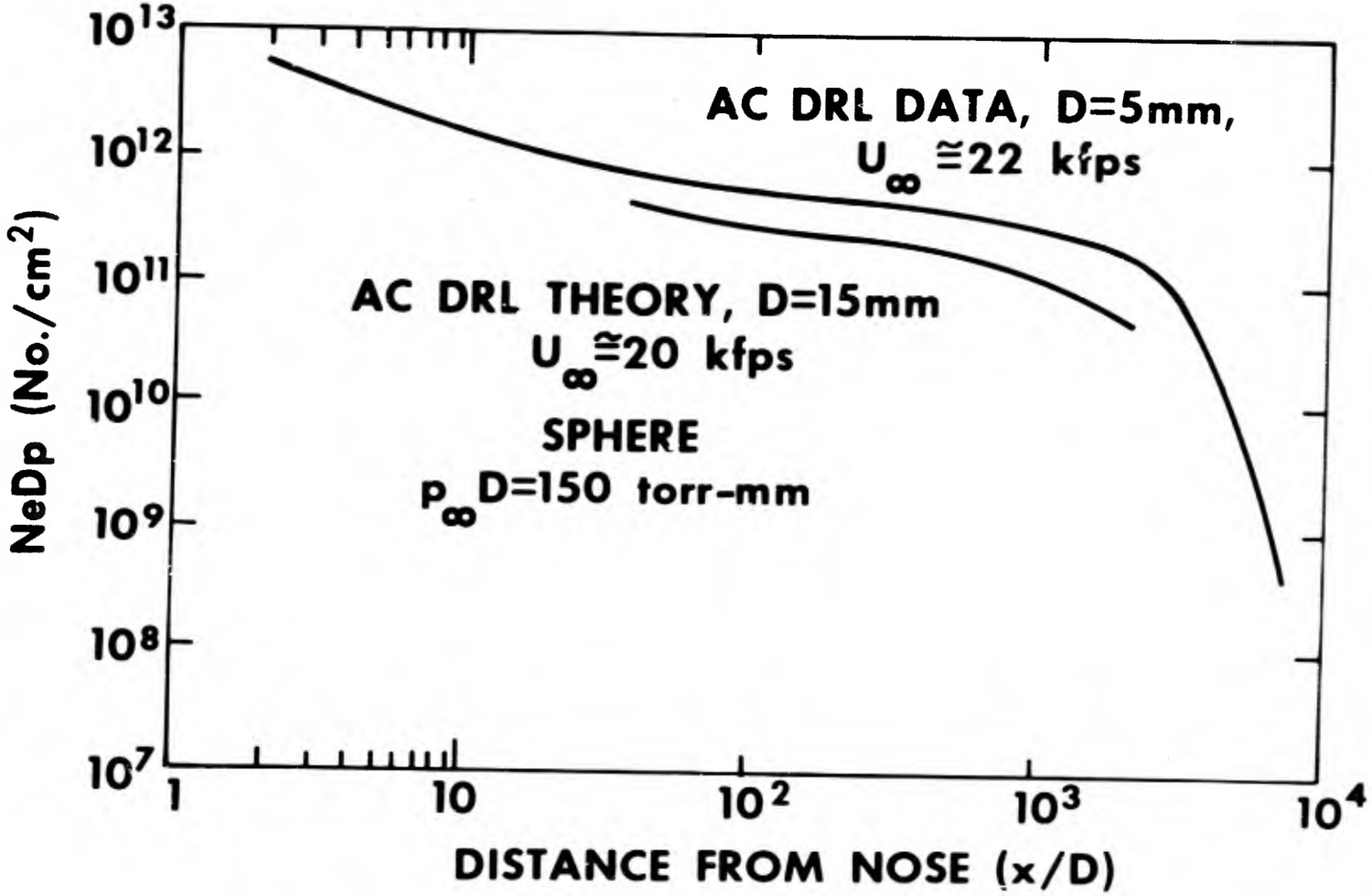

FIG.6 WAKE IONIZATION BEHIND A SPHERE - AXISYMMETRIC CALCULATION FOR SUBCRITICAL REYNOLDS NUMBER

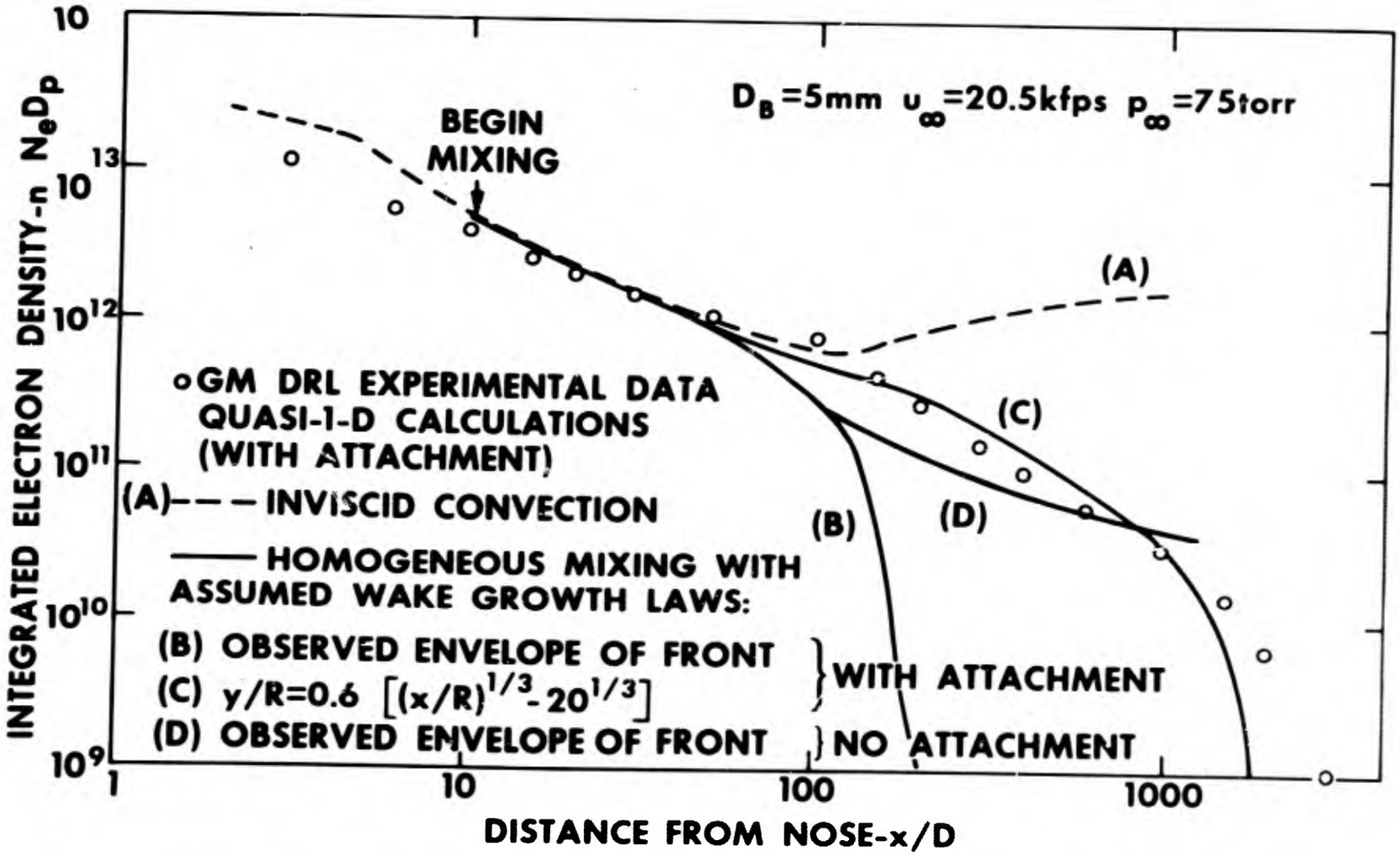

FIG. 7 WAKE IONIZATION BEHIND A SPHERE - QUASI-ONE-DIMENSIONAL CALCULATIONS FOR SUPER-CRITICAL REYNOLDS NUMBER

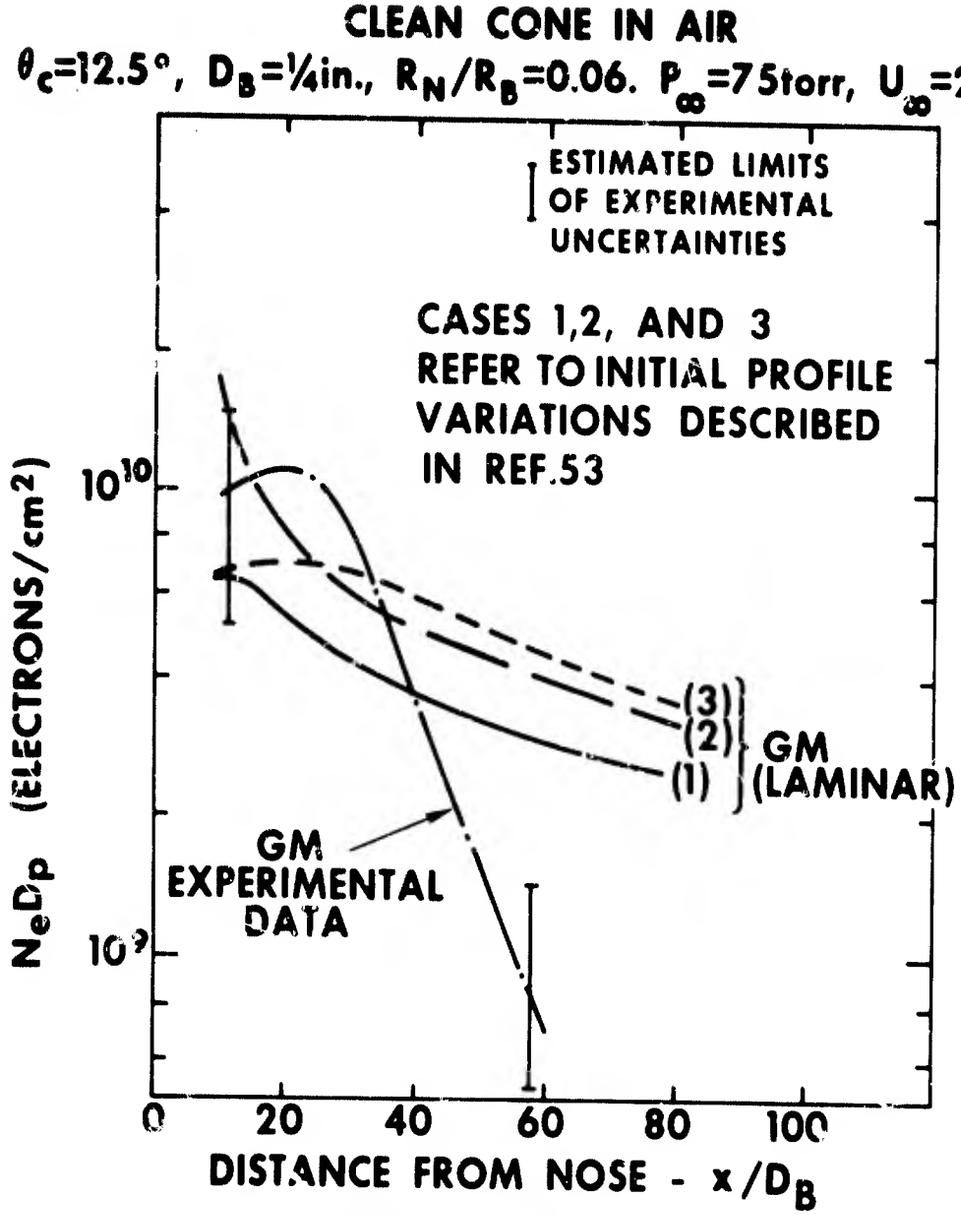

FIG. 8 WAKE IONIZATION BEHIND CONE - INFLUENCE OF INITIAL PROFILES

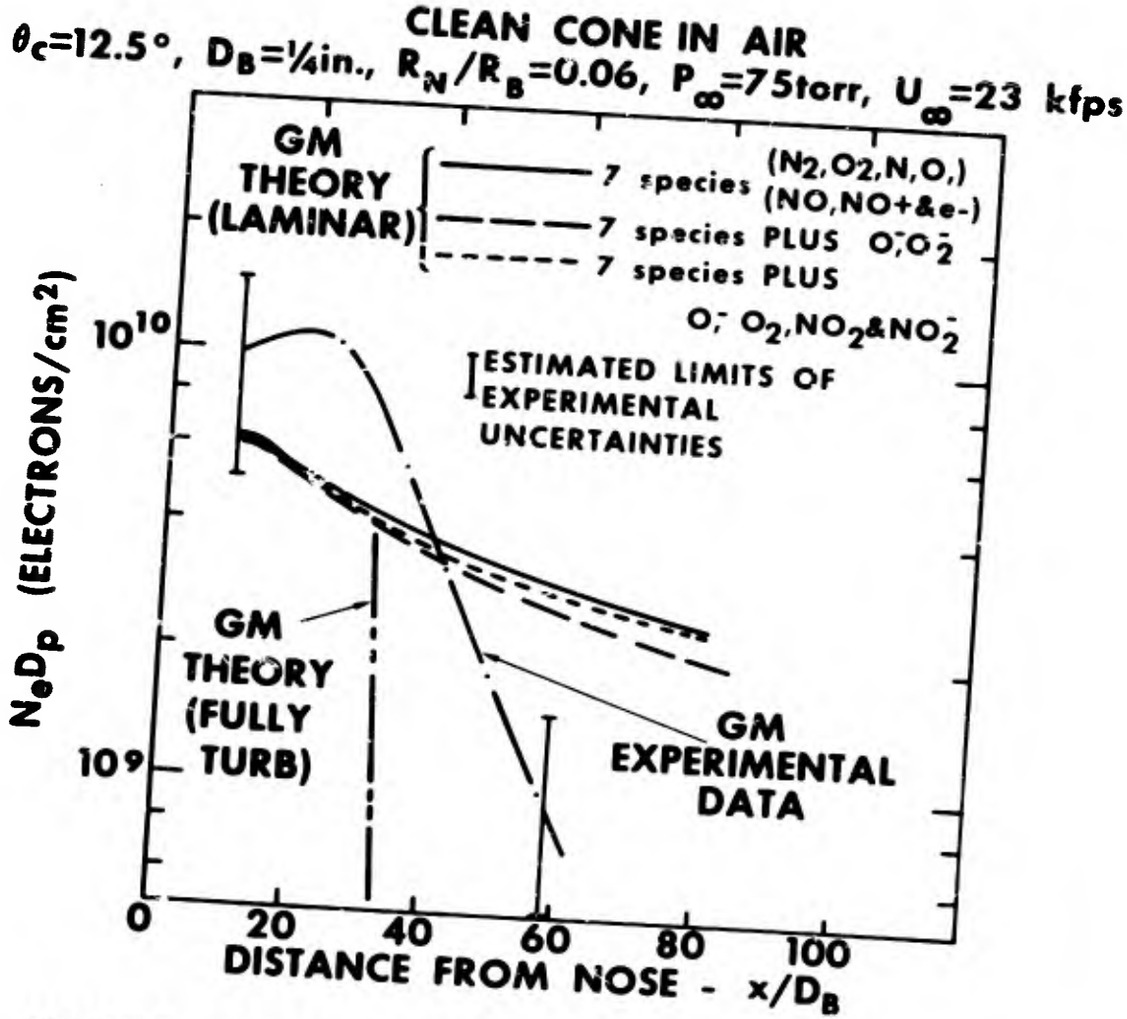

FIG. 9 WAKE IONIZATION BEHIND CONE- CHEMICAL KINETIC AND FULLY TURBULENT EFFECTS

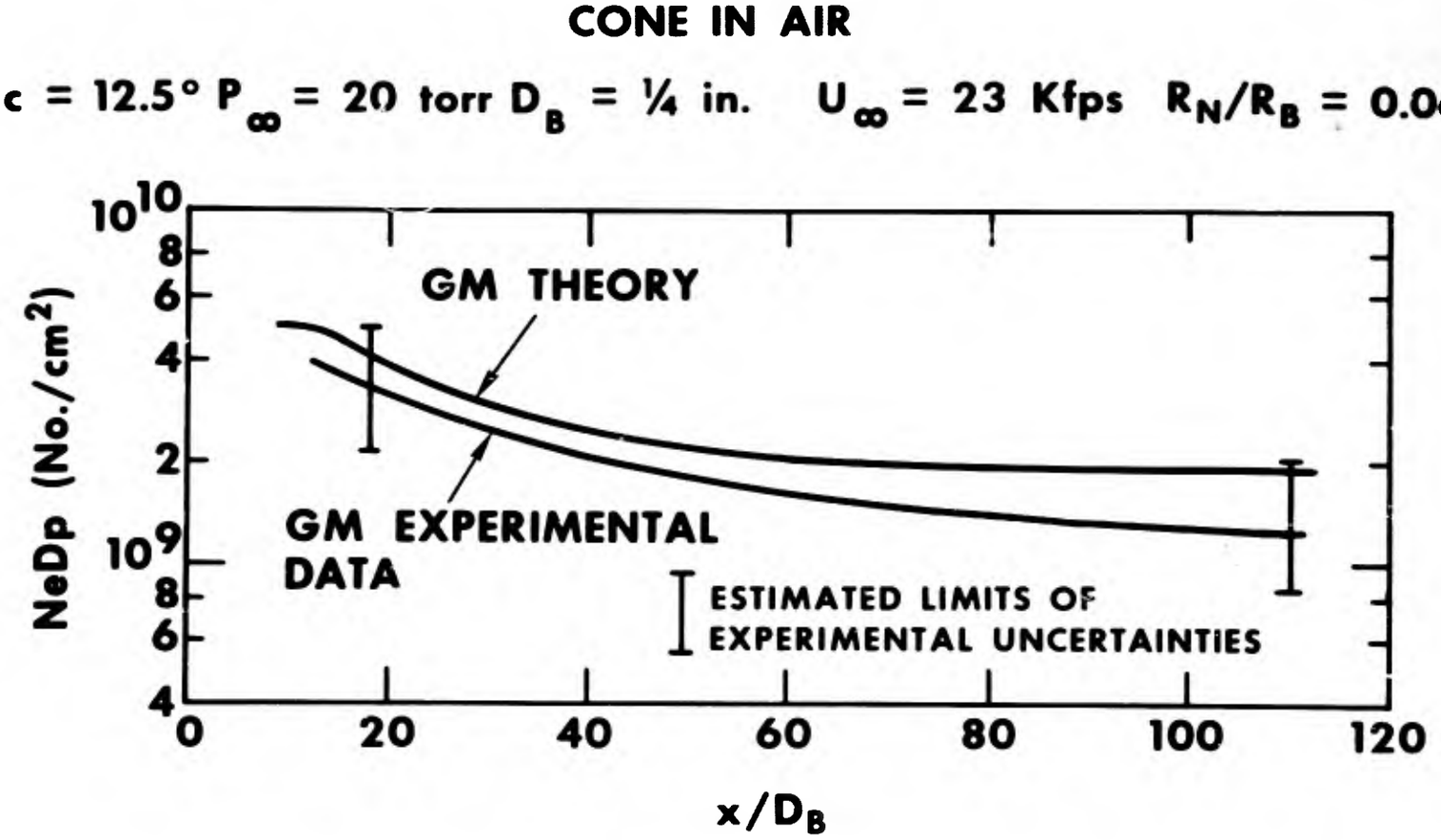

FIG. 10 WAKE IONIZATION BEHIND CONE AT LOW AMBIENT PRESSURE

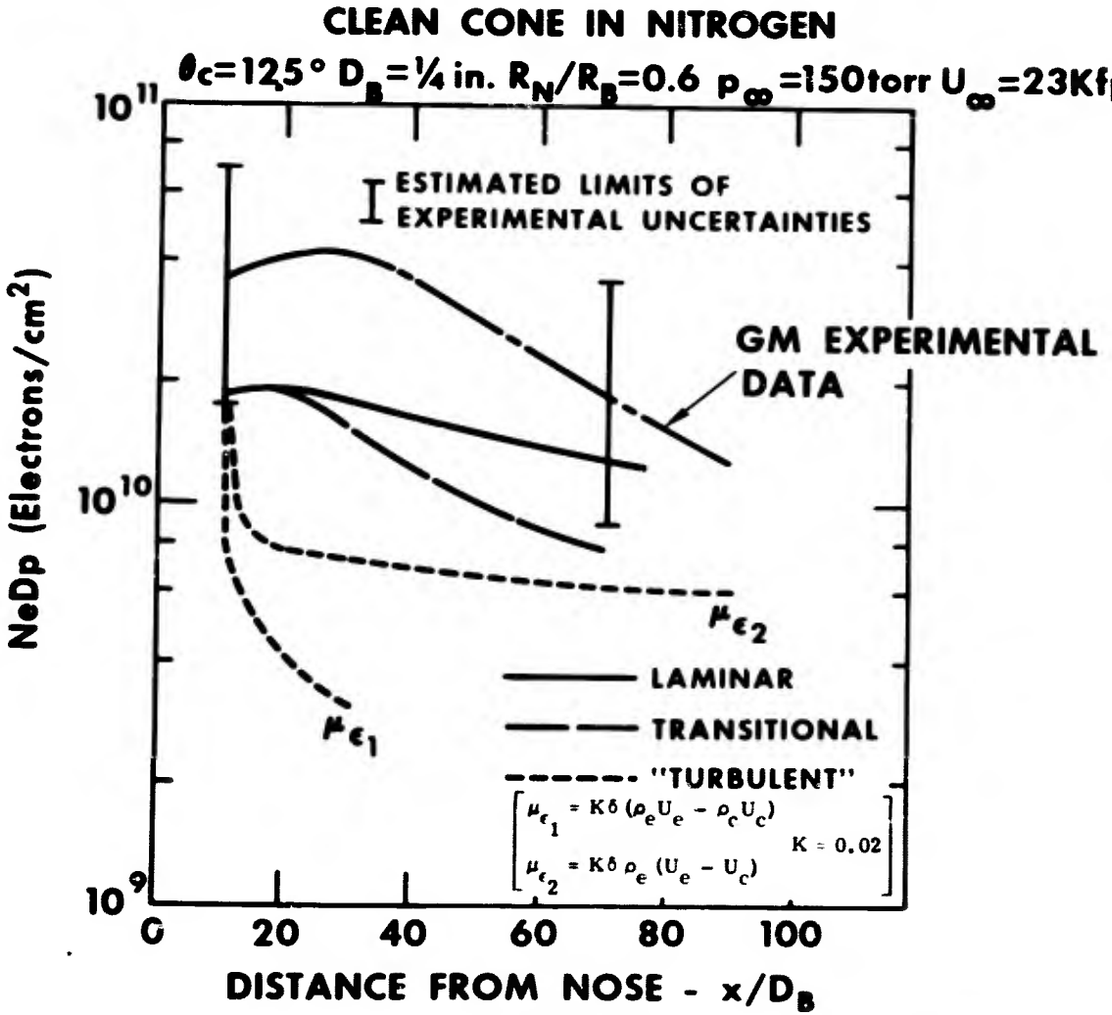

FIG. 11 WAKE IONIZATION BEHIND CONE- DIFFUSION MODEL EFFECTS FOR NITROGEN ATMOSPHERE

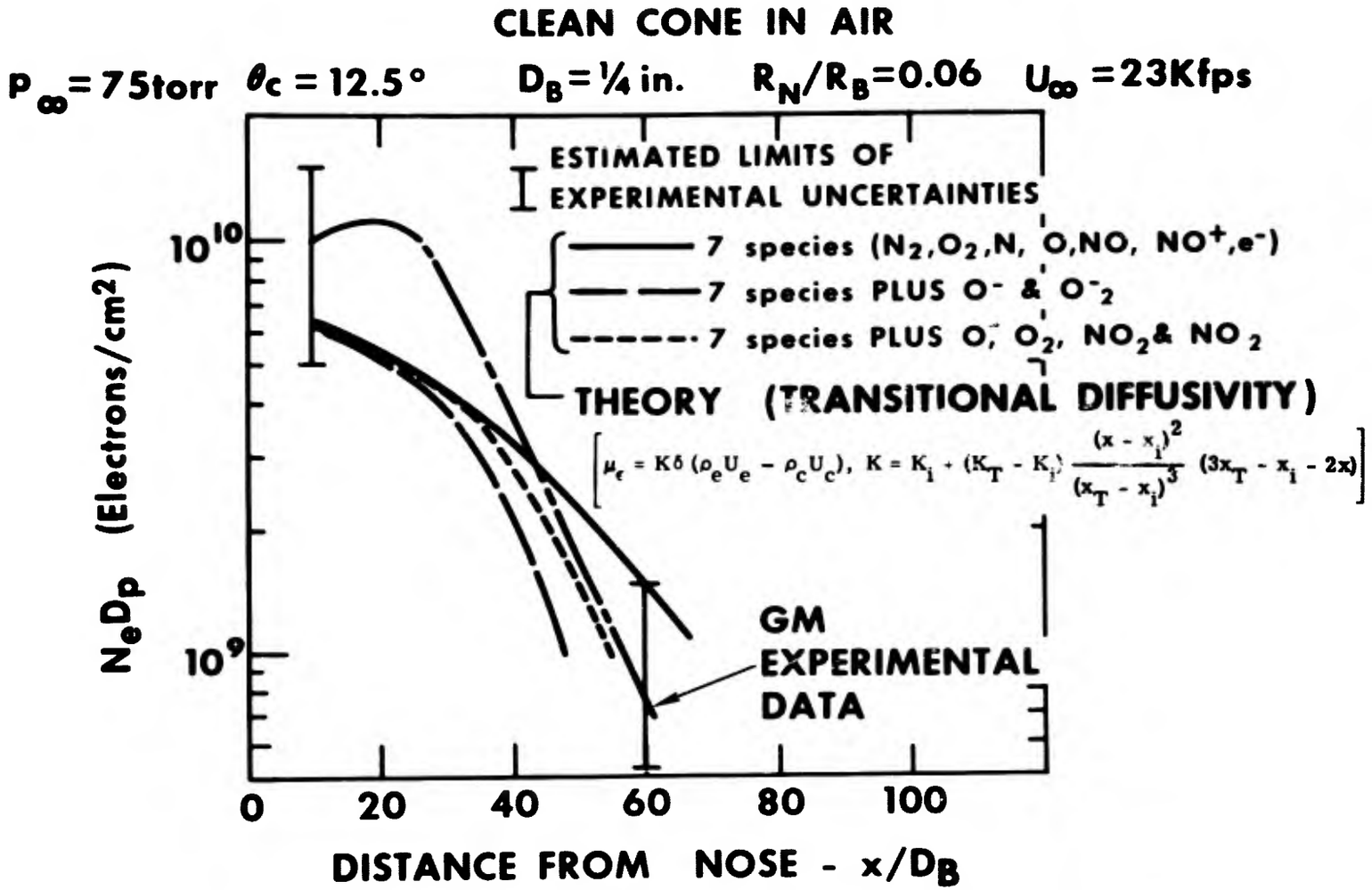

FIG. 12 TRANSITIONAL WAKE IONIZATION BEHIND A CONE WITH VARIOUS KINETIC MODELS

DIAGNOSTIC STUDIES OF LAMINAR HYPERSONIC CONE WAKES[†]

E. M. Murman[*], C. W. Peterson[**] and S. M. Bogdonoff[***]

PRINCETON UNIVERSITY
Gas Dynamics Laboratory
Princeton, New Jersey

† This work has been supported by the Advanced Research Projects Agency (Ballistic Missile Defense Office) and technically administered by the Fluid Dynamics Branch of O.N.R. under Contract Nonr-1858(37).

* NASA Fellow
**Assistant in Research
***Professor of Aeronautical Engineering and Head, Gas Dynamics Laboratory

SUMMARY

This paper reports some new experimental work in the general area of laminar hypersonic wakes behind conical bodies. The experiment is being conducted in a conventional wind tunnel operating at a nominal Mach number of 16 and a free-stream Reynolds number of 120,000/inch. Helium at a stagnation temperature of 525°R. is utilized as a test gas yielding an experiment purely fluid mechanical in nature. A unique feature of the experiment is the use of a magnetic suspension system which is capable of supporting axi-symmetric bodies. This system has been discussed in detail in previous reports and will not be described in this text. Wakes behind conical models of one-inch base diameter, 10° half-angle, and various bluntness ratios from 0 to 17.7% are being studied. All tests have been conducted with the model surface at the adiabatic recovery temperature. These test conditions are such as to yield completely laminar wakes throughout the region of testing (0-15 base diameters).

Several important considerations dictated the design of the experiment. It was desired to survey the wakes of support-free axisymmetric bodies under long duration, steady state conditions. This is a substantial improvement over previous experiments which have been conducted either in short duration facilities or behind two dimensional or mechanically supported three-dimensional bodies. It is important to realize that this experiment utilizes a perfect gas (no ionization, dissociation or radiation) which allows a careful fluid mechanical study to be performed. Such an endeavor yields information which can be used to check various theories without the inclusion of uncertain physiochemical processes.

The conditions discussed above have yielded an experiment in which point measurements can be made in the flow field. Principle methods of measurement are pitot pressure probes, hot-wire anemometry techniques and conventional static pressure probes. Not all of these probing techniques are useful throughout the entire flow field and their various applications will be discussed.

Principal results obtained to date have been with the pitot pressure probes. At the Mach number, Reynolds number and wall temperature of this experiment, the viscous wake behind the body is actually larger than the body base diameter. No "throat" or "neck" in the classical sense is present but other familiar features can be seen. Such an extensive spread of the wake is believed to be the result of the expansion of the highly vortical boundary layer upon separation from the body.

RESUME

Au cours de cette communication sont exposés certains travaux récents de nature expérimentale, intéressant le domaine général des sillages laminaires hypersoniques se produisant derrière des corps coniques. L'expérience est effectuée dans une soufflerie classique fonctionnant à un nombre de Mach nominal de 16 et à un nombre de Reynolds en écoulement libre de 120.000 par pouce. On utilise de l'hélium à une température d'arrêt de 525°R.; c'est en effet un gaz permettant de réaliser des expériences relevant de la pure mécanique des fluides. Cette expérience présente un caractère de nature unique: l'utilisation d'un système de suspension magnétique pouvant servir de support à des corps de révolution. Ce système, exposé en détail au cours de précédents rapports, ne sera pas décrit dans ce texte. On étudie les sillages apparaissant derrière des maquettes de forme conique, présentant une base de un pouce de diamètre, un demi-angle de 10°, et divers rapports d'arrondissement, allant de 0 à 17,7%. Pour tous les essais effectués, la surface de la maquette a été portée à une température de récupération adiabatique. Ces conditions permettent d'obtenir des sillages absolument laminaires pour toute la zone d'essai (diamètres de culot allant de 0 à 15).

La mise au point de l'expérience fut dictée par plusieurs considérations importantes. On désirait étudier le sillage produit par des corps de révolution libres de tout système de sustentation au cours d'essais de longue durée en régime stable. Ceci constitue un progrès substantiel par rapport aux expériences précédentes, menées soit dans des installations pour essais de courte durée, soit sur des corps bi-dimensionnels ou tri-dimensionnels à support mécanique. Il est également important de souligner que le gaz utilisé au cours de cette expérience est un gaz parfait (sans ionisation, dissociation ou radiation), qui permet de procéder à une étude minutieuse relevant de la mécanique des fluides. Les résultats obtenus dans ces conditions peuvent être utilisés pour la vérification de diverses théories, sans qu'il soit nécessaire d'avoir recours à des procédés physico-chimiques incertains.

On a pu, dans les conditions décrites ci-dessus, procéder à des expériences permettant des mesures extrêmement localisées dans le champ d'écoulement. Les principaux procédés de mesure employés sont les sondes de pression dynamique de Pitot, les techniques anémométriques utilisant des fils chauds, et les sondes de pression statique classiques. Cependant, ces techniques de sondages ne sont pas toutes utiles pour la totalité du champ d'écoulement, et les auteurs examinent leurs diverses applications.

Les principaux résultats dont on dispose à ce jour ont été obtenus grâce aux sondes de Pitot. Pour le nombre de Mach, le nombre de Reynolds et la température des parois choisis en vue de l'expérience, le sillage visqueux situé derrière le corps étudié est en réalité plus important que le diamètre de base de ce corps. Aucun rétrécissement, au sens classique, ne se produit, mais on peut observer d'autres caractéristiques bien connues. On suppose qu'un tel étalement du sillage est dû à l'élargissement de la couche limite hautement tourbillonnaire après décollement du corps.

LIST OF SYMBOLS

C_D	Total drag coefficient; $C_D = \frac{\text{Total Drag}}{\frac{1}{2}\rho_\infty u_\infty^2 A_B}$
$C_{D_{sharp}}$	Total drag coefficient for sharp cone
D	Cone base diameter, 1.00 inch
M	Mach number
P	Static pressure
P_o	Tunnel stagnation pressure
P_t	Pitot pressure measured in the wake
R	Distance from axis of wake (R = 0 is wake centerline)
R_B	Cone base radius
R_N	Nose radius
$Re_{\infty,D}$	Reynolds number based on freestream conditions and cone base diameter
T_o	Tunnel stagnation temperature
u	Velocity
Z	Distance behind cone, measured from model base
γ	Ratio of specific heats
δ	Boundary layer thickness
ρ	Density
Ψ	Stream function (see Figure 9)
θ	Inclination of bow shock

Subscripts

s	Edge of boundary layer at cone shoulder
∞	Freestream conditions

1. INTRODUCTION

This paper reports some new experimental work in the general area of laminar hypersonic wakes behind conical bodies. The studies are currently in progress at Princeton University's Gas Dynamics Laboratory. The experiment is purely fluid mechanical in nature (e.g., no physio-chemical effects), and is being conducted in a conventional hypersonic helium wind tunnel. A unique feature of this work is the use of a magnatic suspension system which is capable of supporting axisymmetric bodies. Pitot pressure and hot-wire anemometry probing techniques are being employed to analyze the wake flow fields.

There are two primary objectives of the research: the first is to formulate a basic understanding of the physical processes involved in the initial development of the laminar wake flow field behind conical bodies by constructing an accurate experimental model. The second objective of the research is to provide a set of point measurements in this region to be used as a reference when comparing different theories. Such a result will allow the fluid mechanical formulations of various wake calculations to be verified prior to the inclusion of physio-chemical processes.

2. EXPERIMENTAL TECHNIQUES

A conventional helium wind tunnel is used to generate the flow. Helium gas at a stagnation pressure of 225 psia (1162 cm Hg) and room temperature is expanded through a contoured nozzle to freestream conditions. An inviscid core of about 2.5 inch (6.35 cm) diameter and 18-inch

(45.7 cm) length is present.

At the cone tip, the Mach number is 16.35, the Reynolds number is 121,000/inch, the static pressure equals 151 microns of mercury, and the velocity is 5650 feet/second (1720 m/sec.). Deviations from these nominal freestream conditions occur throughout the test region, but are of less significance than the trends reported for the wake flow field. A calibration of the wind tunnel may be found in Reference 1. Static density levels are too low to allow standard flow visualization techniques to be employed. A testing time of about six minutes is available.

Right circular cones of 10° half angle, one inch (2.54 cm) base diameter and various spherical bluntness ratios from 0 to 17.7% were used as models. The detailed design of the model (Figure 1) was dictated by the requirements of the magnetic suspension system which provided a model support apparatus completely free of mechanical contrivances during a test. The suspension system is fully described in References 2 and 3. A mechanical holder used during starting and shutdown is retracted from the tunnel throughout the data gathering stage of the test. All tests have been conducted with the wall temperature approximately equal to the adiabatic value. The model is maintained fixed and stable to within a few thousandths of an inch.

One of the objectives of the experiment is a complete determination of all the flow field variables (pressure, density, velocity, etc.) and several types of instruments are needed to accomplish this task. The use of any standard aerodynamic tool throughout the entire wake is compli-

cated by the extremes encountered in local flow conditions. The responses of available diagnostic tools were considered susceptible to the following characteristics of the problem:

(a) The local Mach number of the flow varies from subsonic to hypersonic values.

(b) The local Reynolds number changes by about two orders of magnitude from near freestream level in the inviscid wake to a low value on the wake axis.

(c) Gradients in the property being measured may be large over a distance comparable to the probe dimension.

(d) A given probe may interact with the flow field to a sufficient degree to perturb it a measurable amount, or even change its character altogether.

(e) Significant flow angularities could be present.

With these characteristics in mind, the present experimental program was designed to include two important features. The response of each probe was either known to be not adversely affected by these characteristics, or else a suitable calibration scheme was included to investigate the problem. Consistency of the results are to be established by redundant measurements with different instruments. The instruments are expected to depend on the characteristics of the flow field in different ways in order to detect of eliminate spurious effects which may manifest themselves. Data presented in the following two sections have been obtained with pitot and hot-wire probes. Other probing techniques are

currently being employed, but complete results are not yet available.

Several pitot probes were used in the course of the experiment. The majority of the data were gathered with a probe which had an externally chamfered circular orifice of 0.048 inch I.D. and 0.063 inch O.D. (1.22 mm I.D. and 1.59 mm O.D.). Three other geometrically similar probes were used along the wake axis in an experiment to measure viscous corrections for the 0.048 inch I.D. probe. Another probe used in surveys near the model had a rectangular orifice whose internal height was 0.010 inches (0.254 mm). Three pressure transducers were used to attain maximum sensitivity over a range of measured pressures from 0.003 to 3 psia (155μ to 155 mm Hg) and the resultant accuracy of the measurements is $\pm$ 2%. The probe lag time was continually observed, and readings were recorded only after equilibrium had been achieved. No corrections to the instrument's reading were made for pitot pressure gradients across the probe orifice. The information available (4) suggests the corrections are within the accuracy of locating the probe, $\pm$ .010 inch.

Hot-wire anemometer probes were used to measure steady state (or mean level) values of heat transfer rate and probe recovery temperature. A constant current hot-wire anemometer unit manufactured by Shapiro-Edwards was the prime instrumentation. The techniques for gathering and analyzing the data closely paralleled those of Dewey (5). Probes were constructed from 0.00015 inch (0.00381 mm) diameter platinum - 10% rhodium wire attached directly to the support prongs. Each probe had a nominal length to diameter ratio of 500, and were operated at low overheat ratios ranging

from two to twelve percent.

How-wire measurements were needed only in the viscous wake as the inviscid wake was completely determined by the pitot pressure measurement (see below). In the viscous wake, the probe was operating in the free-molecule flow regime where the response of the instrument is known analytically (6). Each probe was calibrated in the inviscid wake where the flow was near free molecule, and an appropriate thermal accommodation coefficient was obtained. The values for the later quantity ranged from 0.48 to 0.58 and remained quite constant for each probe during its lifetime. No particular care was taken to insure a clean probe surface, and there was most probably an absorbed gas layer present. Radiation from the hot-wire probe was negligible compared to convection and conduction cooling (end losses). The latter represented a major error which was accounted for by using Dewey's (5) end loss corrections. For the calibration experiments in the inviscid wake, the end losses reached a maximum of 17%. In the viscous wake the maximum value was about 50%. Complete details of the hot-wire measurements may be found in Reference 1.

Readings from the pitot pressure and hot-wire probes were combined to extract information about the flow field. The execution of this procedure contained several novel features discussed below. (Details of the computations may be found in Reference 1). In the viscous portion of the wake, both probes were needed to determine the flow field. Three independent measurements are needed to completely define all the thermodynamic and dynamic parameters in such a region. One of the measurements

was pitot pressure. The other two measurements were contributed from the hot-wire probe in the form of a heat transfer rate (or Nusselt Number) and an adiabatic cylinder recovery temperature. The actual data reduction technique consisted of guessing initial values of Mach number and stagnation temperature, and performing an iterative calculation until the desired convergence of the solution was obtained.

For regions wherein the local Mach number is less than about 2.5, this scheme will yield a complete description of the flow field providing the three measurements are of sufficient accuracy. Both the pitot pressure and hot-wire probes are blunt bodies, and as such are subject to the well-known hypersonic independence principle. Thus, above Mach numbers of about 2.5, the probe's responses are sensitive only to density and velocity variations. Hence, in regions of the viscous wake when M = 2.5 is exceeded, these are the only parameters recoverable from the probing techniques.

The response of the ideal pitot probe is governed by the Rayleigh pitot probe formula. This expression is written below in a form convenient for the present discussion:

$$P_t = \rho u^2 \left\{ \frac{\gamma+1}{2\gamma} \left[\frac{(\gamma+1)^2}{4\gamma - \frac{2(\gamma-1)}{M^2}} \right]^{\frac{1}{\gamma-1}} \right\}$$

$$= \rho u^2 \frac{\gamma+1}{2\gamma} \left[\frac{(\gamma+1)^2}{4\gamma} \right]^{\frac{1}{\gamma-1}} \left\{ 1 + \frac{1}{2\gamma M^2} + O(M^{-4}) \right\}$$

This expression clearly indicates that pitot pressure response becomes practically independent of Mach number at moderate supersonic speeds. For hypersonic flow, pitot pressure responds exclusively to momentum flux variations (a combination of density and velocity only). This is indeed the

case in the inviscid wakes of many bodies.

Another approximation may be introduced in many situations which further simplifies the interpretation of pitot pressure data. Oblique shock waves in hypersonic flows result in only small reductions of the gas velocity. For example, in the present experiment, the bow shock wave causes about a 2% reduction in total velocity. Furthermore, as the flow traverses the expansion region emanating from the rear of the cone, the gas is accelerated to within less than a percent of its freestream velocity. Thus, in the inviscid wake where no shear forces have acted upon the fluid, the velocity is equal to the freestream value, and pitot pressure variations are synonymous with density variations. These two simplifications together with the pitot pressure measurement result in the complete determination of the flow field as is outlined below.

Density and velocity distributions are known both in the viscous wake and inviscid wake, and hence a mass flow integral (or stream function) may be computed for each location in the flow field. A point with the corresponding stream function may be located on the bow shock wave if the shape of the latter is known. The stagnation pressure loss across the shock wave may then be calculated for each streamline. (Stagnation pressure losses across other shock waves in the flow field may also be included.) Since the inviscid flow field is isoenergetic, the stagnation temperature is known everywhere. At each point in the inviscid wake then, the pitot pressure, stagnation pressure and stagnation temperature are known. This is enough information to determine all the flow field variables. In

practice, the accuracy of the method relies on the determination of the local slope of the shock wave. A series of experiments were performed to accurately measure this.

Several remarks of general interest should be made here. The method outlined above for analyzing the inviscid wake may be extended to much lower Mach numbers than in the present experiment. For instance, a 10° half angle cone in a M = 4 air stream has a velocity deceleration across the bow shock wave of about 3.5% and a surface Mach number of about 3.5. Following the corner expansion, the flow velocity and Mach number should have returned to a sufficient level to accurately use the above analysis. For better accuracy at lower Mach numbers, a suitable iteration procedure could be established incorporating the above scheme as an initial guess. This technique for analyzing the inviscid wake has the distinct advantage of using a simple, reliable probe whose response is well known.

3. SHARP CONE RESULTS

The probing techniques described above have been used to study the wake from zero to fifteen base diameters behind a sharp, 10° half angle cone. The predominant features of the flow field observed are shown to scale in Figure 2. The viscous wake has an almost constant width of 1.25 base diameters. This is somewhat larger than the base diameter plus boundary layer thickness (1.14 base diameters). The classical necking down is not evident for these conditions. A trailing shock is first detected at two diameters behind the model, and reaches the viscous wake edge at about three diameters. Its strength and inclination varies along

its length as is discussed below.

In order to accurately determine the bow shock location, a separate series of experiments were performed. A hot-wire probe whose diameter was comparable with the shock wave thickness (0.001 inch) was used to traverse the shock wave at many stations. A least mean squares curve fit to the data points then yielded a bow shock shape. The local slope was determined from the equation of the fitted curve. Figure 3 presents the results. A constant shock wave angle of 12.7° was observed from $Z/D = -0.13$ to $Z/D \simeq 0.3$. The shock wave slope then monotonically decreased for larger Z/D locations. No measurements were taken upstream of the -0.13 location. Instead, a constant shock wave angle of 12.7° was assumed for this region. This assumption was verified by a pitot pressure trace at the cone shoulder (Fig. 4). A region of near constant pitot pressure was observed between the boundary layer edge and the shock wave indicating a straight shock wave. The level of pitot pressure agreed with that for a 12.7° shock wave to within one percent. The inviscid cone shock wave angle for these conditions is 12.0° and the additional 0.7° inclination is due to the presence of the boundary layer. Shoulder properties based on a 12.7° shock wave are listed in Figure 2. At that location, the boundary layer and shock layer thicknesses are about equal.

The development of the viscous and inviscid wakes is illustrated by the density profiles in Figures 4 and 5. At the cone shoulder, a region of near constant density is visible in the shock layer. The density measurements in this region were calculated from pitot pressure data with a slight

correction for the velocity deceleration across the bow shock wave. Agreement with the theoretical density ratio is excellent. One-half diameter behind the cone, the effects of the shoulder expansion processes are evident. A marked density decrease has occurred in part of the flow field. A small constant density region still exists near the bow shock wave indicating that the leading wave of the expansion fan has not yet intersected the shock wave. The shock wave inclination angle has remained unchanged (Figure 3) within the accuracy of that measurement. At two diameters behind the body, the density gradient through the expansion fan is visible. A slight density increase, recognizable as the forming trailing shock wave has appeared. No indication of a trailing shock was discovered after careful probing at one and one-half diameters. It seems, therefore, that the trailing shock wave forms somewhere between these two locations.

Three diameters behind the sharp cone, the trailing shock wave has approximately reached the edge of the inner or viscous wave. The latter is characterized by a region of constant density around the axis. The level of density in this area is approximately an order of magnitude below the edge value. Outside the trailing shock wave, the density gradient due to the expansion fan is again manifest. At five diameters, a definite inviscid region exists between the viscous wake edge and trailing shock wave. The viscous wake edge is denoted by an arrow. Results calculated in the inviscid wake from pitot pressure measurements alone are denoted by circular symbols. (These are accurate to $\pm$ 2%). The squares denote calculations from pitot pressure and hot-wire data. This

notation is uniform throughout the paper. At ten and fifteen diameters, the character of the viscous wake is the same as three and five diameters. The density level in the wake center has a continual, slight increase. A region between the wake edge and trailing shock wave of near constant density is present at ten and fifteen diameters.

Mach number distributions in the inviscid wake are presented in Figure 6. Unfortunately, at this stage of the experiment, the hot-wire measurements are not refined to a sufficient accuracy to calculate parameters other than density. However, the inviscid wake calculations are themselves quite revealing. The Mach number profiles again illustrate the characteristics of the expansion fan. The Mach number change across the trailing shock wave is seen to decrease rather quickly with axial distance behind the body. Outside of the trailing shock wave, the estimated error is about $\pm$ 3%. A typical inaccuracy inside the trailing shock wave is indicated by the error bar at Z = 5D. The increased error in this region results from the estimate of the trailing shock strength needed to determine the local stagnation pressure. At three diameters, the trailing shock wave causes about a fifteen percent decrease in stagnation pressure. However, due to the rapid decay of the shock strength, there is only about a one percent loss at five diameters.

The character of the region between the trailing shock and the viscous wake is portrayed more fully by the radial pressure profiles (Figure 7). From a high level near the bow shock wave, the pressure decays to a level below p_∞ . A recompression across the trailing shock wave then

raises the pressure above, but to the order of, p_∞ . Between the trailing shock wave and the wake edge, the pressure remains approximately constant at a level of about 1.2 p_∞ . The pressure variations in this region may be the result of either experimental inaccuracy or some sort of secondary wave reflection pattern.

Four representative streamlines are plotted in Figure 8. The general characteristics are quite evident. An important feature to note is that the streamlines downstream of the trailing shock wave are straight and nearly parallel to the axis. The $\psi = 0.5$ streamline is slightly inclined towards the wake axis at a measured angle of about -0.4°. Determination of an angle of that size is probably beyond the accuracy of experimental data. However, it does appear that downstream of the trailing shock wave, the streamlines are approximately parallel to the axis and the pressure is the order of freestream ambient.

The streamlines presented in Figure 8 are obtained by numerically integrating the mass flow from the wake axis to any R/D . A typical mass flow distribution across the wake at one axial location is shown in Figure 9. Also plotted is the freestream distribution measured at a nearby location with no model in the tunnel. The two curves agree to about one percent outside the bow shock wave verifying the accuracy of the inviscid wake mass flow calculations.

Some remarks concerning probe-flow field interaction effects should be made at this point. Three separate experiments were carried out to detect and identify such disturbances. The goal of the first two sets

of tests were to determine if any interaction was occurring between the probe and the viscous wake downstream of the trailing shock wave origin. It was presumed that such a disturbance would be manifest as a large scale change, e.g., a distortion of the wake boundaries, a spreading of the viscous wake as observed by Slattery, et. al. (7), or a change in position of the trailing shock wave. One test involved a pitot pressure survey across the wake at Z = 5D with two probes of quite different geometry. No important differences were noted between the two profiles. The second experiment involved moving a pitot probe on the wake centerline upstream from fifteen diameters behind the cone. At the same time, a second probe mounted from the tunnel wall at about eight diameters was used to monitor the trailing shock wave position. The farthest upstream point the centerline pitot probe could be used was three diameters, at which time its shock wave intersected the monitoring probe. No change in location of the trailing shock wave position was found for any position of the centerline pitot probe between three and fifteen diameters.

The third experiment was designed to uncover changes in the base flow region due to the presence of a probe. The current in the drag coil of the magnetic suspension system was monitored on a sensitive recorder with the largest part of the signal biased off. It was possible to detect changes in total cone drag of about 0.05%. Assuming a base pressure on the order of p_∞ (see below), this represents a change in base pressure (or base drag) of between one and two percent. A significant change in the geometry of the base flow region should produce base pressure changes

greater than this amount.

Results of the above experiment were as follows: No base drag changes could be determined as pitot probes one through four were moved from zero to fifteen diameters. An increase in base pressure of about three percent was caused as the model launcher was moved from three diameters to just behind the model. A description of the launcher can be found in References 1 and 3. Its approximate geometry is that of a side wall mounted wedge shape sting of 1/8 inch base height.

A series of four geometrically similar probes were used to measure the pitot pressure on the wake axis to investigate errors due to viscous mechanisms (4). The 0.048 inch I.D. probe was considered the maximum size acceptable due to spatial resolution requirements in the rest of the wake flow field. For this probe, errors reached a maximum of 26% at Z = 1D (and R = 0D), and decreased to zero at Z = 14D. It is interesting to note that all four probes recorded the same value of pressure when placed directly at the base of the cone model. No significant changes were noted in the total drag of the model indicating that the base drag had changed less than two percent. The value of pressure which the probe recorded at this location, 1.58 $p_\infty \pm 7\%$, appears to be an accurate measurement of the base pressure.

4. BLUNT CONES

A. Pitot Pressure Measurements

It is generally agreed that the properties of the hypersonic wake behind a blunt base body are in some way related to the properties of

the boundary layer at the shoulder. A comparison of several blunted cone wakes to the sharp cone wake may shed some light on the importance of "initial conditions" on the body and their influence on the laminar wake development. The wakes of cones with bluntness ratios (R_N/R_B) of 1.4%, 3%, 5%, 10% and 17.7% are compared to that of the sharp cone at a station five diameters behind the models. For the 10% blunted cone, the wake was examined at other locations. Total drag measurements and pitot profiles across the wake have been made for each configuration.

Figure 10 shows the radial pitot pressure profiles at Z = 5D behind all the models tested, including the sharp cone. It is observed that data for the 1.4% and 3.0% blunted cones fall on the sharp cone data everywhere in the wake (within the $\pm$ 2% accuracy of the measurement). The order of magnitude estimate in Reference 8 indicates that strong interaction effects have a greater influence on the boundary layer at the cone shoulder than such small geometric bluntness, and therefore no noticeable departure from the sharp cone pitot pressure profile is expected.

When bluntness ratio is increased to 10% and 17.7%, the inviscid rotational flow field between the viscous wake and the trailing shock cannot be distinguished from the viscous wake, and only small changes in trailing shock strength and location are observed. For bluntness ratios above 10%, the trailing shock is observed further away from the wake centerline than the sharp cone trailing shock. No change in pitot pressure in the center of the viscous wake is observed as bluntness ratio is increased from zero to 17.7%. No significant difference between the density profiles

at several axial stations downstream of the sharp and 10% blunted cone were observed.

B. Total Cone Drag Measurements

The drag coil of the magnetic suspension system has been calibrated to give total drag of all the cone models (3) and the results of these measurements are given in Figure 11. For bluntness ratios of less than 5%, no noticealbe change from the sharp cone value of 0.1115 is observed. As bluntness ratio is increased from 5% to 10%, total drag coefficient decreases to about 95% of the sharp cone value. Further increases in bluntness causes the total drag to increase.

Although the authors have not encountered other experimental drag data which first decreases and then increases as bluntness ratio is increased, there are drag calculations in the literature which suggest this behavior. References 9 and 10 show that skin friction drag decreases monotonically with increasing bluntness ratio. References 11 and 12 indicate that cone surface pressure drag initially decreases for small cone bluntness and then increases rapidly for larger cone bluntness. These calculations, coupled with rough base pressure measurements which show that base drag is nearly the same for all configurations tested, indicate that the initial decrease in total drag observed is not unlikely for the cone geometries and test conditions in this report.

5. DISCUSSION

The previous three sections of this paper have discussed some experiments currently in progress at Princeton University's Gas Dynamics

Laboratory. This section will elaborate on some aspects of the current findings whose nature may be of general applicability.

Discussions of the sharp cone results in Section 3 demonstrated that the trailing shock wave appeared to have a distinct and identifiable role in the inviscid wake development. Namely, the flow behind the trailing shock wave is nearly uniform, at a pressure level on the order of p_∞, and directed approximately parallel to the freestream and the wake axis. Departures from the ideal conditions suggested above may be due to experimental inaccuracies, tunnel non-uniformities or gradients, or a secondary wave reflection process in the inviscid flow.

Static pressures behind the trailing shock wave from this experiment and that of Ragsdale and Darling (13) are plotted in Figure 12. The results of Ragsdale and Darling are for a turbulent cone wake at a Mach number five; a condition which is quite different from the present experiment. Both sets of data indicate that the static pressure behind the trailing shock wave is approximately at freestream level. Ragsdale and Darling's results also reveal that the pressure between the trailing shock wave and wake edge is uniform to within about $\pm$ 10%.

Data of Chapkins, et. al. behind 6° half-angle wedges at a Mach number of 4.0 reported elsewhere in this volume also reveal a region of uniformity behind the trailing shock wave. Their data is for laminar wakes behind both adiabatic and cold bodies with and without mass injection into the wake. For all of these cases, the static pressure behind the trailing shock wave is at freestream level. (The static pressure was

estimated by the authors using the inviscid wake calculation procedure outlined in Section 2. A straight shock wave for an inviscid 6° wedge was assumed to calculate the stagnation pressure loss for the wake edge streamlines). It is interesting to note that the trailing shock wave location at a given axial station is radically changed by the mass injection process. However, in both cases, a uniform region is produced behind the shock wave.

Streamline patterns from other experimental investigations support the observation noted in the sharp cone experiments. Data of Martellucci, et. al (14) for the turbulent wake behind a 10° half angle circular cone at a Mach number of six indicates that the streamlines downstream of the trailing shock wave are nominally straight. In the region around the shock wave origin, Martellucci's data indicates an additional mechanism besides the trailing shock wave is needed to straighten the streamlines. However, these streamlines appear to be inside the viscous wake. For some experiments, it is possible to deduce the directions of certain streamlines from schlieren or shadowgraph pictures. Slip lines are streamlines, and if such are present in the flow field they may be used to measure streamline direction. Hama's data (15) at a Mach number of 2.61 for turbulent wakes behind wedges indicate that streamlines downstream of the trailing shock wave are straight. Another picture of an 8° half angle cone wake at M = 13 in air (16) demonstrates that the same characteristic is observed for a transitional wake.

The above observations seem to support the conclusion that the

inviscid wake flow behind the trailing shock wave has returned to its downstream boundary conditions for pressure and flow direction. It is interesting at this point to question what might be the implication of this conclusion. There has been some discussion in the literature recently of the nature of the interaction of the viscous shear layer and wake with the inviscid outer flow. These two regions must somehow adjust so as to produce a compatible flow pattern. It now appears that this adjustment takes place near the body. The final manifestation of the adjustment is the trailing shock wave. Behind this shock wave, the viscous wake (whether it be laminar, transitional or turbulent) grows into a uniform pressure field and uniformly directed velocity field. If mass is added to the wake as in the experiments of Chapkins, et. al., it is clear some sort of adjustment in the flow field must result. Whatever the detailed process is, the trailing shock wave again produces a uniform flow in the inviscid wake.

6. CONCLUSIONS

Results have been presented from an experimental study of laminar wakes behind conical bodies. Hot-wire and pitot pressure instruments have been used to probe the flow field. The experiment is purely fluid mechanical in nature and is being conducted in a conventional helium wind tunnel. The major findings to date are:

1. For a sharp cone, in the region between the trailing shock wave and viscous wake edge, the pressure is nearly constant and is on the order of freestream ambient. In the same region, the streamlines are parallel to the wake axis. These two observations, supported by data from other

laboratories, indicate that the trailing shock wave must be the final mechanism in returning the inviscid wake flow to its downstream boundary condition in pressure and flow direction.

2. Surveys across the viscous wake revealed a sharp decrease in density of at least one order of magnitude at the wake edge. The center of the viscous wake is a region of nearly constant density.

3. No significant changes were noted in the wake pitot pressure distribution as the bluntness ratio was increased from 0 to 10%.

4. As bluntness was increased from 0 to 5%, the cone drag remained constant. The drag then decreased to 95% of its sharp cone value as the bluntness reached 10%, and further increases in bluntness caused increases in drag.

REFERENCES

1. Murman, Earll M., PhD Thesis, Princeton University, 1967 (to be published).
2. Dukes, T. A. and Zapata, R. N., "Magnetic Suspension with Minimum Coupling Effects for Wind Tunnel Models", IEEE Transactions on Aerospace and Electronic Systems, Vol. AES-1, No. 1, August 1965, pp. 20-28.
3. Zapata, R. N. and Dukes, T. A., "The Princeton University Electromagnetic Suspension System and its Use as a Force Balance", in F. L. Daum's Summary of ARL Symposium on Magnetic Wind Tunnel Model Suspension and Balance Systems, ARL 66-0135, July 1966.
4. Chambré, P. L. and Schaaf, S. A., The Impact Tube in Physical Measurements in Gas Dynamics and Combustion, Vol. IX, High Speed Aerodynamics and Jet Propulsion Series, Princeton Univ. Press, Princeton, N. J. 1954.

5. Dewey, C. F., Jr., "Hot Wire Measurements in Low Reynolds Number Hypersonic Flows", ARS J., Dec. 1961, pp. 1709-1718. Also Part I, PhD Thesis, California Institute of Technology, 1963.

6. Schaaf, S. A. and Chambré, P. L., Flow of Rarefied Gases in Physical Measurements in Gas Dynamics and Combustion, Vol. IX, High Speed Aerodynamics and Jet Propulsion Series, Princeton Univ. Press, Princeton, N. J., 1954.

7. Slattery, R. E., Clay, W. G., and Stevens, R. R., "Interactions Between a Hypersonic Wake and a Following Hypersonic Projectile", AIAA J. 1, No. 4 (1963), pp. 974-975.

8. Hayes, W. D. and Probstein, R. F., Hypersonic Flow Theory, Academic Press, New York, Chapter 9, 1959.

9. Wilson, R. E., "Laminar Boundary-Layer Growth on Slightly Blunted Cones at Hypersonic Speeds, Journal of Spacecraft and Rockets 2, pp. 490-496, 1965.

10. Wilson, R. E., "Laminar and Turbulent Boundary Layers on Slightly-Blunted Cones at Hypersonic Speeds", United States Naval Ordnance Laboratory, NOLTR 66-54, March 1966.

11. Chernyi, G. G., Introduction to Hypersonic Flow, Translated by R. F Probstein, Academic Press, New York, 1961.

12. Hromas, L. and Lees L., "Effect of Nose Bluntness on the Turbulent Hypersonic Wake", Space Technology Laboratories, BSD-TDR-62-354, October, 1962.

13. Ragsdale, W. C. and Darling, J. A., "Experimental Study of the Turbulent Wake Behind a Cone at Mach 5", NOLTR 66-95, 27 September 1966.

14. Martellucci, A., Trucco, R., Ranlet, J. and Agnone, A., "Measurements of the Turbulent Near Wake of a Cone at M = 6", AIAA Paper No. 66-54, January 1966.

15. Hama, F. R., "Experimental Studies of the Lip Shock", AIAA Paper No. 67-29, January 1967.

16. Gold, H., "Stability of Axisymmetric Laminar Wakes", in AIAA Entry Technology Conference Papers, AIAA Publication CP-9, October 1964.

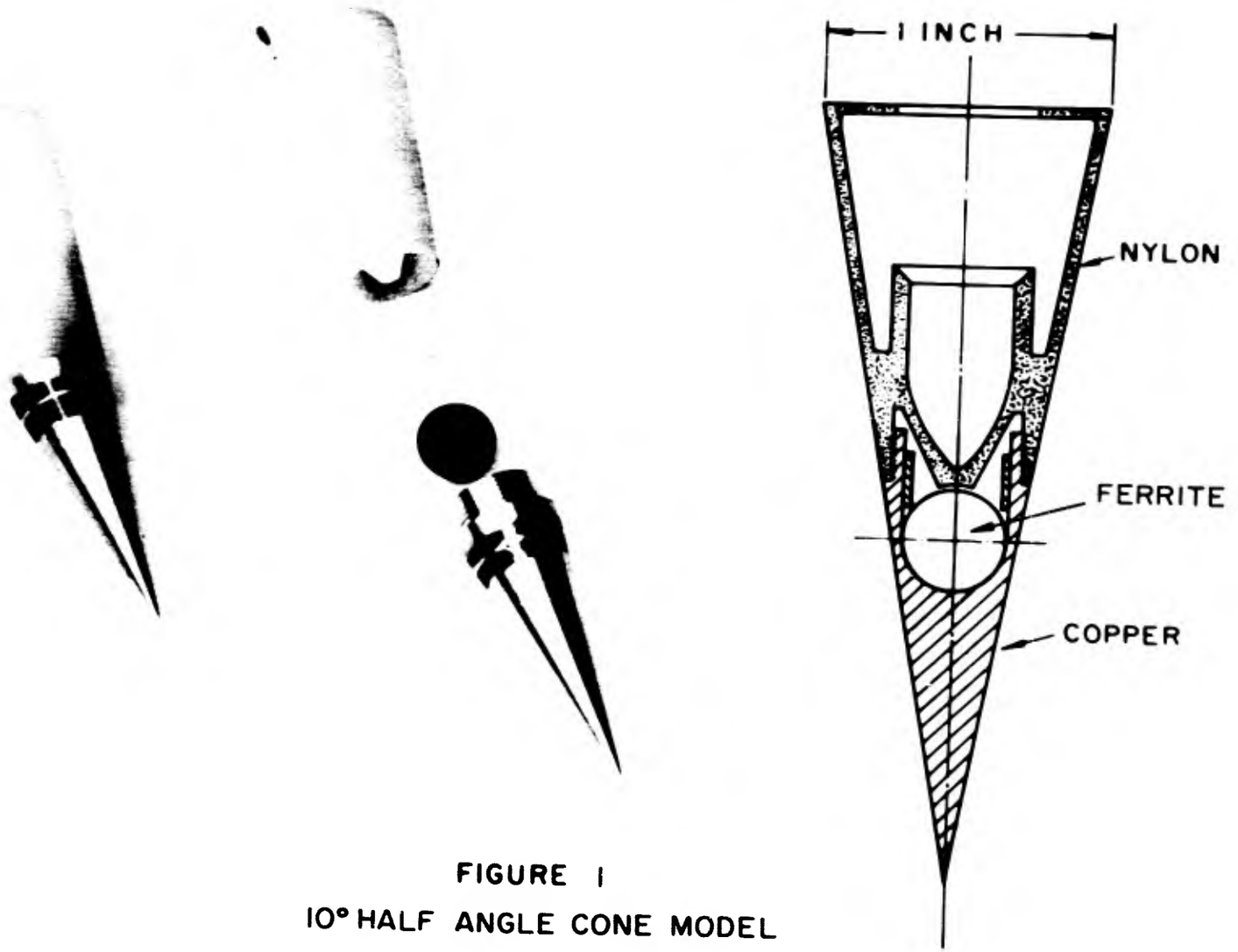

FIGURE 1
10° HALF ANGLE CONE MODEL

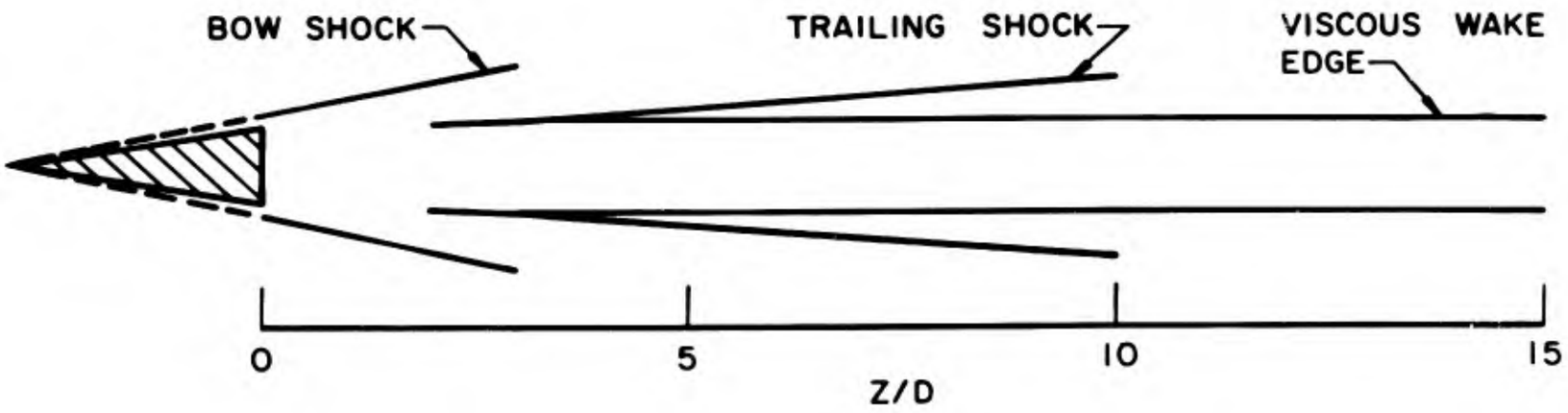

FREESTREAM PROPERTIES

$M_\infty = 16.35$

$P_\infty = 0.00292$ PSIA

$U_\infty = 5650$ FPS

$\rho_\infty = 5.80\ \mu$ SLUGS / FT^3

Re_∞ / IN $= 1.21 \times 10^5$

$To_\infty = 535°R$

CONE SHOULDER PROPERTIES

$M_S = 7.1$

$P_S = 0.0423$ PSIA

$U_S = 5520$ FPS

$\rho_S = 18.6\ \mu$ SLUGS / FT^3

Re_S / IN $= 1.44 \times 10^5$

$\delta / D \simeq 0.07$

FIGURE 2 EXPERIMENTAL FLOW FIELD DIAGRAM

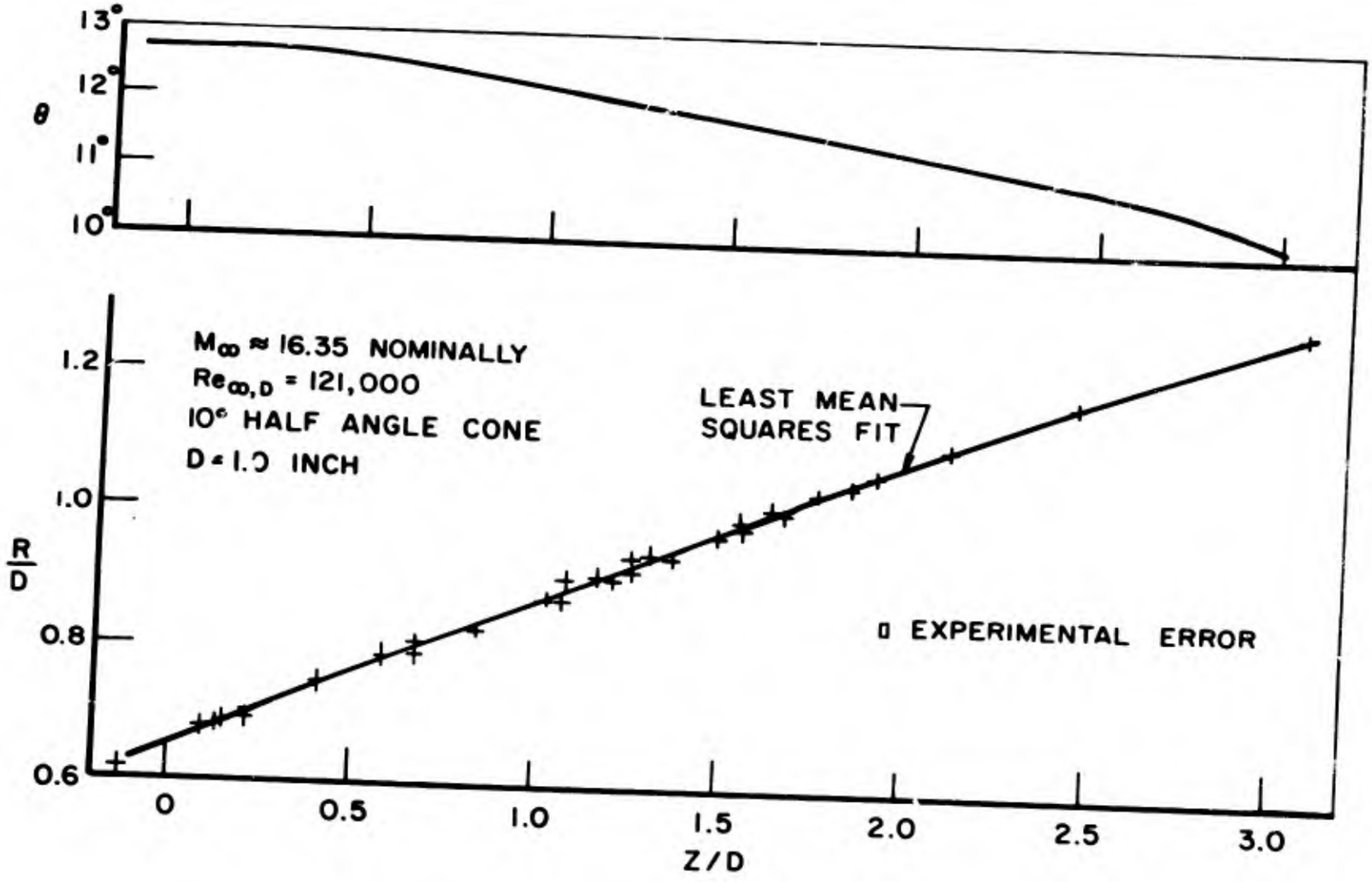

FIGURE 3 SHARP CONE BOW SHOCK

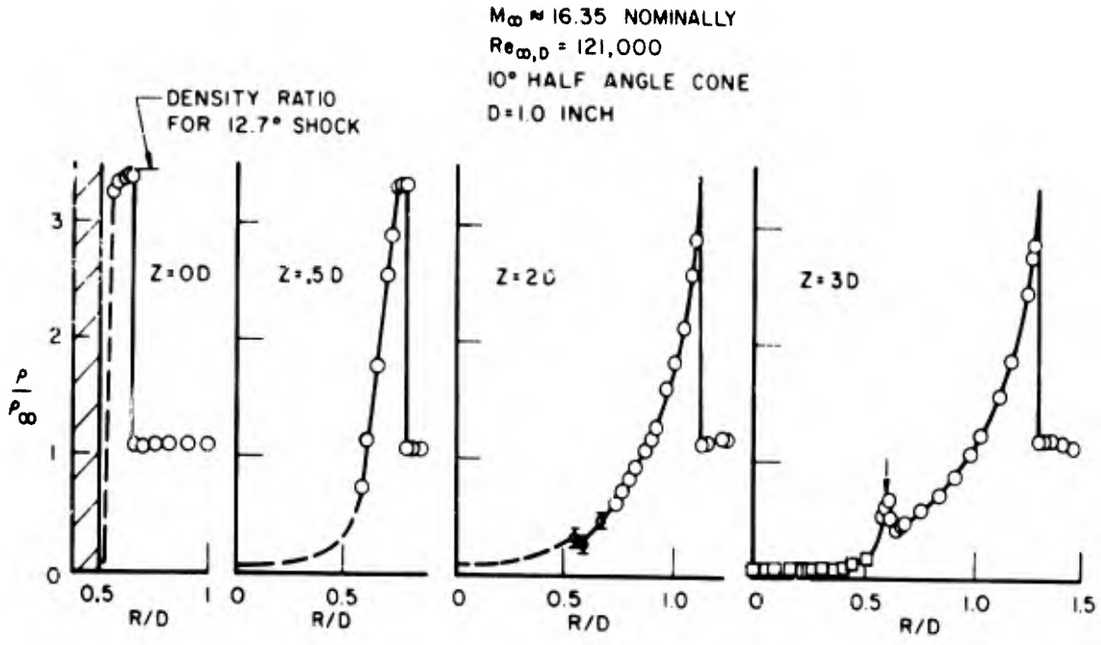

FIGURE 4 SHARP CONE DENSITY PROFILES

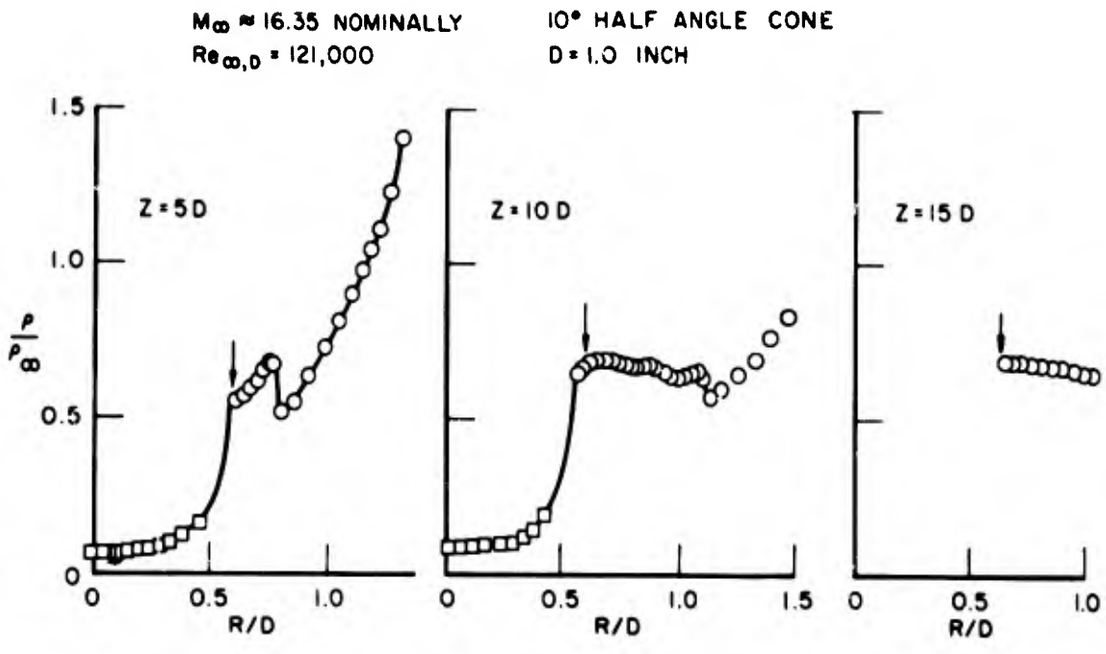

FIGURE 5 SHARP CONE DENSITY PROFILES

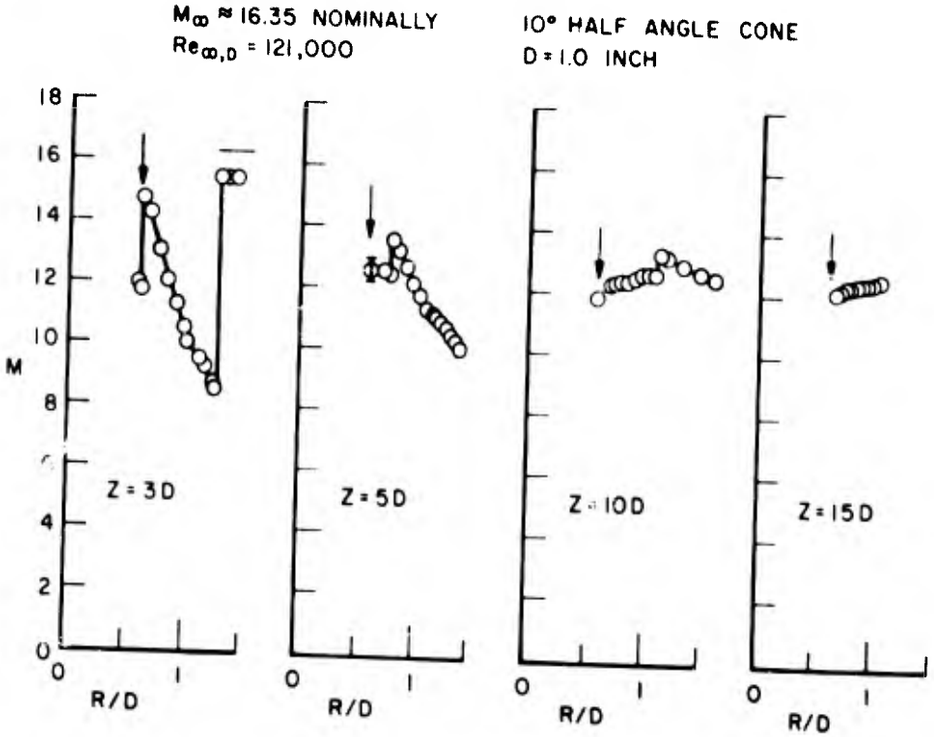

FIGURE 6 SHARP CONE MACH NUMBER PROFILES

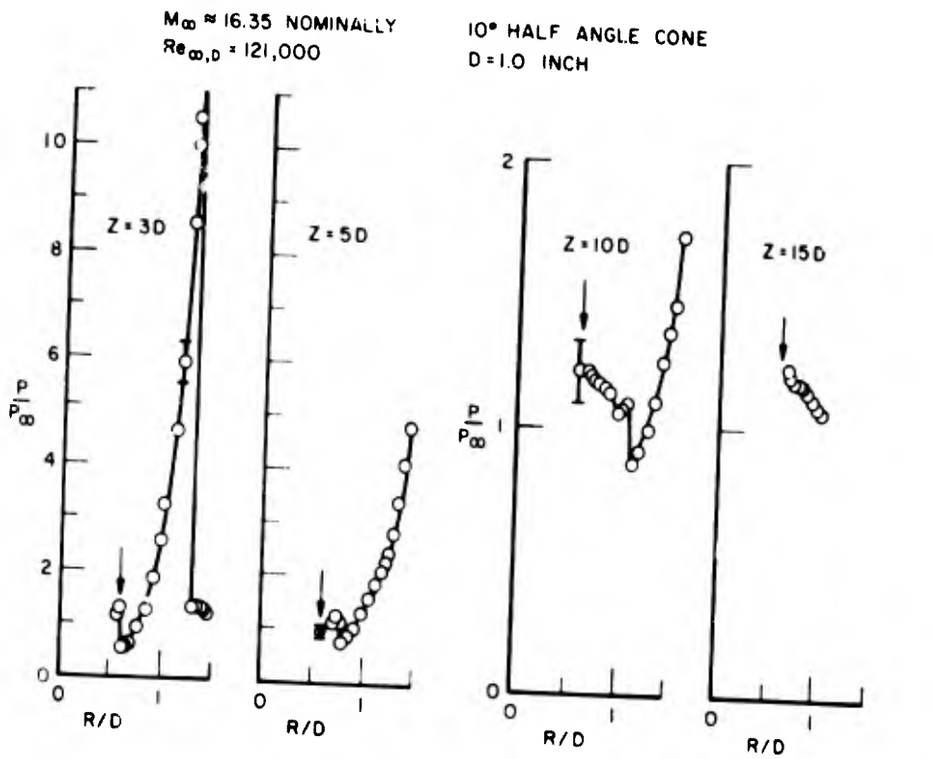

FIGURE 7 SHARP CONE STATIC PRESSURE PROFILES

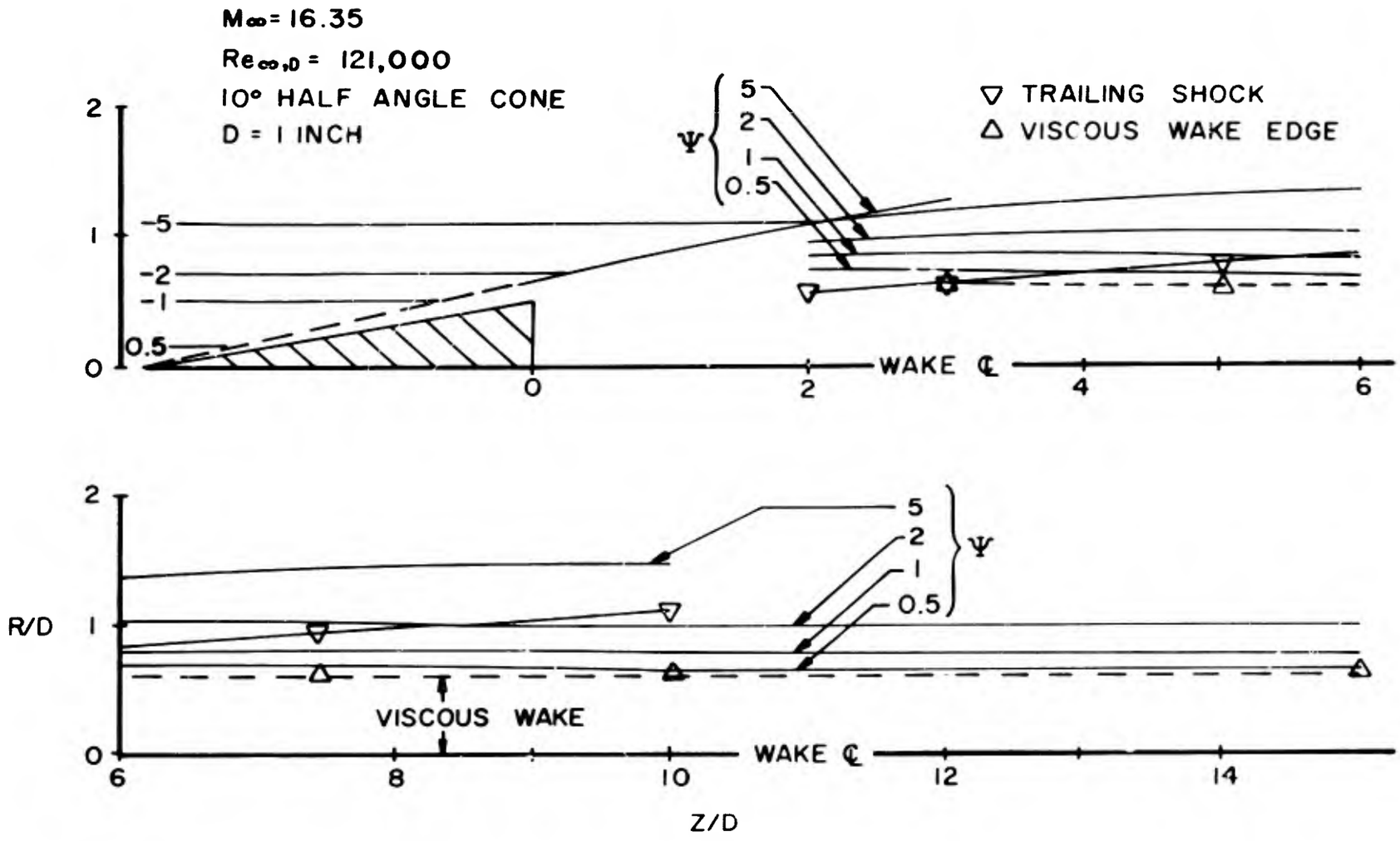

FIGURE 8 SHARP CONE STREAMLINES

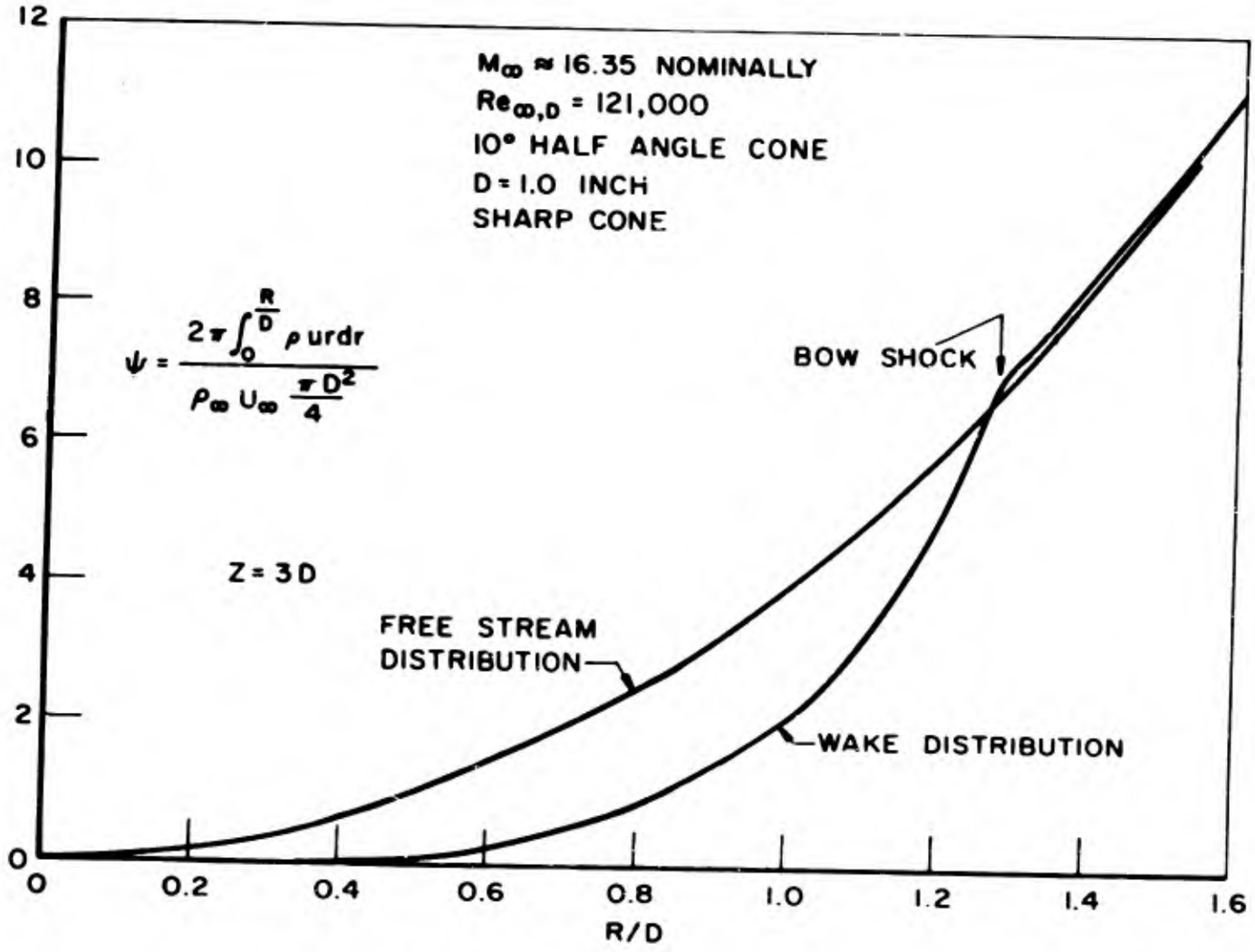

FIGURE 9 RADIAL STREAM FUNCTION

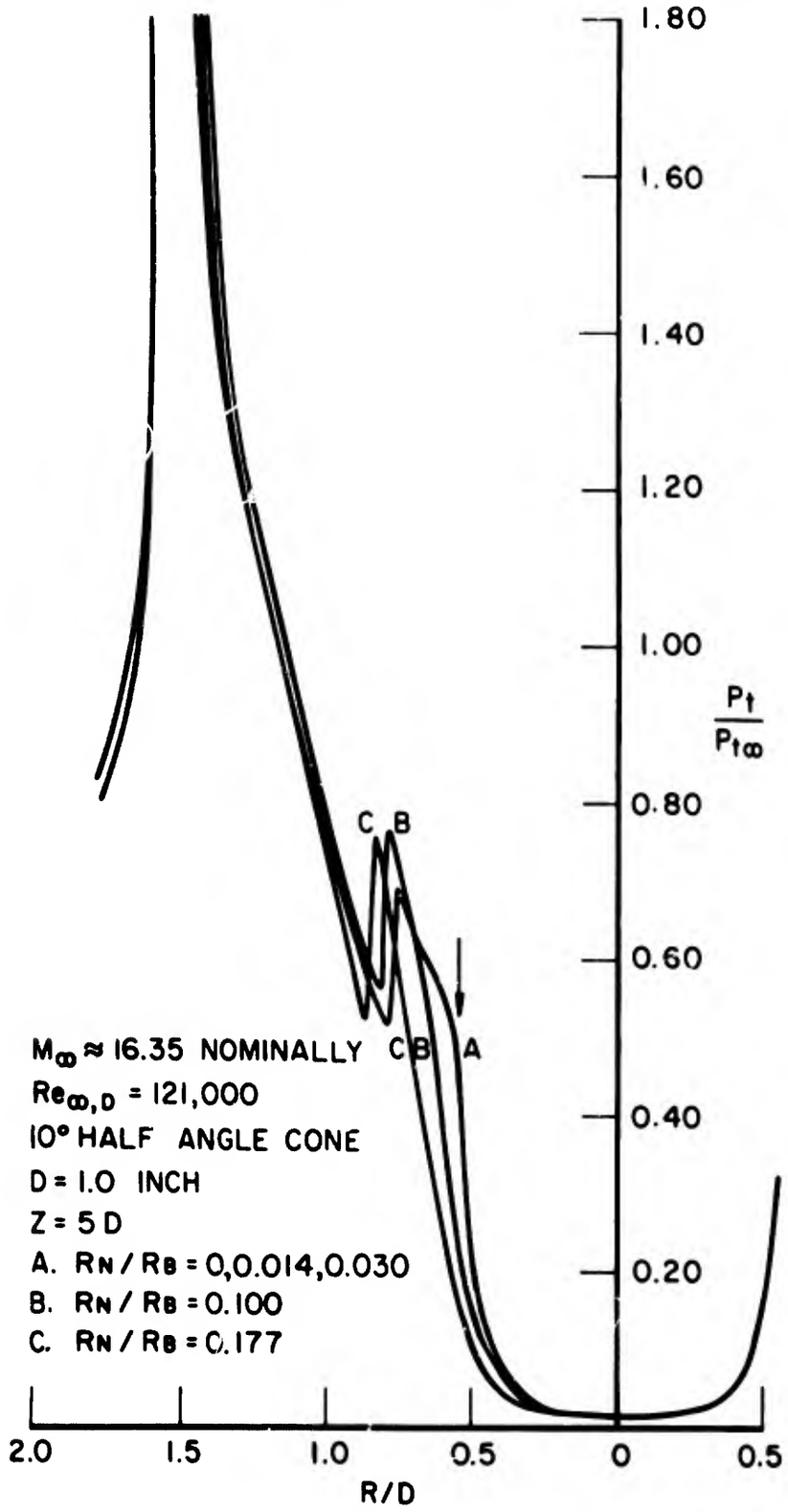

FIGURE 10 RADIAL PITOT PRESSURE PROFILES

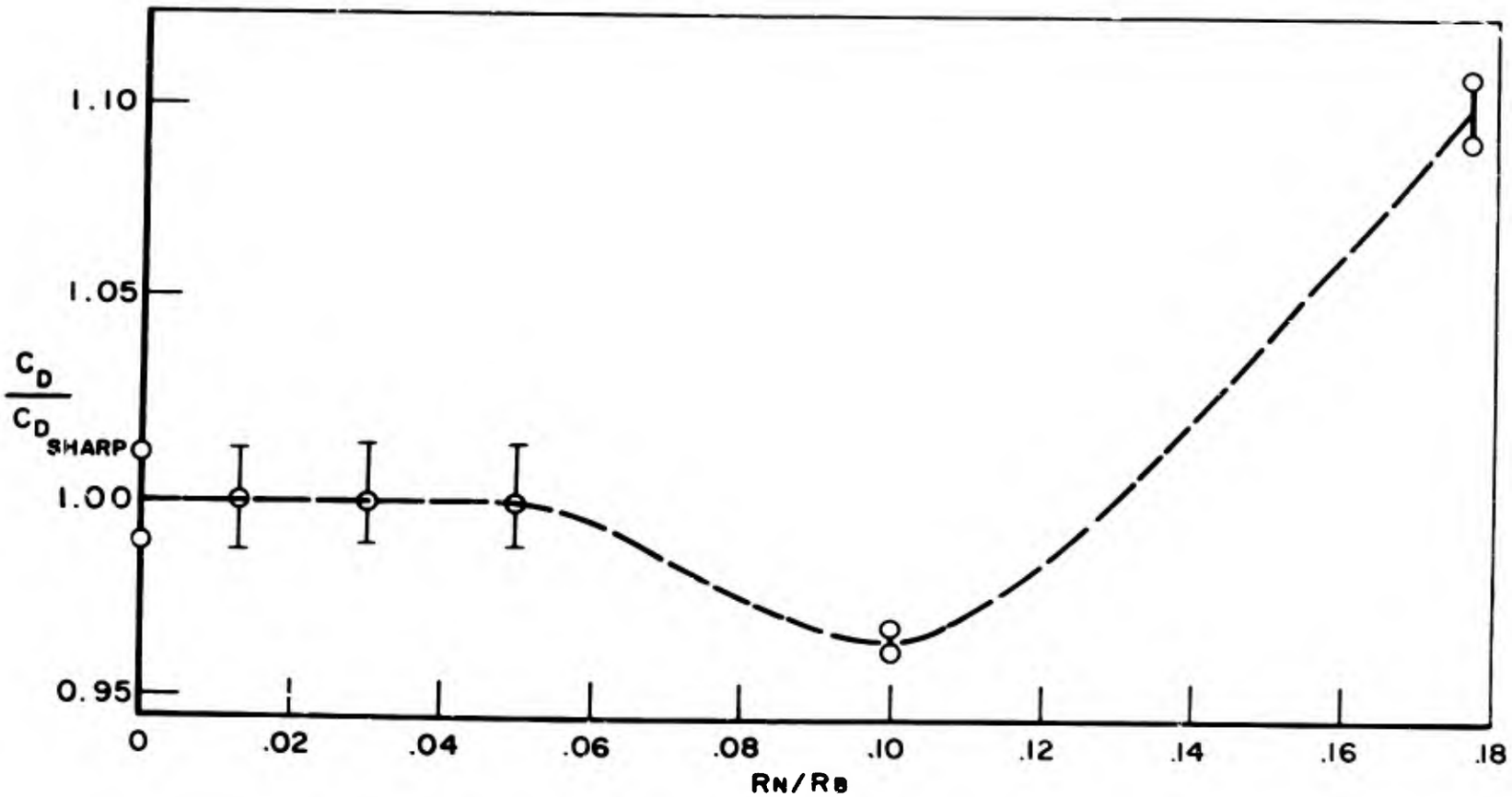

FIGURE II VARIATION OF DRAG COEFFICIENT WITH BLUNTNESS RATIO

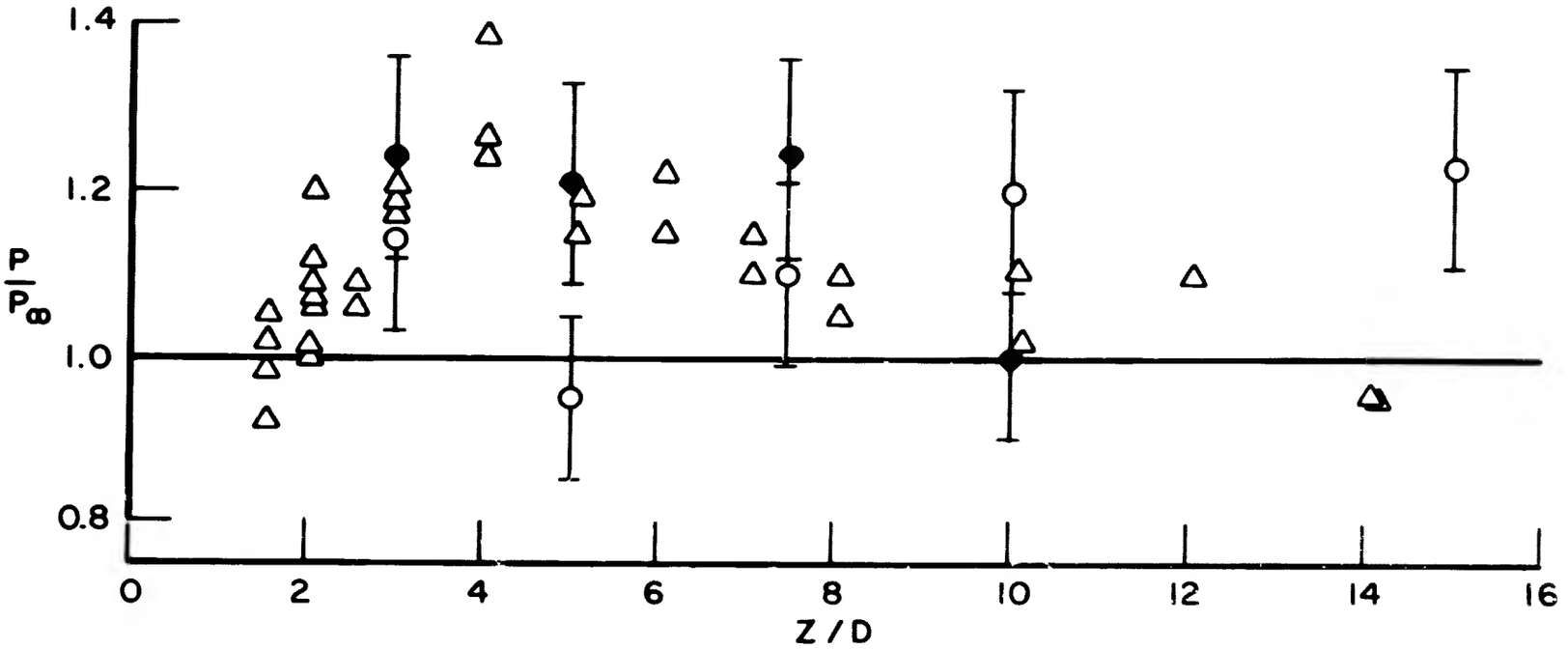

△ NOL TRAILING SHOCK $M_\infty = 5$ 9° SHARP CONE TURBULENT

● PRINCETON TRAILING SHOCK
O " WAKE EDGE
} $M_\infty = 16.35$ 10° SHARP CONE LAMINAR

FIGURE 12 EDGE STATIC PRESSURE

WAKE MEASUREMENTS BEHIND A CONE SUSPENDED MAGNETICALLY IN A MACH NUMBER 4.3 STREAM

by

F.K. BROWAND*, M. FINSTON**, and D.K. MCLAUGHLIN***
Department of Aeronautics and Astronautics
Massachusetts Institute of Technology, Cambridge, Massachusetts, U.S.A.

---

*Assistant Professor

**Professor

***Research Assistant

SUMMARY

The paper will describe the results of continuous pitot pressure surveys behind a 7 degree half angle cone at zero angle of attack. The cone is at recovery temperature. Hot-wire data will probably be limited to qualitative surveys indicating the extent of the base recirculation region and the location of the transition point in the wake. The pitot pressure surveys extend from the base to a distance of about 6 diameters downstream and are sufficiently detailed to accurately indicate the complete geometry of the near wake region including the corner expansion, lip shock, free shear layer, and wake recompression.

Pitot pressure profiles taken over a range of Reynolds numbers will provide information on the Reynolds number dependence of the near wake characteristics, and on body size effects. These data are further supported by Schlieren photographs of the near wake, although these photographs are of poorer quality than those usually obtained in ballistic ranges.

Similar results will be presented for the 7 degree cone at small angles of attack, which forcefully illustrate the sensitivity of the wake flow to this variable.

A brief description of the magnetic suspension system and the data acquisition techniques will also be given.

RESUME

Au cours de cette communication seront décrits les résultats de relevés continus de pression dynamique à l'arrière d'un cône présentant un demi-angle de 7^{o} et placé sous un angle d'attaque nul. Ce cône est à la température de récupération. Les résultats fournis par la technique des fils chauds seront probablement limités à des données qualitatives indiquant l'étendue de la zone de recirculation de la partie postérieure du cône, et l'emplacement du point de transition dans le sillage. Les relevés de pression dynamique par sonde de Pitot s'effectuent de la base du cône à une zone située en aval, à une distance représentant environ six diamètres et sont suffisamment détaillés pour indiquer avec précision la géométrie complète de la région du sillage proche du corps, y compris l'étalement à proximité de l'angle, l'onde de choc attachée au décrochement du culot, la couche de cisaillement libre, et la recompression du sillage.

Les profils de pression dynamique pour toute une gamme de nombres de Reynolds indiqueront dans quelle mesure les caractéristiques de la zone de sillage proche du corps dépendent du nombre de Reynolds, et renseigneront sur l'influence des dimensions du corps. Ces données seront appuyées par des photographies Schlieren du sillage au voisinage du corps, bien que ces images soient de moins bonne qualité que celles généralement obtenues en tunnels balistiques.

Les auteurs présenteront, pour ce cône de 7 degrés orienté suivant de faibles angles d'attaque, des résultats similaires qui illustrent avec conviction la sensibilité de l'écoulement du sillage à cette variable.

Ils décriront enfin brièvement le système de suspension magnétique et les techniques d'acquisition de données.

NOTATION

d	cone model base diameter
M_{ave}	average Mach number of jet
p_p	pitot pressure
p_o	stagnation pressure
$Re_{\infty d}$	Reynolds number based upon free stream conditions and model base diameter
T	temperature
T_o	stagnation temperature
V	velocity
x, y, z	coordinates as defined in Fig. 6, and with origin at the center of the model base
α	angle of attack of the model
δ_M	minimum wake width
δ_b	boundary layer thickness on the cone just before separation at the base
ρ	density
μ	viscosity

Subscript

$( )_\infty$	free stream conditions

1. INTRODUCTION

The study of hypersonic wakes has largely been motivated by the desire to predict observables in the wakes of bodies reentering the atmosphere. To get some idea of the flow conditions encountered during reentry, Fig. 1 shows the Mach number-Reynolds number history for a typical, slender conical body having a base diameter of five feet. An altitude scale is also superimposed on the horizontal axis. At 250,000 feet, the mean free path in the atmosphere is about .1 inch, so the flow can be considered continuous below this altitude. The extremely high Mach numbers experienced during such a reentry pose a difficult problem for the experimenter. At the present time it is impossible to simulate these high Mach numbers in a facility which will allow a reasonably complete exploration of the wake. The MIT Aerophysics Laboratory has undertaken a program to supply experimental data in the near wake ($x/d<10$) of three dimensional bodies at much lower Mach numbers. The ability to test continuously in a support-free wake is the advantage of our facility.

Also plotted in Fig. 1 is an approximate curve which represents the locus of wake neck transition points. The intersection of the reentry trajectory with the transition curve defines the altitude at which transition has moved forward to the wake neck. Above this altitude, the transition point will move downstream into the wake, while below this altitude transition will move ahead of the rear stagnation point. Thus the near wake is probably laminar for about half of the total altitude history in the continuous flow regime.

The measurements to be reported here consist of pitot pressure surveys behind a 7 degree half angle cone for several angles of attack. The Reynolds number is low enough to insure a laminar wake in the region investigated -- from the cone base to 5 1/2 diameters downstream.

2. EXPERIMENTAL EQUIPMENT AND PROCEDURES

2.1 Wind Tunnel

The experiments were carried out in the MIT Aerophysics Laboratory hypersonic wind tunnel, at a nominal Mach number of 4.3. The tunnel is a continuous flow, open jet type with a nozzle exit area of 3.06 in. by 3.88 in. The core of inviscid flow is approximately 2.2 in. by 3 in. Overexpansion of the nozzle flow was controlled by bleeding air into the bell surrounding the free jet. Normally the tunnel was operated with the bell pressure slightly less than the nozzle exit static pressure. Pitot pressure profiles were taken throughout the test section of the jet with no model present to establish flow uniformity. Within the nozzle Mach rhombus the Mach number variations were less than ±0.5 percent. However, outside the Mach rhombus the flow expanded to a Mach number 4 percent higher. Thus an average Mach number can be defined, from which variations are never more than ±2 percent.

2.2 Magnetic Suspension System

The hypersonic wind tunnel is equipped with a five-degree-of-freedom magnetic suspension system (described in Ref. 4). Fig. 2 is a schematic of the relative magnet positions. The function of the magnetic suspension system was to locate the wind tunnel model at a predetermined position while the wake was probed. The model could be placed in a previously determined location within ±0.004 in. and to a given angle of attack within ±0.2 degrees. The control optics in the pitch plane could be rotated as a unit while the wind tunnel was running. (In this way, angles of attack up to 20 degrees are obtainable in principle.)

The position drift in translation was less than ±0.002 in. over a 10 minute period. Since the absolute position of the model was reset for each traverse of the wake, the model position was always within ±0.006 in. in translation and 0.3 degree angle of attack of the set point. In addition, small scale fluctuations in model position were always present. The control optics output was monitored to indicate the level of these fluctuations. Fig. 3 is a typical time history of horizontal translation during a wind tunnel run.

2.3 Models

All models used were 7 degree half-angle cones, 3 in. in length with a base diameter of 0.737 in. The ratio of nose radius to base radius was less than .01. The models were constructed of magnetic ingot iron, counterbored at the rear and fitted with a thin cover disk (see Fig. 4). The purpose of the counterbore was to move the center of mass nearer the center of pressure.

2.4 Instrumentation

Pitot pressure probes were made by drawing 1 mm OD glass tubing to the desired thickness and shape. The tube was then broken at the minimum section and honed square with a smooth stone. The final outside and inside diameters at the tip were of the order of 0.011 in. and 0.007 in. respectively (see Fig. 5). Probe supports were brass double-wedge stems designed to produce as little disturbance as possible. A ±5 lbs/in^2 Hydine differential pressure transducer was located at the base of the pitot probe stem, less than 5 in. from the tip. The internal diameter of the stainless steel tubing joining the glass to the transducer was selected to minimize the time response of the system. Response times of the order of 0.5 second were measured for a 1 lb/in^2 step input and the transducer initially at vacuum.

The hot wire probes originally had the wires supported by jewelers broaches which were epoxied onto the sides of a brass stem. However, preliminary investigation (Ref. 5). showed that these probes presented too much interference in the wake region. The probes were redesigned to be very similar to the pitot probes. In the new design (see Fig. 5), the supports were made of 0.007 in. spring steel fed up through a glass tube, .020 in. in diameter. One of the spring steel supports was coated with epoxy to electrically insulate it. The supports were bent apart like a fork, leaving their tips about 0.070 in. apart. The wires themselves were made from 0.00012 in. diameter tungsten wire, copper plated at each end, with an unplated central portion about 0.020 in. in length. Time constants for such wires were about 1/2 millisecond.

The probe drive mechanism was capable of moving the probe in three orthogonal directions (Fig. 6). Probes were normally mounted in the vertical plane, but could be mounted horizontally for limited investigations. Each degree of freedom was fitted with a mechanical counter and a Helipot potentiometer. For convenience in taking flow profiles, the y and z drives were controlled by reversible, variable speed, d.c. motors. A voltage proportional to position was fed into the y axis of the Moseley Autograph X-Y plotter when profiles were being recorded.

When pitot pressure profiles were taken the voltage output from the pressure transducer was fed into the x axis of the Moseley X-Y plotter. Similarly hot wire voltage or mean square voltage fluctuation was fed into the x axis of the plotter when the hot wire was used. The hot wires were operated with a Shapiro-Edwards constant current system. Mean wire voltage was plotted only for the purpose of establishing the negligible effect of the probe on the wake flow. Mean square voltage fluctuation profiles were used to establish the location of wake transition.

3. EXPERIMENTAL RESULTS

3.1 Test Conditions

All tests were performed with the cone very near recovery temperature. Below is a summary of the test conditions, including an estimate of the boundary layer thickness just before separation at the base.

$P_{o\infty}$	T_o	$Re_{\infty d}$	M_{av}	δ_b	δ_b/d
45.0 lbs/in^2	250°F	156,900	4.28	.025 in.	.034
27.0	250°	94,300	4.28	.032	.043
18.0	250°	55,800	4.28	.040	.054
11.9	250°	40,600	4.28	.051	.069

To avoid modifications to the optical control system, a single cone size was tested. The Reynolds number was varied by changing the tunnel stagnation pressure. Tunnel air has a dewpoint of about -70°F, and the stagnation temperature was high enough to avoid air liquefaction.

3.2 Transition location at zero angle of attack

The location of the transition point in the viscous wake was determined from observation of the mean square hot wire voltage fluctuation (a measure of the energy contained in the longitudinal velocity fluctuation). With the hot wire compensated for wake edge conditions, the wake was traversed horizontally and vertically in planes perpendicular to the stream direction at various axial positions downstream of the rear stagnation point. Profiles of mean square voltage fluctuation indicated a maximum signal in the viscous wake at some distance from the centerline. On the centerline of the wake the fluctuation energy was initially very low. Fig. 7 shows the centerline fluctuation energy normalized by the value outside the wake as a function of axial distance from the cone base at several Reynolds numbers. At some definite axial position, determined by the Reynolds number, the fluctuation energy on the wake axis increases rapidly. Behrens (6) has shown, at least for a two dimensional cylinder in supersonic flow at low Reynolds numbers, that the rapid increase in the centerline fluctuation signal is coincident with the first deviation from laminar behavior in the wake. It is reasonable to suppose the same behavior in the viscous cone wake. The conclusion is that, in this investigation, the cone wake is completely laminar in the region of interest at the two lowest Reynolds numbers; but at the two highest Reynolds numbers deviations from laminar behavior should be expected just downstream of the rear stagnation point.

In any event (for all four Reynolds numbers) the flow upstream of the rear stagnation point should be laminar since the separated shear layer is much more stable than the downstream wake.

The instantaneous hot wire signal was observed on an oscilloscope. At the two highest Reynolds numbers, the fluctuations appeared to be quite random. At the two lowest Reynolds numbers discrete frequencies were observed (although the signal amplitudes were much smaller). Fig. 8 shows an oscillation which was present at $Re_{\infty d} = 55,800$ at $x/d = 6$. The frequency is very nearly 1,100 cycles per second. Kendall (7) has reported discrete oscillations in the wakes of cylinders and spheres in supersonic flow. The oscillation has an amplitude distribution across the wake which exhibits a minimum on the wake axis, where the second harmonic is also present. There is little doubt that these oscillations are a result of the instability of the wake flow.

3.3 Pitot Pressure Errors

It is convenient at this point to discuss some of the uncertainties in the pitot pressure data. Fig. 9 shows a typical wake traverse just as it was recorded. To gain more confidence in the measurements, most of the traverses were recorded by driving the probe completely across the wake in one direction and then back again. The deviations between the two traverses can be attributed to several causes. The most important are: backlash in the probe drive machanism (amounting to about .007 in.), hysteresis effects in the pressure transducer, and model position drift. The deviations are generally much less than the absolute error estimate for the pitot measurements, which is indicated in the figure. For this reason, most of the subsequent presentations will show a single trace which represents an average of the two.

The absolute uncertainty in the pitot measurements is about ±2.8 percent of the free stream pitot pressure. In the inviscid portions of the wake, this represents an error in Mach number of about ± 1 percent. In the viscous portions of the wake where the pitot pressure is small, the error is significant.

No Reynolds number correction was applied to the data. For the lowest free stream Reynolds number tested, the correction would not be more than about 1 percent anywhere in the supersonic portion of the flow. Near the wake stagnation point, the local Reynolds number (based on probe diameter) can be of order unity for the present test conditions. Reynolds number corrections would be large in this region.

3.4 Wake Symmetry

At zero angle of attack, the horizontal and vertical pitot profiles should be symmetrical about the cone axis Fig. 10 shows horizontal and vertical traverses at $x/d = .75$ and $x/d = 4.5$, with one half of each traverse transposed about the axis to facilitate comparison. In general the agreement is good. The results at $x/d = 4.5$ suggest that the wake centerline is displaced slightly from the cone axis in the vertical plane. In addition there is some asymmetry in the viscous portion of the wake. These results are typical.

The horizontal and vertical profiles should also be indistinguishable from each other when the cone is aligned with the flow. Fig. 11 shows the superposition of typical horizontal and vertical profiles at two downstream locations. The agreement is again good but becomes progressively poorer in the outer portions of the wake as the distance from the cone increases. Most of the differences can be explained by non-uniformities present in the empty jet, and by the fact that the wake is affected in the horizontal plane by disturbances which propagate in from the edge of the jet. Thus at $x/d = 4.5$, the bow shock reflection (which becomes an expansion) and also the reflection of the cone base expansion (which becomes a compression) are noticeable in the horizontal profiles. In the vertical plane, the jet dimension is larger, and such reflections always occur downstream of the region of interest.

3.5 The Near Wake at Zero Angle of Attack

Pitot pressure measurements provide a convenient means of determining the geometry of the near wake. Fig. 12 presents a near wake map at a Reynolds number of $Re_{\infty d} = 40,600$. The pitot pressure data from which the map was constructed is shown in Fig. 13. Several features may be mentioned.

The strong corner expansion at the base of the cone is followed by a shock - the lip shock. The origin and strength of the lip shock has been the subject of recent investigation (8). This shock is clearly evident in Fig. 13 although it is a very weak disturbance. From a knowledge of the Mach number ahead of the lip shock and the pitot pressure gain across it, the stagnation pressure loss can be shown to be much less than 1 percent. The lip shock appears to originate in the free shear layer downstream of the base, since it is not present at the station closes to the cone (a distance less than a boundary layer thickness downstream).

In the recirculation region at the base of the cone, the pitot probe is not aligned (even approximately) with the local flow direction. Pitot pressure measurements in this region do not have much significance except as a rough indication of the extent of the recirculation region which appears as a region of relatively constant pitot pressure. Using this criterion, pitot measurements indicate the rear stagnation point to be about 3 1/2 diameters downstream. At higher Mach numbers and lower wall temperatures, many investigators have placed the rear stagnation point about one diameter downstream. This indicates a strong Mach number influence on the length of the recirculation region as, perhaps, one might expect. The outer inviscid flow near the rear stagnation point returns smoothly to the free stream direction without the formation of a wake shock -- although such a shock must eventually appear as a result of the confluence of compression waves.

At the highest Reynolds number tested ($Re_{\infty d} = 156,900$), the wake geometry is qualitatively similar, but an examination of the data reveals several Reynolds number effects. Fig. 14 is a plot of minimum wake width (determined from pitot measurements and hot wire fluctuation measurements) versus Reynolds number. A line representing laminar dependence, $\frac{\delta_M}{d} \propto \frac{1}{\sqrt{Re_{\infty d}}}$ is shown. As expected from previous discussion of wake transition, the wake deviates from laminar

behavior at the two highest Reynolds numbers. This deviation is perhaps most strikingly illustrated by the difference in pitot pressure along the wake axis. Fig. 15 gives the normalized pitot pressure along the wake axis as a function of axial position for several Reynolds numbers. At the two highest Reynolds numbers, where the wake is no longer laminar, the pitot pressure rises very rapidly. Judging from the pressure rise, the rear stagnation point appears to about 3 diameters downstream. For the laminar flow at $Re_{\infty d} = 40,600$, the pitot pressure rise is four or five times smaller at 5 1/2 diameters from the cone base. The rear stagnation point is difficult to estimate, but a position about 3 1/2 to 4 diameters downstream is consistent with observation of the pitot profiles. The pressures recorded with the probe within the recirculation region are very inaccurate, but they can be taken as an indication of the base pressure. The trend of higher pressure in the recirculation region at lower Reynolds numbers is consistent with the increased recirculation region length.

3.6 The Near Wake at Angle of Attack

If the cone was angulated even slightly, an interesting effect appeared downstream. Fig. 16 shows a horizontal pitot pressure traverse taken in the viscous portion of the laminar wake six diameters downstream at an angle of attack of just −.4 degree (the cone was pitched nose down). In the horizontal plane, two off-axis minima appear in the profile. The vertical profile still has a single minimum. This seems to indicate that the wake is bifurcated in the horizontal plane as a result of cone angulation. Of course, one might anticipate such behavior eventually, but it is a little surprising that such a small angle of attack would produce a wake which was bifurcated. (Since the error in cone angle of attack could be as much as ±.2 degree, the procedure for determining zero angle of attack was first to align the cone with the nozzle axis as accurately as possible, and then, to angulate the cone slightly while running until a wake without bifurcation was produced.)

It may be noticed that the pressure probe lies in the vertical plane. To examine the possibility that bifurcation was caused by the probe itself,

and not by slight cone inclination, the probe was inserted into the wake from the side -- that is, in the horizontal plane instead of the vertical plane. The results of this investigation are shown in Fig. 17. The pitot pressure profiles for the two cases are not completely repeatable (due to the difficulty of setting an arbitrarily small angle of attack), but the conclusion is unmistakable. The pressure probe does not cause bifurcation.

When the cone angle of attack was increased to about - 1 1/2 degrees, the bifurcation increased. Figure 18 shows horizontal and vertical pitot profiles recorded at various distances downstream of the cone base. (The vertical profiles were recorded in the vertical plane through the wake centerline; while the horizontal profiles were recorded at a vertical position half way between the top and bottom of the viscous wake. The position of the center of the cone base is indicated by $y = z = 0$.) Horizontal profiles, which should be well upstream of the rear stagnation point, e.g., $x/d = 2.5$, also exhibit two minima. This suggests that the recirculation region is also bifurcated. To see how such an effect might arise, it is helpful to examine the streamlines over a cone at a small angle of attack. A qualitative picture is presented in Fig. 19. Both the inviscid streamlines and the streamlines (in the boundary layer) nearest the surface are shown for the cone at a negative angle of attack. The circumferential velocity, from top to bottom, which exists near the cone surface must also exist in the flow downstream of the base. The most reasonable structure for the recirculation region is one composed of two cells with two separate rear stagnation points. Fig. 20 shows such a bifurcated recirculation region schematically, although the swirl has been exaggerated. This picture can be contrasted to the purely axisymmetric recirculation region also shown.

Figs. 21 and 22 give horizontal and vertical pitot pressure traverses at cone inclinations of -3, and -4 1/2 degrees, respectively.

Next to bifurcation the most striking feature (in Figs. 18, 21, 22) is the asymmetry in the vertical plane. There is a region of very high shear at the top of the viscous wake which does not seem to diminish in

intensity with increasing downstream distance. On the bottom, or leeward side of the wake, the viscous region is much thicker. This behavior can be explained qualitatively by returning again to the boundary layer flow on the cone.

Moore (9) has shown analytically that the effect of angle of attack is to thin the boundary layer on the windward side, and thicken the boundary layer on the leeward side. This is physically reasonable since there is a flow within the boundary layer from windward to leeward. It is not surprising (but comforting) that this effect appears also in the wake.

Generally, inclination appears to produce stronger radial gradients in the inviscid portions of the flow bordering the viscous wake. The lip shock also becomes more pronounced in the vertical plane, although on the leeward side, it forms much farther downstream.

Between 4 1/2 degrees and about 5 1/2 degrees angle of attack, another interesting effect occurs. This can be illustrated by the horizontal and vertical traverses shown in Fig. 23. The horizontal profile now has four minima instead of two, and the vertical profile is very complicated also. This structure is believed to be caused by the separation of two vortices from the leeward surface of the cone, Fig. 24. The two vortices apparently lie close enough to the wake to produce a significant interaction.

The cone angle of attack at which these vortices are first shed is consistent with calculations by Moore (10). He predicts, for a Mach number of about four, that the vortices will first form at an angle of attack which is about 80 percent of the cone semi-vertex angle. In our case this number is about 5.6 degrees.

Such a sketchy description of the effects of angle of attack leaves much to be desired. What is really wanted, of course, is a quantitative determination of wake properties at angle of attack. This would require the measurement of additional fluid properties (a future objective), but several rough comparisons can be made using the present data. Fig. 25 presents the minimum pitot pressure as a function of downstream position for several angles of attack. Pitot pressure errors are large in this region,

but at the farthest downstream position the data seems to be "sorting out", with pitot pressure increasing more rapidly at the larger angle of attack. It is also fair to say that angles of attack up to 4 1/2 degrees have little effect on the length of the recirculation region. Fig. 26 gives a plot of the pitot pressure "jump" at the wake axis as a function of angle of attack for several downstream positions. The purpose of this figure is to indicate, roughly, the sensitivity of wake bifurcation to angle of attack. Looking at the slopes, it can be said that wake bifurcation is at least as sensitive to angle of attack at very small angles as it is at larger angles, and perhaps more sensitive.

Three independent measurements are needed to determine flow properties at a point. In the inviscid portions of the flow, it is a good approximation to assume constancy of stagnation temperature and pressure since the lip shock is negligibly weak, and the wake shock has not yet formed. Thus outside the viscous portions of the wake, the pitot pressure is sufficient to determine flow properties with reasonable accuracy. To obtain a first estimate of the effects of angle of attack, it could also be assumed that the stagnation temperature is constant everywhere, and that the static pressure is uniform across the viscous wake and equal to its value at the wake edge.

Figure 27 presents flow properties, which have been calculated with the above assumptions, at $x/d = 4.5$ for zero cone angle of attack and for an angle of attack of $-1\ 1/2$ degrees. The results indicate that the temperature field is most strongly affected by cone angulation, with differences amounting to about 25 percent near the cone axis. Note however that the maximum temperature is not reduced due to angulation -- at least at this location. Mach number differences are about 25 percent also, while differences in velocity are less.

3.7 Summary

It has been demonstrated that a magnetic support system can be used to obtain reliable data behind suspended models. The measured pitot pressure in the laminar, viscous wake increases very slowly with downstream distance, which indicates that a significant momentum defect

and a high temperature will probably persist far downstream. This situation is contrasted to the blunt body case, in which the favorable pressure gradient created by the strong bow shock produces additional accelerations along the wake axis which rapidly eliminate defects in the viscous wake.

The laminar wake is very sensitive to small cone inclinations. The wake bifurcates at any angle of attack different from zero. Flow properties in the near wake are noticeably affected by cone angulations as small as .4 degree. It is impossible at this time to make a critical assement of the importance of wake bifurcation, but further investigation seems warranted. Differences in wake properties produced by bifurcation could be even more exaggerated if the transition location is significantly affected. Thus for slender bodies subject to small angles of attack, it may not be adequate to use an axisymmetric theory to predict wake properties. If this is true, the hope of determining wake properties analytically is remote indeed.

REFERENCES

1. Levensteins, Z.J. and Krumins, M.V., "Experimental Study of Aerodynamic Characteristics of Hypersonic Wakes," AIAA Paper No. 66-53.

2. Bailey, A.B., "Effect of Unit Reynolds Number on Transition in the Wakes of High Speed Sharp Slender Cones," AEDC-TR-66-137 (July 1966).

3. Wilson, L.N., "Body Shape Effects on Axisymmetric Wakes: Transition", AIAA J, Vol. 4, No. 10 (October 1966).

4. Tilton, E.L., Parkin, W.J., Covert, E.E., Coffin, J.B. and Chrisinger, J.E., "The Design and Initial Operation of a Magnetic Model Suspension and Force Measurement System," J of Roy. Aero. Soc., Vol. 67, p 717 - 744 (1963)

5. Browand, F.K., Finston, M., and McLaughlin, D.K., "Some Preliminary Measurements Behind Cones Magnetically Suspended in a Mach Number 4.3 Stream," MIT Aerophysics Lab. Technical Report 132 (October 1966).

6. Behrens, W., "Flow Field and Stability of the Far Wake Behind Cylinders at Hypersonic Speeds," AIAA Paper No. 67-32.

7. Kendall, J.M., Jr., "Experimental Study of Cylinder and Sphere Wakes at a Mach Number of 3.7", JPL Technical Report 32-363 (November 1962).

8. Hama, F.R., "Experimental Studies on the Lip Shock," AIAA Paper No. 67-29.

REFERENCES (cont'd.)

9. Moore, F.K., "Laminar Boundary Layer on a Circular Cone in Supersonic Flow at Small Angle of Attack", NACA TN 2521 (October 1951).

10. Moore, F.K., "Laminar Boundary Layer on Cone in Supersonic Flow at Large Angle of Attack", NACA TN 2844 (1952)

ACKNOWLEDGEMENTS

This research is supported by the Air Force Office of Scientific Research under contract number AF 49(638)-1328. The Project Officer is Lieutenant Colonel George Stalk.

The magnetic balance system was developed under the sponsorship of the United States Air Force Aerospace Research Laboratories under contract numbers AF 33(616)-7023 and AF 33(615)-1470.

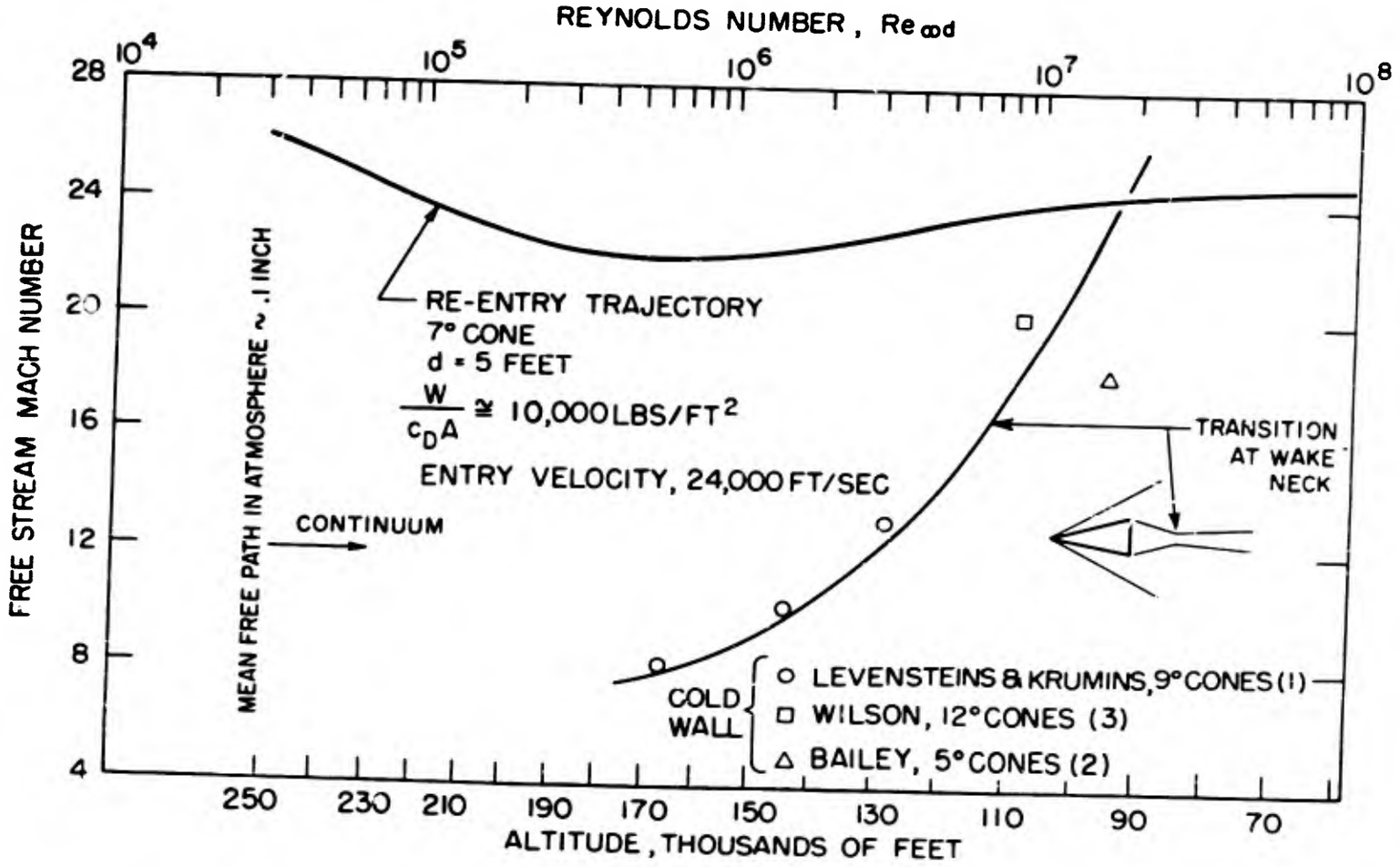

Fig. 1. Typical Reynolds number, Mach number history for a slender reentry vehicle.

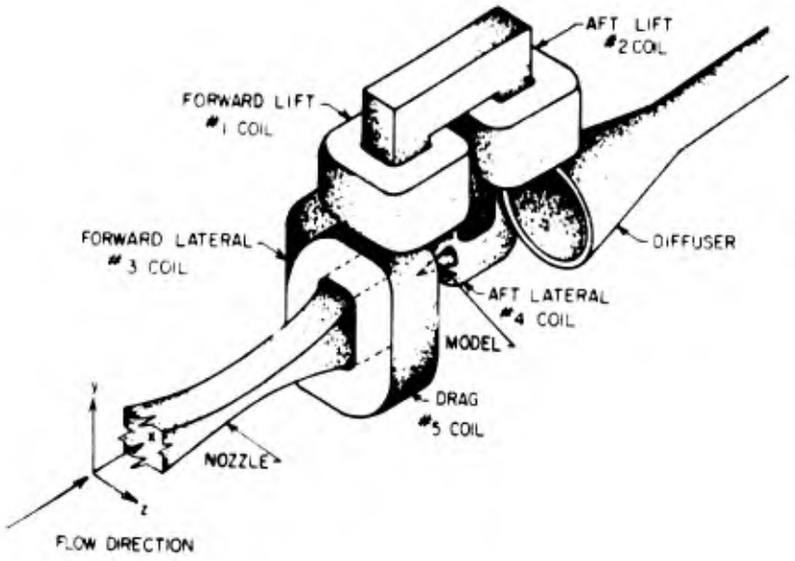

Figure 2. Schematic of the magnetic suspension system

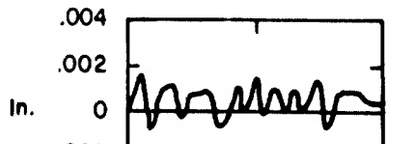

Figure 3. Time history of horizontal translation during wind tunnel run

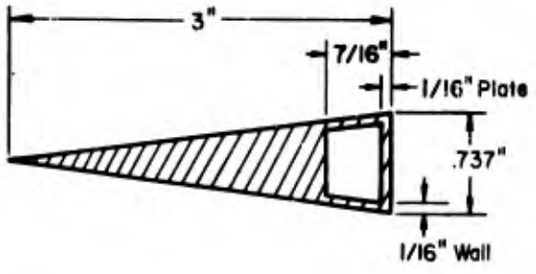

Figure 4. Cross section of cone model

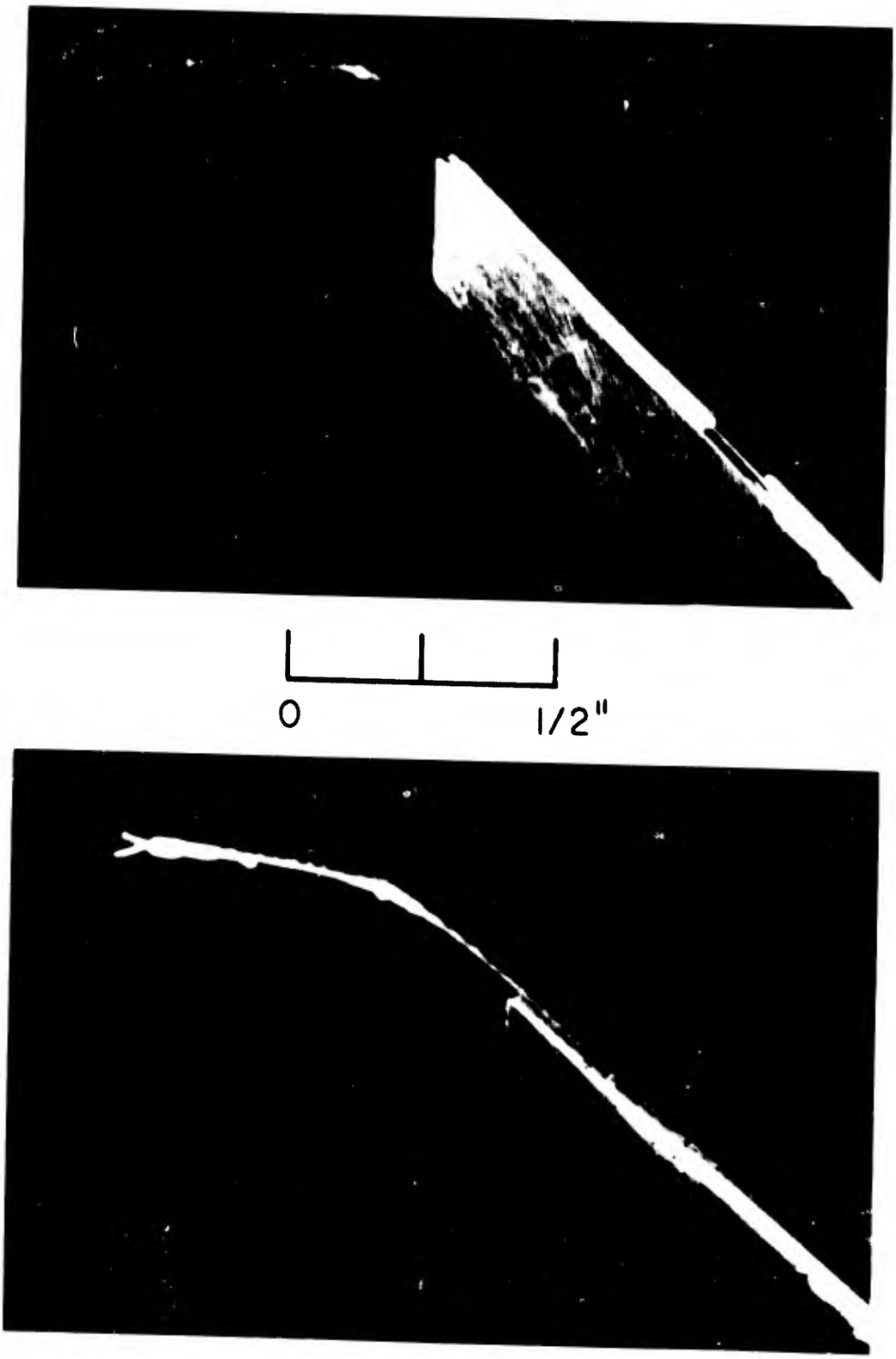

Fig. 5. Pitot pressure probe (upper) and hot wire probe (lower).

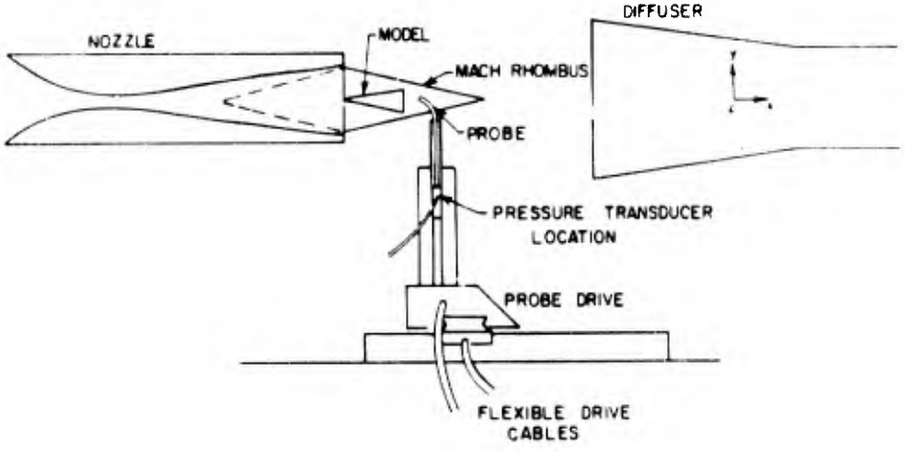

Figure 6. Schematic of test section and probe drive

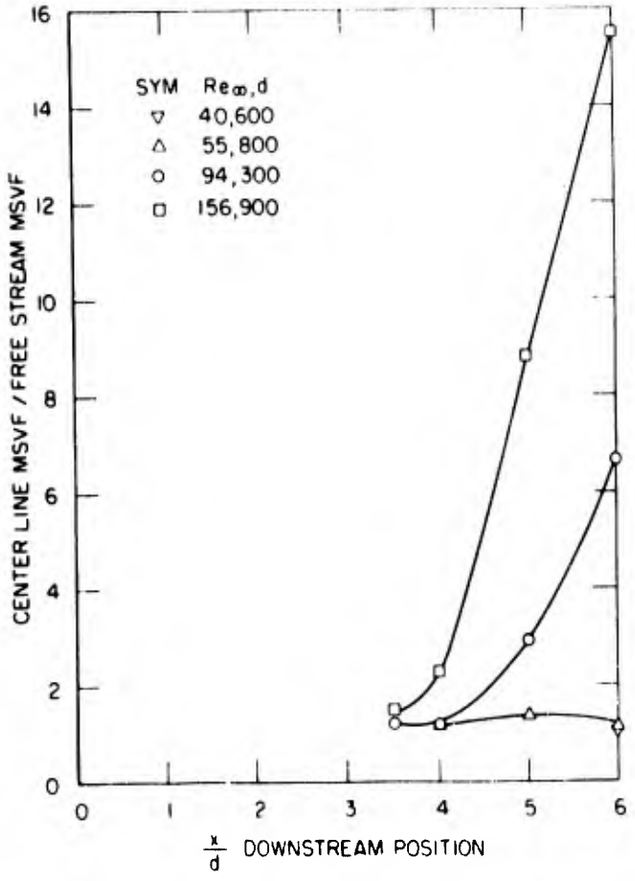

Figure 7. Centerline mean square voltage fluctuation versus downstream position

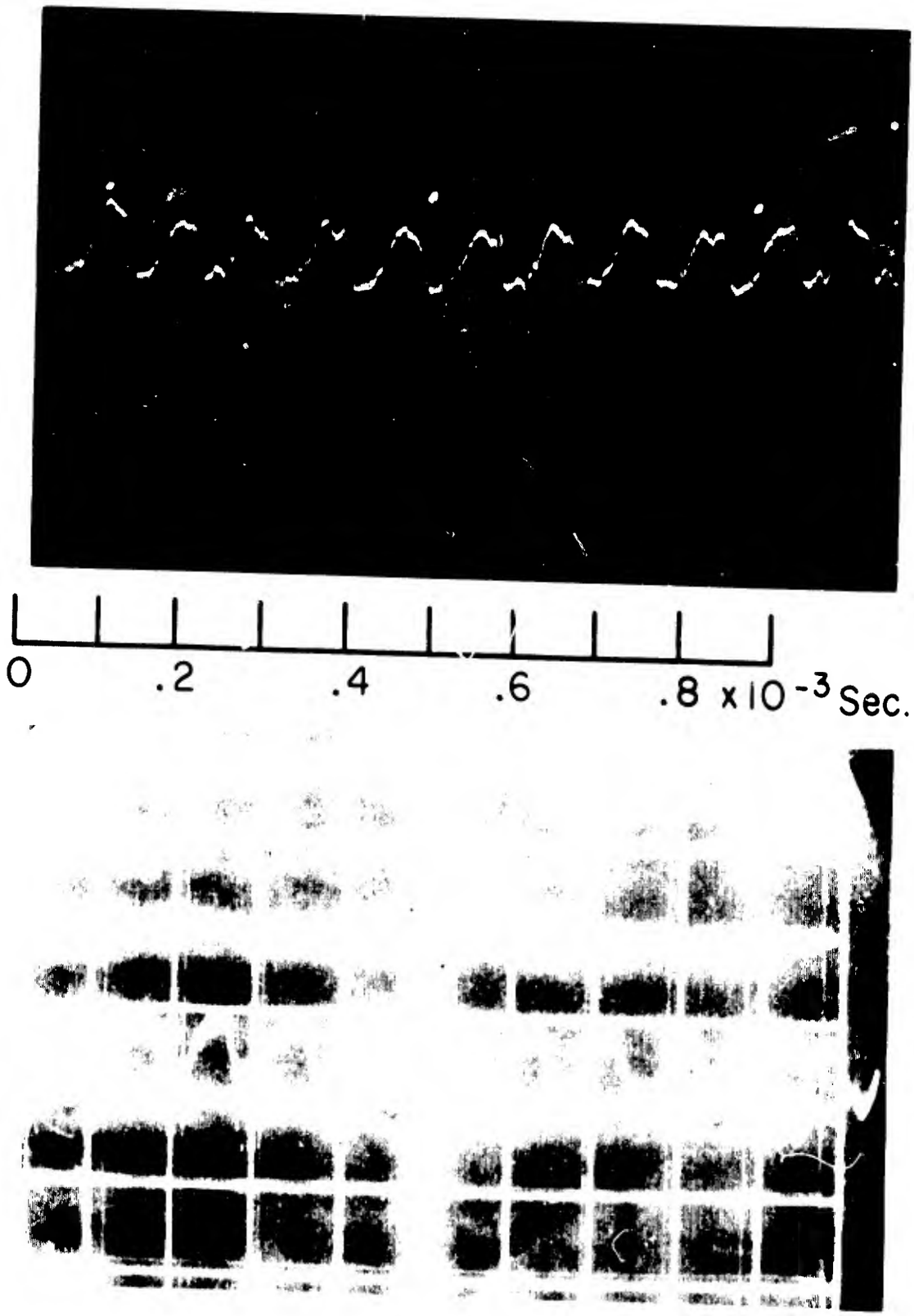

Fig. 8. Oscilloscope traces of mean hot wire voltage oscillation.

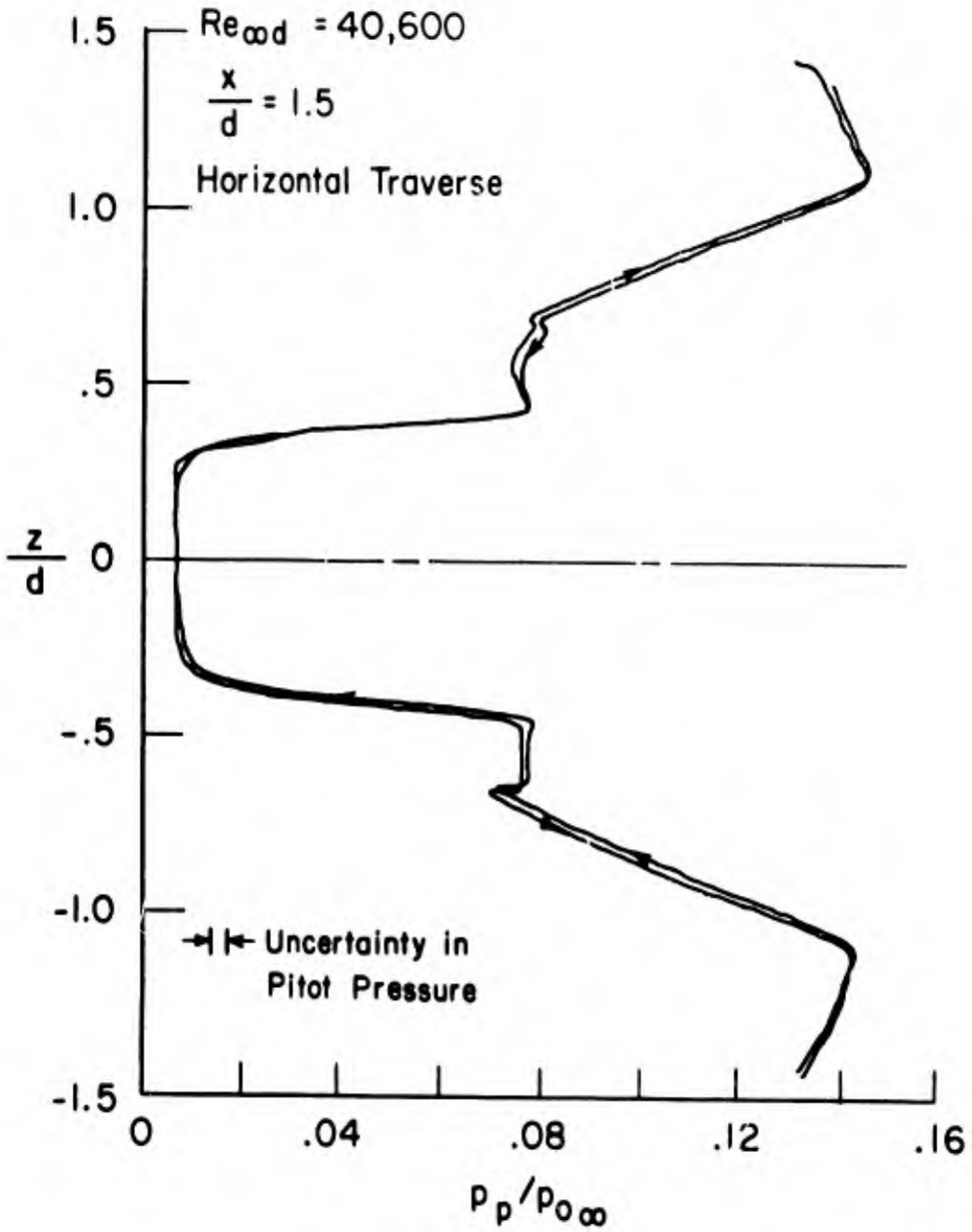

Figure 9. Typical wake traverse

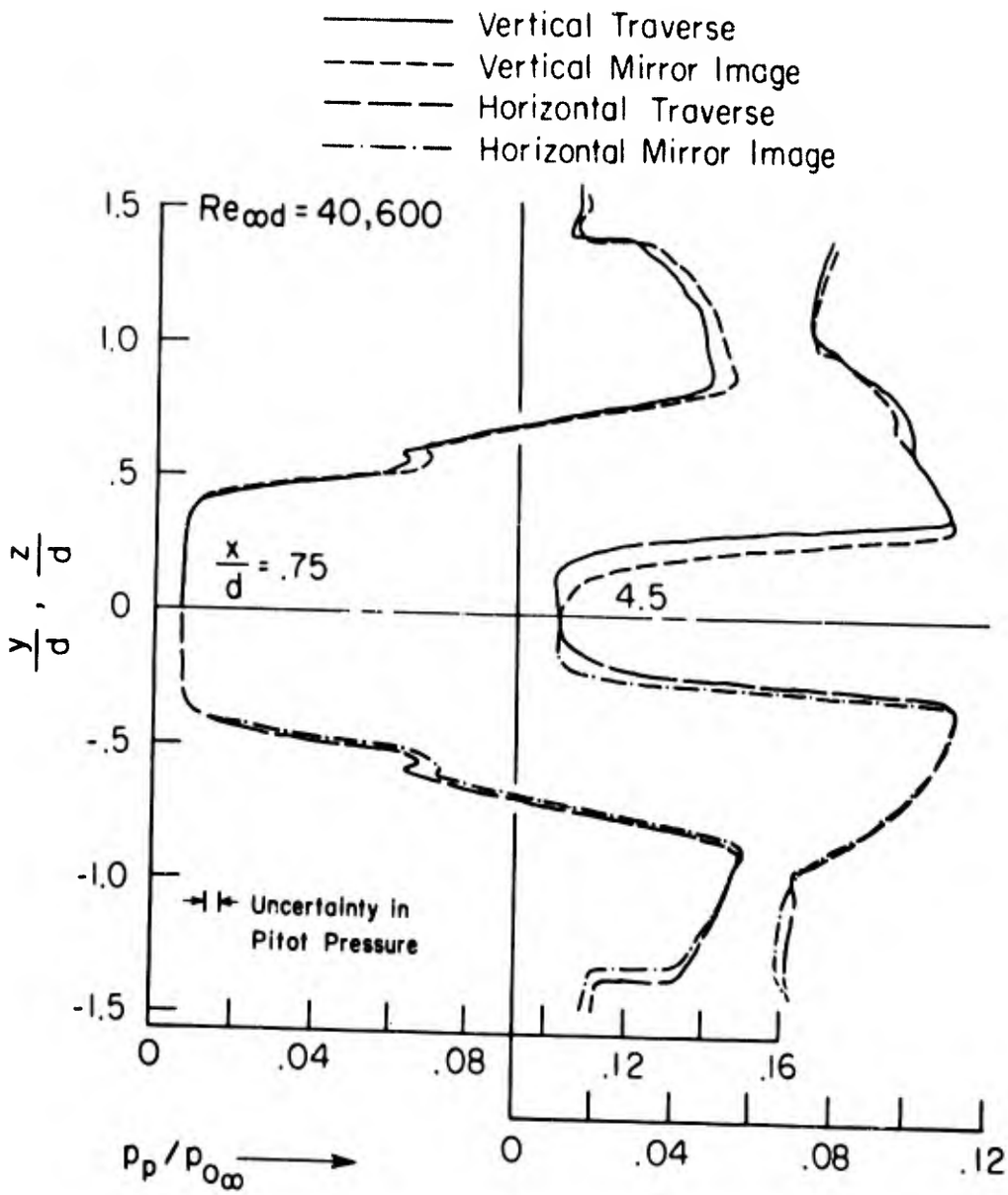

Figure 10. Horizontal and vertical traverses compared with their mirror images

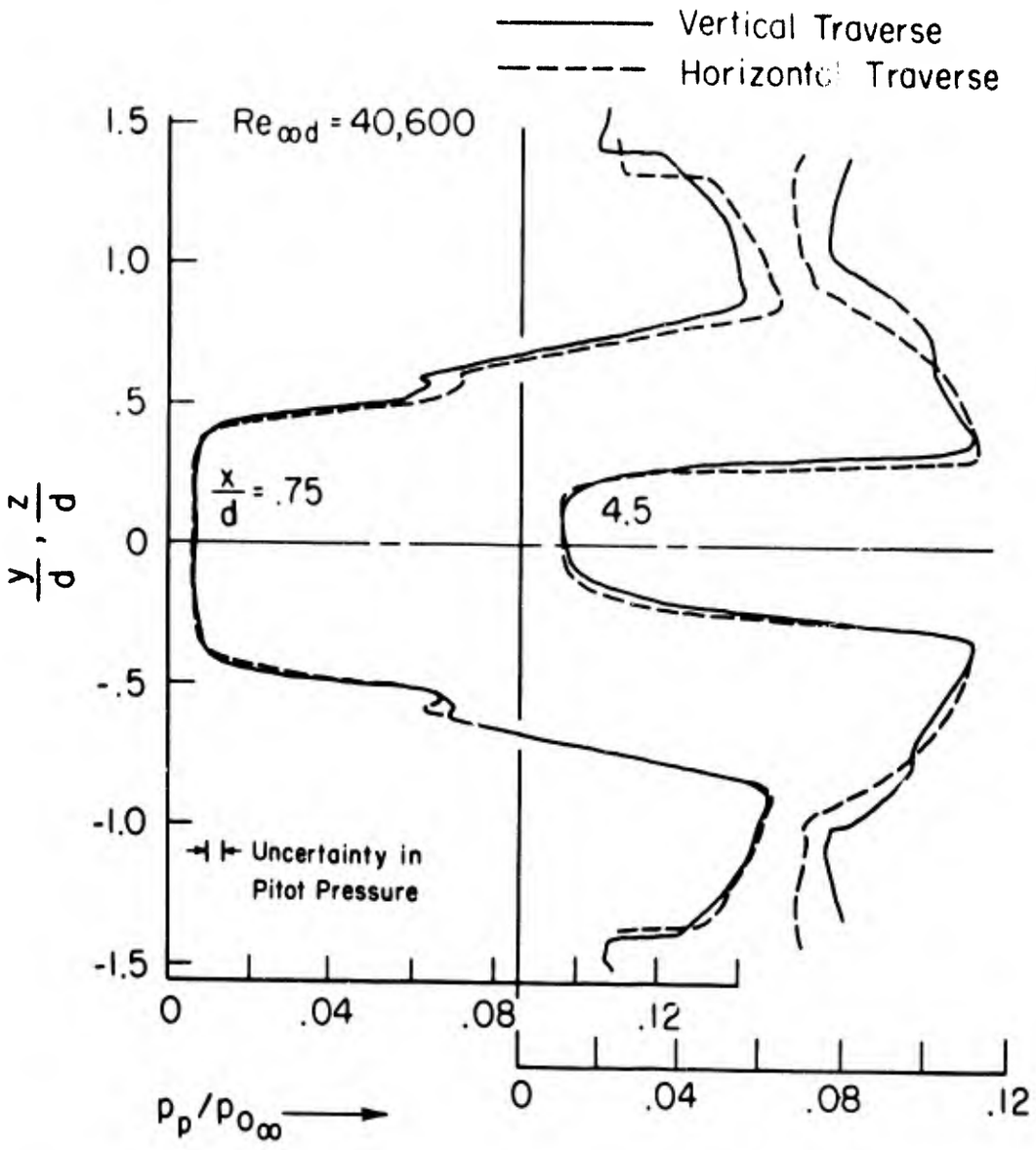

Figure 11. Comparison of horizontal and vertical traverses

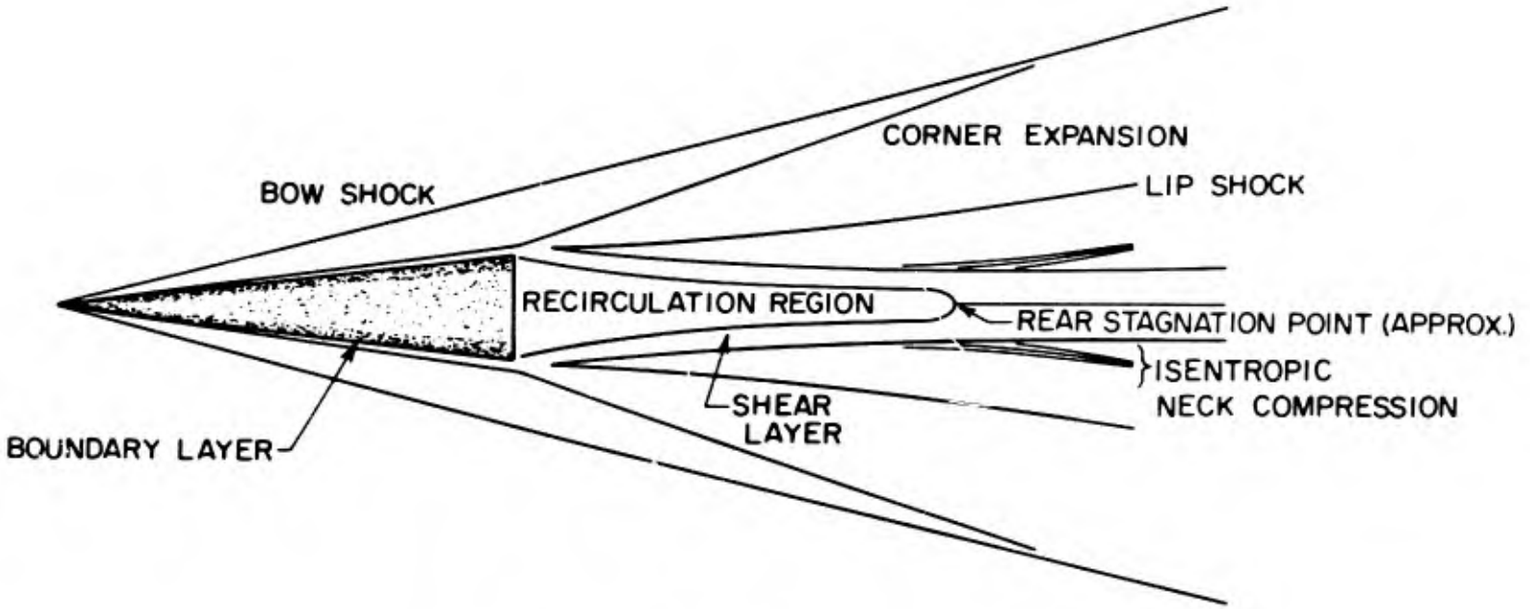

Fig. 12. Near wake map at $Re_{\infty d} = 40,600$

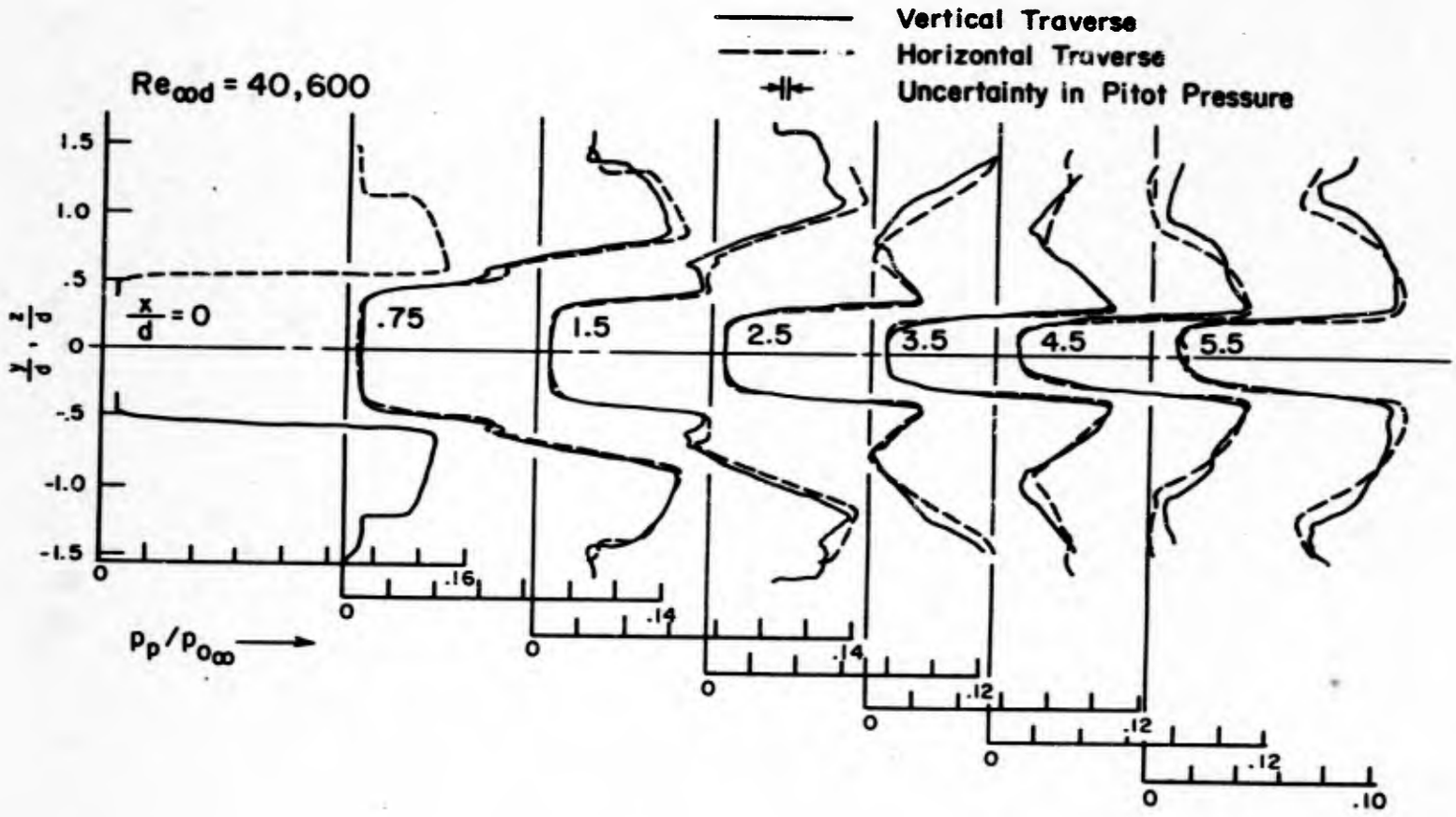

Figure 13. Pitot pressure profiles at zero angle of attack

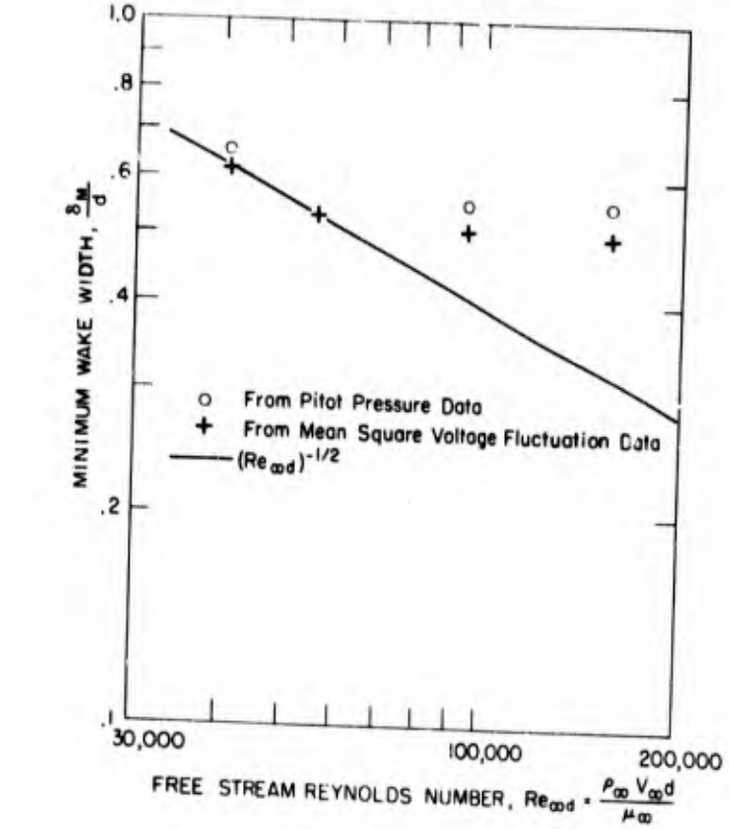

Figure 14. Minimum wake width versus Reynolds number

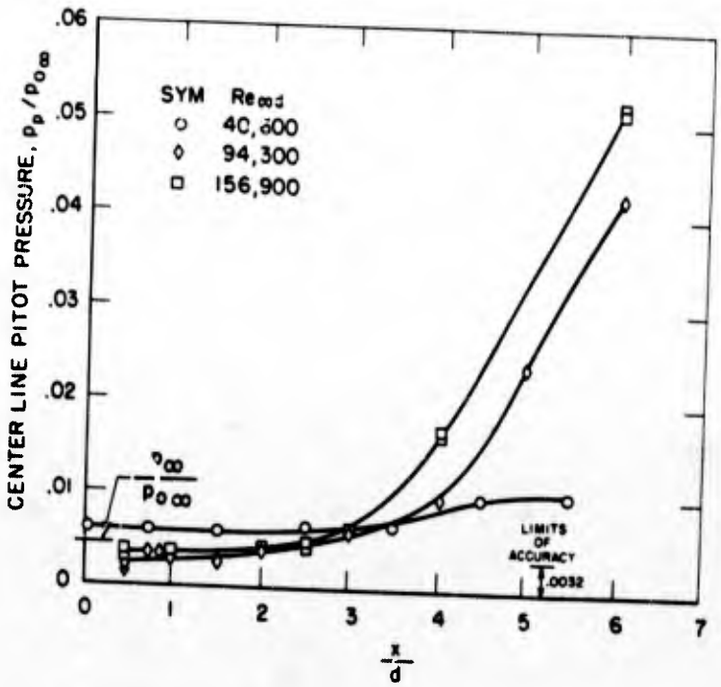

Figure 15. Axial pitot pressure variation

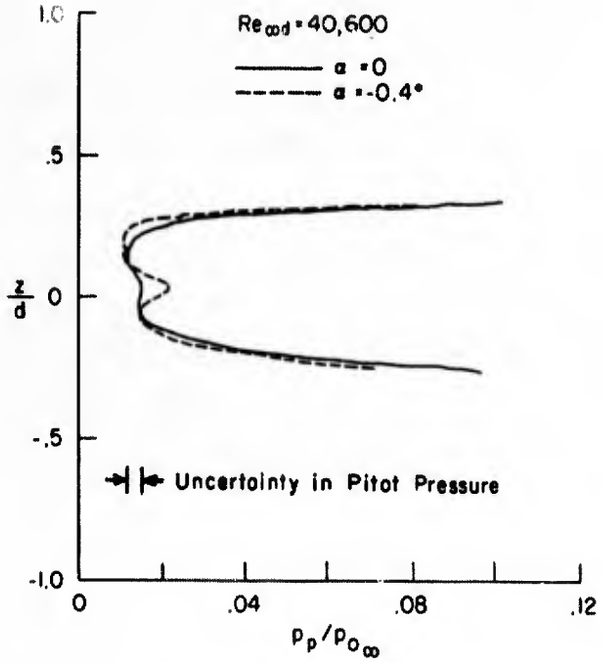

Figure 16. Horizontal pitot pressure traverse at small angle of attack

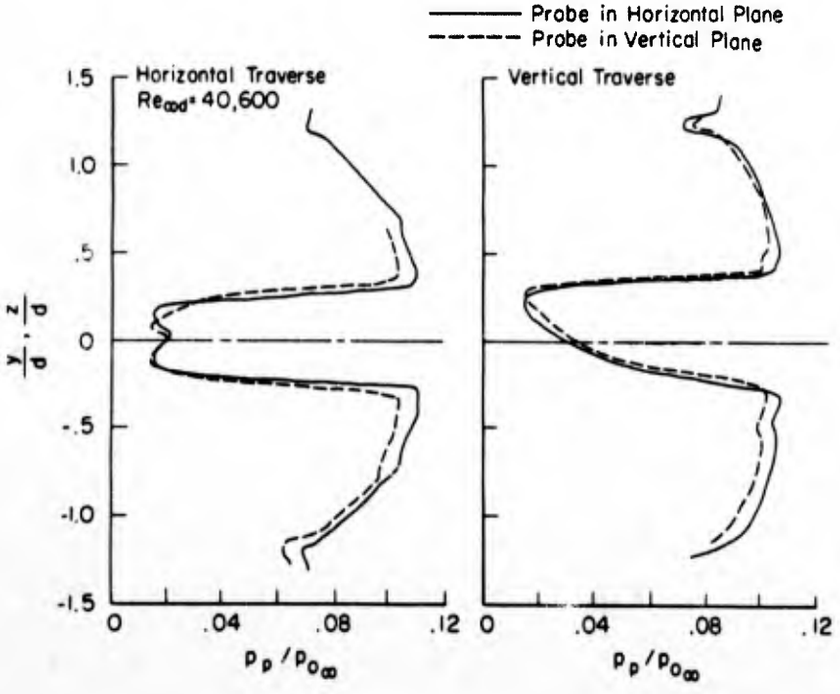

Figure 17. Comparison of pitot pressure profiles measured with horizontally and vertically mounted probes

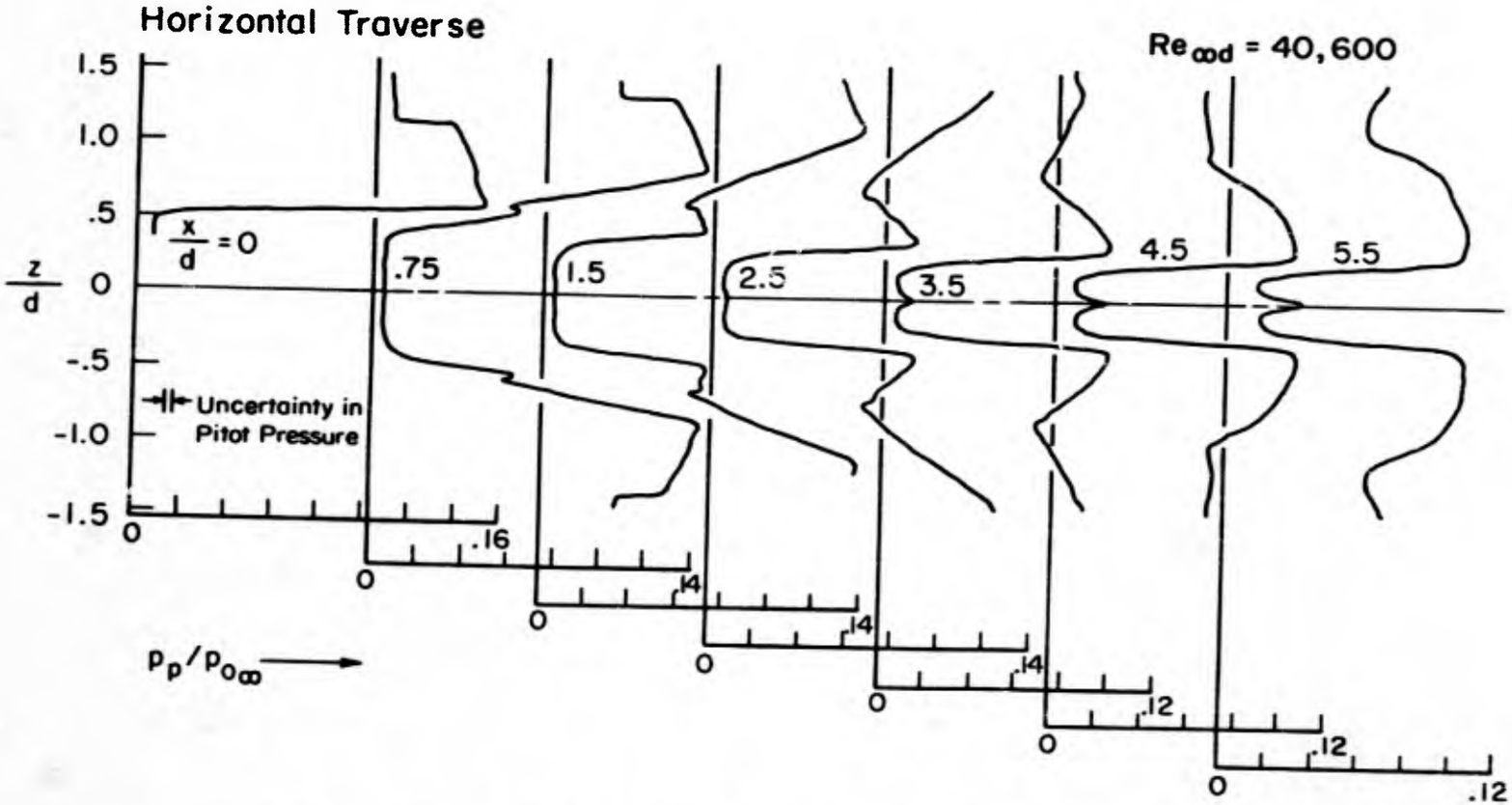

Figure 18a. Pitot pressure profiles at -1 1/2 degrees angle of attack

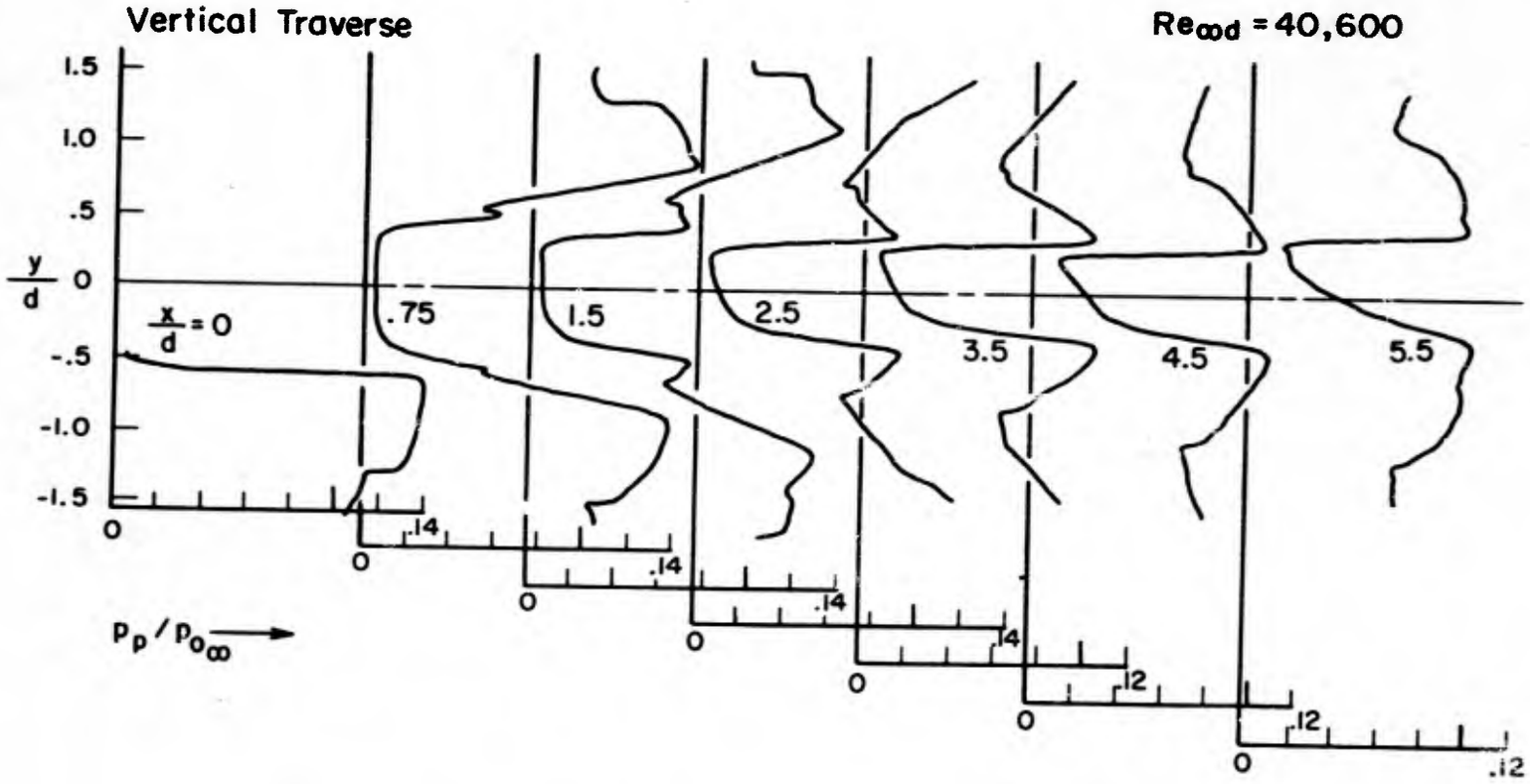

Figure 18b. Pitot pressure profiles at -1 1/2 degrees angle of attack

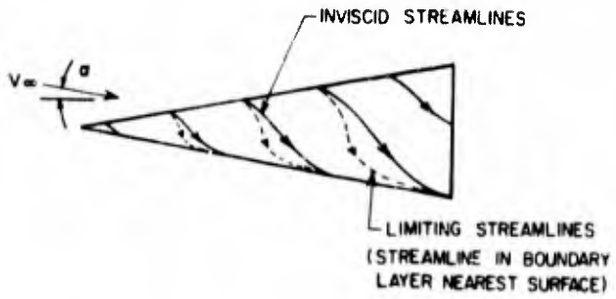

Figure 19. Streamlines over a cone at angle of attack

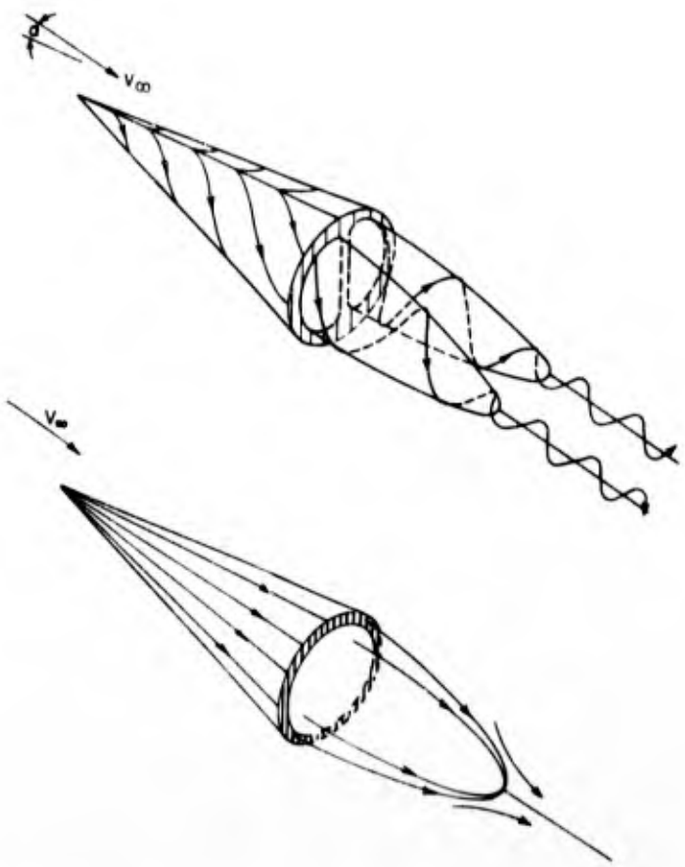

Figure 20. Structure of the recirculation region at small angle of attack

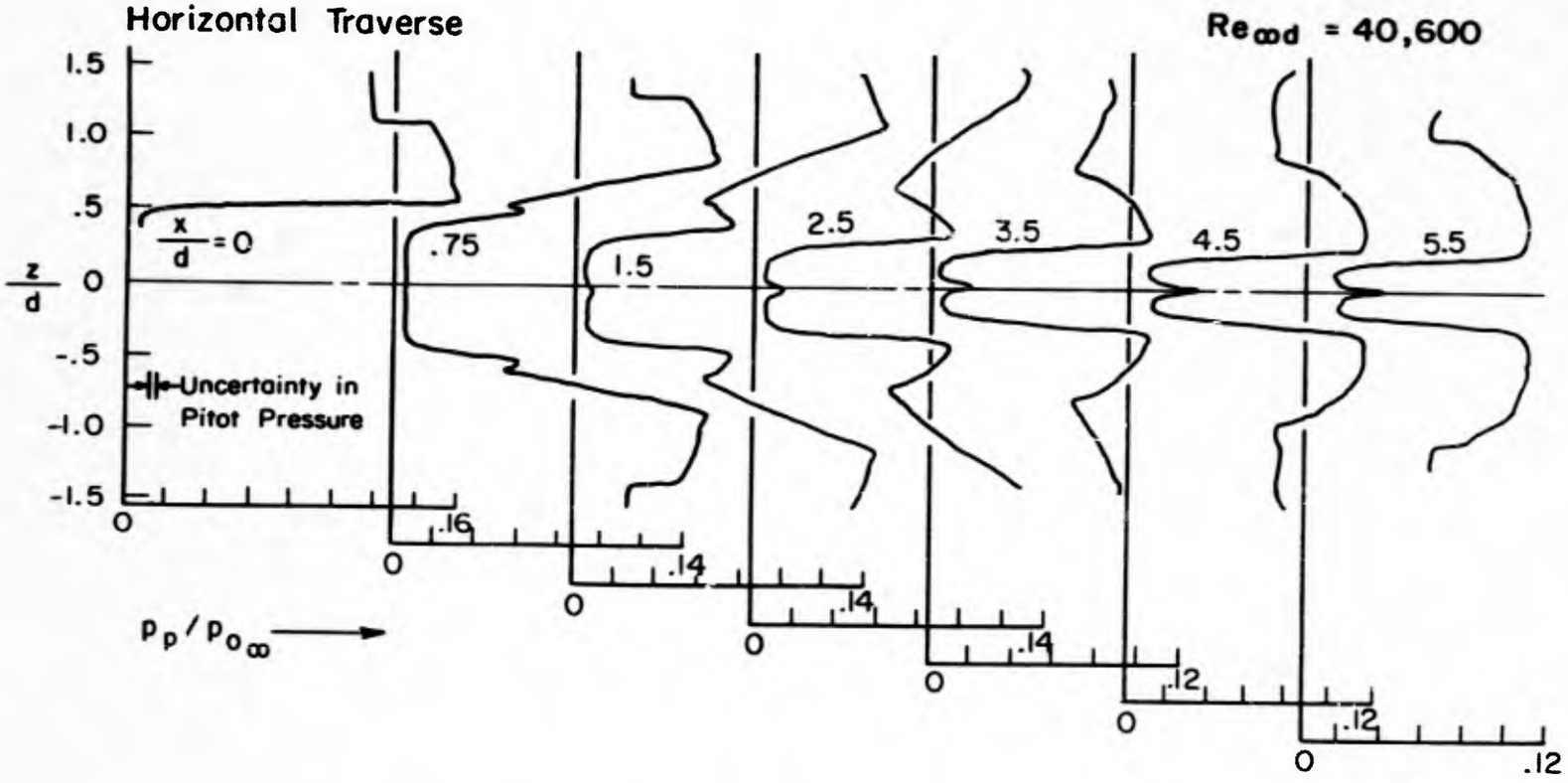

Figure 21a. Pitot pressure profiles at -3 degrees angle of attack

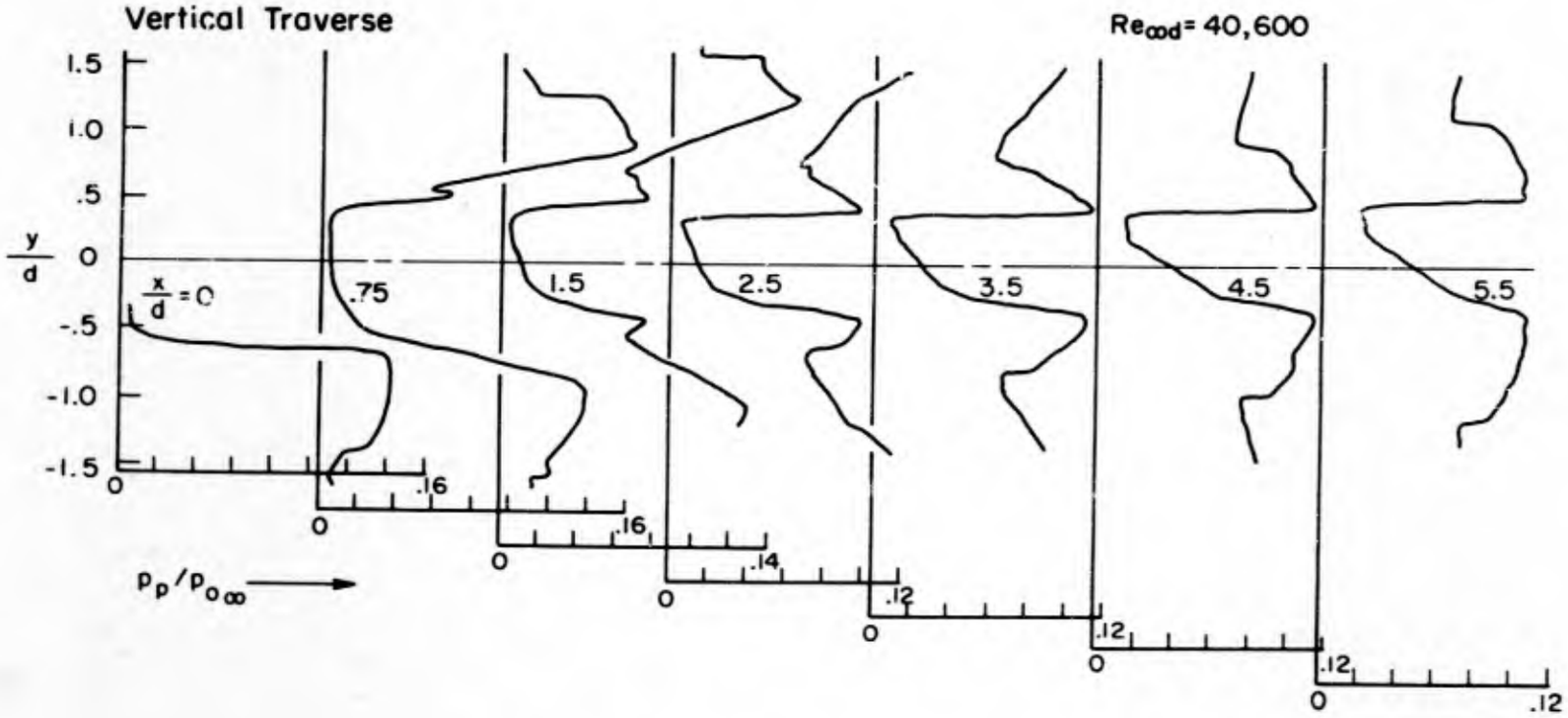

Figure 21b. Pitot pressure profiles at -3 degrees angle of attack

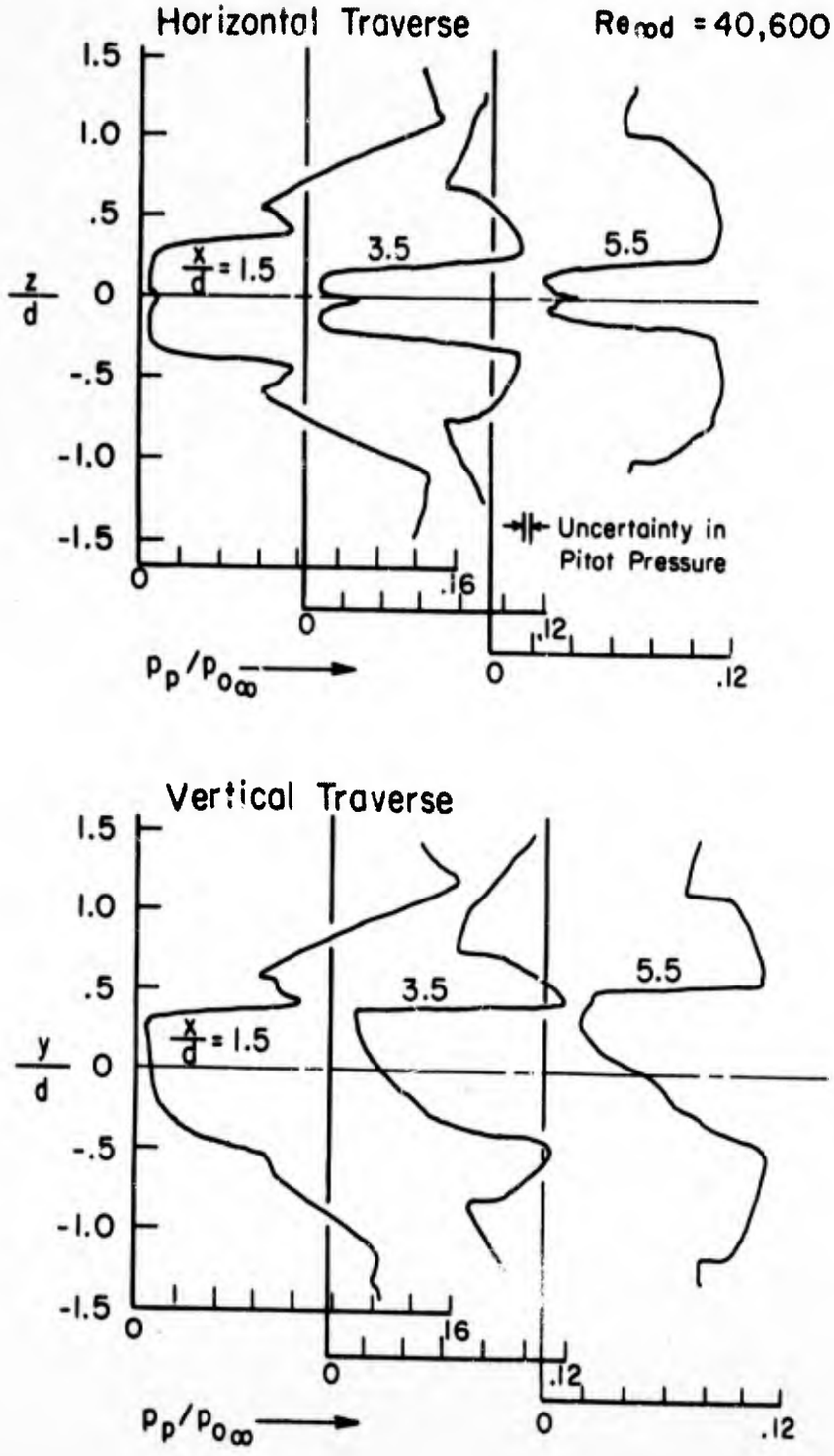

Figure 22. Pitot pressure profiles at -4 1/2 degrees angle of attack

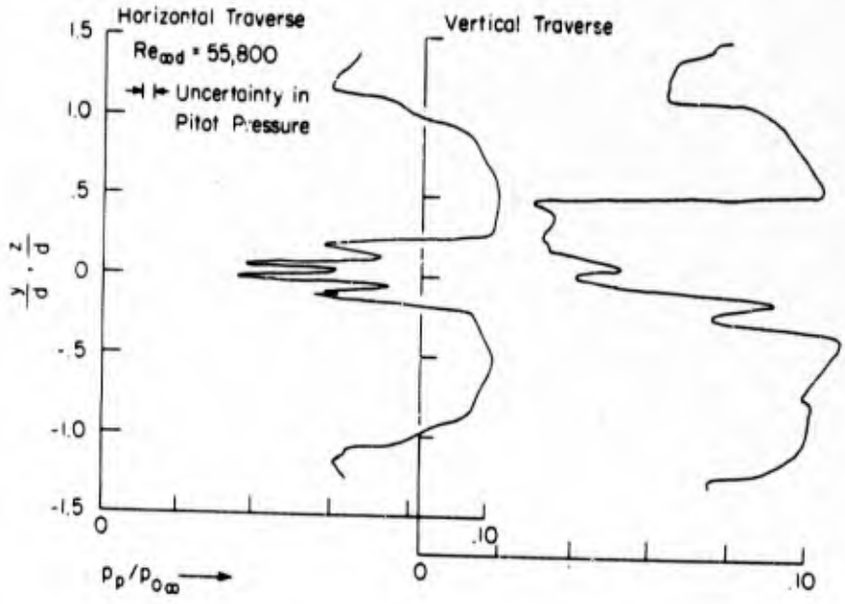

Figure 23. Pitot pressure profiles at -5 1/2 degrees angle of attack

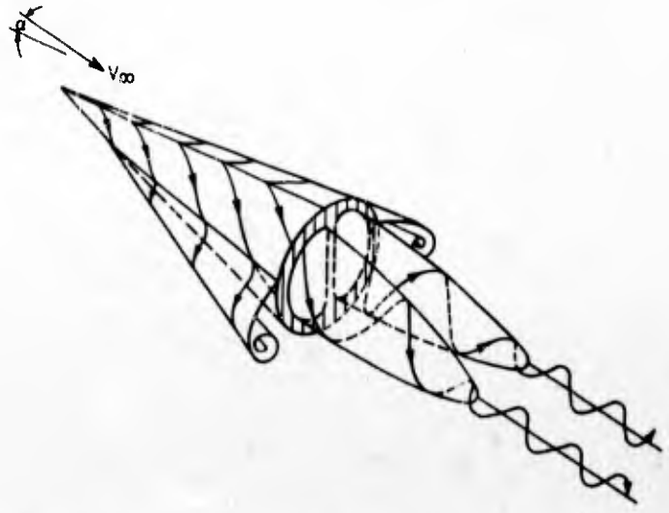

Figure 24. Structure of wake flow at -5 1/2 degrees angle of attack

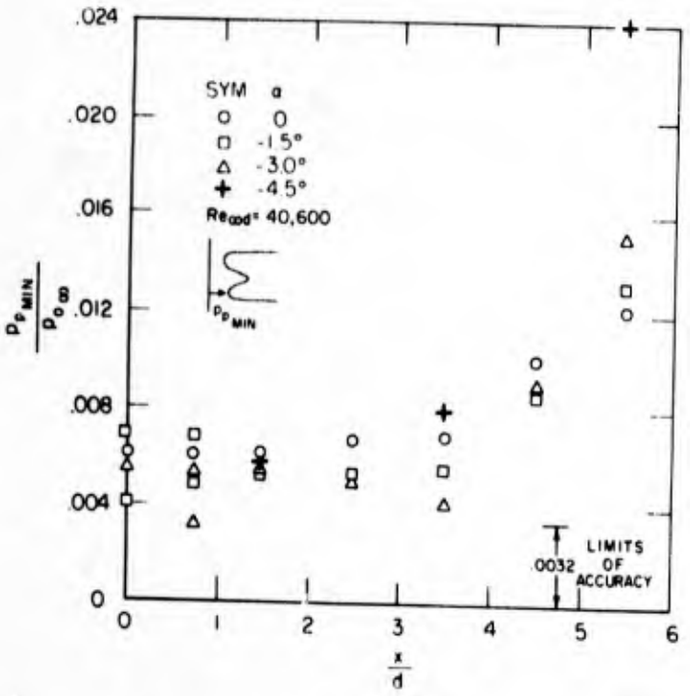

Figure 25. Minimum pitot pressure versus downstream position showing effect of angle of attack

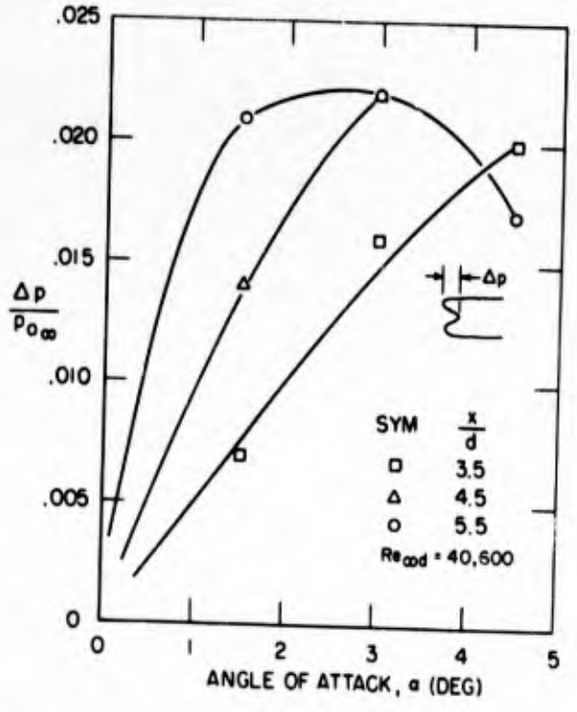

Figure 26. Pitot pressure "jump" versus angle of attack

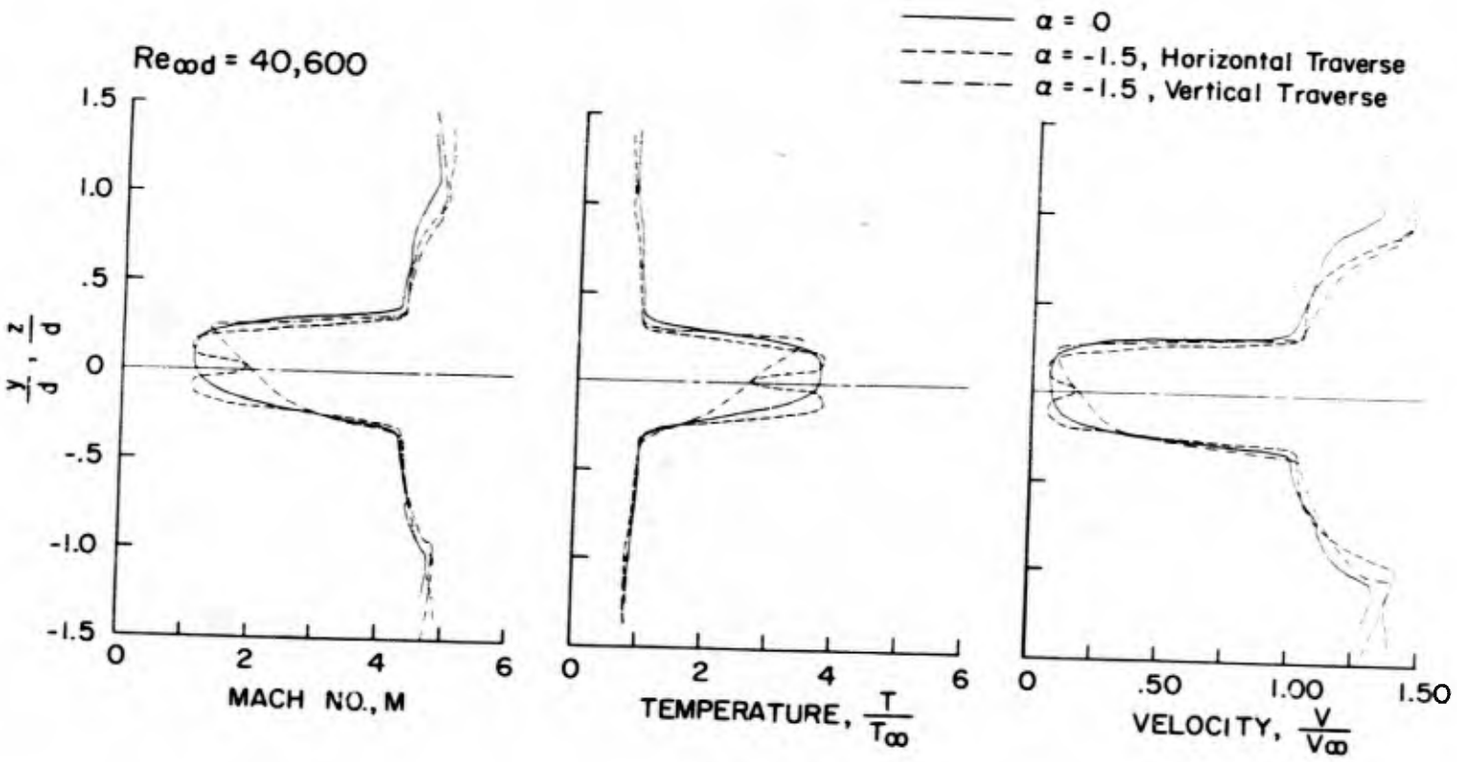

Figure 27. Calculated flow properties x/d = 4 1/2

BLANK PAGE

ANALYSE EXPERIMENTALE DU PROCHE SILLAGE D'UN CORPS ELANCE LIBRE DE TOUT SUPPORT LATERAL

par

M. Sirieix et J. Delery

ONERA, France

RESUME

Pour procéder en soufflerie à l'analyse expérimentale detaillée du proche sillage, il faut éliminer autant que possible les interactions parasites provoquées par les supports traditionnels: dard aval, mât latéral, suspension par fils.

Dans la première partie de cette communication sont décrites brièvement et discutées les méthodes développées à cet effet par l'ONERA.

Un support amont profilé traversant le col de la tuyère a d'abord été utilisé pour étudier le sillage en régime turbulent pleinement établi et en écoulement uniforme.

Bien que ce dispositif ait fourni des résultats déjà très intéressants, il ne permet pas de restituer correctement l'état de l'écoulement autour d'un projectile réel dans le plan du culot (épaisseur et nature laminaire ou turbulence de la couche limite, gradient de pression et d'entropie de l'écoulement extérieur).

Pour éviter cet inconvénient et compléter les informations obtenues, une suspension magnétique de la maquette comportant un dispositif de télémesure a été mise en oeuvre, à un nombre de Mach de 5 et pour une plage étendue de nombre de Reynolds.

Les résultats qui sont ensuite présentés comprennent essentiellement:

- Une analyse, en fonction du nombre de Reynolds, pour différentes configurations d'avant-corps, des pressions et dans certains cas des flux au culot de la maquette,
- un examen détaillé de la structure de l'eau morte, comportant notamment l'étude des profils de vitesse dans la zone de recompression et dans le proche sillage,
- une étude préliminaire de l'évolution de la transition dans le sillage d'un corps élancé de grand allongement.

Cette étude du proche sillage prolonge les études antérieures de l'ONERA concernant les conditions de recollement d'un jet supersoniques. Les développements théoriques permettant d'assurer le raccrod entre les diverses zones d'écoulement sont en cours d'élaboration et on espére pouvoir présenter quelques résultats intéressants en Mai 1967.

SUMMARY

In order to perform a detailed experimental wind-tunnel analysis of the near wake, it is necessary to eliminate as much as possible the parasitic interactions induced by traditional mountings: downstream sting, lateral strut, wire suspension.

The first part of this paper briefly describes and discusses the methods developed by ONERA for this purpose.

An upstream aerodynamically shaped holder passing through the nozzle throat has first been used to investigate the wake in a completely established turbulent state and in a uniform flow.

Although this device has already provided very interesting results, it is not capable of accurately reproducing the state of the flow around a true missile in the body-base plane (thickness and laminar or turbulent nature of the boundary layer, pressure and entropy gradient of the external flow).

In order to avoid this drawback and to complete the data obtained, a magnetic model mounting with a telemetry device has been used, at Mach 5 and for a wide range of Reynolds numbers.

The results which are then presented primarily include:

- an analysis, with reference to the Reynolds number, for various forward body configurations of the pressures, and in certain cases of the flows at the model base,
- a detailed investigation of the dead water structure, including, in particular, a speed profile study in the recompression zone and the near wake,
- a preliminary study of transition development within the wake of a high aspect ratio slender body.

This investigation of the near wake continues previous ONERA studies dealing with reattachment conditions for a supersonic jet. Theoretical developments permitting to achieve the junction of the various flow areas in progress and some interesting results are expected for May 1967.

NOTATIONS UTILISEES

Symboles -

p_s : pression statique

p_i : pression génératrice

p'_i : pression Pitot

T : température absolue

u : composante longitudinale de la vitesse

M : nombre de Mach

R : nombre de Reynolds

P_r : nombre de Prandtl

δ : épaisseur de la couche limite

δ^{**} : épaisseur de quantité de mouvement

H, J : paramètres de forme incompressibles (définis dans le texte)

a : $a = \frac{u_i}{u_e}$ en amont du point de recollement

$a = \frac{u_c}{u_e}$ en aval du point de recollement

ε : coefficient de viscosité turbulente apparente

x : coordonnées suivant l'axe du sillage

Y, Z : coordonnées orthogonales à l'axe du sillage

Y_m : ordonnée pour laquelle $\frac{u_e - u}{u_e - u_c} = 0,5$

D : diamètre du culot

b : largeur du sillage

e' : fluctuation de tension aux bornes du fil chaud

α : proportionnel à $\overline{e'^2}$

N : fréquence de l'oscillation harmonique osculatrice à la couche d'autocorrélation

R : coefficient d'autocorrélation

Indices -

e : caractérise les conditions à la frontière du sillage

o : caractérise les conditions sur l'axe du sillage

i : caractérise les conditions génératrices

∞ : caractérise les conditions dans l'écoulement amont isentropique

1 : caractérise les conditions dans l'eau-morte

p : caractérise les conditions à la paroi de la maquette

j : caractérise les conditions sur la ligne de jet

R : caractérise les conditions au point de recollement.

1 - INTRODUCTION -

L'étude expérimentale du proche sillage d'un corps de révolution, en écoulement supersonique ou hypersonique, constitue le prolongement naturel des recherches effectuées depuis de nombreuses années à l'O.N.E.R.A. sur les conditions de recollement d'un jet et sur les problèmes de mélange.

L'expérience acquise dans ces domaines [1 - 2 - 3 - 4] et l'emploi de techniques expérimentales d'avant garde, en particulier l'utilisation de la suspension magnétique des maquettes [5 - 6 - 7] ont contribué à assurer des conditions d'essais exemptes autant que possible d'interactions parasites.

Dans cet exposé, on passera d'abord en revue et on discutera les montages utilisés ; les premiers résultats expérimentaux actuellement disponibles seront ensuite présentés.

Ils se réduisent pour l'instant à une analyse expérimentale détaillée de la structure du proche sillage dans deux cas typiques, étape qui nous a paru indispensable avant toute tentative d'exploitation théorique.

Le premier cas concerne l'écoulement de culot, en régime turbulent établi, qui se développe en aval d'un arrière-corps cylindrique placé dans un écoulement supersonique uniforme, parallèle à son axe.

Le second cas est relatif à l'écoulement en aval d'un obstacle émoussé et élancé, en régime laminaire ; l'étude correspondante a été effectuée à $M = 5$ sur une maquette du type HB1 [8] maintenue à l'incidence nulle par suspension magnétique.

Dans la dernière partie de cette communication est abordé le problème de la transition laminaire turbulent et de sa détection expérimentale.

Les principaux résultats d'une étude au fil chaud de la transition dans le sillage d'un cylindre normal à un écoulement supersonique,

effectuée avec le concours de l'O.N.E.R.A. par l'Institut de Mécanique Statistique de la Turbulence (I.M.S.T.) [9 - 10], seront brièvement commentés.

2 - MONTAGE D'ESSAIS ET TECHNIQUE EXPERIMENTALE -

2.1 - Généralités -

Jusqu'à ces dernières années, l'attention des expérimentateurs avait été surtout attirée, par la nécessité de minimiser les effets de support, en vue d'obtenir une détermination précise de la résistance de culot, lorsque celle-ci intervient pour une part importante dans la résistance globale.

Des études critiques nombreuses, consacrées à ce sujet [11 - 12 - 13], il ressort en effet que les modes de fixation faisant intervenir des mâts latéraux ou des fils, entraînent des perturbations sensibles de la pression de culot, provenant notamment d'un déclenchement prématuré et dissymétrique de la transition.

Lorsque le but des expériences consiste à effectuer une analyse détaillée du proche sillage, une attention encore plus marquée doit être portée aux conditions d'essais.

Dans ce cas, l'extrême sensibilité que présente le développement transversal du sillage à des variations de pression relativement modérées inégalement réparties sur la périphérie, conduit à des exigences très sévères, tant sur le mode de support à utiliser, que sur l'uniformité de l'écoulement dans la veine d'essai.

A titre d'exemple, est représentée figure 1, l'exploration des pressions d'arrêt effectuée à une distance du culot égale à environ 3 diamètres dans le sillage turbulent d'un arrière-corps cylindrique de révolution. Le modèle est placé dans un écoulement quasi uniforme de nombre de Mach moyen égal à 4.

Cette figure met en évidence une distorsion importante de l'écoulement au voisinage de l'axe, distorsion qui s'atténue d'ailleurs très sensiblement à la périphérie du sillage, et réapparaît ensuite dans l'écoulement extérieur non visqueux montrant ainsi l'existence au sein de cet écoulement de légères dissymétries.

Un sondage très soigné de l'écoulement dans le plan du culot a permis de voir que ces dissymétries correspondraient à une variation ΔM du nombre de Mach local tel que : $\Delta M \leqslant \pm 0{,}06$, tandis que les variations de l'épaisseur de quantité de mouvement δ^{**} de la couche limite à la périphérie du culot n'excédaient pas :

$$\frac{\Delta \delta^{**}}{\delta^{**}} \leqslant \pm 0{,}05$$

Dans ces conditions, il est apparu nécessaire d'observer dans les montages expérimentaux utilisés, les prescriptions suivantes :

a) éviter toute dissymétrie d'écoulement imposée par un support matériel non axial,

b) dans le cas où la couche limite en amont du culot est turbulente, régulariser son développement par un déclenchement artificiel convenablement localisé,

c) utiliser autant que possible la suspension magnétique des maquettes émoussées pour lesquelles notamment un support axial amont modifie profondément les caractéristiques de l'écoulement non visqueux du fait de l'interaction importante qui s'établit entre l'onde de choc de tête et la couche limite du support.

Le choix des montages qui ont été utilisés dans notre étude s'inspire de ces conditions.

2.2 - Montage d'étude d'arrière-corps cylindriques, avec couche limite turbulente -

Ces études ont été effectuées aux nombres de Mach de 1,92 et 4, respectivement obtenus avec les montages représentés fig. 2 a et 2 b. Le premier (fig. 2 a) équipe une soufflerie continue du type Eiffel alimentée en air sec à la pression atmosphérique ; l'arrière-corps cylindrique est supporté par un dard également cylindrique traversant d'amont vers l'aval le col d'une tuyère plane; le nombre de Mach d'essai étant faible, M = 1,92 et le diamètre du dard modéré devant les dimensions de la veine (D = 32 mm), les modifications imposées à l'écoulement non visqueux par la présence du dard n'altèrent pas sensiblement son uniformité ($\Delta M \leqslant \pm 0{,}01$).

Pour éliminer les petites perturbations résiduelles du sillage, les grandeurs retenues (p, p'_i) ont été prises en valeur moyenne à partir des mesures effectuées sur un même parallèle au moyen d'un explorateur, opérant en coordonnées semi-polaires (X, Y, θ) et dont l'axe longitudinal X coïncide avec celui du montage.

La pression génératrice de l'écoulement étant voisine de 1 bar, la transition a été déclenchée sur le dard axial au moyen de rugosités disposées de part et d'autre du col conduisant à une épaisseur relative de la couche limite turbulente au droit du culot $\delta^{**}/D = 0{,}012$.

L'étendue du domaine d'étude du sillage est limitée par la réflexion sur la paroi de la tuyère de la détente au droit du culot (2 a).

Dans le second montage, fig. 2 b, l'arrière-corps cylindrique est disposé à l'extrémité d'une tuyère de révolution à corps central, calculée par la méthode des caractéristiques et corrigée des effets de couche limite de façon à produire un écoulement uniforme de nombre de Mach égal à 4, à partir d'une distance égale à environ 2 D en amont du culot cylindrique.

Il n'a pas été nécessaire d'effectuer un déclenchement artificiel de la transition, la pression génératrice étant élevée (20 bars), celle-ci se produit naturellement au voisinage immédiat du col de la tuyère et la couche limite turbulente atteint une épaisseur relative $\delta^{**}/D = 0,007$ au droit du culot. Les essais correspondants ont été effectués à la soufflerie R1 de CHALAIS-MEUDON, à rafale longue (30 s).

2.3- Suspension magnétique des maquettes -

2.3.1 - L'O.N.E.R.A. a développé depuis 1961 un dispositif de suspension magnétique des maquettes dont le principe et les différentes étapes de réalisation ont fait l'objet de publications détaillées [5 - 6 - 7]. L'aboutissement de ces recherches fut la création d'une installation opérationnelle mise en service dès 1962 dans la soufflerie R2 de CHALAIS-MEUDON, permettant de maintenir à l'incidence nulle des maquettes pesant entre 4 et 6 kg, dans une veine de révolution de 30 cm de diamètre, à des nombres de Mach compris entre 5 et 7, pour lesquels les efforts de résistance aérodynamique peuvent atteindre 10 kg.

2.3.2 - Comme le montre la photographie de la planche 3, la solution retenue est une suspension en V, comportant 4 bobines d'électro-aimant assurant à la fois la compensation de la pesanteur et la stabilisation latérale, auxquelles s'ajoute une bobine concentrique à la veine destinée à contenir les efforts aérodynamiques de résistance longitudinale. 5 faisceaux lumineux permettent de détecter la position de la maquette.

Cette suspension a été complétée par un dispositif mécanique tripode, destiné au maintien de la maquette en position, pendant les phases d'amorçage et de désamorçage de la tuyère au cours desquelles les efforts aérodynamiques peuvent atteindre des valeurs très supérieures à celles qui sont prévues en régime permanent.

Le dispositif s'éclipse pendant la phase d'essai ; sur la photographie de la fig. 3, il est représenté en position rétractée.

2.3.3 - La maquette expérimentée est une variante allongée de la version étalon HB1, dont les caractéristiques et dimensions principales sont données sur la figure 3.

Cette maquette comporte notamment un dispositif de télémesure de la pression de culot, celle-ci étant détectée par un capteur à self.

2.3.4 - <u>Conditions d'essais</u> -

2.3.4.1. - Les essais ont été effectués dans la soufflerie à rafale longue R2 à un nombre de Mach de 5, uniforme à $\pm$ 0,02 près, et pour une gamme de pressions génératrices comprises entre 2 et 10 bars (la suspension magnétique actuelle ne permet pas d'assurer la tenue du modèle pour $p_i > 10$ bars). La température génératrice sensiblement constante au cours des différentes rafales est comprise entre 530 et 570°K.

La température de maquette, légèrement variable au cours des différentes rafales oscille entre 290° et 310°K, ce qui correspond à une valeur moyenne de rapport T_p/T_{i_∞} légèrement supérieure à 0,5.

Les profils de pression et de température ont été obtenus par différents sondages effectués dans le plan vertical de symétrie.

L'incidence et le dérapage de la maquette ont été maintenus à une valeur sensiblement nulle, l'écart maximal étant inférieur à 0,1°.

Des photographies prises au cours des rafales, ont permis de vérifier que la position géométrique de la maquette, était invariante pendant la durée de la rafale, la stabilisation par suspension magnétique, s'effectuant sans mouvements résiduels appréciables.

3 - PROCHE SILLAGE TURBULENT D'UN ARRIERE-CORPS CYLINDRIQUE PLACE EN ECOULEMENT SUPERSONIQUE UNIFORME -

3.1 - Les expériences correspondantes, effectuées à $M_0 = 1,92$ et 4 dans le cas d'écoulements adiabatiques, comprennent :

a) une exploration détaillée de la détente initiale de la couche limite,

b) une détermination précise des caractéristiques locales de l'écoulement suivant l'axe du sillage,

c) une étude des profils de vitesse dans le domaine de recompression, de part et d'autre du point de recollement, limitée à l'heure actuelle au seul cas $M_0 = 1,92$.

Ces résultats bien qu'insuffisants pour fournir les éléments d'une exploitation détaillée, permettent toutefois de présenter quelques remarques de caractère général sur la structure de l'écoulement de culot.

3.2 - Etude de la détente initiale de la couche limite de l'arrière-corps -

Ce problème a été abordé dans une publication antérieure [1] où était proposée une méthode de calcul simplifiée du profil des vitesses de la couche limite détendue.

Cette méthode comporte en particulier l'hypothèse que les forces de viscosité peuvent être négligées devant les forces d'inertie au cours d'un processus de détente rapide ; l'écoulement de couche limite est alors assimilé à un écoulement rotationnel de fluide parfait.

Par une voie différente, ce point de vue a été récemment repris par WEINBAUM [14 - 15] qui propose d'utiliser une technique rigoureuse de calcul d'écoulement supersonique rotationnel et non visqueux (méthode des caractéristiques).

Ce procédé est spécialement bien adapté lorsque la couche limite en amont du décollement est turbulente et l'écoulement extérieur supersonique élevé. La partie subsonique de la couche limite représente alors une très faible fraction de sa hauteur totale δ et peut être négligée.

Par ailleurs, un tel calcul montre, que dans certains cas où la détente initiale est importante, il se produit une focalisation des caractéristiques réfléchies par la frontière isobare du jet, ce qui permet d'expliquer l'existence du "lip shock" observé par de nombreux expérimentateurs.

Pour vérifier le bien fondé de ces hypothèses, une comparaison entre la théorie proposée par WEINBAUM et l'expérience est présentée fig. 4 et 5.

Dans le cas du nombre de Mach amont le plus faible (fig. 4, $M_{\infty} = 1{,}92$) aucune focalisation n'est observée et un accord excellent entre les explorations de pression d'arrêt expérimentales et le calcul est enregistré.

Au nombre de Mach le plus élevé (fig. 5, $M_{\infty} = 4$) une focalisation apparaît qui engendre un choc de faible intensité.

L'expérience confirme la présence de ce choc et vérifie parfaitement la méthode de calcul de WEINBAUM.

L'expérience montre également comment s'établit en fait le processus de mélange turbulent entre l'eau-morte et l'écoulement rotationnel provenant de la détente de la couche limite.

3.3 - Caractéristiques de l'écoulement sur l'axe du sillage -

Les figures 6 et 7 donnent l'évolution de la pression statique, de la pression d'arrêt et du nombre de Mach, suivant l'axe du sillage, tandis que la figure 8 présente un regroupement et une comparaison de ces résultats.

On remarquera spécialement les points suivants :

- contrairement à ce qui est observé en écoulement plan, la pression statique atteint, en fin de recompression, une valeur maximale supérieure à celle de l'écoulement uniforme en amont du culot. En effet, par suite de la courbure que présente en écoulement de révolution la frontière sensiblement isobare du décollement, le retour à une direction de la vitesse parallèle à l'axe conduit à une déviation supérieure à celle que subit l'écoulement lors du décollement,
- la vitesse de recirculation sur l'axe est importante, et augmente avec le nombre de Mach ; elle atteint environ 20% de la vitesse extérieure à $M_\infty = 1,92$ et près de 35% pour $M_\infty = 4$. Dans ce cas, le nombre de Mach local maximum dans le courant de retour est de l'ordre de 0,8,
- la position relative du point de recollement évolue d'une façon notable lorsque M_∞ passe de 1,92 à 4 ; toutefois les effets de couche limite initiale n'étant pas identiques dans les 2 cas, cette variation n'est pas significative.

La distance de recollement X_R, représente une longueur caractéristique du phénomène, ainsi que le montre la courbe de corrélation des pressions fig. 8.

La représentation adoptée permet de regrouper jusqu'au point de recollement, les répartitions de pressions obtenues pour les 2 nombres de Mach expérimentés.

Cette tentative de normalisation est analogue dans son principe à celle qui a été proposée réf. [2] et [3], à l'occasion d'études du recollement.

3.4 - Exploration détaillée du proche sillage ($M_\infty = 1{,}92$) -

Les résultats de mesure (pressions statiques et d'arrêt) sont présentés fig. 9, tandis que les profils de vitesse sont donnés sous forme conventionnelle $\frac{u}{u_e} = f(y/D)$, fig. 10 et en variables réduites $\frac{u_e - u}{u_e - u_c} = f\left(\frac{y}{y_m}\right)$ fig. 11.

u_c représente ici la vitesse axiale, y_m est l'ordonnée pour laquelle $f = 0{,}5$.

Cette dernière représentation, met notamment en évidence, l'existence d'une forme asymptotique du profil des vitesses dans le sillage, qui est très rapidement atteinte, en aval du point de recollement.

La comparaison effectuée fig. 12 a avec une prévision théorique proposée en écoulement plan turbulent incompressible par GINESKII [16] conduit aux remarques suivantes, qui généralisent les conclusions de l'auteur :

- l'effet de compressibilité ne paraît pas modifier sensiblement la forme du profil des vitesses, pratiquement identique en écoulement plan et en écoulement de révolution, ce qui a été constaté à de nombreuses reprises dans les problèmes de mélange turbulent [4],
- le gradient de pression longitudinal affecte peu la forme asymptotique du profil des vitesses.

Ainsi les effets de révolution, de compressibilité et de gradient de pression agissent essentiellement, d'une part sur la loi de vitesse axiale $u_c(X)$, d'autre part sur le taux d'expansion du sillage.

Sur la fig. 12 b est proposée une comparaison entre le profil expérimental de recollement turbulent et un calcul théorique effectué en écoulement plan dans le cadre des hypothèses suivantes [17] :

- similitude des profils de vitesse pour un gradient de pression constant,

- coefficient de viscosité turbulent apparent ε indépendant de Y,

L'excellent accord obtenu demande a être confirmé par d'autres résultats expérimentaux.

4 - ETUDE PRELIMINAIRE EN SUSPENSION MAGNETIQUE, DU PROCHE SILLAGE LAMINAIRE D'UN CORPS EMOUSSE A $M_\infty = 5$ -

4.1 - Les résultats acquis, concernent la maquette HB1 et sont présentés fig. 13 à 17.

Ils comprennent :

a) l'évolution des caractéristiques de l'écoulement (pression, nombre de Mach) sur l'axe du proche sillage (fig. 13),

b) une exploration détaillée des pressions, températures, vitesses à différentes distances du plan de culot (fig. 14 et 15),

c) une comparaison avec différents éléments théoriques disponibles (fig. 16 et 17).

4.2 - Caractéristiques de l'écoulement sur l'axe, influence du nombre de Reynolds (fig. 13)

Celle-ci se traduit par une évolution assez sensible des niveaux de pression relevés dans le proche sillage et conduit à une décroissance continue de la pression de culot avec le nombre de Reynolds, calculé ici en fonction du diamètre de l'obstacle avec les valeurs de vitesse et de viscosité de l'écoulement à la frontière de la couche limite immédiatement en amont du culot.

On observera :

a) le plateau caractéristique des écoulements de culot laminaires ;

b) une diminution sensible de l'étendue de ce plateau lorsque le nombre de REYNOLDS augmente.

Cette décroissance est provoquée en premier lieu par une convergence plus marquée de l'écoulement vers l'axe, lorsque la pression décroît,

mais aussi très vraisemblablement par l'apparition d'une transition dans le domaine de recompression pour la valeur la plus élevée du nombre de REYNOLDS ;

c) l'évolution très rapidement croissante des vitesses u_e sur l'axe lorsque le nombre de REYNOLDS augmente.

4.3 - Structure du proche sillage - Profils de vitesse et de température -

De la même façon que pour le cas turbulent, les profils de vitesse dans le domaine de recompression du proche sillage sont présentés fig. 16 en coordonnées réduites :

$$\frac{u_e - u}{u_e - u_c} = f\left(\frac{y}{y_m}\right)$$

On remarquera le regroupement surprenant auquel conduit cette représentation pour les valeurs de $f \geq 0{,}5$; par contre lorsque f est inférieur à 0,5 les courbes se distinguent et s'étagent régulièrement rendant ainsi compte de l'épanouissement progressif du sillage lorsque la distance relative $\frac{X}{D}$ augmente. A titre de comparaison est représenté sur cette figure, le profil théorique asymptotique proposé par GOLD [18] correspondant au sillage lointain en l'absence de gradient de pression. Le calcul de la solution complète de GOLD, qui tient compte des conditions initiales et du gradient de pression extérieur, actuellement en cours, n'a pu être présenté dans cette communication.

De la comparaison présentée, il ressort que l'établissement de la forme asymptotique du sillage en régime laminaire, nécessite une distance de développement beaucoup plus importante que dans le cas turbulent.

Sur la fig. 16, est également représentée la relation température d'arrêt - vitesse obtenue expérimentalement pour les différentes explorations effectuées. A titre indicatif, faute de disposer actuellement des solutions théoriques de GOLD, est représentée sur ce

diagramme la relation proposée par CHAPMAN dans le cas du mélange laminaire isobare.

Ayant observé que les profils de vitesse du sillage turbulent étaient peu affectés par les effets de révolution et de compressibilité, il a paru intéressant de vérifier si cette propriété s'étendait également aux profils laminaires. Dans ce but, les caractéristiques globales des profils de vitesse expérimentaux ont été comparées à celles proposées par LEES et REEVES [19] et déduites des solutions incompressibles de STEWARTSON. La fig. 17 présente les évolutions théorique et expérimentale des paramètres de forme incompressibles $\mathcal{H}$ et J en fonction du paramètre a qui, en amont du point de recollement est égal au rapport $\frac{u_i}{u_e}$ de la vitesse sur la ligne de jet à la vitesse externe, et en aval de ce point, à $\frac{u_c}{u_e}$, rapport de la vitesse sur l'axe à la vitesse externe. Les paramètres $\mathcal{H}$ et J sont définis par les relations suivantes :

$$\mathcal{H} = \frac{\int_0^\infty \frac{u}{u_e}\left(1-\frac{u}{u_e}\right) dy}{\int_0^\infty \left(1-\frac{u}{u_e}\right) dy}$$

$$J = \frac{\int_0^\infty \frac{u}{u_e}\left(1-\frac{u^2}{u_e^2}\right) dy}{\int_0^\infty \left(1-\frac{u}{u_e}\right) dy}$$

Les résultats portés sur la fig. 17 montrent que les effets de révolution et de compressibilité ne conduisent pas, même en laminaire, à une modification importante des caractéristiques globales déterminées en courant plan dans un cas incompressible. Cette constatation renforce l'idée d'une extension au cas de révolution de la méthode proposée par LEES et REEVES.

5 - OBSERVATION SUR LES METHODES EXPERIMENTALES DE DETECTION DE LA TRANSITION LAMINAIRE - TURBULENT DANS UN SILLAGE -

5.1 - L'étude expérimentale de la transition dans le sillage de la maquette HB1, maintenue par suspension magnétique n'est pas actuellement assez avancée pour que les résultats puissent figurer dans cet exposé.

C'est pourquoi il a paru intéressant de fournir à titre d'exemple quelques résultats typiques d'une étude parallèle menée avec le concours de l'O.N.E.R.A. à l'Institut de Mécanique Statistique de la Turbulence [9], [10].

Le but de cette recherche était d'apporter une contribution aux méthodes expérimentales de détection par fil chaud de la transition en aval de corps émoussés, en écoulement supersonique.

Les expériences correspondantes ont été effectuées à $M = 2,3$ et concernent le sillage d'un cylindre disposé normalement à la direction de l'écoulement.

5.2 - Rappel des méthodes de détection classiques :

La visualisation du sillage (strioscopie, ombroscopie, interférométrie) est utilisée par certains auteurs [20] pour déceler la transition qui se manifeste d'une manière globale par un changement caractéristique du taux d'expansion du sillage, ou encore par l'apparition et la multiplication de singularités tourbillonnaires que l'on peut figer par un temps d'observation très bref.

Une seconde méthode, proposée notamment par DEMETRIADES [21], utilise l'anémométrie à fil chaud.

La courbe $\sqrt{e'^2} = f(X)$, donnant l'évolution de l'écart type de la fluctuation de tension aux bornes d'un fil chaud au cours d'un déplacement X suivant l'axe du sillage, présente un maximum assez net.

DEMETRIADES interprète cette courbe de la manière suivante : la partie croissante correspond à la traversée d'une zone dans laquelle se développent des signaux de prétransition, tandis que la partie décroissante, indique la dissipation en chaleur de la turbulence établie. L'abscisse X_T du maximum est appelée distance de transition.

5.3 - Méthodes utilisées par l'Institut de Mécanique Statistique de la Turbulence :

5.3.1 - L'exploration transversale du sillage au moyen d'un anémomètre à fil chaud, effectuée à différentes distances de la maquette et pour plusieurs valeurs du nombre de Reynolds $\mathcal{R}_{eD}$ (fig. 18) met d'abord en évidence, que la valeur maximale de l'énergie de fluctuation n'est pas nécessairement atteinte sur l'axe, résultat analogue à celui trouvé réf. [21].

Elle permet en outre de définir avec précision des frontières normalisées du sillage de la façon indiquée sur cette figure.

L'épaisseur b du sillage ainsi définie, dépend peu du nombre de Reynolds lorsque l'écoulement est laminaire, croît rapidement dans la zone de transition et plus lentement lorsque la turbulence est développée.

Le coude formé par la courbe $b = f(\mathcal{R}_{eD})$ détermine de façon assez nette un nombre de Reynolds de transition.

Cette méthode est analogue dans son principe à celle qui est utilisée réf. [20].

5.3.2 - Une analyse détaillée du spectre d'énergie de la tension aléatoire e', permet également d'établir une méthode expérimentale de détection de la transition, en même temps qu'elle fournit des indications sur le mécanisme du développement de la turbulence.

Le spectre d'énergie de la tension aléatoire e' comporte :

- des signaux non turbulents dont le niveau est élevé mais dont la fréquence atteint au plus quelques kilohertz,
- des signaux turbulents appartenant aux divers modes, dont la fréquence peut dépasser 100 kilohertz lorsque la turbulence est établie, et dont l'échelle caractéristique λ est du même ordre que celle qui caractérise la dissipation en chaleur de la turbulence.

λ peut être caractérisé par la courbure au sommet des courbes d'autocorrélation, ou ce qui revient au même par la fréquence équivalente N de l'oscillation harmonique osculatrice à la courbe d'autocorrélation.

Un calcul simple montre que :

$$N^2 = \frac{1}{4\pi^2}\left[\overline{\left(\frac{de'}{dt}\right)^2} \Big/ \overline{e'^2}\right]$$

Cette grandeur peut être obtenue par mesure directe au moyen d'un dérivateur de signaux électriques disposé dans le montage expérimental.

Dans les zones laminaires, N^2 est très faible. Lorsque la transition apparaît N^2 croît d'abord rapidement puis plus lentement lorsque la turbulence est établie.

Ces propriétés permettent donc de repérer la transition au moyen des courbes expérimentales $N^2 = f(R_{eD})$ par exemple, ainsi que le montre la figure 19.

5.4 - <u>Comparaison des divers critères expérimentaux</u> -

La figure 20 récapitule les résultats obtenus au moyen des différentes méthodes exposées ci-dessus.

Le critère de DEMETRIADES détermine des distances de transition plus faibles que celles qui sont déduites des méthodes anémométriques

utilisées à l'I.M.S.T.

Leur application comparée semble montrer que le critère de DEMETRIADES permet de déceler un état voisin de la phase initiale de la transition, tandis que ceux de l'I.M.S.T. indiqueraient une transition presque achevée.

On peut ainsi obtenir un ordre de grandeur de la longueur sur laquelle s'opère la transition ; cette longueur est d'autant plus grande que la distance à laquelle apparaît la transition est elle-même plus élevée.

6 - CONCLUSION -

Une étude expérimentale du proche sillage a été effectuée à l'O.N.E.R.A. en utilisant des moyens d'essai destinés à éliminer, autant que possible, toute interaction parasite de support.

Dans le cas du proche sillage turbulent d'un arrière-corps cylindrique, une analyse détaillée de l'écoulement de culot a été effectuée à $M_\infty = 1{,}92$ et 4.

Cette analyse met en évidence les points suivants :

- la détente d'une couche limite turbulente et la formation éventuelle d'un choc ("lip shock") peuvent être prévues avec une bonne approximation en assimilant cette couche limite à un écoulement rotationnel de fluide parfait dont on effectue le calcul par la méthode des caractéristiques [14 - 15].
- la vitesse de recirculation est d'autant plus importante que le nombre de Mach est plus élevé,
- ainsi qu'il a été montré dans des publications antérieures [2 - 3], une corrélation des pressions jusqu'au point de recollement peut être obtenue par un choix de variables réduites convenables,
- en aval du point de recollement, les profils de vitesse, présentés en variables réduites, tendent rapidement vers une forme asymptotique peu sensible aux effets de révolution, de compressibilité et de

gradient de pression et bien représentée par une loi théorique incompressible [16].

L'étude du proche sillage laminaire a été effectuée à $M_\infty = 5$ sur une maquette HB1 tenue par suspension magnétique.

L'exploration des pressions et températures a été effectuée jusqu'à une distance du culot égale à 4 diamètres.

Les résultats montrent que la longueur d'établissement du sillage dans sa forme asymptotique est beaucoup plus importante qu'en écoulement turbulent.

Une comparaison des caractéristiques globales des profils de vitesse (paramètres de forme) dans le domaine de recompression avec celles proposées par REEVES et LEES et déduites des solutions incompressibles de STEWARTSON, confirme également que l'effet de révolution et la compressibilité jouent un rôle peu important.

L'analyse expérimentale au fil chaud du sillage d'un cylindre normal à un écoulement de nombre de Mach égal à 2,3, effectuée à l'Institut de Mécanique Statistique de la Turbulence avec la collaboration de l'O.N.E.R.A., a permis de développer un nouveau critère expérimental de transition basé sur l'évolution de la courbure initiale des courbes d'autocorrélation.

LISTE DES REFERENCES

[1] P. CARRIERE, M. SIRIEIX — Facteurs d'influence du recollement d'un écoulement supersonique. 10ème Congrès de Mécanique Appliquée - STRESA 1960 -

[2] P. CARRIERE — Recherches récentes effectuées à l'O.N.E.R.A. sur les problèmes de recollement. 7ème Symposium de Mécanique des Fluides - JURATA (Pologne) 1965 -

[3] M. SIRIEIX, J. MIRANDE, J. DELERY — Expériences fondamentales sur le recollement turbulent d'un jet supersonique. AGARD CONFERENCE PROCEEDINGS N° 4 - Separated Flows - May 1966 -

[4] M. SIRIEIX, J.L. SOLIGNAC — Contribution à l'étude expérimentale de la couche de mélange turbulent isobare d'un écoulement supersonique AGARD CONFERENCE PROCEEDINGS N° 4 - Separated Flows - May 1966

[5] M. TOURNIER, P. LAURENCEAU — Suspension magnétique d'une maquette en soufflerie. La Recherche Aérospatiale n° 59, 1957 -

[6] R. MOREAU — Utilisation des dispositifs de suspension magnétique dans les souffleries de l'O.N.E.R.A. O.N.E.R.A. - T.P. n° 341 - 1966 -

[7] P. REBUFFET

Effets de support sur l'écoulement à l'arrière d'un corps.

AGARD - Report 302 - March 1959 -

[8] J. DON GRAY
E. LINDSAY

Force test of standard hypervelocity ballistics models HB1 and HB2 at Mach 1,5 to 10.

A.E.D.C. - T.D.R. - 63-137 - August 1963 -

[9] A. FAVRE
J. GAVIGLIO
H. BURNAGE

Observations sur la transition dans un sillage transversal en écoulement supersonique.

A paraître dans La Recherche Aérospatiale - 1967 -

[10] J. GAVIGLIO
H. BURNAGE

Observations en soufflerie de sillages dans un écoulement supersonique par strioscopie et anémométrie à fil chaud.

A.F.I.T.A.E - 3ème Colloque d'Aérodynamique Appliquée - Novembre 1966 -

[11] J.D. WHITFIELD

Support interference at supersonic speeds.

AGARD - Report 300 - March 1959 -

[12] J. DON GRAY

Base pressure measurements with wire supported models at supersonic speeds.

A.E.D.C. - T.N. 61-23 - March 1961 -

[13] A. MARTELLUCCI
H. TRUCCO
A. AGNONE

Measurements of the turbulent near wake of a cone at Mach 6.

A.I.A.A. Journal - Volume 4 N° 3 - p. 385-391 - March 1966 -

[14] S. WEINBAUM — Rapid Expansion of a supersonic Boundary Layer and its application to the near wake.
A.I.A.A. Journal Volume 4 N° 2 - p. 217-226 - February 1966 -

[15] R.F. WEISS, S. WEINBAUM — Hypersonic Boundary Layer Separation and the base flow Problem.
A.I.A.A. Journal Volume 4 N° 8 - p. 1321-1330 - August 1966 -

[16] A.S. GINEVSKII — Turbulent wake and jet in a flow in the presence of a longitudinal pressure gradient.
IZV. AKAD. NAUK. O.T.N. 1959 - U.S.S.R.
TIL/T 5261 - September 1962 -

[17] J. DELERY — Résolution sur calculateur analogique des équations simplifiées d'une couche visqueuse turbulente.
La Recherche Aérospatiale n° 110 - Janvier Février 1966 -

[18] H. GOLD — Laminar wake with arbitrary initial profiles.
A.I.A.A. Journal Volume 2 N° 5 - p. 948-949 - May 1964

[19] B.L. REEVES, LESTER LEES — Theory of Laminar near wake of blund bodies in hypersonic flow.
A.I.A.A. Journal Volume 3 N° 11 - p. 2061-2074 - November 1965 -

[20] R.E. SLATTERY, W.G. CLAY — Measurements of turbulence transition, motion, statistics and gross radial growth behind hypervelocity objects.
The Physics of fluids Volume 5 N° 7 - July 1962 -

[21] A. DEMETRIADES — Some hot wire anemometer measurements in a hypersonic wake.
Proceedings of heat transfer and fluid Mechanics Institute - 1961 -

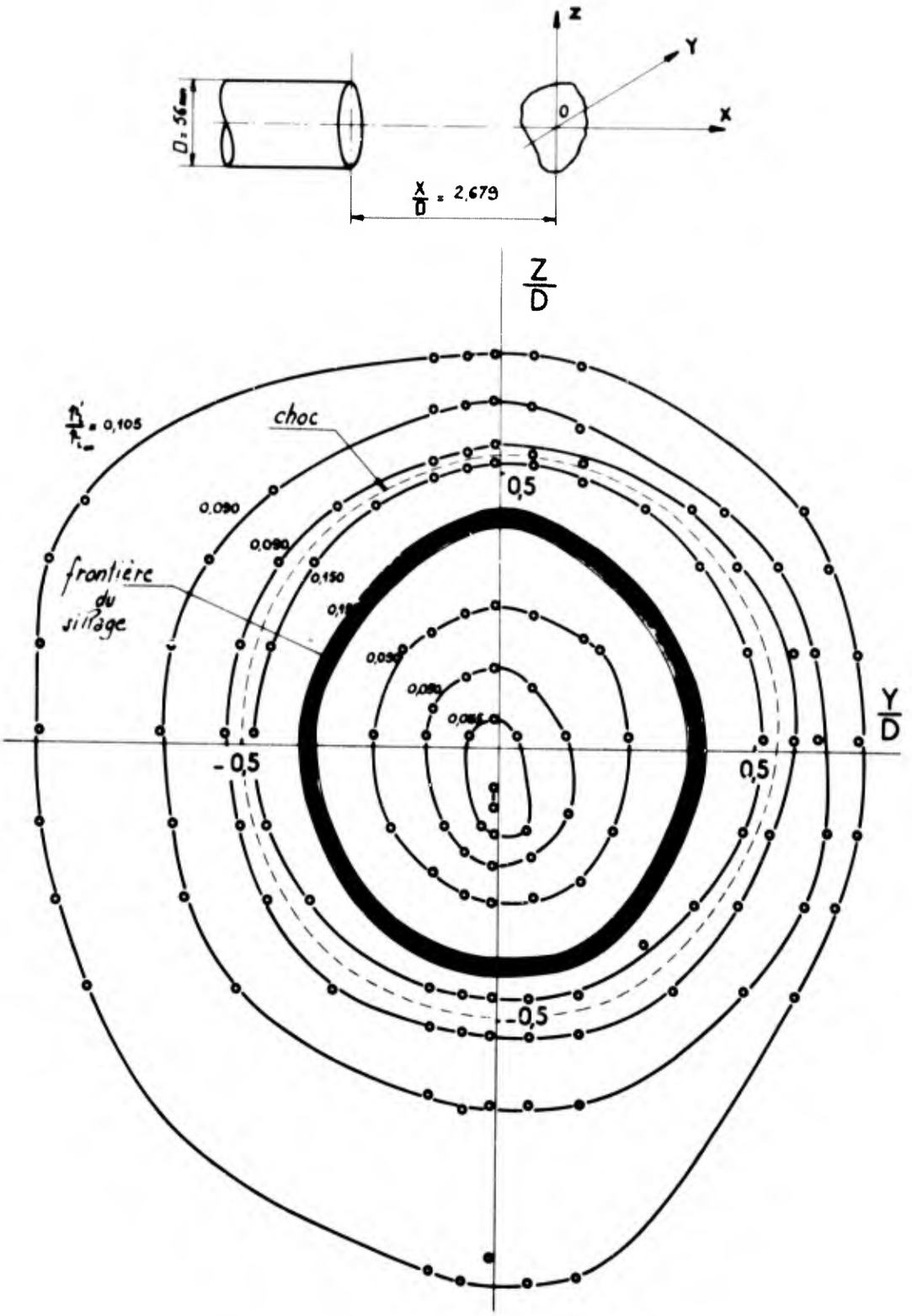

Fig. 1 Exemple de distorsion provoquée par la non-uniformité du champ extérieur. $M_\infty = 4$

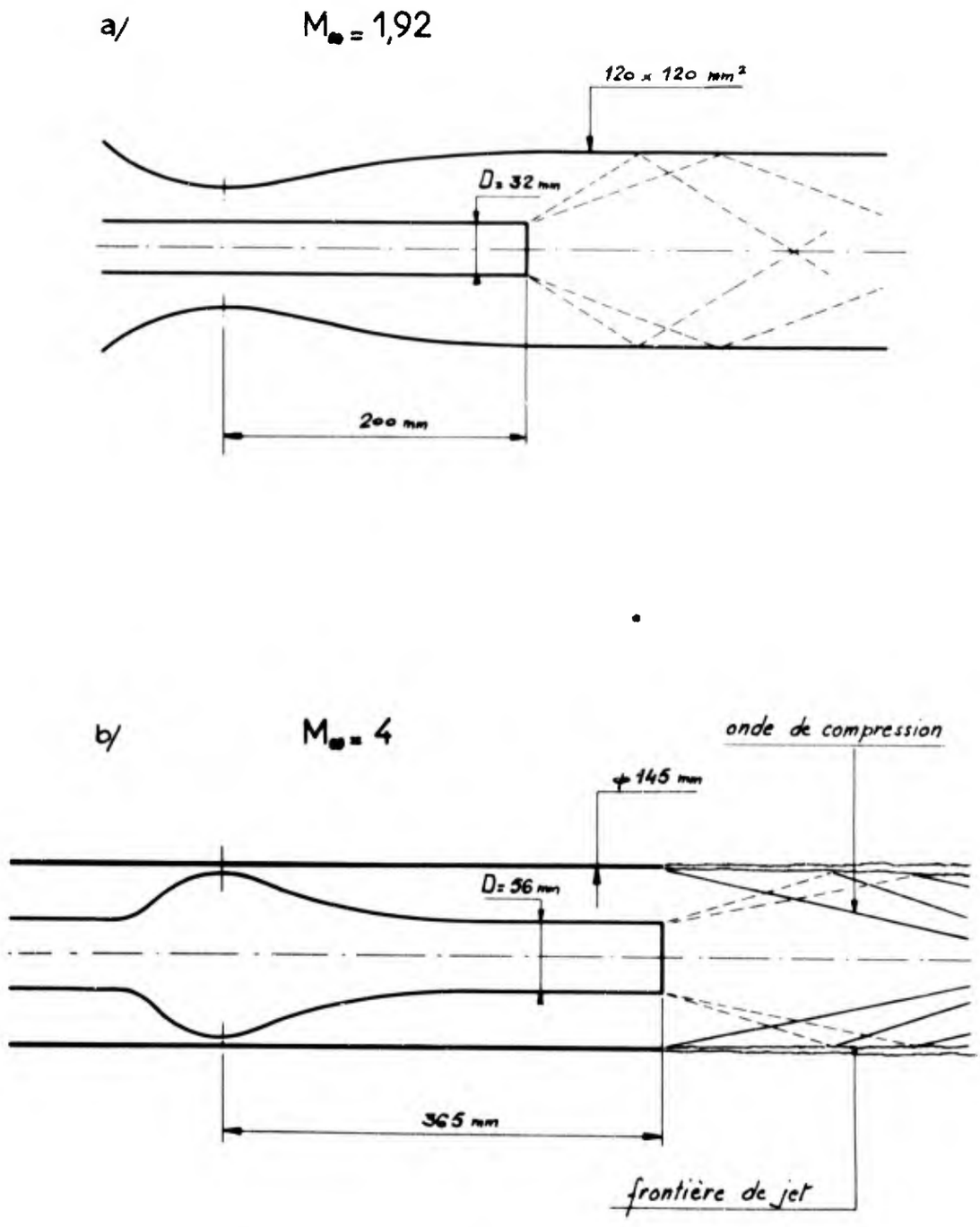

Fig. 2 Etude du proche sillage turoulent - Montage d'essai
a) Tuyère plane - Montage sur dard amont
b) Tuyère de revolution à corps central

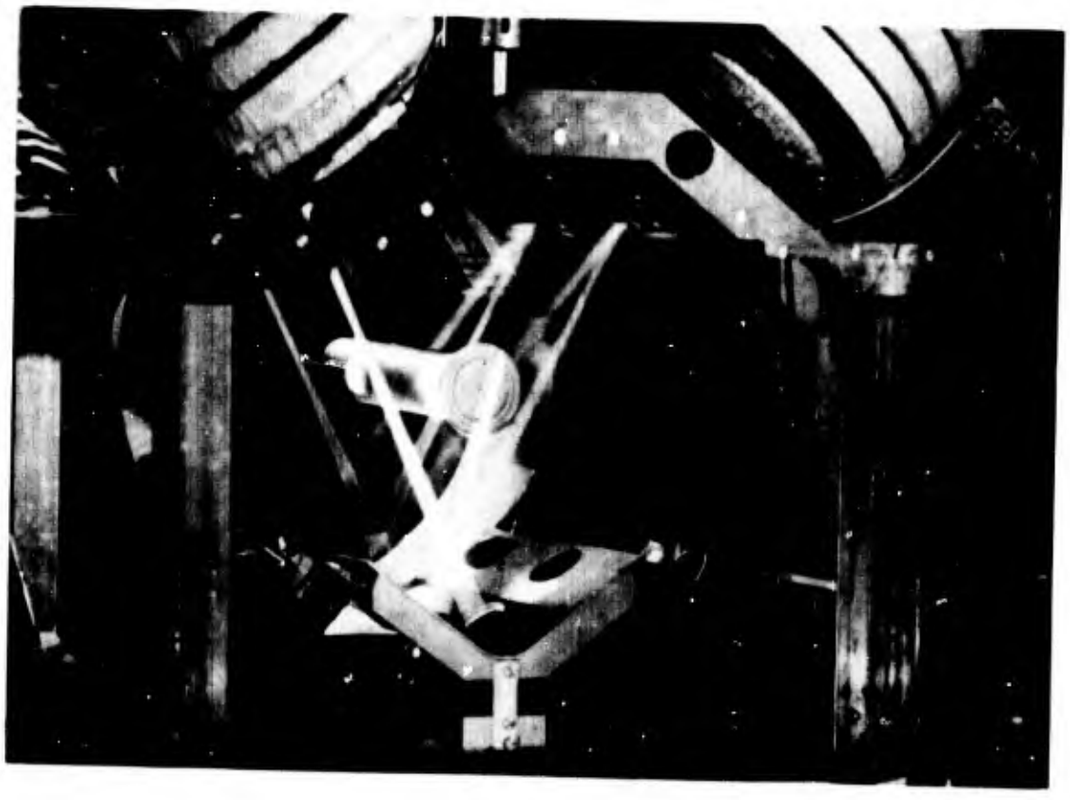

a/

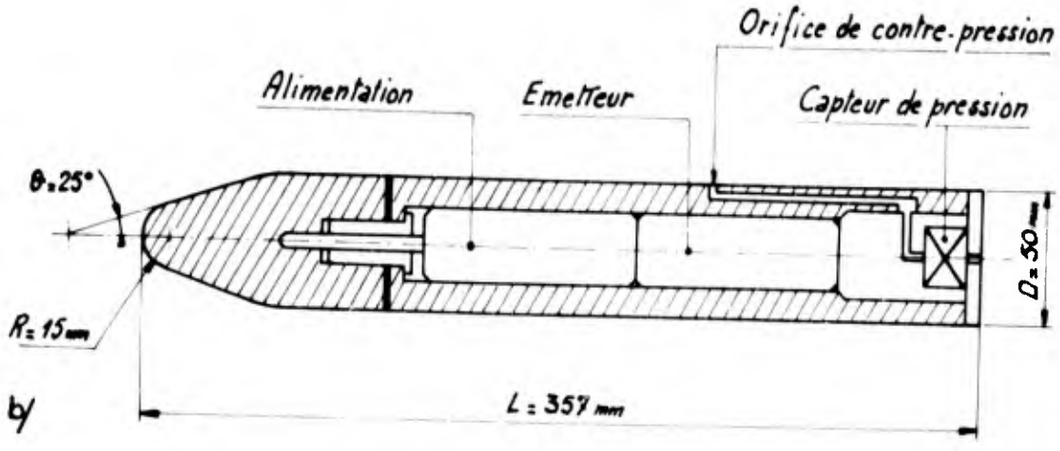

b/

Fig.3 Etude du proche sillage laminaire - $M_\infty = 5$
a) Suspension magnétique b) Maquette

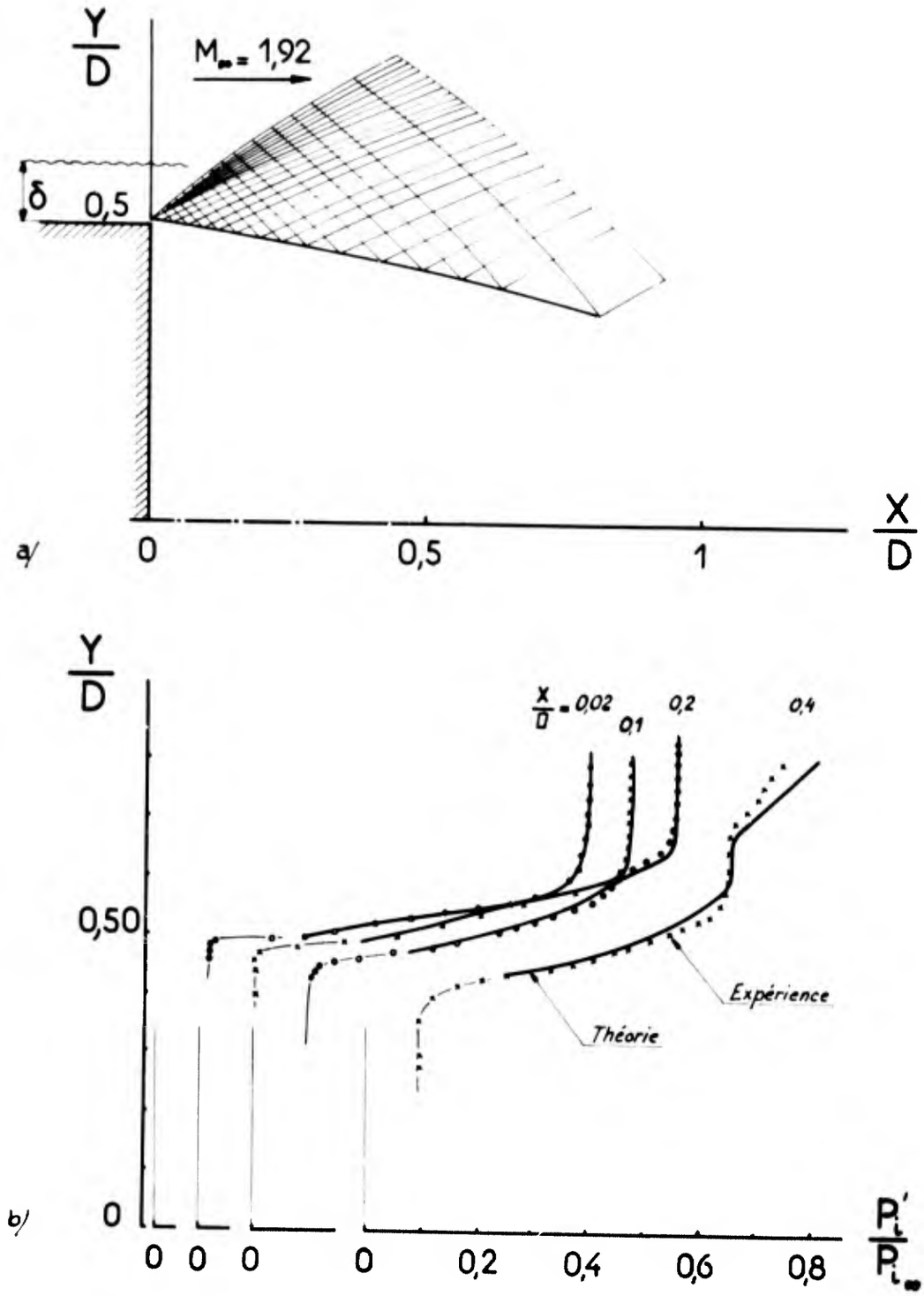

Fig.4 Etude de l'écoulement à l'origine du décollement. $M_\infty = 1,92$
Détente de la couche limite initiale turbulente

a) Réseau des caractéristiques

b) Confrontation théorie-expérience

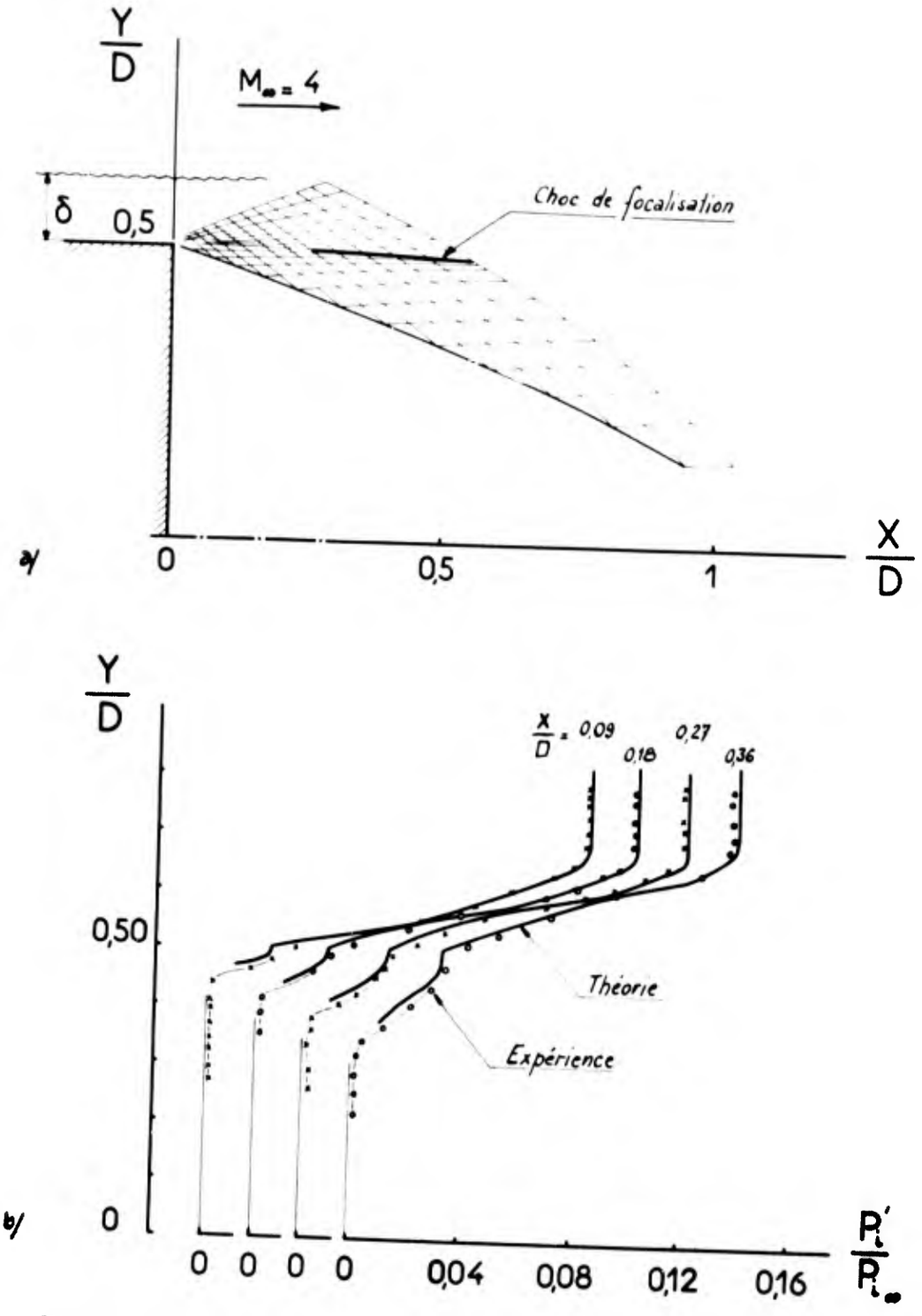

Fig.5 Etude de l'écoulement à l'origine du décollement $M_\infty = 4$
Détente de la couche limite initiale turbulente

a) Réseau des caractéristiques

b) Confrontation théorie-expérience

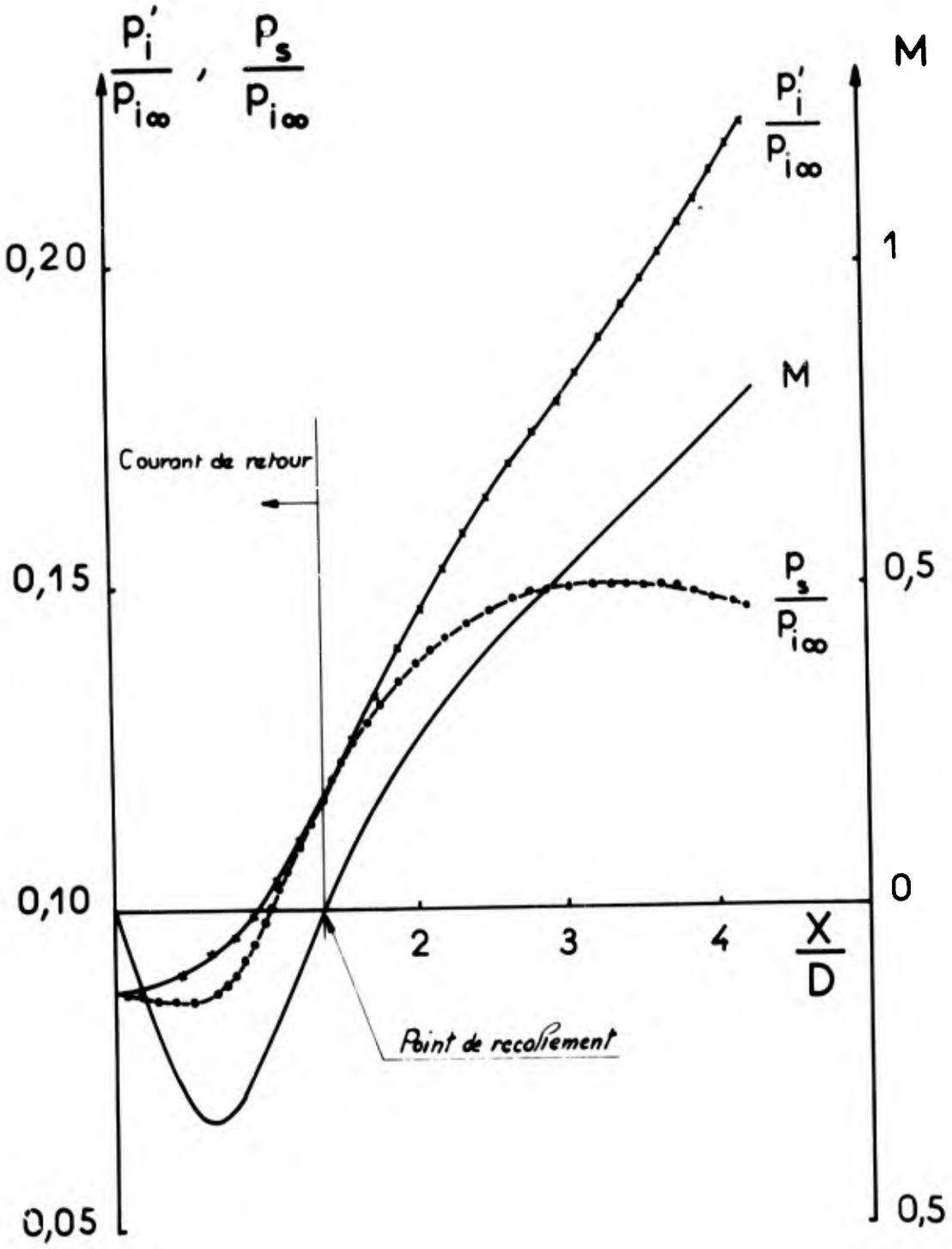

Fig.6 Evolution de l'écoulement suivant l'axe du proche sillage turbulent. $M_\infty = 1,92$

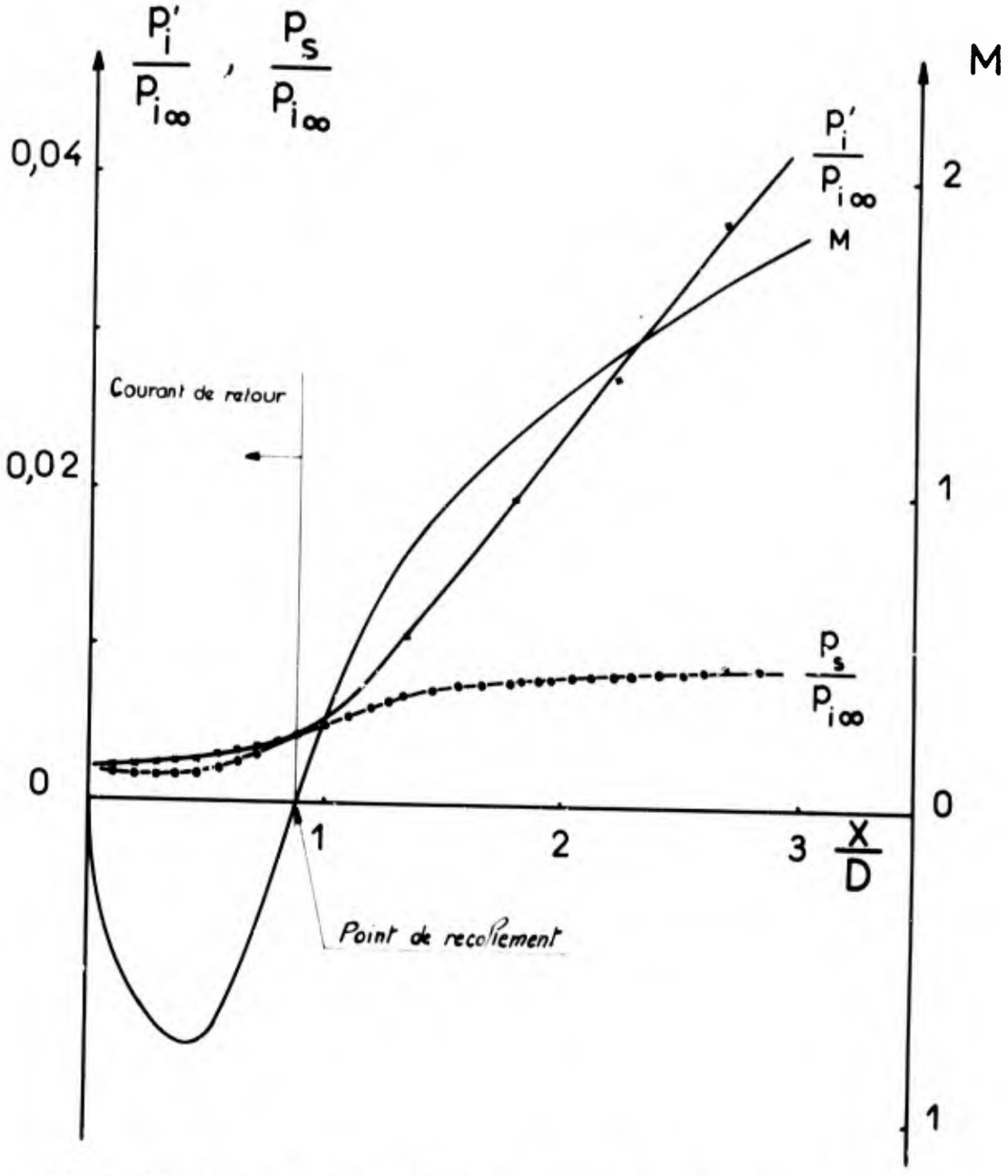

Fig.7 Evolution de l'écoulement suivant l'axe du proche sillage turbulent. $M_\infty = 4$

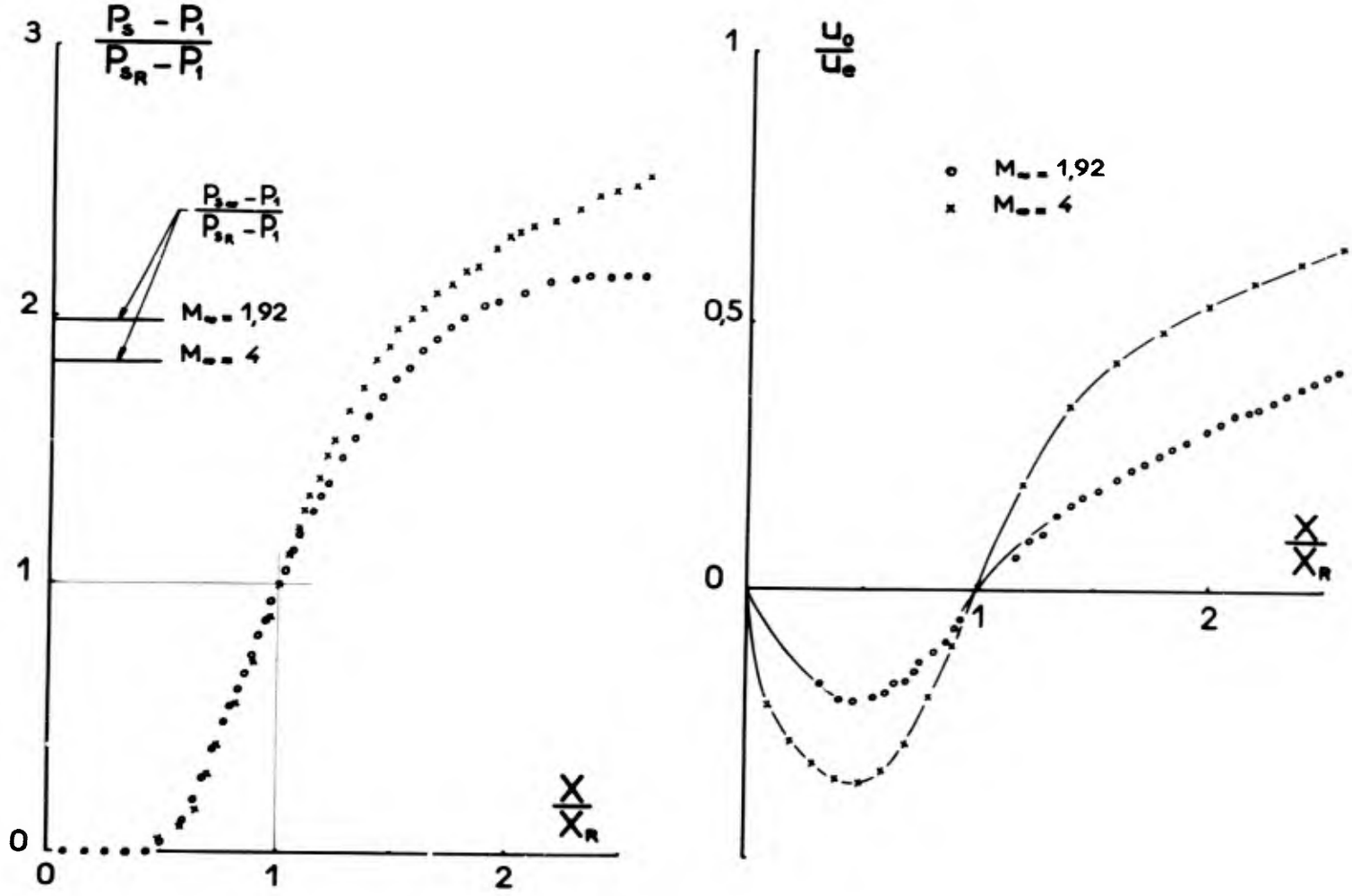

Fig.8 Corrélation des répartitions de pression dans la recompression et la loi de vitesse sur l'axe - Régime turbulent établi

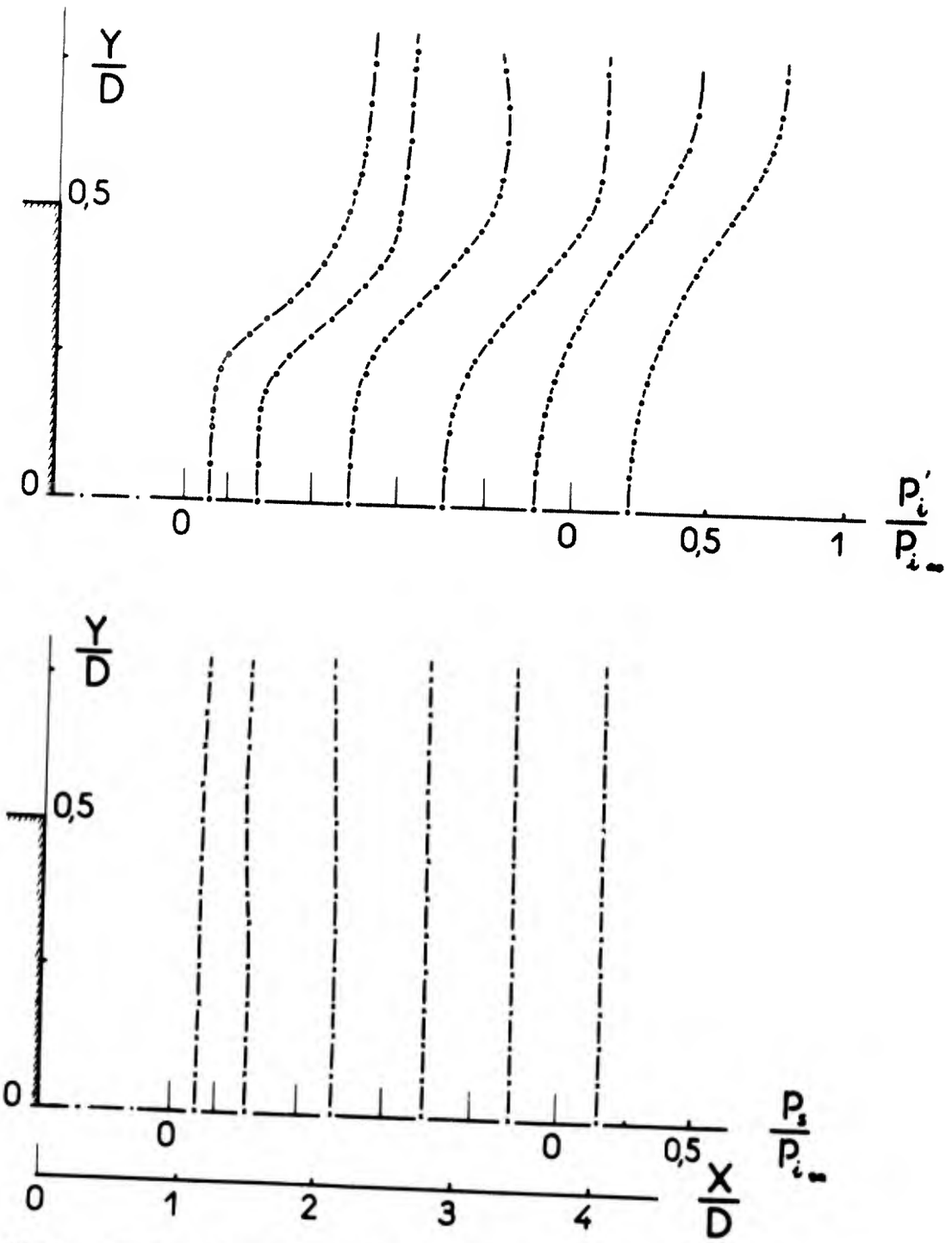

Fig. 9 Exploration des pressions - Régime turbulent établi $M_\infty = 1,92$

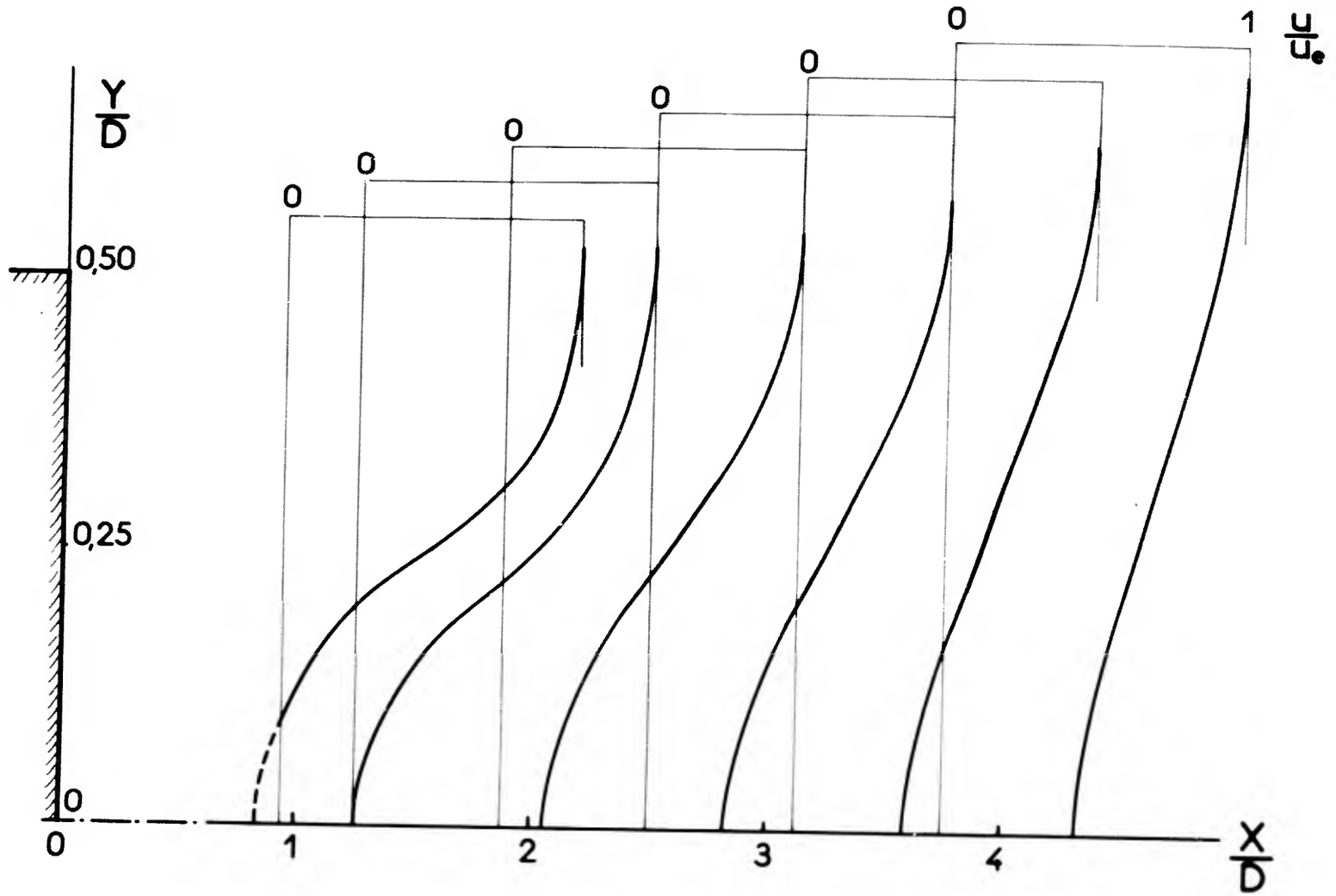

Fig. 10 Profils de vitesse dans le proche sillage turbulent $M_\infty = 1,92$

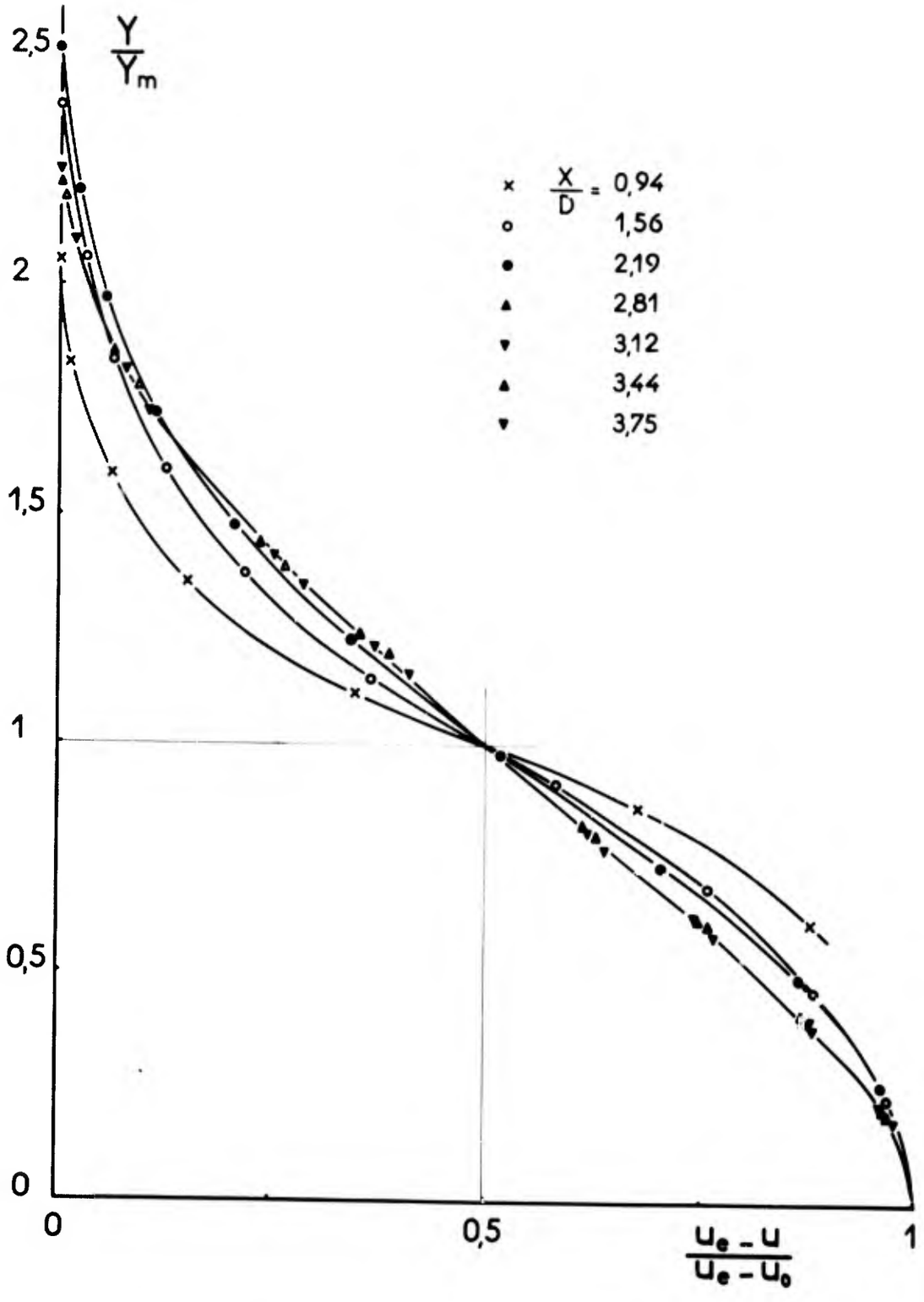

Fig. 11 Evolution des profils de vitesse normalisés dans la zone de recompression - Régime turbulent établi $M_\infty = 1,92$

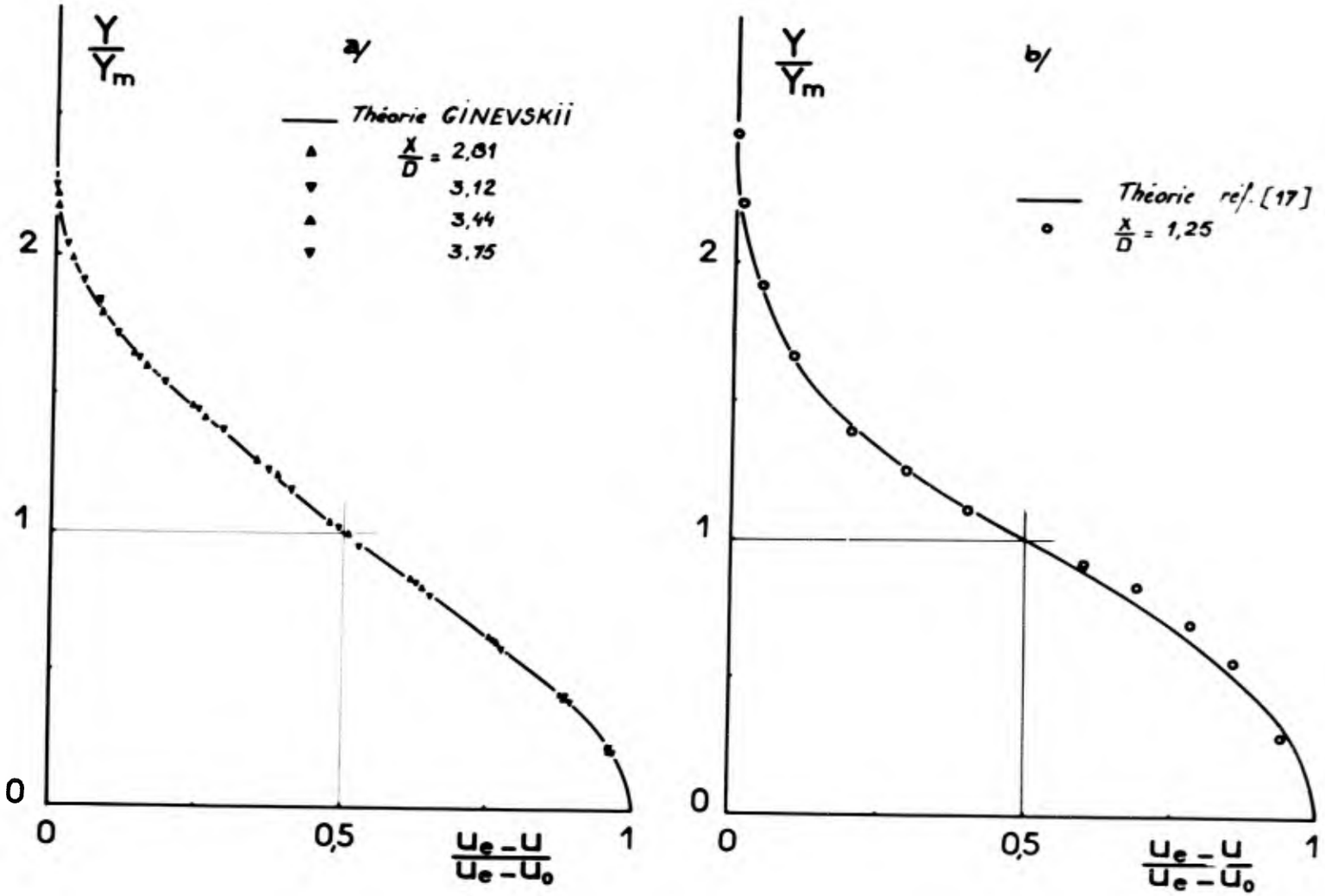

Fig. 12 Profils de vitesse normalisés - Régime turbulent établi $M_\infty = 1,92$
a) en fin de recompression b) au point de recollement

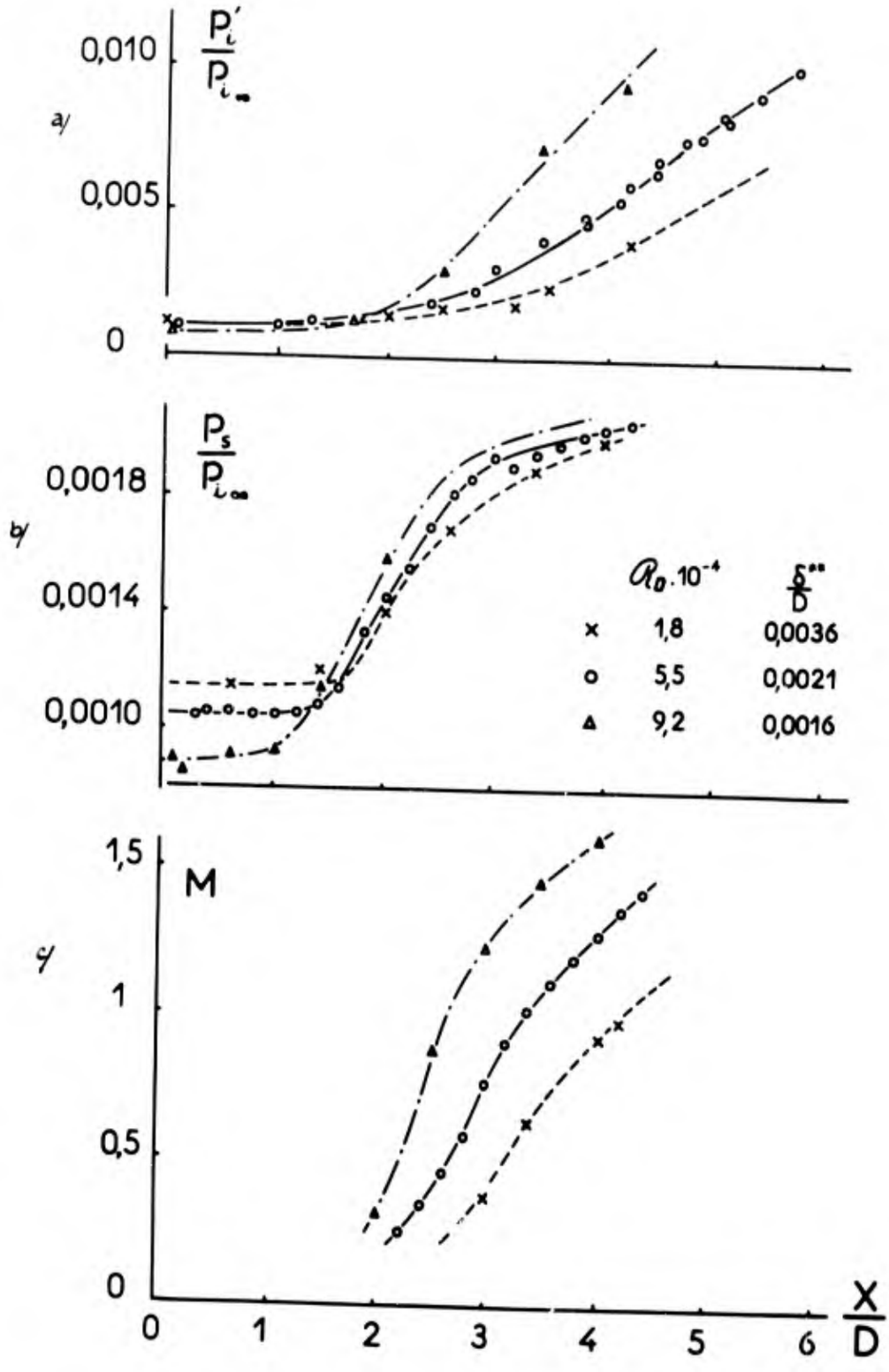

Fig. 13 Evolution de l'écoulement suivant l'axe du proche sillage laminaire $M_\infty = 5$

a) pression totale b) pression statique c) nombre de Mach

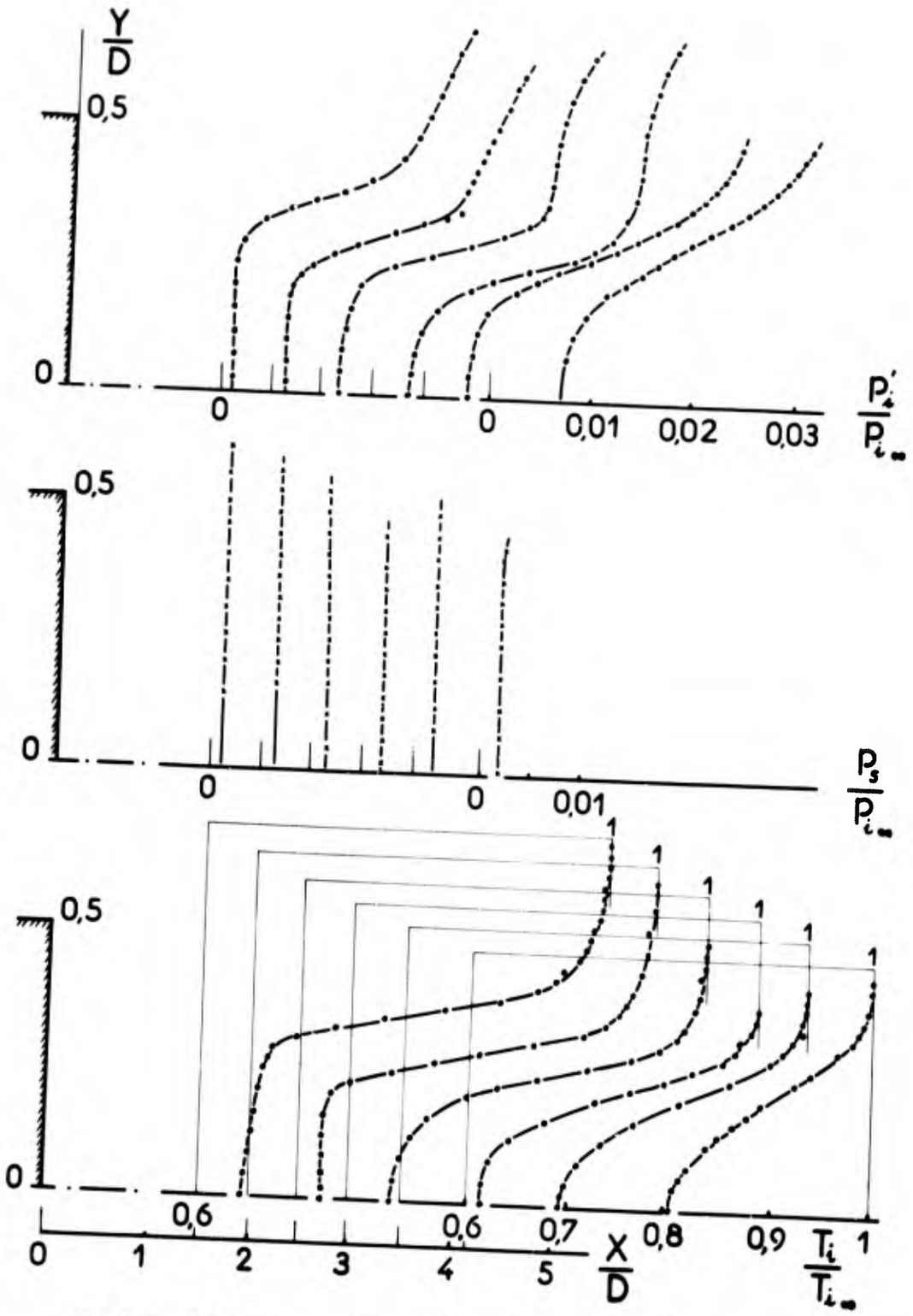

Fig. 14 Exploration radiale des pressions et températures
Régime laminaire $M_\infty = 5$ $R_D = 5,5.10^4$

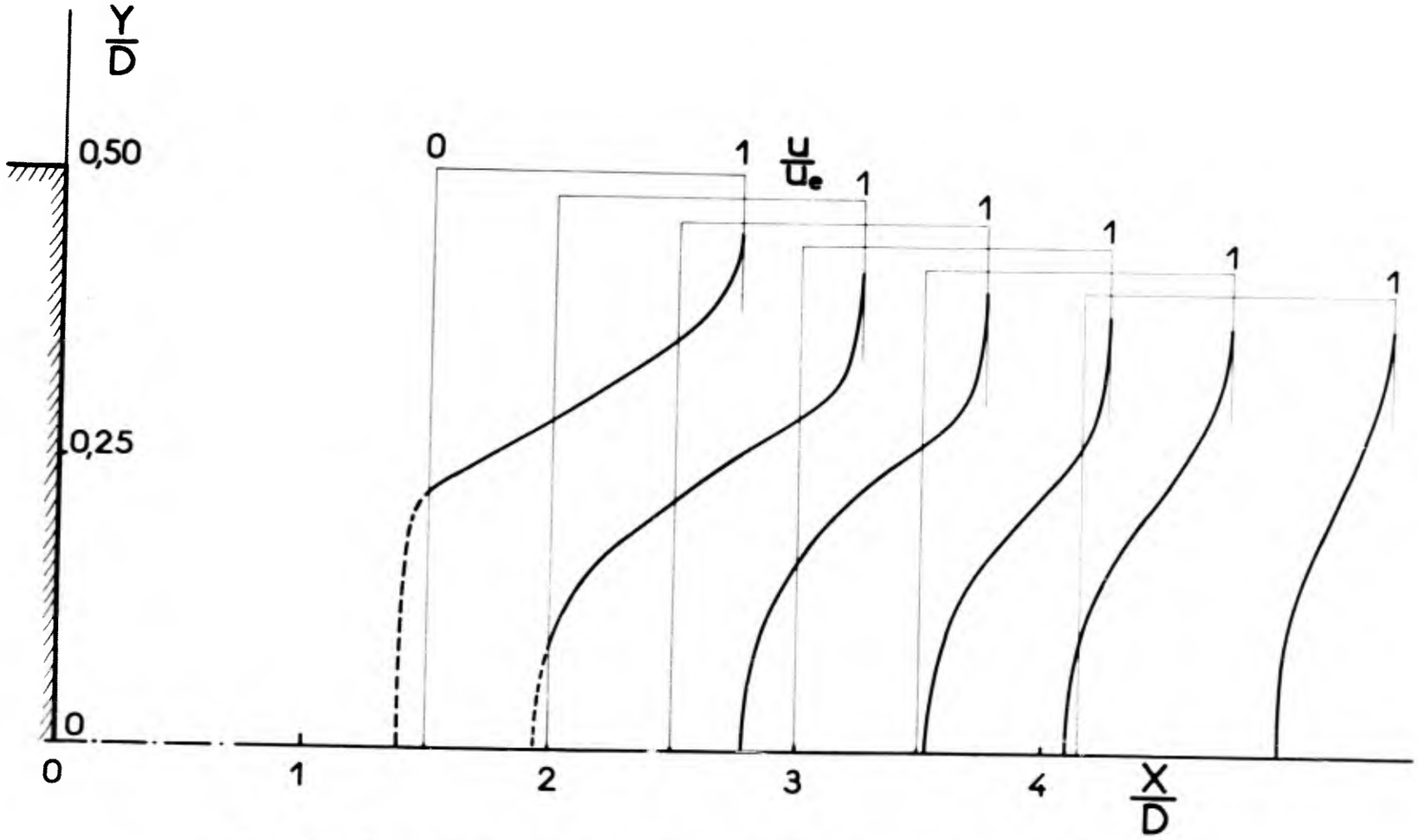

Fig. 15 Profils de vitesse dans le proche sillage laminaire $M_\infty = 5$
$R_D = 5,5.10^4$

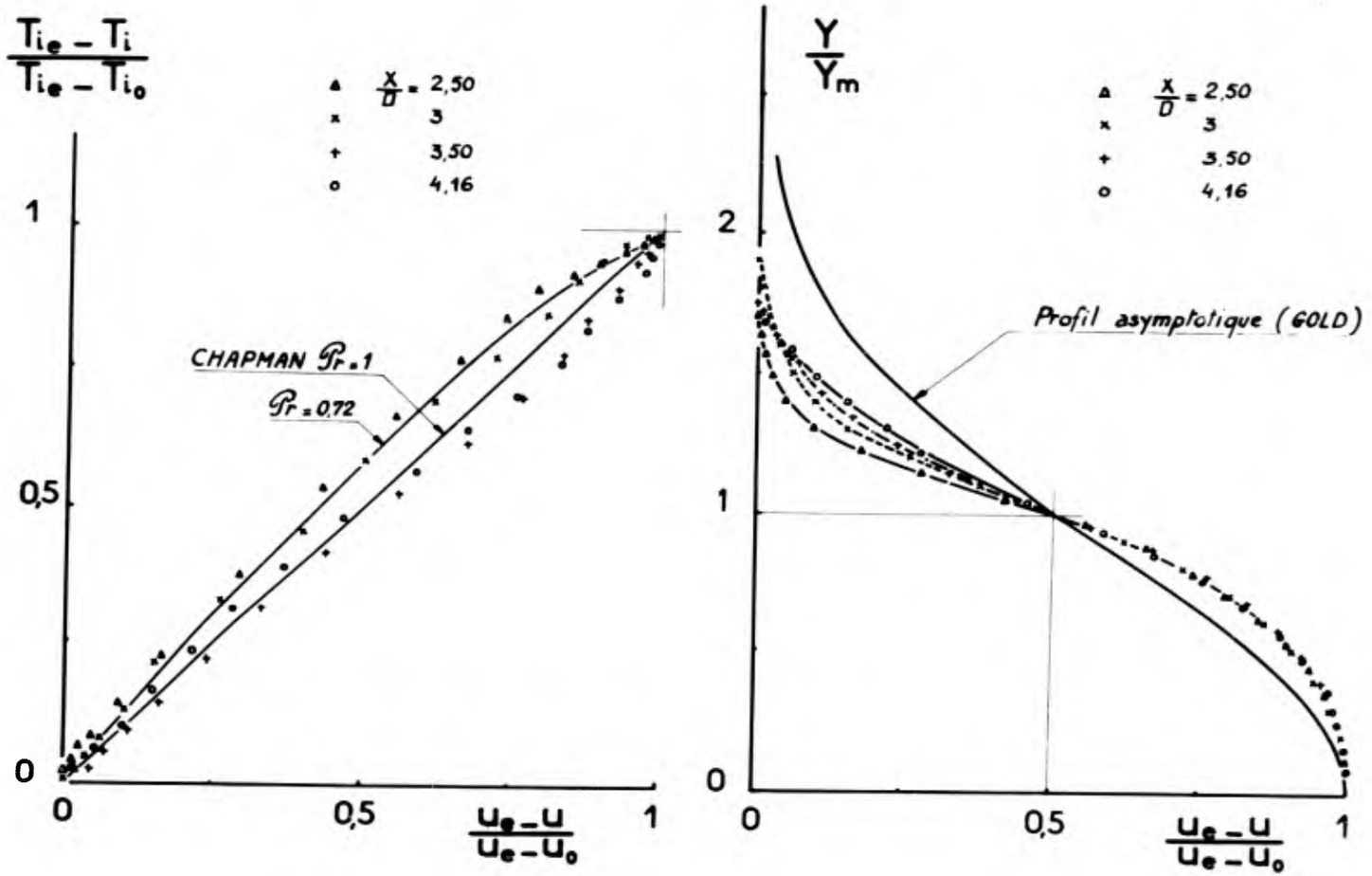

Fig. 16 Loi température - vitesse et évolution des profils de vitesse réduite dans la recompression - Régime laminaire $M_\infty = 5$

$\frac{T_p}{T_{1\infty}} = 0,5$ $\qquad$ $R_D = 5,5.10^4$

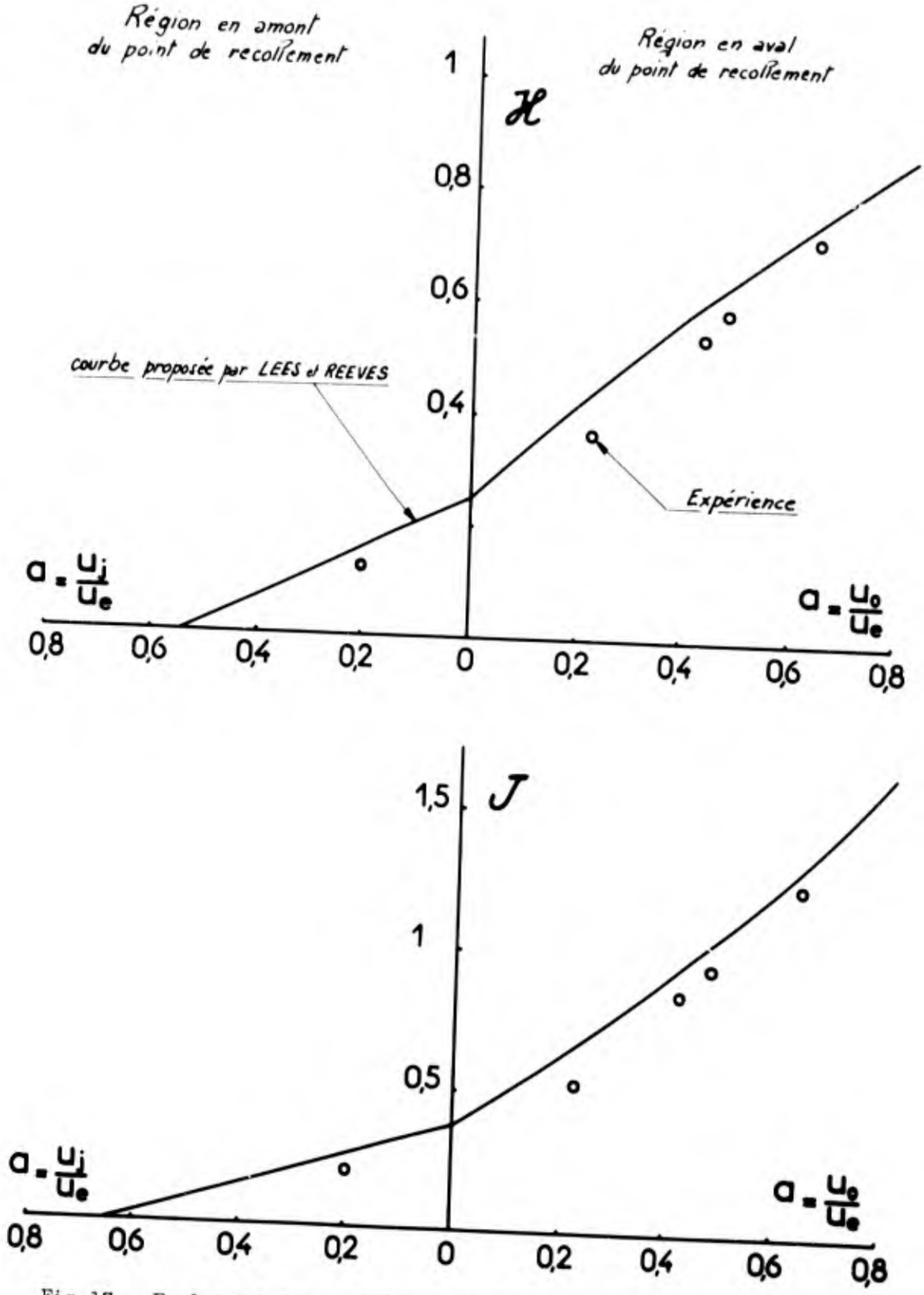

Fig. 17 Evolution des paramètres de forme incompressibles $\mathcal{H}$ et J
Régime laminaire $M_\infty = 5$

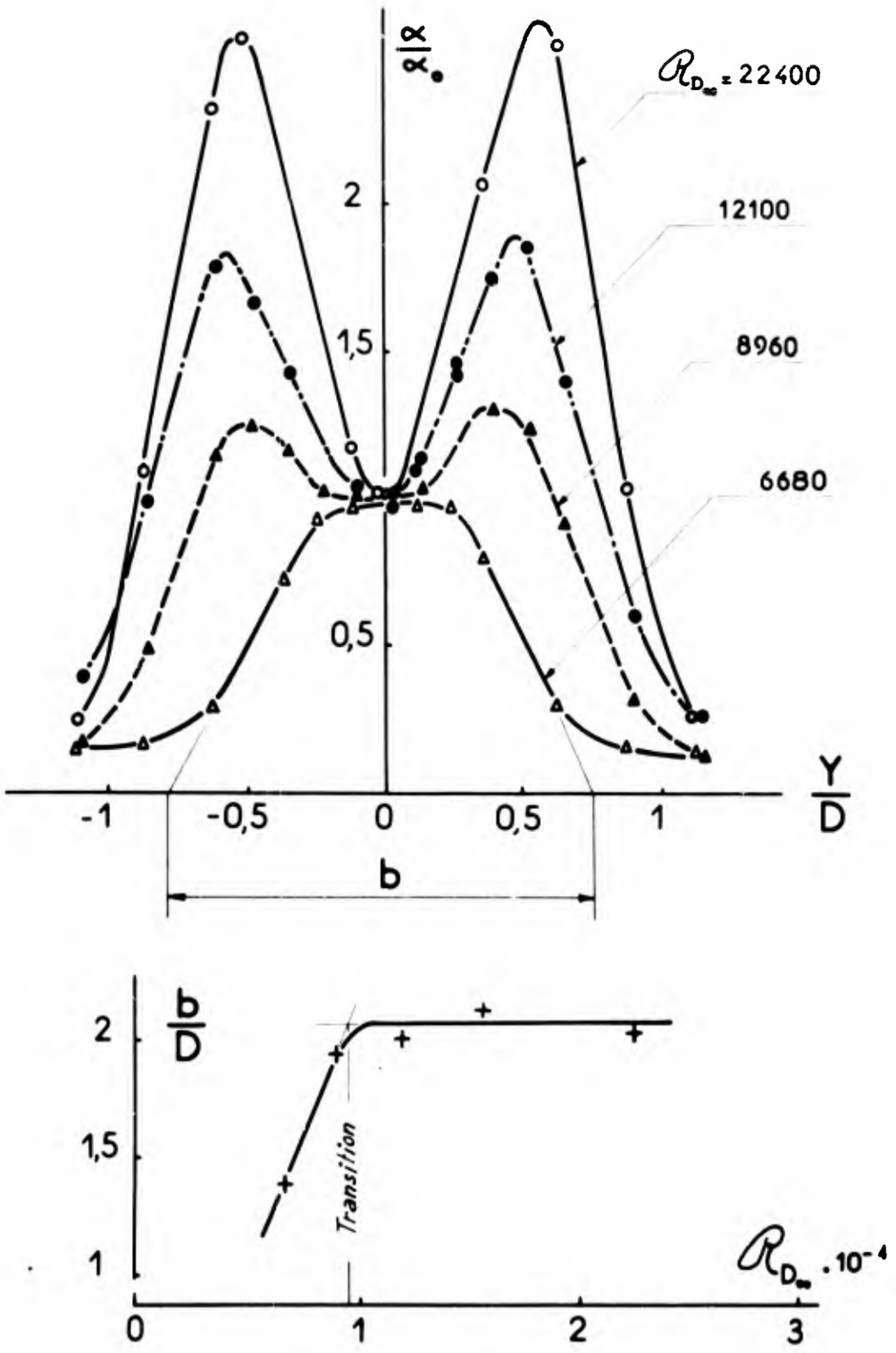

Fig. 18 Détermination du nombre de Reynolds de transition à partir de la largeur du sillage

X/D = 24,5 D = 4 mm M_∞ = 2,3

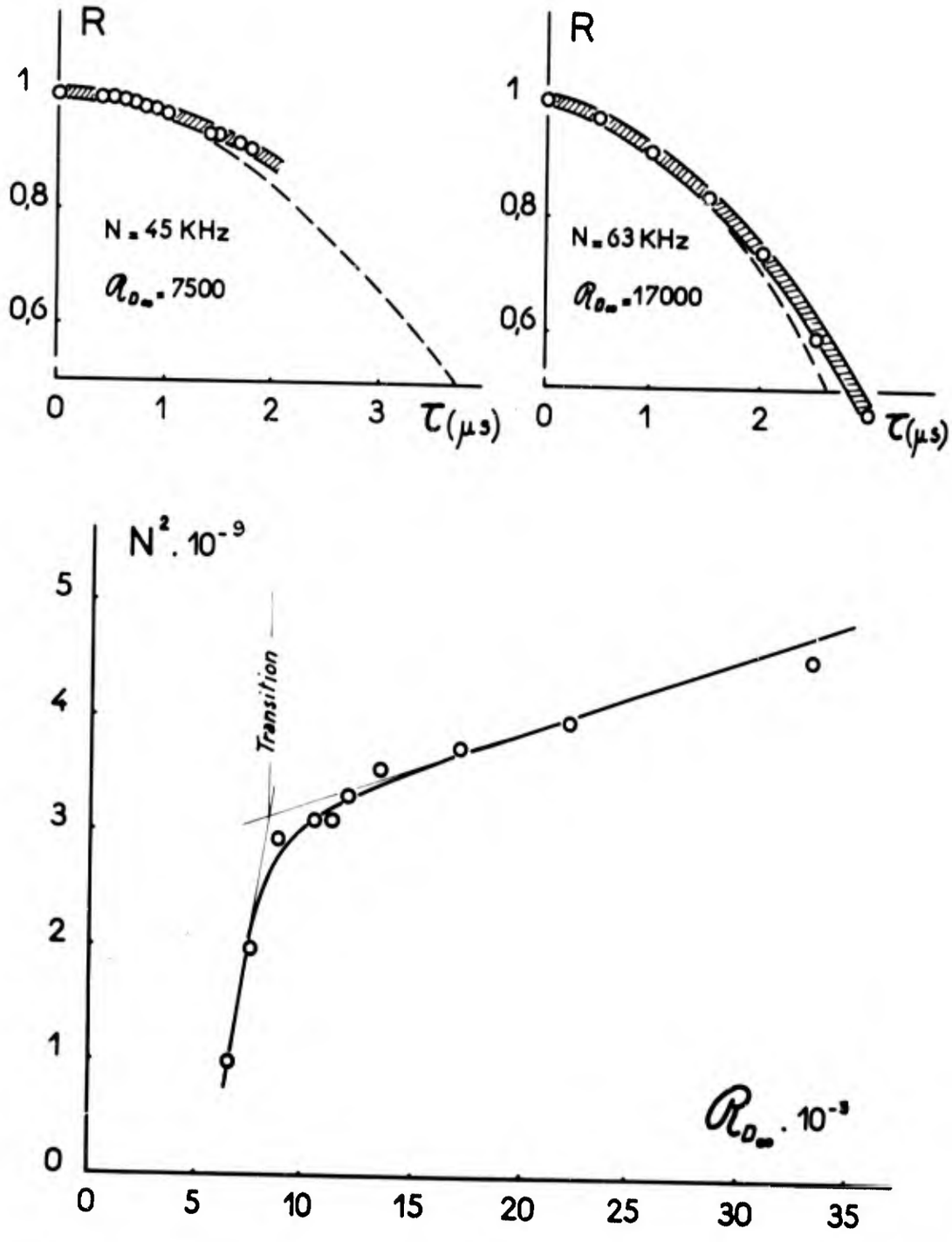

Fig. 19 Détermination du nombre de Reynolds de transition à partir de mesures d'autocorrélation

X/D = 24,5 D = 4 mm M_∞ = 2,3

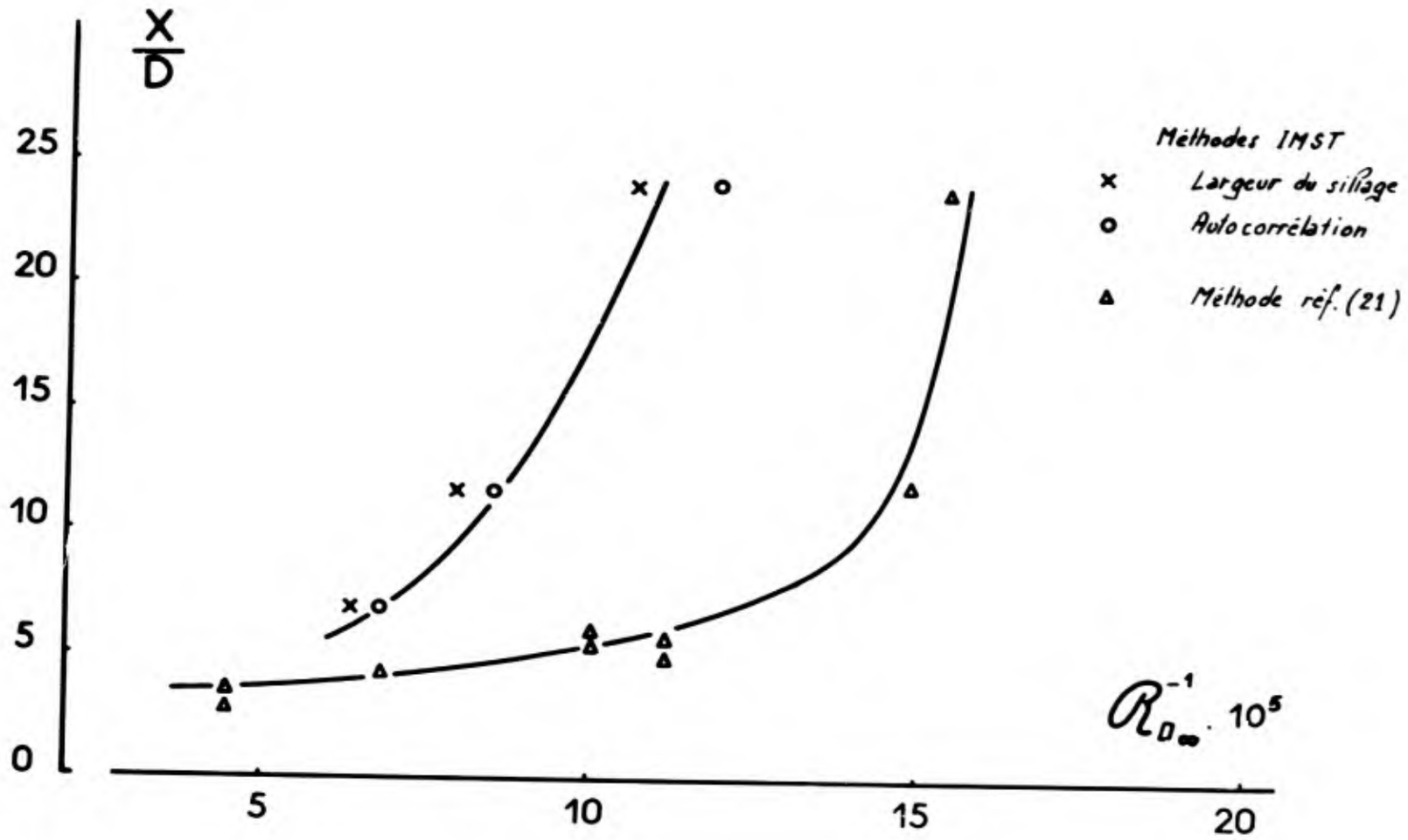

Fig. 20 Evolution de la distance de transition en fonction du nombre de Reynolds D = 4 mm

NEAR WAKE OF A SLENDER CONE IN HYPERSONIC FLOW

by

Edward M. Schmidt and Robert J. Cresci

Department of Aerospace Engineering
and Applied Mechanics
Polytechnic Institute of Brooklyn
Farmingdale, New York

This research study was supported by the Office of Naval Research
Under Grant No. NONR 839(33)

SUMMARY

This abstract presents a study of the flow field in the near wake region of a slender cone in a hypersonic free stream flow. Both experimental data and theoretical investigations of the overall flow field are included.

There is an inherent difficulty in obtaining data in the near wake region since most standard types of model support interfere with the flow region wherein the detailed measurements are to be carried out. For slender cones at zero angle of attack, various experimental techniques have been evolved to circumvent this difficulty. Shock tube studies were originally performed using wire supports that melt away as the starting shock passes the test section. It was subsequently found that no alteration of the flow occured if the wires were allowed to continue supporting the model throughout the test. This result was also substantiated in blow down wind tunnel tests using fine braided wires for model supports, thus, this method of support was utilized in the present experiments.

The experimental investigation consists of a study of the flow on the surface and near wake regions of a sharp 10° half angle cone with an 8" base diameter. Heat transfer and pressure measurements were made on the cone surface to give an indication of the nature of the boundary layer at the separation point under various test conditions. In the near wake region a complete pressure survey was made which includes base pressure measurements, static, and pitot pressure profiles at various axial locations downstream of the base. Measured stagnation temperature profiles enabled the computation of all desired flow properties and therefore provided a basis for comparison with the theoretical work.

The theoretical analysis of the near wake régime consists of an application of the method of rotational characteristics to the expansion of the cone boundary layer around the shoulder. This basic approach has also been used by Weiss and Weinbaum; the basic difference in the method and a comparison of the present method with experimental data is presented.

RESUME

Les auteurs présentent une étude du champ d'écoulement dans la zone de sillage située au voisinage immédiat d'un cône fusiforme placé dans un écoulement libre hypersonique. Cette étude comprend données expérimentales et résultats de recherches théoriques pour la totalité du champ d'écoulement.

La difficulté inhérente à l'obtention de données dans le sillage proche réside dans le fait que la plupart des modèles standard de support de maquette créent des interférences dans la région de l'écoulement où l'on doit effectuer des mesures détaillées. Dans le cas des cônes fusiformes à angle d'attaque nul, on a mis au point diverses techniques expérimentales afin d'obvier à cet inconvénient. Pour les essais en tubes à choc, on avait recours, précédemment, à des supports consistant en fils métalliques qui fondent dès que l'onde de choc initiale franchit la veine d'essai. Toutefois, on a découvert, par la suite, que l'écoulement ne subissait pas de modification si on laissait à leur place les fils de support pendant toute la durée de l'expérience. Ceci fut également confirmé par des essais en souffleries à rafales, où les maquettes étaient maintenues en place par des fils tressés d'une grande finesse; on a donc utilisé cette méthode au cours des expériences décrites ici.

L'expérience consiste en une étude de l'écoulement sur la surface et dans le sillage proche d'un cône effilé, au demi-angle de 10° et au diamètre de base de 8 pouces. On a procédé à des mesures de pression et de transfert de chaleur à la surface du cône pour obtenir des données sur la nature de la couche limite au point de décollement dans diverses conditions d'essais. Dans la zone du sillage située au voisinage immédiat du cône, on a effectué une étude complète des pressions, consistant en mesures des pressions à la base du cône et tracés des profils de pression statique et dynamique en divers points axiaux en aval de la base. Les profils des témperatures d'arrêt ont permis de calculer toutes les caractéristiques désirées de l'écoulement, fournissant ainsi une base de comparaison avec les résultats théoriques.

L'analyse théorique du régime du sillage proche consiste à appliquer la méthode des caractéristiques de rotation à l'élargissement de la couche limite du cône autour du ressaut. C'est également de cette façon que Weiss et Weinbaum ont abordé le problème. Les auteurs présentent la différence essentielle de la méthode et comparent la méthode actuelle aux résultats expérimentaux.

NOTATION

C_p		specific heat at constant pressure
D		cone base diameter (8.0 inches)
h		enthalpy
k		coefficient of thermal conductivity
M		Mach number
Nu	$\equiv$	$q_w C_{p_\infty} D/k_\infty (h_{s_\infty} - h_w)$ - Nusselt number
p		static pressure
q		heat transfer rate
Re_D	$=$	$\rho_\infty V_\infty D/\mu_\infty$ - Reynolds number
r		radial coordinate measured from centerline
s		cone surface coordinate
T		temperature
V		velocity
x		coordinate in free stream direction measured from cone base
$\bar{(\ )}$		coordinate normalized with respect to base diameter
α		angle of attack
ρ		mass density
μ		coefficient of viscosity
φ		azimuthal angle measured from windward axis

Subscripts

s	stagnation conditions
w	conditions evaluated at cone surface
∞	free stream conditions
1	local conditions
2	conditions behind a normal shock

NEAR WAKE OF A SLENDER CONE IN HYPERSONIC FLOW

Edward M. Schmidt and Robert J. Cresci

1. INTRODUCTION

The near wake of blunt-based slender bodies represents a fundamental fluid mechanical problem which derives its basic features from the separated flow regime. The necessity of studying this region in detail has been dictated by the effect of its local flow properties on communications, guidance, and identification of high speed vehicles. A comprehensive review of the available literature connected with this problem is presented in reference (1) while the current development of theoretical analyses of the near wake region is typified by the results of references (2) and (4). These analyses are presently applicable to two dimensional bodies with laminar boundary layers. Even in this some what limited context, moreover, there arise certain difficulties which restrict the solutions to limited ranges in free stream Reynolds numbers and Mach numbers, cf. reference (4). For the more practical problem of an axisymmetric body with either a laminar or turbulent boundary layer, the inherent complexity of analyzing such a region is even greater so that no current analyses is capable of predicting the flow properties in the near wake region.

Certain properties of the base flow region are significant from the viewpoint of design and advanced development of reentry bodies, e.g. the temperature of the fluid in the recirculating region, and near wake velocity profiles, which are necessary initial conditions for far-wake computations. Since theoretical analyses for the prediction of these

properties are not yet available, attempts have been made to correlate this information in terms of the free stream conditions and vehicle configurations from experimental data. cf. references (5) through (7). It has therefore become necessary to obtain a large amount of experimental data for this purpose; this data also provides information for comparison with proposed theoretical analyses, and indicates the basic flow pattern from which the theoretician can gain insight into mechanisms governing the flow in this region. The experimental data has been obtained by various techniques including ballistic range firings, shock tunnels and blowdown wind tunnels. A comprehensive summary of the experimental reports issued over the past several years on this subject has been presented in reference (8) and includes near wake data for a variety of vehicle configurations, free stream Mach numbers, Reynolds numbers, wall temperature ratios, etc. Although there is a reasonably large amount of data available, certain aspects of the flow pattern have not yet been satisfactorily resolved and require further investigation.

A configuration which has received little attention as yet is the asymmetric body, or slender body at angle of attack. This problem is of extreme practical importance since a re-entering hypersonic vehicle will not necessarily be at zero attitude throughout its entire flight trajectory. In fact, if maneuvers are desired, the angle of attack developed can be quite large. Even without this consideration, however, small oscillations of the vehicle about the zero angle of attack attitude are possible and may have a significant influence on the general behavior of the base flow. Some data is currently available concerning this phenomenon and has been presented in reference (9). It consists of a 10° half angle cone tested at $M_{\infty} = 6.0$ and at a 10° angle of attack. The

free stream Reynolds number is sufficiently large so that fully turbulent flow is achieved both on the cone surface and in the near wake. The corresponding data for $\alpha = 0$ are presented in reference (6). Significant differences in the flow field were observed due to the angle of attack of the body. In addition to this basic inviscid flow field effect, it is of considered importance to determine whether a change of vehicle attitude can sufficiently alter the surface boundary layer characteristics and the base flow to change the near wake from a laminar to a turbulent flow. In other words, if the free stream Reynolds number is sufficiently low so that both the surface boundary layer and the near wake are laminar at $\alpha = 0$, and then a change in attitude produces an angle of attack, the question arises as to whether the altered nature of the boundary layer on the surface of the body can signicantly alter the mixing processes occuring in the near wake.

It is the purpose of this investigation, therefore, to examine the flow characteristics in the near wake of a slender body at angle of attack for reasonably low Reynolds numbers. A detailed study of the surface properties on the cone is performed both at zero and non-zero angle of attack to accurately ascertain the nature of the boundary layer under these conditions. This is necessary if a more complete understanding of the measured wake data is to be obtained. The flow field is surveyed between the base and several base diameters downstream of a sharp, 10° half angle cone which is wire supported at a 10° angle of attack. Tests were conducted at a free stream Mach number of 7.7 in the PIBAL hypersonic facility over a free stream Reynolds number range of 0.3×10^6 to 1.5×10^6 based on model diameter. The average stagnation temperature is $1700^{\circ}R$ producing a wall to stagnation temperature ratio of 0.32. The same model was also tested previously at zero inclination, thus, a comparison of results

may be performed between the zero and non-zero angle of attack configurations.

2. MODEL DESIGN AND INSTRUMENTATION

The model, illustrated in figure (1), is a 10^{o} half angle cone which was rolled and machined to 0.05 inches thickness from a stainless steel sheet. The surface is instrumented for local heat transfer and static pressure measurements; these are required to determine the nature of the boundary layer both at the zero and non-zero angle of attack configurations. For the surface measurements, the model is supported by a base sting to facilitate removal of the instrumentation leads from the wind tunnel. Heat transfer gauges, which are located at various positions along a generator of the cone, consist of fine thermocouple wires spot welded to the inside of the model skin. The local heat transfer rate is calculated by the thin skin technique, utilizing the basic assumptions that no heat is transferred along the cone surface, and that the inner surface is adiabatic. Static pressure taps are also located along a conical ray, the peripheral distribution of surface pressure being obtained by rotating the model about its axis on the model mount.

To obtain data in the near wake, the model is supported by six braided cables with a diameter of 0.03 inches; three of these support the model at the nose and three just slightly aft of the model center of gravity. In this manner, the rear wires penetrate the model boundary layer at a location of more than 250 wire diameters upstream of the model base. This is done to assure no wire interference effects on the base region, since in this distance the major influence of the wires has been dissipated.

The wake survey data obtained corresponds to radial variations of flow parameters at selected axial positions. These measurements of local values of the pitot and static pressures are obtained only in the supersonic portion of the near wake region. The rakes and probes used in the wake survey are illustrated in figure (2). The total pressure rake consists of standard pitot tubes with blunt leading edges connected to Statham 0.5, 2.5, and 15 lb./in.^{2} transducers. The static probes consist of tubes with six static holes drilled around their periphery at a distance of 15 tube diameters from the tip; slender (5°) cones are installed at the tips of the probes to facilitate the decay of local static pressure on the probe surface to that of the local free stream. The static pressure is measured using Hastings DV-13 thermocouple type gauges. The static probes measure the local static pressure directly while the total head probes measure the pitot pressure. From the pitot and static pressure data, the local Mach number is obtained and the corresponding value of the local stagnation pressure can then be computed.

The tests were performed at Mach 7.7 with air as the test gas. The duration of sustained hypersonic flow in this blow down tunnel is on the order of 30 seconds, however, to obtain wake data at a relatively constant value of the wall temperature ratio, a run length of about 5 seconds is used. This is sufficient to achieve stabilization of the pressure instrumentation and still have a relatively uniform surface temperature. The tunnel stagnation pressure was varied from 30 psia to 500 psia to obtain the desired variation in Reynolds number necessary to compare with the theoretical analyses of the boundary layer. The complete wake survey at $\alpha = 10^\circ$ was conducted at a nominal tunnel stagnation pressure of 250 lb./in.^{2} and roughly 1700°R stagnation temperature, which corresponds

to a free stream Reynolds number of 0.83×10^6 per foot.

3. PRESENTATION AND DISCUSSION OF RESULTS

One method which has been utilized extensively in the past to ascertain the nature of the boundary layer characteristics on a surface is to measure the local heat transfer rate and compare this to theoretical analyses. This has been done for the test model at both zero and non-zero angles of attack and the results are shown in figure (3). The data is presented in terms of Nusselt number versus a Reynolds number based on free stream conditions and the base diameter of the cone. This particular variation of heat transfer corresponds to a surface location ($\bar{s} = 2.80$) on the cone which is close to the shoulder ($\bar{s}_b = 2.88$). Also included on the data plot of figure (3a) are the laminar boundary layer predictions of reference (10) and the fully turbulent theory of reference (11). It is observed that by varying the stagnation pressure of the tunnel, complete range of boundary layer behavior can be obtained corresponding to either completely laminar, transitional, or fully turbulent at the shoulder. For Reynolds numbers less than 0.7×10^6, the boundary layer on the entire surface is seen to be laminar.

For the angle of attack configuration, the corresponding data for the same surface location is presented in various meridian planes. The angle φ is measured from the windward plane and for $\varphi = 0$, the theoretical laminar boundary layer analysis of reference (12) is included for comparison. The comparison of experimental data and the theoretical analysis indicates that the boundary layer is laminar in this plane over the entire test Reynolds number range. The corresponding data and analysis is also shown in the cross plane ($\varphi = 90^\circ$) and again it is observed that the boundary layer is laminar. Along the cone surface in the leeward plane, the experimentally

obtained surface heat transfer is also presented. In this case, there is no theoretical analysis available since the cross flow is toward the plane of symmetry and the inviscid flow field is not accurately known. The cone surface in this plane is parallel to the free stream direction, however, a highly vortical flow exists due to the large inviscid cross flow velocities existing for this configuration. The observed variation of heat transfer with Reynolds number appears to indicate that the flow is transitional along this surface. Of further significance is the fact that although the flow is completely laminar on the windward surface, it appears to be transitional on the leeward surface at a value of the free stream Reynolds number which is less than required to achieve a transitional boundary layer on the cone at zero angle of attack. The near wake characteristics of axisymmetric bodies have been found to be strongly dependent on the surface boundary layer at the model shoulder, thus, it is of interest to determine for the present configuration, the near wake conditions that are produced. With this in mind the centerline variation of local properties such as Mach number and pressure will be examined for the non-zero angle of attack configuration.

Figures (4) through (6) present the axial distributions of static pressure, Mach number, and local stagnation pressure along the model centerline as a function of distance from the base of the cone. The static pressure measurements presented in figure (4) are normalized with respect to the corresponding free stream values thereof and the zero angle of attack data of references (13) through (15) are also included for comparison. This data corresponds to a range in free stream Mach number between 5.0 and 12.0 and a range in Reynolds numbers which produce either laminar or fully turbulent boundary layers on the cone surface. The peak over-pressure obtained is seen to increase as the Mach number increases or

or as the Reynolds number decreases. In addition, the axial extent of the region of increased pressure is quite large for laminar layers while for turbulent conditions it is reduced considerably. Examination of the Mach 8.0 data, at zero angle of attack, for different Reynolds numbers indicates this trend quite conclusively. For the low Reynolds number laminar tests ($Re_D \approx 0.20 \times 10^6$) the static pressure in the near wake is seen to reach a value of 2.5 times the free stream pressure at a distance of roughly 5 diameters downstream of the base, while for the turbulent condition ($Re_D = 1.1 \times 10^6$), the peak pressure is only 1.3 p_∞ and is achieved at a downstream distance of only three base diameters. Compare this with the angle of attack configuration (solid symbols) and it is observed that the data compares with the fully turbulent, zero inclination condition. It should be noted that although the data presented in figures (4) through (6) correspond to the geometric centerline distribution for the zero angle of attack configuration, when the cone is inclined at an angle with the free stream this centerline does not correspond to the "local symmetry axis." Therefore, the angle of attack data corresponds to the maximum local static, or minimum local pitot pressures, rather than the centerline distributions. These occur slightly off axis as can be seen in figures (7) and (8).

Figure (5) presents the centerline variation of Mach number for the various experimental data available and trends similar to those observed in the pressure variation are seen to occur. The zero angle of attack, Mach 8.0, data for laminar flow indicate that recovery to half of the free stream Mach number occurs roughly six diameters downstream, while for turbulent flow, the same wake Mach number is achieved at five diameters. When the cone is placed at an angle of attack, however, recovery to free stream conditions is seen to occur even more rapidly

than for the zero angle condition with a fully turbulent surface boundary layer. Since these two configurations produced similar static pressure distributions, it is evident that the stagnation pressure recovery in the near wake will also be dissimilar due to the difference in Mach number variation. This can be seen in figure (6) which presents the variation of local stagnation pressure (normalized with respect to the free stream stagnation pressure) along the axis. Again, it is seen that the recovery to free stream conditions occurs more rapidly than for the zero angle of attack condition with a fully turbulent boundary layer. The recovery of the near wake flow parameters thus appears to be influenced by two different factors in the angle of attack configuration. First, the angle of attack produces a localized region on the cone surface wherein the boundary layer which was originally laminar has become transitional or turbulent at lower Reynolds numbers than expected for the axisymmetric flow case. This effects the mixing processes and therefore the behavior of the local flow conditions in the wake. In addition, it appears that for the angle of attack configuration there is a large scale mixing caused by the vortical inviscid flow over the cone surface which further increases the pressure recovery in the wake to its free stream value.

Pitot pressure profiles are presented in figures (7a) through (7f). The trailing shock shape can be roughly determined from the observed discontinuity in the pitot profiles; this is shown to scale in figure (9) with the corresponding zero angle of attack shock shape as determined from the high Reynolds number (turbulent boundary layer) tests. As noted previously, the symmetry axis in the viscous core is displaced toward the leeward side of the cone by an amount approximately equal to one tenth of the base diameter. As the distance downstream of the

base increases, this radial shift decreases until it is essentially zero ($\bar{x}$ = 4.5). The trailing shock shape is also displaced in the same direction although it is seen to require a longer distance to approach the axisymmetric shock configuration. In order to determine the range of validity of the measured profiles, the conical shock and base expansion fan are also shown in figure (9). Reflection of this shock from the tunnel wall (using the displacement thickness as an approximate wall correction) on the windward side of the model indicates an intersection with the trailing shock between four and five base diameters downstream of the model. Although additional radial surveys were obtained for values of $\bar{x}$ up to 7.5, these are not included since the data is of questionable value. Centerline conditions, however, are expected to be reasonable for distances up to seven base diameters downstream of the model. The disturbance from the leeward surface of the cone is seen to have no effect on the measured flow variables for considerably larger distances.

The static pressure profiles are shown in figures (8a) through (8e). In these plots, the shock location is not as evident since the pressure readings on the static probes are affected for some distance on either side of the exact impingement location. In addition, the off-axis data incur a larger percentage error due to the possibility of local flow inclinations.

4. CONCLUDING REMARKS

In addition to providing some profiles of pitot and static pressure in the near wake of a cone at angle of attack, some overall effects on the pressure recovery have been observed. Comparison of the Mach 6.0 data, for fully turbulent flow, indicates that the effect of angle of attack on the inviscid flow increases the stagnation pressure ratio by roughly a factor

of three. The present tests at Mach 7.7 indicate an increase by a factor of five above the laminar axisymmetric flow conditions. This increase is believed to be caused in part by the inviscid flow field over the cone and partially by the local alteration of the boundary layer on the cone surface from a laminar to a transitional condition.

REFERENCES

1. Lykoudis, P.S. — A Review of Hypersonic Wake Studies. AIAA Journal Vol. 4, No. 4, April 1966, p. 577-590

2. Golick, R.J.; Webb, W.H.; Lees, L. — Further Results of Viscous Interaction Theory for the Laminar Supersonic Near Wake. AIAA Paper No. 67-61, January 1967.

3. Webb, W.H.; Golik, R.J.; Vogenitz, R.W.; Lees, L. — A Multimoment Integral Theory for the Laminar Supersonic Near Wake. Proceedings of the Heat Transfer and Fluid Mechanics Institute, 1965, p. 168-189.

4. Weiss, R.F. — A New Theoretical Solution of the Laminar, Hypersonic Near Wake. AIAA Paper No. 67-63, January 1967.

5. Zakkay, V.; Cresci, R.J. — An Experimental Investigation of the Near Wake of a Slender Cone at M_∞ = 8 and 12. AIAA Journal Vol. 4, No. 1, January 1966, p. 41-46.

6. Martellucci, A; Trucco, H. — Measurements of the Turbulent Near Wake of a Cone at Mach 6. AIAA Journal Vol. 4, No. 3, March 1966, p. 385-391.

7. Muntz, E.P.; Softley, E.J. — A Study of Laminar Near Wakes. AIAA Journal Vol. 4, No. 6, June 1966, p. 961-968.

8. Todisco, A.; Pallone, A. — Measurements in Laminar and Turbulent Near Wakes. AIAA Paper No. 67-30, January 1967.

9. Schlesinger, A.J.; Martellucci, A. — Wind Tunnel Investigation of the Near Wake of a Cone at Angle of Attack. GASL TR No. 581, March 1966.

10. Eckert, E. R. G. Engineering Relation for Friction and Heat Transfer to Surfaces in High Velocity Flow. Journal of the Aeronautical Sciences Vol. 22, 1955, p. 585-586.

11. Cresci, R. J.
MacKenzie, D. A.
Libby, P. A. An Investigation of Laminar, Transitional, and Turbulent Heat Transfer on Blunt-Nosed Bodies in Hypersonic Flow. Journal of the Aero/Space Sciences, Vol. 27, No. 6, June 1960, p. 402-414.

12. Reshotko, E. Laminar Boundary Layer with Heat Transfer on a Cone at Angle of Attack in a Supersonic Stream. NACA TN 4152, December 1957.

13. Schmidt. E. M. An Investigation of Hypersonic Flow Around a Slender Cone. AIAA Student Journal, Vol. 3 No. 4, December 1965, p. 126-129.

14. Martellucci, A.
Schlesinger, A. Measurements in the Near Wake of a Cone at Mach 12. GASL TR No. 582, March 1966.

15. Ragsdale, W. C.
Darling, J. A. An Experimental Study of the Turbulent Wake Behind a Cone at M= 5. Proceedings of the 1966 Heat Transfer and Fluid Mechanics Institute. p. 198-209.

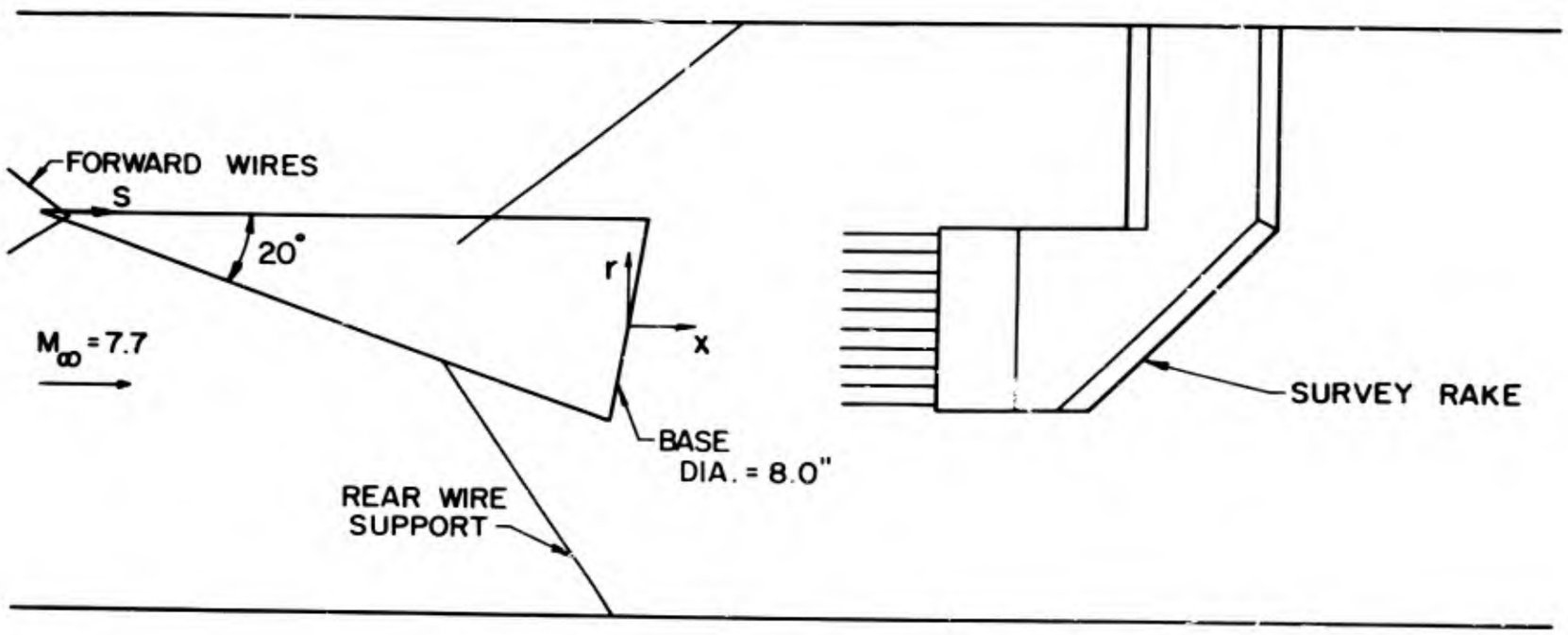

FIG (1) SCHEMATIC OF TEST CONFIGURATION

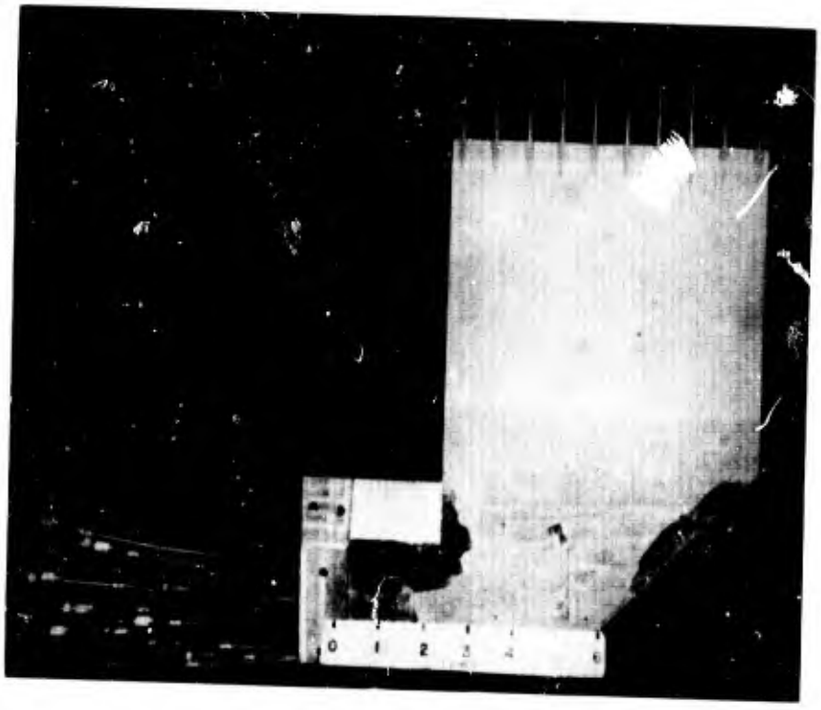

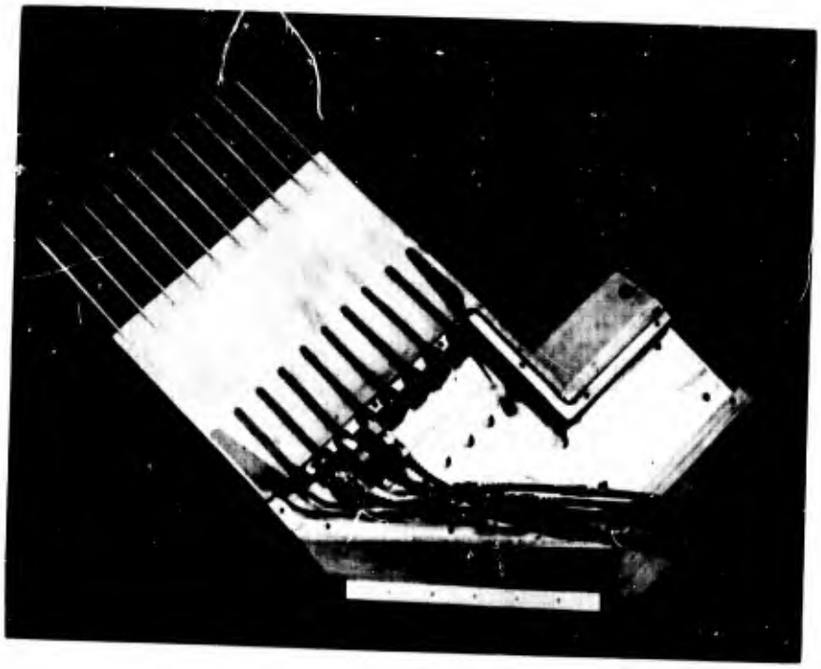

FIG (2) PHOTOGRAPHS OF WAKE SURVEY RAKES

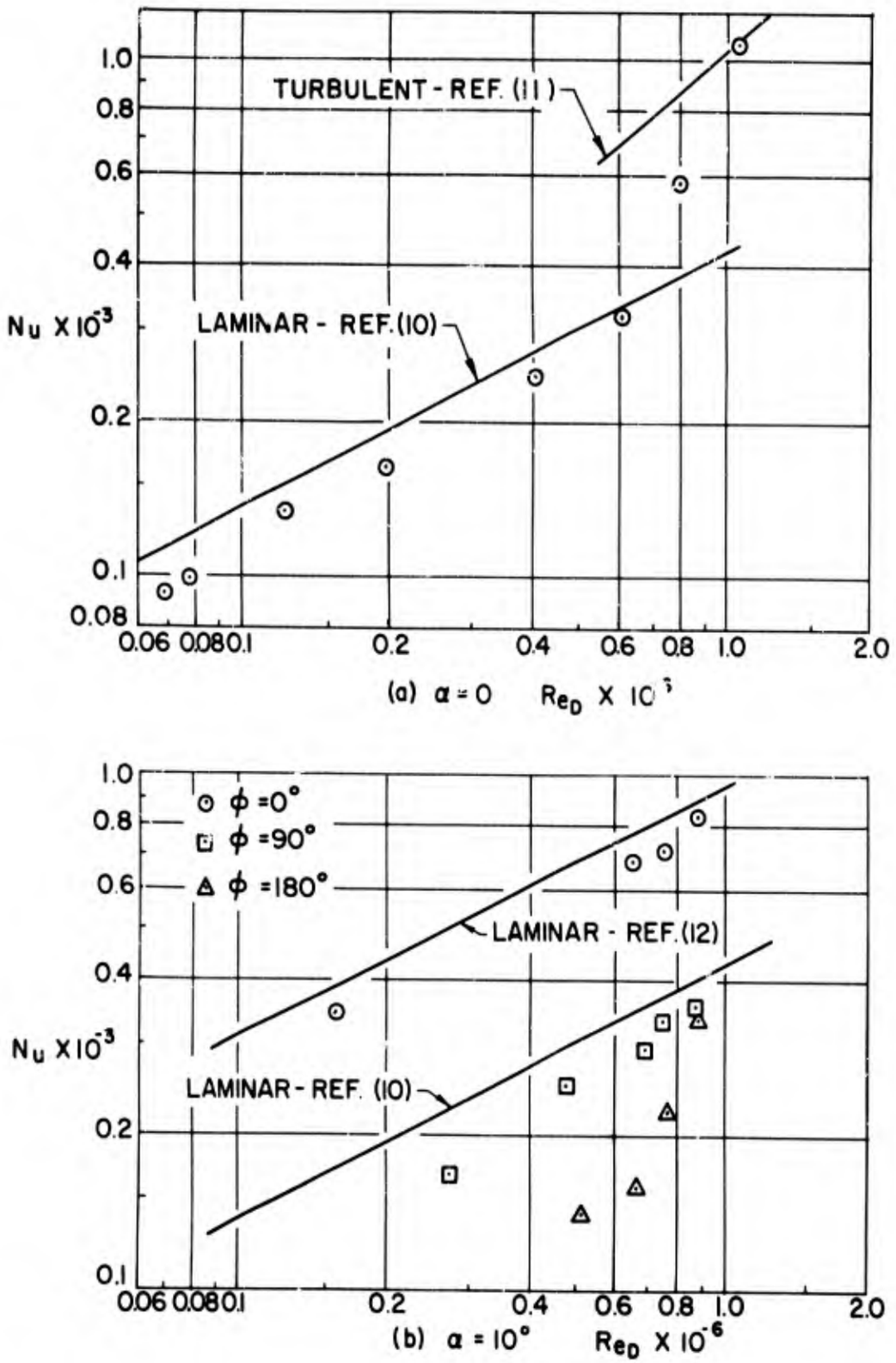

FIG (3) HEAT TRANSFER TO CONE SURFACE ($\bar{S} = 2.8$)

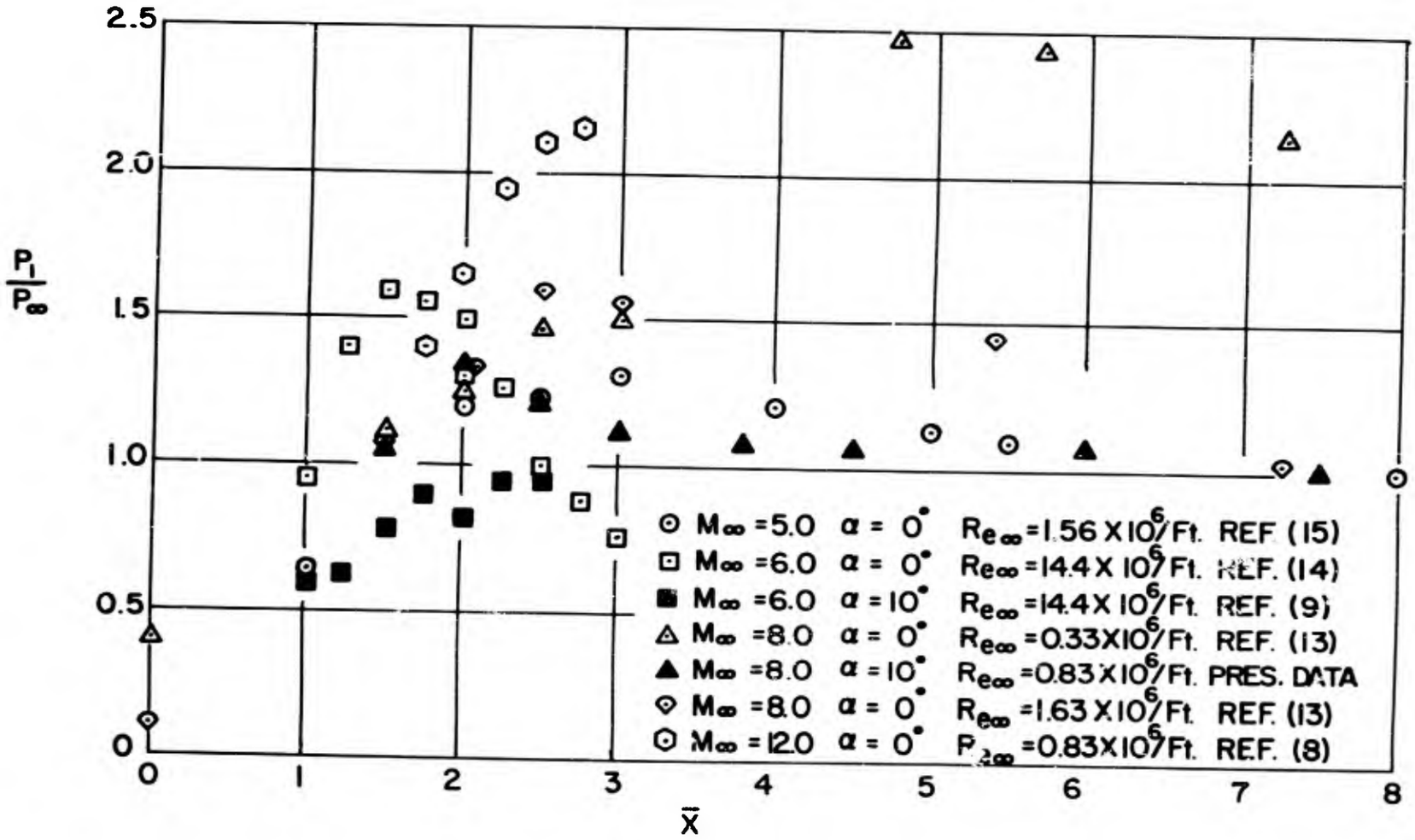

FIG (4) CENTERLINE DISTRIBUTION OF STATIC PRESSURE

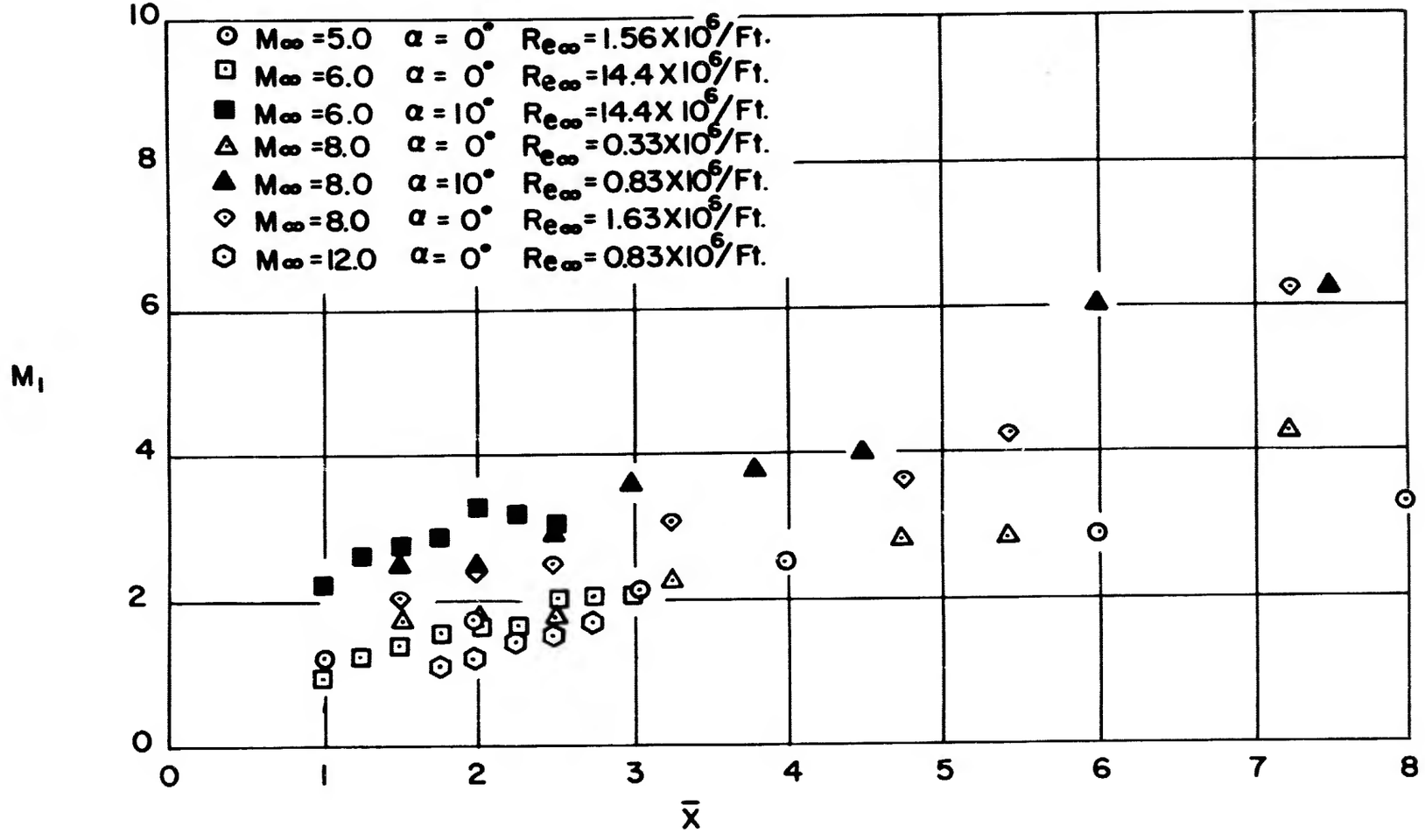

FIG (5) CENTERLINE DISTRIBUTION OF MACH NUMBER

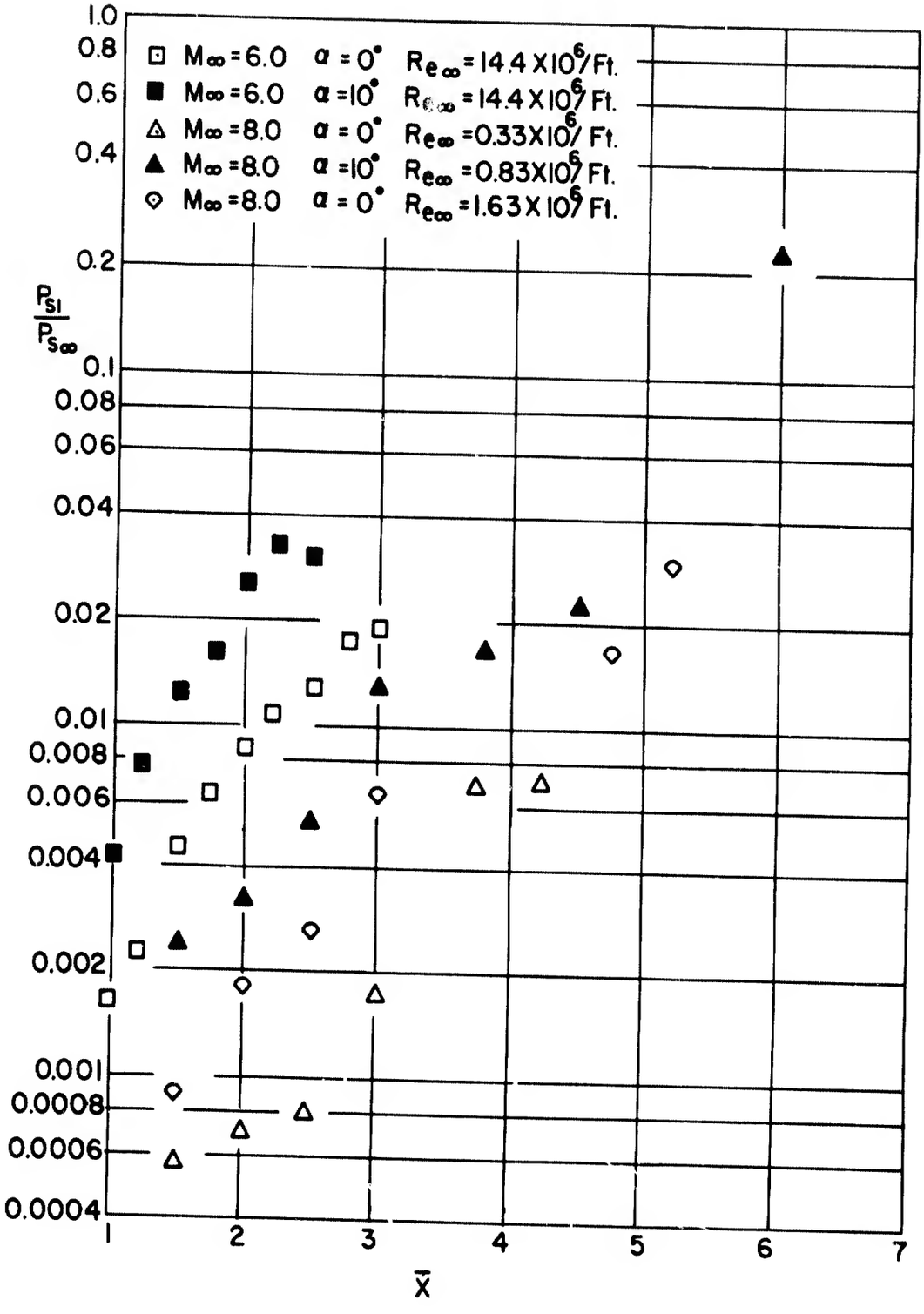

FIG. (6) CENTERLINE DISTRIBUTION OF STAGNATION PRESSURE

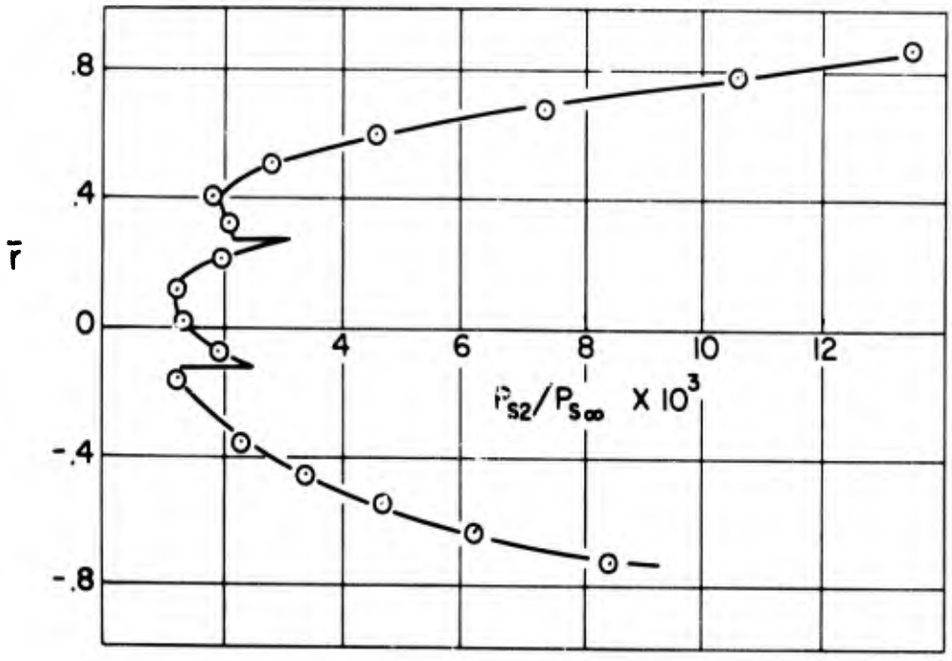

(a) $\bar{X}$ = 1.5

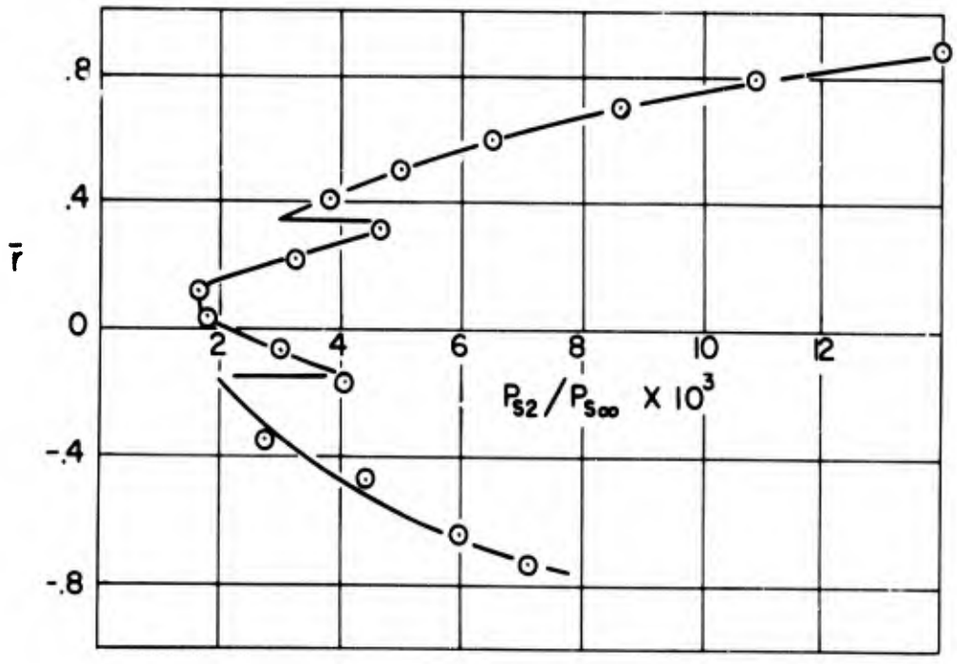

(b) $\bar{X}$ = 2.0

FIG (7) PITOT PRESSURE PROFILES

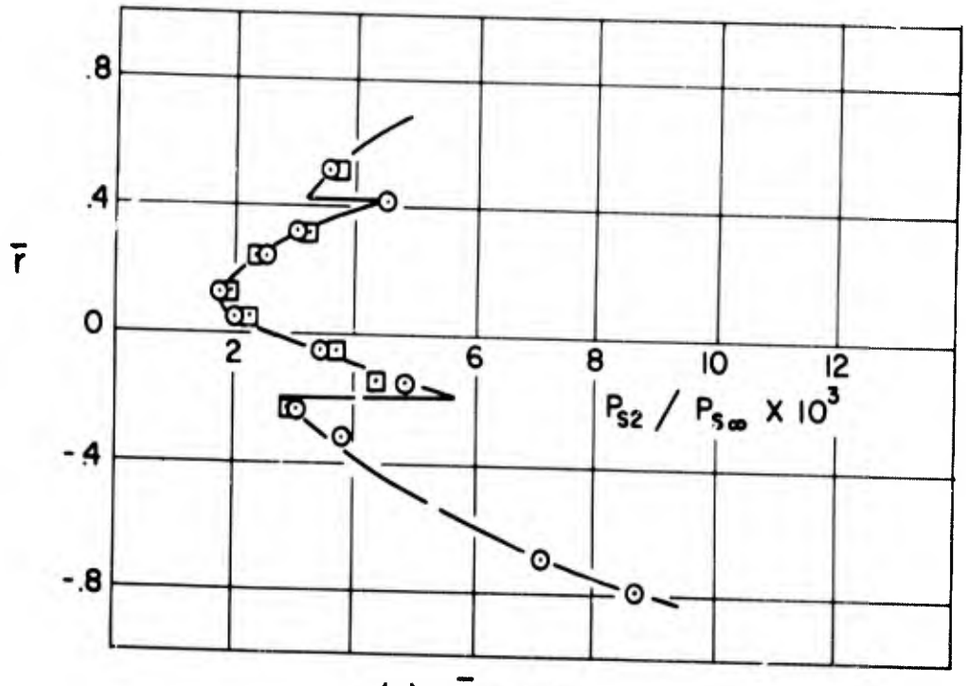

(c) $\bar{X} = 2.5$

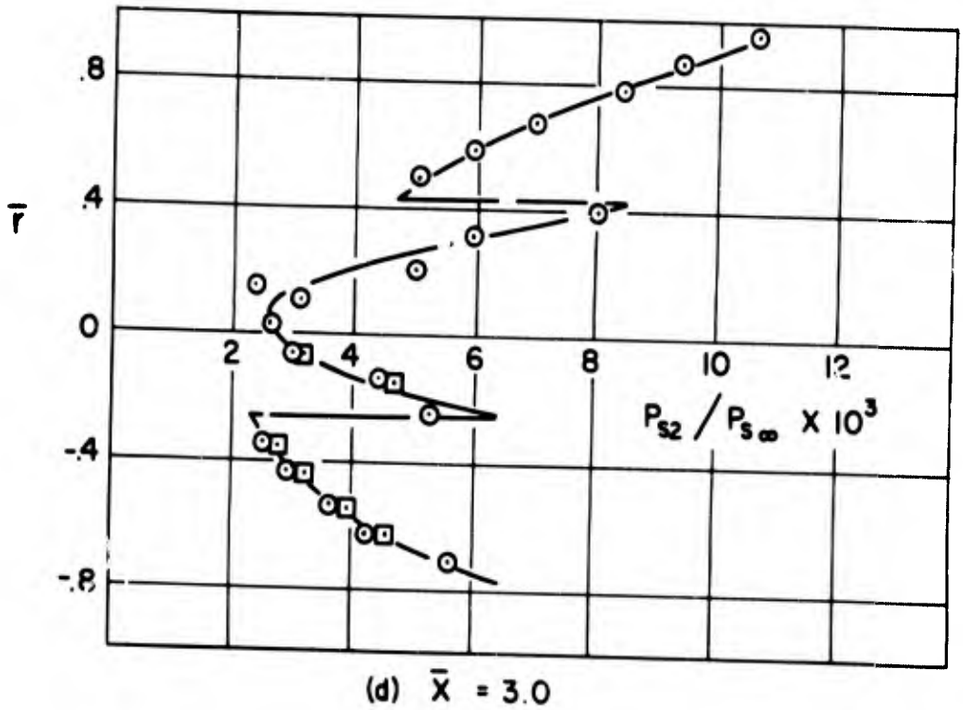

(d) $\bar{X} = 3.0$

FIG (7) PITOT PRESSURE PROFILES

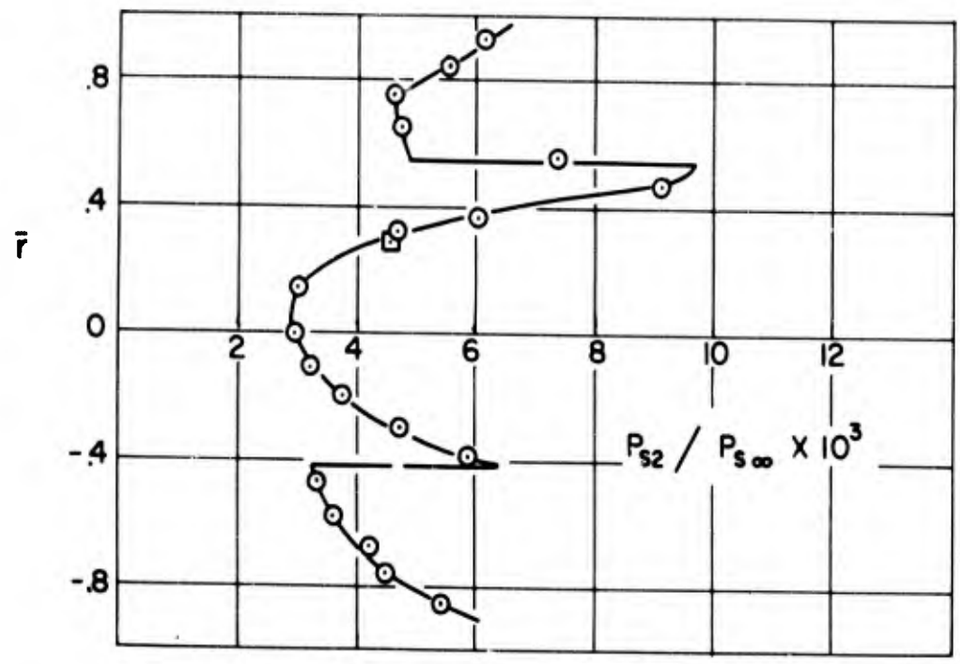

(e) $\bar{X} = 3.8$

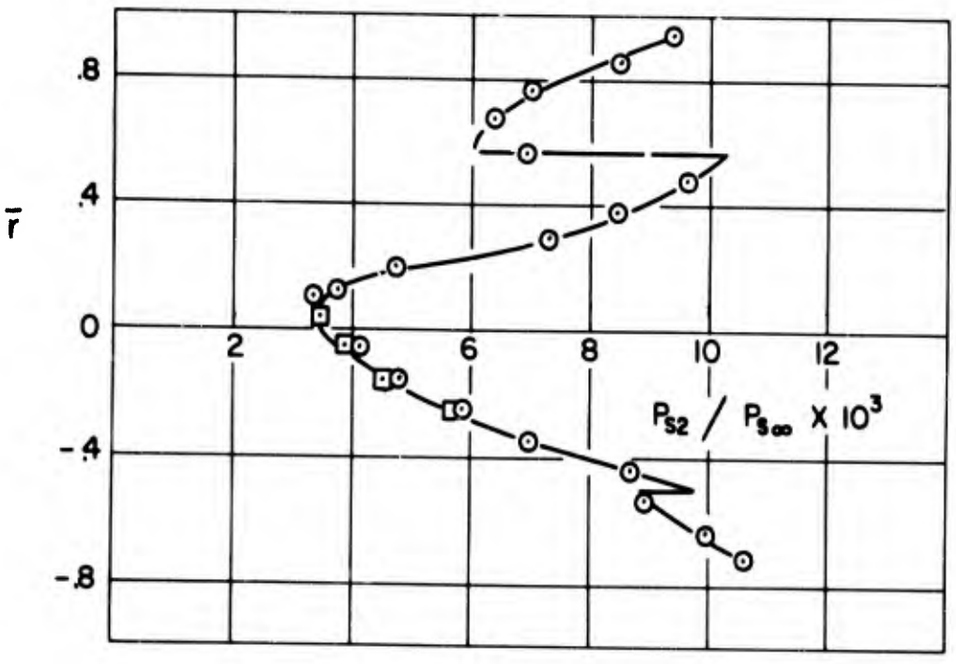

(f) $\bar{X} = 4.5$

FIG (7) PITOT PRESSURE PROFILES

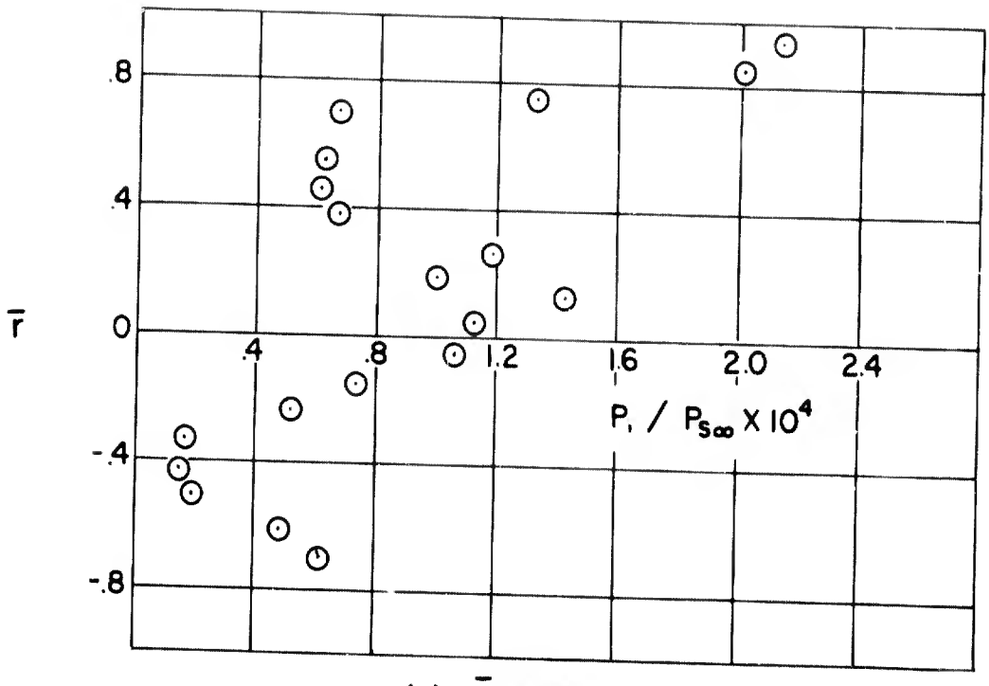

(a) $\bar{X}$ = 1.5

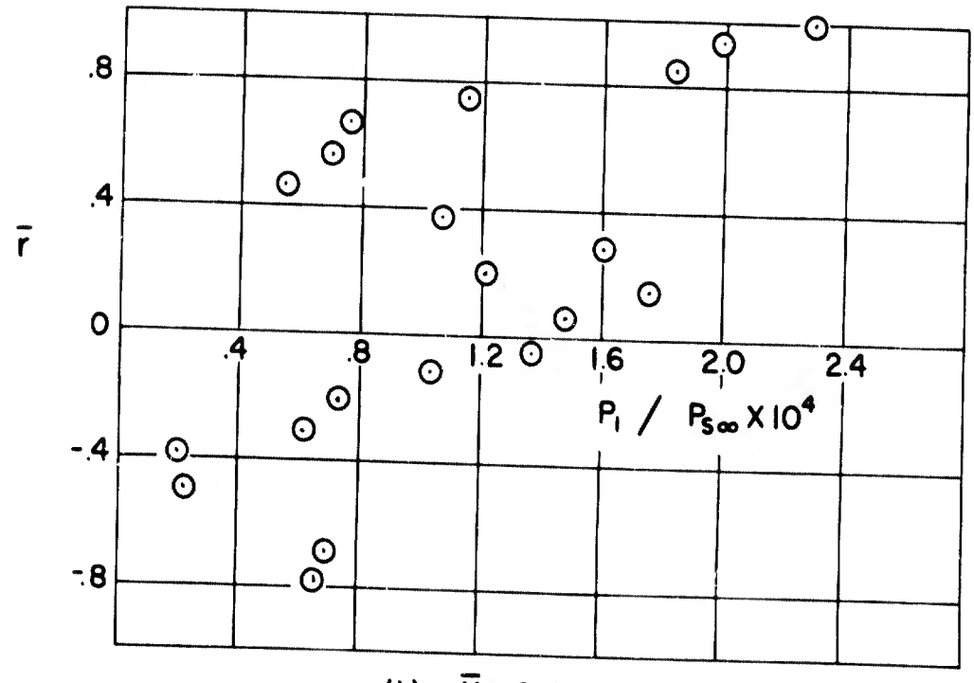

(b) $\bar{X}$ = 2.0

FIG (8) STATIC PRESSURE PROFILES

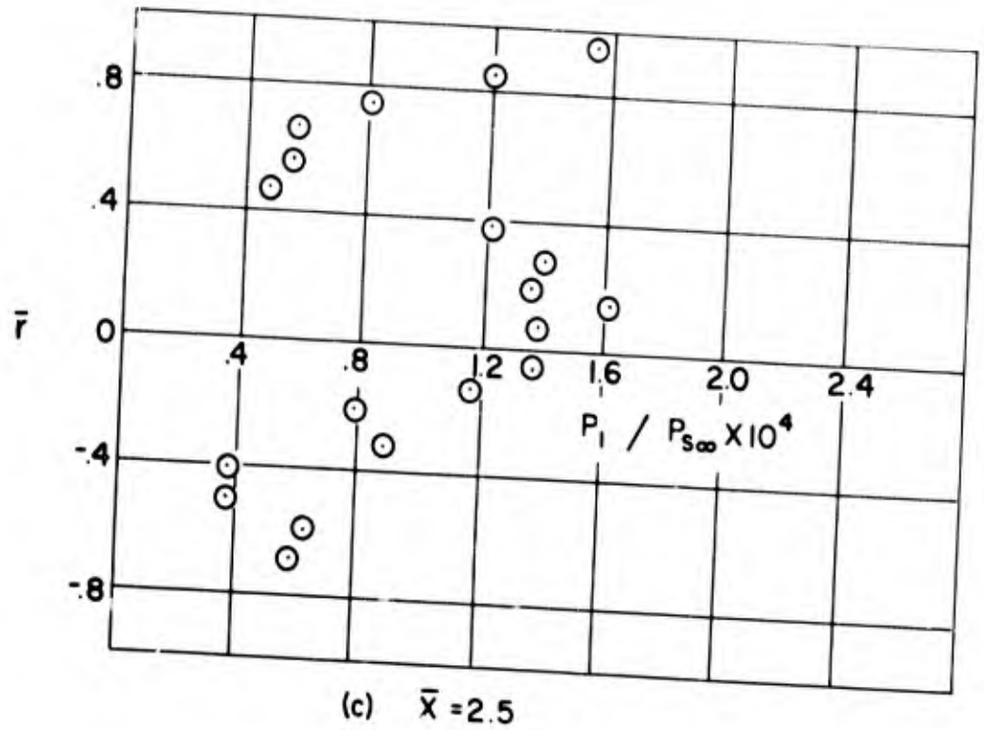

(c) $\bar{X} = 2.5$

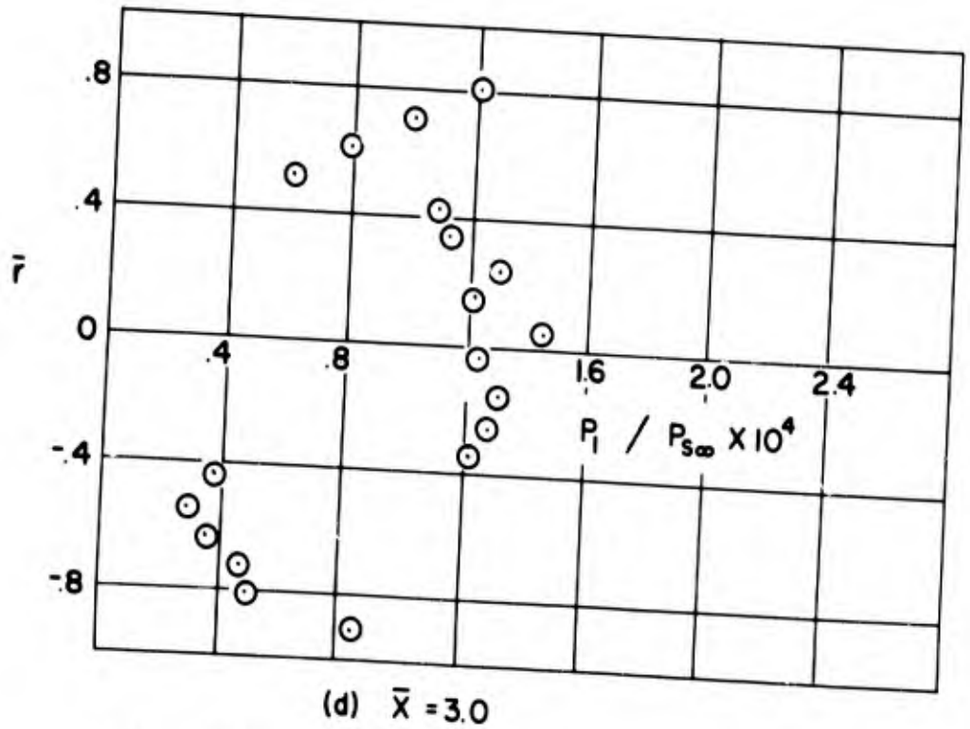

(d) $\bar{X} = 3.0$

FIG (8) STATIC PRESSURE PROFILES

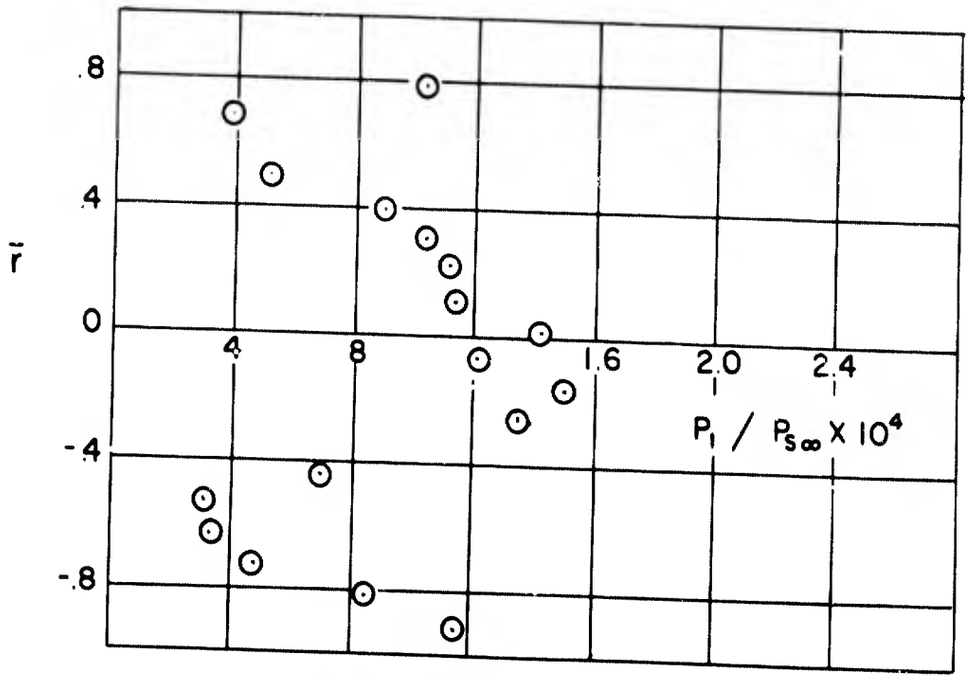

(e) $\bar{X} = 3.8$

FIG (8) STATIC PRESSURE PROFILES

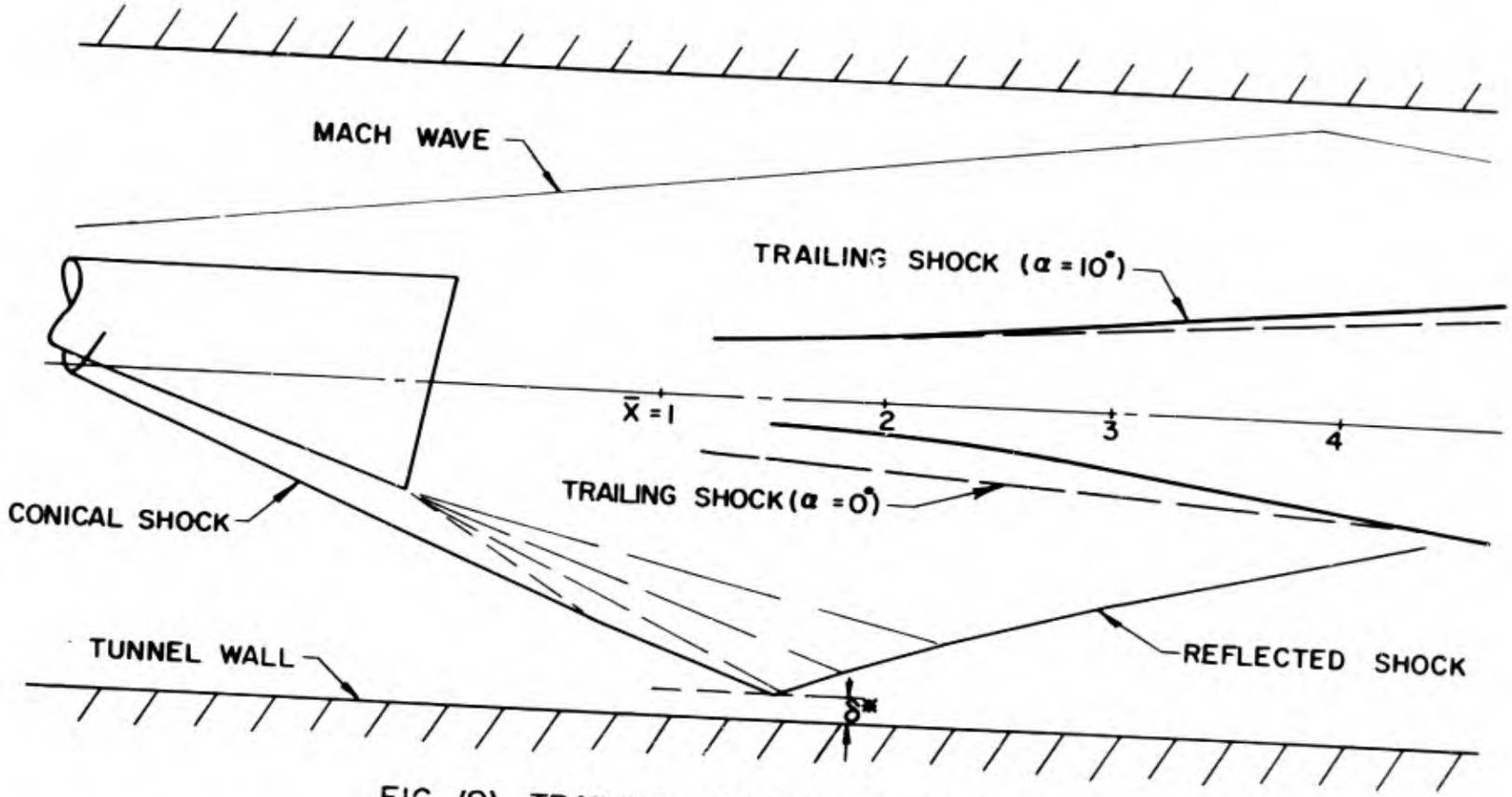

FIG (9) TRAILING SHOCK CONFIGURATION

INVESTIGATION OF THE BOUNDARY LAYER AND OF THE NON VISCOUS WAKE, ON SHARP AND BLUNTED CONES AT INCIDENCE, IN HYPERSONIC FLOW

by

Jacques VALENSI, Raymond GUILLAUME,
Daniel GUFFROY, Bernard ROUX et Jacques MARCILLAT,
de l'INSTITUT de MECANIQUE des FLUIDES de l'Université
d'Aix-Marseille.

RESUME

La plupart des recherches poursuivies dans le domaine des sillages hypersoniques portent sur des écoulements symétriques à un axe. Afin d'étudier la configuration du sillage de corps inclinés selon un angle d'incidence, on effectue des expériences sur des cônes effilés et arrondis placés suivant un angle d'incidence dans un écoulement hypersonique; ces études portent sur l'écoulement de la couche limite, en particulier au voisinage du culot, et sur la région non visqueuse s'étendant entre le choc d'onde qui se produit à la partie antérieure et la couche limite du corps. On espère étendre ces recherches à des points situés plus loin en aval.

Les expériences effectuées jusqu'ici ont démontré que, lorsque l'angle d'incidence auquel est soumis le cône est inférieur au demi-angle de ce dernier, la transition de la couche limite se produit sur la partie de la surface la moins inclinée vers le vent. Cette transition semble être due à une inflexion dans la forme du profil de vitesse de la couche limite. Les résultats des mesures portant sur la pression, la densité et le taux de transfert de chaleur concordent parfaitement avec ceux des calculs basés sur la théorie de la couche laminaire ou turbulente tri-dimensionnelle.

Dans le cas d'un cône effilé, lorsque l'angle d'incidence est supérieur au demi-angle de ce cône, le décollement de la couche limite survient, avec la formation de deux tourbillons, à partir du sommet. On peut également observer la formation de tourbillons sur des cônes arrondis, même si l'angle d'incidence est très faible. Dans ce cas la transition peut se produire dans les zones non décollées, là où l'épaisseur de la couche limite est maximale.

SUMMARY

Most investigations on hypersonic wakes concern axisymmetric flow. In an attempt to study wake configuration for bodies at incidence, an investigation is carried out on sharp and blunted cones at incidence in hypersonic flow, which concerns the boundary layer flow, especially near the base, and also the non viscous region between the bow shock and the body boundary layer. It is hoped to extend the investigation to stations farther downstream.

So far the experiments have shown that boundary layer transition occurs, when the incidence is smaller than the semi-angle of the cone, on the part of the surface least inclined to the wind. The transition appears to be due to an inflexion in the shape of the boundary layer velocity profile. The measured values of pressure, density and heat transfer rate, are in excellent agreement with those calculated by the three dimensional laminar or turbulent boundary layer theory.

For sharp cones, when the incidence exceeds the cone semi-angle, separation of boundary layer is observed together with the formation of two vortices from the apex. The vortices are also observed on blunted cones even when the incidence is very small. Transition can occur in this case, in non separated regions, when the thickness of the boundary layer is a maximum.

NOTATIONS

C_f = Coefficient de frottement

i = Incidence

M = Nombre de Mach

n = Abscisse curviligne transversale

p = Pression

p'_o = Pression d'arrêt

P_r = Nombre de Prandtl (pris égal à 0,7)

q = Densité de flux de chaleur convectée pariétal

R = Rayon de l'émoussement

Re = Nombre de Reynolds

s = Abscisse curviligne longitudinale

St = Nombre de Stanton

T = Température

T_f = Température de frottement

T_o = Température d'arrêt

u = Composante longitudinale de vitesse

w = Composante transversale de vitesse

y = Coordonnée normale à la paroi

α = Demi-angle du cône

φ = Azimut

μ = Viscosité

ρ = Masse spécifique

INDICES

∞ = Ecoulement amont non perturbé

w = Surface du modèle

$+$ = Conditions à la température de référence *

e = Frontière de la couche limite

1 = Ecoulement entre le choc et le corps

---

* Prise égale à T_w en laminaire, et donnée par la relation de Monaghan en turbulent.

1. - INTRODUCTION

La plupart des recherches théoriques et expérimentales déjà effectuées sur les sillages hypersoniques, concernent les écoulements à symétrie axiale, ou les écoulements plans.

Comme première tentative d'étude de sillages dissymétriques, une recherche a été entreprise * à l'Institut de Mécanique des Fluides de Marseille, qui concerne le sillage de cônes circulaires à pointe vive ou émoussée placés en incidence dans un écoulement à M =7.

Dans une première phase l'étude a porté sur la configuration de l'écoulement pariétal et sur celle de l'écoulement entre le choc et le modèle.

L'étude de la configuration du sillage proche fait l'objet d'une seconde phase, actuellement en cours d'exécution.

Les résultats obtenus ont en particulier mis en évidence suivant l'incidence et l'émoussement, l'existence de deux tourbillons d'apex ou d'une transition précoce de la couche limite à l'intrados des modèles en incidence, résultant du caractère tridimensionnel de l'écoulement.

2. - MAQUETTES- CONDITIONS DES ESSAIS

Les essais ont été effectués dans la soufflerie hypersonique à rafales de l'Institut de Mécanique des Fluides dans les conditions suivantes :

---

* La présente étude a été effectuée dans le cadre d'un contrat de recherche confié à l'Institut de Mécanique des Fluides à Marseille par l'Office National d'Etudes et de Recherches Aérospatiales.

Nombre de Mach : 7

Pression génératrice : 24,5 bars

Température génératrice : 600 °K

Diamètre de la section d'essai : 20 cm

Durée maximale de la rafale : 1 minute

Nombre de Reynolds par cm : 125.000

Température initiale des maquettes : 300 °K

Les maquettes sont constituées par des cônes tronqués de demi-angle au sommet $\alpha = 9°$ et 15° pouvant recevoir soit une pointe vive, soit une pointe émoussée en secteur sphérique (Longueur du cône à pointe vive : $\alpha = 9°$, L = 230 mm; $\alpha = 15°$, L = 130 mm; rayon de la pointe émoussée R = 5 mm).

Pour obtenir une connaissance plus détaillée de l'écoulement au voisinage de l'émoussement, il a été utilisé des maquettes non démontables reproduisant à plus grande échelle la partie antérieure des cônes émoussés ($\alpha = 9°$: R = 15 mm, L = 139,12 mm; $\alpha = 15°$: R = 15 mm, L = 87,05 mm).

Les maquettes sont équipées à la paroi de prises de pression disposées de 10 en 10 mm le long d'une génératrice, et de pastilles calorimétriques disposées de façon identique, le long d'une autre génératrice.

3.- RESULTATS

3.1. Ecoulement pariétal

3.1.1. Cône à pointe vive, cas des incidences faibles

Les essais montrent qu'à faible incidence, la couche limite laminaire autour de $\varphi = 0°$ devient turbulente vers l'aval au voisinage de la génératrice la moins inclinée sur le vent, d'azimut $\varphi = 180°$ (1) (2) (3) La transition ainsi observée peut s'expliquer de la façon suivante. Comme le montrent la théorie et l'expérience (méthode du film d'huile, figure 1 a), les lignes de courant pariétales divergent à partir de la génératrice

de part et d'autre de cette génératrice, qui est une ligne de partage, pour converger de part et d'autre de la génératrice $\varphi = 180°$, qui constitue une ligne de confluence.

L'épaisseur de la couche limite est donc maximale vers l'aval, sur la portion de surface du cône la moins inclinée sur le vent, en particulier le long de la génératrice $\varphi = 180°$, et la transition peut se produire, bien que le nombre de Reynolds, rapporté aux conditions de l'écoulement non perturbé et à l'abscisse le long de la génératrice, soit relativement faible ($\sim 10^6$) * . Les observations strioscopiques permettent de préciser que la transition le long de la génératrice $\varphi = 180°$ se produit entre les abscisses 75 et 120 mm.

De plus, comme le montrent les mesures de flux de chaleur (fig. 2) et le confirment les observations strioscopiques, la couche limite est turbulente à 120 mm du sommet, sur une région étroite autour de la génératrice $\varphi = 180°$. Les courbes, ensemble des maxima et des minima des courbes $q\ (\varphi)_{s = Cte}$ tracées sur la figure 2 délimitent approximativement la zone de transition. Cette représentation met en évidence l'élargissement vers l'aval de la zone turbulente.

Les courbes de répartition de la pression (fig. 2)montrent que la pression sur chaque parallèle décroit constamment, lorsque φ varie de 0 à 180°, tout en demeurant supérieure à p_∞ .

La distribution de la pression ainsi que celle de la densité de flux de chaleur q, relevées sur le cône $\alpha = 15°$ pour $0° < i < 13,5°$, présentent des caractères tout à fait analogues.

---

* Le nombre de Reynolds de transition rapporté aux conditions locales de l'écoulement à la frontière de la couche limite et à l'épaisseur de cette dernière est voisin de 10^4.

3.1.2 Cône à pointe vive à forte incidence -Cône à pointe émoussée

La configuration de l'écoulement pariétal est très différente sur le cône à pointe vive, lorsqu'il est placé à une incidence supérieure ou égale au demi-angle au sommet, ainsi que sur le cône à pointe émoussée, aussi faible que soit son incidence.

En effet, dans de telles conditions la couche limite se sépare sur une certaine zone autour de la génératrice la moins inclinée sur le vent, zone étroite d'abord, éloignée de la pointe du cône, qui s'élargit en se rapporchant de la pointe, et s'étend à toute la longueur du modèle lorsque l'incidence augmente. C'est ainsi qu'aux grandes incidences, sur le cône à pointe vive, la zone de décollement est limitée par deux génératrices de part et d'autre de $\varphi = 180°$, (fig. 1b, $i = 20°$, méthode du film d'huile). Bien entendu le décollement provoque la formation de deux tourbillons qui dans ce dernier cas sont des tourbillons d'apex. La génératrice $\varphi = 180°$ devient génératrice d'arrêt de l'écoulement pariétal. Autour de cette génératrice le film d'huile se trouve balayé dans une zone limitée par deux génératrices symétriques par rapport à $\varphi = 180°$, ensemble des points de rattachement de l'écoulement pariétal.

Les génératrices de décollement et de rattachement de la couche limite coïncident respectivement avec le lieu des minima et le lieu des maxima des courbes $q(\varphi)_{s=Cte}$ (fig. 3).

Les phénomènes observés sont identiques sur le cône émoussé, à toute incidence différente de zéro.

Aucune transition n'a été constatée à faible incidence en amont de la région séparée. Il y a lieu de remarquer cependant que le caractère tridimensionnel de l'écoulement doit rendre cette transition possible, pourvu que le nombre de Reynolds soit suffisamment élevé.

3.2. Ecoulement entre le choc et le corps

3.2.1. Cône à pointe vive

La configuration du sillage visqueux dépend évidemment du régime de l'écoulement dans la couche limite du modèle, ainsi que de la configuration de l'écoulement entre l'onde de choc et l'obstacle

La forme de l'onde de choc peut être obtenue par l'observation strioscopique. Dans le cas du cône à pointe vive, l'onde de choc a sensiblement la forme d'une nappe conique issue du sommet du cône, car l'effet de déplacement dû à la couche limite est insensible. C'est ce que montre la figure 4 a, image strioscopique de l'intersection de l'onde de choc avec le plan de symétrie de l'écoulement, pour le cône placé à l'incidence de 5°. Dans ce plan, et dans chacun des domaines délimités par l'onde de choc et la couche limite, l'entropie peut être considérée comme constante.

Des mesures de pression d'arrêt ont été effectuées dans la région comprise entre le choc et le corps, dans les différents plans méridiens de la maquette, à l'aide d'une sonde de O,8 mm de diamètre extérieur, déplacée perpendiculairement à la surface du modèle. Cette sonde est reliée à une capsule manométrique différentielle à jauge de contrainte. Le vide assuré par une petite pompe à palettes dans une capacité auxiliaire et mesuré à l'aide d'une jauge de McLeod, est utilisé comme pression de référence.

Les résultats concernant les génératrices d'azimuts 0, 90°, 180°, sont représentés sur la figure 5. Ils montrent que pour chaque génératrice, et dans la région non visqueuse, la pression d'arrêt varie peu en fonction de y/y_c et demeure pratiquement indépendante de s, ce qui confirme l'hypothèse de l'écoulement conique.

Des mesures de densité de débit ρu, ont été effectuées dans la même région, à l'aide d'une sonde constituée par un tube dont la section d'entrée, de 0,6mm de diamètre, est à bord vif. La

sonde est reliée à une pompe à palettes suivie d'un refroidisseur et d'un débitmètre. Lorsque le débit d'aspiration est suffisant pour que l'onde de choc soit avalée à l'intérieur du tube, le débitmètre mesure exactement le flux traversant le tube de courant de l'écoulement non perturbé s'appuyant sur la section d'entrée de la sonde.

Il est théoriquement possible de calculer la distribution du nombre de Mach et de la température à partir des distributions de T_o et du rapport $\frac{\rho u}{p'_{o1}}$. Malheureusement, le calcul est peu précis, car le rapport $\frac{\rho u}{p'_{o1}}$ demeure pratiquement constant dans un domaine de variation étendu de M et de T.

3.2.2. Cône à pointe émoussée

Les photographies strioscopiques de la figure 4 mettent en évidence la modification de la forme du choc avec l'émoussement ainsi qu'une zone à fort gradient de densité, immédiatement à l'aval de l'émoussement, là où l'onde de choc est la plus proche de la surface du cône (au voisinage de la génératrice $\varphi = 0°$).

Les figures 7 et 8 montrent les variations de la pression d'arrêt et de la densité de débit à travers cette zone, lorsqu'on déplace les sondes le long d'une normale à la surface de l'obstacle. Cette zone au voisinage de la pointe correspond à une couche à forte entropie, dont l'effet, par le jeu de la réflexion des ondes de détente issues de la surface à partir de la ligne sonique, se fait également sentir sur la distribution longitudinale de la pression à la paroi. Cette pression ne garde une valeur constante que pour $s/R > 20$.

La figure 10 représente l'évolution de la pression d'arrêt entre le choc et l'obstacle ainsi que dans le sillage proche, aux incidences 0 et 5°.

A l'aval de la base du modèle, la pression à l'incidence nulle (non visible sur la figure) est égale à 0,4 p_∞ . A l'incidence 5°, cette pression varie entre 0,23 et 0,4 p_∞ .

4. - COMPARAISON DES RESULTATS EXPERIMENTAUX AVEC LES THEORIES EXISTANTES ET DISCUSSION

4.1. Etude du sillage non visqueux

Jusqu'à ces dernières années, les seuls calculs effectués en écoulement tridimensionnels étaient basés sur des solutions des équations linéarisées du mouvement valables pour $\frac{i}{\alpha} \ll 1$. Ainsi Kopal [4], puis Sims [5] ont calculé l'écoulement autour des cônes circulaires placés à des incidences inférieures à leur demi-angle, lorsque l'onde de choc est attachée.

Une méthode exacte de résolution numérique, par différences finies, du système des équations aux dérivées partielles du mouvement a été proposée par Babenko [6]. Cette méthode valable pour tout obstacle suffisamment régulier, a été appliquée par les auteurs au cas du cône circulaire en incidence, avec onde de choc attachée. L'application de la méthode de Babenko n'a pas été traitée dans le cas où l'onde de choc est détachée. Dans ce cas, comme il est bien connu, le problème est celui du calcul d'un écoulement mixte subsonique-supersonique, très difficile à traiter. Une instabilité apparait dans les calculs.

La comparaison entre les résultats expérimentaux concernant la pression d'arrêt et la densité de débit dans le sillage non visqueux et les calculs théoriques effectués d'après Babenko, n'a donc pu être effectuée que dans le cas du cône à pointe vive. La comparaison met en évidence en dehors des couches limites, un accord satisfaisant (fig. 5 et 6).

4.2. Etude de la couche limite et du flux de chaleur convectée pariétal

4.2.1. Conditions à la frontière de la couche limite

La connaissance de l'écoulement non visqueux ne suffit pas pour déterminer les conditions de l'écoulement à la frontière de la couche limite. En dehors des effets de déplacement, deux phénomènes principaux se dégagent :

-pour le cône à pointe vive, il existe uné région à fort gradient d'entropie près de la paroi, dite "couche tourbillonnaire" [7].

-pour le cône à pointe émoussée, à la frontière de la couche limite, par suite de l'existence d'une région à fort gradient d'entropie, l'écoulement est encore rotationnel. Un tel effet, remarqué à l'incidence zéro par R. Rogers [8], est amplifié contre la génératrice au vent, par la mise en incidence, d'une façon analogue à ce qui a été observé sur le bord d'attaque d'une aile en delta en dérapage [9].

Dans ce qui suit, l'entropie à la frontière de la couche limite a été prise égale :

-en ce qui concerne le cône à pointe vive, à l'entropie en aval de la section de la nappe de choc par le demi plan méridien contenant la génératrice considérée.

-en ce qui concerne le cône à pointe émoussée, à l'entropie en aval de la partie droite de l'onde de choc détachée. Le calcul n'est dans ce cas valable que près de la pointe.

La donnée de la pression statique permet alors de connaitre tout l'écoulement. Celle-ci étant supposée constante sur une normale à la paroi, à travers la couche limite, peut donc être mesurée sur l'obstacle. La pression peut être d'ailleurs calculée théoriquement dans le cas du cône à pointe vive. La figure 11 relative

au cône de demi-angle 15° à l'incidence 5°, montre un excellent accord entre le calcul de Babenko et les résultats expérimentaux.

4.2.2. Méthodes de calcul du flux de chaleur convectée (paroi isotherme)

Lorsque l'écoulement transversal est faible, il est possible, pour calculer le flux de chaleur, de trouver un écoulement à symétrie axiale localement équivalent. Ce dernier peut alors être traité, par exemple, en cherchant des solutions de similitude locale au système que l'on obtient après application des transformations de Mangler et Stewartson.

Une telle méthode a été appliquée en utilisant le principe de prévalence, c'est-à-dire en négligeant la composante transversale de vitesse et toutes ses dérivées [9].

Les résultats obtenus étant sensiblement inférieurs aux valeurs mesurées, une correction a été apportée [10] en tenant compte du terme précédemment négligé dans l'équation de continuité. Celle-ci s'écrit alors :

$$\frac{\partial (\rho u)}{\partial s} + \frac{\partial (\rho v)}{\partial y} + \rho u \left(\frac{1}{e}\frac{de}{ds} + \frac{1}{u}\frac{\partial w}{\partial n}\right) = 0$$

Le calcul de la correction est effectué en supposant constant le terme $\frac{1}{u}\frac{\partial w}{\partial n}$ à travers la couche limite, et égal à sa valeur à la frontière.

Le corps de révolution équivalent possède alors une méridienne dont l'équation $r_o(s)$ satisfait la relation :

$$\frac{1}{r_o}\frac{dr_o}{ds} = \frac{1}{e}\frac{de}{ds} + \frac{1}{u_e}\left(\frac{\partial w}{\partial n}\right)_e$$

Que le cône soit à pointe vive ou émoussée, la divergence des lignes de courant $\frac{1}{e}\frac{de}{ds}$ doit vérifier l'équation différentielle :

$$\frac{d}{ds}\left(\frac{1}{e}\frac{de}{ds}\right) + \left(\frac{1}{e}\frac{de}{ds}\right)^2 = \frac{1}{\gamma M_e^2 s^2 \sin^2 \alpha} \cdot \frac{1}{p(\varphi = 0)}\frac{\partial^2 P}{\partial \varphi^2}$$

4.2.3. Flux de chaleur sur les génératrices du plan de symétrie du cône à pointe vive

Dans le cas du cône à pointe vive, la divergence des lignes de courant, qui est l'opposée de la courbure géodésique des lignes orthogonales, doit être inversement proportionnelle à s. Deux solutions sont alors trouvées de la forme $\frac{1}{e}\frac{de}{ds} = \frac{A}{s}$. La première qui vérifie :

$$2A_1 = 1 + \sqrt{1 - \frac{4}{\rho_e U_e^2 \sin^2 \alpha} \frac{\partial^2 p}{\partial \varphi^2}}$$

correspond à des lignes de courant divergentes (donc à la génératrice au vent)

La seconde :

$$2A_2 = 1 - \sqrt{1 - \frac{4}{\rho_e U_e^2 \sin^2 \alpha} \frac{\partial^2 p}{\partial \varphi^2}}$$

correspond à des lignes de courant convergentes ou parallèles (Donc, à la génératrice sous le vent).

Le nombre de Nusselt divisé par la racine carrée du nombre de Reynolds sera donné par :

$$\frac{Nu}{\sqrt{Re}} = 0,33 \; P_r^{0,4} \sqrt{2A' + 1}$$

où $$A' = A + \frac{1}{u_e \sin \alpha} \frac{\partial w}{\partial \varphi}$$

Et le flux de chaleur q par :

$$q = 0,33 \frac{k_w}{\sqrt{s}} \sqrt{\frac{\rho_w u_e}{\mu_w} (2A' + 1)} (T_f - T_w) P_r^{0,4}$$

Sur la figure 12, les valeurs mesurées de flux de chaleur ont été comparées aux valeurs obtenues par la présente méthode, pour les cônes de 9° et 15° à l'incidence 10° sur la génératrice $\varphi = 0°$. L'accord est excellent. Sur cette figure, ont également été portées les valeurs déduites du calcul effectué avec l'hypothèse du principe de prévalence, qui sont inférieures aux précédentes, comme l'on pouv ait s'y attendre.

Il faut également noter un excellent accord entre la présente méthode et celle proposée par Reshotko[11], les résultats obtenus par l'une et l'autre méthode différant entre eux de moins de 5%.

Comme le laisse prévoir la description de l'écoulement donnée au paragraphe 3.1.1., la comparaison entre les résultats donnés par la présente méthode pour $\varphi = 180°$ et $i = 5°$ et les flux de chaleur mesurés n'est satisfaisante que pour les faibles abscisses en amont de la transition (fig. 13).

4.2.4. Flux de chaleur sur la génératrice au vent du cône à pointe émoussée

Les conditions de l'écoulement extérieur ne sont pas encore connues. La figure 14 met cependant en évidence que, pour le cône de demi-angle 15°, si l'on rapporte les pressions mesurées à leur valeur sur la génératrice $\varphi = O°$ au point de même abscisse, les points obtenus se groupent autour d'une courbe moyenne. Celle-ci ne peut être distinguée à la précision des mesures, de la courbe théorique établie pour le cône à pointe vive de même angle.

L'équation différentielle écrite à la fin du paragraphe 4.2..2. doit être alors intégrée numériquement à partir de la valeur initiale à l'épaule :

$$\left(\frac{1}{e}\frac{de}{ds}\right)_{s = s_1} = \frac{tgi}{R}$$

La figure 14 montre qu'un bon accord est observé entre les valeurs théoriques et expérimentales dans le cas du cône de 15° à l'incidence 5°.

4.3. Etude de la couche limite sur la génératrice $= 180°$

La transition mentionnée au paragraphe 3.1.1. est également confirmée :

-par la comparaison des flux de chaleur mesurés avec ceux calculés à l'aide des relations établies pour le cône de révolution en écoulement turbulent [12]. Ces relations sont appliquées en utilisant les conditions locales de l'écoulement. Il vient pour le nombre de Stanton:

$$St = 0,026 \left(\frac{\rho^+}{\rho_e}\right)^{5/6} \left(\frac{\mu^+}{\mu_e}\right)^{1/6} Re^{-1/6}$$

-par des explorations effectuées à l'aide d'une sonde de pitot de 0,4 mm de diamètre, et dont les résultats pour trois abscisses différentes représentés sur la figure 1.3. montrent une modification notable du profil de pression d'arrêt à travers la couche limite.

-par la comparaison des résultats de mesure du flux de chaleur dans la région supposée être en écoulement turbulent, avec les valeurs que l'on peut déduire du coefficient de frottement en supposant applicable l'analogie de Reynolds. Ce dernier coefficient peut être calculé à partir de la distribution de la pression d'arrêt au voisinage immédiat de la paroi. Il vient :

$$C_f = 2 \frac{\rho_w \; a_w}{\rho_e \; u_e^2} \left(\frac{\partial M}{\partial y}\right)_{y = 0}$$

On remarque que les nombres de Stanton restent compris entre 0,85 et 0,9 10^{-3}, qu'ils soient déterminés à partir des mesures de flux de chaleur ou calculés à partir du coefficient de frottement.

REFERENCES

(1) J. VALENSI, R. GUILLAUME
Transition dans la couche limite autour d'un cône à pointe vive placé en incidence
Comptes-rendus t. 263 Série A 1966 p. 138

(2) J. VALENSI, R. GUILLAUME, J. MARCILLAT
Pression et densité de flux de chaleur convectée sur un cône à pointe vive placé en incidence
Comptes-rendus t. 263 Série A 1966 p. 396

(3) J. VALENSI, R. GUILLAUME, J. MARCILLAT
Sillage hypersonique d'un cône en incidence
3ème Colloque d'Aérodynamique Appliquée A.F. I.T.A.E.
Novembre 1966

(4) KOPAL Z.
Tables of supersonic flow around yawing cones
M.I.T. TR n° 3 1947

(5) SIMS
Tables for supersonic flow around right circular cones at small angle of attack
NASA SP 3007 1964

(6) K.I. BABENKO , G.P. VOSKRESSENSKY, A.N. LIOUBIMOV
V.V. ROUSSANOV
Three dimensional flow of an ideal gas past smooth bodies
NASA TT F 380 1965

(7) A.FERRI
Supersonic flow around circular cones at angles of attack
NACA Report 1045 1951

(8) R. ROGERS
Boundary layer development in supersonic shear flow
AGARD Report 269 Avril 1960

(9) J. VALENSI, R. MICHEL, D. GUFFROY
Résultats expérimentaux et théoriques sur le transfert de chaleur au bord d'attaque des ailes à forte flèche en hypersonique.
Colloque AGARD (Naples Mai 1965) AGARDograph n° 97 p. 881

(10) J. VALENSI, D. GUFFROY, B. ROUX
Sur le calcul du coefficient de convection local le long de la ligne d'arrêt d'un corps de révolution en dérapage (écoulements hypersoniques, couche limite laminaire).
Comptes-rendus t. 263 Série A. 1966 p. 425

(11) E. RESHOTKO
Laminar boundary layer with heat transfer on a cone at angle of attack in a supersonic stream
NACA TN 4152 Décembre 1957

(12) R. MICHEL
Couches limites turbulentes et calcul pratique des couches limites en fluides compressibles
E. N. S. A. Cours d'Aérodynamique 1962.

Fig 1

ECOULEMENT D'HUILE A LA SURFACE DES MAQUETTES

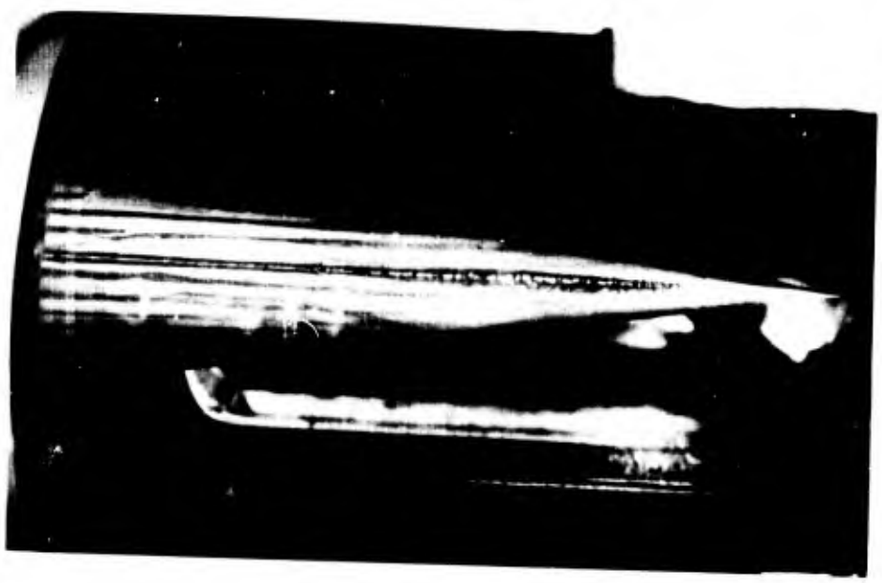

a) Incidence 5°

b) Incidence 20°

Fig : 2

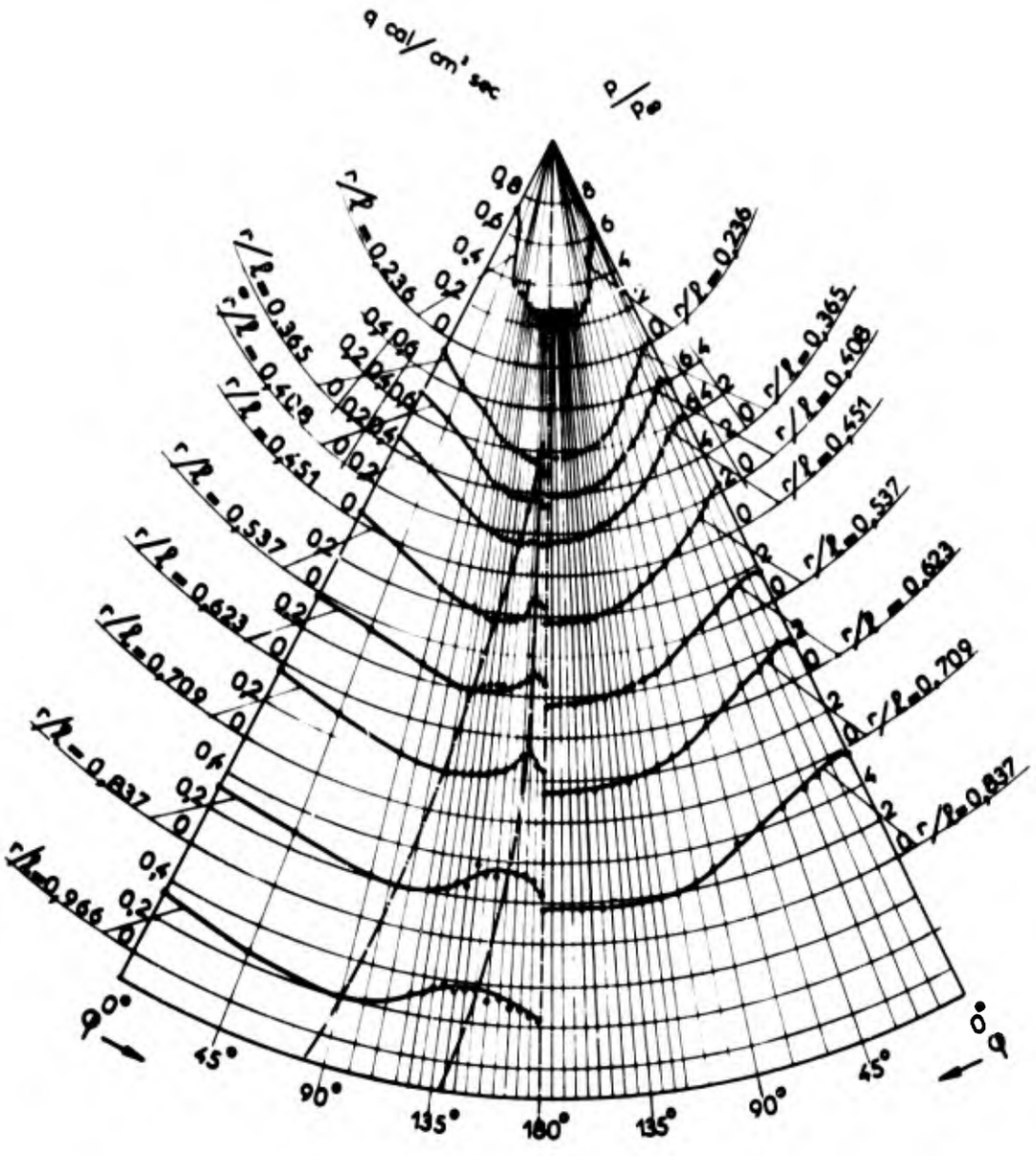

PRESSION ET FLUX DE CHALEUR PARIETAUX

$\alpha = 9°$ $i = 5°$

Fig: 3

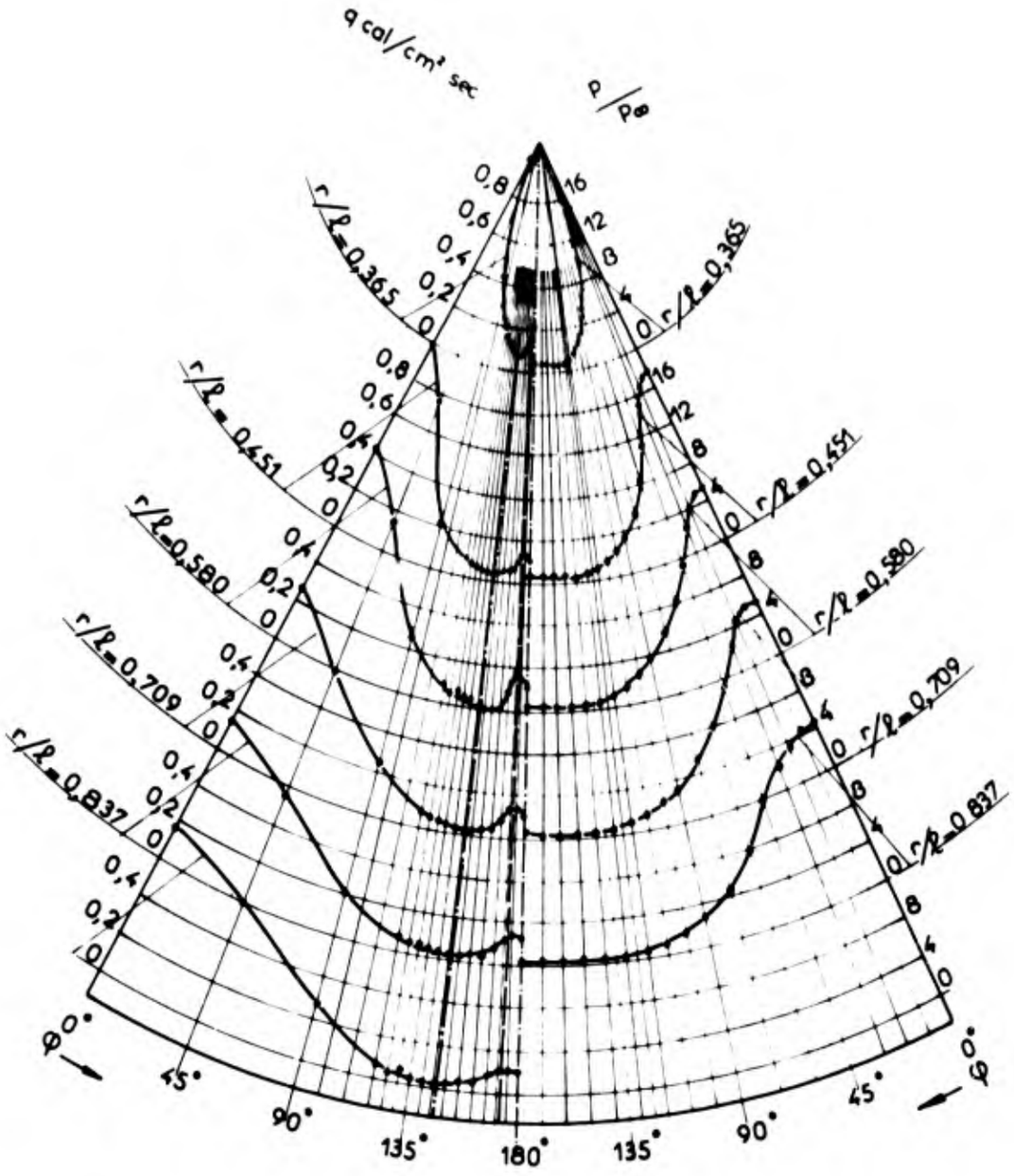

PRESSION ET FLUX DE CHALEUR PARIETAUX

$\alpha = 9°$ $i = 20°$

STRIOSCOPIE DE L'ECOULEMENT $\alpha = 5°$ Fig: 4

a) Pointe vive

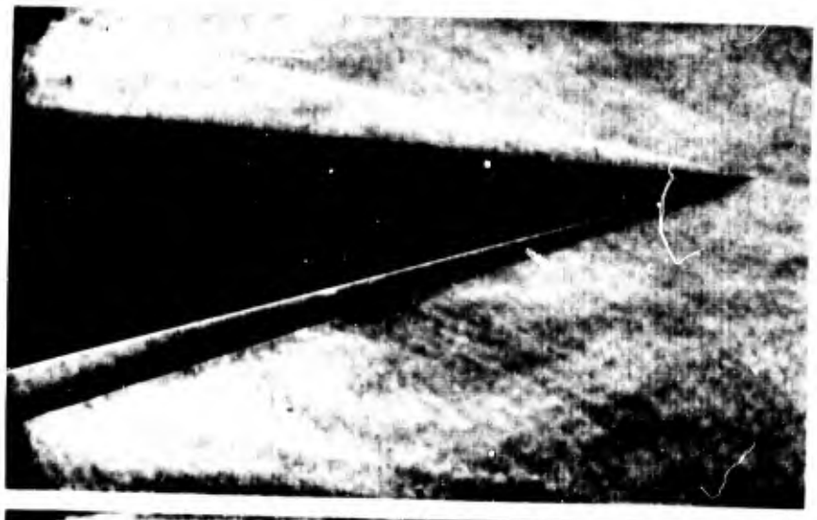

b) R = 5mm

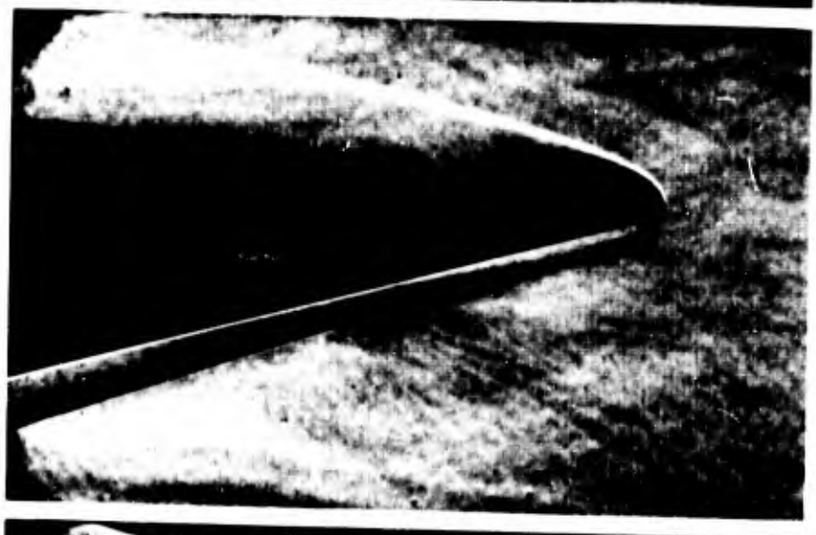

c) R = 15mm

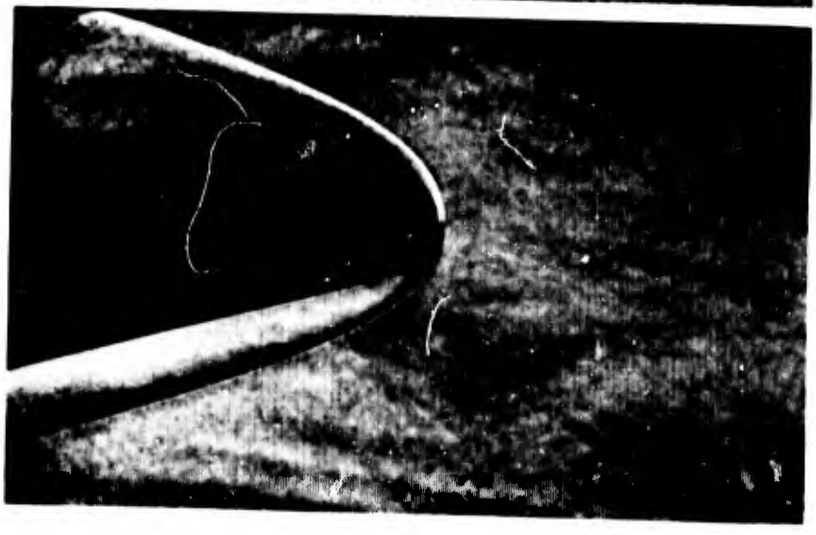

Fig : 5

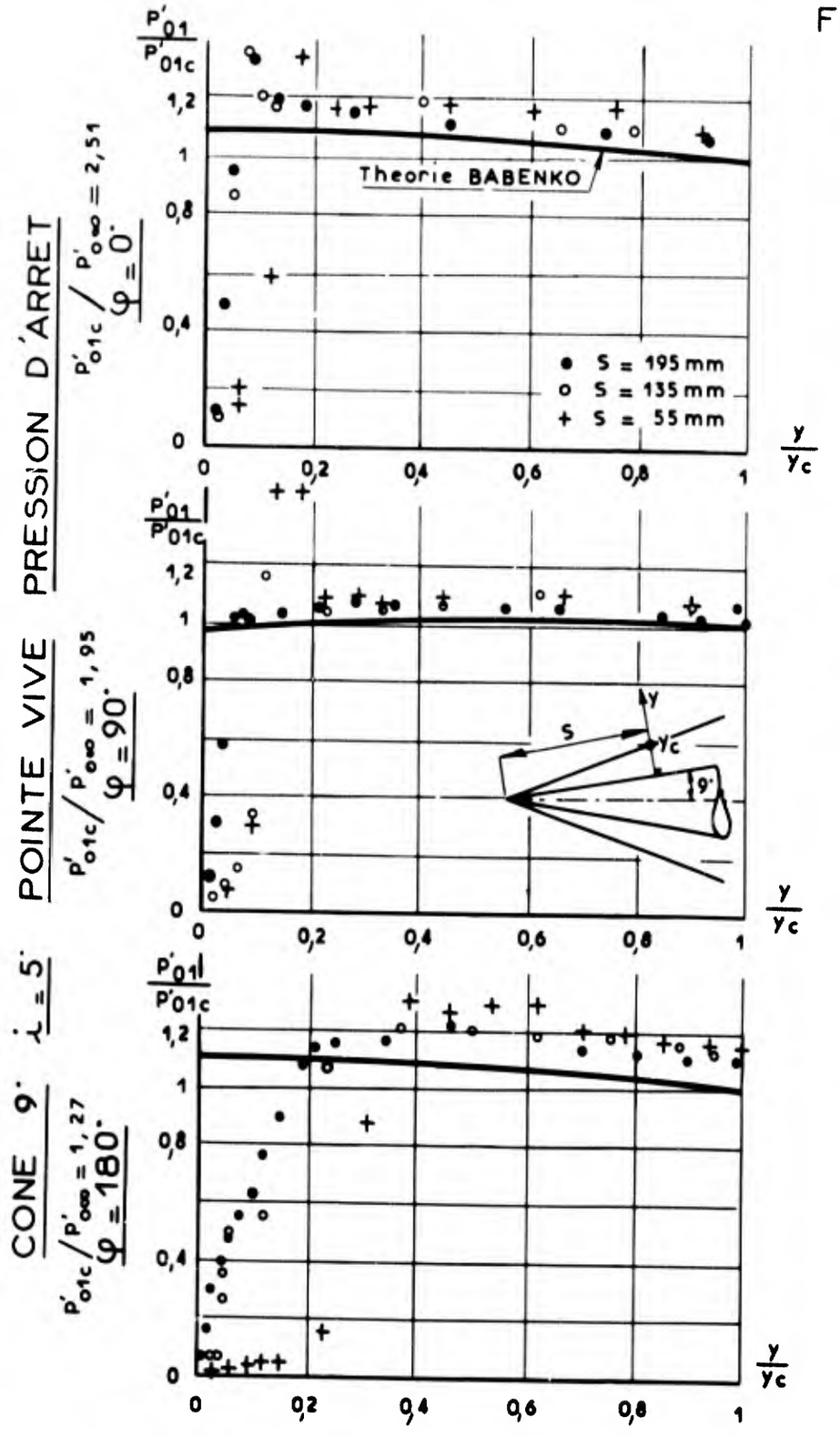
CONE 9° i = 5°
POINTE VIVE
PRESSION D'ARRET
$\frac{P'_{01}}{P'_{01c}}$
$P'_{01c} / P'_{0\infty} = 2,51$
$\varphi = 0°$
Theorie BABENKO
● S = 195 mm
○ S = 135 mm
+ S = 55 mm
$P'_{01c} / P'_{0\infty} = 1,95$
$\varphi = 90°$
S
y
y_c
9°
$P'_{01c} / P'_{0\infty} = 1,27$
$\varphi = 180°$
$\frac{y}{y_c}$
0
0,2
0,4
0,6
0,8
1
1,2

Fig : 6

DEBIT MASSE POINTE VIVE CONE 9° i=5°

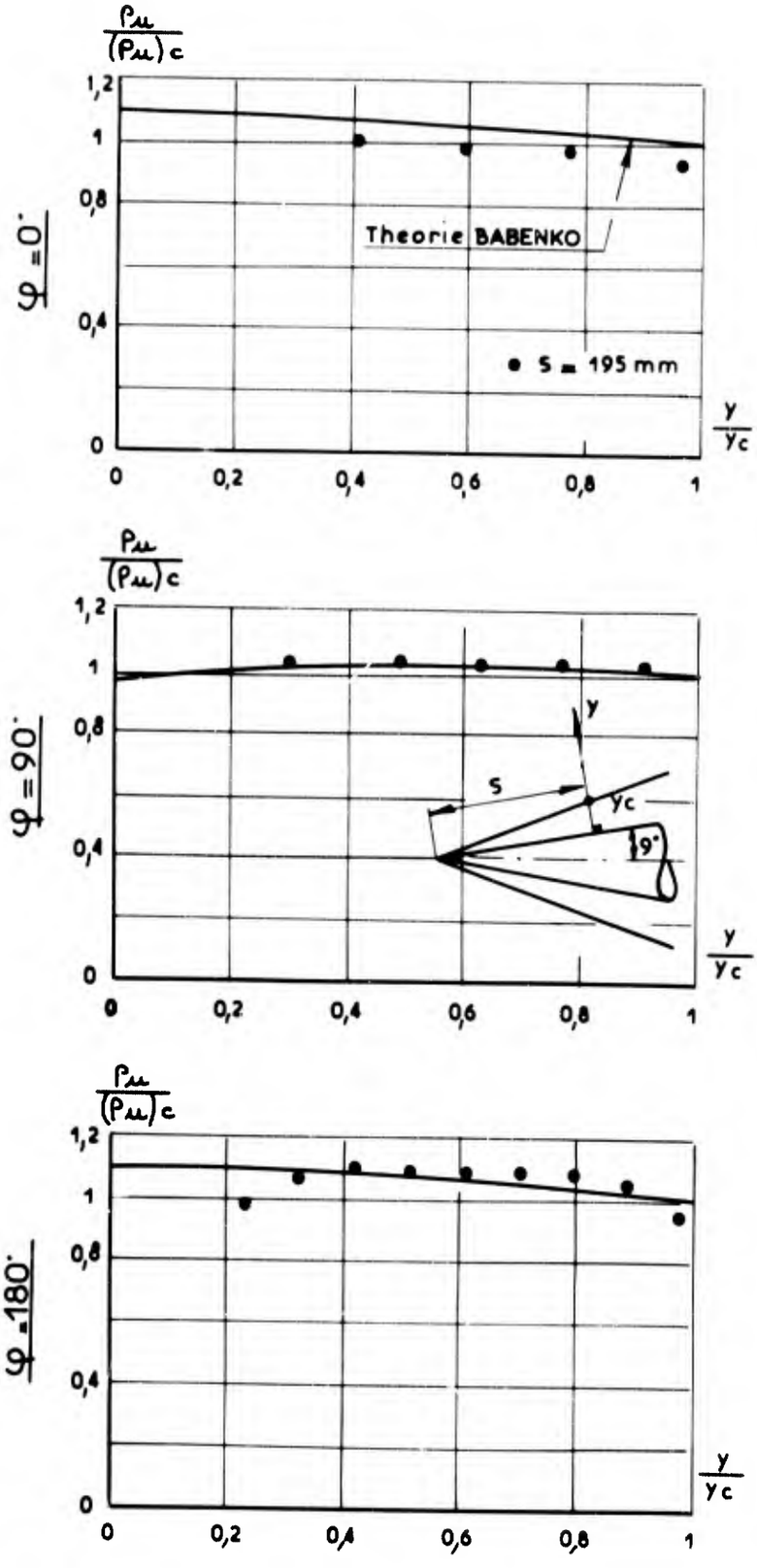

Fig: 7

CONE 9° λ=5° POINTE EMOUSSEE PRESSION D'ARRET.

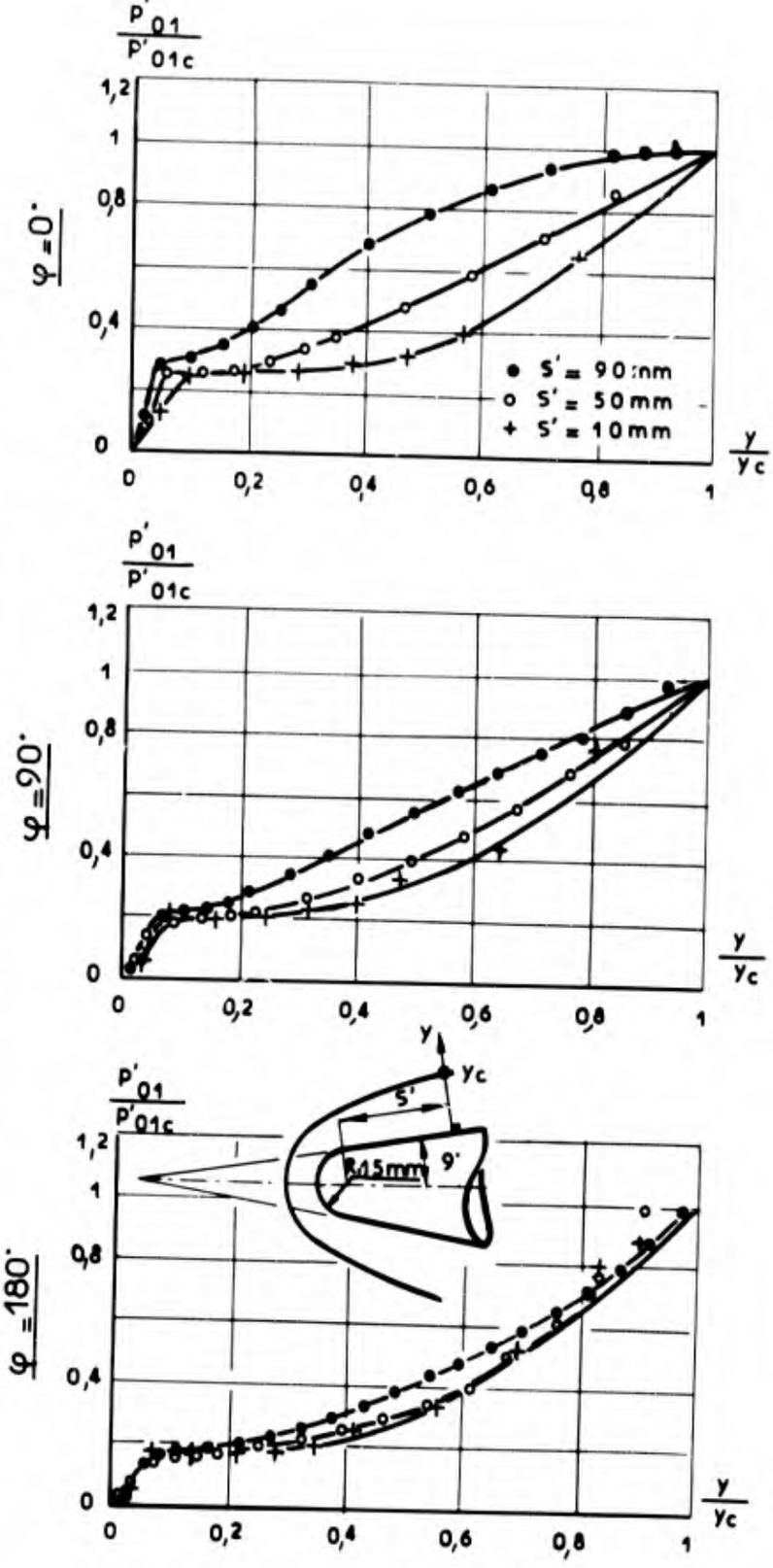

Fig: 8

CONE 9° $\lambda = 5°$ POINTE EMOUSSEE DEBIT MASSE

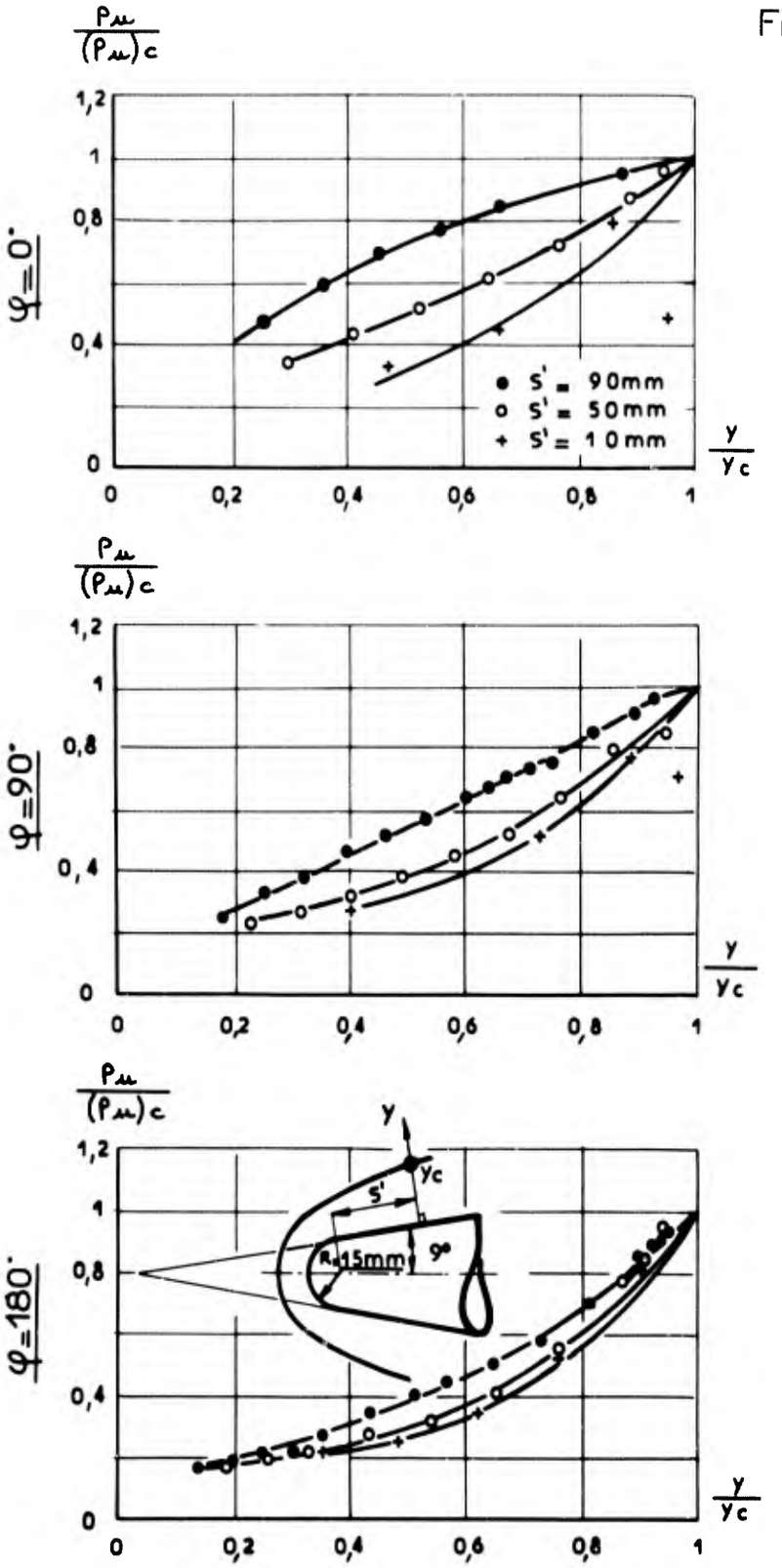

CONE 9° POINTE EMOUSSEE PRESSION PARIETALE

Incidence 5°

φ = 0° φ = 45°
φ = 10° φ = 60°
φ = 20° φ = 90°
φ = 30° φ = 135°
φ = 180°

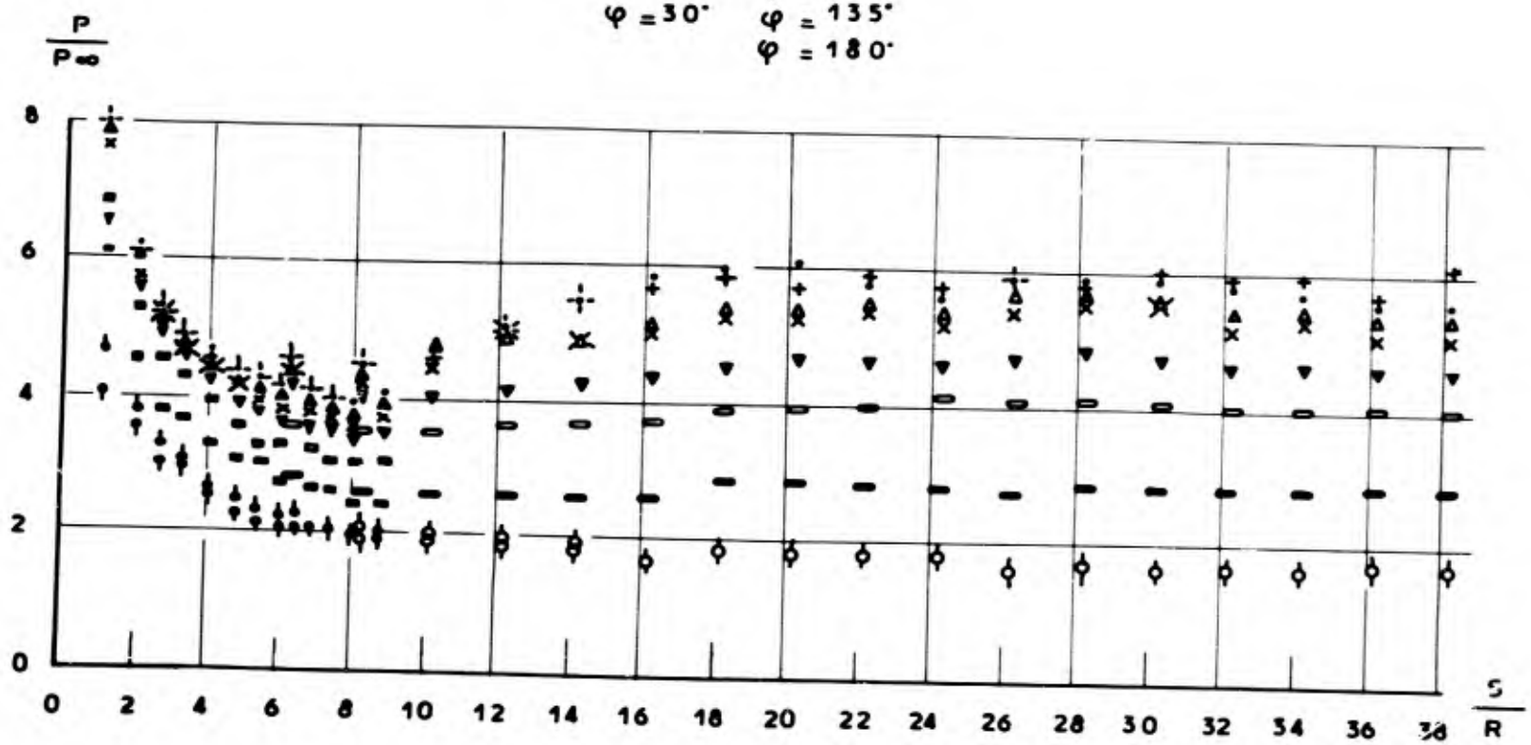

Fig : 9

Fig: 10

CONE 9° POINTE EMOUSSEE PROFILS DE PRESSION D'ARRET

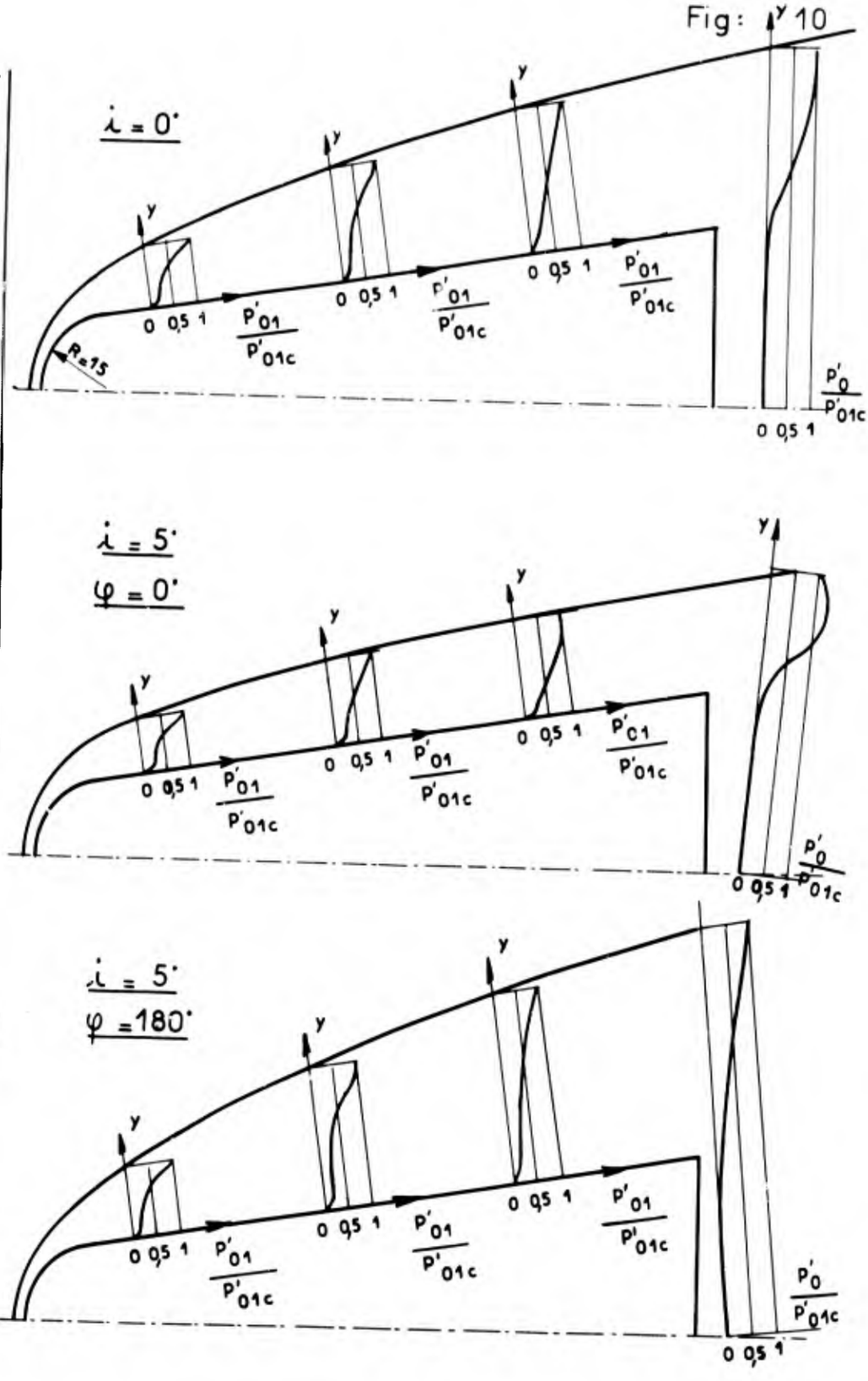

CONE $\alpha = 15°$ $i = 5°$ POINTE VIVE PRESSION PARIETALE

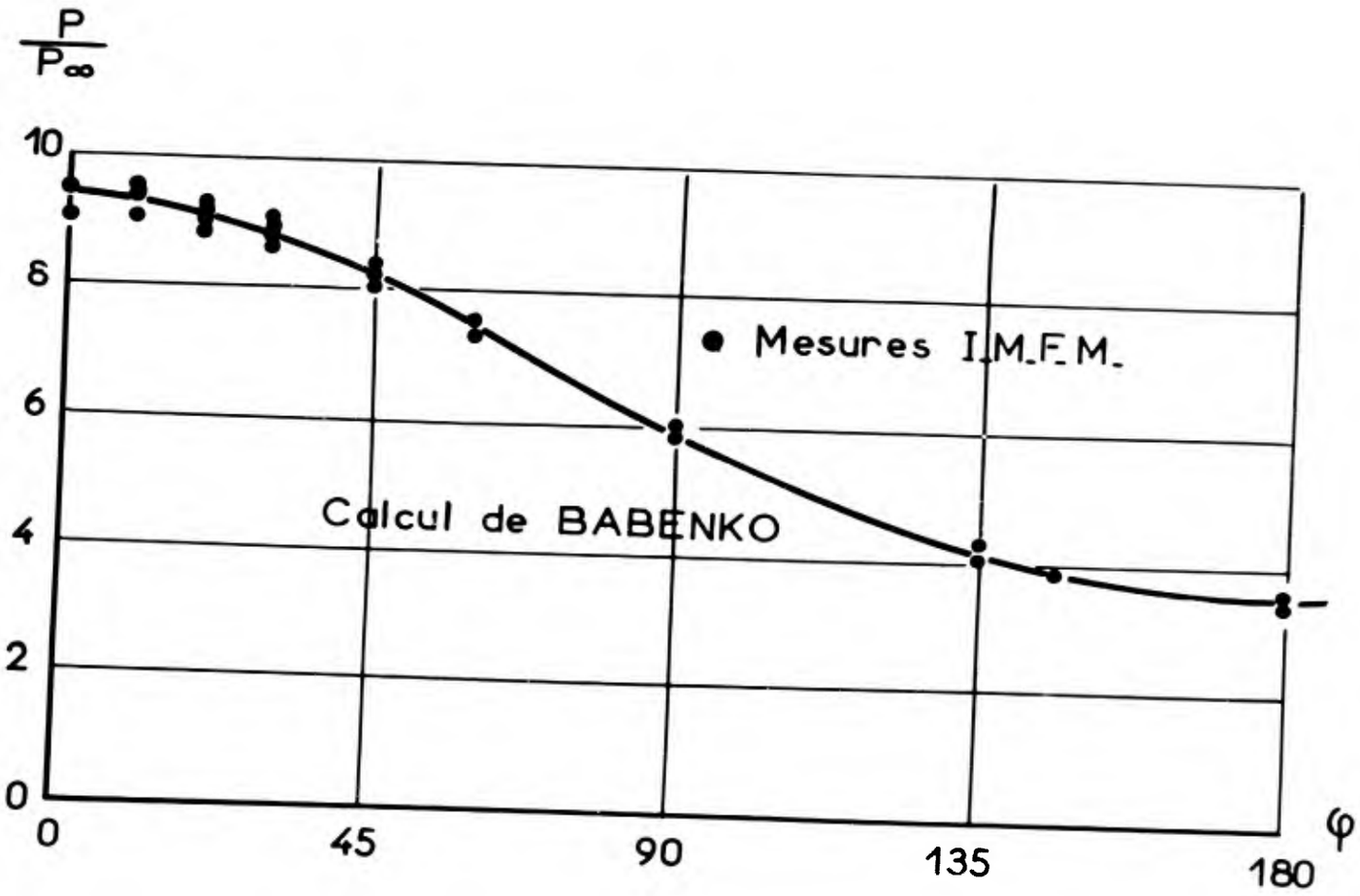

Fig: 11

FLUX DE CHALEUR (Cône à pointe vive)

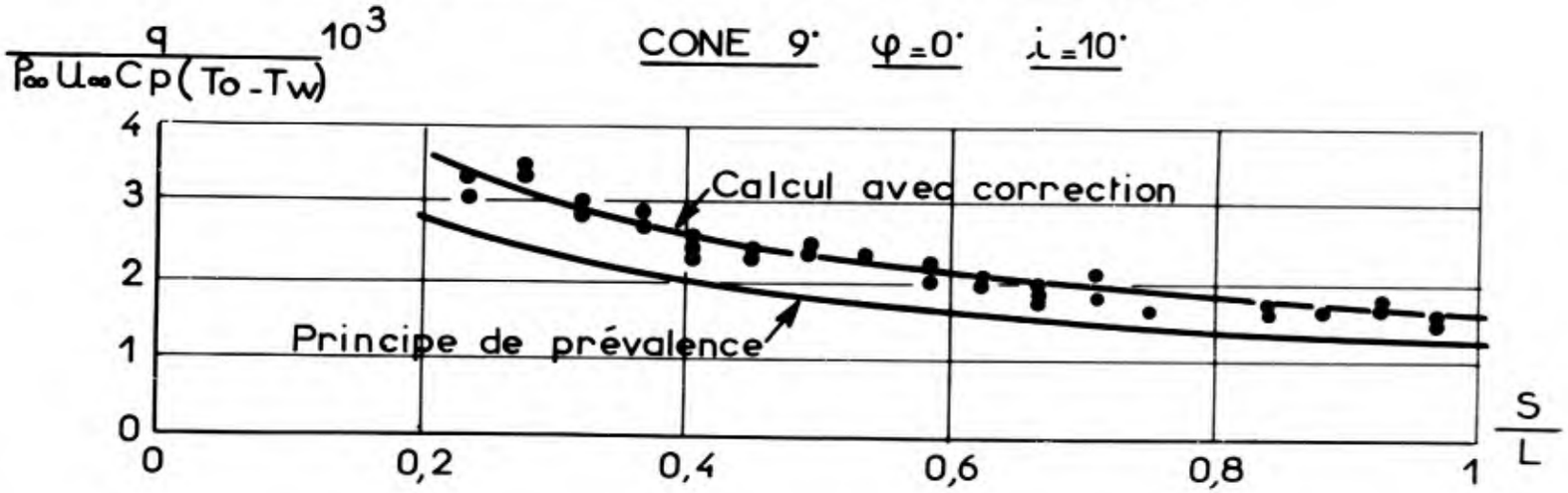

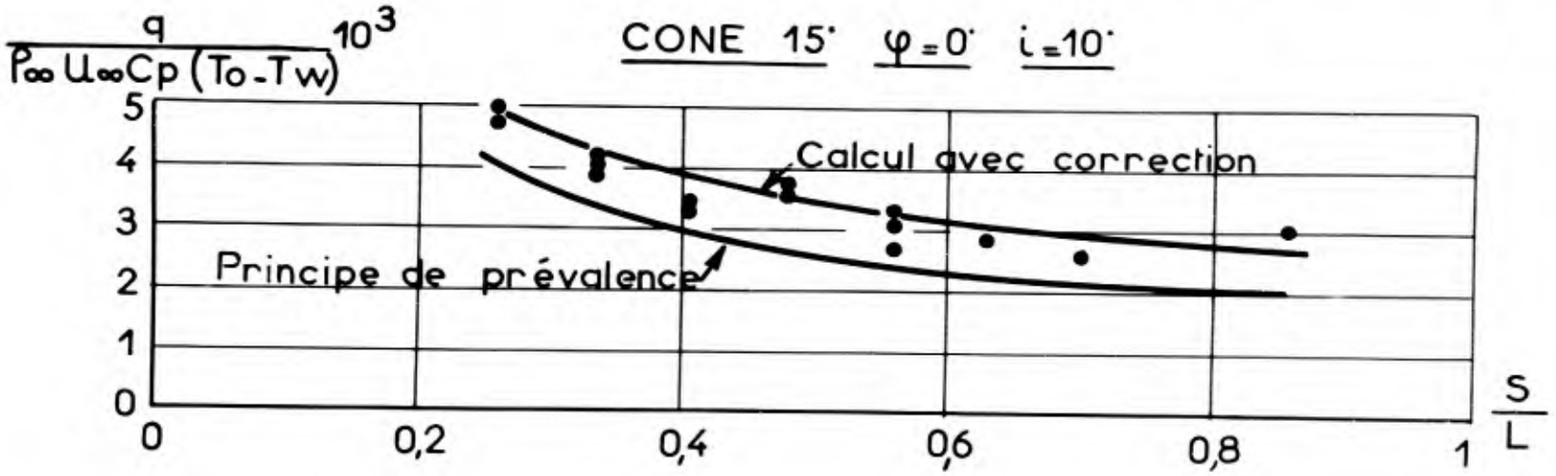

Fig : 12

FLUX DE CHALEUR ET PRESSION D'ARRET DANS LA ZONE DE TRANSITION

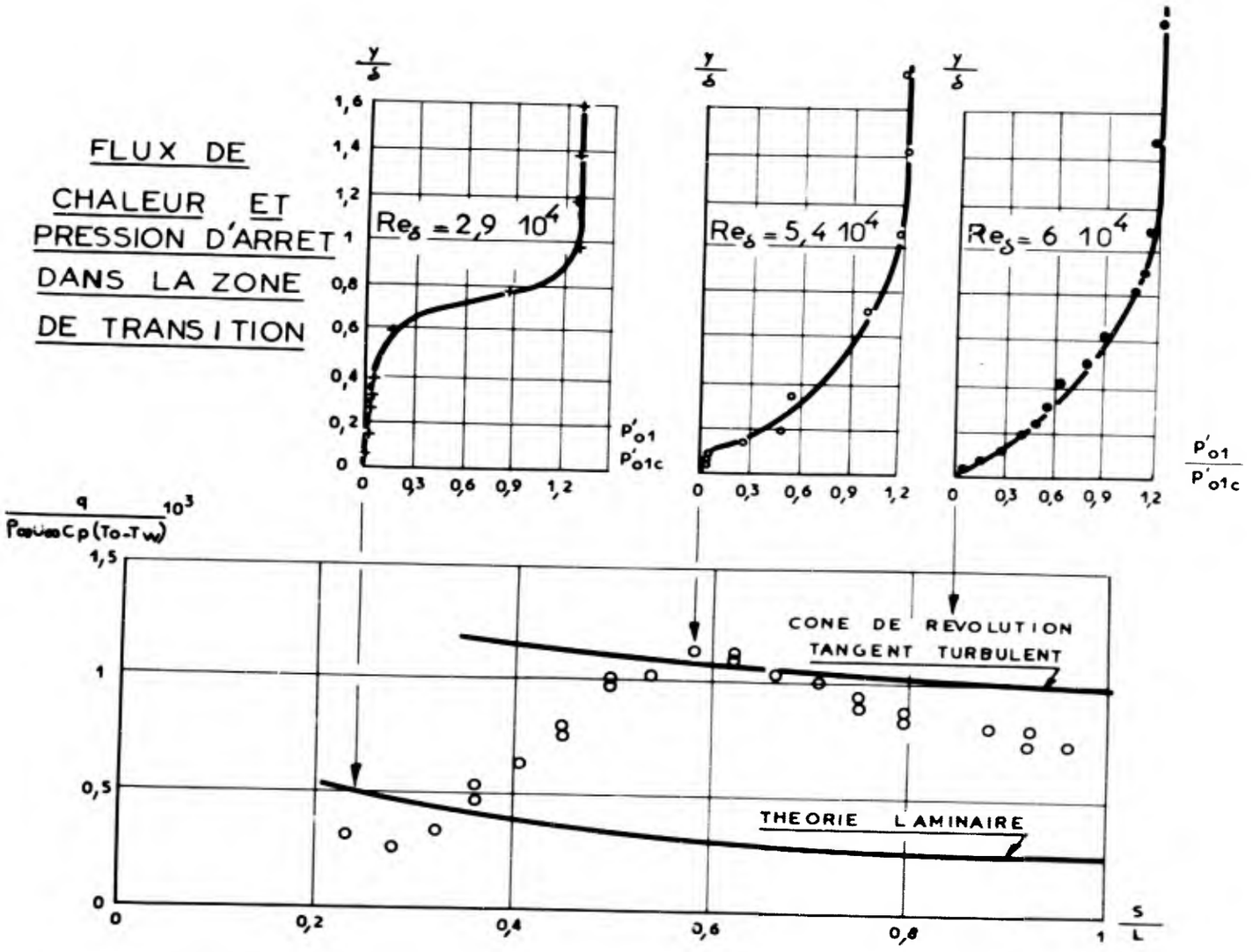

Fig: 13

FLUX DE CHALEUR ET PRESSION PARIETALE

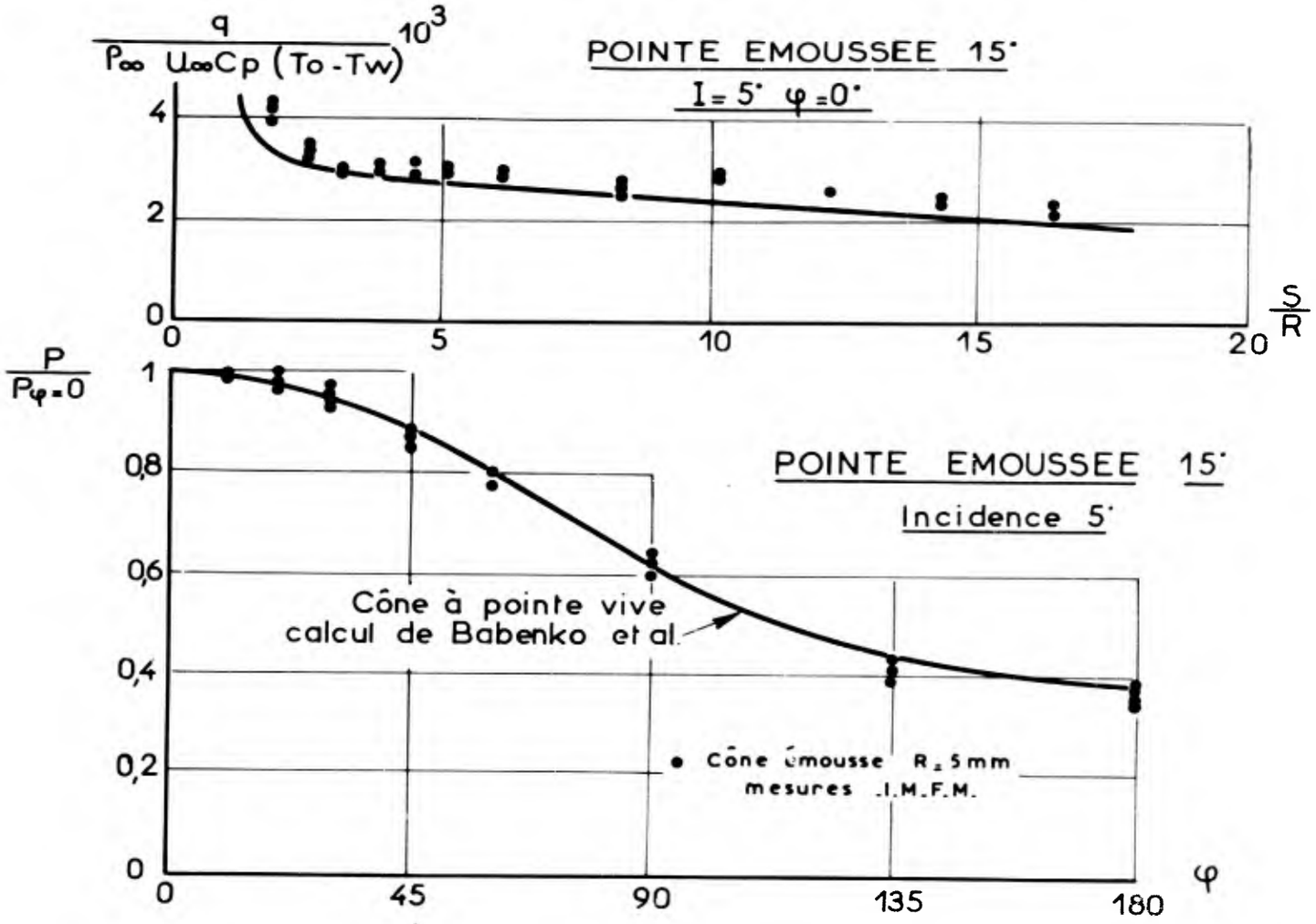

Fig: 14

REYNOLDS NUMBER EFFECTS IN THE NEAR WAKE BEHIND A WEDGE AT SUPERSONIC AND HYPERSONIC SPEEDS

by

Wolfgang F. Merzkirch

Ernst-Mach-Institut
Freiburg i. Br., Germany

SUMMARY

Near wake studies behind blunt or sharp-nosed bodies in supersonic and hypersonic flow are important, e.g. from the standpoint of determining base pressure, base drag as well as base heating rates. According to Chapman's model for the recompression process at the wake neck the determination of base drag is reduced to the problem of finding a solution for the free shear layer flow in the near wake. The analytical studies by Chapman and by Denison and Baum based on assumption similar to those of boundary layer theory, predict that the base drag is independent of Reynolds number. These results are not in agreement with numerous experimental data obtained at supersonic speeds.

Measurements of several near wake characteristics (base pressure, wake angle, pitot profiles) were carried out behind a wedge in hypersonic helium flow and show a strong influence of Reynolds number. The two-dimensional, wedge-shaped model is of experimental advantage since it allowed for optical visualization of the free shear layer in the near wake. A discrepancy between the measured base pressure and the visualized wake angle leads to the conclusion that the body boundary layer expands into a wide fan of diverging streamlines in the near wake.

The influence of Reynolds number on near wake characteristics which is verified experimentally here for hypersonic flow can be attributed to several factors, e.g.

> mixing and diffusion in the free shear layer; interaction with the recirculating "dead air" region; viscous interaction with the recompression process at the wake neck; non-isentropic expansion of the body boundary layer and formation of a lip-shock.

It is not known by what order of magnitude these factors determine the total amount of Reynolds number influence and whether some factors might predominate in certain ranges of Reynolds number. Some of the above-mentioned factors have been treated separately in the literature and consideration will be given here to the last point.

It can be shown by experiment that the strength of the lip-shock is not negligibly small. An analytic explanation of the lip-shock formation has been given by Weinbaum. A simplified model is used here to describe the lip-shock formation at supersonic speeds. A criterion is given for the existence of the lip-shock; the strength of this shock depends on Reynolds number. The assumptions used for this simplified model are not applicable to hypersonic speeds. It is shown that the small Mach angles (at hypersonic Mach numbers) and the geometry of the near wake do not allow for the development of a lip-shock and that the near wake is governed by strong viscous interaction processes. This model is discussed by means of the above-mentioned experimental results of the hypersonic near wake.

RESUME

L'étude de la zone du sillage qui se forme immédiatement à l'arrière d'un corps effilé ou arrondi en régime supersonique et hypersonique est importante pour la détermination de la pression de culot, de la traînée de culot ainsi que des taux d'échauffement du culot. Grâce à la maquette de Chapman qui met en lumière le processus de recompression au point de resserrement du sillage, déterminer la traînée de culot se ramène à résoudre le problème de l'écoulement de la couche de cisaillement libre dans le sillage proche. Selon les études analytiques de Chapman, et de Denison et Baum, basées sur des hypothèses semblables à celles de la théorie de la couche limite, la traînée de culot n'est pas affectée par le nombre de Reynolds. Ces résultats ne concordent pas, cependant, avec les nombreux résultats expérimentaux obtenus aux vitesses supersoniques.

On a en effet mesuré diverses caractéristiques (pression de culot, angle de sillage, profils de pression dynamique) du sillage proche à l'arrière d'un corps en forme de diédre placé dans un courant d'hélium; or ces mesures révèlent que l'influence du nombre de Reynolds est importante. La maquette bi-dimensionnelle en forme de diédre présente l'avantage du point de vue expérimental, de permettre une visualisation optique de la couche de cisaillement libre dans le sillage proche. Il apparait entre la pression de culot telle qu'elle est fournie par les mesures et l'angle de sillage révélé par les procédés de visualisation, un écart qui indique que la couche limite du corps soumis à l'expérience s'épanouit en un large évantail de courants dans le sillage proche.

L'influence du nombre de Reynolds sur les caractéristiques du sillage proche, influence que l'expérience établit ici pour un écoulement hypersonique, peut être attribuée à plusieurs facteurs: - mélange et diffusion dans la couche de cisaillement libre; interaction avec la région morte du courant qui effectue une recirculation; interaction visqueuse avec le processus de recompression dans la zone d'étranglement du sillage; amplification non isentropique de la couche limite du corps et formation d'une onde de choc attachée au décrochement du culot (lip-shock).

On ignore dans quelle mesure ces facteurs déterminent la somme totale de l'influence du nombre de Reynolds, et si certains facteurs pourraient prédominer pour une certaine game de nombres de Reynolds Parmi ces facteurs, ci-dessus mentionnés, certains ont été traités séparément dans la littérature scientifique, et l'auteur se consacrera ici à l'étude du dernier point.

On peut démontrer expérimentalement que l'influence de l'onde de choc attachée au décrochement de culot n'est pas une valeur négligeable. Weimbaum a donné une explication analytique de la formation de cette onde. On a recours ici à une maquette simplifée pour décrire sa formation aux vitesses supersoniques, et l'on donne un critère pour son existence; son intensité dépend du nombre de Reynolds. Les hypothèses utilisées pour cette maquette simplifiée ne sont pas applicables aux vitesses hypersoniques. On démontre que de faibles angles de Mach (au nombre de Mach hypersoniques) et la géométrie du sillage proche ne permettent pas la formation d'une onde de choc attachée au décrochement du culot et que le sillage proche est régi par de puissants processus d'interaction. La maquette en question est étudiée à l'aide des résultats expérimentaux sur le sillage proche hypersonique, résultats mentionnés plus hauts.

NOTATION

C_1, C_2	characteristic numbers according to [12]
h	base height
L	length of wedge
M	Mach number
M' , M''	Mach numbers on both sides of an entropy discontinuity
p_b	base pressure
p_t	stagnation pressure
Re	Reynolds number
s	distance between base and wake neck
tan α	see eq. [2]
ß	wake angle
γ	ratio of specific heats
δ, ε	numbers describing the reflection and refraction of a wave at an entropy discontinuity

Further subscripts:

1, 2, 3	inviscid flow regimes according to figure 1

1. INTRODUCTION

One of the most important goals of supersonic and hypersonic near wake studies is the prediction of base pressure or base drag. The theories given by Chapman [1), 2)] and by Denison and Baum [3)] allow for analyzing the free shear layer behind a two-dimensional body (wedge) and thereby determining the base pressure; it is shown that - for a Prandtl number $Pr=1$ - it is not necessary to include into the analysis thermodynamic or physical gas effects and that the base pressure is predicted only by analyzing the fluid mechanical aspects of the flow field. The resulting base pressure is then a function of the Mach number but independent of Reynolds number.

The latter prediction is not in agreement with numerous experimental data obtained at supersonic speeds and which display a strong influence of the Reynolds number on the base drag. A representative base pressure profile, measured over a wide range of Reynolds numbers, has been presented by Kavanau [4)] for an axisymmetric model and a free stream Mach number $M_1 = 3$. Lehnert and Schermerhorn [5)] compared the Prandtl-Meyer deflection angles β, calculated by using the measured base pressures, with the wake angles β (see figure 1) visualized by optical means, and they found good agreement at a local Mach number $M_2 = 2.75$. Base pressure and wake angle measurements carried out in hypersonic flows, e.g. [6)], also display a strong Reynolds number dependence.

The influence of the Reynolds number on near wake characteristics which has been verified experimentally can be attributed to several factors, e.g.

mixing and diffusion in the free shear layer;
interaction with the recirculating "dead-air" regime;

viscous interaction with the recompression process at the wake neck;

non-isentropic expansion of the body boundary layer and formation of a separation or lip shock.

It is not known by what order of magnitude these factors determine the total amount of Reynolds number influence and whether some factors might predominate in certain ranges of Reynolds number. Some of the above mentioned factors have been treated separately in the literature and consideration will be given here to the last point. Since the discussion and results of this note are related to some of the experimental data obtained by H. K. Larson and the present author [6], these experiments will first be briefly reported.

2. EXPERIMENTAL RESULTS FOR THE HYPERSONIC NEAR WAKE

Measurements of both base pressure and wake angle behind a 7.5^{o} half angle wedge were taken in the Ames 1-foot helium tunnel at free stream Mach numbers of 11 and 18. The total variation of Reynolds number, $Re_{2,\,L}$, was between 2 and 15 million and had been achieved by varying the model length and/or the tunnel stagnation pressure. The recorded base pressure, plotted in figure 2, decreases with increasing Reynolds number; also shown in fig. 2 are some hypersonic base pressure values measured by Softley, Muntz and Zempel [7] and by Dewey [8] respectively, although the test gas and model shapes were different from the present conditions.

A schlieren-interferometer system had been used to visualize the wake angle ß which was found to increase with increasing Reynolds number, see figure 3. Less accurate methods, a separating oil-film technique and a pitot-pressure-survey of the near wake, displayed the same quali-

tative results. The measured base pressure, p_b, and the inviscid stream parameters M_2, p_2 can be used to calculate the deflection angle ß; however, the Prandtl-Meyer-angles obtained in this way, are not consistent with the visualized wake angles ß: the measured angle being much greater than the Prandtl-Meyer-angle. This led to the conclusion that the body boundary layer expands into a wide fan of diverging streamlines, the inner streamlines with a lower local Mach number expanding at larger angles than the outer streamlines near the inviscid flow. The visualized angles thus correspond to streamlines in the low Mach number part of the separated boundary layer. The following shows that this conclusion needs some modification.

3. INVISCID MODEL OF SEPARATING BOUNDARY LAYER

An inviscid model for the supersonic and hypersonic boundary layer separation and its application to the near wake problem has recently be given by Weinbaum [9] and by Weiss and Weinbaum [10]. A characteristic solution for the non-isentropic flow expansion at the wedge shoulder yields - as well as a second order theory by Weinbaum - that the streamlines leave the expansion fan under different deflection angles corresponding to their local Mach number. This fan of diverging streamlines is compensated by a secondary wave system: rarefaction (expansion) waves or compression waves depending on whether the deflection angles are decreasing or increasing with local Mach number in the boundary layer. The boundary layer is represented in this model by a layer of streamlines each of which being at a different entropy level, and the secondary waves can be regarded as reflections of the Prandtl-Meyer-expansion waves at the entropy discontinuities.

The secondary waves travel through the free shear layer into the lower Mach number region and are reflected - according to this inviscid

model - at the local M = 1-surface as waves of the opposite sign (figure 4). Secondary expansion waves are reflected as compression waves, and the ... are supposed to form a separation shock or "lip shock" downstream of the expansion. The net effect of this process is that all streamlines of the free shear layer - after having passed through the primary expansion and the complete system of secondary and secondary reflected waves - are at equal static pressure and equal direction β'. If β_o be the Prandtl-Meyer-angle for the inviscid, outer flow through the primary expansion, then $\beta' < \beta_o$, and the expansion of a hypersonic flow would only yield small deflection angles once the secondary wave process can be completed.

This secondary wave system is an inviscid model to describe a flow pattern which underlies viscous effects. It has been shown, [11], that this model allows for drawing some conclusions concerning the influence of Reynolds number, e. g. on the strength of the lip shock. However, this model does not allow for explaining the large deflection angles which have been measured in the near wake of the wedge, as described in [6]. The interaction of the secondary waves with the entropy discontinuities in the free-shear-layer flow will be studied in the following paragraphs to yield a better agreement with the experimental data.

4. INTERACTION OF EXPANSION WAVES WITH A LAYER OF ENTROPY DISCONTINUITIES

The interaction between a (rarefaction or compression) wave of intensity 1 and an entropy discontinuity has been analyzed by Ferri [12]. Following his notation of characteristic numbers C_1, C_2, the process of reflection and refraction of the incident wave (of intensity 1) is described by the values of δ and ϵ (see figure 5):

$$\delta_1 = \frac{1 - \tan\alpha}{1 + \tan\alpha} \quad , \quad \varepsilon_1 = 1 - \delta_1 \qquad (1)$$

$$\tan\alpha = 1 + \frac{1 + \frac{\gamma - 1}{2} M'^2}{M'^2 (M'^2 - 1)} (2 - M'^2) \ln \frac{p_t''}{p_t'} \qquad (2)$$

p_t and p_t are the stagnation pressures on both sides of the entropy discontinuity. If the intensity of the incident wave is not 1 but k, then

$$\delta_k = k \cdot \delta_1 \quad , \qquad \varepsilon_k = k \cdot \varepsilon_1$$

The refracted wave which is of intensity ε_1 may interact with a second entropy discontinuity where the same process takes place, etc. After the interaction with the n-th discontinuity the characteristic numbers in the 5 regimes 1, 2, 3, 4, 5 (see figure 5) are:

1: $C_1^{(n)}, \quad C_2^{(n)}$

2: $C_1^{(n+1)}, \quad C_2^{(n+1)}$

3: $C_1^{(n)} - \varepsilon_1 \cdot \varepsilon_2 \cdots \varepsilon_{n-1}, \quad C_2^{(n)}$

4: $C_1^{(n)} - \varepsilon_1 \cdot \varepsilon_2 \cdots \varepsilon_{n-1}, \quad C_2^{(n)} - \varepsilon_1 \cdot \varepsilon_2 \cdots \varepsilon_{n-1} \cdot \delta_n$

5: $C_1^{(n+1)} - \varepsilon_1 \cdot \varepsilon_2 \cdots \varepsilon_n, \quad C_2^{(n+1)}$

The refracted wave has now the intensity $\varepsilon_1 \cdot \varepsilon_2 \cdots \varepsilon_n = \prod_{i=1}^{n} (\varepsilon_i)$, an intensity smaller than unity as long as always $\varepsilon_i < 1$, e.g. in the case of $p_t' > p_t''$ and $M' < \sqrt{2}$. The intensity of the wave is continuously weakened when the local Mach numbers on the path of the wave are decreasing and approaching 1. To show that the intensity of the wave vanishes when it approaches the M = 1-surface requires a separate investigation of the product $\prod_{i=1}^{n} (\varepsilon_i)$, see Appendix.

DISCUSSION

The interaction phenomena may now be applied to the secondary wave system occuring in the supersonic and hypersonic near wake. On their way to the lower Mach number regime in the free shear layer the secondary expansion waves are refracted, and are partly reflected in form of (tertiary) compression waves as long as the local Mach number $M' > \sqrt{2}$. The intensity of these tertiary compression waves is vanishingly small. Between the $M = \sqrt{2}$ - and the $M = 1$-surface the total intensity of the incident wave is reflected in form of waves of the same sign, so that the intensity of the incident wave becomes zero when it approaches the $M = 1$-surface: the incident secondary wave cannot be reflected, therefore, as a wave of opposite sign at the $M = 1$-surface, and the streamlines near the $M = 1$-surface are not deflected significantly by the secondary wave system from their original direction. A rough approach to this process is that the secondary expansion waves be reflected as expansion waves at the $M = \sqrt{2}$ -surface, which represents the situation fairly good once the inviscid stream Mach number M_3 is much greater than $\sqrt{2}$.

The formation of the lip shock can be explained by secondary compression waves which are reflected below the $M = \sqrt{2}$ -surface as waves of the same sign, and by the above mentioned tertiary compression waves. Whether these compression waves can converge to form the lip shock depends on both Reynolds number and Mach number: The secondary wave reflections and the formation of the lip shock must be completed within a regime close to the wedge shoulder, i.e. long before the recompression process at the wake neck begins. The average distance between the wake neck and the wedge base, s, is between $h/2$ and h, h being the base height. The length of the regime in which the secondary waves are reflected must be much

smaller than this distance s to allow for forming the lip shock. At supersonic velocities the separation shock appears, therefore, only when the thickness of the separating boundary layer is small compared to the base height, i.e. at high Reynolds numbers. The strength of the separation shock decreases with decreasing Reynolds number and disappears completely when the boundary layer thickness is of the same order of magnitude as the base height.

Figure 6 shows the development of the free shear layer in the near wake behind a 7.5^{o} half angle wedge in helium flow at a free stream Mach number of 11, thus representing a case that corresponds to the before mentioned experiments, [6]. The inviscid flow Mach number at the outer edge of the body boundary layer is $M_2 = 6.45$; the Mach number profile in the boundary layer has been calculated according to Nicholl [13]. It is assumed that the $M = 1$-streamline be deflected by an angle of $\beta_o = 30^{o}$. The Prandtl-Meyer-expansion at the wedge shoulder is concentrated into one single line. The secondary expansion (rarefaction) waves, calculated as reflections of the primary expansion at the entropy discontinuities, travel through the free shear layer and are reflected - according to the above rough assumption - at the $M = \sqrt{2}$ -surface as waves of the same sign. Because of the high local Mach numbers or the relatively small Mach angles the reflection process can only be completed for a few secondary waves within a distance smaller than $h/2$ from the wedge base; therefore, a separation shock cannot be formed, and the divergence of the streamlines in the free shear layer cannot be compensated before the recompression at the wake neck starts. The initial direction of the streamlines near the $M = 1$-surface, however, remains nearly unchanged, since the intensity of the secondary waves becomes zero near that surface, and this explains the relatively large deflection angles which had been observed in the experiments.

All streamlines in the free shear layer have the same direction once the process of the secondary wave reflections can be completed; this may be realized - as shown above - only in the supersonic, high-Reynolds-number near wake, and it explains the agreement between the Prandtl-Meyer angles calculated from the measured base pressure and the visualized wake angles, as reported by Lehnert and Schermerhorn [5].

To summarize: A separation shock can be formed in the supersonic near wake at high Reynolds numbers only, when the boundary layer thickness is small compared to the base height, whereas this shock cannot be formed in hypersonic flow, even at high Reynolds numbers, due to the small Mach angles.

REFERENCES

1) Chapman, D.R. — Laminar mixing of a compressible fluid. NACA TN 1800, 1949.

2) Chapman, D.R., Kuehn, D.M., Larson, H.K. — Investigations of separated flows in supersonic and subsonic streams with emphasis on the effect of transition. NACA Report 1356, 1958.

3) Denison, M.R., Baum, E. — Compressible free shear layer with finite initial thickness. AIAA J. 1, 1963, pp. 342-349.

4) Kavanau, L.L. — Base pressure studies in rarefied supersonic flow. J. Aero. Sci. 23, 1956, pp. 193-207.

5) Lehnert, R., Schermerhorn, V.L. — Correlation of base pressure and wake structure of sharp and blunt nose cones with Reynolds number based on boundary layer momentum thickness. J. Aero. Sci. 26, 1959, pp. 185-186.

6) Merzkirch, W. F.
Larson, H. K.
Base flow measurements behind a 7.5° half angle wedge in hypersonic helium flow.
NACA TN (to be published)

7) Softley, E. J.
Muntz, E. P.
Zempel, R. E.
Experimental determination of pressure, temperature, and density in some laminar hypersonic near wakes.
General Electric, Tech. Inf. Series R64SD35, 1964.

8) Dewey, C. R.
Near wake of a blunt body at hypersonic speeds.
AIAA J. 3, 1965, pp. 1001-1010.

9) Weinbaum, S.
Rapid expansion of a supersonic boundary layer and its application to the near wake.
AIAA J. 4, 1966, pp. 217-226.

10) Weiss, R. F.
Weinbaum, S.
Hypersonic boundary layer separation and the base flow problem.
AIAA J. 4, 1966, pp. 1321-1330.

11) Merzkirch, W. F.
Zum Einfluß der Reynolds-Zahl auf die Heckströmung hinter einem Keil bei Überschall- und Hyperschallgeschwindigkeiten.
Paper presented at the DGRR/WGLR Annual Meeting, October 1966, Bad Godesberg, Germany.

12) Ferri, A.
The Methods of Characteristics. In: General Theory of High Speed Aerodynamics (W. R. Sears, Editor), Princeton University Press, 1954, pp. 638-642.

13) Nicoll, K. M.
Investigation of the laminar boundary layer on a flat plate in helium using the Crocco method.
ARL Report 62-345, 1962

APPENDIX

The logarithmic term in equation (2) may be replaced by an expression containing the local Mach numbers M' and M'' ; the static pressure on both sides of the discontinuity is the same, therefore:

$$\tan\alpha = 1 + \frac{1 + \frac{\gamma-1}{2} M'^2}{\gamma M'^2 (M'^2-1)} (2 - M'^2) \frac{\gamma}{\gamma-1} \ln \frac{1 + \frac{\gamma-1}{2} M''^2}{1 + \frac{\gamma-1}{2} M'^2}$$

If the net work of entropy discontinuities is chosen very narrow so that the difference $\Delta M = M' - M''$ be small and $(\Delta M)^2$ and terms of higher order may be neglected, then

$$\tan\alpha = 1 - \frac{2-M'^2}{M'^2-1} \cdot \frac{\Delta M}{M'}$$

The i-th factor of the product $(\overline{|}_i \varepsilon_i)$ can be written:

$$\varepsilon_i = \frac{2 \cdot \left[M_i'^2 - 1 - (2 - M_i'^2) \cdot \frac{\Delta M}{M_i'} \right]}{2 \cdot (M_i'^2 - 1) - (2 - M_i'^2) \cdot \frac{\Delta M}{M_i'}} = \frac{f(M_i')}{g(M_i')}$$

and

$$\varepsilon_{i+1} = \frac{f(M_i') - a_i}{g(M_i') - a_i} ; \qquad a_i = 4 M_i'^2 \cdot \frac{\Delta M}{M_i'}$$

For the secondary waves between the $M = \sqrt{2}$ - and the $M=1$-surface: $M' > M''$, $\varepsilon_i < 1$, and therefore

$$\varepsilon_{i+1} \leqslant \varepsilon_i .$$

The network of entropy discontinuities may be chosen infinitely narrow, i.e. $\Delta M \rightarrow 0$; one needs then an infinite number of steps to approach the $M=1$-surface. The last step on this way ($M'' = 1$) is described by the limiting value

$$\lim (\tan \alpha) = \frac{1}{2}$$
$$M'' = 1,$$
$$\Delta M \to 0$$

and therefore

$$\lim (\varepsilon_i) = \frac{2}{3}$$
$$M'' = 1,$$
$$\Delta M \to 0$$

From this and the condition $\varepsilon_i < 1$ one may deduce that the product

$$\lim \left(\prod_{i=1}^{\infty} \varepsilon_i \right) \to 0 \quad \text{for} \quad M'' \to 1.$$

The intensity of the incident wave therefore becomes zero when the wave approaches the M=1-surface.

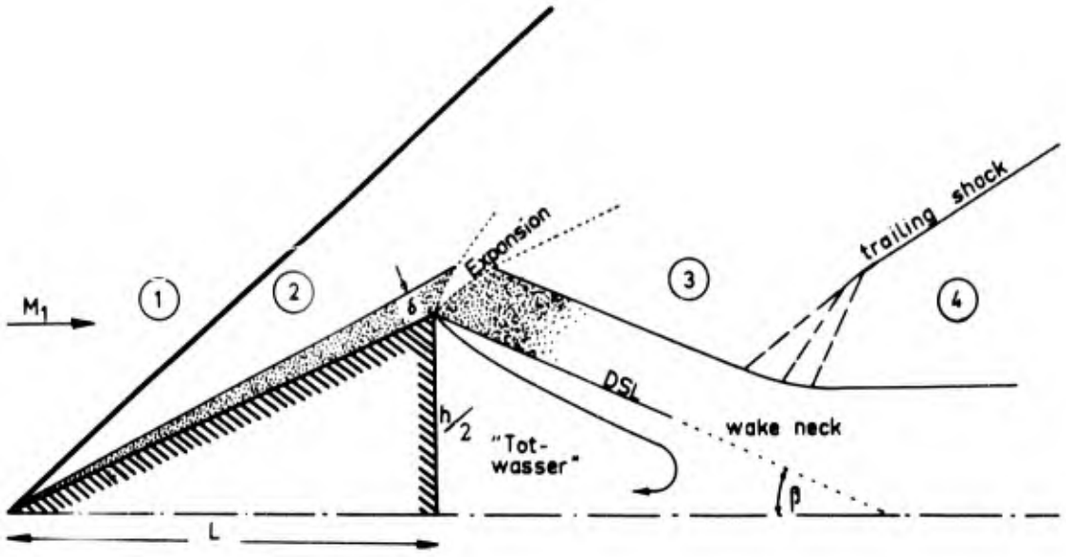

Fig. 1 Near wake model

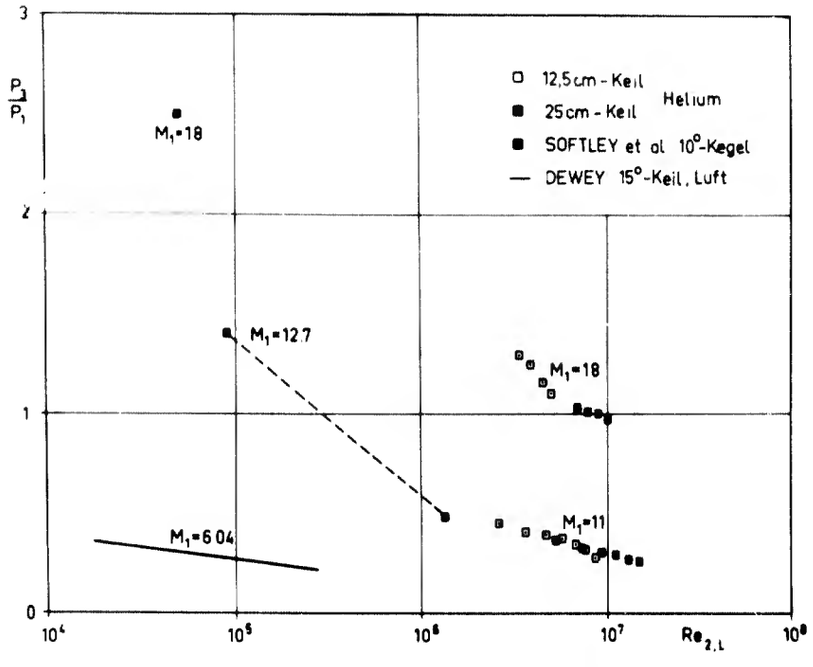

Fig. 2 Base pressure measurements behind a 7.5° half angle wedge in helium flow at free stream Mach numbers of 11 and 18.

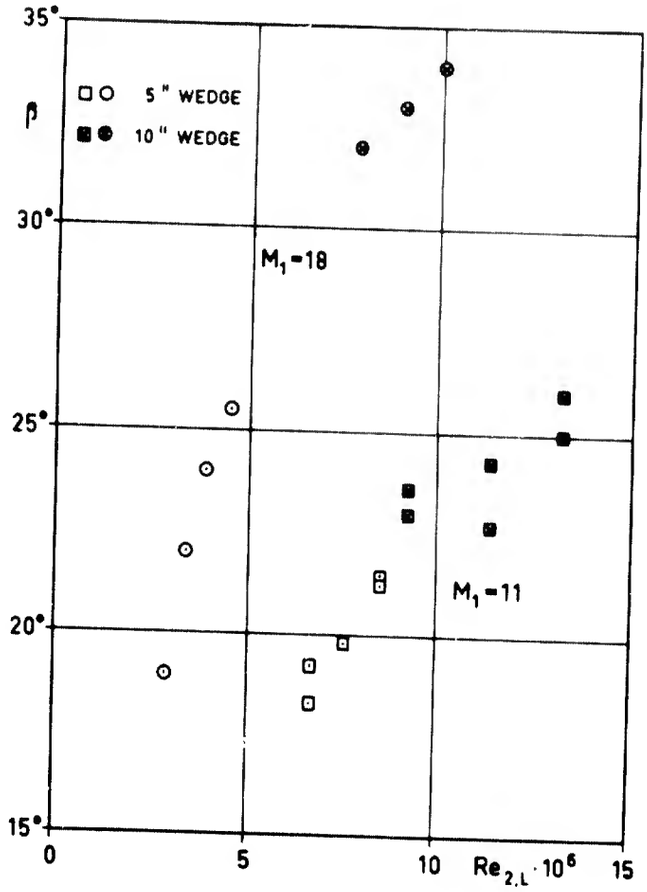

Fig. 3 Wake angle ß behind a 7.5° half angle wedge in hypersonic helium flow.

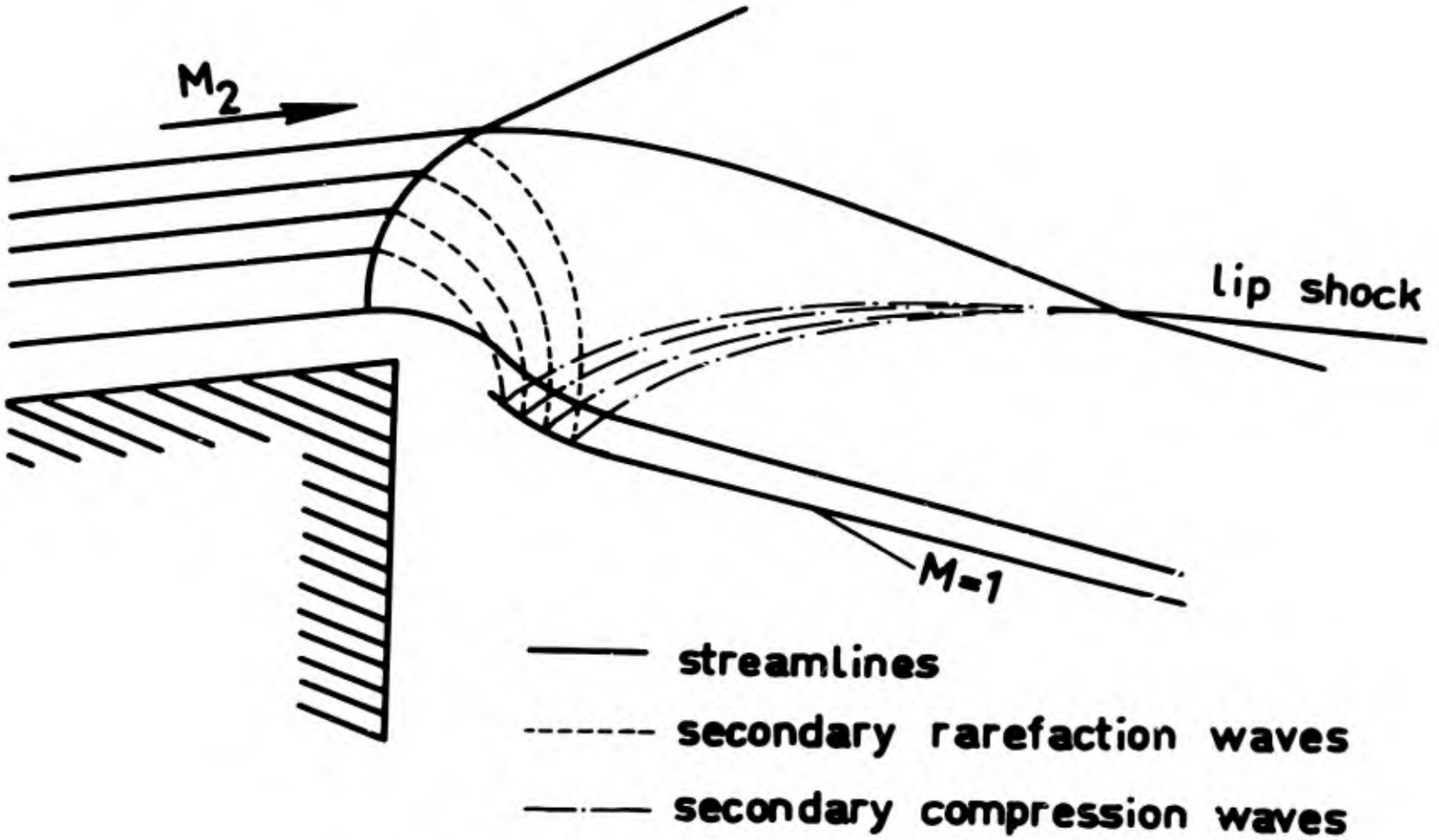

Fig. 4 Inviscid model for the separating supersonic boundary layer according to Weinbaum [9].

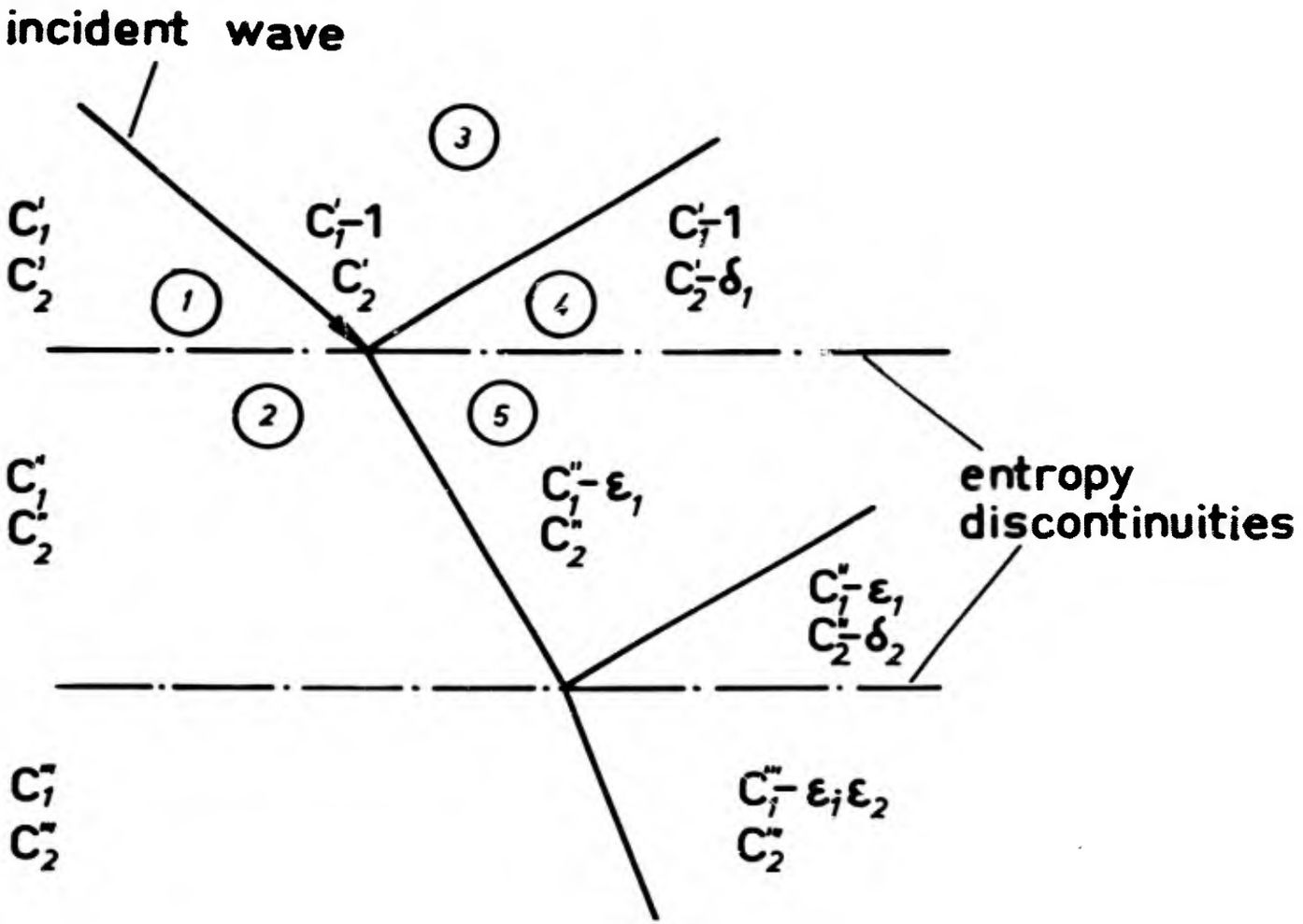

Fig. 5 Incident wave of intensity 1 interacting with two entropy discontinuities.

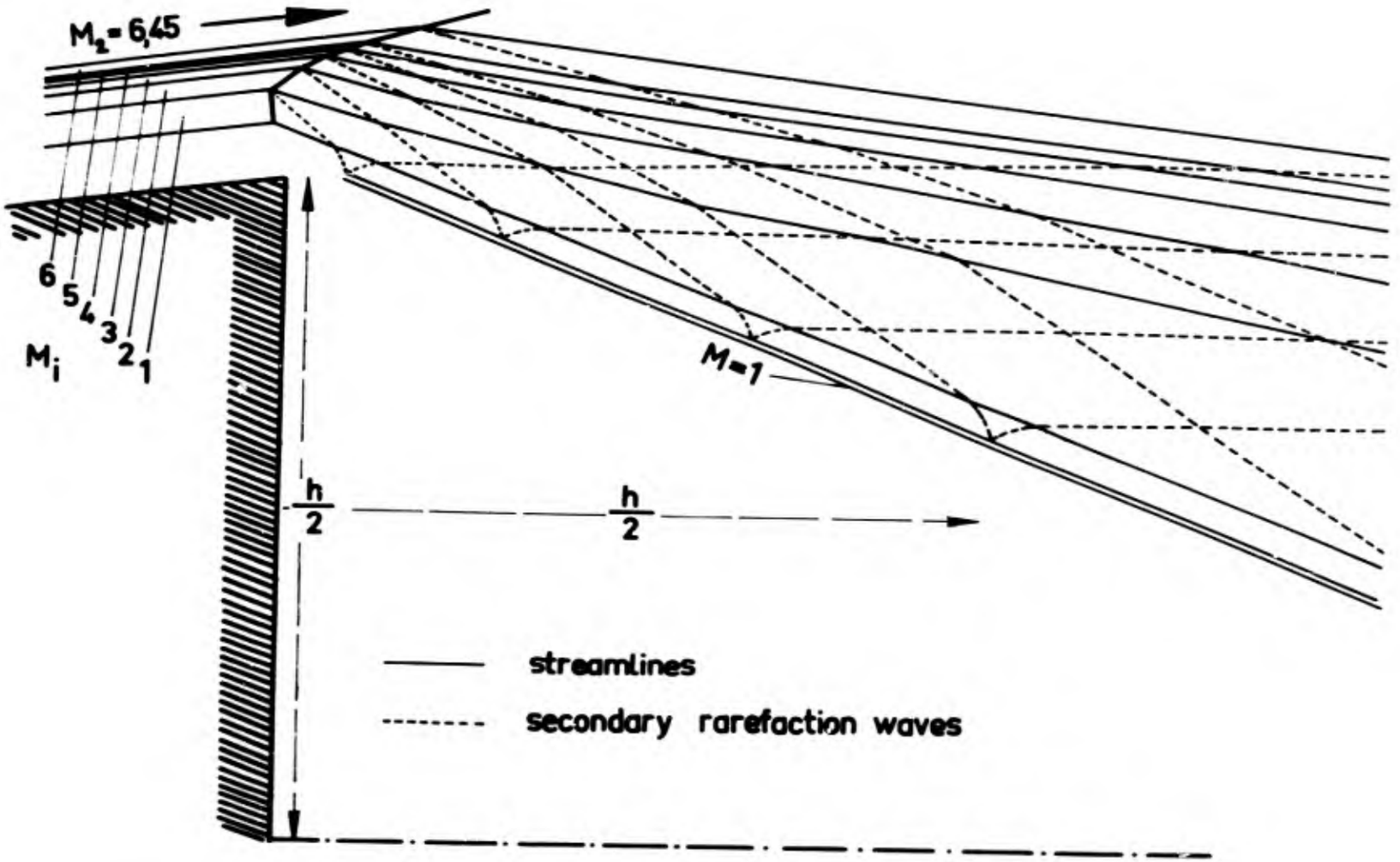

Fig. 6 Separating boundary layer and secondary wave system in the near wake of a 7.5° half angle wedge in $M_1 = 11$ - helium flow.

BLANK PAGE

ETUDE DE SILLAGES DE CYLINDRES ET DE DIEDRES EN ECOULEMENT DE GAZ RAREFIE

par

P. TREPAUD *
R. PERY *
J.P. BOEHLER *
H. VIVIAND **
E.A. BRUN ***

Laboratoire d'Aérothermique
du Centre National de la Recherche Scientifique
4ter, route des Gardes
92 - MEUDON FRANCE

* Ingénieur de recherche
** Chargé de recherche
*** Professeur à la Sorbonne, Directeur du laboratoire d'Aérothermique

SOMMAIRE

On présente les résultats d'une étude expérimentale de sillages de cylindres et de dièdres (d'angle au sommet 10°), en écoulement de gaz raréfié. Le nombre de Mach est voisin de 4; le nombre de Reynolds, basé sur le diamètre du cylindre ou la longueur du dièdre, est égal à 533 et 870 pour le cylindre, et 2540 pour le dièdre. Les techniques expérimentales utilisées sont décrites : explorations de l'écoulement à l'aide d'un tube de Pitot et d'un fil chaud, et visualisation. Le proche sillage n'a plus une structure nettement définie, comme aux grands nombres de Reynolds ; les effets de viscosité rendent les caractéristiques du sillage de plus en plus diffuses, lorsque le nombre de Reynolds décroît, et ceci beaucoup plus rapidement pour le dièdre que pour le cylindre.

Cette étude a été complétée par des mesures de pressions de paroi et de pressionsde culot à des nombres de Mach 2 et 4, et pour des nombres de Reynolds variant de 34 à 1400 pour le cylindre, et de 137 à 2660 pour le dièdre.

SUMMARY.

The results of an experimental study of wakes behind cylinders and wedges (total angle = 10°), at Mach number 4, in rarefied gas flow, are presented. The values of the Reynolds number, based on cylinder diameter or wedge length, are 533 and 870 for the cylinder, and 2540 for the wedge. The experimental techniques used are described : measurements with a Pitot tube and a hot wire, and visualization. The results show that the near wake has lost the well defined structure found at high Reynolds numbers ; viscous effects make the wake characteristics more and more diffuse, as the Reynolds number decreases, this phenomena being more rapid for the wedge than for the cylinder.

Measurements of surface pressure and base pressure have been carried out at Mach numbers 2 and 4, and over a range of Reynolds numbers 34 to 1400 for the cylinder, and 137 to 2660 for the wedge.

NOTATION

A	surface latérale du fil
a	demi-épaisseur du culot pour le dièdre
C	constante de Chapman-Rubesin
C_p	coefficient de pression = $(p - p_\infty)/\frac{1}{2}\rho_\infty U_\infty^2$
d	diamètre du cylindre
h	coefficient de convection = $Q_c/A(T_{eq} - T_f)$
i	intensité du courant électrique
L	longueur du dièdre
M	nombre de Mach de l'écoulement libre
p	pression, pression de paroi
p_b	pression de culot (pression à $\theta = 180°$ sur le cylindre)
$\overline{p}_b$	pression moyenne de culot (pour le dièdre)
p_t	pression effectivement mesurée par un tube de Pitot
p_w	pression totale derrière une onde de choc droite
Q_c	puissance reçue par le fil par convection
Q_r	puissance perdue par le fil par rayonnement
R	résistance électrique
$\mathcal{R}$	nombre de Reynolds = $U_\infty \rho_\infty d/\mu_\infty$
$\mathcal{R}_0$	nombre de Reynolds basé sur la viscosité à la température d'arrêt = $U_\infty \rho_\infty d/\mu_0$
$\mathcal{R}_x$	nombre de Reynolds à la distance x de l'arête du dièdre = $U_\infty \rho_\infty x/\mu_\infty$
$\mathcal{R}_{1x}$	nombre de Reynolds basé sur les conditions qui existeraient à la paroi du dièdre en fluide non-visqueux = $U_1 \rho_1 x/\mu_1$
T	température
T_{eq}	température d'équilibre du fil
T_f	température de frottement du fil
T_o	température génératrice
T_p	température de la paroi interne de la jauge
U_∞	vitesse de l'écoulement libre
x	distance sur une face du dièdre mesurée à partir de l'arête ; distance sur l'axe du sillage

δ^*	épaisseur de déplacement de la couche limite
θ	azimut d'un point sur le cylindre mesuré à partir du point d'arrêt
$\tilde{\chi}_1$	paramètre d'interaction visqueuse modifié (equ. 1)
μ	coefficient de viscosité
ρ	masse spécifique
ε	émissivité

Indices

∞	caractérise l'écoulement libre
1	caractérise les conditions sur le dièdre en fluide non-visqueux

1. - INTRODUCTION

Une quantité importante de résultats expérimentaux et théoriques est déjà disponible en ce qui concerne les sillages supersoniques et hypersoniques à des nombres de Reynolds élevés. Par contre, les études dans des conditions d'écoulement caractérisées par un nombre de Reynolds faible ou modéré, sont beaucoup moins nombreuses (1 , 2). De telles conditions se rencontrent à des altitudes très élevées, là où les premiers effets de la raréfaction de l'atmosphère se traduisent principalement par une diminution du nombre de Reynolds, c'est-à-dire une augmentation, qui peut être considérable, des épaisseurs de couche limite. Lorsque l'altitude augmente encore, les effets de glissement et de saut de température à la paroi interviennent ; ce régime, dit de glissement, correspond approximativement aux valeurs du paramètre $M/\mathcal{R}^{1/2}$ comprises entre 0,01 et 1. L'écoulement entre ensuite dans le régime de transition et enfin dans le régime moléculaire libre, domaines de la théorie cinétique des gaz.

L'étude expérimentale de sillages présentée ici se rapporte à des conditions d'écoulement allant du régime continu à nombre de Reynolds modéré, de l'ordre de 10^3, au régime de glissement. Les expériences ont été faites dans la soufflerie à basse densité SR 3 du Laboratoire d'Aérothermique, pour des nombres de Mach de 2 et de 4, à des pressions statiques comprises entre 15 et 60 microns de mercure. L'étude expérimentale comporte des mesures de pression de paroi et de pression de culot, des explorations du proche sillage au tube de Pitot et au fil chaud,et des visualisations de l'écoulement.

L'étude des sillages de cylindresa fait l'objet d'une thèse(1) ; en ce qui concerne les sillages de dièdre s,les résultats présentés ici sont des résultats préliminaires obtenus à l'aide d'un seul modèle. L'étude doit être poursuivie à des nombres de Reynolds plus variés, et à des nombres de Mach plus élevés.

2. - DISPOSITIFS EXPERIMENTAUX

2.1 Mesure des pressions

Les mesures de pression ont été faites à l'aide de jauges à fil chaud construites au laboratoire. Elles fonctionnent sur le principe de la jauge de Pirani. Si T_p est la température de la paroi intérieure de la jauge, et si le fil chaud, parcouru par un courant d'intensité i, prend une température d'équilibre T_{eq}, la pression p dans la jauge est de la forme :

$$p = f(i, T_p, T_{eq})$$

Il faudrait opérer à intensité i et à température T_p constantes, aussi bien au cours des mesures qu'au cours de l'étalonnage pour que la pression p soit fonction de la seule température T_{eq}. Pour ne pas courir le risque de variations accidentelles de i et de T_p, nous avons préféré opérer de manière différentielle (fig. 1) en plaçant, dans le pont de Wheatstone qui contient le fil de la jauge, un fil identique placé dans une ampoule vide. Un même fluide, maintenu à température constante T_p, circule autour de la jauge et de l'ampoule. Ainsi une légère variation sur l'intensité i ou sur la température T_p agit pratiquement de la même façon sur les deux éléments symétriquement placés dans le même pont et, par suite, n'influence pas la mesure fournie par un millivoltmètre placé dans la diagonale du pont.

La jauge est constituée par une double enveloppe cylindrique suivant l'axe de laquelle est tendu un fil en platine de diamètre 0,02 mm. (fig. 2). Avant chaque mesure, les jauges sont étalonnées en maintenant le caisson à diverses pressions, et en mesurant ces pressions à l'aide d'une jauge de Mac Leod. On obtient ainsi, pour chaque jauge, une courbe donnant le déséquilibre du pont, mesuré en millivolts, en fonction de la pression.

2.2. Mesure à l'aide d'un fil chaud

2.2.1. Principe

Les difficultés inhérentes à l'emploi d'une sonde à fil chaud (perte de chaleur par rayonnement et perte de chaleur par conduction vers les extrémités) prennent une importance relative accrue quand cette sonde est utilisée dans un écoulement à basse pression.

Nous avons supprimé les pertes de chaleur par conduction en portant les supports à la même température que le fil : une résistance de chauffage entoure chacun des supports. La mesure de la température des supports est faite à l'aide d'un thermocouple. Un asservissement permet de fixer cette température à la valeur voulue.

Pour corriger les pertes par rayonnement, nous avons déterminé expérimentalement l'émissivité ε du fil : le fil étant maintenu à température constante, nous faisons varier la pression du gaz dans l'enceinte ; par extrapolation à une pression nulle, on en déduit ε, qui est voisin de 0,1.

2.2.2. Réalisation

Le fil de platine, de 0,02 mm de diamètre et de 2,2 cm de long, est tendu entre deux aiguilles de 0,5 mm de diamètre, qui constituent les supports. Ce fil, de résistance R, est parcouru par un courant d'intensité i. Il prend alors une température d'équilibre T_{eq} qui est définie par le bilan thermique suivant : il reçoit une puissance Ri^2 par effet Joule et une puissance Q_c par convection. Il perd une puissance Q_r par rayonnement ; le chauffage du support empêche les pertes par conduction. Le bilan se résume par l'équation :

$$Ri^2 + Q_c = Q_r$$

La connaissance de la température des parois de la soufflerie et de la température du fil (par mesure de sa résistance), permet de connaître Q_c, que l'on écrit :

$$Q_c = Ah\ (T_{eq} - T_f)$$

où A est l'aire latérale du fil et h le coefficient de convection.

En mesurant ainsi Q_c pour diverses valeurs de T_{eq}, on peut tracer la droite donnant Q_c en fonction de T_{eq}. La pente de cette droite permet de calculer h. On peut, d'autre part, déterminer la température de frottement du fil puisque $T_f = T_{eq}$ pour $Q_c = 0$.

Le fil étant très fin, l'écoulement autour de la sonde est moléculaire libre ; la mesure faite avec une telle sonde ne dépend donc pas de l'état de raréfaction local du gaz par rapport à la sonde. D'autre part, l'interprétation des mesures ainsi obtenues est rendue plus facile du fait que les transferts de chaleur sont bien connus pour ce type d'écoulement.

2.3. Visualisation

La visualisation de l'écoulement autour de la maquette est obtenue par ionisation du gaz par excitation électronique dans un champ électrique alternatif haute fréquence. La luminosité de l'écoulement provient de la désexcitation des molécules qui suit la recombinaison,et ses variations suivent celles de la densité. Pour obtenir une meilleure luminosité, nous avons remplacé l'air par l'azote.

Cette technique a déjà été beaucoup utilisée à Mach = 2; la bobine d'induction est placée autour d'un tube en pyrex prolongeant en amont la chambre de tranquillisation où règne une pression de l'ordre de 500 microns de mercure. A des nombres de Mach plus élevés, la pression de la chambre de tranquillisation atteint quelques millimètres de mercure et, avec un générateur de fréquence d'environ 20 MHz, l'ionisation n'est plus possible avec le dispositif précédent. La bobine d'induction est donc placée autour d'une tuyère en matériau isolant (fibre de verre moulée), entre le col et le plan de sortie, à l'intérieur de la chambre de tranquillisation. Dans la tuyère, la pression au droit de la bobine est très proche de la pression de la veine et l'ionisation s'amorce bien ; nous avons même constaté, que, par phénomène de rétrodiffusion, cette ionisation arrive à s'étendre jusqu'au col. Par contre, la pression géné-

ratrice, autour de la tuyère, est suffisamment élevée pour que la décharge haute fréquence ne puisse s'amorcer aux bornes de la self, si l'on prend quelques précautions relatives à la distance entre les conducteurs et à la tension d'alimentation.

Dans ces conditions, la fréquence de collision des électrons avec les particules neutres est très supérieure à la pulsation du champ électrique, et seuls les électrons gagnent de l'énergie ; l'échange d'énergie entre les électrons et les particules neutres est très faible compte-tenu du rapport des masses, et ainsi le gaz ne subit qu'une très faible élévation de température ; les caractéristiques aérodynamiques de l'écoulement ne sont donc pas modifiées par l'ionisation.

3.- ETUDE DU CYLINDRE

3.1 Pression de paroi

3.1.1. Dispositif expérimental

Les maquettes utilisées sont des cylindres de laiton de diamètre 10 mm, 14,8 mm et 15,6 mm. Ces cylindres sont solidaires de l'arbre d'un moteur du type Stéro-Moteur pas à pas 1 200 positions, placé dans la soufflerie. Le moteur est relié à un coffret d'asservissement placé à l'extérieur de la soufflerie. Cet ensemble permet de faire tourner le cylindre et de fixer l'azimut de la prise de pression à 1/3 de grade près. L'orifice de mesure de pression a un diamètre de 0,4 mm. Le fil de la jauge est placé dans le cylindre à la hauteur du palier qui supporte ce cylindre.

Pour un nombre de Mach donné, nous avons fait varier le nombre de Reynolds et le nombre de Knudsen, soit en agissant sur la pression statique de l'écoulement, soit en faisant varier le diamètre du cylindre.

3.1.2. Résultat général

A titre d'exemple, nous avons porté sur la figure 5 , pour divers nombres de Reynolds, la variation du coefficient de pression C_p en fonction de l'azimut θ pour un nombre de Mach de 2. La courbe correspondant à $\mathcal{R} = 10^5$ a été obtenue dans la soufflerie supersonique SS 1 du laboratoire d'Aérothermique.

On peut constater, sur cette figure, pour tous les points situés sur la face amont du cylindre, que le coefficient de pression C_p augmente quand le nombre de Reynolds diminue. Ce résultat s'explique par l'augmentation importante de l'épaisseur de la couche limite le long de la paroi du cylindre quand le nombre de Reynolds diminue.

3.1.3. Pression de culot

Nous avons porté, sur la figure 6, les courbes donnant p/p_w à l'arrière du cylindre pour divers nombres de Mach et de Reynolds, ainsi que deux courbes obtenues par Dewey (5) à des nombres de Reynolds supérieurs. Considérons celle correspondant à un nombre de Reynolds $\mathcal{R}_o$ de $7{,}9\ 10^3$: pour des valeurs de θ comprises entre 140° et 170°, la courbe présente un "plateau". L'existence de cette région à pression constante justifie l'hypothèse classique d'une zone de mélange isobare. Dewey a également noté, sur cette courbe, une très légère augmentation de pression à des angles voisins de 180°. Cette augmentation de pression serait due à la présence du point d'arrêt de l'écoulement recyclé se dirigeant vers le cylindre.

On remarque que la courbe correspondant à un nombre de Reynolds de $1{,}4\ 10^3$ ne présente plus de "plateau". Ceci veut dire que, déjà, à ces nombres de Reynolds, l'hypothèse de la zone de mélange à pression constante n'est plus valable. Ce phénomène est encore plus marqué sur les courbes que nous avons obtenues pour des nombres de Reynolds beaucoup plus faibles, à savoir 154, 86 et 52. Si l'on admet que la région de décollement de la couche limite correspond à la partie de la courbe où la pression est minimale,on remarque que cette région correspond à des angles de plus en plus grands à mesure que le nombre de Reynolds diminue, ce qui veut dire que la couche limite pénètre de plus en plus dans la région

située immédiatement à l'aval du cylindre. Sur la courbe correspondant à un nombre de Mach 2 et à un nombre de Reynolds 22, on ne décèle pratiquement plus de minimum de pression, ce qui voudrait dire qu'il n'y a plus réellement de décollement de la couche limite et que la zone de recirculation a pratiquement disparu.

La figure 7 donne les valeurs expérimentales du rapport p_b/p_w en fonction du nombre de Reynolds $\mathcal{R}_o$, pour des nombres de Mach 2 et 4. p_b est la pression de paroi pour $\theta = 180°$, et $\mathcal{R}_o$ le nombre de Reynolds calculé pour une température égale à la température d'arrêt du gaz. Sur cette figure, on remarque que les points expérimentaux correspondant à un nombre de Mach 4 se trouvent sur une courbe déjà obtenue par d'autres auteurs (5,6,7) pour des nombres de Reynolds plus élevés, alors que les points expérimentaux correspondant à un nombre de Mach 2 se trouvent tout à fait en dehors de cette courbe. Le fait que, pour des nombres de Mach supérieurs à 4, tous les points expérimentaux se trouvent sur une courbe unique, signifie que la valeur du rapport p_b/p_w ne dépend que du nombre de Reynolds pourvu que le nombre de Mach soit supérieur à 4 environ. Ce résultat semble se vérifier même aux très faibles nombres de Reynolds $\mathcal{R}_o$ que nous avons obtenus.

3.2 Etude à l'aide d'un tube de Pitot

Les mesures au tube de Pitot fournissent surtout une description géométrique du sillage, car il est pratiquement impossible d'effectuer, sur les mesures, les corrections dues à la viscosité et à la raréfaction du gaz. Cependant, les mesures que nous citons ici ont été effectuées à des pressions supérieures à 40 microns de mercure à l'aide d'un tube de Pitot de diamètre relativement grand (2,5 mm). Ces corrections restent donc faibles, et la valeur p_t de la pression ainsi mesurée à l'aide de ce tube est assez proche de la pression d'arrêt locale.

A titre d'exemple, nous donnons, sur la figure 8, les lignes d'égale pression d'arrêt dans le sillage d'un cylindre pour un nombre de Mach de 3,85 et un nombre de Reynolds 533. Ces lignes sont obtenues à partir de la figure 9 où l'on a traçé la variation de p_t/p_{t_∞} en fonction de y pour diverses valeurs de x. Sur cette dernière figure, on peut

remarquer la forte élévation de pression p_t à la traversée de l'onde de choc (par exemple $p_t/p_{t\infty} = 2$ pour $2x/d = 1$ et $2y/d = 4$), qui s'explique par le fait que le tube de Pitot mesure alors la pression d'arrêt derrière une onde de choc oblique.

Les courbes correspondant à des explorations faites dans le sillage du cylindre présentent de la même façon un maximum, mais beaucoup moins aigu (par exemple $2y/d = 2$, $2x/d = 9$). Par analogie, nous pensons que cette augmentation de pression est due à la présence d'une zone de recompression, correspondant à l'onde de choc du sillage aux grands nombres de Reynolds.

3.3. Exploration au fil chaud

3.3.1. Expériences

L'indication donnée par cette sonde est indépendante de l'orientation du vecteur vitesse, pourvu que ce vecteur soit contenu dans un plan perpendiculaire au fil. Par conséquent, cette sonde est tout indiquée pour étudier l'écoulement de culot, immédiatement à l'aval du cylindre, région où les lignes de courant peuvent être très inclinées. Les expériences ont été faites pour un nombre de Mach 4 et une pression statique de 60 microns de mercure. Le diamètre du cylindre était de 15 mm.

Les figures 10 et 11 montrent la variation en fonction de y, et pour diverses valeurs de x, du rapport $(h - h_x)/h_\infty$, où h est le coefficient de convection entre le gaz et le fil en un point du sillage ; h_x et h_∞ sont les valeurs que prend h respectivement sur l'axe du sillage et dans l'écoulement libre.

Les résultats concernant la température de frottement T_f du fil sont donnés dans la figure 12 sous la forme de courbes où le rapport $(T_f - T_o)/(T_{f\infty} - T_o)$ est constant. Dans cette expression, T_f est la température de frottement du fil, relative à un point du sillage, $T_{f\infty}$ est la valeur de T_f au loin et T_o est la température génératrice.

3.3.2. Interprétation des résultats

On peut voir sur la figure 11 qu'il existe toute une région, à l'aval du cylindre, où le coefficient h est minimal pour chaque

section. Cette région correspond à une zone où la vitesse elle-même est faible. Par conséquent, la ligne pointillée que nous avons indiquée délimite la zone d'air mort où se trouve l'écoulement recyclé, zone de mélange exclue. Le point d'arrêt B de cette ligne se trouve à une distance d'environ 3/4 d en aval du cylindre. Dewey (5), pour M = 6 et $\mathcal{R} = 2{,}2\ 10^4$, trouve que le point d'arrêt du sillage est situé à environ 1,9d du cylindre. On voit que la longueur de la zone de recirculation diminue rapidement lorsque $\mathcal{R}$ diminue. En extrapolant la ligne pointillée vers le cylindre, on trouve que le point de décollement A correspond à un angle de 132°. Si l'on se reporte à la figure 6 et que l'on considère la courbe $\mathcal{R}_0 = 154$ ($\mathcal{R} = 565$) en admettant que le minimum de cette courbe définisse la région de décollement de la couche limite, on voit que le décollement se produit à 134° environ, valeur qui concorde à peu près avec la précédente.

A l'extérieur de cette région, le coefficient h augmente rapidement lorsque l'on s'éloigne de l'axe du sillage ; cette variation correspond à l'augmentation de la vitesse à la traversée de la zone de mélange qui prolonge la couche limite décollée au point A. Lorsqu'on s'éloigne encore de l'axe et que l'on quitte cette couche visqueuse, la valeur du coefficient h diminue à nouveau ; cette région où le coefficient h est plus faible correspond à l'onde de choc très faible qui accompagne la séparation. La figure 12 met en évidence la zone de mélange très épaisse ; dans cette zone, la température de frottement varie très rapidement et les lignes d'égale température de frottement y sont très resserrées.

Considérons maintenant l'écoulement au delà de la zone de recirculation (fig. 10) : la partie de la courbe 1 comprise entre les points O et A correspond à une région de l'écoulement où le coefficient h est relativement faible et augmente à mesure que l'on s'éloigne de l'axe. Nous attribuons cette variation du coefficient h à une variation de la vitesse. La partie OA de la courbe 1 définit donc le sillage visqueux proprement dit. Entre les points B et C, on note un brusque abaissement du coefficient h puis, à partir de C, ce coefficient augmente réguliè-

rement à mesure que l'on s'éloigne de l'axe. La brusque variation de h est due à la présence de l'onde de choc du sillage, qui semble, en fait, être plutôt une zone assez large de recompression. La frontière du sillage visqueux montre un col, situé à environ 1,1 d en aval du cylindre, et d'épaisseur voisine de 0,4 d. Dans la région du col, la courbe 2 présente deux bosses, qui sont sans doute dues à l'influence combinée de l'onde de choc de séparation et l'onde de choc du sillage.

4. - ETUDE DU DIEDRE

4.1 Généralités

Nous présentons les résultats obtenus dans le cas d'un écoulement autour d'un dièdre d'angle au sommet de 10°, de longueur L = 5,71 cm et d'épaisseur au culot 2 a= 1 cm. L'arête du dièdre a une épaisseur inférieure à 0,07 mm. Des mesures de pression de paroi et de pression de culot ont été effectuées pour les conditions d'écoulement données dans la table I. Le diamètre des orifices de pression est de 0,3 mm. Les conditions thermiques sont celles d'une paroi adiabatique, la température d'arrêt étant de 20°C environ. Une exploration de l'écoulement autour du dièdre et dans la région initiale du sillage à l'aide d'un tube de Pitot, a été faite pour un nombre de Mach 3,86 et une pression statique dans la veine de 53,5 microns de mercure. Le montage en soufflerie, pour les mesures de pression de paroi, est présenté dans la figure 3.

4.2 Pression de paroi

Les pressions de paroi mesurées sont données dans la figure 13 sous la forme p/p_1 en fonction du paramètre d'interaction visqueuse modifié, $\tilde{\chi}_1$, défini par :

$$\tilde{\chi}_1 = \frac{M_1^3 C^{1/2}}{\mathcal{R}_{1x}^{1/2}} \frac{M_1}{\left(M_1^2 - 1\right)^{1/2}} \left(1 + \frac{3,9}{M_1^2}\right) \qquad (1)$$

L'indice 1 se rapporte aux conditions qui existeraient à la paroi du dièdre en fluide non visqueux. Les valeurs de M_1, p_1/p_∞, $\mathcal{R}_{1L}$, $\tilde{\chi}_{1L}$ sont données dans la table I.

La définition de $\tilde{\chi}_1$ résulte du calcul de la pression induite, dans le cas d'une interaction visqueuse faible, par la formule des écoulements supersoniques linéarisés :

$$\frac{p}{p_1} = 1 + \frac{\gamma M_1^2}{(M_1^2-1)^{1/2}} \frac{d\delta^*}{dx} \qquad (2)$$

Pour $M_1 \gg 1$, la relation (2) devient identique à celle que l'on obtient par la méthode dite du dièdre tangent, toujours dans le cas d'une interaction faible. Cette méthode a été utilisée par Cheng (8). Pour calculer δ^*, nous prenons, comme Hayes et Probstein (9), la solution obtenue par Crocco, c'est-à-dire, dans le cas d'une paroi adiabatique, et pour un facteur thermique pariétal égal à 0,85 :

$$\delta^* = x\, C^{1/2} \mathcal{R}_{1x}^{-1/2} \left(1{,}73 + 0{,}444\, M_1^2\right) \qquad (3)$$

Les équations (2) et (3) donnent ainsi :

$$\frac{p}{p_1} = 1 + 0{,}31\ \tilde{\chi}_1 \qquad (4)$$

relation valable aussi bien pour un écoulement supersonique que pour un écoulement hypersonique.

Les valeurs de $\mathcal{R}_L$, dans les conditions d'expérience, sont trop faibles pour que la relation (4) soit bien vérifiée. Cette formulation n'a en fait pour but que de mettre en évidence l'influence des phénomènes complexes qui entrent en jeu lorsque $\mathcal{R}_L$ décroît. Ces phénomènes sont, principalement, le glissement à la paroi, qui tend à diminuer l'effet de l'interaction visqueuse, le passage progressif d'une couche limite classique à un écoulement visqueux où les approximations de la couche

limite ne sont plus justifiées,et enfin l'influence du culot qui se fait sentir de plus en plus près du bord d'attaque. Il est difficile de séparer ces effets et la figure 13 donne seulement l'influence globale. On constate que les courbes de p/p_1 en fonction de $\tilde{\chi}_1$ se composent d'une partie, près du culot, où la pression décroît très rapidement, et, en amont, d'une partie à peu près linéaire et parallèle à la courbe théorique. Dans cette partie linéaire, pour des valeurs de M, $\mathcal{R}_{1x}$, et donc de $\tilde{\chi}_1$ fixées, la pression décroît lorsque $\mathcal{R}_L$ décroît.

4.3 Pression de culot

La pression sur le culot a été mesurée en quatre points situés à des distances différentes de l'axe (fig. 14). La pression décroît du centre vers le bord, phénomène déjà observé par Kavanau (2) et Cheng (10), et qu' une étude théorique (11 et 12), valable en écoulement incompressible, a mis aussi en évidence. Cette théorie a montré, en outre, que la décroissance de la pression est d'autant plus rapide que le rapport δ/a est plus petit, c'est-à-dire que le nombre de Reynolds est plus grand (δ représente l'épaisseur de la couche visqueuse à x = L). C'est ce que l'on vérifie très nettement sur la figure 14, puisque la pression redevient presque uniforme aux plus faibles nombres de Reynolds. Il semble donc que le phénomène de décroissance de la pression sur le culot doive passer par un maximum pour une certaine valeur du nombre de Reynolds, puisqu'aux grandes valeurs de $\mathcal{R}_L$ la pression est uniforme sur le culot.

La variation de la pression avec la distance y,est bien représentée par une loi parabolique ; mais nous n'avons qu'un petit nombre de points et il est possible que cette loi soit moins bien vérifiée près du bord du culot. Une pression moyenne de culot $\bar{p}_b$ a été calculée en utilisant cette loi parabolique : le rapport $\bar{p}_b/p_1$ est donné, sur la figure 15, enfonction de $\mathcal{R}_{1L}$, le nombre de Reynolds calculé d'après les conditions qui existeraient sur le dièdre en fluide non visqueux. Les mesures de Cheng (10) pour un dièdre de même angle

au sommet, à M = 4 et 6, sont aussi portées sur cette figure. On note une certaine dispersion qui, sans être très importante, empêche de conclure définitivement quant au sens de variation de $\bar{p}_b$. En fait, la pression moyenne du culot varie peu, dans les domaines de Mach et de Reynolds considérés, et nos résultats semblent indiquer l'existence d'un minimum.

4.4 Exploration au tube de Pitot

Une exploration de l'écoulement a été faite à l'aide d'un tube de Pitot de diamètre extérieur 3 mm, pour les conditions suivantes : M = 3,85, p_∞ = 53,5 microns de mercure, soit $\mathcal{R}_L$ = 2540. Le résultat est représenté sur la figure 16, où l'on a porté d'une part les profils de pression Pitot mesurée, $p_t/p_{t\infty}$, en fonction de y, pour différentes distances axiales, et d'autre part les principales caractéristiques de l'écoulement, déduites de ces profils de pression. L'origine des pressions, pour un profil correspondant à $x = x_1$, est décalée de telle sorte que le point $x = x_1$ corresponde à la pression $p_t/p_{t\infty}$ sur l'axe.

La position de l'onde de choc est ainsi déterminée avec une assez bonne précision. La frontière de la couche limite sur le corps est aussi bien définie, mais celle du sillage visqueux devient de plus en plus imprécise lorsque l'on s'éloigne du dièdre. A x = 6a, la courbe de pression ne montre plus le changement rapide de pente qui caractérise la frontière entre le sillage visqueux et l'écoulement non visqueux ; on peut en déduire que les gradients transversaux de vitesse deviennent partout du même ordre de grandeur et que la distinction entre sillage visqueux et sillage extérieur n'est plus valable. Pour $x \geqslant$ 12a, on remarque une légère diminution de la pression Pitot entre deux valeurs rapprochées de y ; par analogie avec la variation de p_t à travers une onde de choc, nous pensons que cette diminution de p_t correspond à une zone de recompression, analogue à l'onde de choc du sillage que l'on observe aux grands nombres de Reynolds. La figure 16 indique un rapport δ/a, au culot, voisin de 1,8, alors que l'équation (3) donne, pour δ^*/a , une valeur égale à 1,4. Il est évident qu'il

n'existe plus de zone de mélange proprement dite, distincte de la zone de recirculation ; en fait, l'écoulement au voisinage du culot est entièrement visqueux et proche d'un écoulement du type de Stokes.

La méthode de visualisation, déjà décrite, a été utilisée dans le cas du dièdre, pour M = 4, p_{∞} = 15 et 60 microns de mercure. Pour une pression de 60 microns de mercure (fig. 17), on retrouve sur la photographie la zone de recompression mise en évidence par l'exploration au tube de Pitot ; le sillage est visible à des distances du culot égales à 2 ou 3 fois la longueur du dièdre. Au contraire, à la pression de 15 microns (fig. 18), la zone de recompression n'est plus visible et le sillage semble extrêmement court.

Les figures 17 et 18 montrent comment évolue la structure du proche sillage lorsque le nombre de Reynolds décroît. Les régions à forts gradients (onde de choc, zone de mélange, sillage visqueux), nettement définies aux grands nombres de Reynolds, sont de plus en plus diffuses au faibles nombres de Reynolds, et laissent finalement la place à un écoulement entièrement visqueux où les gradients de pression et de vitesse sont partout d'un même ordre de grandeur.

REFERENCES

1. TREPAUD, P. — Etude des Sillages de Cylindres placés dans un Ecoulement de Gaz Raréfié. Thèse de Doctorat d'Etat, Université de Paris, Avril 1966.

2. KAVANAU, L.L. — Base Pressure Studies in Rarefied Supersonic Flows. Univ. of Calif. Eng. Proj. Rep. HE-150-125, November 1954, aussi J.A.S., Vol. 23, n°3, 1956, pp. I93-207.

3. TREPAUD, P. — Quelques Résultats Concernant les Mesures de Pression à la Paroi en Ecoulement de Glissement. C.R. Acad. Sc. Paris, t. 26I, pp. I457-I460, Août 1965.

4. MALEGUE, D.; TREPAUD, P.; BRUN, E.A. — Sonde à Fil Chaud pour l'Etude d'Ecoulements à Basse Pression et son Emploi dans l'Etude du Sillage d'un Cylindre. C.R. Acad. Sc. Paris, t. 263, pp. 376-379, Septembre 1966.

5. DEWEY, C.F, Jr. — Measurements in highly Dissipative Regions of Hypersonic Flows. Part II. The Near Wake of a Blunt Body at Hypersonic Speeds. Ph. D. Thesis, California Institute of Technology, Pasadena, Calif. I963. Aussi A.I.A.A. Journal, Vol. 3, n°6, pp. IOOI-IOIO, June 1965.

6. TEWFIK, O.K.; GIEDT, W.H. — Heat Transfer, Recovery Factor, and Pressure Distribution around a Cylinder Normal to a Supersonic Rarefied Air Stream. Part I. Experimental Data. Univ. of Calif. Eng. Proj. Rep. HE-I5O-I62, January 1959.

7. WALTER, L.W.; LANGE, A.H. — Surface Temperature and Pressure Distributions on a Circular Cylinder in Supersonic Cross-Flow. Naval Ordnance Lab. Rep. NAVORD 2854, June 1953.

8. CHENG, R.T. Analytical Study of the Characteristics of Wedges in Supersonic Viscous Flow. Univ. of Calif. Aero. Sci. Rep. AS-64-8, 1964.

9. HAYES, W.D.
PROBSTEIN, R.F. Hypersonic Flow Theory. Academic Press, New-York and London, 1959, p. 343.

10. CHENG, R.T.
SCHAAF, S.A.
HURLBUT, F.C. The Measurement of Base Pressure on Wedges in Supersonic Low Density Flow. Univ. of Calif. Aero. Sci. Rep. AS-64-17, 1964.

11. VIVIAND, H.
BERGER, S.A. The Base-Flow and Near Wake Problem very Low Reynolds Numbers. Part I. The Stokes Approximation. J. Fluid Mech. Vol.23, Part 3, 1965, pp. 417-438.

12. VIVIAND, H.
BERGER, S.A. L'Ecoulement de Culot aux Faibles Nombres de Reynolds. AGARD Specialists' Meeting on Separated Flows, Rhode-Saint-Genèse, Belgium, May 1966. Part 1, pp. 1-29.

TABLE I

	A 1	A 2	A 3	B 1	B 2	B 3
M	1,92	2,02	1,96	3,85	3,95	3,85
P_∞ (μ Hg)	19,9	40	66,7	16,5	37,8	56
$\mathcal{R}_L$	137	308	483	785	1965	2660
$M/\mathcal{R}_L^{1/2}$	0,164	0,115	0,089	0,137	0,089	0,075
M_1	1,74	1,836	1,76	3,50	3,60	3,50
P_1 / P_∞	1,302	1,318	1,300	1,598	1,612	1,598
$\mathcal{R}_{1L}$	146	334	512	960	2430	3250
$\tilde{\chi}_{1L}$	1,16	0,83	0,74	1,82	1,225	0,99

Table I Conditions expérimentales et valeurs des principaux paramètres dans l'étude du dièdre.

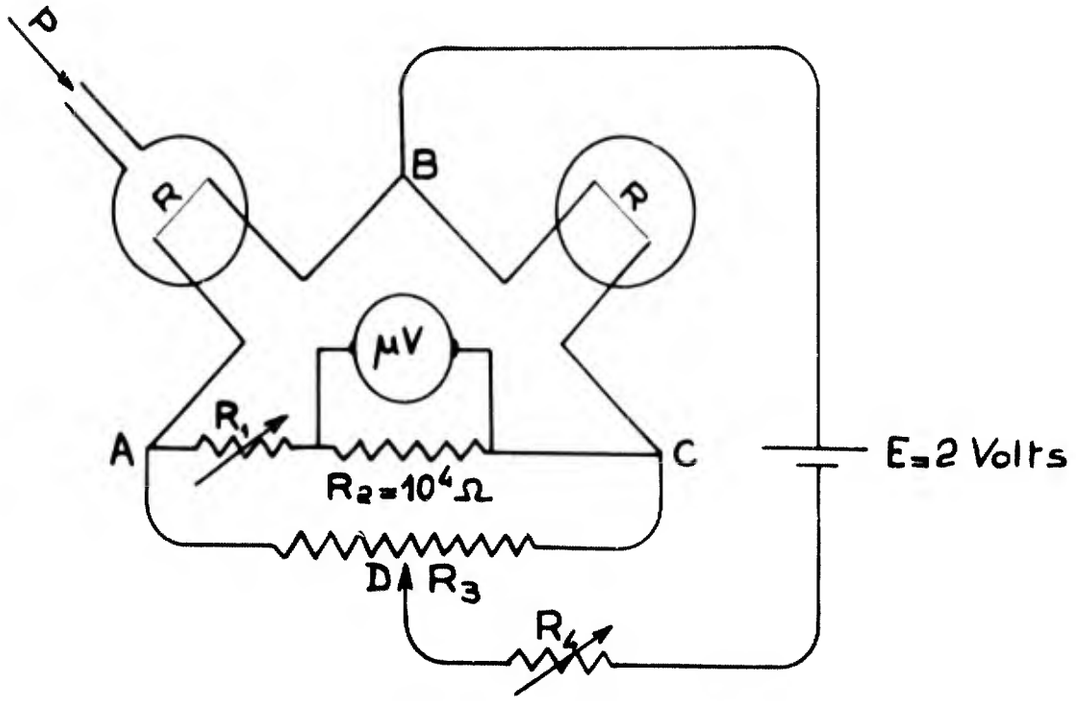

Fig. 1 Circuit électrique de la jauge de pression.

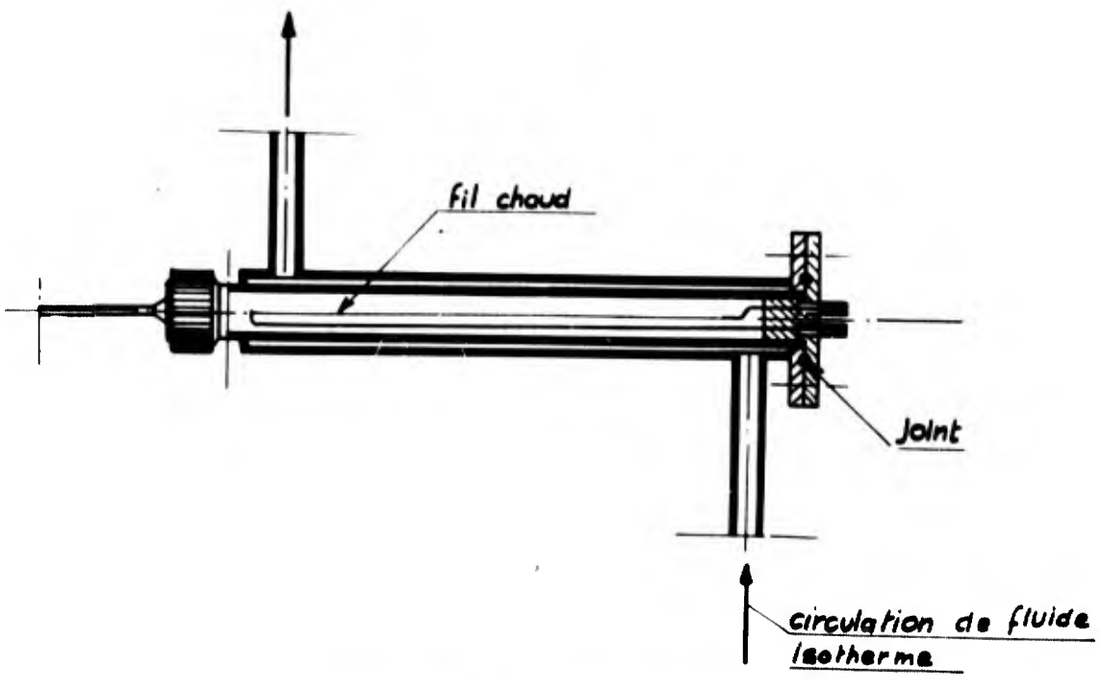

Fig. 2 Elément sensible de la jauge de pression.

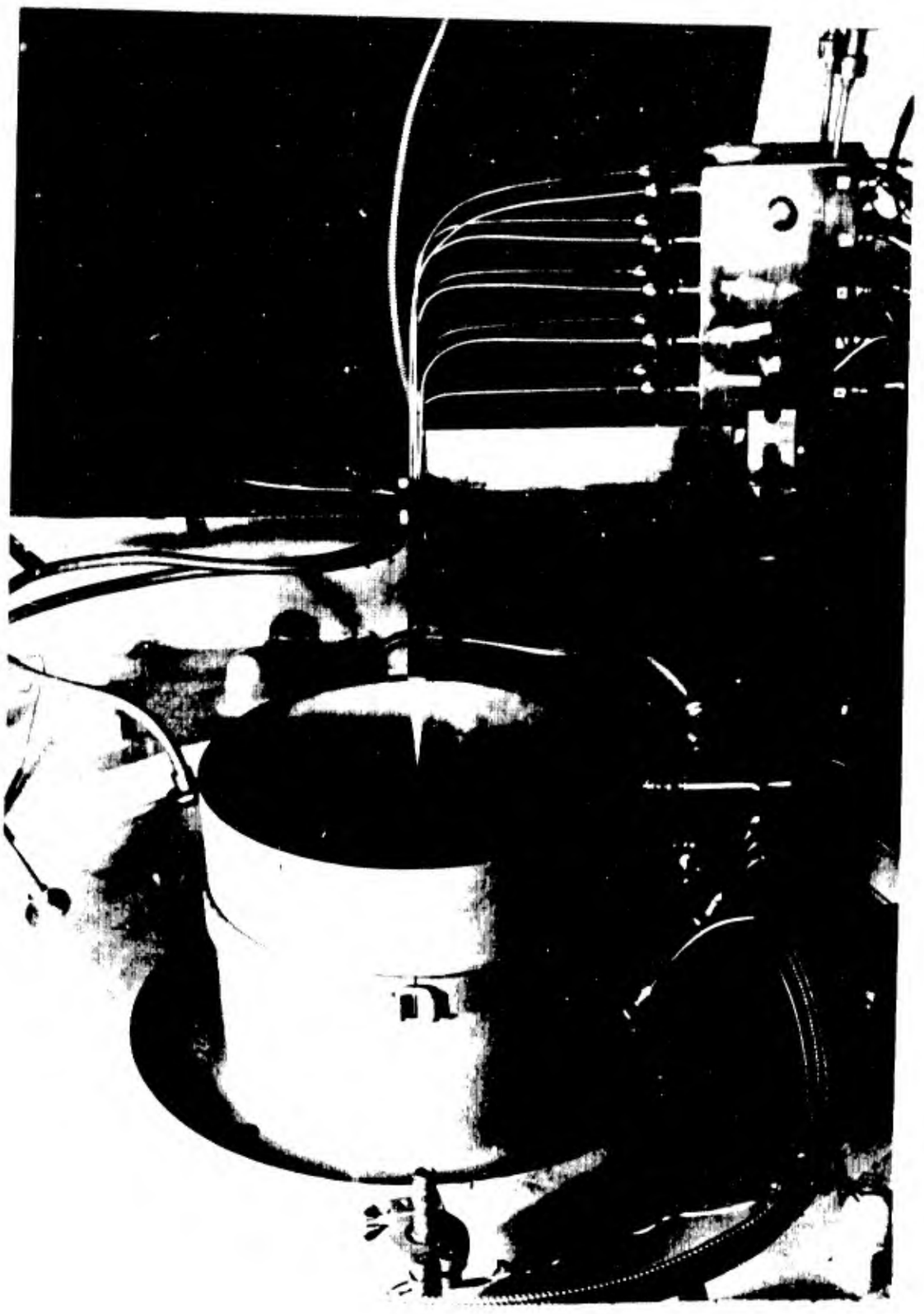

Fig. 3 Montage des jauges de pression en soufflerie (pour le dièdre).

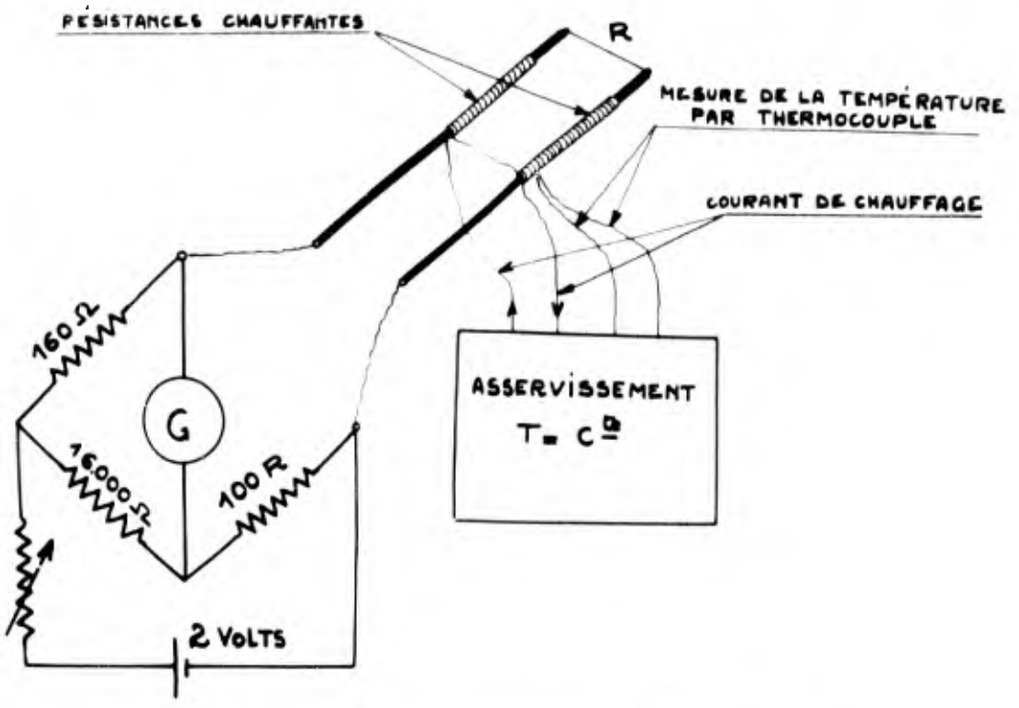

Fig. 4 Schéma électrique du fil chaud.

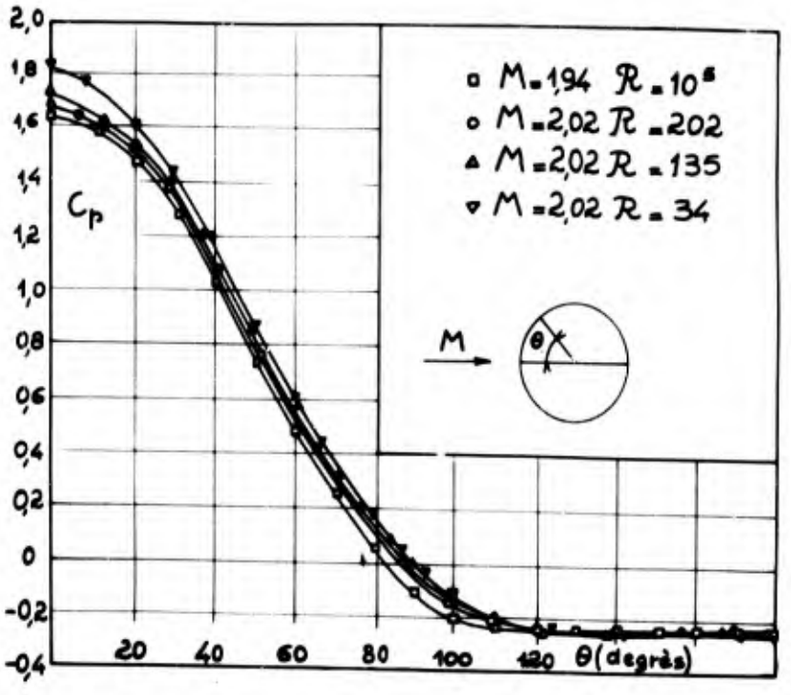

Fig. 5 Coefficient de pression en fonction de l'azimut sur un cylindre.

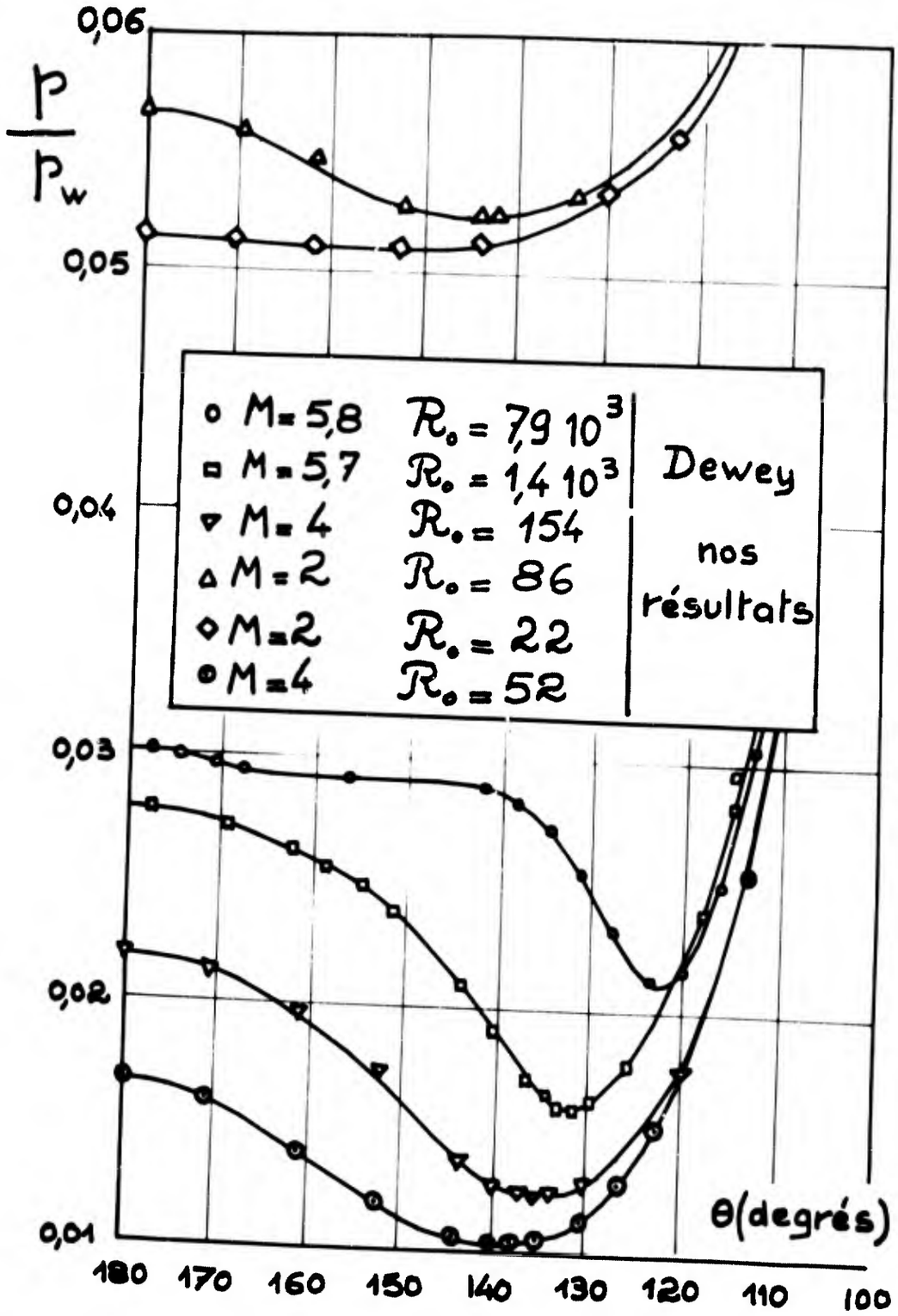

Fig. 6 Distribution de la pression sur la face arrière d'un cylindre.

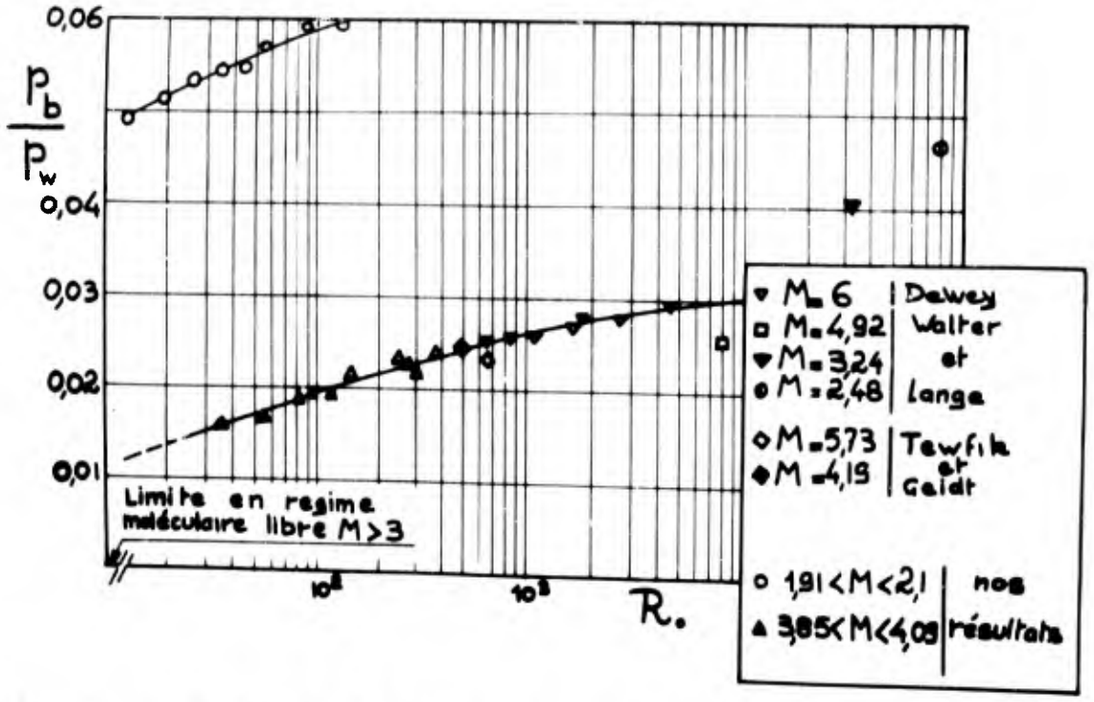

Fig. 7 Variation de la pression de culot sur un cylindre (à $\theta = 180°$) en fonction du nombre de Reynolds.

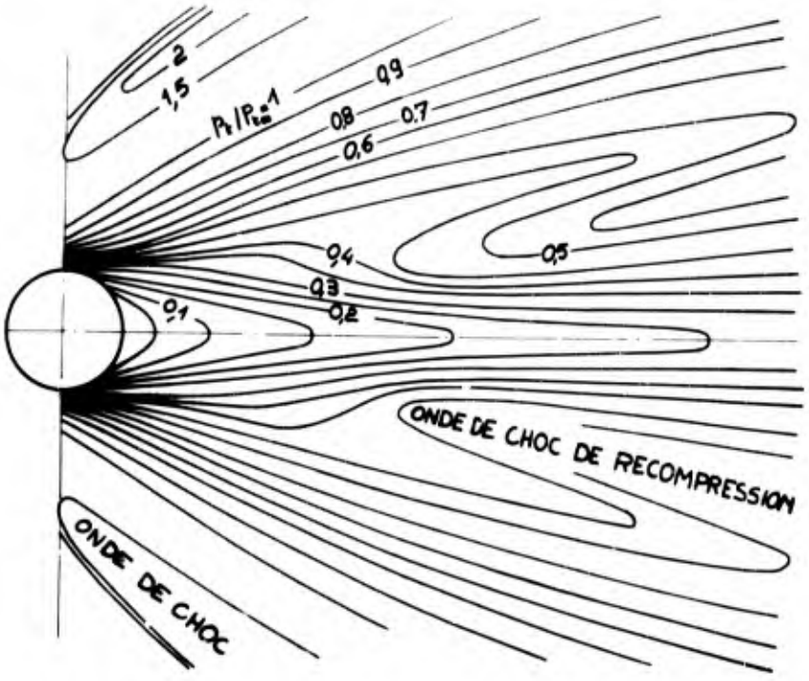

Fig. 8 Courbes d'égale pression Pitot dans le sillage d'un cylindre). ($M = 3,85$, $\mathcal{R} = 533$).

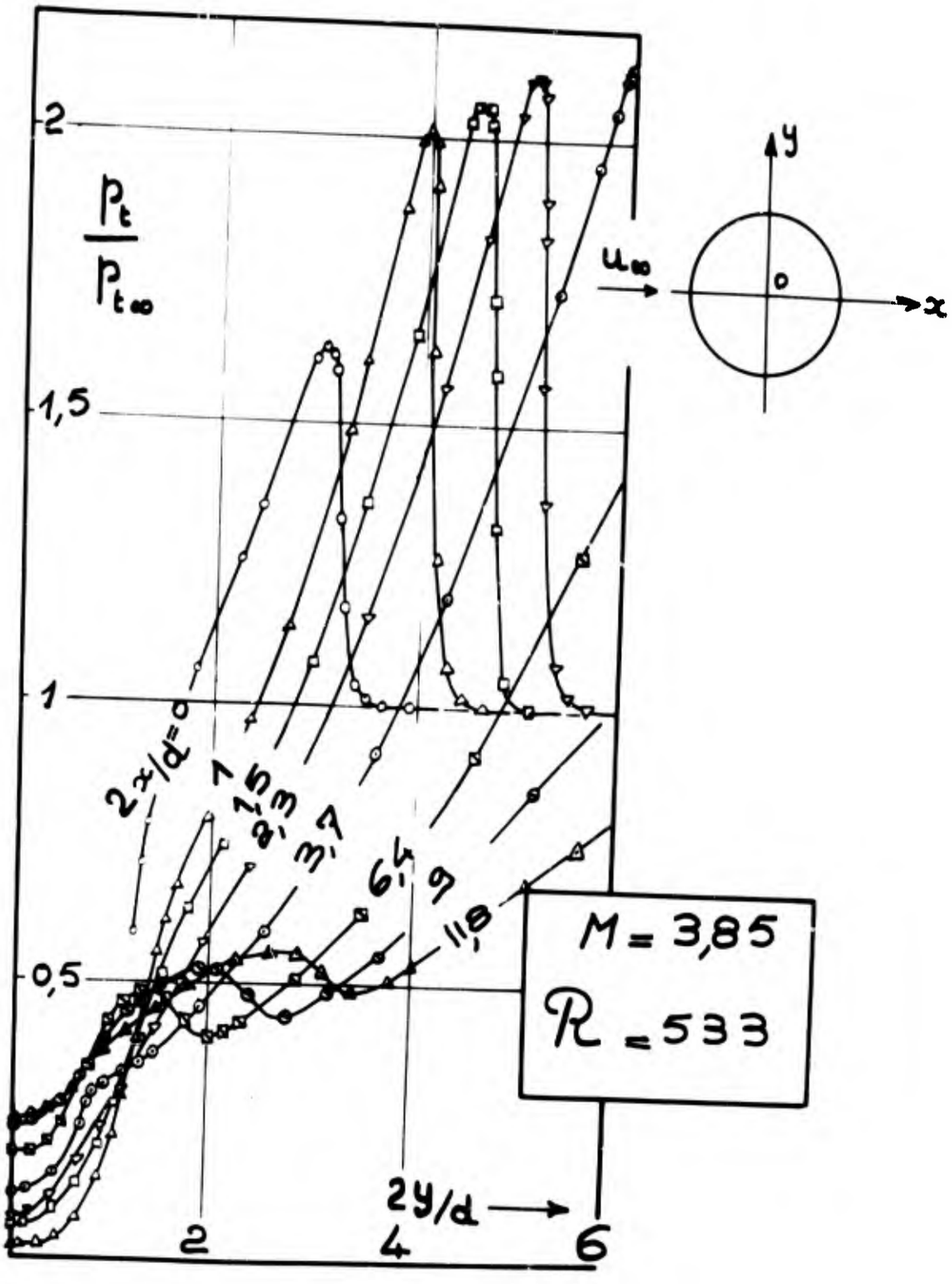

Fig. 9 Profils, en fonction de y, de la pression Pitot dans le sillage d'un cylindre.

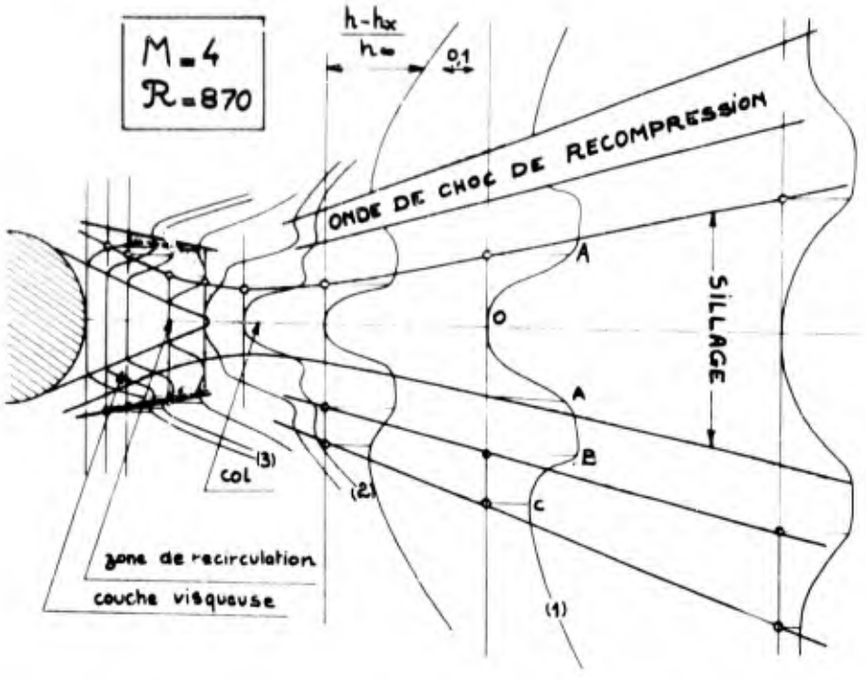

Fig. IO Exploration au fil chaud dans le sillage d'un cylindre (M = 4 , $\mathcal{R}$ = 870).

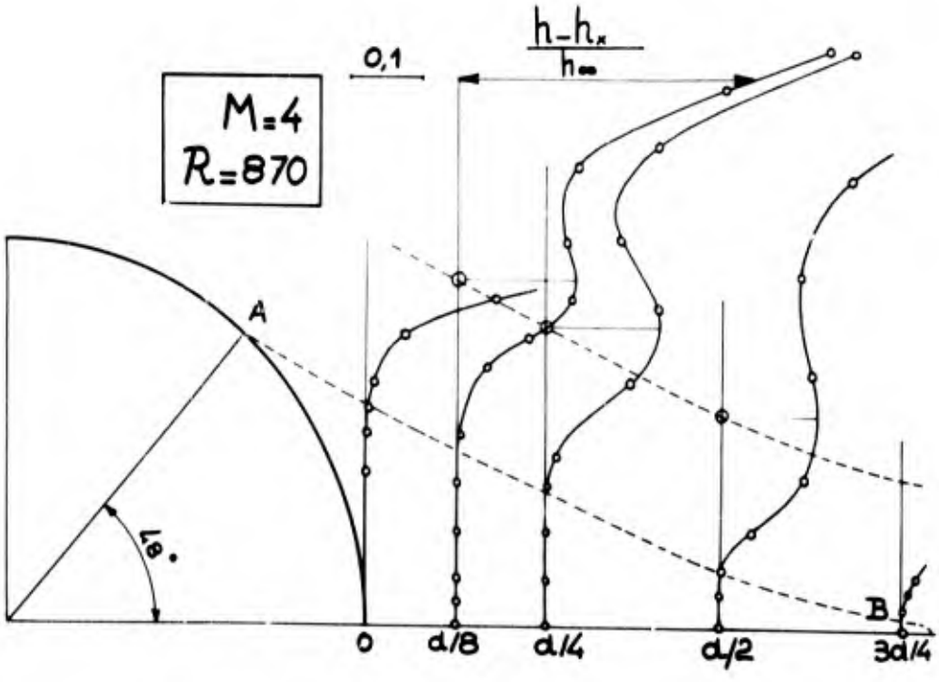

Fig. 11 Exploration au fil chaud dans l'écoulement de culot d'un cylindre (M = 4 , $\mathcal{R}$ = 870).

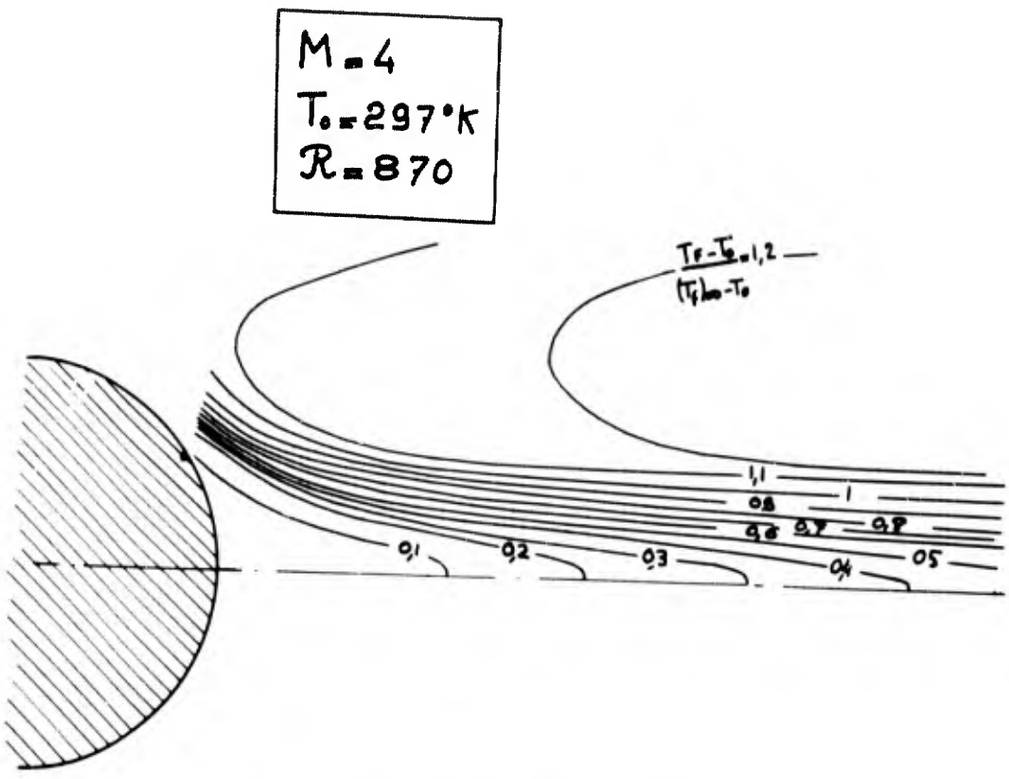

Fig. 12 Courbes d'égale température de frottement dans le sillage d'un cylindre (M = 4 , $\mathcal{R}$ = 870).

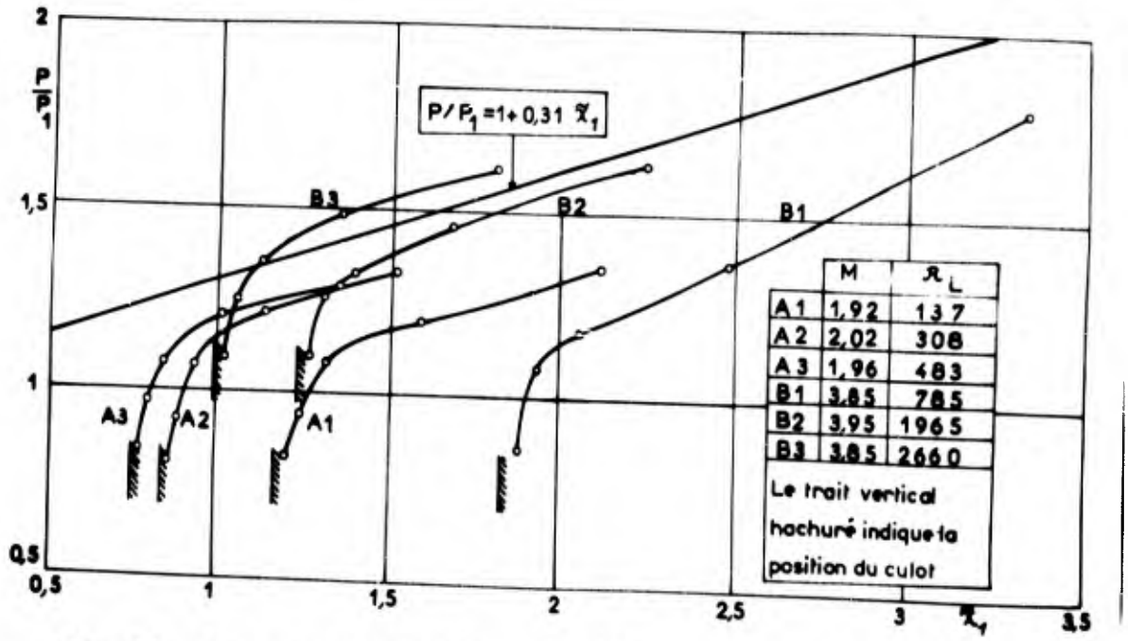

Fig. 13 Pressions de paroi sur le dièdre ; comparaison avec une théorie valable en régime continu.

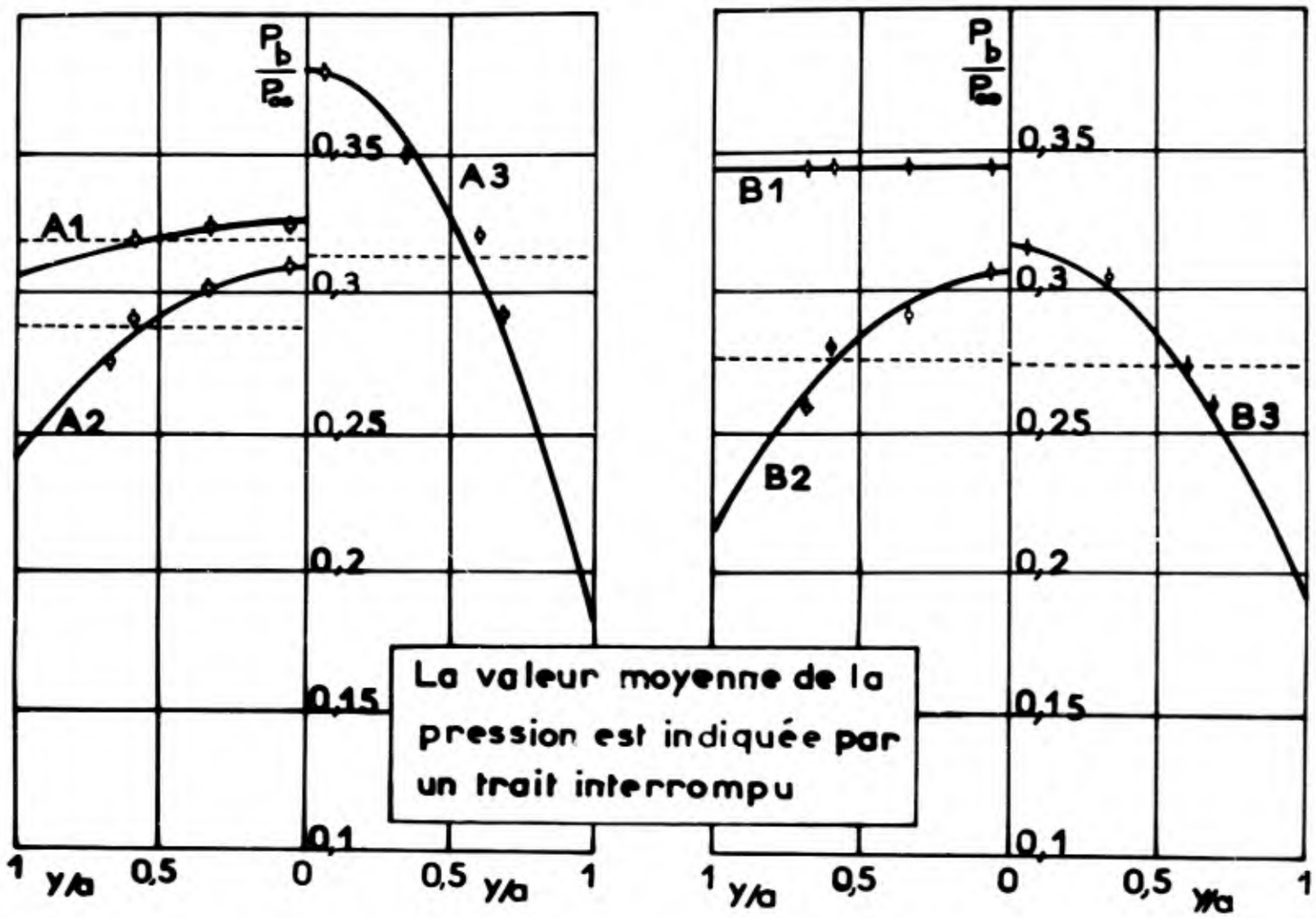

Fig. 14 Pression sur le culot du dièdre et comparaison avec une loi parabolique.

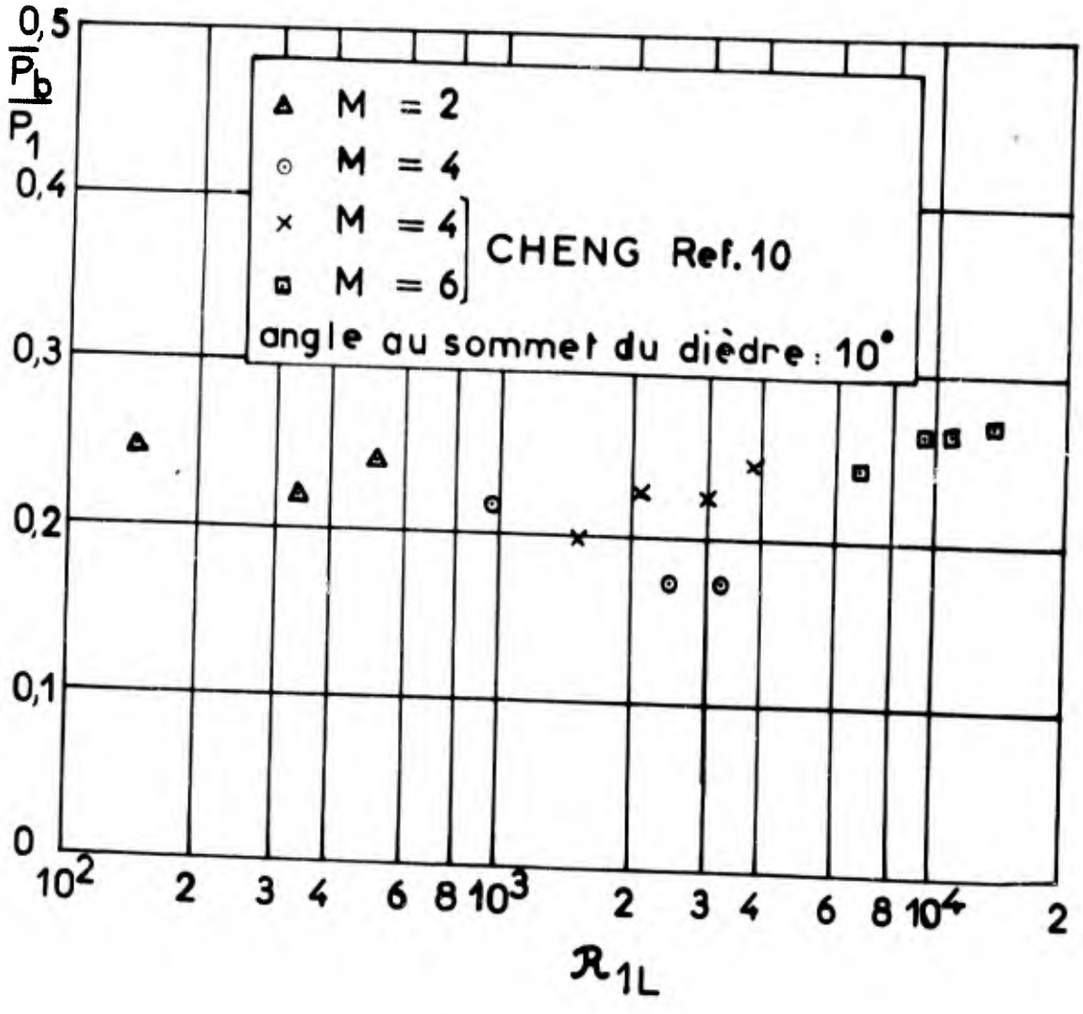

Fig. 15 Pression moyenne de culot, pour le dièdre, en fonction du nombre de Reynolds.

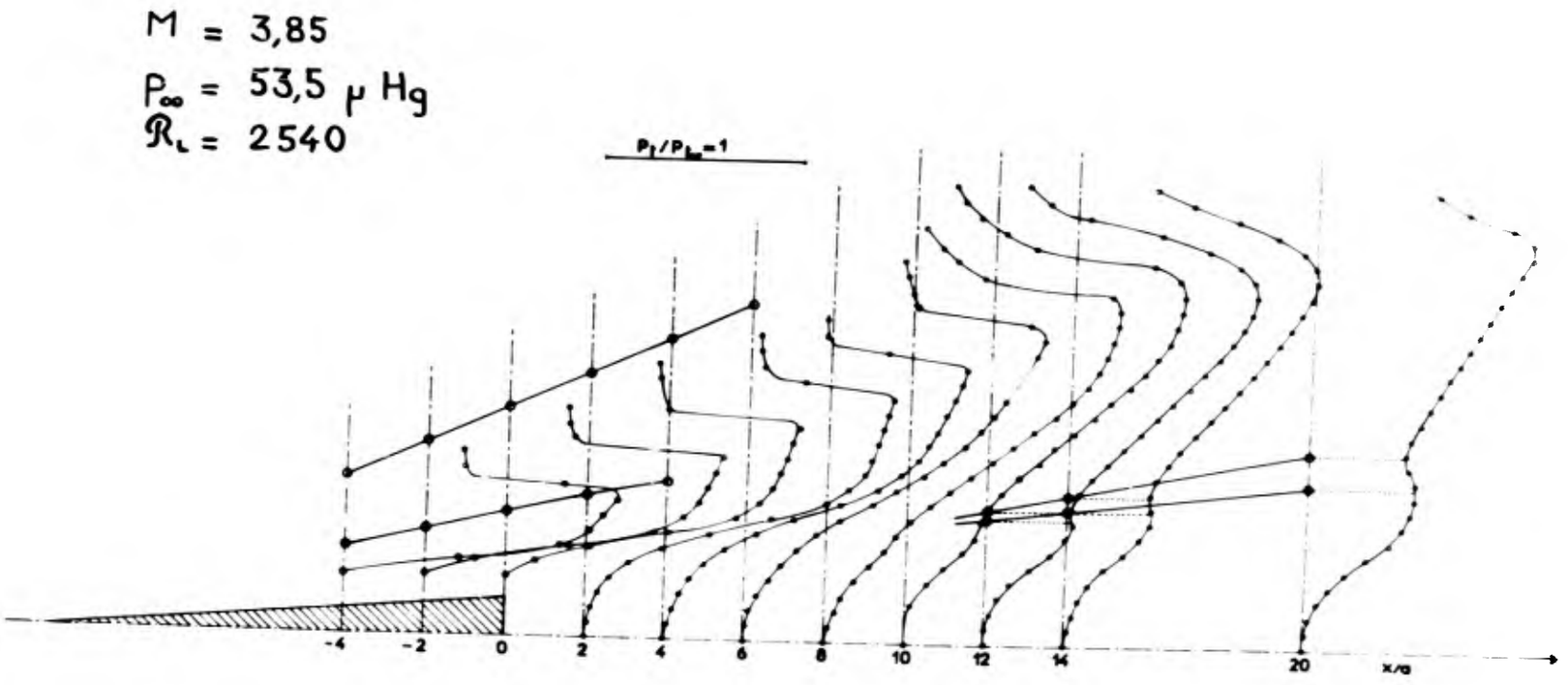

Fig. 16 Exploration du sillage du dièdre à l'aide d'un tube de Pitot ($M = 3,85$, $\mathcal{R}_L = 2540$).

Fig. 17 Visualisation de l'écoulement autour du dièdre à M = 4
P_∞ = 60 microns de mercure.

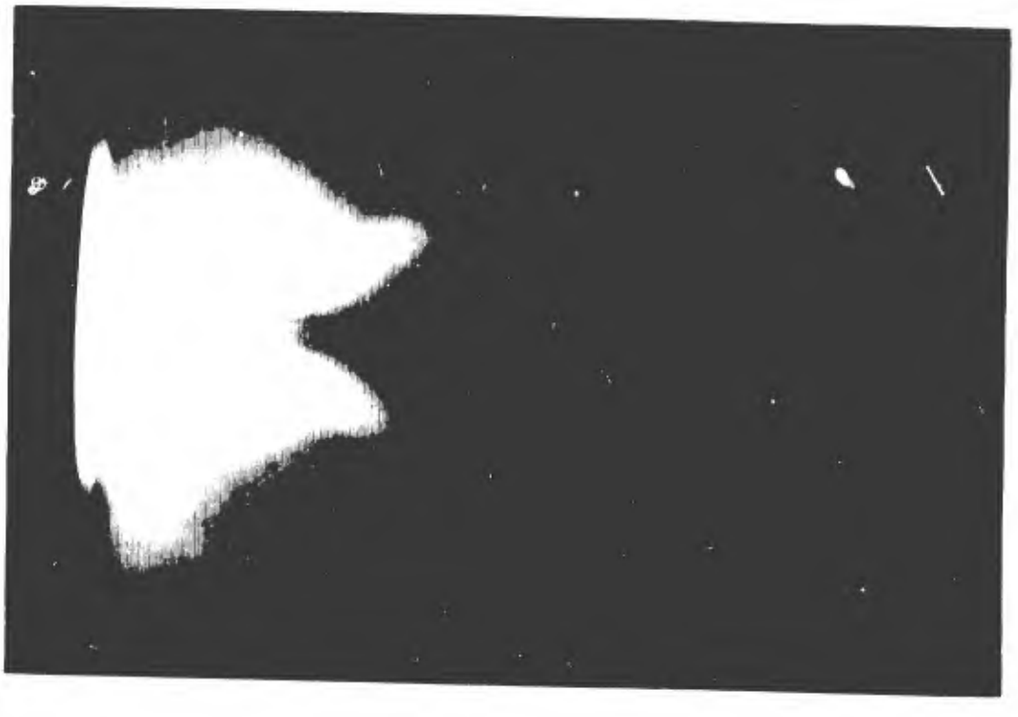

Fig. 18 Visualisation de l'écoulement autour du dièdre à M = 4
P_∞ = 15 microns de mercure.

BLANK PAGE

AN EXPERIMENTAL INVESTIGATION OF BASE MASS INJECTION ON THE LAMINAR WAKE BEHIND A 6-deg. HALF-ANGLE WEDGE AT M = 4.0*

by

Robert L. Chapkis, Jay Fox, Leslie Hromas
and Lester Lees

TRW Systems, Redondo Beach, California

* This work was carried out under the sponsership of the Advanced Research Projects Agency under Contract No. AF 04(694)-638.

SUMMARY

A series of tests were performed in the Jet Propulsion Laboratory (JPL) 20-inch supersonic wind tunnel in order to determine the effects of injecting nitrogen through the base of a wedge. These tests have shown that dramatic and significant changes to the wake structure are caused by a relatively small rate of injection.

The tests were performed at a Mach number of 4.0, a Reynolds number per inch of about 0.25×10^5 and stagnation temperature of about 100°F. Under these conditions the wake behind the model is laminar for at least eight inches (the maximum distance available). The model itself is a six-degree half angle wedge having a one-inch high porous base through which gaseous nitrogen can be injected. In addition, the model has cooling passages through which liquid nitrogen can be circulated, thus allowing tests to be run with either adiabatic or very cold-wall conditions.

The basic measurements made in the wake were pitot pressure, wake-centerline static pressure, and hot-wire anemometer measurements. In these tests the hot wire was used primarily as a device for obtaining mean flow quantities, not fluctuating quantities. The hot-wire-data, corrected for end loss effects, were used in conjunction with the pressure data to determine all of the flow quantities in the wake. To do so, however, one must use a rather complicated data reduction scheme, developed primarily by Dewey, Herzog, and Batt, at GALCIT, which makes use of "universal" hot-wire curves relating local Nusselt number, Reynolds number, recovery temperature, and total temperature, and which also takes into account the characteristics of the particular hot-wire used for the measurements.

The measurements described above were obtained for both adiabatic and cold-wall model conditions and for the cases of zero base injection and an injection mass flow rate equal to four per cent of the mass flow intercepted by the projected frontal area of the wedge.

RESUME

La soufflerie supersonique de 20 pouces du Jet Propulsion Laboratory (JPL) a été le siège d'une série d'essais ayant pour but de déterminer les effets d'injections d'azote à travers la base d'un corps en forme de coin. Ces essais ont montré que des injections relativement faibles amènent des modifications importantes dans la structure du sillage.

Les essais furent effectués à Mach 4, à un nombre de Reynolds, par pouce, d'environ de 0.25×10^5, et à une température d'arrêt de 100°F approximativement. Dans de telles conditions, le sillage produit à l'arrière de la maquette est laminaire pendant au moins huit pouces (distance maximale disponible). La maquette elle-même a la forme d'un coin au demi-angle de 6 degrès, doté d'une base poreuse de un pouce de haut à travers laquelle on peut injecter de l'azote gazeux. En outre, la maquette présente des passages de refroidissement par lesquels on peut faire circuler de l'azote liquide, ce qui permet de procéder à des essais soit dans des conditions adiabatiques, soit avec des parois froides.

Les mesures fondamentales effectuées dans le sillage furent celles de la pression dynamique, de la pression statique suivant une ligne passant par le centre du sillage, ainsi que des mesures réalisées à l'aide d'un anémomètre à fil chaud. Au cours de ces expériences, on utilisa essentiellement le fil chaud pour obtenir des valeurs quantitatives moyennes de l'écoulement; et non des valeurs quantitatives fluctuantes. Les données fournies par le fil chaud, et corrigées pour tenir compte des effets de déperdition, furent utilisées conjointement avec les données sur la pression pour déterminer toutes les valeurs d'écoulement du sillage. On doit toutefois avoir recours, pour ce faire, à un procédé assez compliqué d'exploitation de résultats, mis au point originairement par Dewey, Herzog et Batt, au GALCIT. Ce procédé utilise des courbes "universelles" de mesures obtenues par fil chaud et reliant le nombre de Nusselt local, le nombre de Reynolds, la température de récupération et la température totale; il tient compte des caractéristiques du fil chaud particulier utilisé pour les mesures.

Les mesures décrites ci-dessus ont été obtenues à la fois pour des conditions adiabatiques et des maquettes à parois froides, et pour le cas d'une injection nulle à la base, et le cas d'un taux de débit-masse d'injection égal à 4% du débit-masse intercepté par la surface frontal en saillie du corps en forme de coin.

BLANK PAGE

AN EXPERIMENTAL INVESTIGATION OF BASE MASS INJECTION ON THE LAMINAR WAKE BEHIND A 6-deg. HALF-ANGLE WEDGE AT M = 4.0*

Robert L. Chapkis, Jay Fox, Leslie Hromas
and Lester Lees

TRW Systems, Redondo Beach, California

Tests were conducted in the Jet Propulsion Laboratory (JPL) 20-inch supersonic wind tunnel to determine the effects of base mass injection on the laminar wake behind a six-degree half-angle wedge with a one-inch high porous base. The tests were conducted at Mach 4.0 and a Reynolds per inch of 2.5×10^4. It was found that striking changes in the wake properties were caused by an injectant mass flow rate equal to 2.8 percent of the mass flow intercepted by the projected frontal area of the wedge. At this rate of injection the rear stagnation point is completely blown off and the center portion of the wake consists of a uniform stream of injected gas. The wake shock wave is shifted laterally away from the centerline of the wake and is greatly weakened. These effects occurred for both the adiabatic wall condition and the cooled wall condition. Furthermore, the effects of the injectant persist at least as far back as eight base heights aft of the base.

1. INTRODUCTION

A considerable amount of emphasis has been given recently to the analysis of supersonic and hypersonic wake flows. One aspect of the overall problem is that of ejecting fluid from the body in order to

*This work was carried out under the sponsership of the Advanced Research Projects Agency under Contract No. AF 04(694)-638.

modify the wake flow. This can be done either by ejection from the forward surface or from the base of the body. The present report describes an experimental study conducted in the supersonic wind tunnel at JPL to investigate the effect of ejection from the base of a two-dimensional wedge. The wake region considered extends from the base of the body to 8.0 base-heights back.

Analytical techniques to describe some aspects of the base flow region are being developed by a number of investigators. For example, the analyses of Reeves and Lees (1), Golik, Webb and Lees (2), and Baum and Denison (3) consider the neck and near wake as an effective "throat" with a Crocco-Lees (4) type of critical point behavior. Primarily, only adiabatic conditions have been considered to the present time. Reeves (5) and Weiss (6) have recently analyzed the reverse flow region, i.e., the region between the body and the rear stagnation point. Of these analyses only Reeves (5) considers base injection, but such a modification should be feasible in the others.

Parallel to the analytical efforts of recent years, a number of experimental programs have been undertaken to map in detail the base flow region (with no injection) behind blunt and slender bodies. Kingsland (7) and Dewey (8) have taken detailed measurements behind a cylinder. References 9-15 describe other recent measurements taken behind slender cones, again without any fluid injection.

The amount of mass entrained in the base region is relatively small, and thus this region is quite sensitive to changes in flow conditions. In particular, if a small amount of fluid is ejected from the body into the base region, a strong effect could be expected to occur. Furthermore, for any amount of mass ejected, the same amount must escape the base region and pass on downstream. Thus mass ejected from the base of the body will cause the reverse flow region to move away from the body and form a bubble behind the body. As this ejected mass flow rate is increased, the velocity along the dividing streamline decreases until finally the recirculation region, or bubble, is completely eliminated.

Herzog (16) has made measurements with nitrogen injection into the base region of a cylinder transverse to the flow at Mach 6.0. It was found for those conditions that an injectant rate of 1.5 percent of the mass flow intercepted by the projected frontal area of the cylinder completely eliminated the reverse flow region, i.e., no rear stagnation point existed. Similar effects were obtained more recently by Demetriades and Bauer (17), who made measurements of the effects of air injection into the base region of a 12-degree half-angle cone at Mach 3.0. Other recent tests were performed by Hill and Luce (18) who examined the effect of changing the injected gas momentum for cones and found distinctly different cooling behavior depending on this parameter.

The present experiment conducted in the JPL supersonic wind tunnel is a logical extension of the work of Herzog (16). In the present case, a wedge was used with the wind tunnel providing the capability of obtaining both laminar and turbulent base flow conditions. However, only laminar flow results are reported here. The one-inch base-height model also allows for cooling of the model surface.

Certainly, a very critical question to be considered in all wake measurements made in wind tunnels is that of effects of the support system. Even very fine wire supports have been shown to affect measurements behind axisymmetric models (19, 20). In the present measurements the two-dimensionality of the flow must be considered. While the existence of fences or side plates large enough to contain the subsonic portion of the wake will prevent outflow and effectively isolate any interaction with the wind tunnel boundary layers, the possibility of a disturbance created by the plates themselves is a troublesome point. There have, however, been a substantial number of investigations into this effect, notably the experiments of Dewey (8), Herzog (16) (with injection) and more recently Lewis (21) and Batt (9). These appear to confirm that for aspect ratios greater than about 10, the disturbance created by the side plates is minimal. The TRW model has an aspect ratio of approximately 16 which is assumed to be sufficient to assure the approximation of two-dimensionality.

2. EXPERIMENT

2.1 Test Conditions and Equipment

The tests were conducted in the JPL 20-inch supersonic continuous-flow wind tunnel. The wind tunnel has an 18 by 20-inch test section and a flexible-plate nozzle which allows the Mach number to be set at any value from 1.33 to 5.02. The present tests were all conducted at Mach 4.0 and a Reynolds number per inch of 2.5×10^4. The stagnation pressure was set at 18 cm/Hg and the stagnation temperature at about 100°F.

The model itself which is shown in Figure 1 is a six-degree half-angle wedge with a one-inch-high porous base through which gaseous nitrogen can be injected. The external dimensions of the model were chosen to be those of the wedge tested extensively by Hama (10) in the same JPL wind tunnel. This was done in order to be able to make direct use of some of his carefully obtained wake pictures and pressure data. In particular, his shadowgraphs taken at the same Reynolds number, but lower Mach number, as for the present tests indicate that the wake is laminar for at least eight inches aft of the base (the maximum distance available from the probe traversing mechanism). The model is made of stainless steel, and the porous base consists of three layers of fine-mesh (2-micron) stainless-steel screen covered by a single protective layer of relatively coarse screen. In addition to the porous base, the model has cooling passages through which liquid nitrogen can be circulated, thus allowing tests to be run with either adiabatic or very cold-wall conditions. In order to prevent boiling of the liquid nitrogen inside the model the liquid nitrogen is subcooled just prior to its entry into the model. This is done by passing the coolant through coils of copper tubing which are immersed in an insulated tank full of liquid nitrogen. The tank is vented to the atmosphere, and evaporation of the bath of liquid nitrogen causes its temperature to drop below the temperature of the liquid nitrogen passing through the copper tubing, thus sub-cooling the model coolant.

The liquid nitrogen coolant is circulated through the model through three separate cooling passages each having its own inlet and outlet tube, whereas the gaseous nitrogen injectant is brought into the base plenum chamber of the model through tubes in each end of the model. In addition, for the cold-wall tests, a thermostatically controlled Chromalox Circulation Heater was used to heat the gaseous nitrogen injectant to 165°F prior to its entry into the model. This was done in order to prevent possible liquefaction of the gaseous injectant inside the model. The injectant mass-flow rate was measured by means of a Fisher-Porter flow meter Model 10A 2735 CA. The flow meter was calibrated at the mass flow rate used by measuring the time necessary to displace 20 liters of water from a container. The pressure and temperature of the nitrogen introduced into the container were measured, and the mass of nitrogen computed from the perfect gas law. It is estimated that the mass flow rate could thus be determined within $\pm$ 5 percent of the desired value.

The model was installed so that it spanned the width of the wind tunnel. In order to minimize the effect of the wind tunnel boundary layer on the two-dimensionality of the flow about the wedge, thin fences were attached to the base. One of these is shown in Figure 1. Three pressure ports were also located on the model: One on the top surface halfway from the leading edge to the base; a second one directly opposite on the bottom surface; and a third port at the center of the base. The base-pressure port was designed so that rearward facing probes could be attached in order to make static pressure measurements in the region very close to the base. Two of these probes are shown in Figure 1. However, none of the rearward facing probes were used in the present tests. The remaining wedge instrumentation consists of eight thermocouples, four of which are located on the top surface of the wedge and four on the bottom.

2.2 Measurements

The basic measurements made in the wake were pitot pressure, wake-centerline static pressure, and hot-wire anemometer measurements. The

static-pressure probe was a copy of one developed at the Graduate Aeronautical Laboratory, California Institute of Technology (GALCIT) by Hehrens (22). The hot-wire anemometer was used to measure mean flow quantities, not fluctuations. The wire itself was a 0.0001 inch in diameter platinum-rhodium wire about two hundred diameters long. The wire was mounted between the tips of sewing machine needles that pointed upstream from a slender support strut. On one needle, a small thermocouple was mounted near the tip to facilitate end-loss corrections. Similar probe configurations are described in References (18) and (19).

Wire resistance and power were measured with four currents of one to four milliamperes and the results were extrapolated to zero power. Oven calibrations of the wire temperature-resistance characteristics were combined with measurements of needle temperature, pitot pressure and static pressure to comprise information needed for correcting the measurements for end-loss conduction. A consistent flow field was calculated, using universal recovery factor relations, to obtain the local stagnation temperature. Universal heat transfer relations were also used together with a correction factor deduced from the measurements. For a detailed description of the data reduction method, see Reference (9).

In addition to the wake measurements, other auxiliary measurements were made such as wedge surface pressure and temperature, base pressure and injectant mass flow rate. For the present tests the injectant mass flow rate was set at either zero or 2.8 percent of the mass flow intercepted by the projected frontal area of the wedge.

2.3 Effects of Frost

Frost build-up on the liquid nitrogen cooled model was a serious problem. Although the layer of frost appeared to be rather thin, it covered the pressure ports on the wedge, thus preventing measurement of the wedge surface pressures and base pressure during the cooled-wall tests. Even more troublesome was the fact that, apparently, tiny particles of frost were swept into the wake and would hit the hot-wire anemometer, thus breaking the fragile wire. This behavior made it impossible to make hot-wire measurements for the cooled-wall condition.

In addition, the frost pattern was not perfectly symmetric and thus some asymmetries in the pressure measurements were noted for the cooled-wall condition. However, these asymmetries appear to be rather small, except perhaps in the region between the bow shock wave and the first corner expansion wave.

3. RESULTS AND DISCUSSIONS

3.1 Wedge Surface Pressures

The wedge surface pressures as measured by the two pressure ports on the top and bottom surfaces of the model were used primarily as a check on the angle of attack of the wedge. These pressures were measured at least once during each pitot and static pressure traverse of the wake. The measured ratios of surface pressure to freestream static pressure for the top surface of the wedge had a range of from 2.00 to 2.08. For the bottom surface the range was from 1.95 to 2.06; however, the maximum difference between top and bottom values measured at the same time was 0.05, and usually was 0.02 to 0.03. A difference in the pressure ratios of 0.05 corresponds to a wedge angle of attack of about a quarter of a degree.

It is interesting to compare the measured wedge pressures with theoretical predictions: Inviscid theory predicts a ratio of wedge surface pressure to freestream static pressure of 1.79, which is a little more than ten percent lower than our average value of about 2.0. Viscous effects can be taken into account be considering the displacement effect of the boundary layer as in hypersonic weak interaction theory (23). The value of the hypersonic interaction parameter $\chi = M_\infty^3/\sqrt{Re_\infty}$ for the present tests is about 0.18, where the Reynolds number is based on the distance from the wedge leading edge to the pressure port. For this value of χ weak interaction theory predicts an increase in pressure ratio of about five percent over the inviscid value of 1.79. However, the experiments of Kendall (24) indicate an increase of about ten percent which is closer to our measured values.

3.2 Wake Pressures

Typical pitot pressure plots are shown in Figures 2 to 7. These figures show a comparison of the pitot pressures measured with and

without base injection at various stations downstream of the base and for both adiabatic and cooled wall conditions. It is immediately apparent from the pitot pressure plots that base injection significantly alters the wake structure: The wake shock wave is shifted laterally away from the wake centerline and greatly weakened, and the viscous wake "bucket" is widened. Furthermore, it appears that the effects of the injectant persist quite far downstream of the base.

The location of various regions of the wake can be deduced from the pitot pressure plots as indicated in Figures 2 and 3. By combining the results of all of the pitot pressure plots, a satisfactory picture of the main features of the wake can be obtained. This has been done and is shown in Figures 8 to 13. Figures 10 and 13 show clearly the widening of the viscous wake and the outward shift of the wake shock wave caused by base injection. Also, a comparison of Figures 8 and 11 shows that the viscous wake is narrowed by cooling the wedge surface.

Base injection also changes the static pressure distribution markedly. This is shown in Figures 14 and 15 which compares the centerline static pressure distributions with and without injection for both adiabatic and cooled wall conditions. It can be seen that base injection creates a remarkably uniform centerline static pressure distribution. Furthermore, the centerline pitot pressures too are changed markedly by base injection, as shown in Figures 16 and 17. It can be seen from Figure 17 that base injection creates extremely uniform centerline pitot pressure and static pressure distributions for the cooled wall condition. Similar results were obtained for the adiabatic wall condition. It thus appears that for the amount of base injectant employed, the rear stagnation point has been completely "blown off" and the center portion of the wake consists of a very uniform stream of constant velocity injectant.

The picture with injection is thus one of the mixing of two nearly parallel streams of almost constant pressure. One stream is composed of the injectant and the other of the fluid in the region between the corner expansion fan and the edge of the mixing region (see Figure 18). Actually, the edge of the mixing region is not exactly parallel to the

centerline of the wake; the streamlines in that region are inclined downward toward the axis. Thus a slight compression is required in the downstream direction corresponding to the turning of the flow back to parallel.

3.3 Temperature

Total temperature distributions as determined from the hot-wire-anemometer measurements are shown in Figures 19 and 20. The open symbols represent total temperature measurements that incorporate uncertain corrections for end conduction between the wire and the supports. The corrections were calculated using static pressure measurements together with the other necessary inputs; but no verification was obtained when the reduction was repeated using the universal heat transfer relations. Flow variations along the wire in the locally transonic and subsonic conditions may have caused the uncertainty in the data reduction. Under these conditions, the needles that support the wire also alter the flow over much of the length of the wire. For the closed symbols, the data reduction was certain, the heat transfer verification having been obtained where appropriate. The total temperature variation across the wake at various locations aft of the base is shown in Figure 19 for the case of no base injection. The corresponding distributions with injection are shown in Figure 20 for two locations aft of the base along with a no injection plot for comparison. Again, the widening of the viscous bucket caused by base injection is clear.

As stated previously, no wake temperature measurements were made for the cooled-wall wedge due to continual breakage of the hot wire by particles of frost. However, the wedge surface temperatures were measured by means of the thermocouples on the model and the ratio of model temperature to free-stream total temperature was found to be equal to 0.27, compared to 0.92 for the adiabatic model.

4. CONCLUSIONS

The experiments conducted in the JPL 20-inch supersonic wind tunnel at $M = 4.0$ and a Reynolds number per inch of 2.5×10^4 showed that

base mass injection had a significant effect on the properties of the wake behind the 6° half-angle wedge tested. At the mass flow rate used, which was 2.8 percent of the mass flow rate intercepted by the projected frontal area of the wedge, the rear stagnation point was completely eliminated and the center portion of the wake consisted of a uniform stream of injected gas separated from another uniform region between the wake shock wave and the injectant by a mixing layer. The wake shock wave was greatly weakened and was shifted laterally away from the wake centerline. These effects were still strong eight base-heights aft of the base, and occured for both the adiabatic wall condition and the cooled wall condition.

REFERENCES

1. Reeves, B.L. and Webb, L., "Theory of the Laminar Near Wake of Blunt Bodies in Hypersonic Flow", AIAA Second Aerospace Sciences Meeting, New York (1965), Paper No. 65-52.

2. Golik, R.J., Webb, W.H., and Lees, L., "Further Results of Viscous Interaction Theory for the Laminar Supersonic Wake", AIAA Fifth Aerospace Sciences Meeting, New York (1967), Paper No. 76-61.

3. Baum, E. and Denison, M.R., "Interacting Supersonic Laminar Wake Calculations by a Finite Difference Method", AIAA Fourth Aerospace Sciences Meeting, Los Angeles (1966), Paper No. 66-454.

4. Crocco, L. and Lees, L., "A Mixing Theory for the Interaction Between Dissipative Flows and Nearly Isentropic Streams", J. Aero. Sci. 19, (1952), 649-676.

5. Reeves, B.L. and Buss, H., "On the Flow in Regions of Laminar Separation", AIAA Fifth Aerospace Sciences Meeting, New York (1967), Paper No. 67-64.

6. Weiss, R.F., "A New Theoretical Solution of the Laminar, Hypersonic Near Wake", AIAA Fifth Aerospace Sciences Meeting, New York (1967), Paper No. 67-63.

7. Kingsland, L., Jr., "Experimental Study of Helium and Argon Diffusion in the Wake of a Circular Cylinder at M = 5.8", GALCIT Hypersonic Research Project Memo. No. 60 (1961).

8. Dewey, C.F., Jr., "Near Wake of a Blunt Body at Hypersonic Speeds", AIAA J. 3, (1965), 1001-1010.

9. Batt, R., "Experimental Investigation of Hypersonic Wakes Behind 20° Wedges at M = 6", Ph.D. Thesis, California Institute of Technology, Pasadena (1967).

10. Hama, F.R., "Experimental Studies on the Lip Shock", AIAA Fifth Aerospace Sciences Meeting, New York (1967), Paper No. 67-29.

11. Browand, F.K., Finston, M., and McLaughlin, D.K., "Some Preliminary Measurements Behind Cones Magnetically Suspended in a Mach Number 4.3 Stream", MIT Technical Report 132, AFOSR 66-2510 (1966).

12. Zakkay, V. and Cresci, R.J., "An Experimental Investigation of the Near Wake of a Slender Cone at M = 8 and 12", AIAA J. 4, (1966), 41-46.

13. Martellucci, A., Trucco, H. and Agnone, A., "Measurements of the Turbulent Near Wake of a Cone at Mach 6", AIAA J. 4, (1966), 385-391.

14. Todisco, A. and Pallone, A., "Measurements in Laminar and Turbulent Near Wakes", AIAA Fifth Aerospace Sciences Meeting, New York (1967), Paper No. 67-30.

15. Munty, E.P. and Softley, E.J., "A Study of Laminar Near Wakes", AIAA J. 4, (1966), 961-968.

16. Herzog, R., "Nitrogen Injection into the Base Region of a Hypersonic Wake", GALCIT Hypersonic Research Memo. No. 71, (1964).

17. Demetriades, A. and Bauer, A.B., "Supersonic Wind-Tunnel Experiments with Axisymmetric Wakes", AIAA Fourth Aerospace Sciences Meeting, Los Angeles (1966), Paper No. 66-453.

18. Hill, J.A.F. and Luce, R.W., "Wind Tunnel Measurements of Turbulent Wake Cooling with Base Injection", Mithris, Inc., Cambridge, Mass., Rept. No. MC 64-85-R3 (1966).

19. Dayman, B., Jr., "Support Interference Effects on the Supersonic Wake", AIAA J. 1, (1963), 1921-1923.

20. Gamage, R. and Chapkis, R.L., "An Experimental Investigation of the Turbulent Wake Behind Sharp and Blunted Wire-Supported Cones at M = 4", TRW IOC 67-3321.1-6 (1967).

21. Lewis, J.E., "Experimental Investigation of Supersonic Laminar, Two-Dimensional Boundary Layer Separation in a Compression Corner With and Without Cooling", Ph.D. Thesis, California Institute of Technology, Pasadena (1966).

22. Behrens, W., "Viscous Interaction Effects on a Static Pressure Probe at M = 6", AIAA J. 1, (1963), 2864.

23. Hayes, W.D. and Probstein, R.F., Hypersonic Flow Theory, First Edition Academic Press, New York (1959), 349-350.

24. Kendall, J.M., Jr., "An Experimental Investigation of Leading-Edge Shock-Wave-Boundary-Layer Interaction at Mach 5.8", J. Aero. Sci. 24, (1957), 47-56.

ACKNOWLEDGEMENTS

The authors have greatly benefited from discussions with Richard Batt of GALCIT, Francis Hama and James Kendall, Jr. of JPL, and Raymond Golik and John Lewis of TRW Systems. The authors also would like to thank the staff of the JPL Wind Tunnel and in particular the test engineers Billy Walker and W. Russell Kerr for their expert operation of the wind tunnel and facilities during the testing.

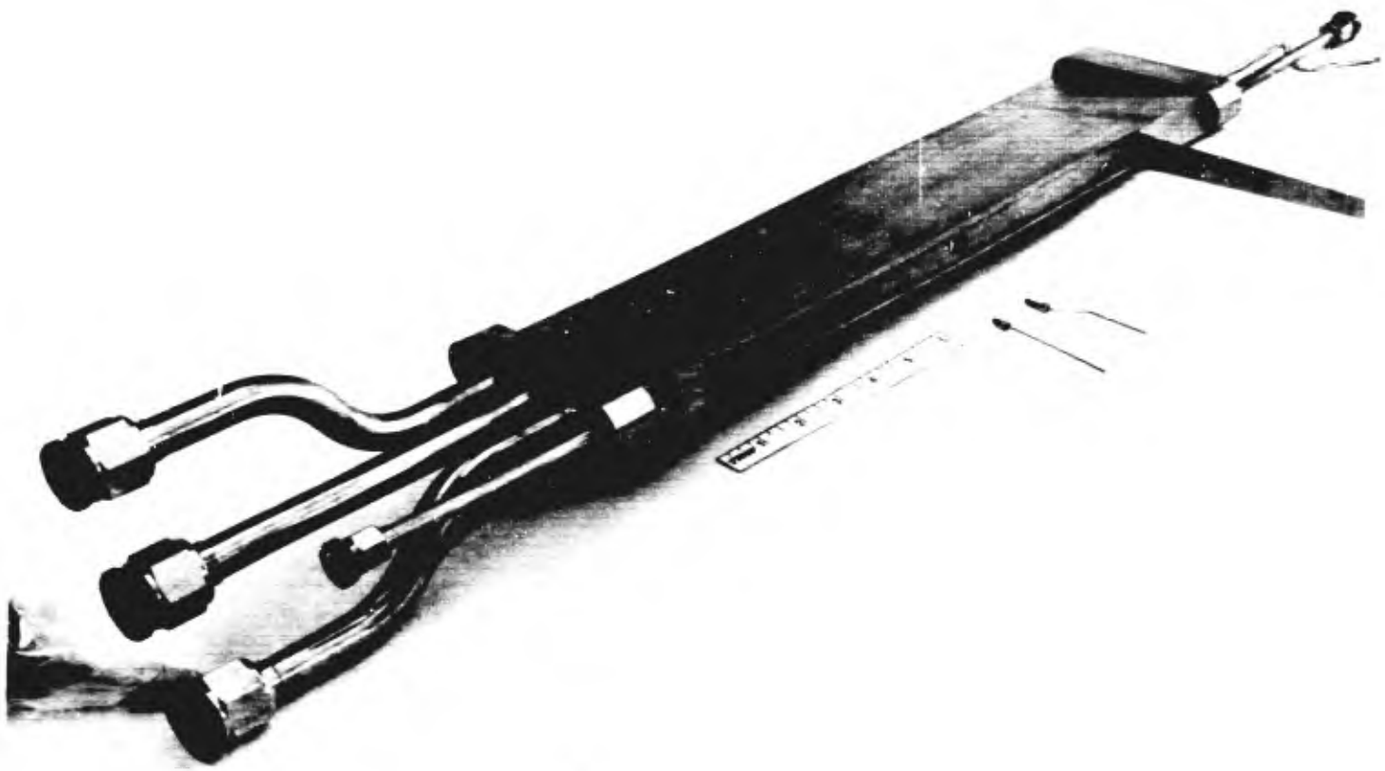

Fig. 1. Wind tunnel model

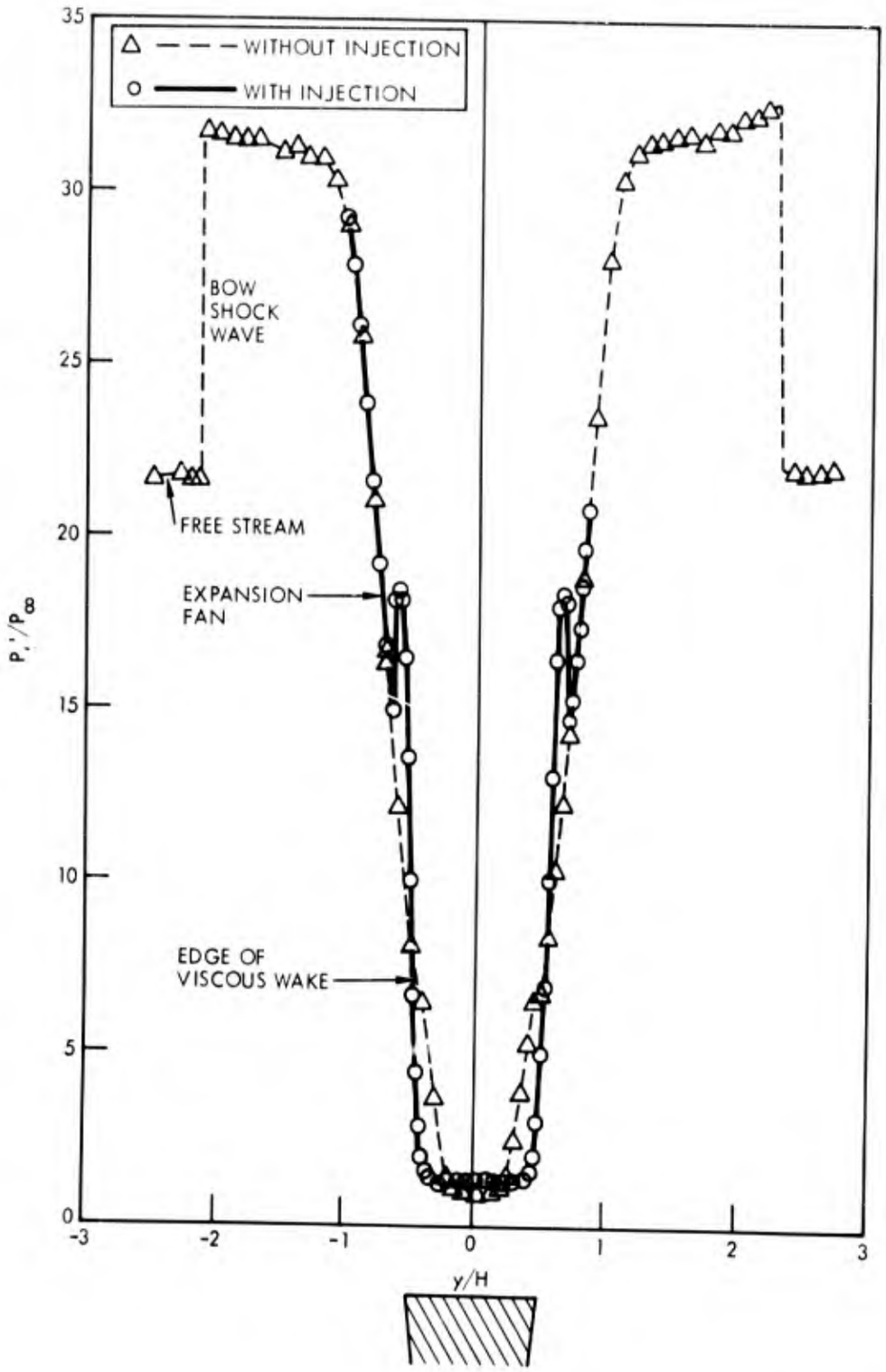

Fig. 2. Comparison of pitot pressures with and without injection for the adiabatic-wall wedge at $x/H = 1.0$

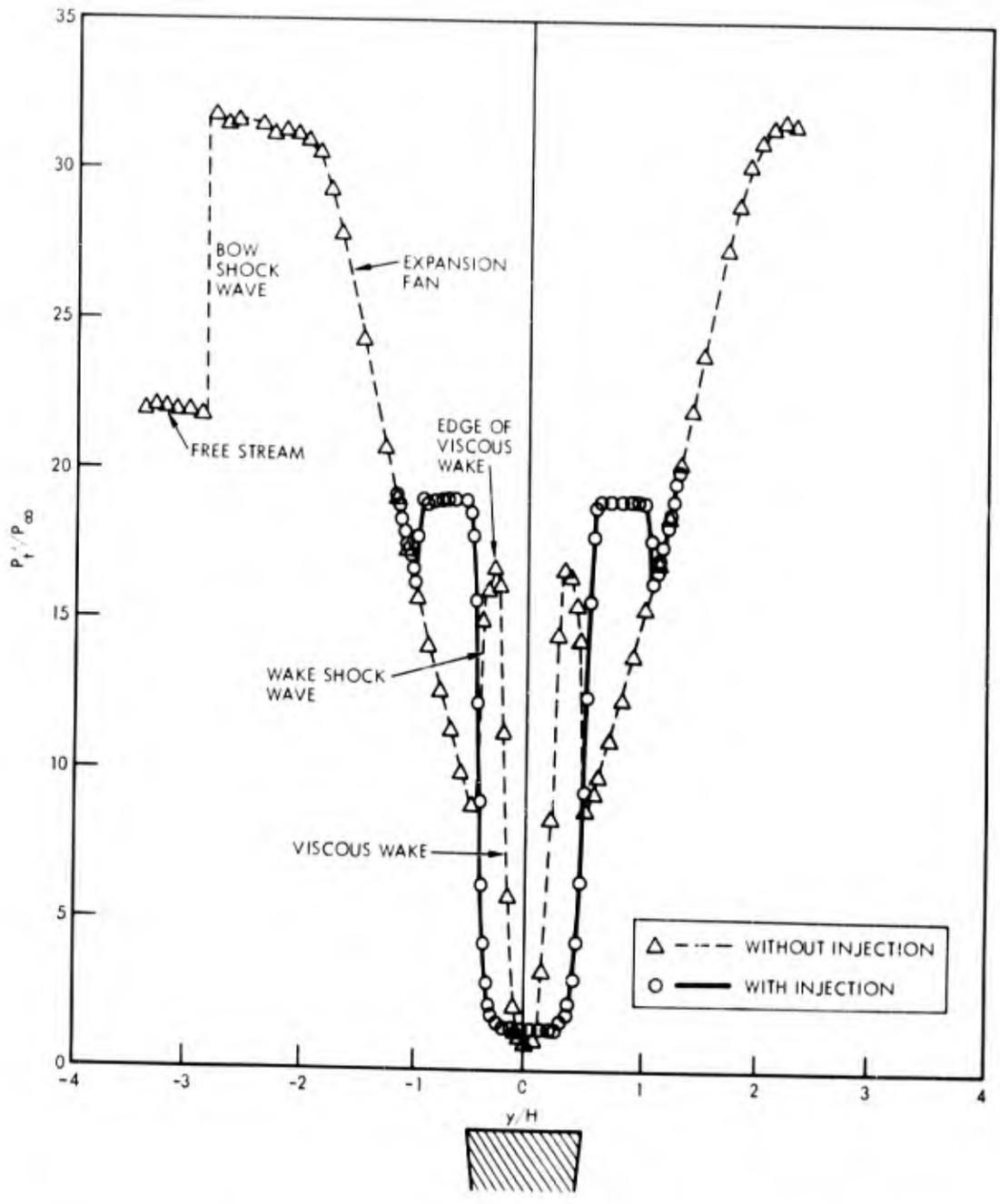

Fig. 3. Comparison of pitot pressures with and without injection for the adiabatic-wall wedge at $x/H = 3.0$

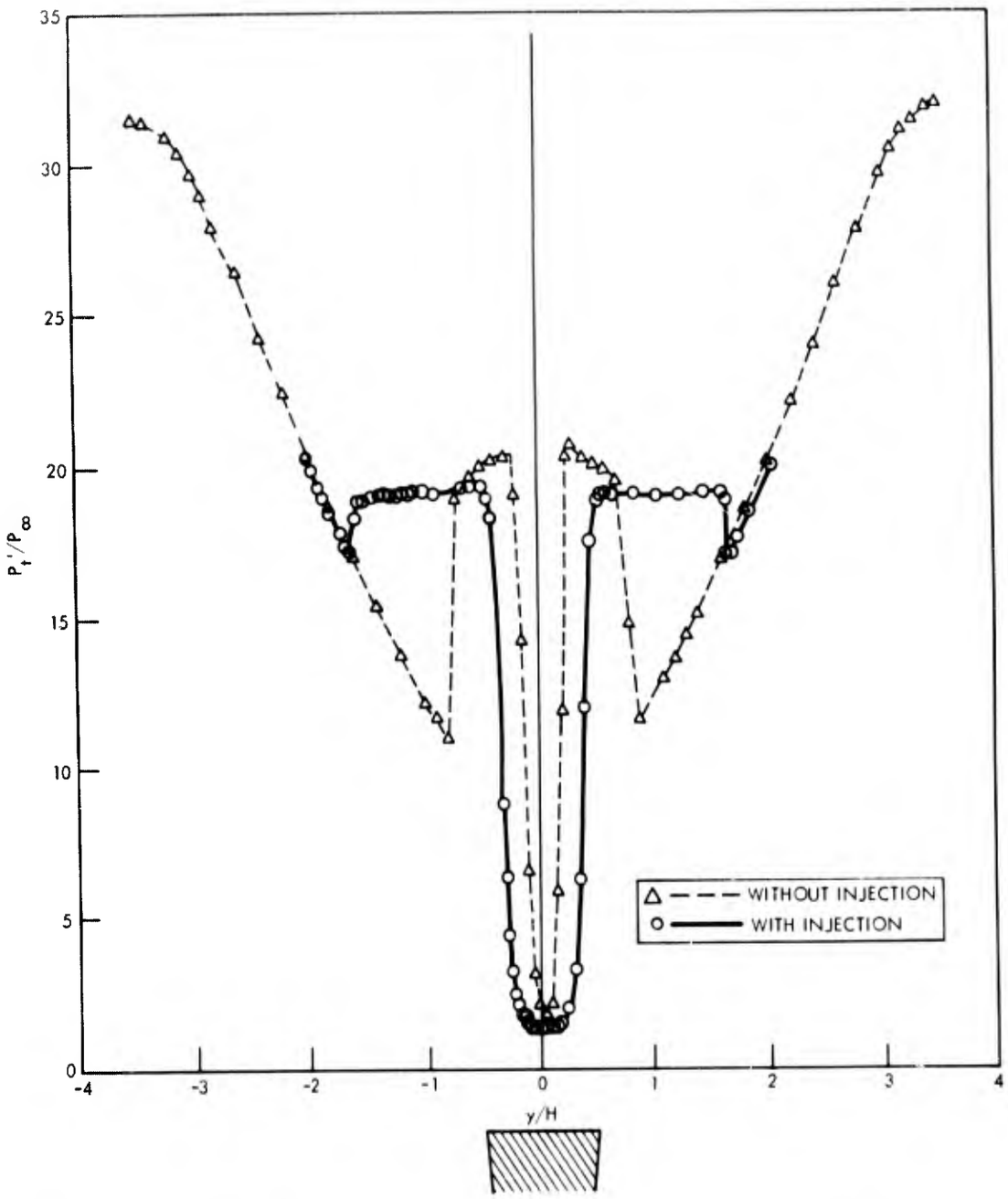

Fig. 4. Comparison of pitot pressures with and without injection for adiabatic-wall wedge at x/H = 6.0

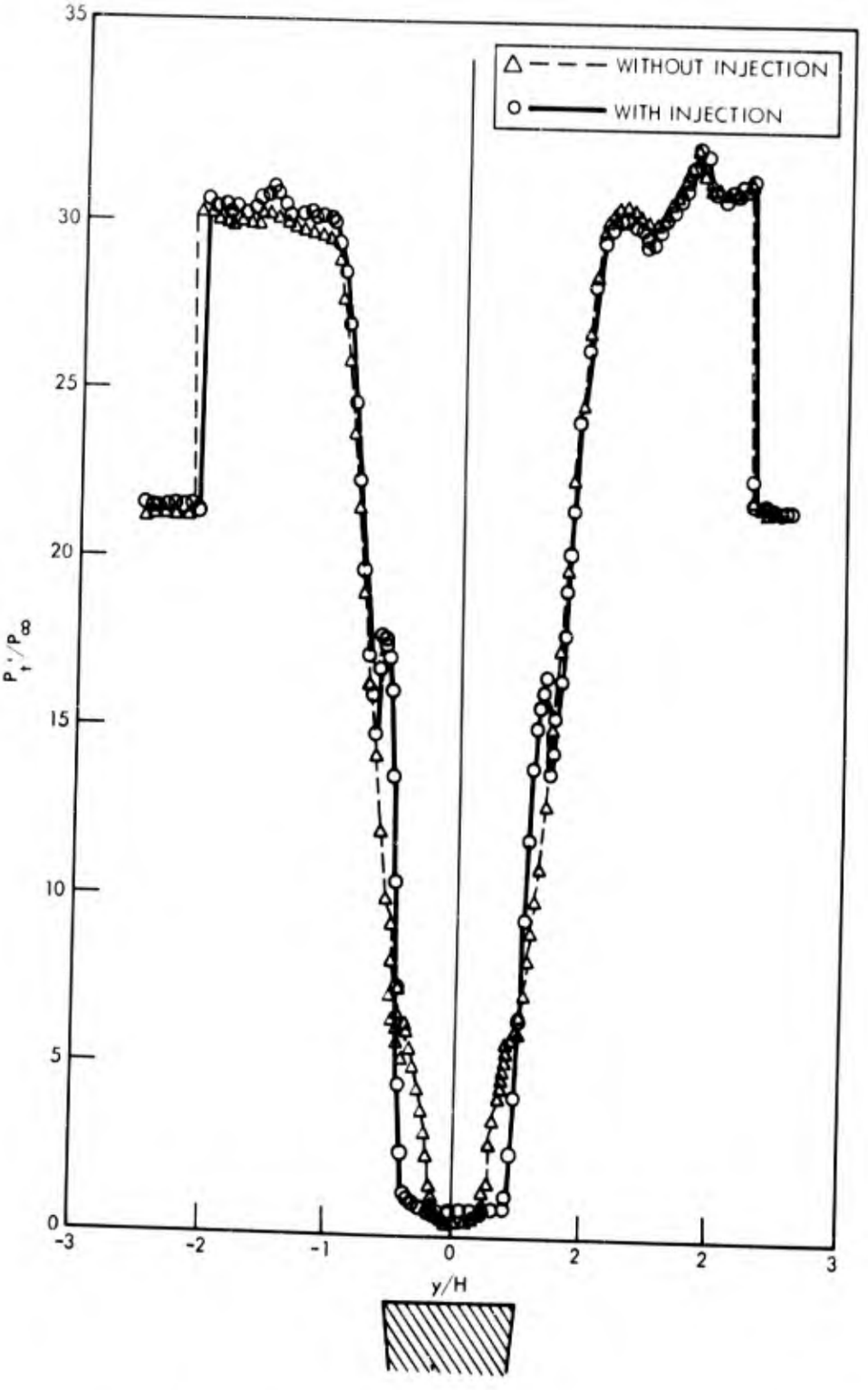

Fig. 5. Comparison of pitot pressures with and without injection for the cooled-wall wedge at $x/H = 1.0$

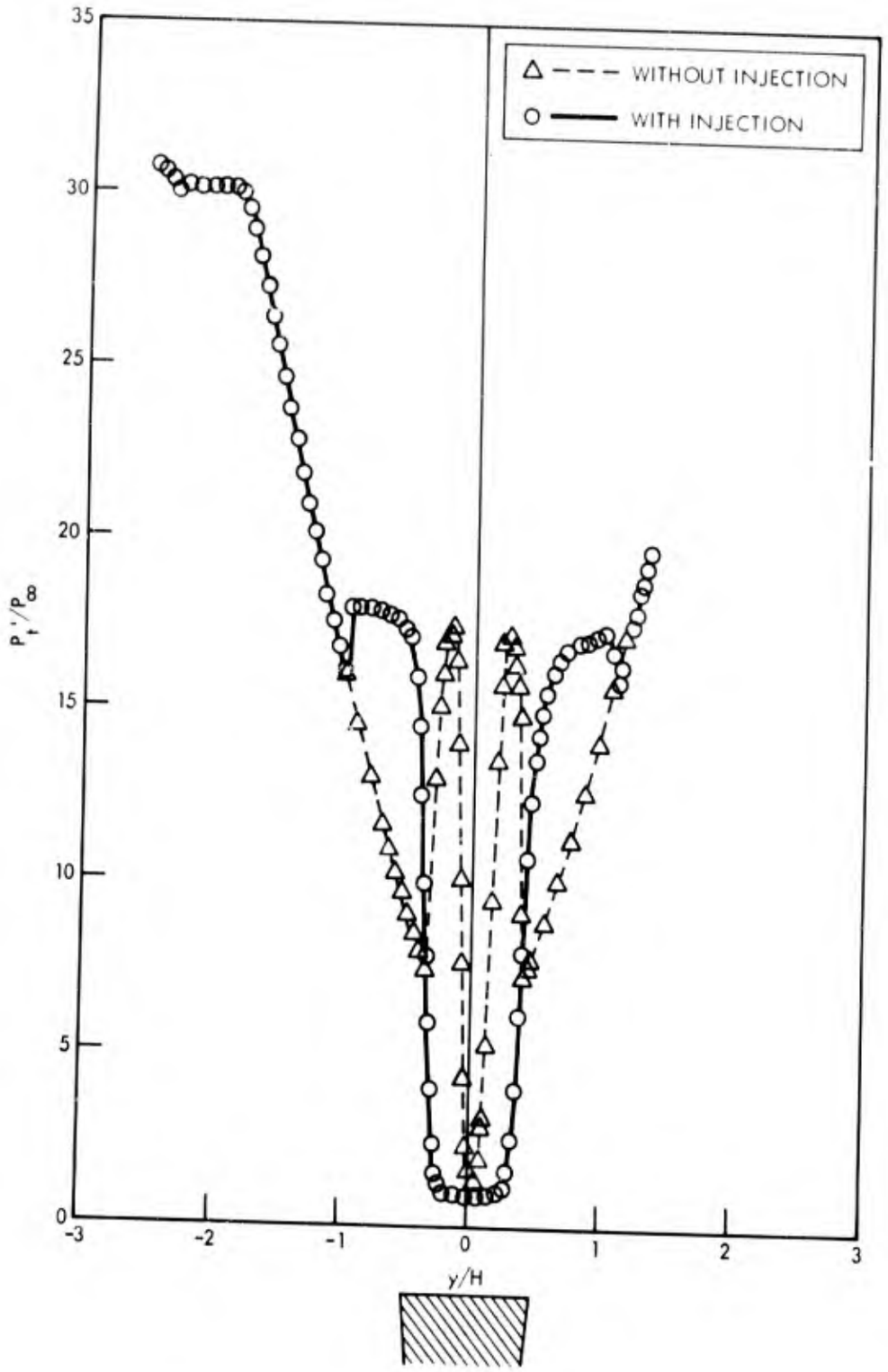

Fig. 6. Comparison of pitot pressures with and without injection for the cooled-wall wedge at x/H = 3.0

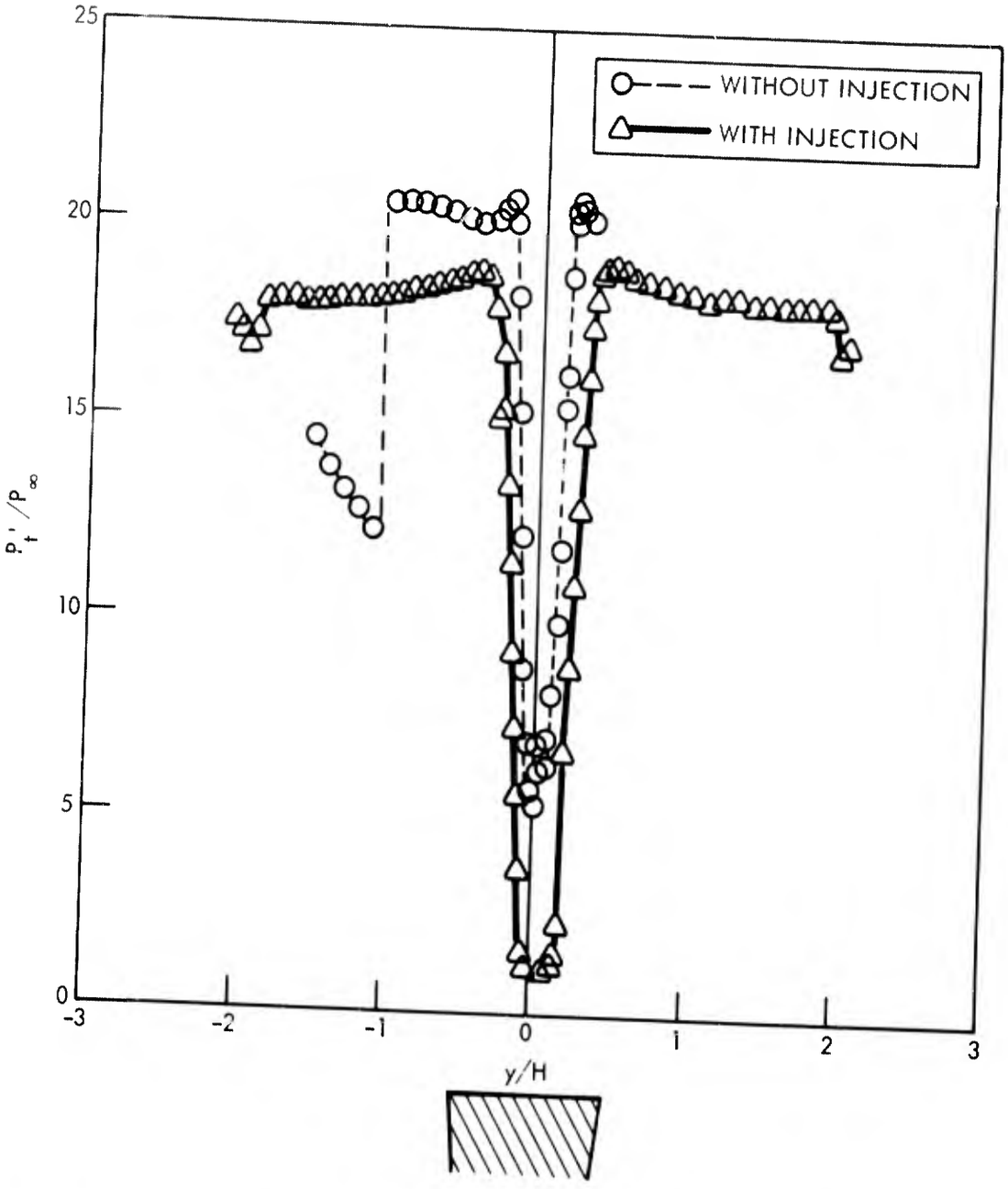

Fig. 7. Comparison of pitot pressures with and without injection for the cooled-wall wedge at $x/H = 8.0$

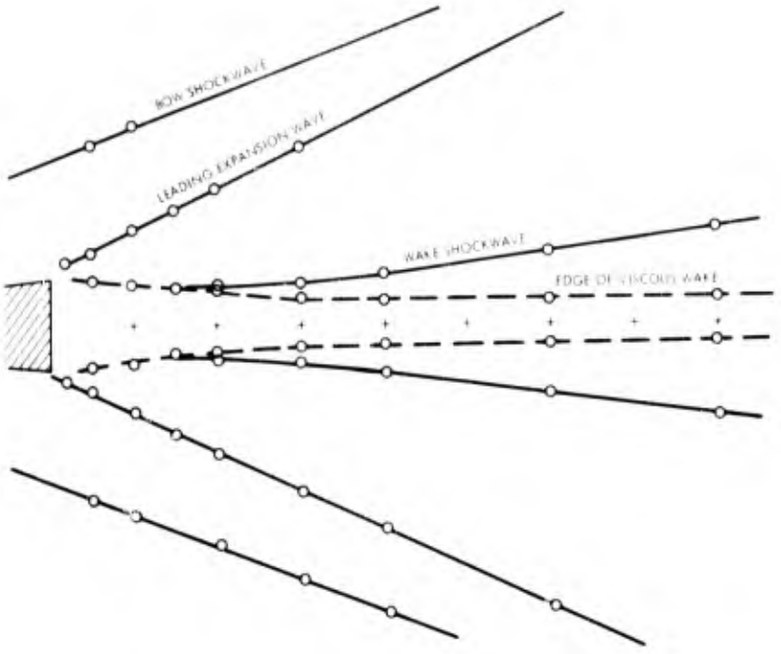

Fig. 8. Flow field boundaries obtained from pitot pressure plots for the adiabatic-wall wedge without injection

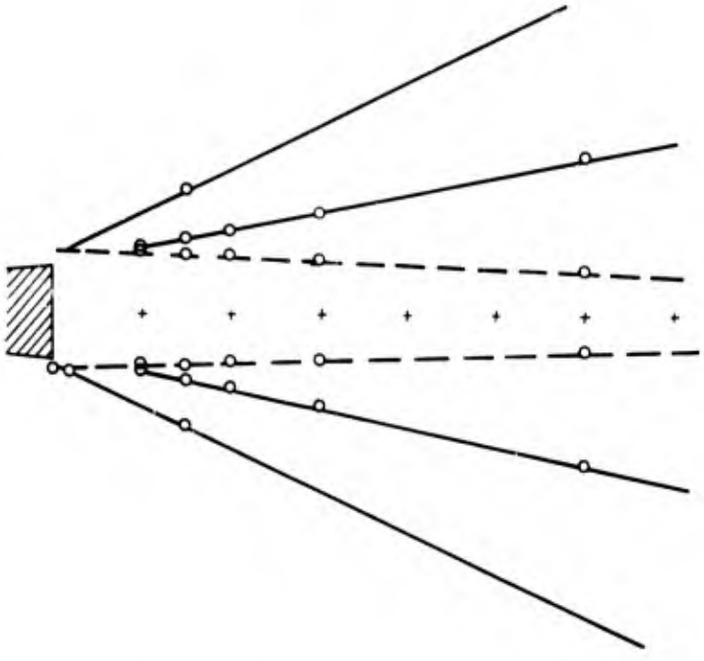

Fig. 9. Flow field boundaries obtained from pitot pressure plots for the adiabatic-wall wedge with injection

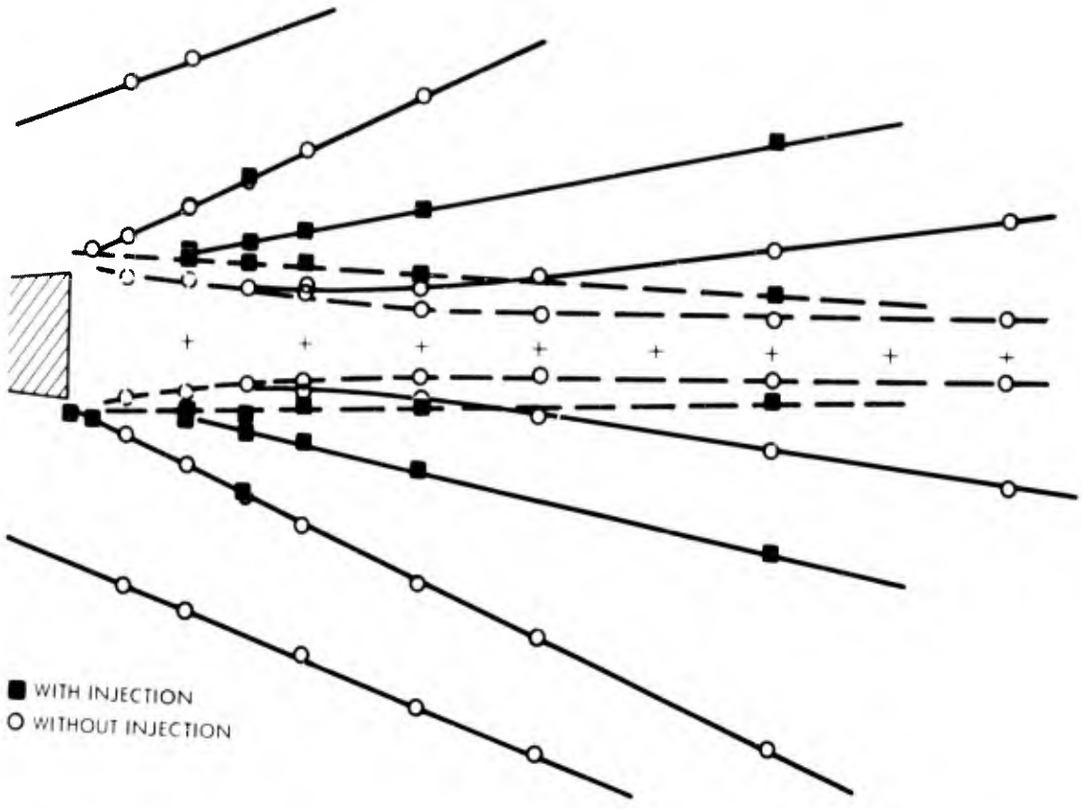

Fig. 10. Comparison of flow field boundaries with and without injection for the adiabatic-wall wedge

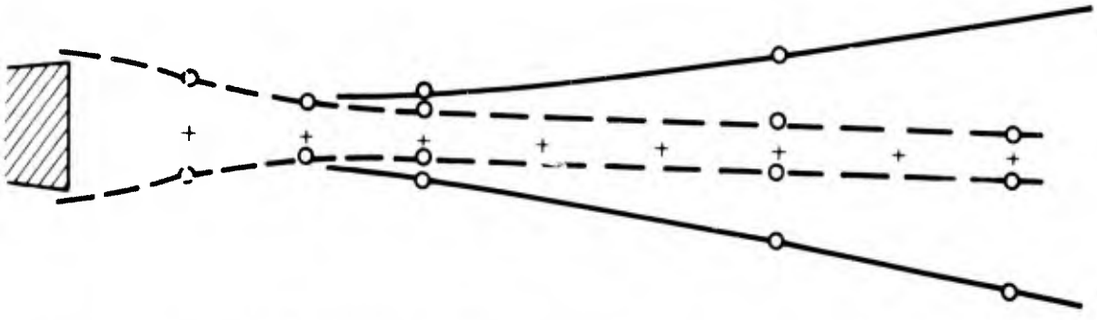

Fig. 11. Flow field boundaries obtained from pitot pressure plots for the cooled-wall wedge without injection

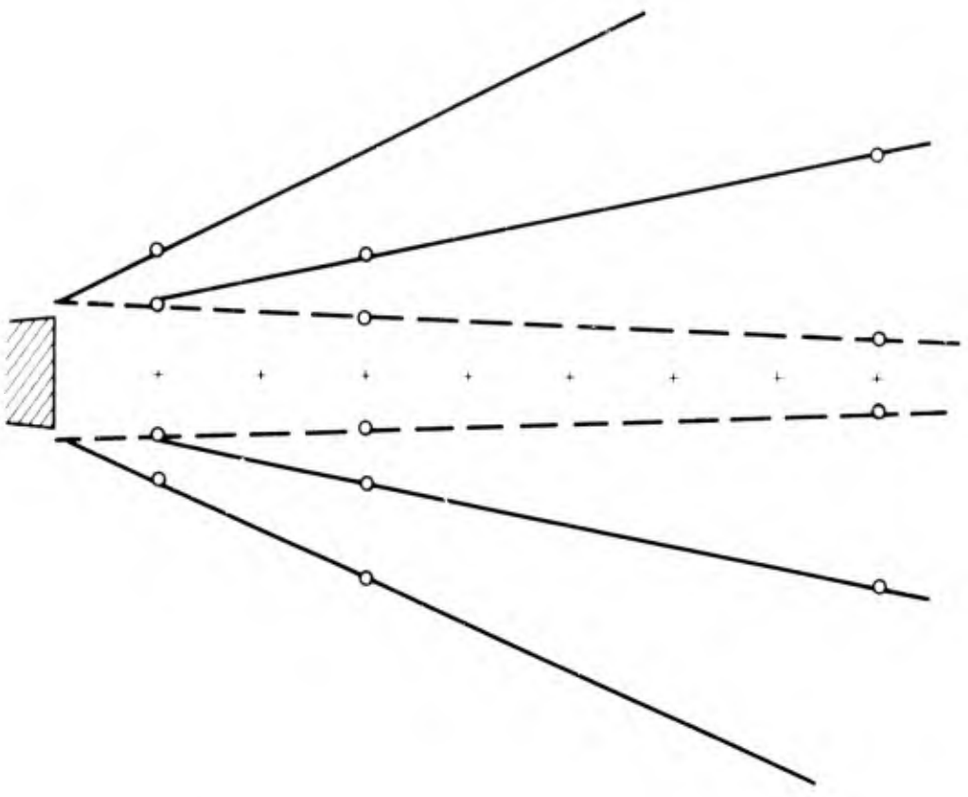

Fig. 12. Flow field boundaries obtained from pitot pressure plots for the cooled-wall wedge with injection

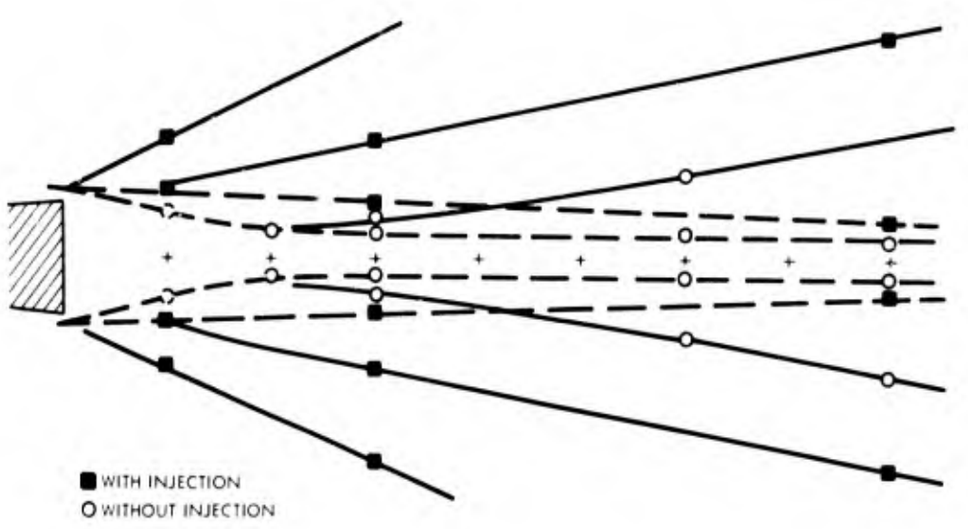

Fig. 13. Comparison of flow field boundaries with and without injection for the cooled-wall wedge

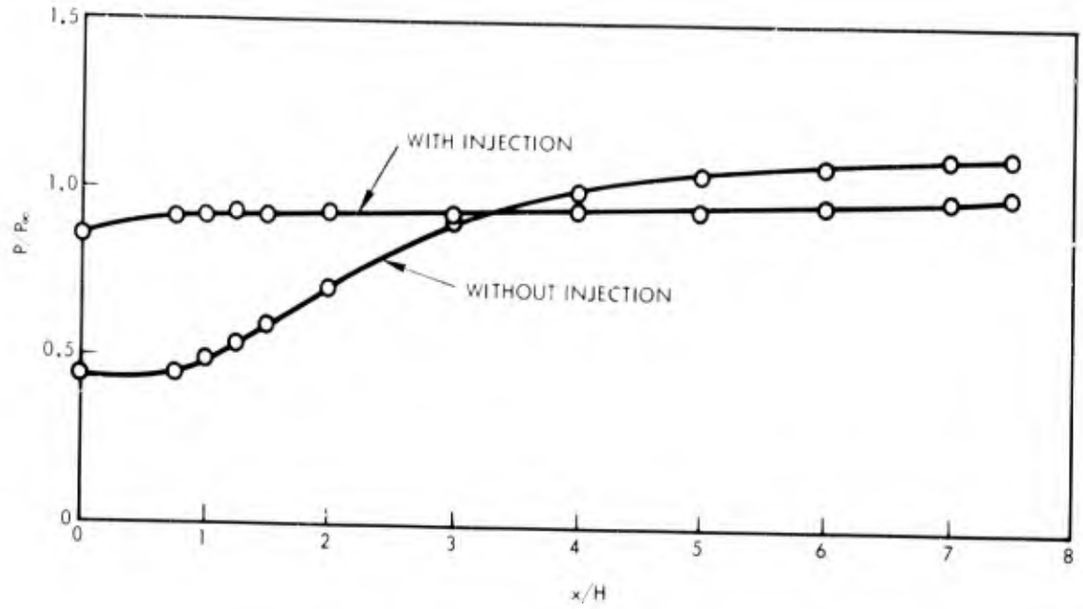

Fig. 14. Comparison of centerline static pressures with and without injection for the adiabatic-wall wedge

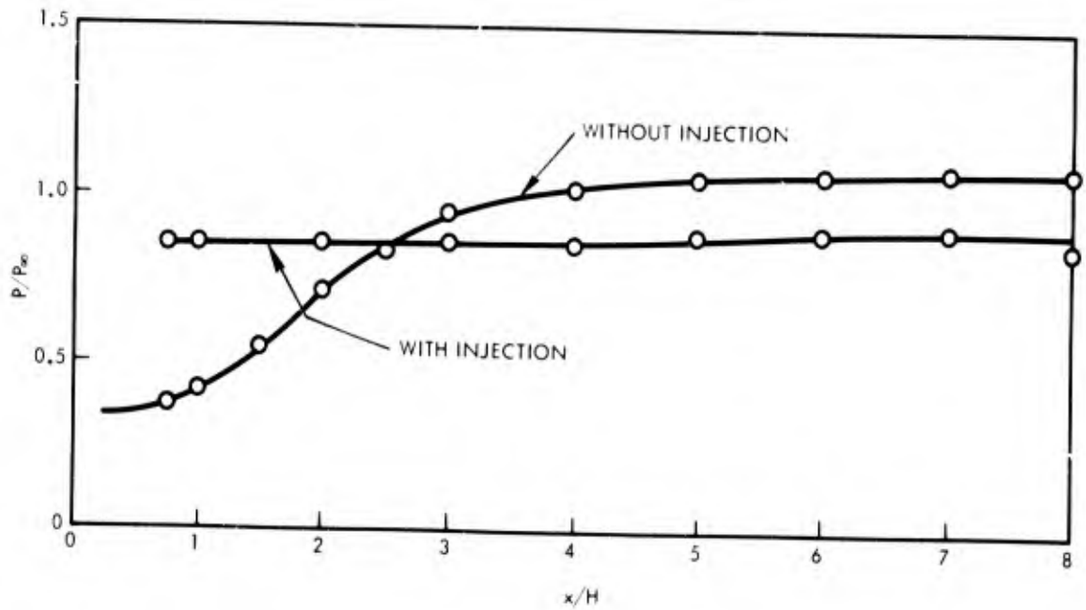

Fig. 15. Comparison of centerline static pressures with and without injection for the cooled-wall wedge

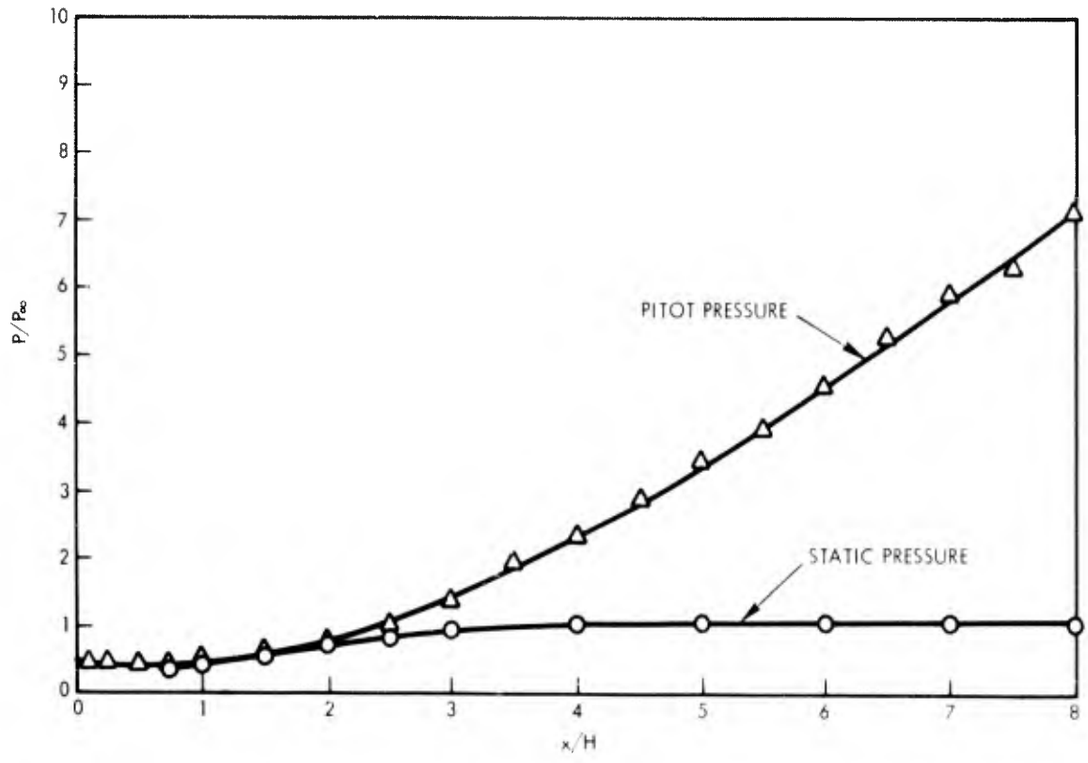

Fig. 16. Centerline static and pitot pressures without injection for the cooled-wall wedge

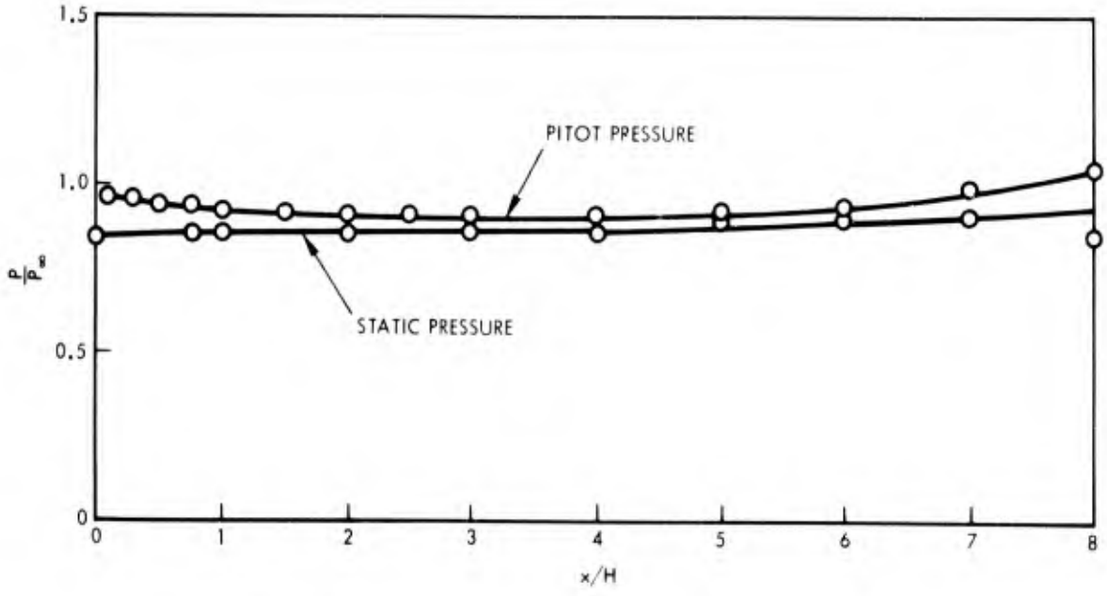

Fig. 17. Centerline static and pitot pressures with injection for the cooled-wall wedge

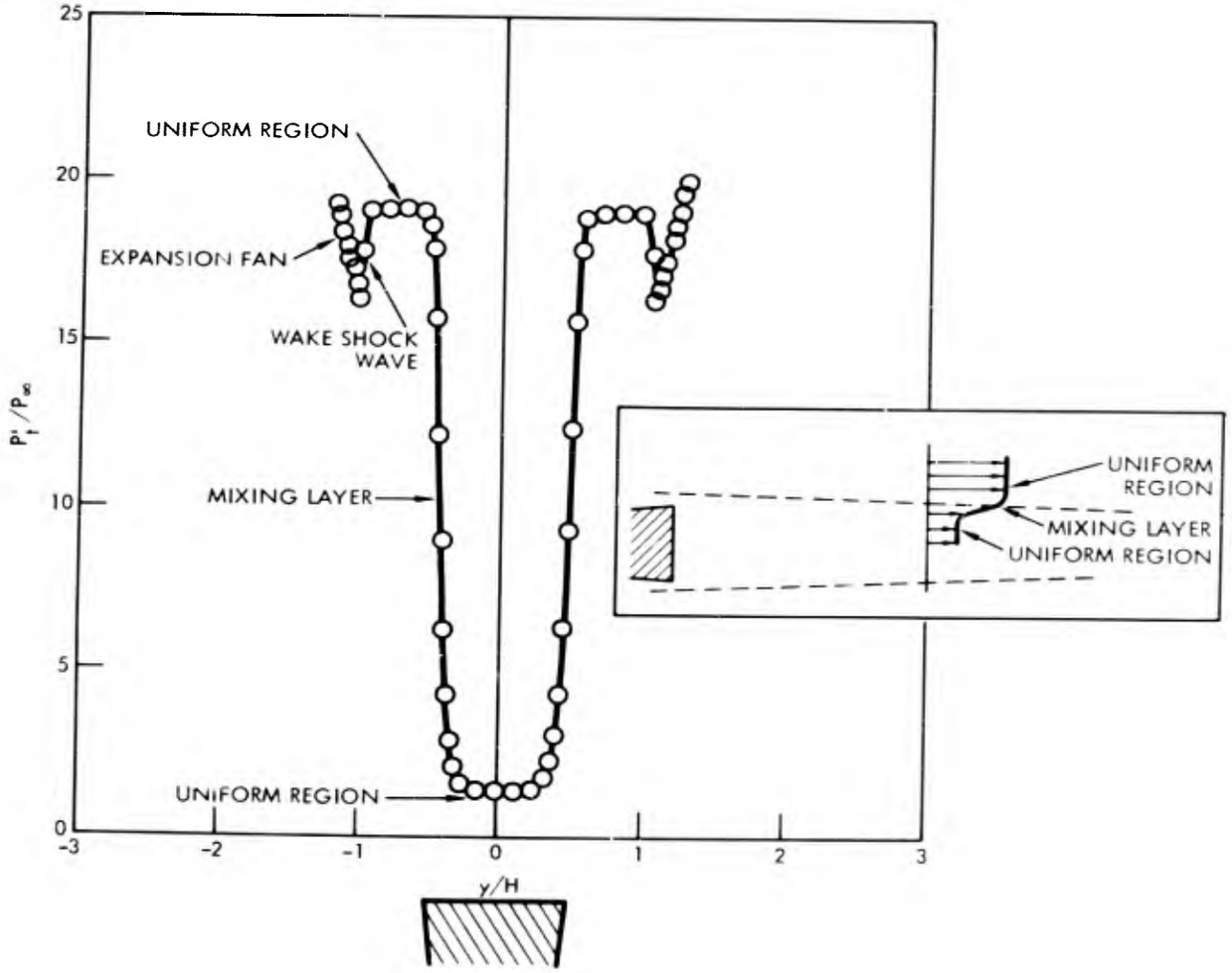

Fig. 18. Pitot pressures with injection at x/H = 6.0 and schematic of mixing region

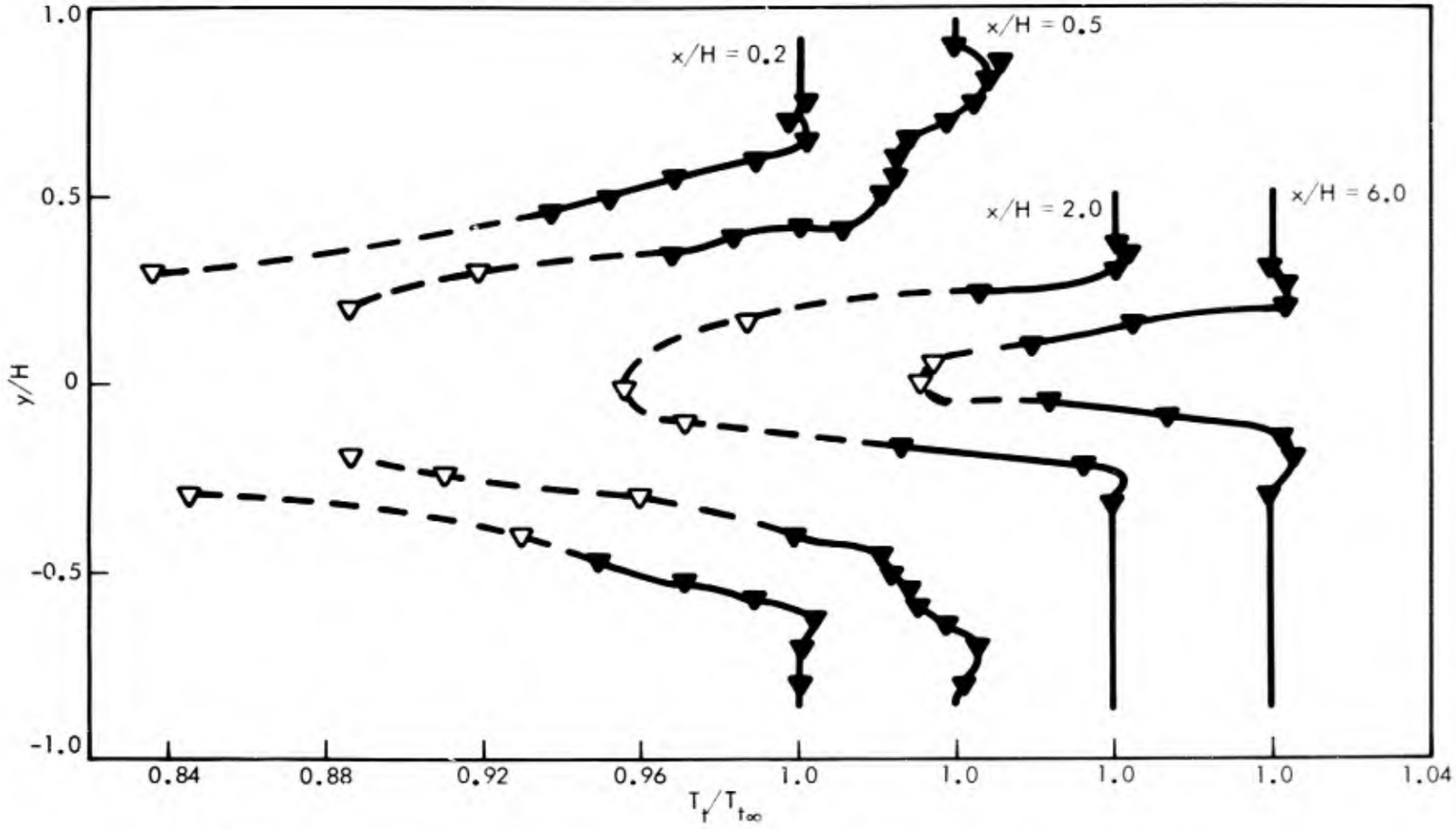

Fig. 19. Total temperature variation across the wake for the adiabatic-wall wedge without injection

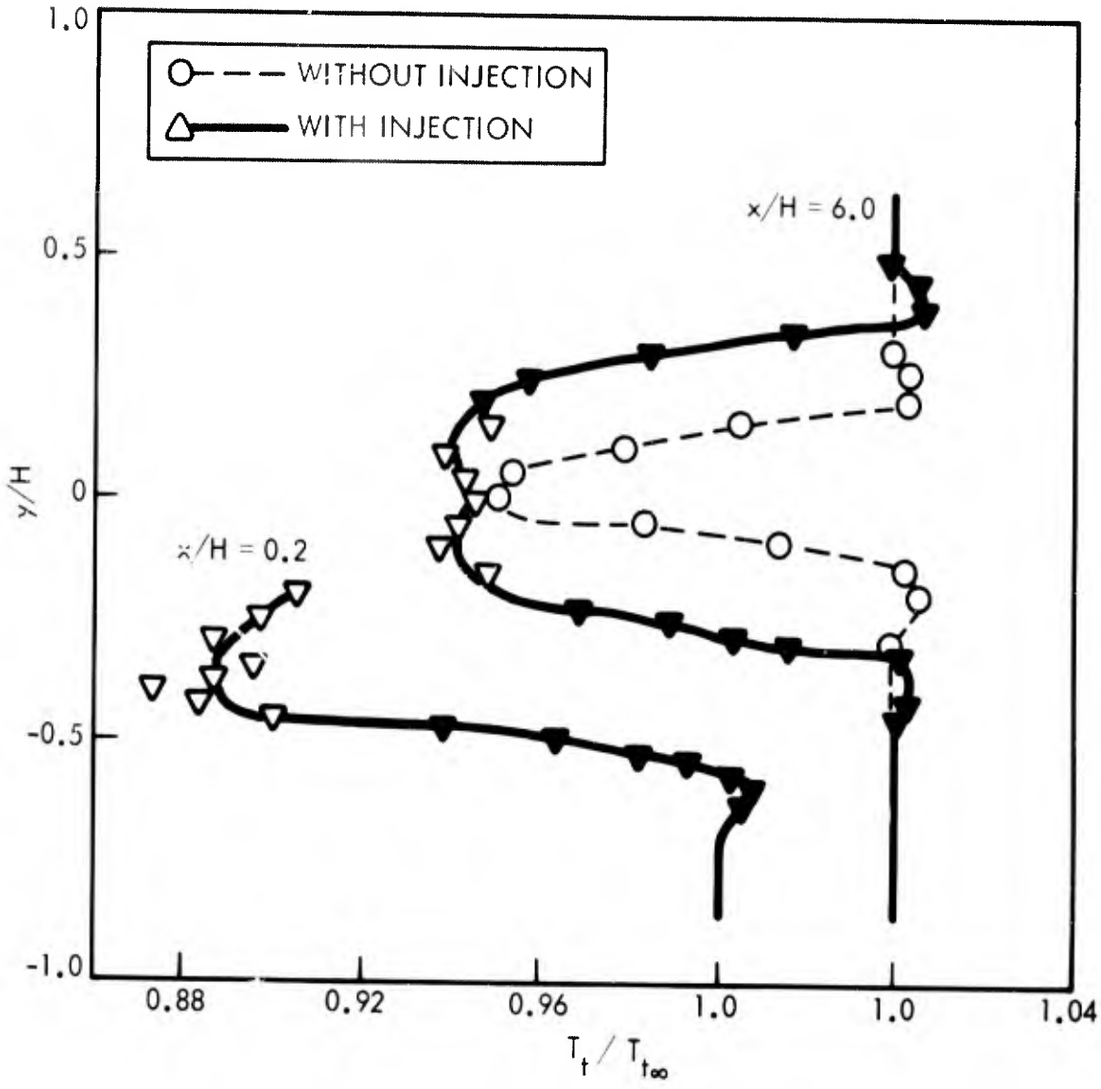

Fig. 20. Total temperature variation across the wake for the adiabatic-wall wedge with and without injection

RADIAL AND AXIAL VELOCITY PROFILES OF HYPERSONIC AND SUPERSONIC WAKES MEASURED BY THE SEQUENTIAL SPARK METHOD

by

C. Lahaye, E.G. Leger, and A. Lemay

This paper is generated under the
CARDE-ARPA co-operative re-entry physics program
of ARPA Order 133.

CANADIAN ARMAMENT RESEARCH AND DEVELOPMENT ESTABLISHMENT
VALCARTIER, P.Q., CANADA

February 1967

SUMMARY

The technique of using a sequence of sparks for velocity profile measurements across the wake of hypersonic projectiles is briefly described and the data reduction method is outlined using one particular case. Measured radial velocity profiles in wakes of hypersonic (15000 fps) and supersonic (4000 fps) spheres are presented for various positions in the wake and for various ballistic range pressures. These results are then discussed. The axial profiles constructed from these radial profiles are then presented and the measurements are compared with the available theoretical estimates and measurements obtained using other methods.

RESUME

Après une brève description de la technique qui consiste à faire jaillir une succession d'étincelles pour procéder à des mesures de profils de vitesse en travers du sillage de projectiles hypersoniques, les auteurs exposent leur méthode d'exploitation des résultats à l'aide d'un cas particulier. Ils présentent les profils de vitesse radiaux obtenus à partir de mesures effectuées dans les sillages de sphères hypersoniques 457.2 m/s et supersoniques 121.9 m/s pour diverses positions dans le sillage et divers nombres de Reynolds. Ils examinent ensuite ces résultats. Puis il présentent les profils axiaux élaborés à partir de ces profils radiaux, et comparent les mesures aux évaluations et aux mesures théoriques obtenues selon d'autres méthodes.

LIST OF SYMBOLS

d	Diameter of the Projectile
D_w	Diameter of the Wake
P	Range Pressure in Millimeters of Mercury (mm Hg)
R	Radial Distance From Flight Axis
V_w	Axial Velocity of the Wake in fps.
V_{yw}	Lateral Velocity of the Wake in fps.
V_∞	Velocity of the Projectile in fps.
X	Distance behind the Projectile
x/d	Distance behind the Projectile in Body Diameters (B.D.)
B.D.	Body Diameters
D.P.	Data Points
fps	Feet per second
RMS D	Root Mean Square Deviation

BLANK PAGE

Radial and Axial Velocity Profiles of Hypersonic and Supersonic Wakes measured by the Sequential Spark Method

by

C. Lahaye, E.G. Leger and A. Lemay

1.0 INTRODUCTION

With the advent of the space age, extensive studies have been initiated of the flow properties around hypersonic vehicles and of their wakes. Many problems have arisen in the understanding of hypersonic wakes because of the presence of high temperatures, ionization and chemical kinetics. The mutual interaction of chemistry and turbulence has introduced an additional complication and leads one to ask what relation the hypersonic wake bears to its predecessors, the supersonic and subsonic wakes.

In our studies we have investigated both hypersonic and supersonic turbulent wakes generated by projectiles travelling at high velocities in free flight ranges. In these studies various probes have been employed to obtain spatio temporal statistical data. This data can be analysed to yield power spectra in the frequency domain. A knowledge of mean velocity distribution in the wake is required in order to transform these power spectra to the wave number domain. This requirement led us to search for methods of measuring wake velocities under a wide range of experimental conditions and the sequential spark method was developed and applied to these studies.

2.0 MEASUREMENT METHOD

The technique of using a sequence of sparks has been applied by various authors (1, 3) to the measurement of flow velocities. This measurement technique operates on the following principle: The passage of an electric spark creates a low resistance ionized path in the fluid which persists for a period of time of the order of 10^{-4} seconds. If a second spark is produced during this interval, it will follow the ionized path traced by the first spark. If such a series of sparks of short duration is made across a flow of gas at properly selected time intervals, the ionized path due to the first spark is displaced at the velocity of the flow and each succeeding spark re-illuminates the ionized path. By open-shutter photography of the spark traces, a profile of the displacements of the flow is obtained and the velocity can be calculated if the time interval between the sparks is known.

The application of this technique to the measurement of wake velocities placed stringent conditions on the instrumentation requirements and on the data reduction method. Because of the dispersion of projectiles and in order to cover the full wake width, gaps of the order of 5 to 7 inches between electrodes were used and these in turn necessitated very high voltage pulses in order to obtain short duration breakdown at ambient pressures between 10 and 200 millimeters of mercury (mm Hg). A modified Model 9 radar hard tube modulator (4) is used to generate 0.8 microsecond pulses at 90 kilovolts across the electrodes with a current of approximately 20 amperes available to produce the sparks.

Preliminary measurements indicated that the sparks did not necessarily pass through the center of the wake along a straight path and therefore, three-dimensional analysis of the spark path was required. A precision stereo system was constructed using two cameras at 60° from the flight axis together with horizontal and vertical reference lines to define the geometry. A film reader reproducing the geometry of the stereo system used on the range was constructed to perform the three-dimensional data reduction. The flight path of the projectile with respect to the sparks is determined to an accuracy of .050 inch by means of a stereo-flash X-Ray photo attitude system using the same reference lines as the film reader.

3.0 DATA REDUCTION METHOD

An example of the data reduction procedure is now given using the sequence of sparks shown in Figure 1. In this case, a series of sparks were obtained at a distance of approximately 600 body diameters behind a one inch diameter aluminum sphere travelling at 14,560 feet per second (fps) in an ambient air pressure of 40 mm Hg. The pulse interval was 40 microseconds and the sequence of 7 sparks seen by the two stereo cameras is shown together with a schlieren photograph taken immediately after the occurrence of the fourth spark. It is seen that, in this case, the diameter of the turbulent wake is greater than the electrode gap.

In order to obtain radial velocity profiles from this data, it is necessary first of all to locate accurately the flight path of the projectile with respect to the horizontal reference lines. The plates from the stereo spark cameras are then mounted in the stereo projector

reading assembly which is aligned by using the vertical and horizontal reference lines. The co-ordinates of numerous points of each spark in the xz and yz planes are determined using standard photogrammetric techniques. Projections of the sparks are shown in Figure 2 where the x axis is the direction of flight, the z axis is the vertical direction and the y axis is the horizontal one. This figure also shows the displacement of three of the sparks in the yz plane and it is seen that none of them passes through the axis of the wake. This was the case for all seven sparks of this sequence. In this analysis it is assumed that the velocity in the z direction is zero and the distance between points on consecutive sparks are measured and the velocities computed using the measured time interval between the sparks.

Graphs of the resulting velocity profiles obtained from every pair of consecutive sparks are shown in Figure 3a. The notation V_{23} means the velocity profile computed from the second and third sparks. A profile averaged for the total duration of the sequence can then be computed. It is seen in this figure that no measurements closer than 0.3 body diameters from the axis are available because of the sparks did not pass through the center of the wake.

Lateral wake velocities are shown in Figure 3b.where the convention is adopted that the direction towards the cameras is positive.

4.0 SUPERSONIC WAKES

4.1 Experimental Conditions

The experimental determination of the wake velocity of supersonic spheres travelling at 4000 fps was made with the purpose

of gathering data which could be used to develop a better theoretical model of the wake. At these low velocities the fluid dynamical properties of the wake can be calculated without the complications of chemistry. All the results presented here were obtained with one inch diameter aluminum spheres. At distances greater than approximately 300 body diameters no measurable spark displacement can be obtained on the photographic plates due to the low absolute velocity of the wake and the short persistence of the ionized path. The photograph of Figure 4 presents a typical result obtained behind a supersonic sphere. This result was obtained at 300 body diameters behind the model travelling at 4000 fps in an ambient pressure of 40 millimeters of mercury. The schlieren picture shown was taken at the time of the fourth spark and the shock waves produced by the preceeding sparks can be seen. A series of 10 voltage pulses spaced by 100 microseconds was used. The first pulse produced a glow whereas succeeding ones produced well defined sparks.

In the very near wake, (3-15 B.D.) the velocity measurements can be made but a few difficulties are encountered. A first difficulty arises in forming a well defined spark at low ambient pressures (lower than approximately 40 mm Hg), but well defined sparks were obtained at an ambient pressure of 100 mm Hg. This behaviour is due to the low gas density where too few molecules are left to produce sparks. Another difficulty is caused by the very large velocity gradients encountered in the very near wake. These large gradients occur within the small diameter of the inner wake and produce sharp curvatures of the ionized path which cannot be followed by the spark. Instead of following the ionized path,

the spark traces a new one. An example of these large gradients can be seen in Figure 5 which is a shadowgraph picture taken at approximately nine body diameters behind a 4000 fps sphere at an ambient pressure of 200 mm Hg. A large velocity increase can be seen at the boundary of the viscous wake and it is believed that a new spark path was traced in the viscous core. In this illustration the V shaped electrodes are seen together with part of the bow and recompression shocks and their reflections on the electrodes. The difficulty of measuring in high gradient flow near the body can be overcome by using a shorter time interval between the sparks. A short time interval will permit measurement of the large axis velocity and a longer time interval will give the edge velocity. By combining these results, the data where spark jumping occured can be rejected and a complete velocity profile can be obtained.

A total of 28 velocity profiles were measured in the viscous wakes of one inch diameter spheres travelling at approximately 4000 fps. These measurements were made at nominal axial distances of 15, 50, 100, and 300 body diameters and at ambient pressures of 10, 40, 100 and 200 mm Hg.

4.2 Velocity Profiles of Viscous Wakes

The velocity profiles gathered during the low velocity firing program are given in Figures 6,7,8 and 9. In these graphs the wake velocity normalized with respect to the sphere velocity (Vw/V_{∞}) is traced as a function of radial distance normalized with respect to the sphere diameter (R/d). Profiles measured at approximately the same

distances behind the spheres have been grouped together and the ambient pressure is indicated on the graphs. It should be noted that two profiles corresponding to two different rounds are usually given for each condition of axial distance and pressure. In order to keep the graphs simpler, only the points printed by an automatic plotter are given and no attempt at distinguishing between profiles under the same conditions has been made.

The velocity profiles of Figure 6, measured at a nominal axial distance of 15 body diameters are suspected to show lower values than actual. These errors are a consequence of the large reduction of gas density and of the strong axial velocity gradient encountered in the near wake. A time interval of 25 microseconds between sparks was used for these measurements, and with such a pulse spacing jumping of the spark has probably occurred across the viscous wake. The error will be smaller further away from the axis. In order to measure the wake velocity more accurately in this region, a pulse spacing of 10 microseconds will be required, and the small diameter of the wake dictates the use of an array of electrodes with a capability of selecting the spark position. The velocity profiles given in Figures 7,8 and 9 measured at nominal axial distances of 50, 100, and 300 body diameters respectively are believed accurate. At these distances behind the model the axial velocity gradient is considerably reduced and no spark jumping is expected.

The velocity profiles in Figures 6 to 9 have been collected at four different ambient pressures in order to study the effect of Reynolds number and no large changes in velocity have been observed. The statistical fluctuations tend to mask any possible effect of Reynolds

number and a large number of profiles would have to be studied in order to draw a conclusion. However, the profiles reveal a slight tendency for higher axis velocities at higher ambient pressures.

4.3 Velocity Distributions

Since the velocity profiles show very little dependence on Reynolds number, all the profiles measured were used to obtain velocity distributions. The normalized mean velocity values of each radial profile (average of eight displacements produced by 9 sparks) are plotted and linear interpolation is made between points of the mean curve to obtain the velocity at fixed radial distances of 0.2, 0.4, 0.6, 0.8 and 1 body diameter. A least mean squares fit of an equation of the form

$V_w/V_\infty = a + b \log x/d$ where a and b are functions of radial position

was made on the computer with a set of data points obtained at each pre-selected radial distance, over a finite distance of the wake. The result of the least mean squares fit is given in Figure 10 for radial distances previously mentioned. The number of data points used in the least mean squares fit together with the standard deviation are indicated on the graph for each axial velocity profile. Less confidence can be placed on some of these axial velocity profiles, especially those very near the axis (0.2 R/d) and near the body (15 B.D.), where spark jumping could have occured. This error will tend to decrease the slope of the 0.2 R/d profile only. The velocity measurement errors associated with low gas density will have a tendency to shift the axial profile downward.

In order to trace the axial velocity profiles of Figure 10,

both inviscid and viscous wake data have been used; at an axial distance of 15 body diameters for example, the viscous wake is approximately one body diameter in width and data points at radial distances of .6, .8 and 1 body diameter are inviscid data.

5.0 HYPERSONIC WAKES

5.1 Experimental Conditions

The measurement of hypersonic wake velocities behind one inch diameter aluminum spheres presents in some respects a different problem than the measurement at supersonic velocities. At hypersonic speeds, the wake velocity measurements can be made as far as 1500 body diameters behind the projectile due to the high absolute velocity of the flow. At these large axial distances however, the size of the viscous wake exceeds 10 body diameters and the electrodes are immersed in the viscous wake. Measurements of the edge velocity can be made by offsetting the pair of electrodes.

Figure 11 shows a typical result obtained behind a hypersonic sphere. The velocity of the sphere was 14,600 fps the pressure was 40 mm Hg and the velocity measurement was taken at approximately 300 body diameters downstream. At this axial distance the viscous wake almost completely filled the gap between the electrodes and it is seen that strong velocity gradients occur inside the viscous wake width as defined by the schlieren method.

At distances up to approximately 150 body diameters, it is very difficult to form a well defined spark in the center of the viscous wake of a hypersonic sphere because of the high conductivity of the gas

due to ionization, ablation products and low gas density. The sequence of sparks shown in Figure 12, taken at approximately 140 body diameters behind a sphere travelling at 14,240 fps at ambient pressure of 76 mm Hg illustrates this problem. The spark traces which are well formed on the edge of the viscous wake become completely diffused in the central core. A slight reduction of the sphere velocity to 13,500 ft/sec. at 40 mm Hg permits the formation of a continuous spark across the center of the viscous core.

Up to the present time some 50 hypersonic profiles have been gathered. They oover a large range of different conditions of pressure, velocity and axial distance.

5.2 Velocity Profiles of Viscous Wakes

A comparison of the velocity profiles measured at distances of approximately 150, 300, 600 and 1000 body diameters behind a hypersonic sphere is given in Figure 13. Two or three rounds are plotted for each axial distance and the velocity varied between 14500 to 15,000 fps for all rounds except for those at 150 body diameters where lower velocities of 12,700 and 13,200 fps were used to obtain the profiles. This type of presentation, with normalization to the wake width at any axial distance has been selected because it reduces the overlap of the traces; the flattening of the velocity profiles as a function of distance behind the body becomes evident at a glance.

A rather good coverage of the viscous wake is achieved at 150 and 300 body diameters although the edges are difficult to measure because of the relatively short time gap between the sparks. At 600 and

1000 body diameters the width of the measurable wake between the electrodes determines the width of the profiles. One peculiarity about these profiles is that sharp gradients in velocity still exist close to the axis at distances of the order of 150 body diameters.

5.3 Velocity Distribution

The variation of the normalized wake velocity (V_w/V_∞) with distance behind the body has also been studied under hypersonic conditions and a graph illustrating the results found is given in Figure 14. A least mean squares fit was made on the data points using the method described previously for the supersonic wake. The velocity of the projectiles varied from 15,000 to 12,500 fps at ambient pressures varying from 27 to 76 mm. of Hg. The data points found were for measurements from 150 to 1000 body diameters behind the projectile. A total of 30 different velocity profiles were used to construct the curves. For each curve, the number of data points and RMS deviations are given. It can be seen that the velocity in all curves decreases regularly with increasing distance behind the body and all curves tend to a common value of approximately .03 V_w/V_∞ at 1000 body diameters. A comparison of the hypersonic and supersonic data reveals a steeper axial velocity gradient in the hypersonic case. Theoretical calculations using the Lees and Hromas method are in agreement with the experimental results.

5.4 Average Velocity Profiles

Velocity profiles have been obtained on different rounds for the same experimental conditions and some are shown in Figure 13. An examination of these graphs reveals that important divergences between profiles taken under identical conditions are evident in both the shape

of the profiles and the relative wake velocities. This can be attributed to the superposition of a random turbulent eddy velocity upon the mean velocity of the turbulent wake.

The magnitude of these fluctuations can only be bracketed by analyzing a large number of firings under identical experimental conditions and this has not yet been achieved. However a certain number of firings where the conditions were similar and the measurements made at the same distance behind the body were averaged and the average profiles are shown in Figure 15. The number of rounds used to obtain these average profiles is indicated for each condition and readings at both sides of the wake have been used to generate the average. The velocity fluctuations computed using this limited number of data points are of the order of 20% at radial distances of 0.4 to 1.0 R/d.

Velocity profiles calculated by Ellington (2) using the method of Lees and Hromas (7) are also shown for conditions of 76 mm Hg and 15,080 fps and at approximately the same distances in the wake. The theoretical profile lies below the measurements at the center and above at the edge of the wake. This is more apparent at 600 body diameters than at 1000 body diameters because at this latter position, only the central part of the wake lies between the electrodes and can be measured.

An influence of pressure on the axis velocity for the two curves at 1000 body diameters is apparent.

6.0 COMPARISON BETWEEN SUPERSONIC AND HYPERSONIC RESULTS

The first few measurements in wake velocity behind supersonic spheres reveal a large reduction in normalized wake velocity when compared with hypersonic results. An appreciable difference is also noted in the growth of the viscous wake.

6.1. Viscous Wake Width

The growth of the turbulent wake has been studied among others by Lees and Hromas (5). The result of their theoretical calculations for the turbulent wake width versus axial distance in the case of thermodynamic equilibrium and locally similar turbulence is given in Figure 16 for a blunt nosed body travelling at 9500 fps at atmospheric pressure. Also given in Figure 16 are some experimental measurements of wake widths measured from schlieren photographs of the wake which were taken at the same time as the spark sequence for wake visualisation purposes. Wake widths measured behind 1 inch spheres travelling at 4000 fps fall below the Lees-Hromas curve while those measured behind 1 inch sphere travelling at 15,000 fps fall above this theoretical curve. This dependence of the turbulent wake width on flight velocity or Mach number was predicted by the Lees-Hromas theory. It has to be noted that the experimental wake width curves given in Figure 16 are only tentative due to the small amount of data available at the present time. No appreciable change in the wake width with ambient pressure was noted from the measurements of schlieren pictures taken at pressures of 40, 100 and 200 mm Hg.

6.2 Viscous Wake Velocity

Due to the difficulties encountered in measuring velocity of a hypersonic wake at distances closer than 300 body diameters and due to the low absolute velocity of supersonic wakes far behind the model which again preclude measurement, the only point available at the present time for the comparison of velocity profiles is 300 body diameters. Figure 17 shows four velocity profiles measured at 300 body diameters behind one inch diameter spheres travelling at 14,600 and 4,000 fps. In all cases the ambient pressure was 40 mm Hg. Much higher normalized wake velocities are measured behind hypersonic spheres than behind supersonic spheres. A factor of about 2 in normalized velocity is observed. To establish a better figure, more data would be necessary because of the turbulent fluctuations of the wake velocity.

This same figure also shows the same velocity profiles but normalized with respect to the viscous wake width. Values of the wake widths used to normalize the profiles were taken from the curves of Figure 16. It can be seen that, at this axial distance for radial distances between 0.3 and 0.4 close to the edge of the viscous wake the hypersonic profile coincides with the supersonic one.

7.0 COMPARISON WITH OTHER DATA

A comparison has been made between the axial velocity distributions at a radial distance of 1.6 body diameter, as measured by electrostatic probes and sequential sparks. These results are shown in Figure 18. In general the results are in good agreement especially at distances greater than 400 body diameters: however at small axial distances, the electrostatic probe measurements tend to be slightly higher than those obtained from the

sequential spark although lower than the theoretical curve calculated by Ellington using the Lees and Hromas method.

8.0 CONCLUSION

The sequential spark technique has been used to obtain velocity profiles behind wakes of spheres travelling at supersonic and hypersonic velocities. It has been demonstrated that the sequential spark method can yield valuable information in establishing average velocity distributions in the wakes of hypersonic and supersonic projectiles.

The sequential spark results at hypersonic speeds indicate that steep velocity gradients occur well within the boundaries of the viscous core as defined by flow visualization techniques. It appears that velocity profiles are narrower than the profiles heretofore assumed for use in theoretical calculations where the maximum gradient is taken to occur at the wake boundary. Relative velocities are much higher in the hypersonic wake as compared to the supersonic wake. Also the normalized axial velocity decay is greater in the hypersonic wakes.

It should be borne in mind that the amount of information obtained at the time of writing of this paper is limited. To increase the confidence level more data is necessary. This data is being steadily accumulated as part of the CARDE turbulent wake study program.

REFERENCES

1. Bomelburg, H.J., Herzog, J., and Weske, J.R. "The Electric Spark Method for Quantitative Measurements in Flowing Gases." AFOSR TN-59-273, ASTIA AD212707 - University of Maryland, 1959.

2. Ellington, D. "The Lees-Hromas Method for Wake Turbulent Diffusion at Hypersonic Speeds".
PART I - Analysis. CARDE T.N. 1740/66. December 1966.
PART II - Numerical Solutions. CARDE T.N. 1744/67. January 1967.

3. Frungel, F.B.A., "High Speed Pulse Technology". Vol. 11 Academic Press - New York - 1965 Pages 162 - 182.

4. Glasoe and Lebacqz. "Pulse Generators". - Radiation Laboratory Series, McGraw-Hill, Pages 152 - 160.

5. Heckman, D.E. Private Communication. February 1967.

6. Kirkpatrick, A., Cantin, A. and Heckman, D. "Progress in Electrostatic Probe Measurements in a Hypersonic Turbulent Wake". CARDE T.N. 1733/66 - October 1966.

7. Lees, L., Hromas, L. "Turbulent Diffusion in the Wake of a Blunt-Nosed Body at Hypersonic Speeds". - Journal of the Aerospace Sciences. August 1962, Pages 975 - 993.

ACKNOWLEDMENTS

The authors are grateful to Mr. G.H. Tidy for his continued interest in this work. Many helpful discussions were held with Mr. D. Ellington and Dr. D. Heckman. The authors also express their appreciation to the members of Aerophysics Wing for their cooperation.

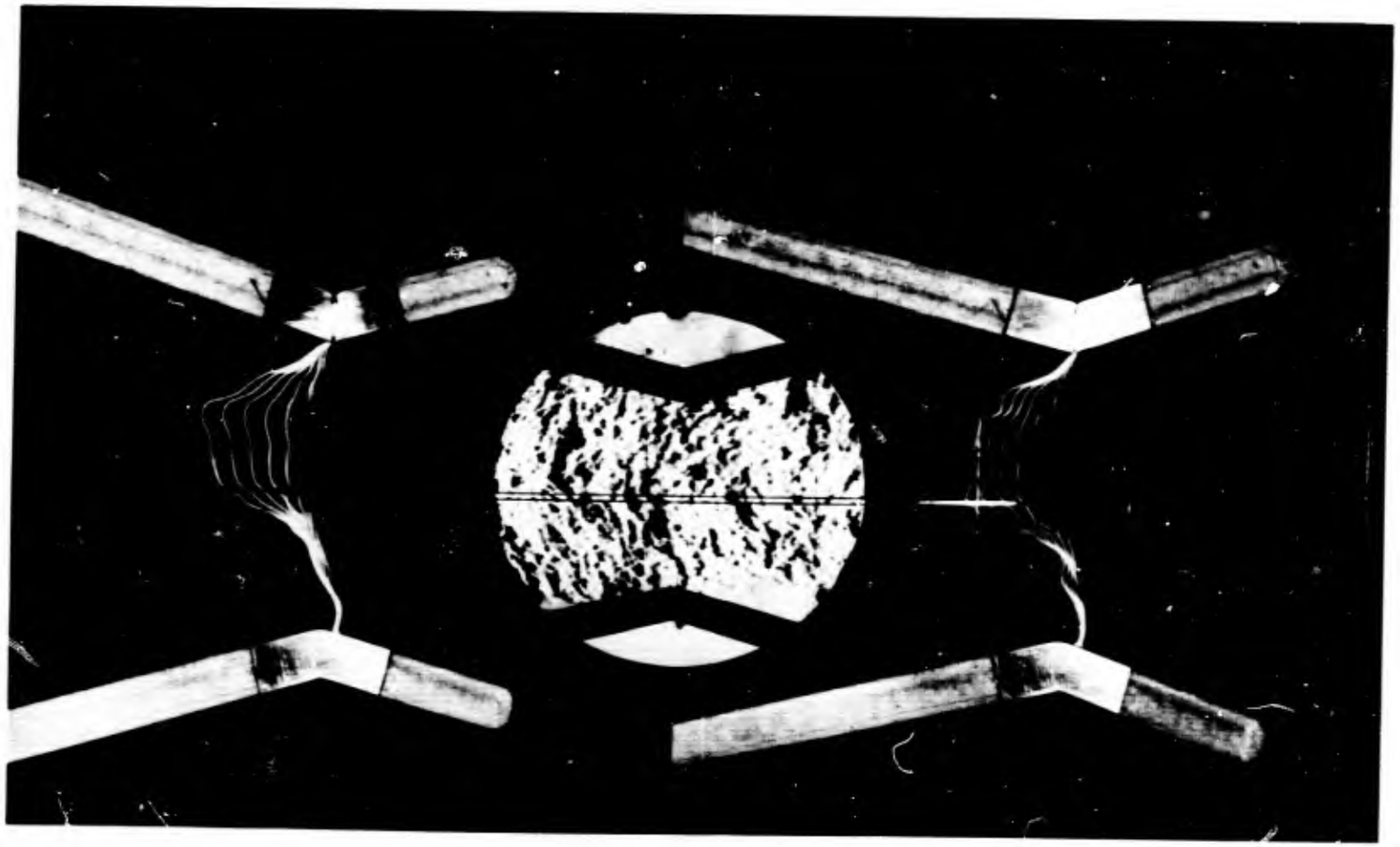

Fig. 1 Stereo photographs of a sequence of sparks together with a Schlieren photograph taken at the time of the fourth spark.
V_∞ = 14560 fps x/d = 600 body diameters
P = 40 mm Hg Pulse interval = 40 microseconds

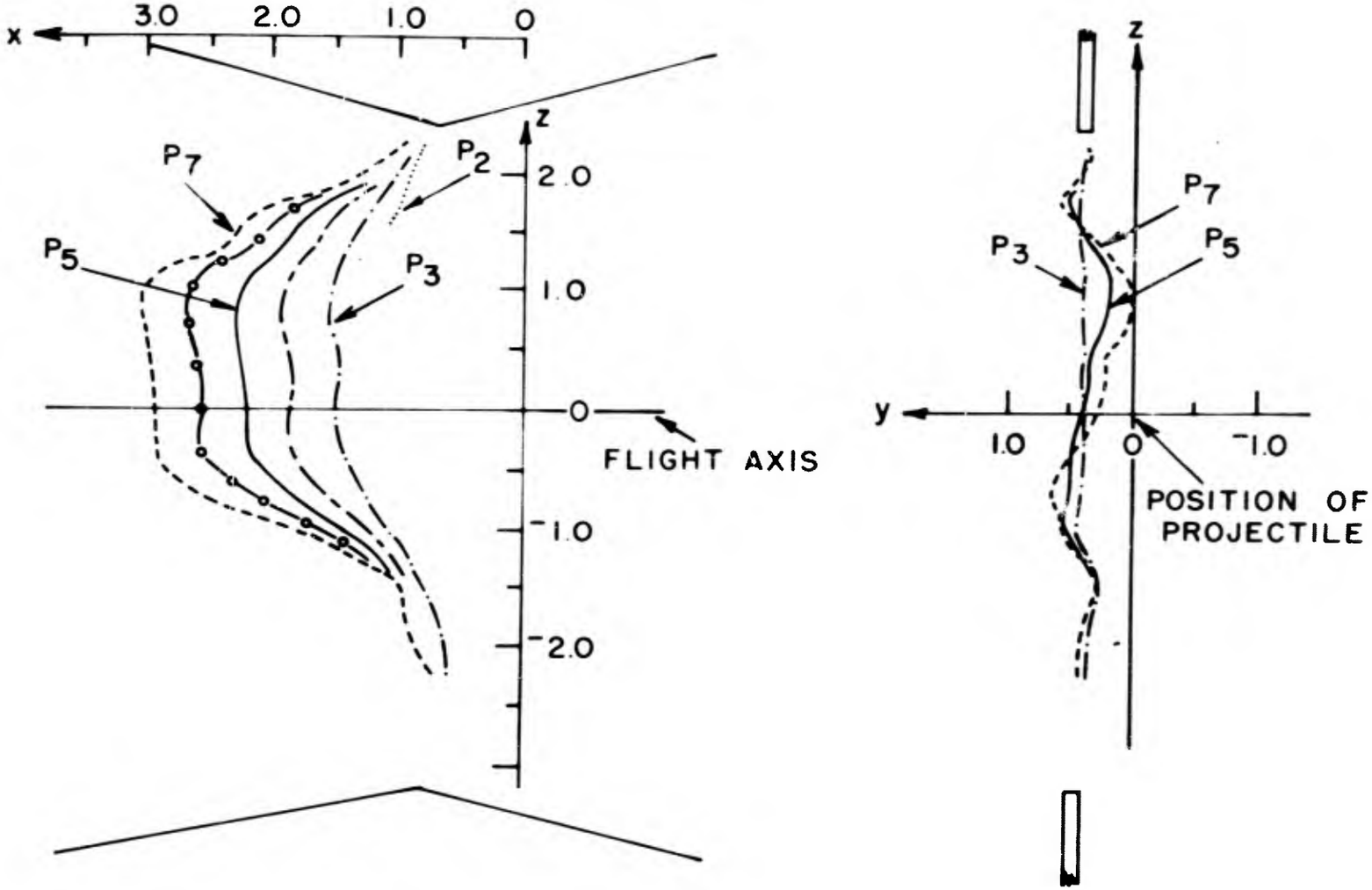

Fig. 2 Projections in the XZ and YZ Planes of the spark sequence shown in Figure 1

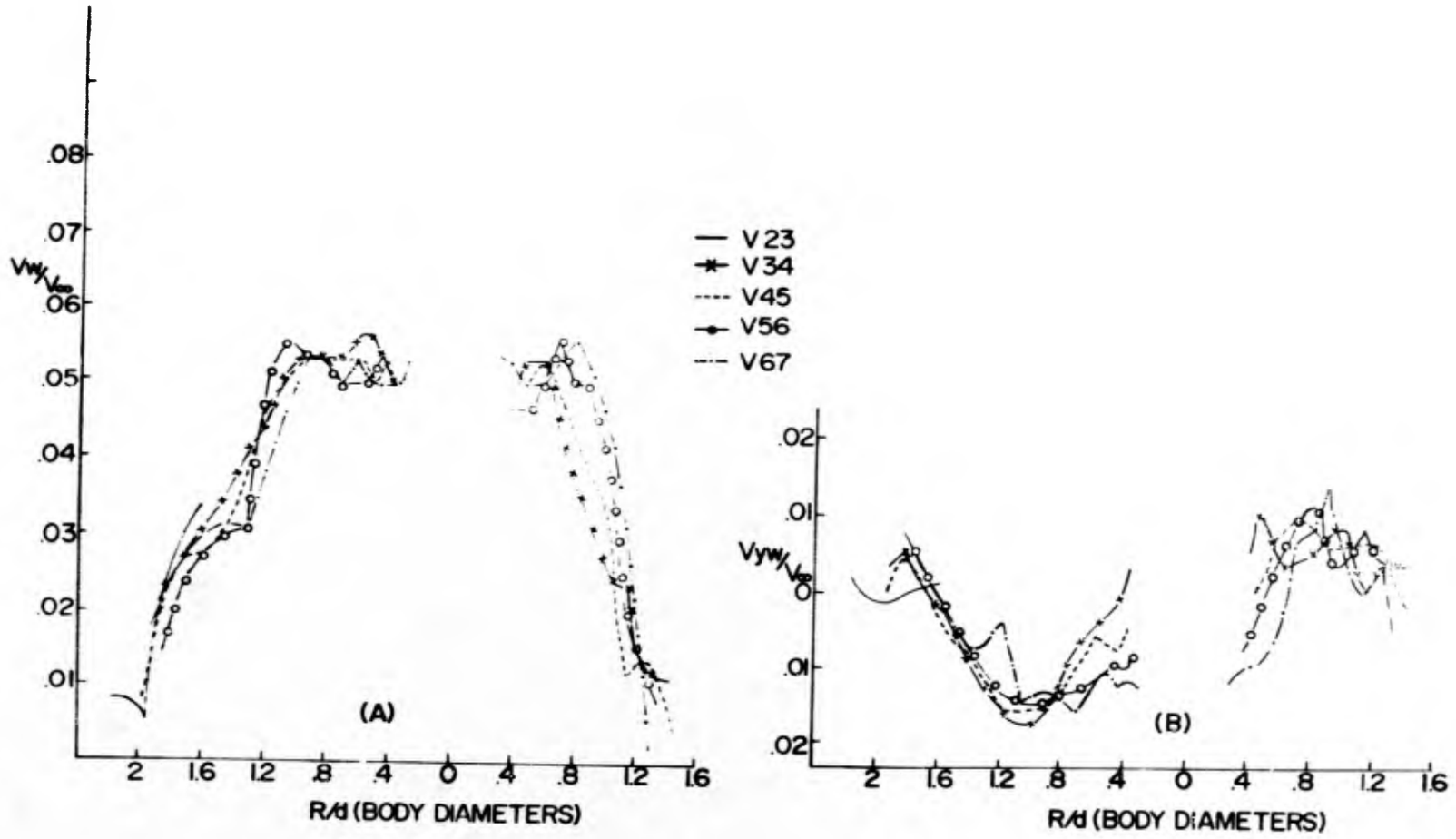

Fig. 3 Axial and lateral velocity profiles calculated from the projections of the sparks shown in Figure 2

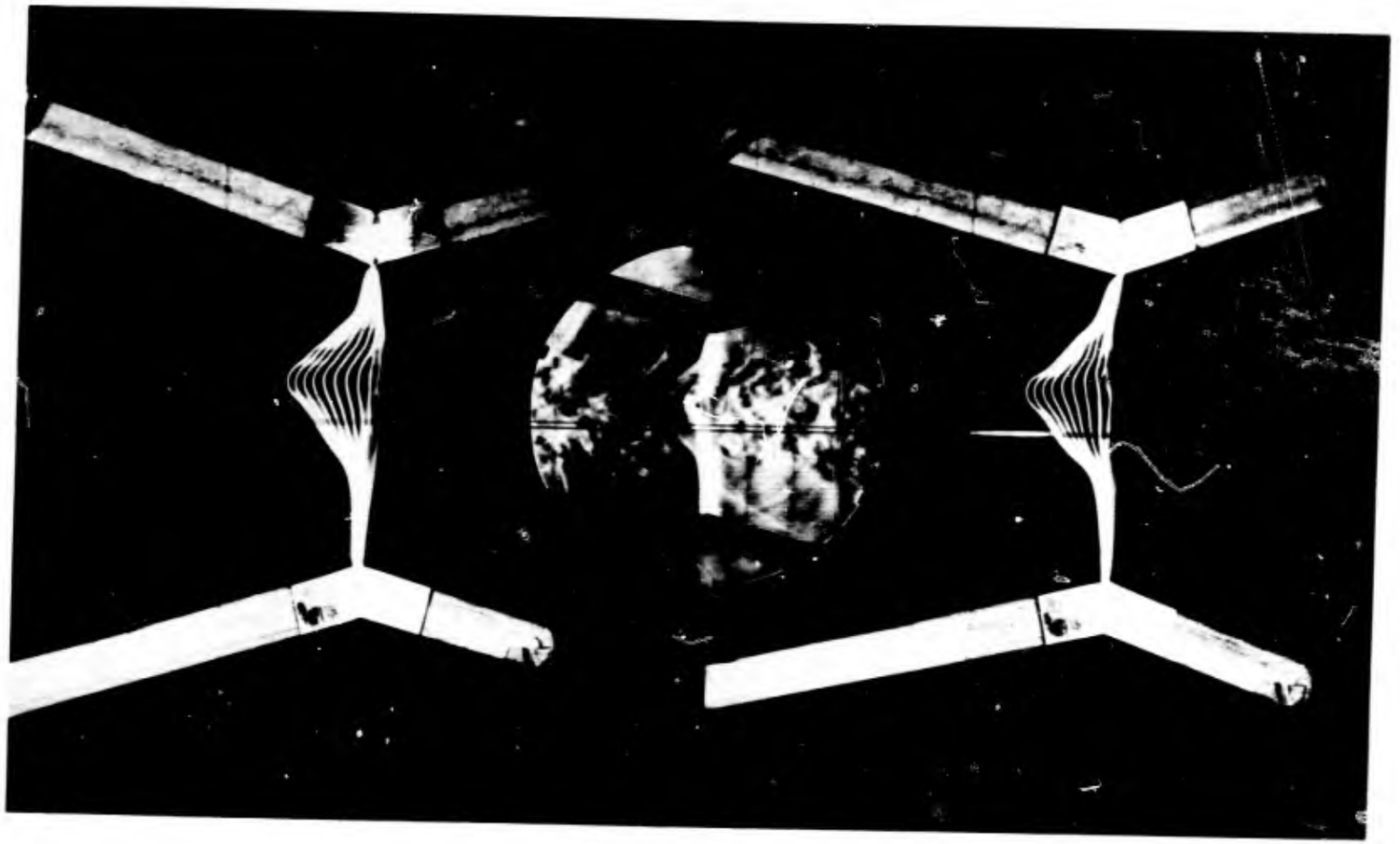

Fig. 4 Stereo photographs of a sequence of sparks together with a Schlieren photograph taken at the time of the fourth spark.
V_∞ = 4185 fps x/d = 300 body diameters
P_∞ = 40 mm Hg Pulse interval = 100 microseconds

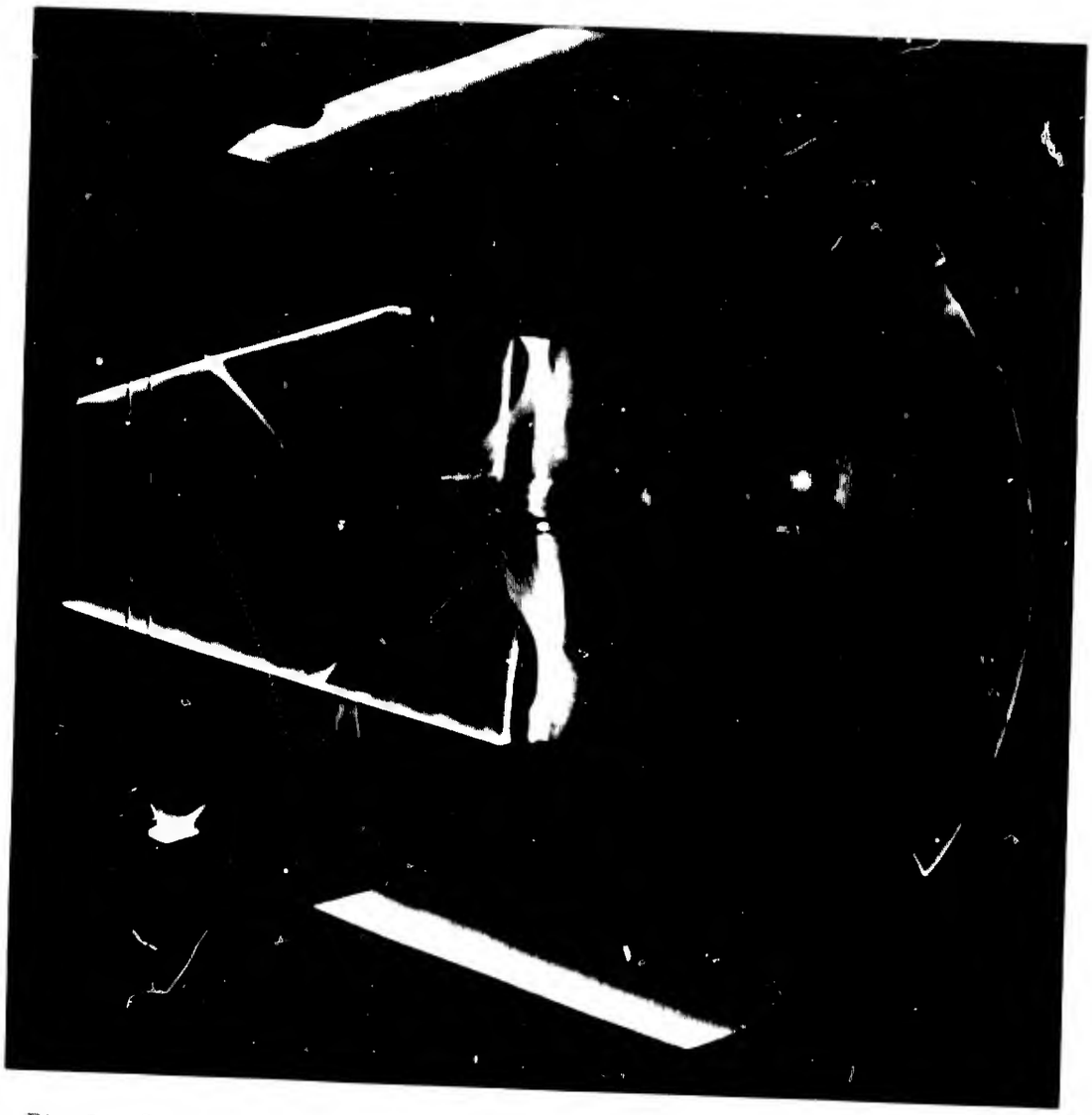

Fig. 5 Shadow photograph of the near wake also showing a sequence of sparks. The shadowgraph was taken at the time of the first spark

V_∞ = 3970 fps
P = 200 mm Hg
x/d = approximately 10 body diameters
Pulse interval = 20 microseconds

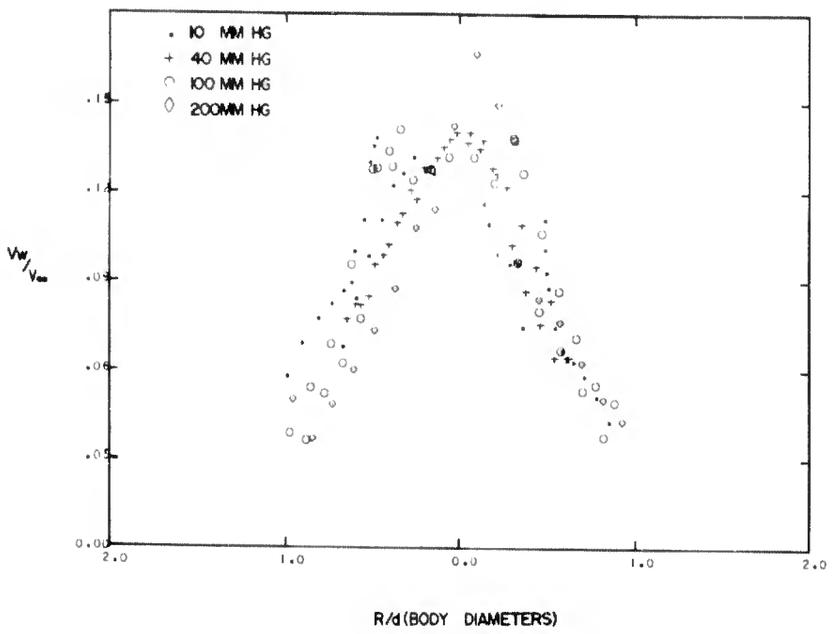

Fig. 6 Radial velocity profiles measured at a nominal axial distance of 15 body diameters at various pressures
V_∞ = approximately 4000 fps

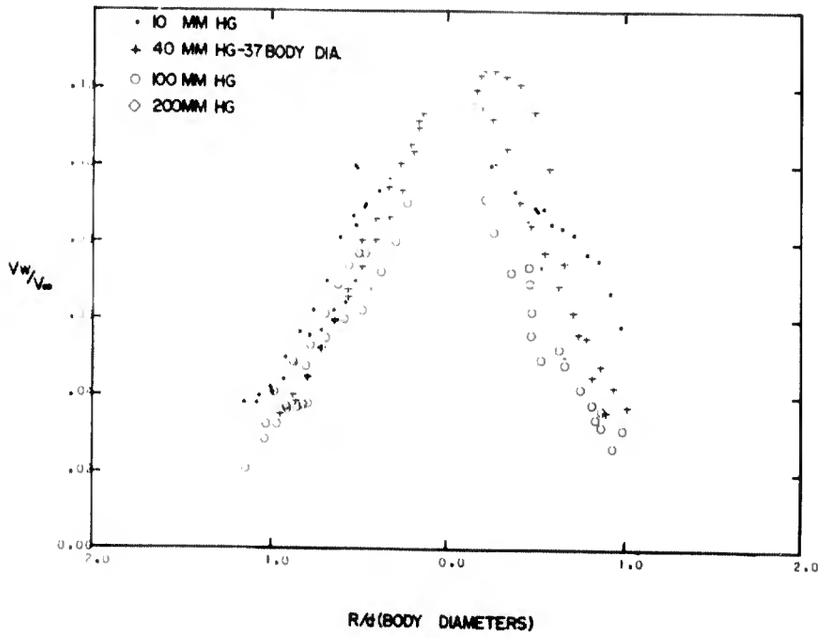

Fig. 7 Radial velocity profiles measured at a nominal axial distance of 50 body diameters at various pressures
V_∞ = approximately 4000 fps

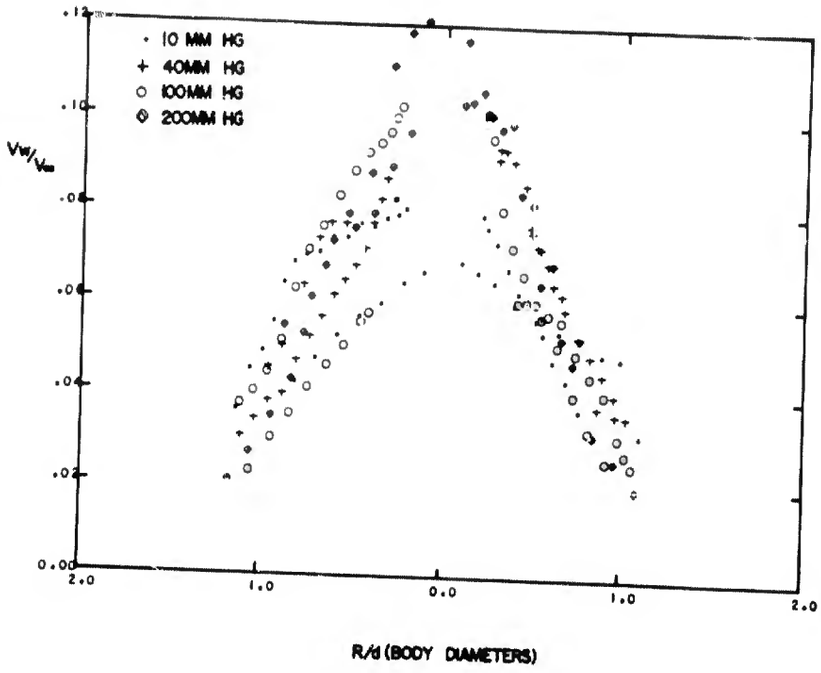

Fig.8 Radial velocity profiles measured at a nominal axial distance of 100 body diameters at various pressures
V_∞ = approximately 4000 fps

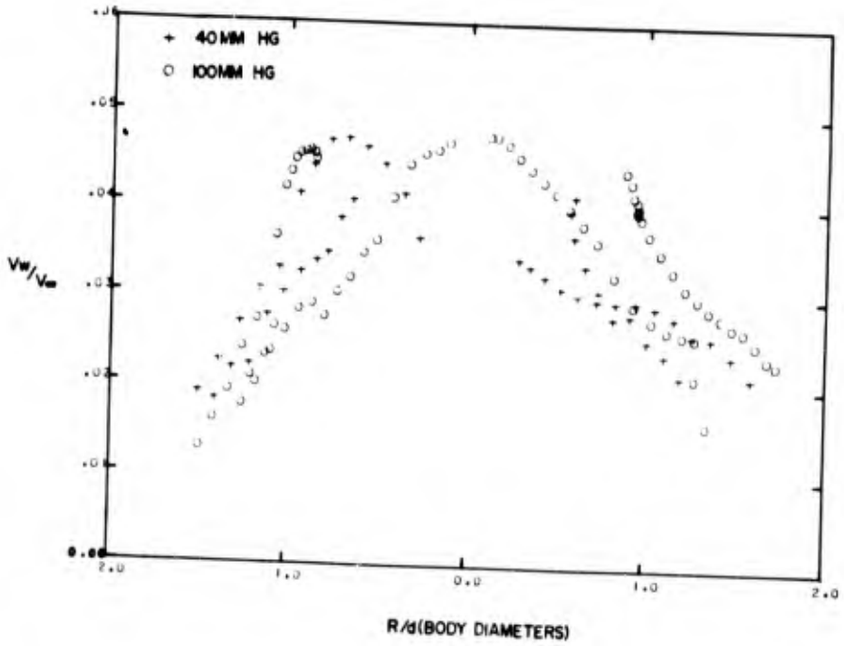

Fig.9 Radial velocity profiles measured at a nominal axial distance of 300 body diameters at various pressures
V_∞ = approximately 4000 fps

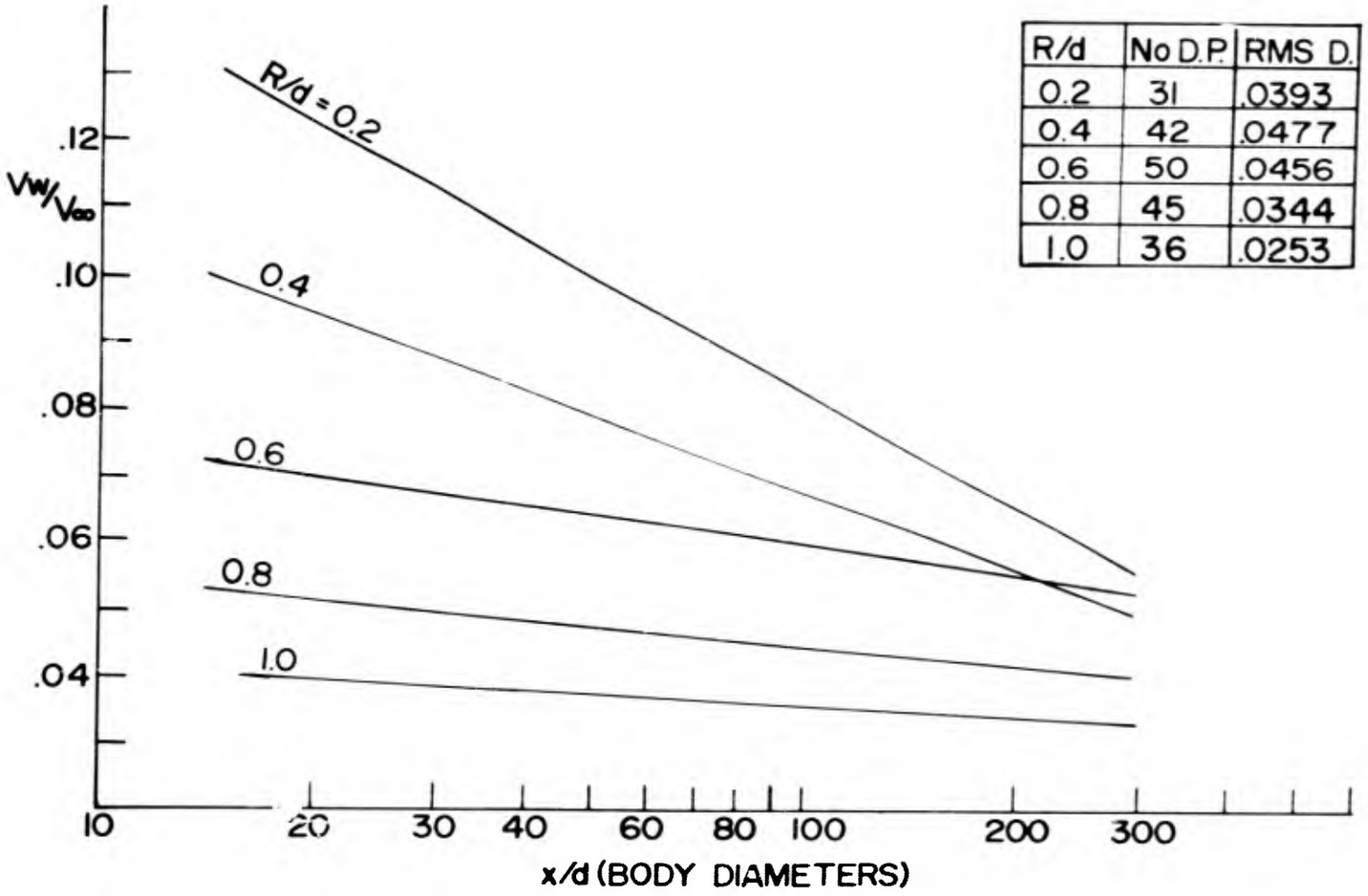

R/d	No D.P.	RMS D.
0.2	31	.0393
0.4	42	.0477
0.6	50	.0456
0.8	45	.0344
1.0	36	.0253

Fig. 10 Wake velocity distribution behind supersonic spheres
V_∞ = approximately 4000 fps
10 mm Hg < P < 200 mm Hg

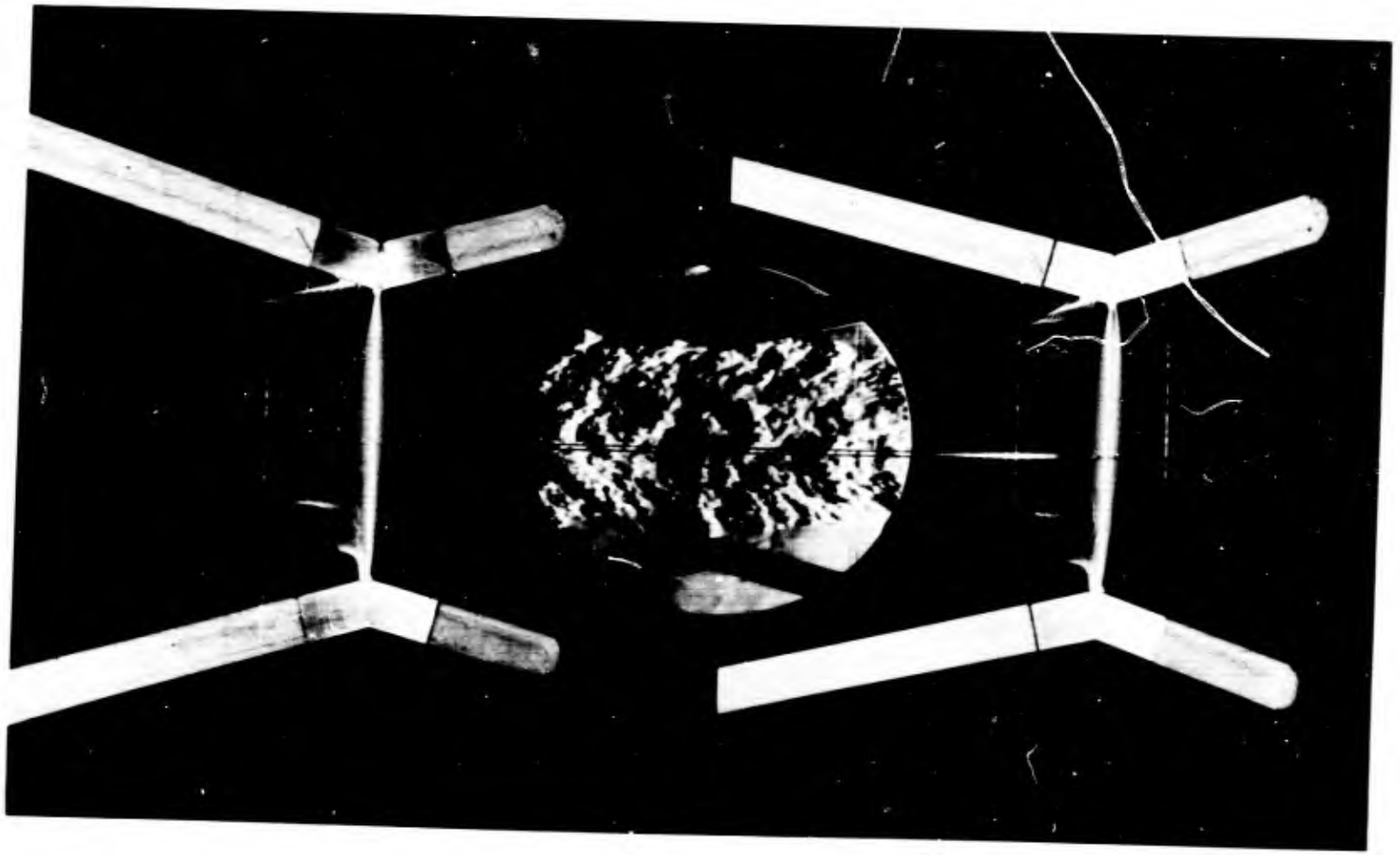

Fig. 11 Stereo photographs of a sequence of sparks together with a Schlieren photograph taken at the time of the fourth spark.
V_∞ = 14600 fps x/d = 300 body diameters
P_∞ = 40 mm Hg Pulse interval = 25 microseconds

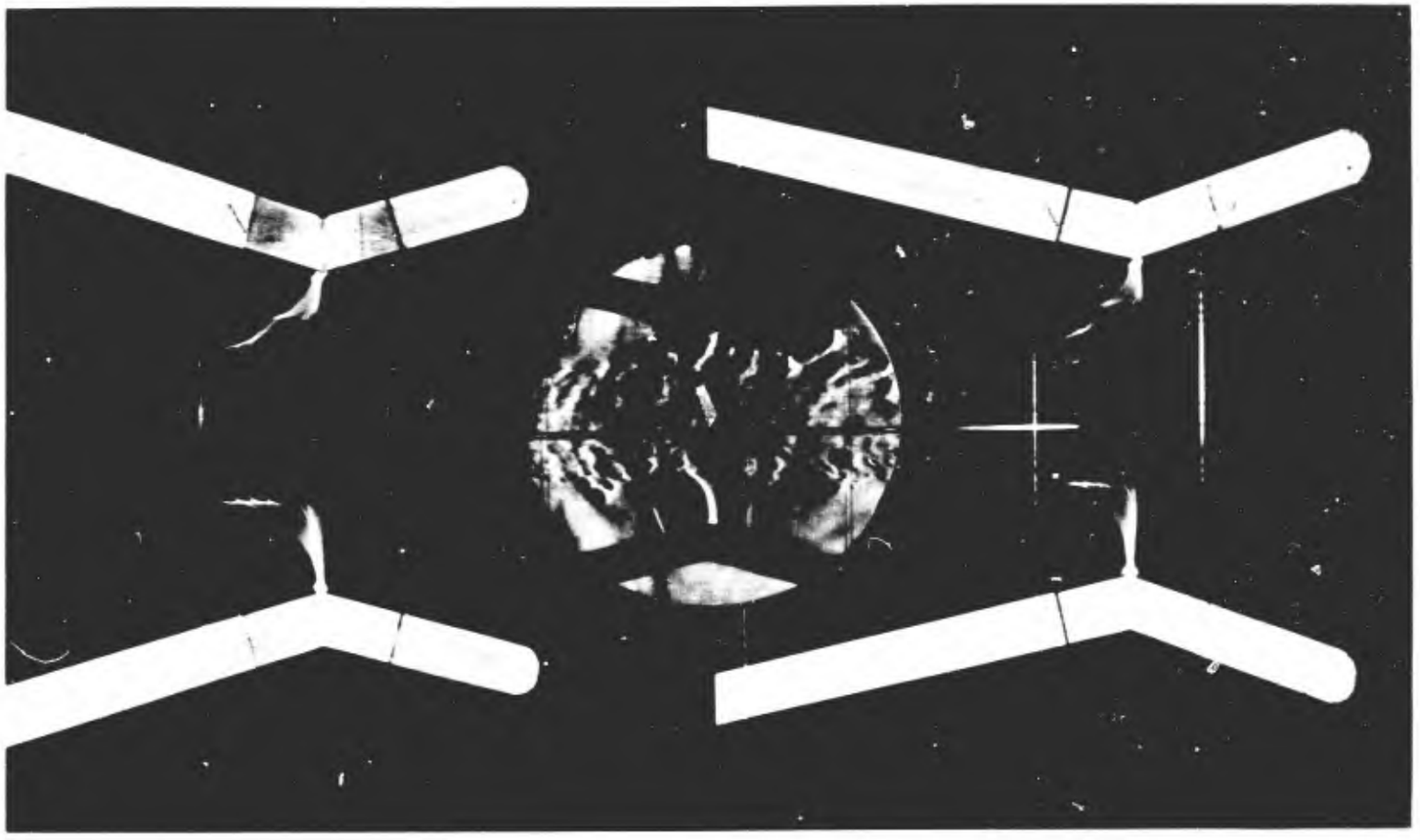

Fig. 12 Stereo photographs of a sequence of sparks together with a Schlieren photograph taken at the time of the fourth spark.
V_∞ = 14240 fps x/d = 140 body diameters
P_∞ = 76 mm Hg Pulse interval = 15 microseconds

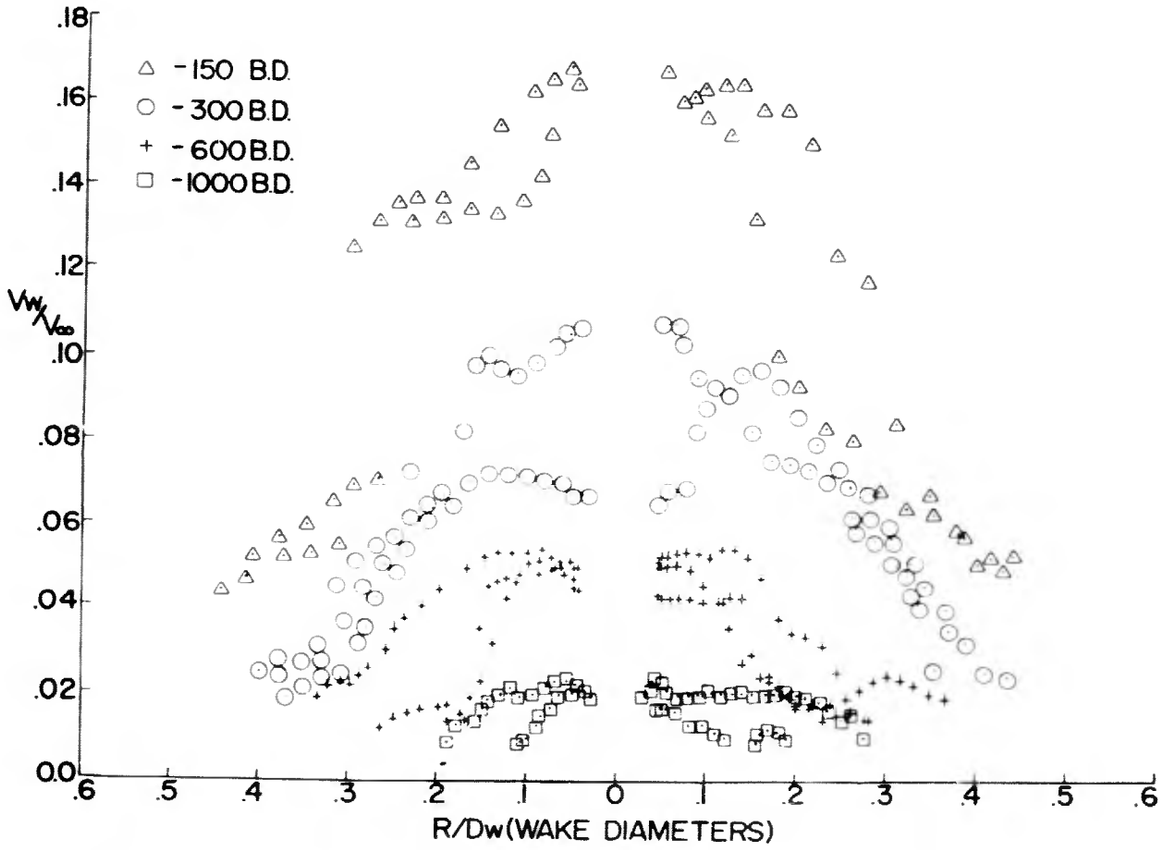

Fig. 13 Radial velocity profiles measured at a range pressure of 40 mm Hg as a function of radial distance normalized to the width of the viscous wake
V_∞ = approximately 14600 fps
At 150 B.D.,
V_∞ = approximately 13000 fps

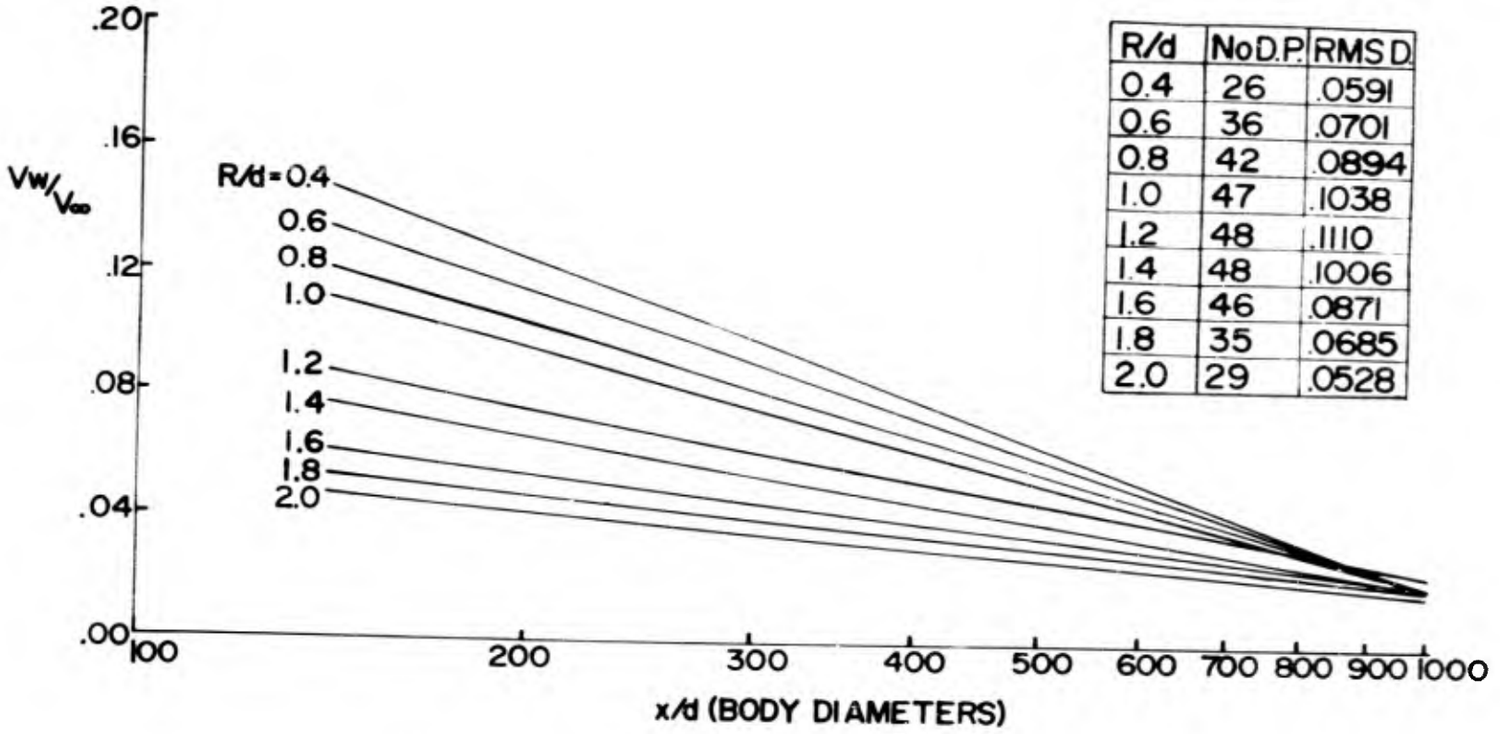

R/d	No D.P.	RMS D.
0.4	26	.0591
0.6	36	.0701
0.8	42	.0894
1.0	47	.1038
1.2	48	.1110
1.4	48	.1006
1.6	46	.0871
1.8	35	.0685
2.0	29	.0528

Fig. 14 Wake velocity distribution behind hypersonic spheres
V_∞ = approximately 14500 fps
26 mm Hg < P < 76 mm Hg

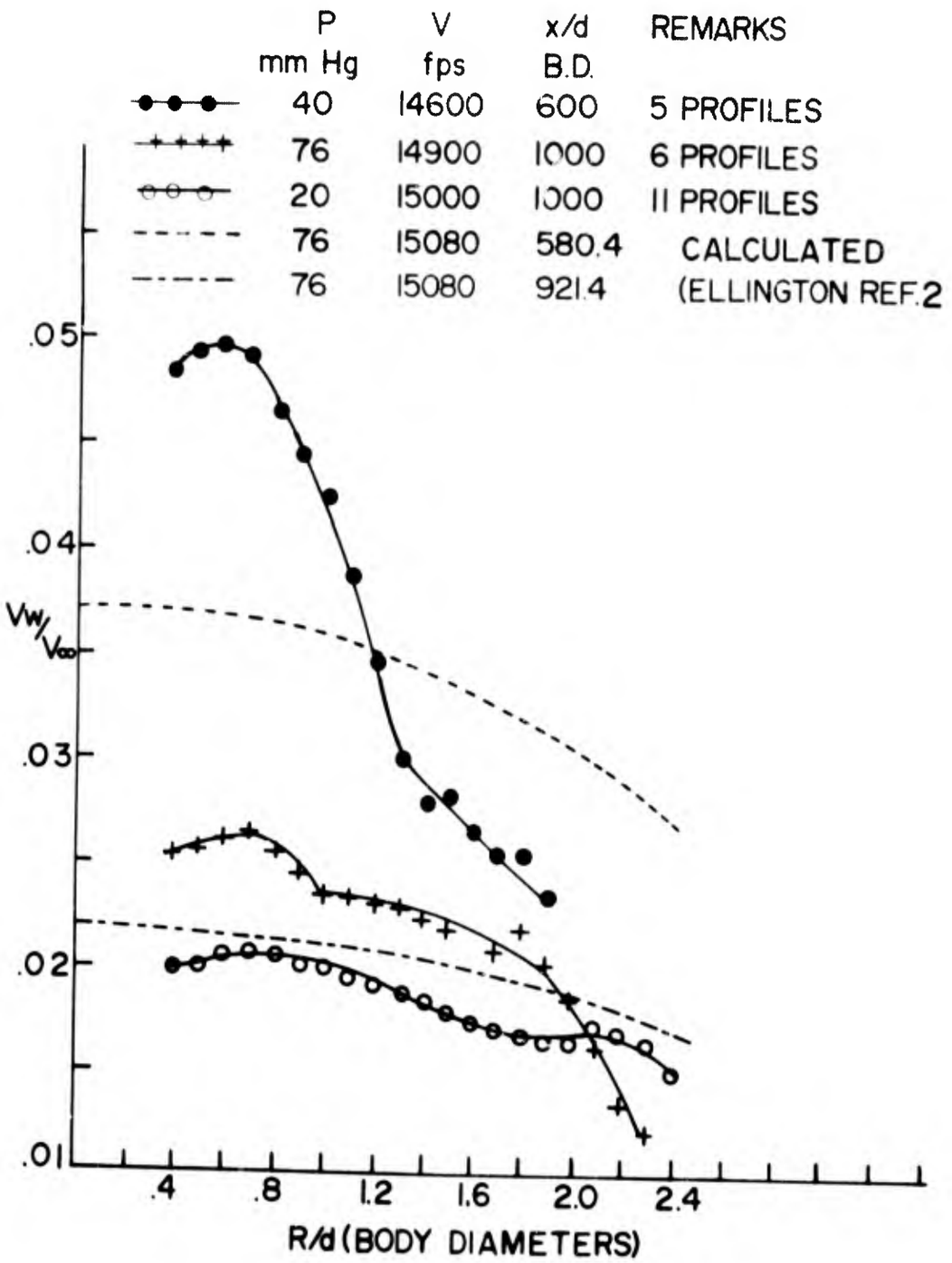

Fig. 15 Comparison of averaged velocity profiles with calculated profiles

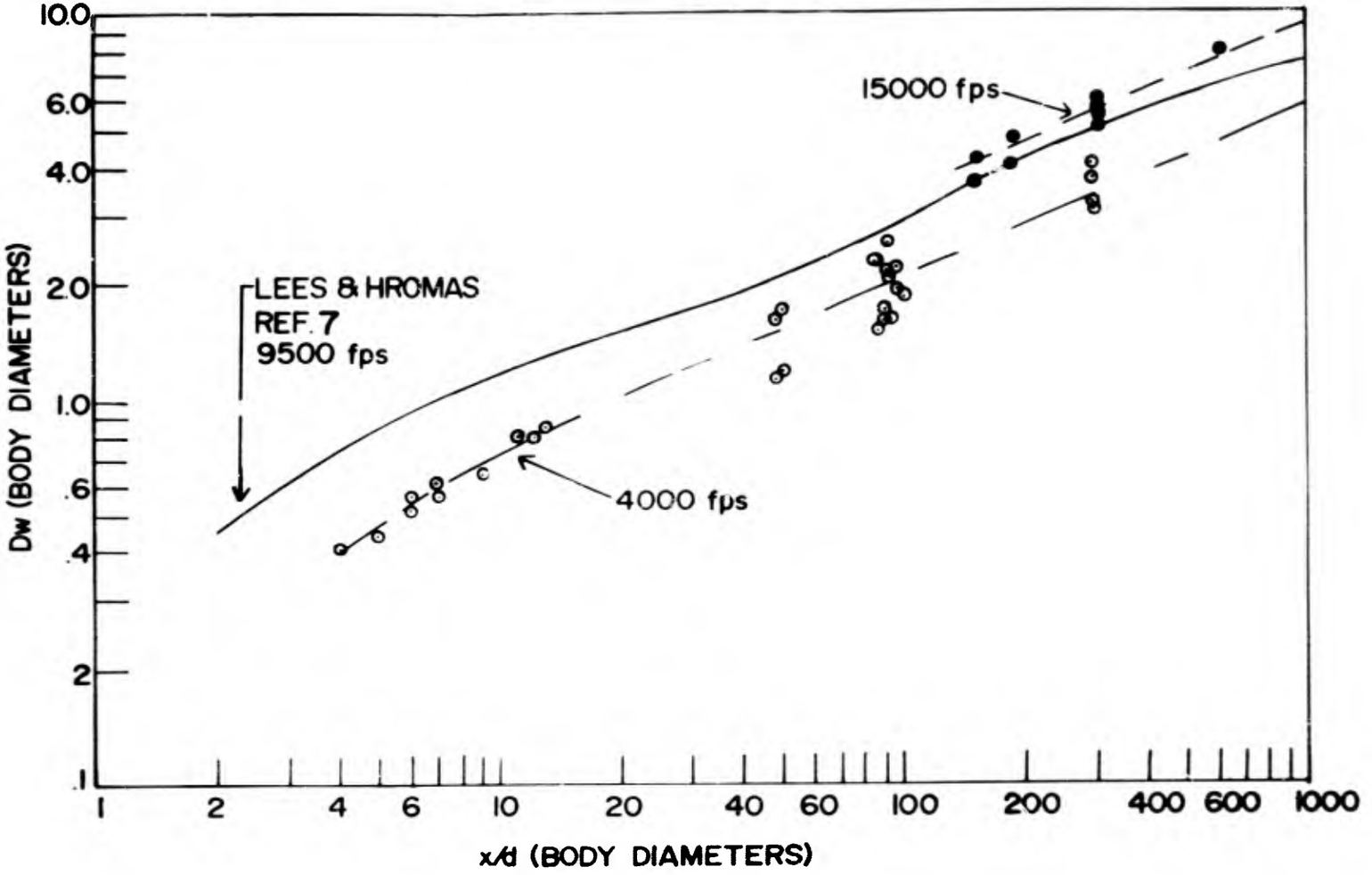

Fig. 16 Wake growth measured from Schlieren photographs at supersonic and hypersonic velocities

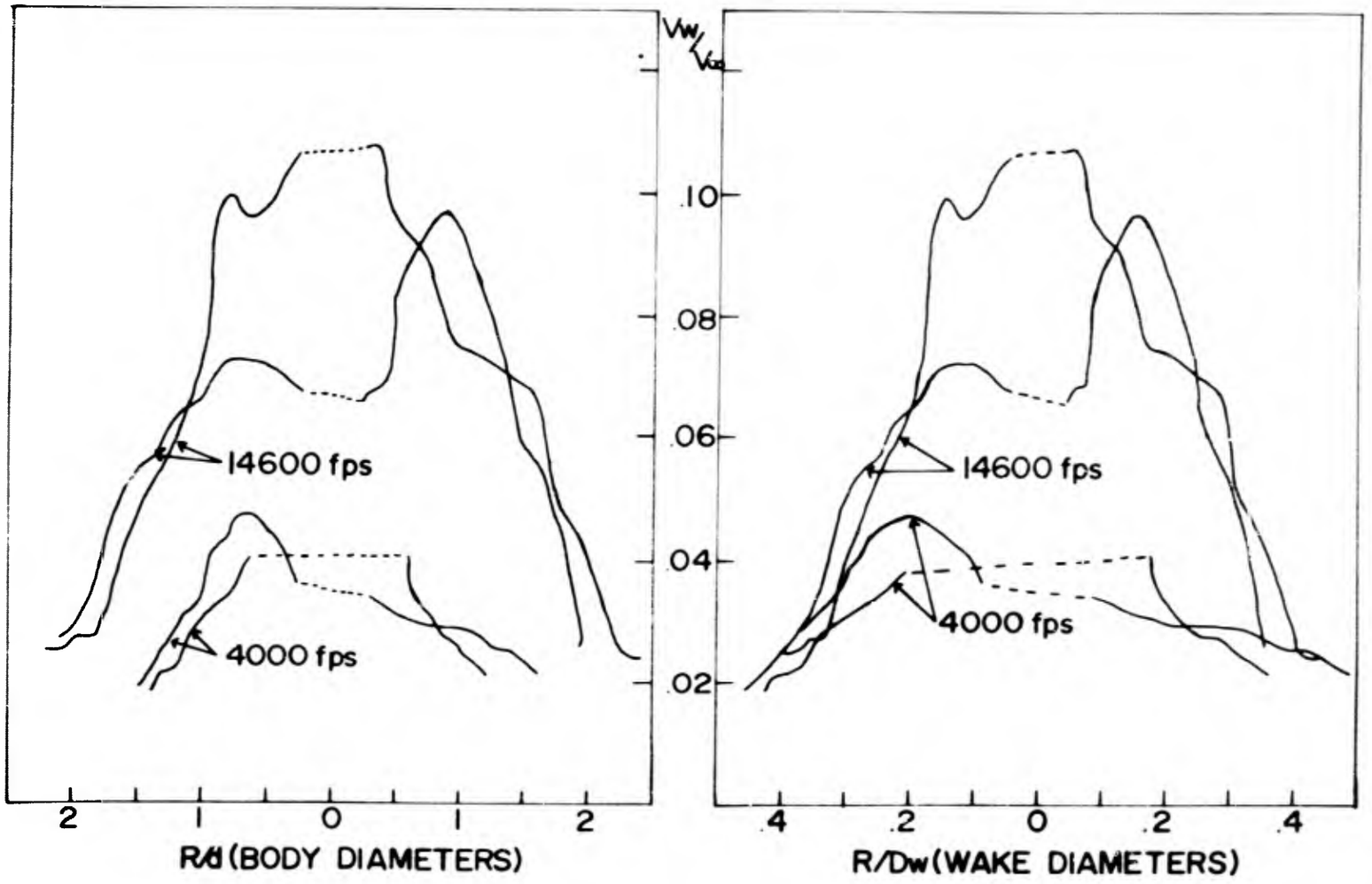

Fig. 17 Comparison of supersonic and hypersonic wake velocity profiles versus body and wake diameters

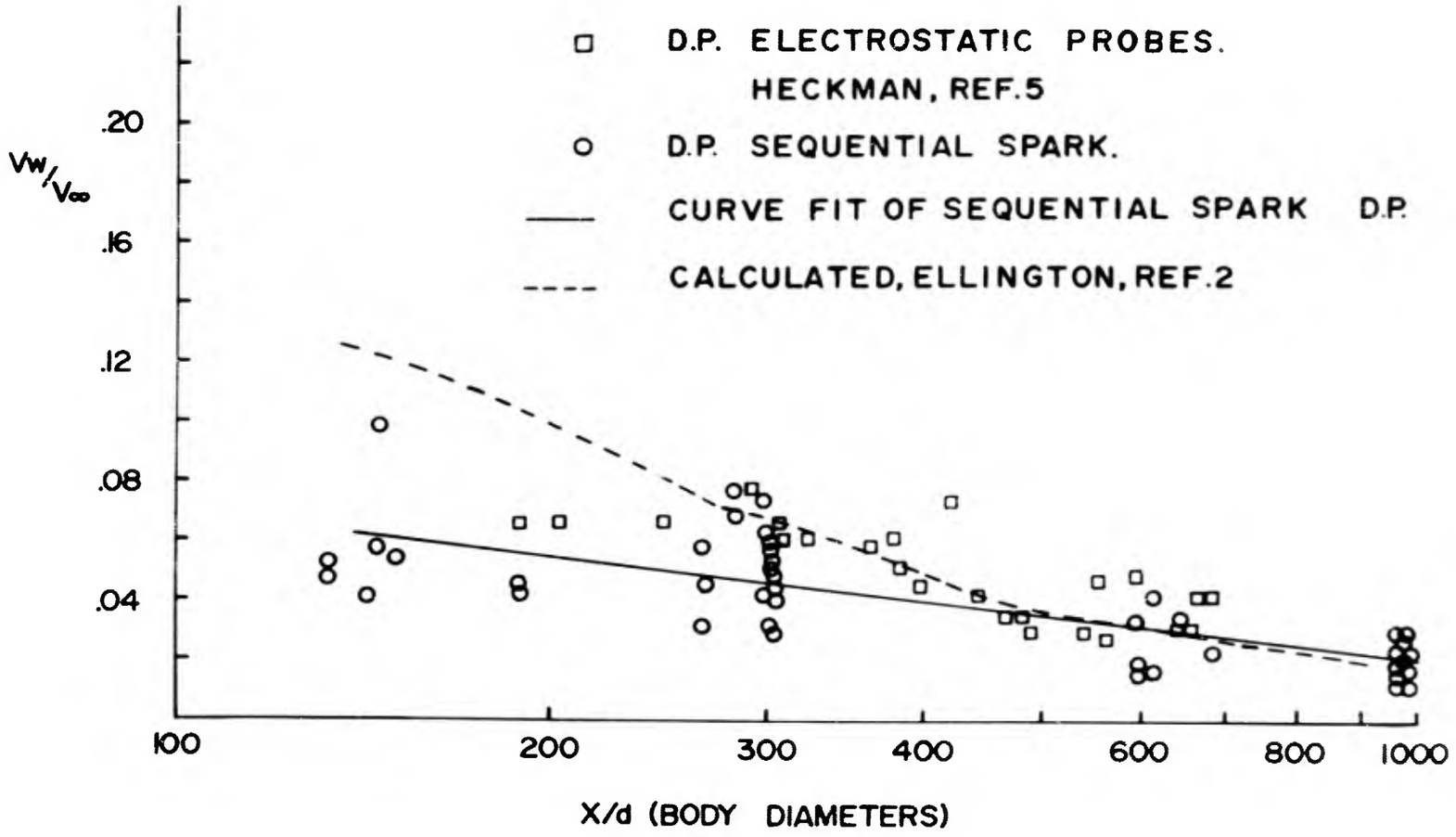

Fig. 18 Comparison of the velocity decay in the wake at a radial distance of 1.6 B.D. with the one obtained with conductivity probes and a calculated one

AN EXPERIMENTAL STUDY OF THE PRESSURE AND HEAT TRANSFER ON THE BASE OF CONES IN HYPERSONIC FLOW

by

E. J. Softley
B. C. Graber

Space Sciences Laboratory
General Electric Company
Valley Forge, Pa.

This work was done under the auspices of the Ballistic Missile Division, United States Air Force.

SUMMARY

Experimental measurements of the base pressure and heat transfer on flat based 9^{o} cones have been made. These measurements were made in a hypersonic shock tunnel. Free stream Mach numbers varied from 12.6 to 20. Independent variations of Reynolds number and wall temperature ratios were made at $M_{\infty} = 12.6$. Nose bluntness varied from "sharp" ($R_N/R_B < .005$) to $R_N/R_B = 0.3$. Only limited angle of attack effects were noted. In all cases the boundary layer on the cone surface was laminar.

Previous reports have described the techniques used. Advantage is taken of the pulse nature of the flow and the model is "free flown" during testing. Hence the biggest interference problem, that of a support sting, is eliminated. Trailing instrument leads of small diameter are run back through the wake flow, parallel to the free stream and away from the sensitive inner core of the wake. Early experiments verified the negligibility of these wires on the flow.

The experiments were hampered by the extreme low level signals typical of base measurements. Special instrumentation was developed for the study and this helped significantly when extending the parameters (particularly the Reynolds and Mach numbers).

Measurements were made in both a conical flow and parallel flow facilities. The basic difference observed was in the starting time of the wake flow. In the short conical nozzle with a model size of 2" base diameter wake flows were steady in approximately 1 millisecond. In the 22" long parallel flow nozzle with a $4\frac{1}{2}$" base diameter model the flows took 4 milliseconds to become steady. On the 2" model only two measurements were made per model. On a larger model 7 position data was obtained. The latest series provides for data at 12 positions on the cone and base surfaces.

The base pressure measurements are in general agreement with the flow field measurements of the electron beam. The extreme effects near the corner support the arguments of Weinbaum that the profiles of viscous flow at separations from the body (where it becomes the free shear layer) cannot be calculated using boundary-layer assumptions (i.e., no cross flow component).

Indeed the effect of Reynolds number on pressure distributions on the base near the corner suggests that the separation streamline does not leave the base at the corner but from a point on the base and the

distance of this point from the corner increases as the cone boundary layer thickness increases. This is an important point of Weinbaum's paper.

The heat transfer has been correlated with the flow temperature measurements of Muntz. The heat transfer rates follow the wall temperature variation shown in the temperature measurements. The Reynolds number effect on the heat flux opposes that on the recirculation flow enthalpies and the difference is attributed to changes in the other recirculating flow properties. (P, U, etc.)

RESUME

On a procédé à des mesures expérimentales de la pression de culot et du transfert de chaleur sur des cônes de 9^{o} à partie postérieure plate. Ces mesures furent effectuées dans un tunnel à choc hypersonique. Les nombres de Mach en écoulement libre variaient de 12,6 à 20. On a fait varier, indépendamment les rapports du nombre de Reynolds et de la témperature des parois à Mach = 12,6. La forme de la partie antérieure du cône allait d'un aspect effilé ($R_N/R_B < .005$) a $R_N/R_B = 0.3$. Seuls des effets limités de l'angle d'attaque furent observés. Dans tous les cas, la couche limite sur la surface du cône était laminaire.

Les techniques utilisées ont été décrites au cours de précédents rapports. On met à profit la nature "à impulsions" de l'écoulement et, pendant l'essai, la maquette est lâchée en vol libre. On élimine ainsi le problème d'interférence le plus important, celui du montage sur dard. On fait remonter à travers l'écoulement du sillage, suivant une trajectoire parallèle à l'écoulement libre et éloignée de la partie centrale sensible du sillage, des fils de raccordement aux instruments, flottant librement, et de faible diamètre. Des expériences précédentes ont démontré que l'influence de ces fils sur l'écoulement était négligeable.

Les signaux de niveau extrêmement faible, caractéristiques des mesures effectuées sur les bases de cônes, entravaient la conduite des expériences. On a donc mis au point, pour cette étude, des instruments de conception spéciale, ce qui a facilité dans une large mesure l'extension des paramètres (en particulier les nombres de Mach et de Reynolds).

Des mesures furent effectuées à la fois dans des installations à écoulement conique et à écoulement parallèle. La différence essentielle que l'on put observer portait sur le temps de démarrage de l'écoulement du sillage. Dans la courte tuyère conique, avec une maquette dont la base mesurait 2 pouces de diamètre les écoulements du sillage se stabilisèrent au bout d'environ une milliseconde. Dans la tuyère de 22 pieds, à courant parallèle, avec une maquette de 4 pouces et demi de diamètre à la base, il fallut 4 millisecondes aux écoulementes pour se stabiliser. Sur la maquette de 2 pouces, on procéda seulement à deux mesures par maquette. Sur une maquette de dimensions plus importantes, on recueillit des résultats en 7 emplacements. La série la plus récente permet d'obtenir des données en 12 endroits sur la surface du cône et de sa partie postérieure.

Les mesures de la pression de culot concordent de façon générale avec les mesures du champ d'écoulement effectuées à l'aide du rayon

d'électrons. Les effets extrêmes se faisant sentir au voisinage de l'angle viennent appuyer la thèse de Weinbaum selon laquelle les profils d'un écoulement visqueux aux points où celui-ci se sépare du corps (et où il se transforme en couche de cisaillement libre) ne peuvent être calculés à l'aide des hypothèses portant sur la couche limite (il n'y a pas, de composante transversal du courant).

En effet, l'influence du nombre de Reynolds sur les répartitions des pressions sur la base du cône, au voisinage de l'angle, suggère que la ligne de courant issue du point de décollement ne s'éloigne pas de la base à partir de l'angle, mais à partir d'un point sur cette base dont la distance avec l'angle augmente au fur et à mesure que la couche limite du cône s'épaissit. Cette observation constitue l'un des points importants de la communication de Weinbaum.

On a comparé le transfert de chaleur aux mesures des températures d'écoulement de Muntz. Le taux de transfert de chaleur suivent les variations de température des parois, variations indiquées par les mesures. L'influence du nombre de Reynolds sur le flux de chaleur s'oppose à celle qui affecte les enthalpies du courant de recirculation; la différence est attribuée aux modifications des autres caractéristiques du courant de recirculation.

Symbols

M_∞		Free Stream Mach Number
h_R	(Btu/lb)	Recovery Enthalpy
h_W	(Btu/lb)	Wall Enthalpy
$P_b(r_B)$	(lb/in^2)	Base Pressure at Radius r_B
P_S	(lb/in^2)	Stagnation Pressure (As read by stagnation probe)
P_5	(lb/in^2)	Reflected Region Pressure (Plenum Pressure)
$P_{\infty B}$	(lb/in^2)	Static Pressure at Location of Base of Model
$\dot{q}(r_B)$	($Btu/ft^2 sec$)	Heat Transfer Rate on Base at Radius r_B
$\dot{Q}_B$	(Btu/sec)	Total Base Heat Transfer Rate
$\dot{Q}_W$	(Btu/sec)	Total Cone Surface Heat Transfer Rate
r_B	(in.)	Radius On Base of Model
R_B	(in.)	Model Base Radius
R_N	(in.)	Nose Radius
R_W	(in.)	Support Wire Radius
Re/ft	(1/ft)	Reynolds Number per ft.
$Re_{\infty L}$		Reynolds Number Based on Free Stream Conditions and Wetted Length
T_0, T_5	(^oK)	Stagnation Temperature in Free Stream
T_W	(^oK)	Wall Temperature

1. Introduction

Measurements of pressure and heat transfer on the surfaces of bodies in the hypersonic flow produced in ground simulation facilities is usually aided by the existence of definite cones of influence in the flow fields. This makes it possible to use strong supports for the model, arranged suitably, so that no effects from the support influence the flow near the body surface. Whilst this simple visualization of the situation is not exactly true, since there is usually a subsonic region in the boundary layer through which disturbances can feed, it is good enough that, with care, reasonable experimental measurements can be made.

If the flow behind the body however, is considered, this simplification does not exist. Fig. 1 shows a typical, assumed flow pattern in the "near wake" region. For the purposes of this report the near wake is defined as that region of the wake flow across which there is some region of subsonic flow. It is apparent therefore that a sting or other significantly sized support may easily affect the flow across the base of the body. It is therefore desirable to eliminate or minimize any source of disturbance in the near wake region when making measurements on the base of the body.

Several approaches have been used in various facilities. A free flying model with data telemetered from the model will result in

complete freedom from support interference. A modification of this, using trailing wires to transmit the signal was used initially to obtain base measurements. Measurements with larger models have used fine support wires together with the trailing wires.

In support of a study of near wakes data have been obtained on base pressure and heat transfer using the latter two techniques above. This data has been accumulated in three series of measurements.

The experimental details are briefly described here. A more complete description showing tables of the flow conditions and with a thorough analysis of the instrumentation is given in Softley and Graber (1).

2. Facilities, Models and Supports, Instrumentation

2.1 6"/30" Shock Tunnel

This facility has been adequately described in earlier publications. It is useful to note here that a six inch diameter shock tube is fitted with a convergent-divergent conical nozzle of 15^{o} 1/2 angle and 30" exit diameter. The result is a facility where test conditions vary considerably along the axis. Fig. 4 shows the Mach number gradient along the axis of the nozzle.

2.2 Parallel Flow Conversion - 6"/54" Shock Tunnel

To allow larger models and remove the problem of severe axial gradients of the flow properties and their effect on hypersonic flows, a contoured nozzle was designed and fabricated. This is approximately

22 ft. long and with a 54 inch exit diameter. Fig. 2 shows a sketch of the facility. The nozzle was designed for an exit Mach number of 20 and has been operated off-design over a range of conditions, using different throats, as low as $M_\infty = 12$. Fig. 4 shows the center line Mach number variation for two flow conditions.

An important feature of this long nozzle is the time to form the flow. There is a considerable time delay in establishing flow from two causes; the time for the flow to travel the length of the nozzle, called the transit time, and the time for the boundary layer to develop on the nozzle walls. In computing flow conditions at any part in time it is important to relate to the right instant on the P_5 (plenum pressure) trace. The transit time is calculated for each run and each instant of time for which data is required by integrating over the velocity along the center line of the nozzle from the throat to the exit. Fig. 7 shows the time variations of P_{s/P_5} and the calculated transit time for a typical run.

2.3 Models and Supports

The models for the conical nozzle tests were 10^o, 1/2-angle cones of 2" base diameter. Nose radius ratio R_{N/R_B} were .03 and .30. Pressure measurements were made at the center of the base and used one trailing wire (see Fig. 1) of .030 inch diameter. The model support consisted of fine threads of .001 to .002 inch diameter. For the higher density conditions these threads were swept away with the

initial flow such that the model was "free flying" during the time of measurement with the threads outside the flow field. This latter fact was checked by photography. For the lower density conditions the flow density was too low for the threads to break and they remained intact. The heat transfer measurements were similar except that up to three gauge locations on the model were used with up to six trailing wires (of .020 inch diameter).

For the contoured model tests larger models were used. For one series of tests a 9^{o}, 1/2-angle cone of 4 1/2 inch diameter was used with a distribution of pressure taps across the base. Due to internal vibrations in the model influencing the gauge output few satisfactory measurements were obtained with this model. However, experience with this led to the model shown in Fig. 3. This has a thick base plate isolated from shock from the forward section by a thick rubber section. The forward section was approximately 6 pounds weight to minimize acceleration correction to the measured pressures. The gauge locations for the pressure measurements are also shown in Fig. 3. For the heat transfer measurements the gauges were similarly located. Of 12 locations six were used for any one run with six trailing wires of .030 diameter.

The support wires for these larger models were .016 inch diameter maximum. These wires were present for all measurements

as the sophistication of the model precluded allowing the model to fall after the tests.

2.4 Instrumentation

Pressure and heat transfer measurements on the base of cones in hypersonic shock tunnels have some awkward characteristics. The transducers must be located in the tunnel, away from subsequent amplifiers and must measure very low level quantities. The result is low signal levels together with high noise and spurious signal pick-up. To help overcome these difficulties all instrumentation uses a primary amplifier located in the vicinity of the transducer (i.e. in the model) with the amplified signal transmitted to further amplifiers outside the tunnel.

A detailed description of the instrumentation is given in reference 1. The pressure measurements were obtained with piezo-electric type transducers and with field effect transistor (F.E.T.) and the newer insulated gate F.E.T. amplifiers. The heat gauges were painted thin films on quartz substrates and used constant voltage transistor amplifiers. For telemetry specially built frequency modulated transmitters were used with commercial receivers.

3. Base Measurements

3.1 Effect of Trailing Wires and Support Wires

Before any discussion of the base data obtained in the study the

effect of the wires that are present in the flow field should be considered. It was clear that these should be kept as small as possible and their sizes have been noted throughout the earlier description.

The location of the trailing wires was chosen to minimize their influence on the flow field. By aligning them with the axis of the overall flow system the normal velocity component of any incident flow was kept small. By keeping them close to the outer rim of the base the wires were kept as remote as possible from the neck of the wake.

Some experiments were made as a check on any effect from the trailing wires. Data was obtained on base heat transfer while the number of wires was reduced from 6 to 4 to 2 and finally, using telemetry, to zero. The result is included in Fig. 5. Within the accuracy of the experiment no change in base heat transfer (at the center of the base) was observed.

In addition some local densities were measured using the electron beam excitation technique of Muntz (2) with and without trailing wires from the model. Here again, within the accuracy of the experiment, no change in density was observed.

It is interesting to observe that the "compression strut" technique of Martellucci and Ranlet (5) has very similar geometry (with somewhat larger components) and their conclusion also is that these struts give minimal interference to the flow.

The other wires present are support wires. For the 2" base diameter model these, when present, were .002 inch diameter. Cresci and Zackay (6) introduced as a parameter the ratio of the support wire size to model base size or R_W/R_B. Their conclusion was that for $R_W/R_B < .006$ no measureable off axis change in the flow could be observed. For the conical flow tests $R_W/R_B = .001$ and for the worst case, the 5 inch base diameter model with .016 inch wires $R_W/R_B \sim .003$. Todisco and Pallone (7) observed no change in stagnation temperatures when R_W/R_B was increased from .005 to .0075. In a more recent paper (8) these authors reported the effect of wire size on pressure measurements in the near wake and concluded for $R_W/R_B < .0083$ these pressures were unchanged by the presence of the wire. Dayman (9) observed, optically, a definite change in near wake characteristics due to the presence of support wires. However this was for $R_W/R_B \sim .027$ and with "tags" on the wire. Dayman's results do not appear to disagree with those of Cresci and Zackay. Note that R_W/R_B is only a useful parameter in these remarks because the flow conditions, in particular local densities, are very similar from tunnel to tunnel.

The conclusion drawn is that while a complete definitive study of the effect of support wires is not available all evidence indicates that for $R_W/R_B \sim .003$, as used in the present work, any influence of support wires is lost in the results of the experimental data.

3.2 Flow Formation Time and Stability

A critical feature of studies in hypersonic shock tunnels is the short time period available for measurement. With the conical nozzle, approximately 3 feet in length, the time to establish nozzle flow was quite short (i.e. considerably less than one millisecond). The wake flows, with 2 inch base diameter models, also established quite quickly. Fig. 6 shows traces and time resolution of the non-dimensional base pressure while Fig. 5 shows time resolution of the non-dimensionalized heat transfer. It is apparent that the wake flows are quasi-steady after approximately 1 1/2 milliseconds and continues until at least 5 milliseconds after flow establishment.

The flows in the contoured nozzle were somewhat different. Fig. 7 shows time resolved data for a stagnation probe in the free stream, the cone pressure and a base pressure location. As can be seen the establishment of the free stream flow takes considerably longer than in the conical nozzle. Moreover the base flow indicates a definite ending of the quasi-steady flow about 5 milliseconds after initial flow establishment (or approximately 8 milliseconds after P_5). It should be noted that a few runs were made when a quasi-steady base flow was not established, consequently no data was obtained from these runs. It can also be observed that for quasi-steady wake flow the wake formation time is absorbed with the formation of the free stream. No additional time was needed.

3.3 Base Pressure Results

Base pressure data, including profiles across the base and on to the rear of the cone surface, has been obtained for 9 and 10° cones and for bluntness ratios (R_N/R_B) from .01 to .30. The parameter considered are nose bluntness ratio (R_N/R_B), Reynolds Number and Mach Number. For convenience the 9 and 10° cones are considered equivalent and no distinction is made between them in the data presentation. Only flat bases were considered. A small amount of data on angle of attack was obtained.

Consider first the base pressure as measured at the center of the base for zero angle of attack. This is denoted by Pb(0). From the profiles this was generally a maximum in pressure (excluding the corner flow). Conical nozzle and contoured nozzle data for the ratio $\frac{Pb(0)}{P_{\infty B}}$ are compared in Fig. 8 for sharp cones at $M_\infty = 12$. Note that $P_{\infty B}$ denotes the free stream static pressure at the location of the base of the model and that conical data here differs from that presented earlier in reference 4 since there the static pressure at the nose was used as a reference. With the exception of one data point there is excellent agreement between the two series of measurements.

For free stream Mach number of 12, Fig. 8 clearly indicates that the base pressure is a function of Reynolds number, decreasing as the Reynolds number increases. This means that as the boundary layer on the cone surface increases in thickness the base pressure increases.

This trend was predicted by Weiss (10), when the boundary layer is laminar on the cone surface. Also shown in Fig. 8 are two data points for Martellucci and Ranlet (5). These were for a 10" base diameter 10° cone and used the "compression strut" support referred to earlier. These points agree with the trend already observed.

Fig. 9 shows data for various free stream Mach numbers. Data of Martellucci and Ranlet (5) at $M_{\infty} = 8$, 10, 12, of Ward and Choate (11) at $M_{\infty} = 10$ and Cassanto (12) at $M_{\infty} = 19$ is shown with data obtained in this study for $M_{\infty} = 12$, 18 and 20. This data is all for sharp ($R_N/R_B \sim .03$) 9° and 10° 1/2-angle cones with flat bases. It is apparent that the Reynolds number effect seen earlier at $M_{\infty} = 12$ is also true at other Mach numbers. It is apparent that increasing the free stream Mach number significantly increases the base pressure.

Varying the nose radius also changes the base pressure. Fig. 10 demonstrates this. At high Reynolds number ($\sim 10^6$) increasing the nose bluntness ratio increases the base pressure. As the Reynolds number is decreased, however, the effect of increasing nose bluntness diminishes until at a Re/ft of 8.5×10^4 little change in base pressure was observed. This result is distinctly different from the results reported earlier from conical nozzle blunted cone tests c.f. Muntz and Softley (4). The reason for this is not known; however, these earlier results were seriously influenced by acceleration of the relatively light models and inaccurate correction for acceleration to the

blunt body data could be a clue to the difference.

Information was also obtained on pressure distribution across the base. Indeed, following a suggestion of Dr. Sheldon Weinbaum of GE-SSL, particular effort was applied to obtaining information near the corner of the base and on the rear cone surface. Fig. 11 shows two profiles for the 9^{o} sharp ($R_N/R_B = .01$) flat based cone for two Reynolds numbers and the free stream Mach number of 12. At $Re_{\infty_L} = 2.3 \times 10^6$ the base pressure drops continuously as the corner is approached, while the cone pressure does not show any indication of the presence of the corner (within, of course, the extent of the instrumentation). At $Re_{\infty_L} = 7 \times 10^5$, however, the influence of the corner on the pressure distribution can be clearly seen both in a pressure rise on the base as the corner is approached and in a corresponding drop in cone pressure. At lower Re_{∞_L} this corner influence was also observed.

Compare these profiles with two obtained on a slightly blunted cone ($R_N/R_B = .10$) (see Fig. 12). For condition 1 (free stream Reynolds number/ft$= 1.7 \times 10^6$) the increase in nose radius from $R_N/R_B = .01$ (see Fig. 11) to $R_N/R_B = .10$ (Fig. 12) gives a somewhat higher base pressure level. In addition there is evidence of corner influence in the cone pressure for the blunt cone.

The second curve in Fig. 12 demonstrates a greatly reduced

Reynolds number. The pressure variation across the base is greatly reduced while the influence of the base on the cone flow is more marked than at higher Re/ft. Similarly some data for a blunter cone ($R_N/R_B = .275$) are shown in Fig. 13. Again at the higher Reynolds number condition the base pressure drops continuously toward the corner. At a slightly lower Reynolds number, however, the drop in pressure at the corner is no longer sharp but spreads over both the cone and base surfaces.

Such a corner influence with the cone flow turning before it reaches the corner is not completely new. Weinbaum (13) has suggested it in recent reports. Hama (14, 15) has observed experimentally this phenomenon on a wedge and Kavanau (16) (in 1956) certainly recognized it. The importance in theoretical calculations is evident since the flow at the corner is no longer described by the boundary layer simplifications.

It is interesting to note the dramatic change of the corner effect for a relatively small variation in Reynolds number (Fig. 11). The distance of upstream influence is clearly not directly proportional to boundary layer thickness as might be expected. One acceptable explanation is that the boundary layer on the cone at the high Reynolds number is transitional or turbulent. Some as yet unreported data on boundary layer transition on a cone obtained in this facility indicates that,for the case above,transition will indeed have started on the cone

surface.

3.4 Base Heat Transfer Results

Base heat transfer measurements were obtained for 9 and 10° cones, with nose bluntness variation at a matrix of conditions, all at approximately free stream Mach number of 12. The parameters considered were Reynolds number, nose bluntness and wall temperature ratio. Profiles were obtained at each condition.

A more complete discussion on these results is given in Ref. 1. Remarks here will be limited to a few sharp cone results.

Some profiles of base heat transfer are shown in Fig. 14. In general, a maximum in heat transfer occurs at or near the center of the base. More interesting is the fact that the heat transfer does not follow a given pattern as r_B is increased. The influence of the pressure field near the corner of the base is clearly seen.

The high value of heat transfer away from the center of the base (demonstrated clearly by the half filled symbols) is not due to a faulty gauge. It was in fact repeated for three separate instrumentation systems. It is felt that this is indicative of the separating streamline leaving the base at a point distinctly removed from the corner.

Since the base heat transfer is clearly dependent on local conditions especially the local total temperature an attempt was made

to correlate the measurements with near wake measurements. The electron beam measurements of Muntz (2, 3, 4) were used to provide values for h_R, the recovery enthalpy of the recirculation region. Fig. 15 shows the result of this correlation. Heat transfer values with well over an order of magnitude in variation are reduced to a very weak dependence on free stream Reynolds number. The conclusion is drawn that the trends of near wake temperatures observed by Muntz are supported by the base heat transfer measurements.

Comparison of base heat transfer with theoretical analysis is difficult due to the lack of theoretical calculations at the correct range of parameters. However, an attempt was made to compare with the work of King (17). In Fig. 16 the total base heat transfer obtained by integrating across the measured profiles are non-dimensionalized with the total cone heat transfer and considered as a function of free stream Reynolds number. The open symbols are data shown in an earlier comparison and for these a linear profile of heat transfer i.e. $\dot{q}(r_B) = \dot{q}(0)\ (1-r_B/R_B)$ was used. As can be seen neither the level nor the Reynolds number dependence for $\dot{Q}_B/\dot{Q}_W$ agrees with the theory. Moreover the linear dependence assumed earlier is clearly a poor assumption. Indeed the integrated base heat transfer is very dependent on the quantities near the corner and hence on the flow geometry referred to earlier. This geometry was not included in the

analysis of reference 17 (or Ref. 18, Baum, King and Denison).

4. Conclusions

The shock tunnel has been used as a facility to study base flows. Within the model size limitation used it has always been possible to establish a quasi-steady wake flow. Comparison between data obtained in conical and contoured nozzle tunnels indicates good agreement provided local pressures are used as reference.

The problem of obtaining data without interfering with the flow can be solved by carefully chosen geometry. The trailing wire technique with the wires carrying amplified signals provides reasonable signal and signal/noise ratios under the most extreme conditions. (The lowest values measured in this program were 5×10^{-4} lb/in^2 pressure and 3×10^{-3} Btu/ft^2 sec heat transfer).

Base pressures and profiles of base pressure were measured at a number of flow conditions. The levels obtained were in good agreement with the axial profiles obtained by Muntz and Softley (4) and with the data of Martellucci and Ranlet (5) and Ward and Choate (11). Mach number, Reynolds number and nose bluntness influenced the pressure level. Wall temperature ratio did not appear to have any influence on the base pressure ratio. In addition the sharp drop of pressure around the corner of the base diminishes as the Reynolds number decreases and considerable upstream influence of the base on the cone pressure was observed.

The influence of Reynolds number and wall temperature ratio on base heat transfer has been observed. The levels and Reynolds number dependence measured were not in general agreement with King (17). The behavior of recirculation flow enthalpy observed by Muntz and Softley (4) appears consistent with the base heat data observed.

References

1. Softley, E.J. and Graber, B.C., "Techniques for Low Level Pressure and Heat Transfer Measurements and Their Application to Base Flows", GE TIS R67SD2*.

2. Muntz, E.P. and Marsden, D.J., "Electron Excitation Applied to the Experimental Investigation of Rarefied Gas Flows", p. 395 in Third International Rarefied Gas Dynamics Symposium Vol. II, J. Laurmann ed., New York, Academic Press, 1963.

3. Softley, E.J., Muntz, E.P. and Zempel, R.E., "Experimental Determination of Pressure, Temperature and Density in Some Laminar Hypersonic Near Wakes", GE TIS R64SD35, May 1964.

4. Muntz, E.P. and Softley, E.J., "A Study of Laminar Near Wakes", AIAA Journal, Vol. 4, pp. 961-968, June 1966.

5. Martellucci, A. and Ranlet, J., "Experimental Study of Near Wakes, GASL Technical Progress Rpt., October 1966.

6. Cresci, R.J. and Zakkay, V., "An Experimental Investigation of the Near Wake of a Slender Cone at M_∞ = 8 and 12", Aeronautical Research Lab. 65-87, May 1965.

7. Todisco, A. and Pallone, A., "Near Wake Flow Field Measurements", AIAA Paper 65-53, January 1965.

8. Todisco, A. and Pallone, A., "Measurements in Laminar and Turbulent Near Wakes", AIAA Paper 67-30, January 1967.

* General Electric Company Technical Information Series.

9. Dayman, B., Jr., "Optical Free-Flight Wake Studies", Jet Propulsion Lab., TR-32-364, November 1962.

10. Weiss, R.F., "Base Pressure of Slender Bodies", AIAA Journal Vol. 4, pp. 1557-1559, September 1966.

11. Ward, L.K., and Choate, R.H., "A Model Drop Technique for Free Flight Measurements in Hypersonic Wind Tunnels Using Telemetry", AEDC-TR-66-77, May 1966.

12. Cassanto, J.M., "Base Pressure Results at Mach 19 in AEDC Tunnel F", GE/RSD Aerodynamics Technology Component Data Memo. #67 - 04., February 1967.

13. Weinbaum, S., "On the Singular Points in the Laminar Two-Dimensional Near Wake Flow Field", submitted Journal of Fluid Mechanics, January 1967.

14. Hama, F.R., "Experimental Investigations of Wedge Base Pressure and Lip Shock", Jet Propulsion Lab. TR-32-1033, December 1966.

15. Hama, F.R., "Experimental Studies On the Lip Shock", AIAA Paper 67-29, January 1967.

16. Kavanau, L.L., "Base Pressure Studies in Rarefied Supersonic Flows", J. of the Aeronautical Sciences, Vol. 23, pp. 193-207, March 1956.

17. King, H.H., "An Analysis of Base Heat Transfer in Laminar Flow", E.O.S. Research Note No. 14, Electro-Optic Systems, Sept. 1963.

18. Baum, E., King, H.H. and Denison, M.R., "Recent Studies of the Laminar Base-Flow Region", AIAA Journal, Vol. 2, pp. 1527-1534, September 1964.

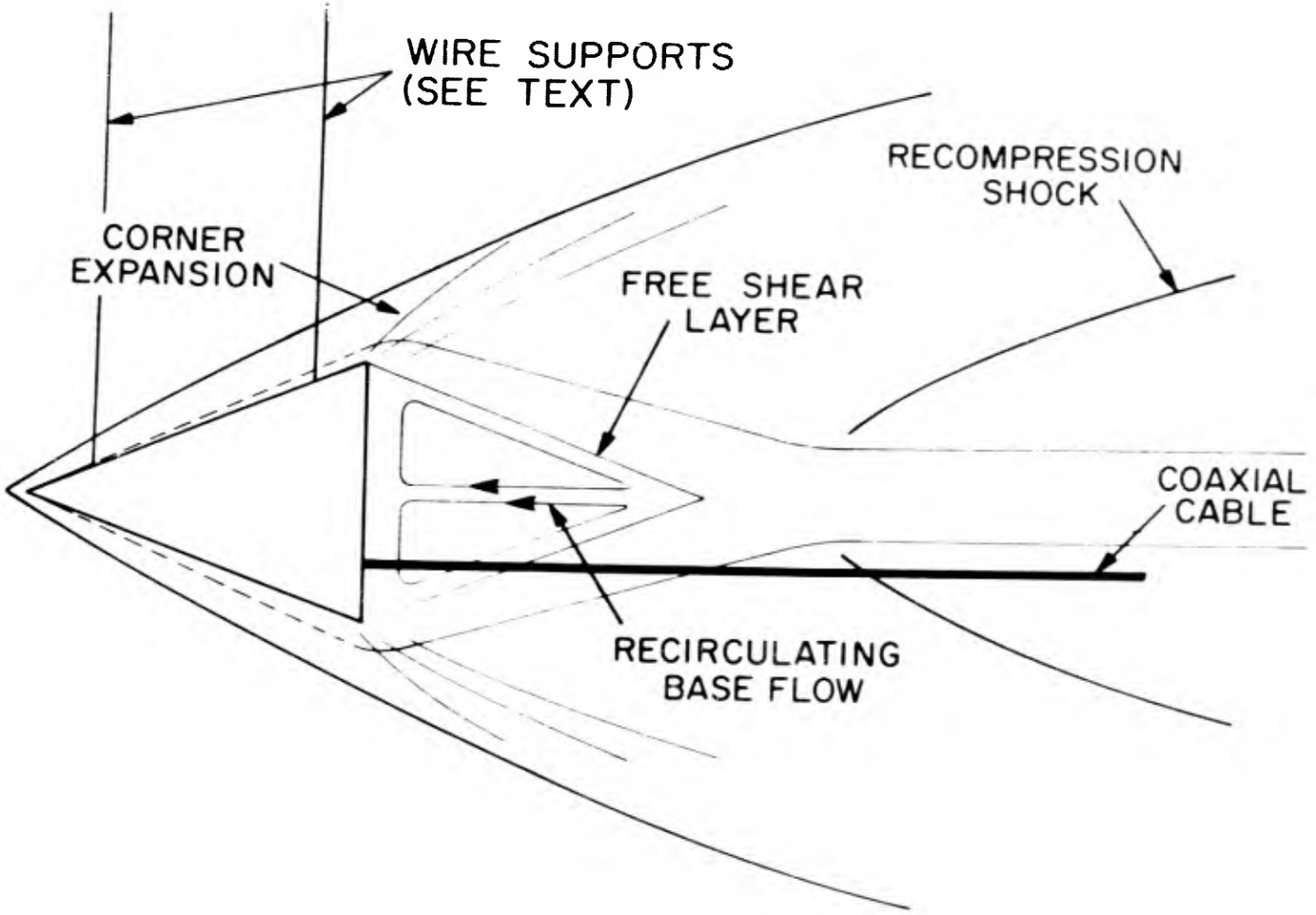

Fig. 1 Classical Near Wake Flow Showing Cable Position For Base Measurements.

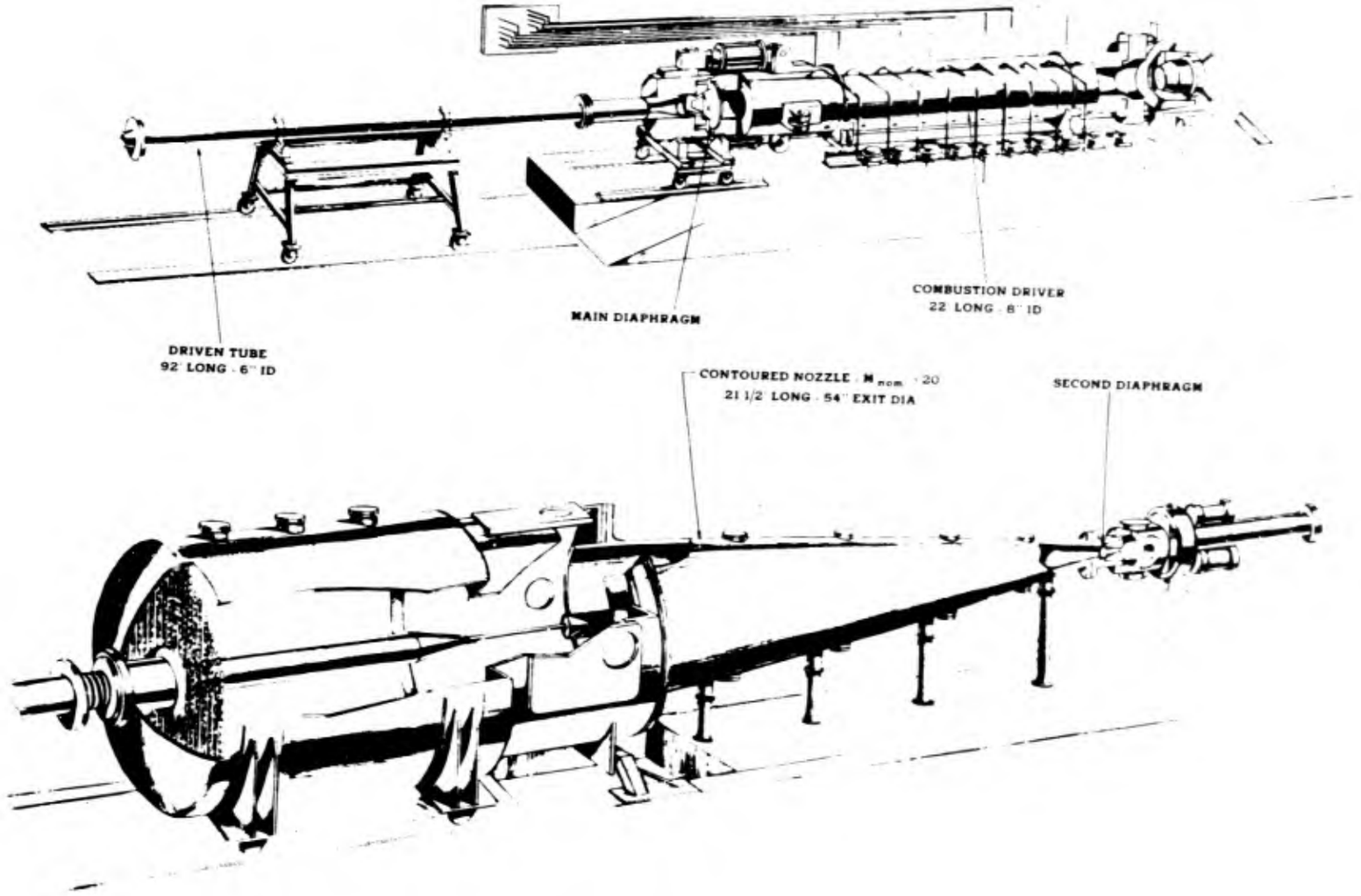

Fig. 2 Sketch of Large Shock Tunnel With Contoured Nozzle Installed.

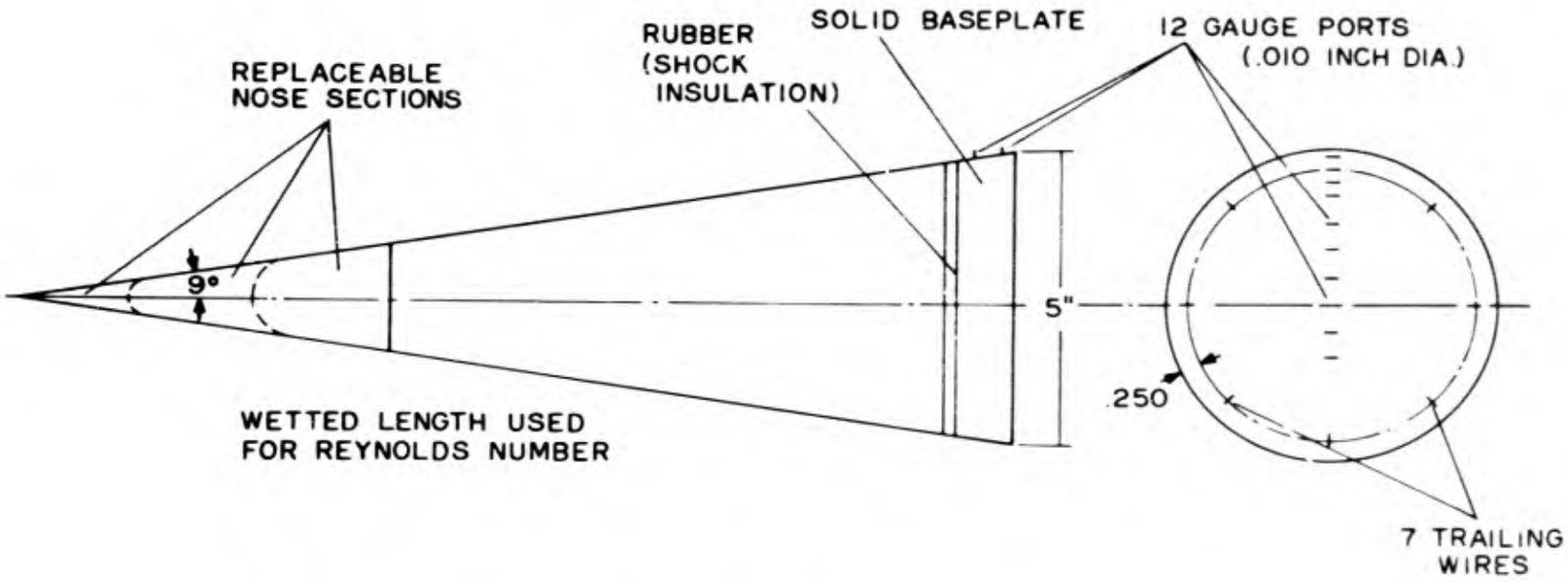

Fig. 3 Base Pressure Model Used For Profile Measurements.

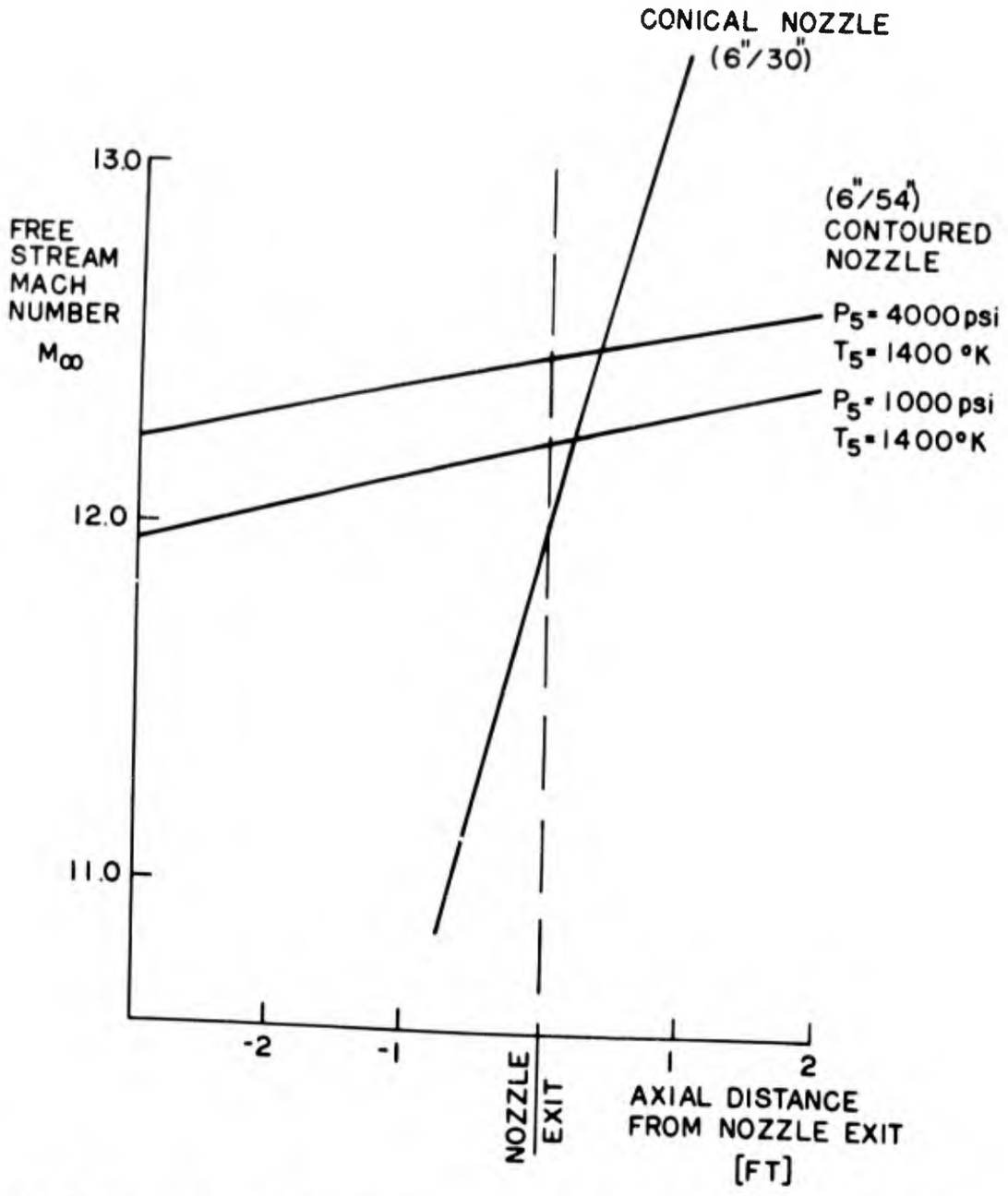

Fig. 4 Mach Number Along Center Line of Nozzle (6"/30" and 6"/54" Shock Tunnels).

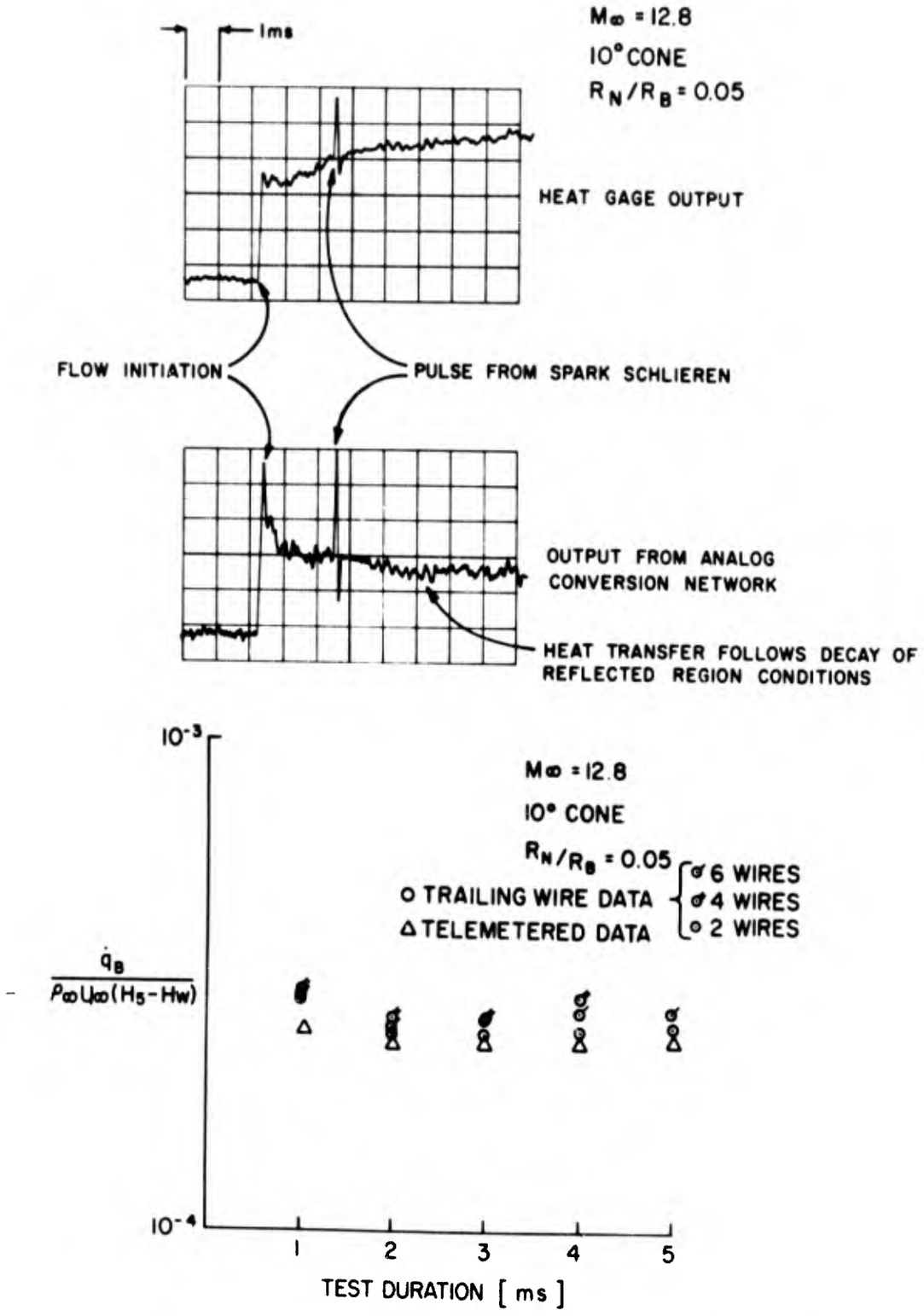

Fig. 5 Oscilloscope Traces and Time Resolved Base Heat Transfer Data (6"/30" Conical Nozzle Shock Tunnel).

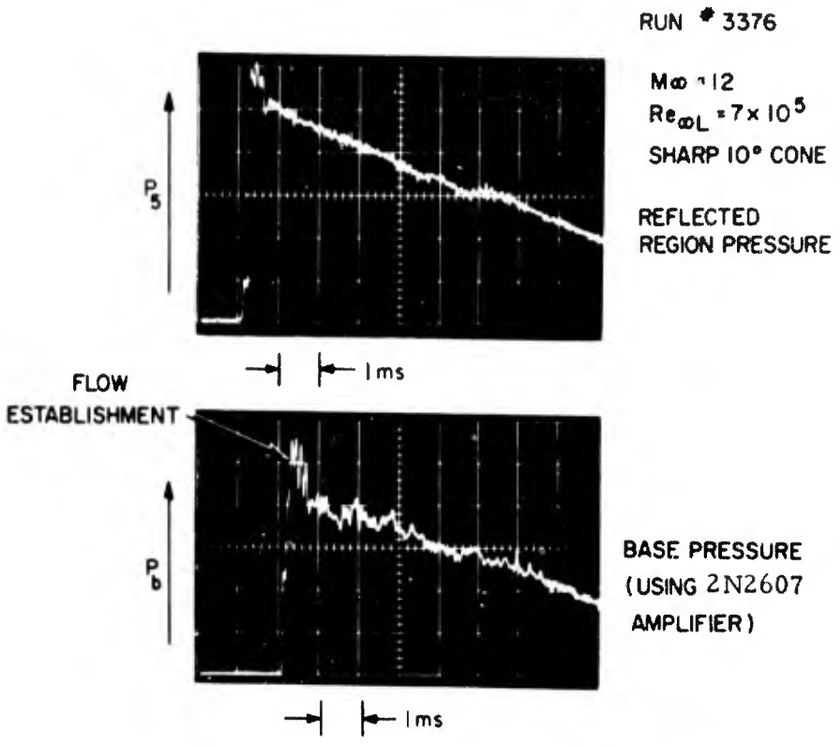

Oscilloscope Traces

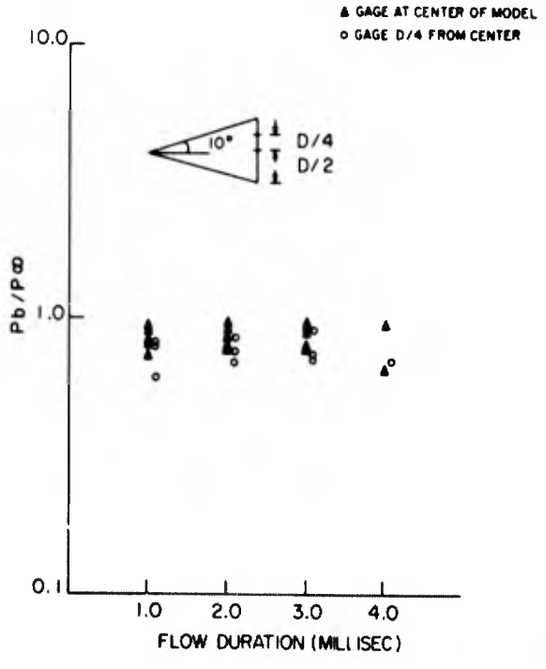

Fig. 6 Oscilloscope Traces and Time Resolved Base Pressure Data (6"/30" Conical Nozzle Shock Tunnel).

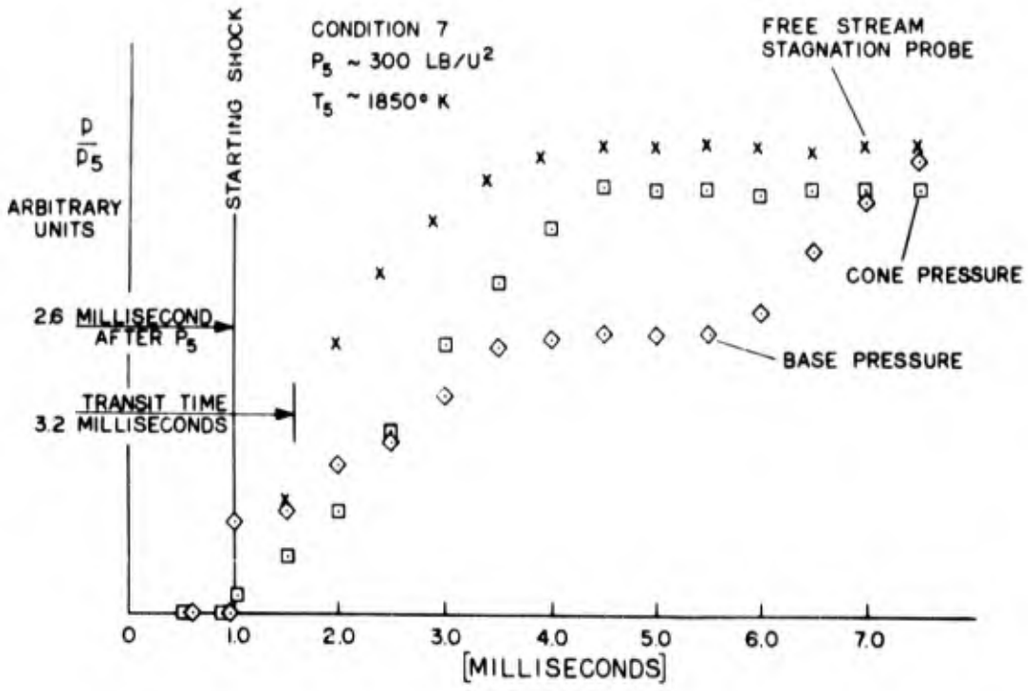

Fig. 7 Time Resolved Free Stream and Base Pressures (Contoured Nozzle and 5 Inch Base Diameter 9° Cone).

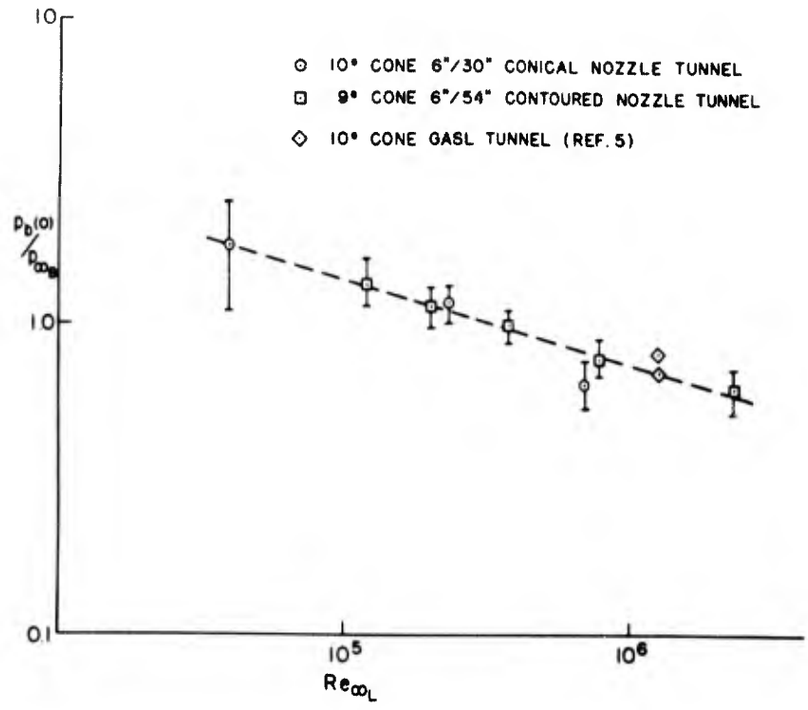

Fig. 8 Comparison of Conical Nozzle and Contoured Nozzle Base Pressures.

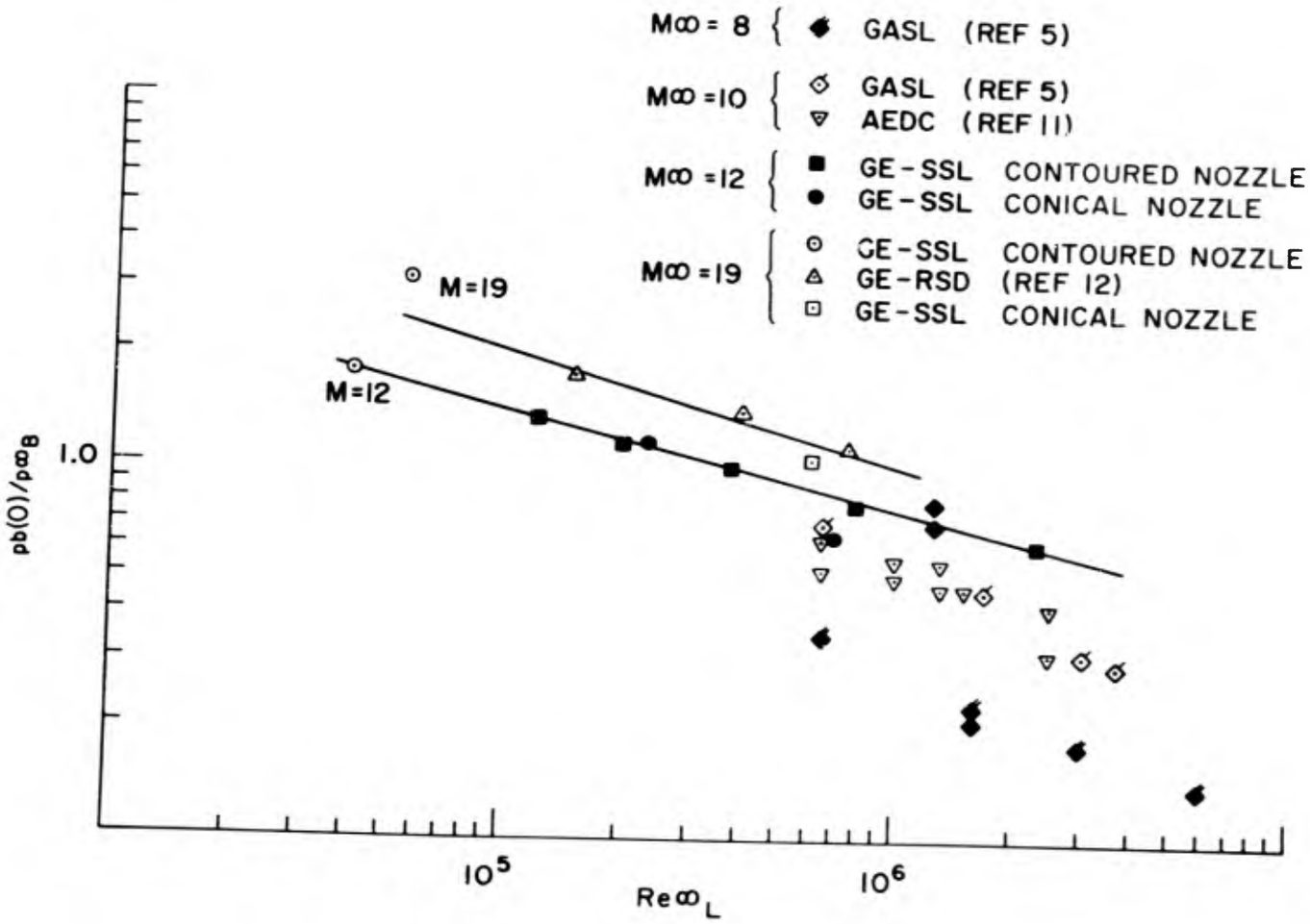

Fig. 9 Effect of Mach Number and Reynolds Number on Sharp Cone Base Pressures.

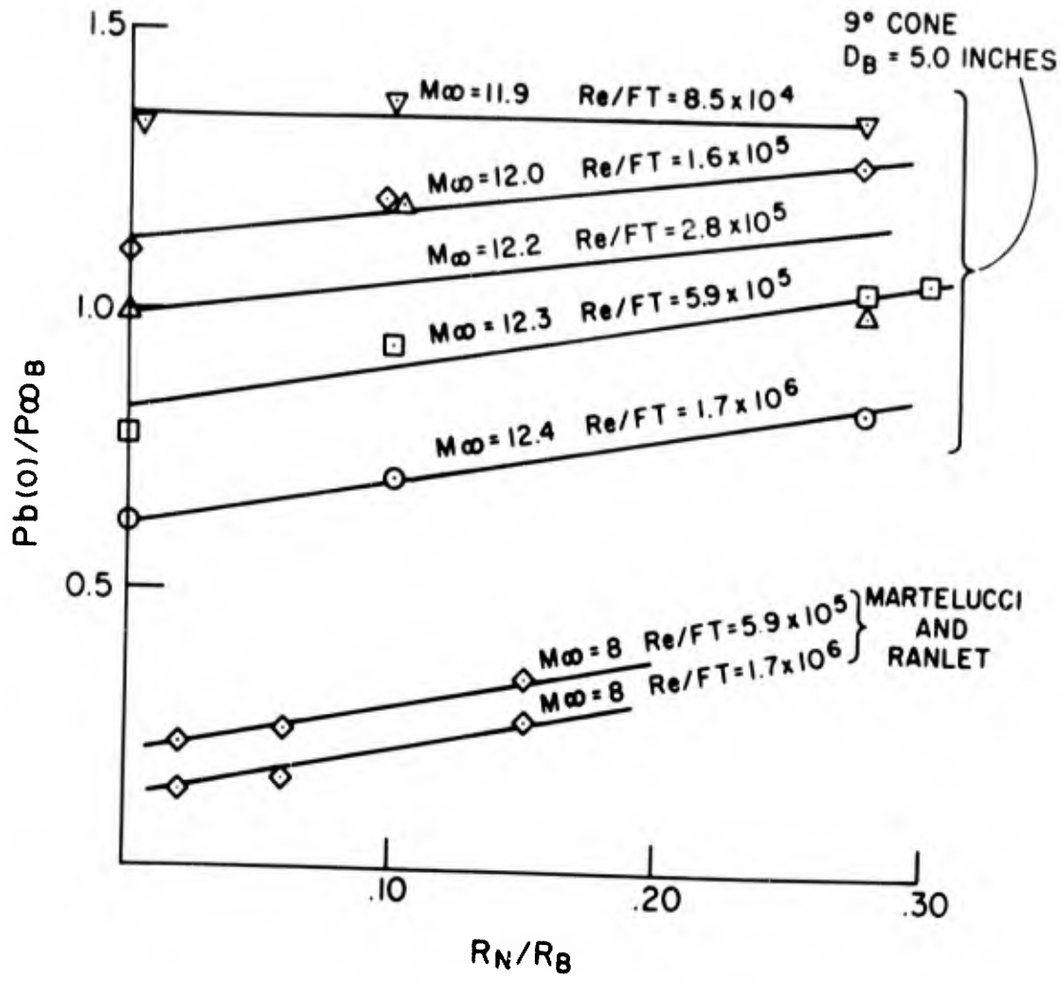

Fig. 10 Effect of Nose Bluntness on Base Pressure.

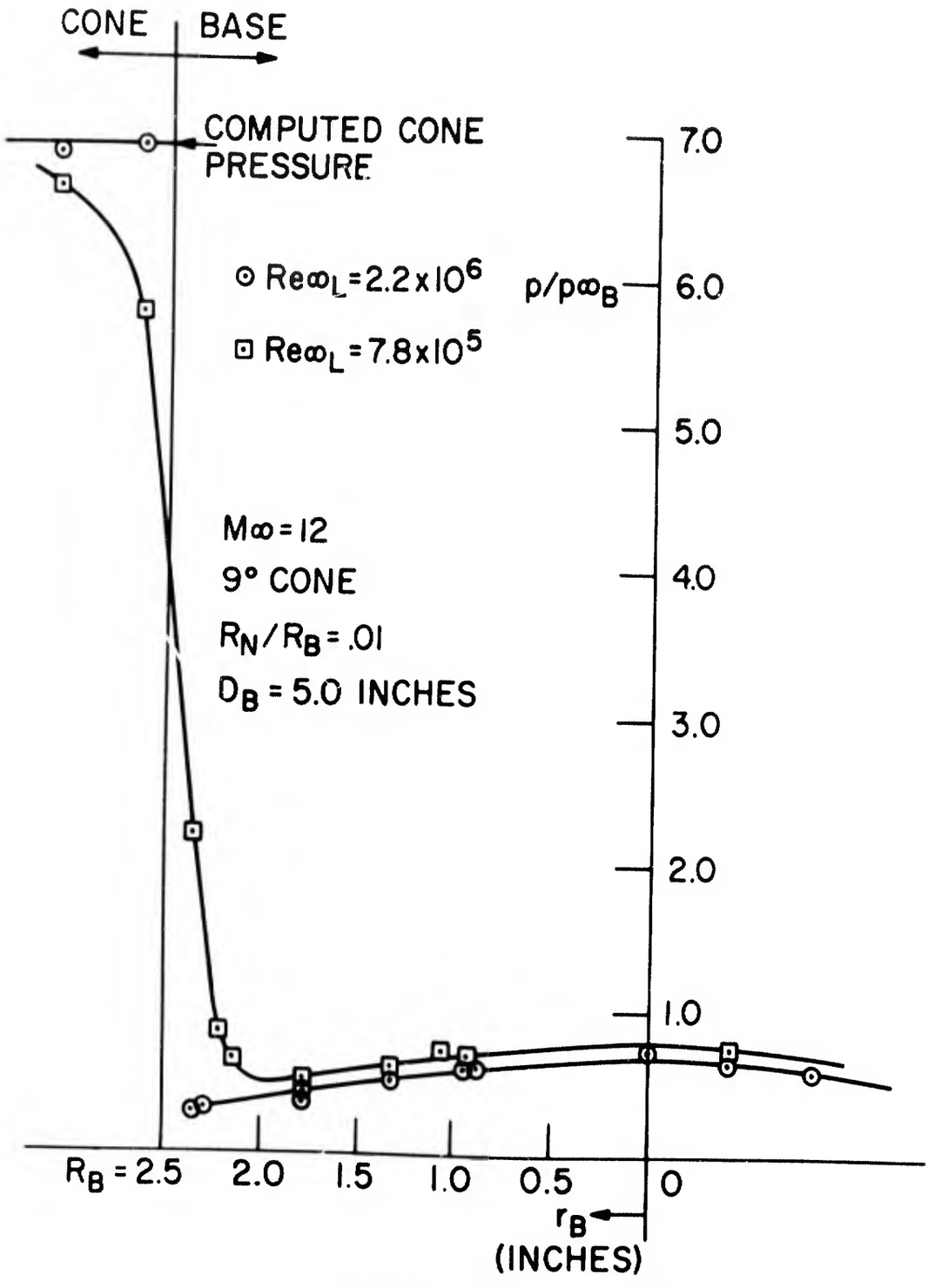

Fig. 11 Base Pressure Profiles on a Sharp Cone.

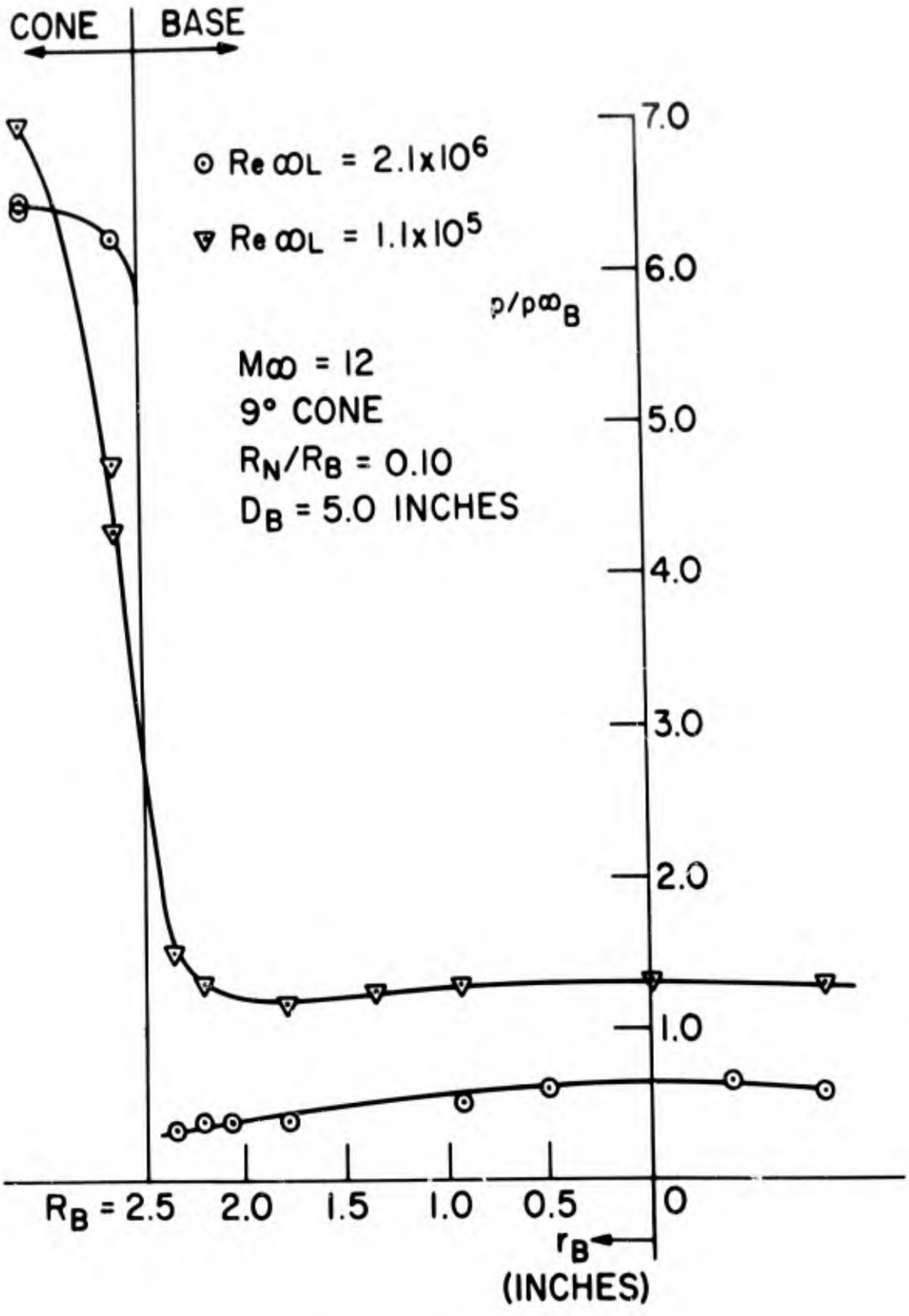

Fig. 12 Base Pressure Profiles on a Slightly Blunted Cone.

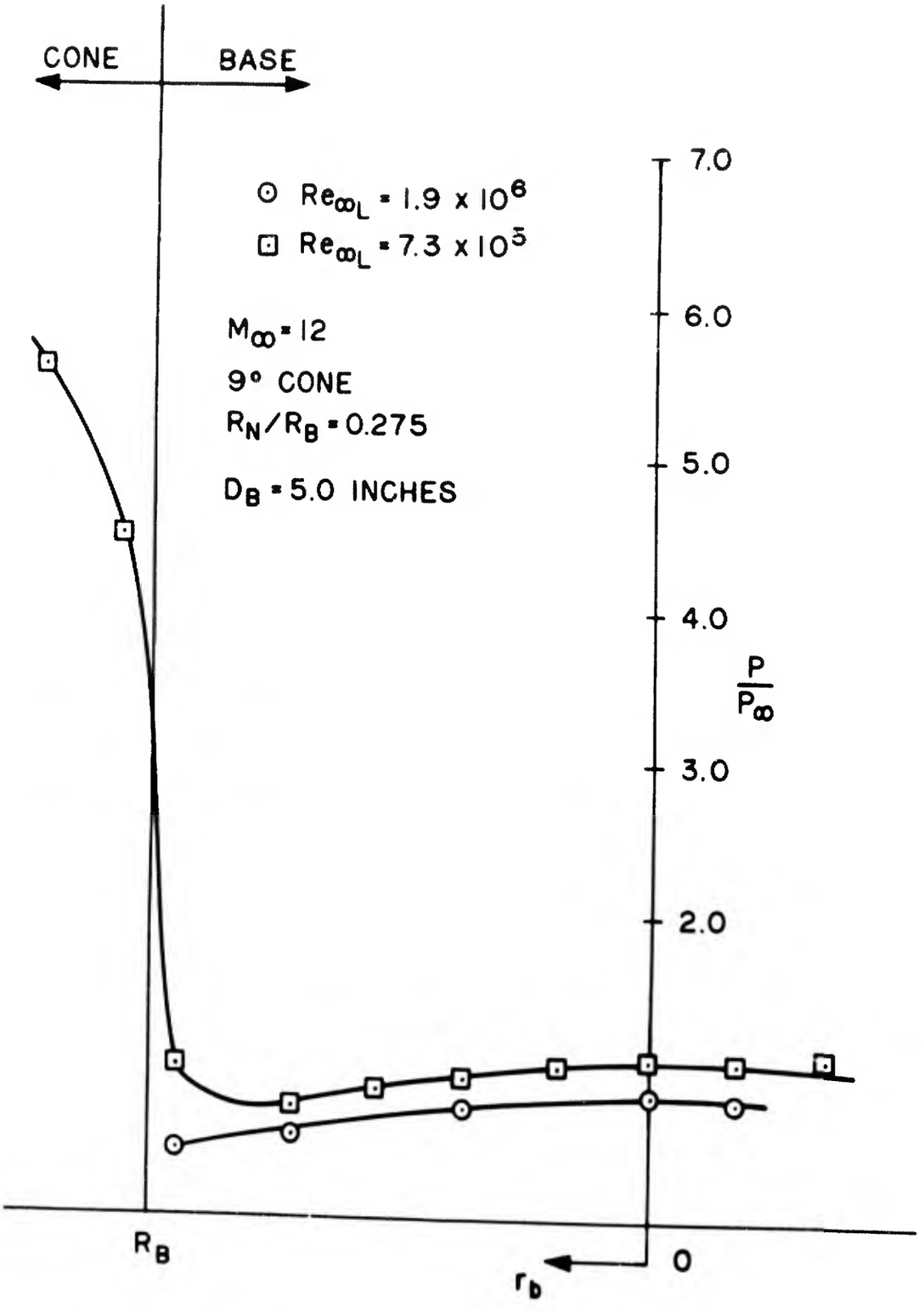

Fig. 13 Base Pressure Profile on a Blunted Cone.

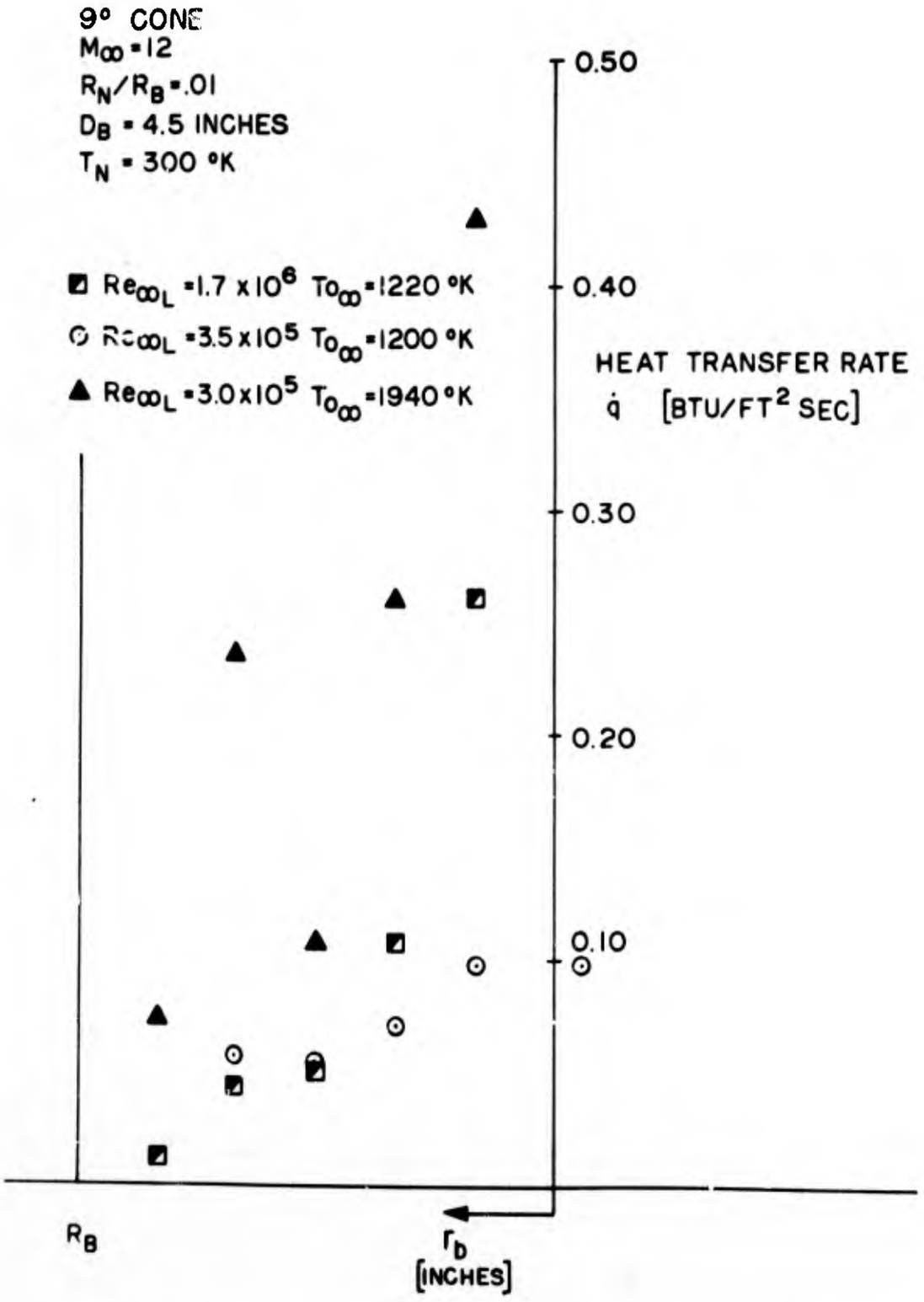

Fig. 14 Base Heat Transfer Profiles on a Sharp Cone.

HYPERSONIC INVESTIGATIONS ON THE LOCAL AND AVERAGE HEAT TRANSFER IN CAVITIES AND AFTER STEPS OF BODIES OF REVOLUTION

by

W. Wyborny, H.-P. Kabelitz and H.-J. Schepers

Deutsche Versuchsanstalt für Luft- und Raumfahrt E.V.

Institut für Angewandte Gasdynamik

Porz-Wahn

SUMMARY

In axi-symmetric cavities and after steps of bodies of revolution measurements of heat transfer and pressure were made at Mach-numbers till 16 and varying Reynolds numbers. The heat transfer tests were made by means of a thin film calorimeter method; they concern local as well as average heat transfer rates. By optical observation detailed results on the flow behaviour could be gained. The measurements were made in the DVL-gun-tunnel. The results are compared with theoretical solutions.

RESUME

On a effectué sur des corps de révolution, dans les cavités symétriques à l'axe ainsi que dans les parties postérieures au redan, des mesures de pression et de transfert de chaleur, pour des nombres de Mach allant jusqu'à 16 et différents nombres de Reynolds. Pour des mesures de transfert de chaleur on a eu recours à une méthode utilisant un calorimètre à pellicule fine; ces mesures portèrent sur les taux de transferts de chaleur locaux et moyens. Grâce à des observations optiques, on a pu obtenir des résultats détaillés sur le comportement de l'écoulement. Les mesures furent effectuées dans le tunnel de tir du DVL, et les résultats obtenus sont comparés aux solutions théoriques.

NOTATION

d	sting diameter
h	heat transfer
q	heat flux
u	velocity
C	condensor
D	diameter of basic model
H	cavity depth
L	cavity length
M	Mach number
P	pressure
$R = D/2$	radius of the basic model
T	temperature
X	cartesian coordinate
R_Ω	resistance
Re_D	Reynolds number related to the body diameter D
Θ_{total}	total angle of the conical nose
τ	time factor

Subscripts

a	related to the average value
r	related to the reattachment zone behind a cavity
s	stagnation conditions
t	total conditions
fl	related to cavity flank
sep	related to the separation point
∞	free stream conditions
–	related to the corresponding cylinder

HYPERSONIC INVESTIGATIONS ON THE LOCAL AND AVERAGE HEAT TRANSFER IN CAVITIES AND AFTER STEPS OF BODIES OF REVOLUTION

W. Wyborny, H.-P. Kabelitz and H.-J. Schepers

1. INTRODUCTION

Among the re-entry problems of space vehicles investigations of cavities and wakes at hypersonic speeds become more and more important. One of the problems of these vehicles is to reduce the heat flux to the body surface in spite of high drag coefficients. The estimations of ALLEN and EGGERS (Ref. 1) have shown that the smallest heat flux to the body surface will be attained if the ratio of friction to drag is minimized. For the reduction of the heat flux cavities are proposed.

For long cavities the flow field becomes similar to the flow field of wakes, but there exists no detailed description of the physical features of the flow in the wake and the cavity. Important for both cases are: the separation process of the boundary layer, the development of a free shear layer with a core in the cavity or the base flow region of a vehicle, and the reattachment of the free boundary layer. The measurements of heat transfer in cavities and behind rotationally symmetric steps presented in this paper were made in order to study these features for cavities of different lengths.

2. APPARATUS AND TEST CONDITIONS

2.1 Facility and Instrumentation

The tests were performed in the DVL gun tunnel. A complete description of the tunnel and operating conditions is given in References 2 and 3. The tunnel consists of a high pressure vessel with a volume of $V = 0{,}15\ m^3$, a barrel with a length of 6 m and an internal diameter of 6 cm, a 12° angle conical nozzle with a 22 cm exit diameter, a closed test section, and a vacuum tank. Diaphragms exist between the high pressure section and the barrel and between barrel and nozzle inlet. After bursting of the diaphragms at the high pressure section a light piston is accellerated along the barrel and compresses the test gas (air) in the barrel upstream of the nozzle.

The instrumentation of the gun tunnel is also fully described in References 2 and 3. Measurements of the speed of the piston and of the shock wave in front of it are carried out with platinum film pick-ups mounted in the wall of the barrel. For the pressure measurements crystal transducers are used. The flow pattern becomes visible by use of a schlieren apparatus. The spark for photographic illumination is triggered by the delayed signal of a pressure transducer.

2.2 Test Conditions

The free stream conditions in the test section are depending on the Mach number which is determined by the nozzle throat and the fixed test section diameter, the total pressure in front of the nozzle

depending on the initial pressure in the high pressure vessel, and the stagnation temperature depending on the pressure ratio of the test gas in the high pressure vessel and the barrel. From these data the free stream velocity and the Reynolds number in the test section can be calculated. For the heat transfer measurements discussed in this paper the following conditions are chosen:

Free stream Mach number	M_∞	8,75	13,37
Total pressure	$P_t \left[\frac{kg}{cm^2}\right]$	155	155
Stagnation temperature	T_s [°K]	980	1370
Free stream velocity	$u_\infty \left[\frac{m}{sec}\right]$	1365	1600
Reynolds number	Re_D	$0,48 \times 10^6$	$0,1 \times 10^6$

2.3 Models and Instrumentation

Two cylindrical bodies having a base diameter of D = 3 cm are used for the tests. One of it is spherical nosed, the other one has a conical nose with a cone angle of 90 degrees. Two different cavity depths are obtained by altering the sting diameter (d). The diameter d = 2 cm corresponds to a cavity depth of H/R = 0,33, the diameter d = 1,5 cm to a cavity depth of H/R = 0,5. Different cavity lengths L are obtained by moving a cylindrical hollow afterbody in the axial direction. For all cavities and steps the length of the forebody (nose and cylinder) is 1,7 x R = 2,5 cm, it is equal for both nose shapes. For the cavity measurements only the configuration with the spherical nose is used.

The heat transfer measurements are carried out with platinum thin film

resistance thermometers (Ref. 4). These platinum films prepared on a cylinder of pyrex glass (Figure 1) have a resistance of 200 Ohms and a temperature coefficient of

$$\frac{\Delta R}{R \times \Delta T} = 0{,}3 \times 10^{-3}\ {}^{o}K^{-1}$$

The delay time of the films is about 1 μsec. The time dependent temperature of the films is transformed directly into heat transfer rates by a T-section analogue network (Ref. 5). These analogue networks are characterized by a time constant $\tau = 100\ \mu$sec and a running time of 20 msec using 30 idential RC sections (Figure 2). An example of the measured surface temperature and the transformed heat transfer rate is shown in Figure 3. The film thermometer was located in a cavity and the testing time available was 15 msec at a Mach number of $M_\infty = 8{,}75$.

At the same point on the model the heat transfer rate at Mach number $M_\infty = 8{,}75$ was nearly three times of the rate at Mach number $M_\infty = 13{,}37$. Consequently, the measurements at the higher Mach number show more scatter.

3. HEAT TRANSFER IN CAVITIES

3.1 Basic Models

The first heat transfer measurements were made at the stagnation point of a hemisphere and on the cylinder part of both basic models. The stagnation point heat transfer was measured at two stagnation temperatures and two Mach numbers with a copper thick film calorimeter and

with a platinum thin film thermometer. The stagnation point heat transfer rates measured by these two methods had a misrate of less than 5 % and were in good agreement with the data calculated by FAY and RIDDEL (Ref. 6) for both stagnation temperatures and both Mach numbers.

Figure 4 shows the measured heat flux on the cylinder related to the stagnation point heat flux of the hemisphere for the two basic models and the Mach numbers $M_\infty = 8{,}75$ and $M_\infty = 13{,}37$. As experimental data have shown, the concept of the local similarity (Ref. 7, 8 and 9) gives a good description of the heat transfer for such models if the pressure distribution on the model is known. This is not measured in the present case. As known the calculated pressure on the cylinder is given too low by Newtonian theory and too high by the blast wave analogy (Ref. 10, 11 and 12). Similar results were obtained for the heat transfer rate near the shoulder.

For both Mach numbers indeed the measured heat transfer rates are being between the data calculated from this two methods. The better approximation is the result using the pressure distribution obtained by the blast wave analogy. In best agreement with our experimental data are the data calculated by HANAWALT, BLESSING and SCHMIDT (Ref. 13) with a modified blast wave pressure distribution.

3.2 Measurements on the Cavity Bottom

At Mach number $M_\infty = 8{,}75$ the trend of the measured heat transfer rates

on the cavity bottom is shown in Figure 5 and Figure 6 for two cavity depths and different cavity lengths. For the deeper cavity (H/R = 0,5, Figure 5) schlieren photographs show (Figure 7) that in the case of the longer cavities the boundary layer reattaches to the cavity bottom. Reattachment is not observed when using the smaller cavity depth (H/R = 0,33, Figure 6) even for long cavities. Corresponding to the observed flow pattern for longer cavities the difference in the heat transfer rates for the two cavity depths may be explained. In those cases where the free shear layer reattaches the heat flux properties in the reattachment zone are nearly the same as are observed in the wake. In this case (Figure 5) a clear division of the cavity flow in three parts is possible, i.e. the zone of the wake flow, the reattachment zone of the boundary layer, and the following separation zone. In the reattachment zone one finds for the different cavity lengths a qualitative and a quantitative agreement of the measured heat transfer rates. Short cavities without reattachment of the separated boundary layer at the cavity bottom have a similar trend of heat transfer versus L/H as long cavities in the downstream separation zone.

If the flow conditions in the cavity are characterized by a recirculation the origin of the boundary layer on the cavity walls must be the stagnation point of the free shear layer. On the basis of the above flow model, Figure 8 shows the measured heat transfer rates and it is obvious that cavities without reattachment of the separated boundary layer at the cavity bottom all lie within a particular region (hatched in Figure 8). In contrast, cavities with reattachment have a

characteristic trend. As Figure 9 shows, the main parameter for the heat transfer in cavities without reattachment does not seem to be the length built by the cavity length L plus the cavity depth H, but the length of the cavity bottom. The results of the theory from BURGGRAF (Ref. 15) which is based on the assumption of an inviscid core in the region of recirculation are shown in Figure 9 for comparison. The measured data do not show for fixed Mach numbers the strong dependence on the ratio of cavity length to cavity depth as BURGGRAF's theory predicts. The difference of the results for the two Mach numbers seem to be influenced by the different Reynolds numbers. The heat transfer rates seem to be nearly independent of the cavity depth and they can be normalized by the cavity length in this case. Moreover, the trend of the heat transfer does not follow a known exponential law of the boundary layer theory as for example in the theory of BURGGRAF. This result is in good agreement with the measured data presented by NICOLL and BOGDONOFF (Ref. 16), though their cavity was located in a conical body and had rounded corners.

3.3 Measurements on the Flanks of the Cavities and in the Reattachment Zone Behind the Cavity

For the estimation of the influence of a cavity to the overall heat transfer a knowledge of the heat transfer rates on the cavity flank and on the cylinder behind the cavity is necessary because the highest heat transfer rates are expected there. In the measurements heat transfer on the cavity flank increased in the direction of the cavity bottom,

while the product of the local value q x d seemed to be constant for the cavity. The average heat transfer for the cavity flank q_{fl} increases with the increased cavity length (Fig. 10). The fla at transfer at Mach number $M_\infty = 8,75$ is the same for both cavity depths for the same ratio L/H and increases with increasing L/H. At a critical value of L/H, depending on L/R, an unsteady change in the slope of q_{fl} occurs, there the so called transitional trend begins. The heat transfer rates for the reattachment zone at the cavity flanks are calculated by a theory of CHUNG and VIEGAS (Ref. 17) and are shown for comparison in Figure 10.

The heat flux in the reattachment zone behind the cavity is characterized by the velocity on the dividing streamline, which increases with increasing distance from the separation point (Ref. 18). For short cavities, where the shear flow has not developed to the CHAPMAN profile, the heat flux relative to the heat flux of the basic model in the reattachment zone is lower than for longer cavities and the slope of the heat flux versus X/D increases with increasing cavity length. The basic explanation of this observation is that the free shear layer develops to the CHAPMAN profile with increasing cavity length. Measurements of NICOLL and BOGDONOFF (Ref. 16) show the same trend (Fig. 11). The same measurements are crossplotted in Figure 12 and it is obvious that for short cavities until L/H = 1,5 the heat flux at the reattachment zone is reduced by the influence of the cavity. For increasing cavity lengths the heat flux increases and exceeds the heat flux obtained for the basic model.

3.4 Comparison of the Average Heat Flux to the Cavities and the Basic Model

To gain an impression of the real heat transfer rates at and in the cavities and the corresponding cylinder, the measured heat transfer rates for a long cavity without reattachment of the separated boundary layer on the cavity bottom and for the corresponding cylinder are shown in Figure 13. It may be clearly seen that for the cavity the heat transfer rates in the stagnation and reattachment zone at the downstream end of the cavity bottom, on the cavity flank, and on the cylinder behind the cavity are greater than the cylinder, so that the reduction of the heat transfer in the cavity is considerably compensated by the other parts. In Figure 14 the average heat transfer is shown for cavities of different lengths related to the heat transfer of the corresponding cylinder. Considering only the average heat transfer on the cavity bottom, one finds a nearly constant slope of heat transfer versus cavity length, but the slope and the range is different for the two Mach numbers. If one looks at the average heat transfer of the whole of the cavity, one recognizes that for the lower Mach number and higher Reynolds number the measured heat transfer rates for short cavities only agree with the theoretical data calculated by CHAPMAN (Ref. 19), while the average heat transfer for long cavities increases. For the long cavities it reaches higher values than the heat transfer of the corresponding cylinder. At the Mach number $M_\infty = 13{,}37$ this trend will be transplanted to much longer cavities, but the main reason for this effect seems to be the influence of the Reynolds number.

The assumption that the free shear flow is laminar in the region where $(h/\bar{h})_a$ is independent of the cavity length and then has a transitional trend corresponding to the increasing heat transfer, as predicted by CHAPMAN's theory (Ref. 19) and proved by LARSON's experiments (Ref. 20), may be valid in the case of the deeper cavity (H/R = 0,5) at Mach number $M_\infty = 8,75$ (Fig. 10). But the same Figure shows that the flow for the less deep cavity (H/R = 0,33), corresponding to the heat transfer on the flanks, seems to be laminar for longer cavities, although the average heat transfer in Figure 14 increases and reaches values which are higher than those of the corresponding cylinder.

4. MEASUREMENTS OF HEAT FLUX BEHIND ROTATIONALLY SYMMETRIC STEPS

Figures 15 and 16 show the heat flux on the sting behind axisymmetric steps for two basic body noses at two Mach numbers and two different sting diameters. In the region of the free shear layer flow the heat transfer rates are as high as in the cavities. In all cases the region of the highest heat transfer is behind the reattachment point as determined from schlieren pictures. The maximum heat transfer rate at the higher Mach number and the lower Reynolds number is nearly one half the corresponding value for the lower Mach number and the higher Reynolds number. The discontinuous development of the heat transfer rate in the region of the reattached boundary layer which was reproduced for several models and platinum film thermometers during several tests is probably associated with pressure gradients in this region.

5. CONCLUSIONS

The heat transfer measurements in the DVL gun tunnel show that for the estimation of the heat transfer to a cylinder with a cavity not only the heat flux on the cavity bottom is important but also the heat transfer on the flank and behind the cavity. It is shown that the flow in a cavity and behind rotationally symmetric steps has nearly the same characteristic behaviour. The measurements in the reattachment zone behind a cavity lead to the conclusion that the reduction of the heat flux is possible using short cavities until a length-height ratio of $L/H \approx 1{,}5$ is reached. Similar considerations show the advantage of short cavities with regard to the heat transfer in the whole cavity. In view of technical application these facts lead to the conclusion that the reduction of heat transfer at hypersonic speeds is possible by a series of short cavities.

This work was sponsored by the Deutsche Gesellschaft für Flugwissenschaften (DGF). The authors also like to thank Professor A. Naumann and Professor A. Heyser for their help and interest in this work.

REFERENCES

1. Allen, H.J.
Eggers, A.J.
A Study of the Motion and Aerodynamic Heating of Ballistic Missiles Entering the Earth's Atmosphere at High Supersonic Speeds
NASA Rep. 1381 1957

2. Wyborny, W.
Kabelitz, H.-P.
Funktionsuntersuchungen und erste Versuchsergebnisse im Stoßwellenwindkanal mit freifliegendem Kolben
DVL-Bericht Nr. 452, DLR FB 65-43, 1965

3. Heyser, A.
Wyborny, W.
Kabelitz, H.-P.
Der Stoßwellenwindkanal der DVL
- Grundlagen und erste Untersuchungen -
Kolloquium für Hyperschallaerodynamik und Meßverfahren der Kurzzeitphysik
14.6. bis 16.6.1966 St. Louis, France

4. Vidal, R.J.
Model Instrumentation Techniques for Heat Transfer and Force Measurements in a Hypersonic Shock Tunnel
Cornell Aeronautical Laboratory, Inc.
Rep. No 40-917-A-1 Febr. 1956

5. Meyer, R.F. Further Comments on Analogue Networks to Obtain Heat Flux from Surface Temperature Measurements
National Research Council of Canada
Aeronautical Rep. LR-375 March 1963

6. Fay, J.A.
Riddel, F.R. Theory of Stagnation Point Heat Transfer in Dissociated Air
Journ. of the Aeron. Sci. Vol. 25 No 2 Febr. 58

7. Lees, L. Laminar Heat Transfer Over Blunt-Nosed Bodies at Hypersonic Flight Speeds
Jet Propulsion 26 1956 page 259-269

8. Kemp, N.H.
Rose, P.H.
Detra, R.W. Laminar Heat Transfer Around Blunt Bodies in Dissociated Air
Journ. of the Aero/Space Sci. Vol. 26 July 59

9. Rose, P.H.
Stark, W.J. Stagnation Point Heat-Transfer Measurements in Dissociated Air
Journ. of the Aeron. Sci. Vol. 25 No 2 Febr. 58

10. Lees, L.
Kubota, T. Inviscid Hypersonic Flow Over Blunt Nosed Slender Bodies
Journ. of the Aero/Space Sci. Vol. 24 1957

11. Sakurai, A. On the Propagation and Structure of the Blast Wave
Journ. of the Phys. Soc. of Japan
Part I Vol. 8 No 5 1953
Part II Vol. 9 No 2 1954

12. Van Hise, V. Analytic Study of Induced Pressure on Long Bodies of Revolution with Varying Nose Bluntness at Hypersonic Speeds
NASA TR R-78 1961

13. Hanawalt, A.J.
Blessing, A.H.
Schmidt, C.M. Thermal Analysis of Stagnation Regions with Emphasis on Heat-Sustaining Nose Shapes at Hypersonic Speeds
Journ. of the Aero/Space Sci. Vol. 26 May 59

14. Crawford, D.H. Investigation of the Flow Over a Spiked-Nosed Hemisphere-Cylinder
NASA TN D-118 Dec. 1959

15. Burggraf, O.R. A Model of Steady Separated Flow in Rectangular Cavities at High Reynolds Number
Proc. of the 1965 Heat Trarsfer and Fluid Mechanics Institute

16. Nicoll, K.M.
Bogdonoff, S.M.
Experimental Studies of a Specific Cavity Configuration in Laminar Hypersonic Flow
Fluid Dynamics Transaction Vol. 2 1965

17. Chung, P.M.
Viegas, J.R.
Heat Transfer at the Reattachment Zone of Separated Laminar Boundary Layers
NASA TN D-1072 Sept. 1961

18. Reeves, B.L.
Lees, L.
Theory of Laminar Near Wake of Blunt Bodies in Hypersonic Flow
AIAA Journ. Vol. 3 No 11 Nov. 1965

19. Chapman, D.R.
A Theoretical Analysis of Heat Transfer in Regions of Separated Flow
NACA TN 3792 Oct. 1956

20. Larson, H.K.
Heat Transfer in Separated Flows
Journ. of the Aero/Space Sci. Vol. 26 No 11 59

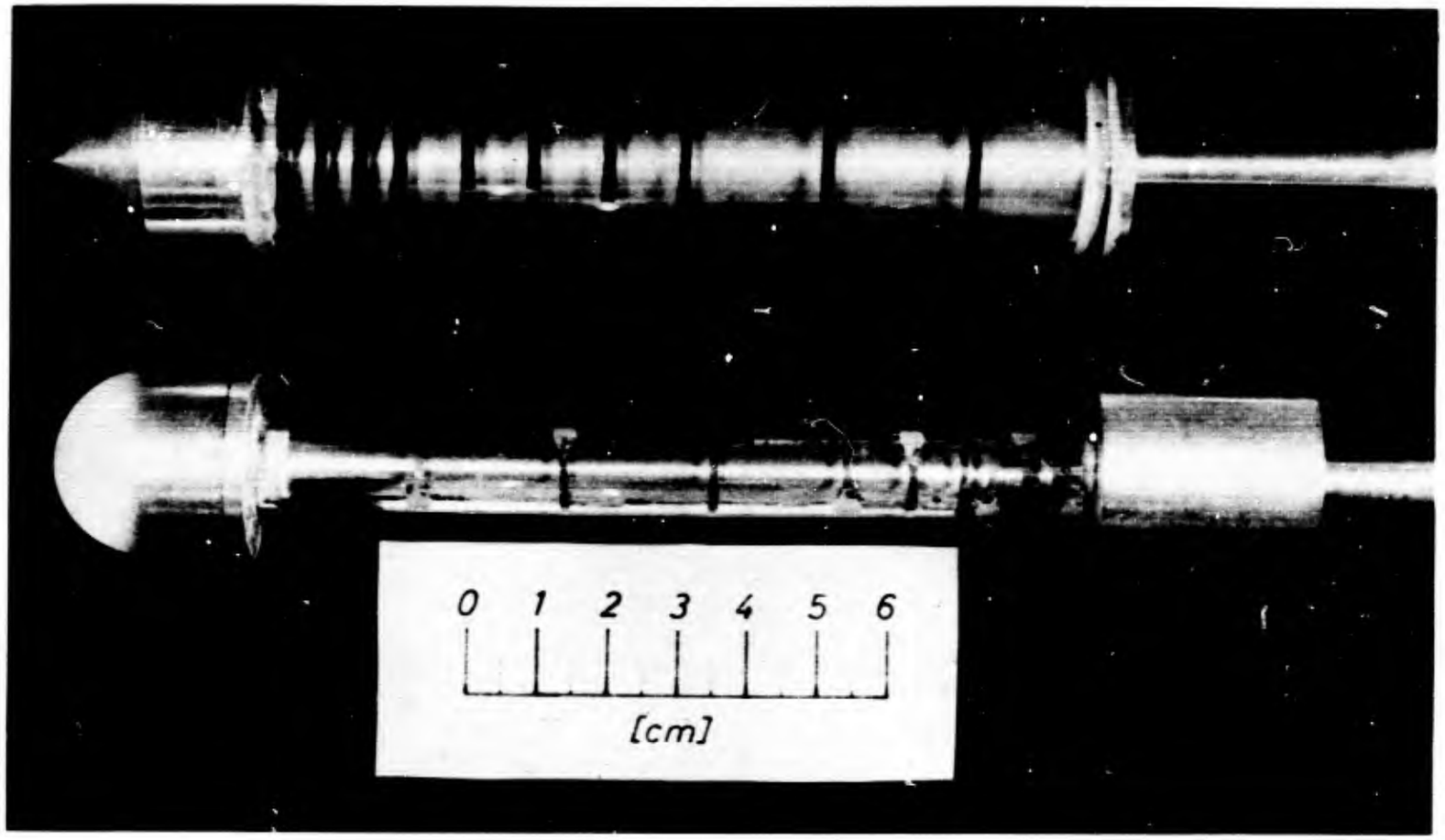

Fig. 1 Heat transfer models

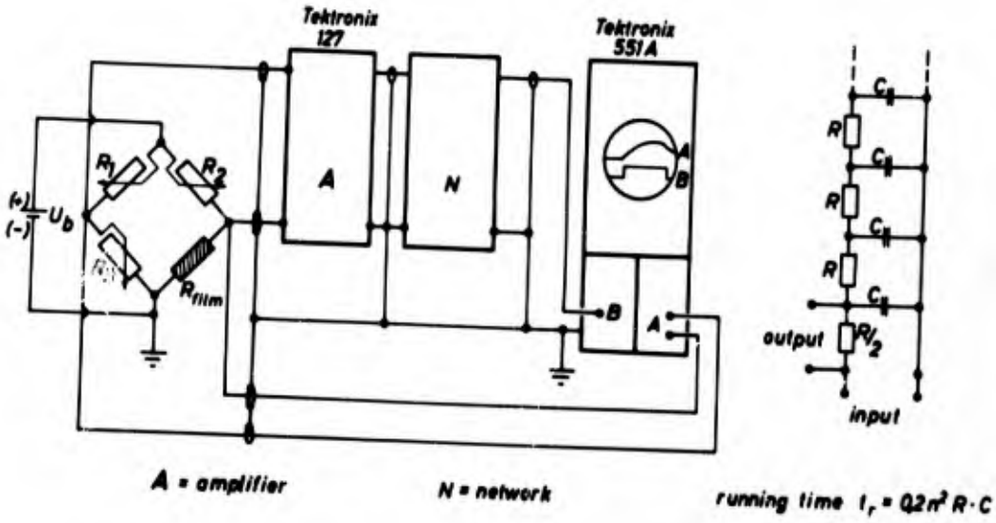

Fig. 2 Scheme for temperature and heat flux measurements

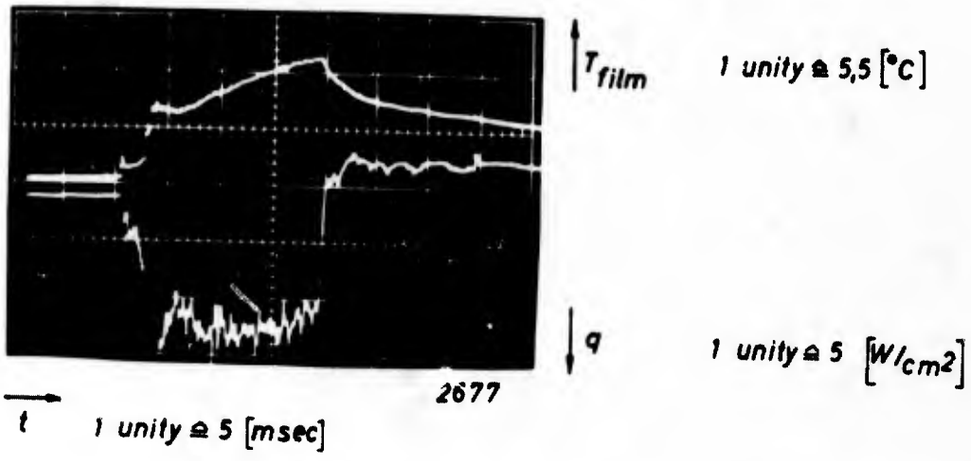

Fig. 3 Heat transfer measurement in a cavity

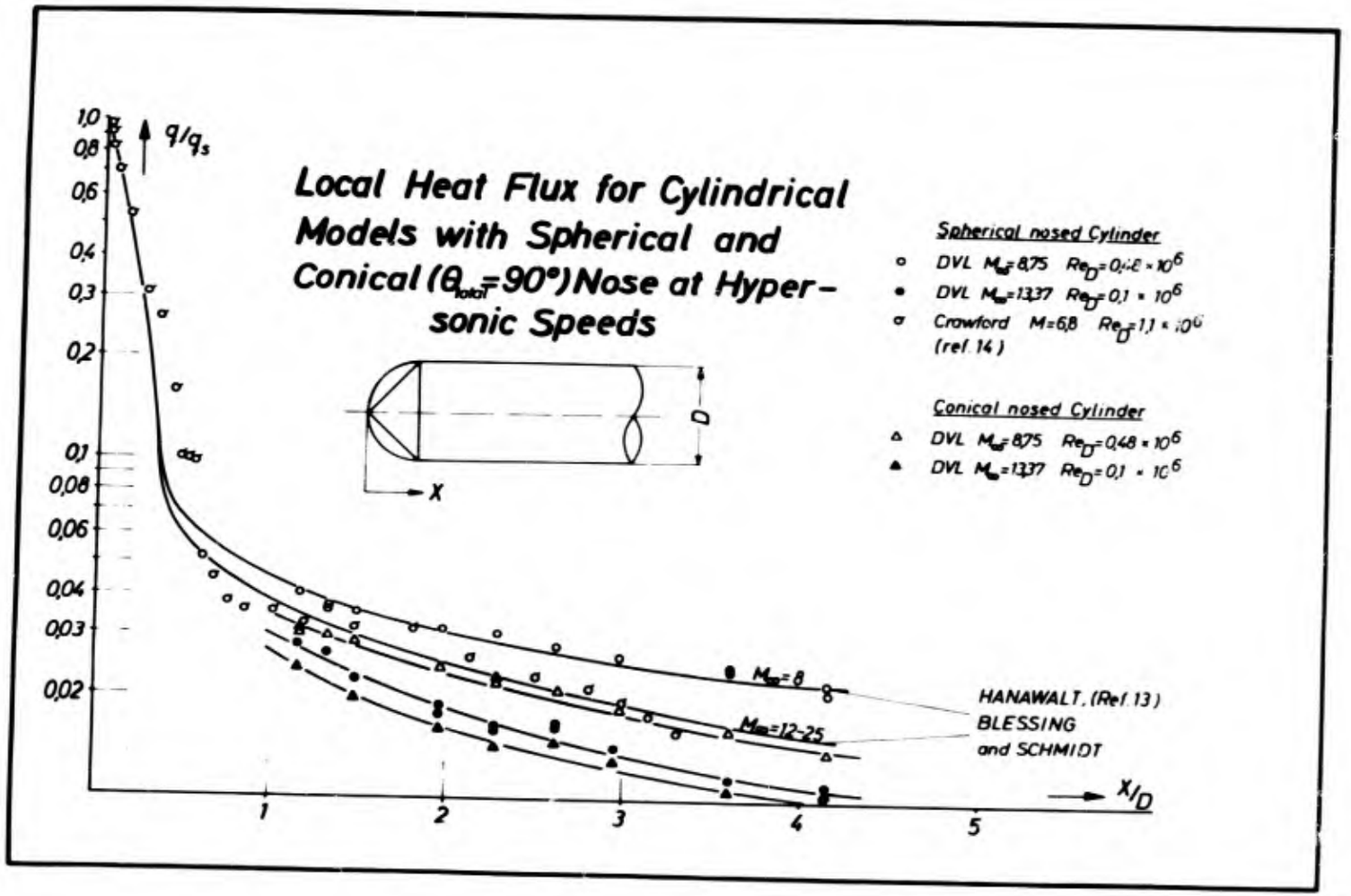

Fig. 4 Local heat flux for cylindrical models with spherical and conical nose

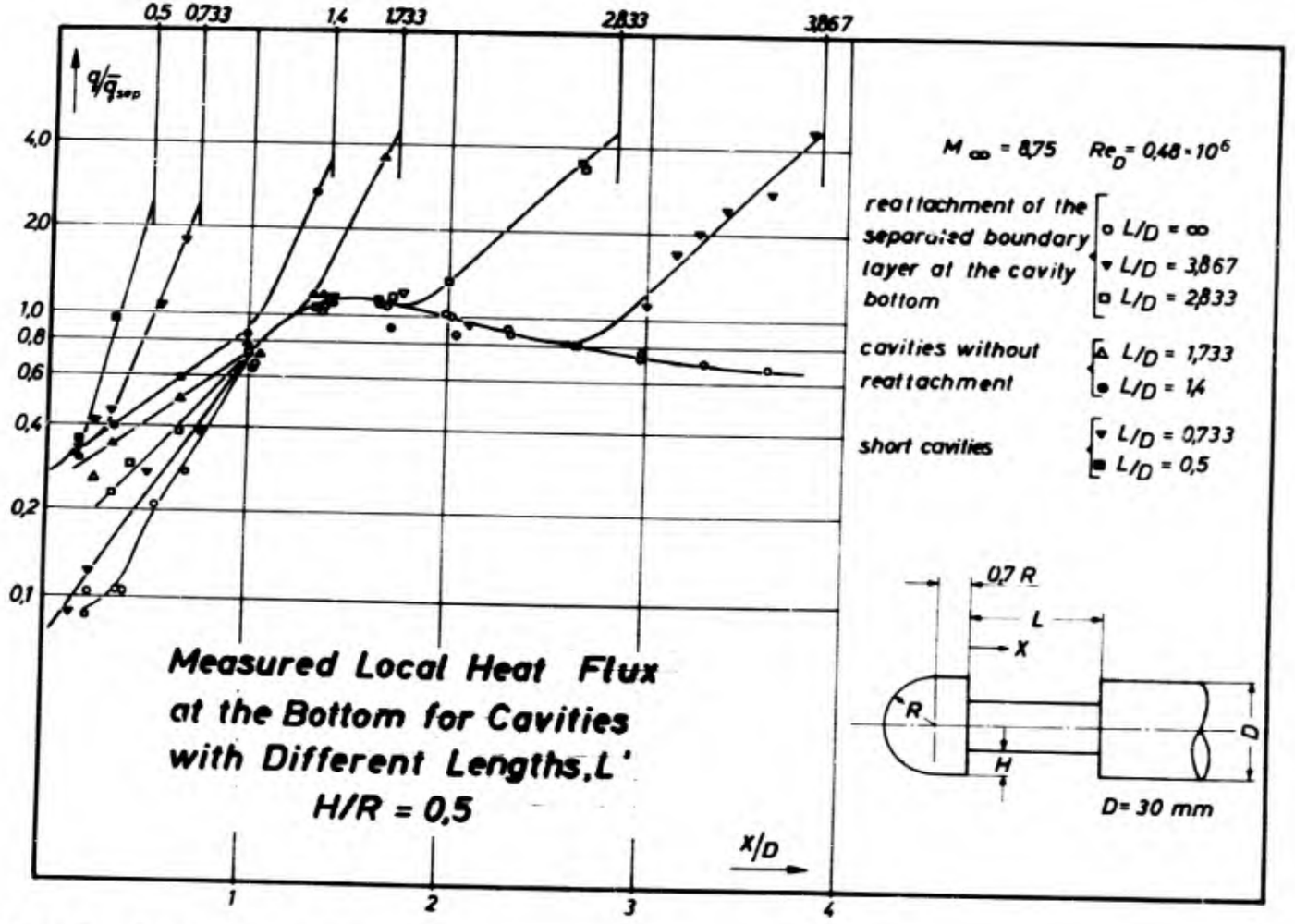

Fig. 5 Local heat flux at the bottom for cavities of different lengths for H/R = 0,5

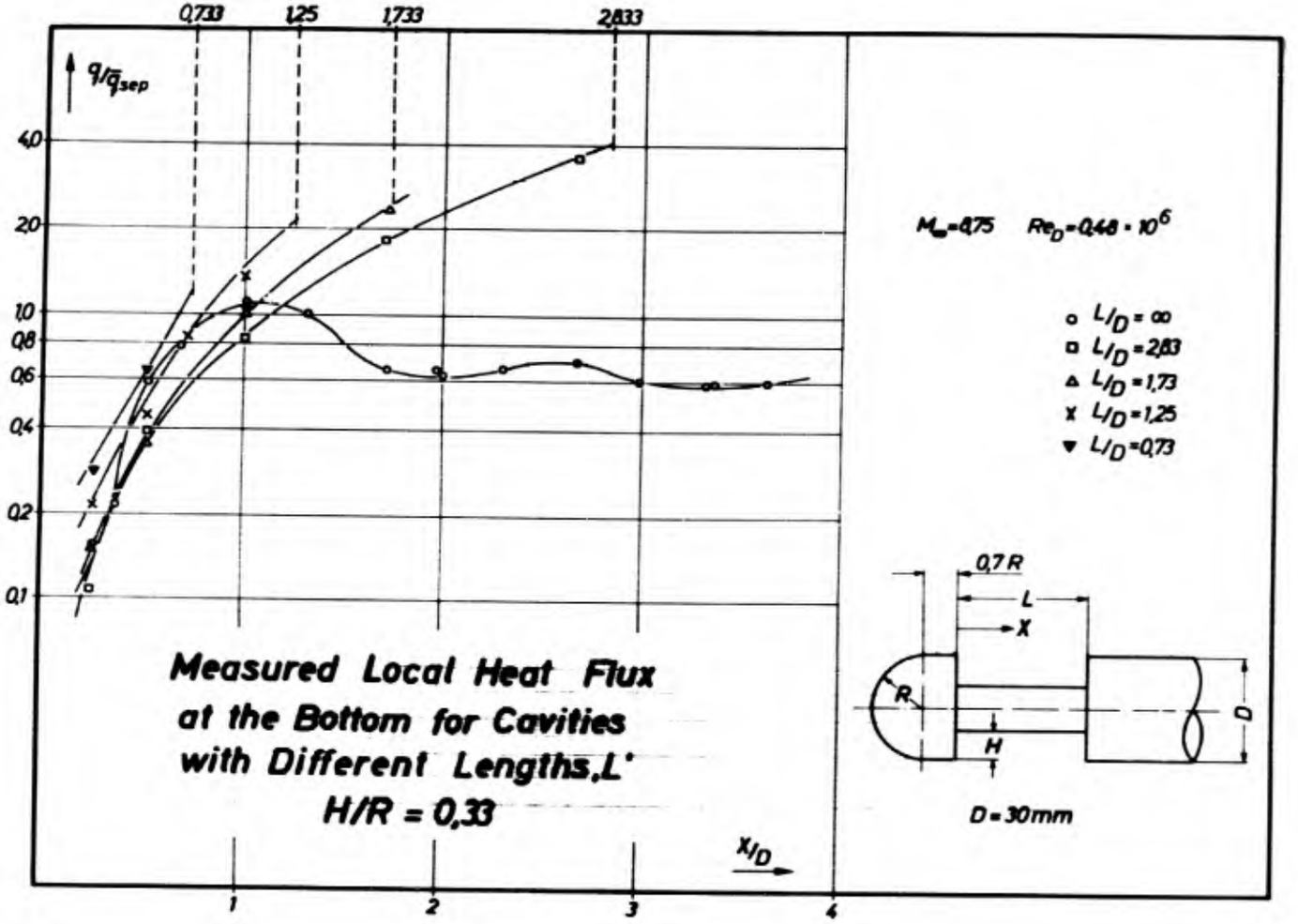

Fig. 6 Local heat flux at the bottom for cavities of different lengths for H/R = 0,33

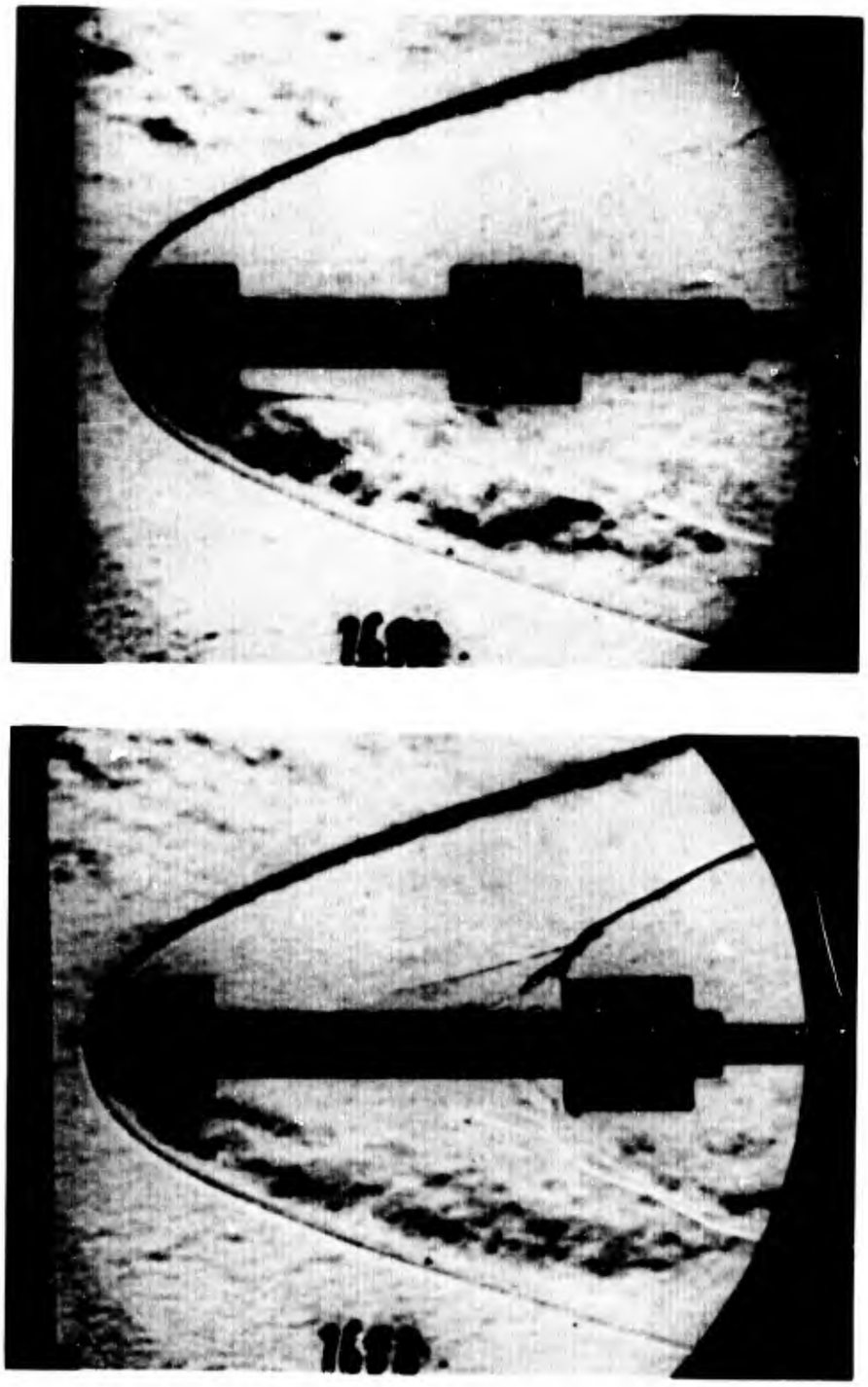

Fig. 7 Schlieren pictures from cavities (H/R = 0,5) at M_∞ = 8,75 and Re_D = 0,48x10^6 L/H = 6,93 (above) L/H = 11,33 (below)

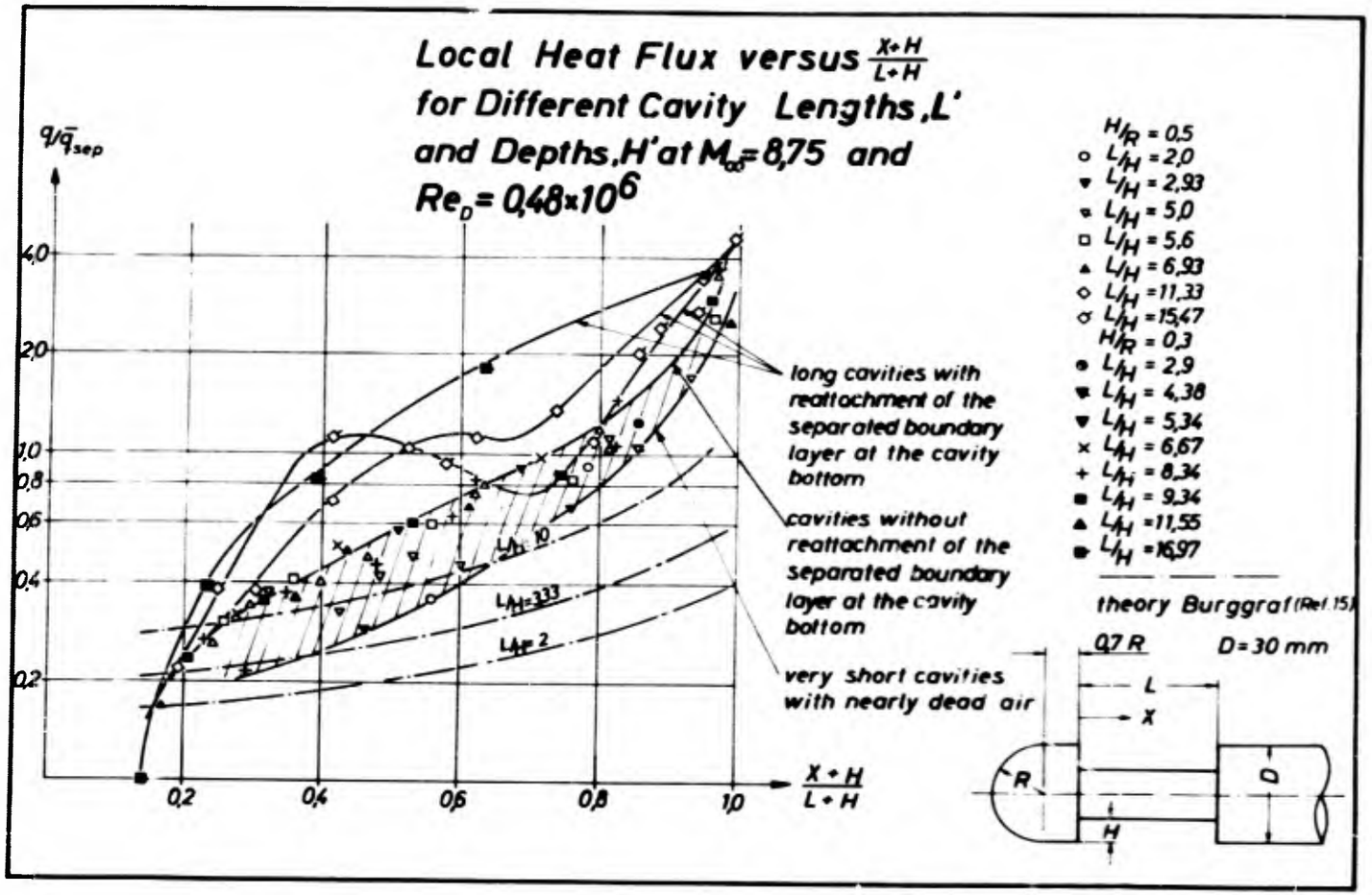

Fig. 8 Heat flux at the cavity bottom versus $\frac{X+H}{L+H}$

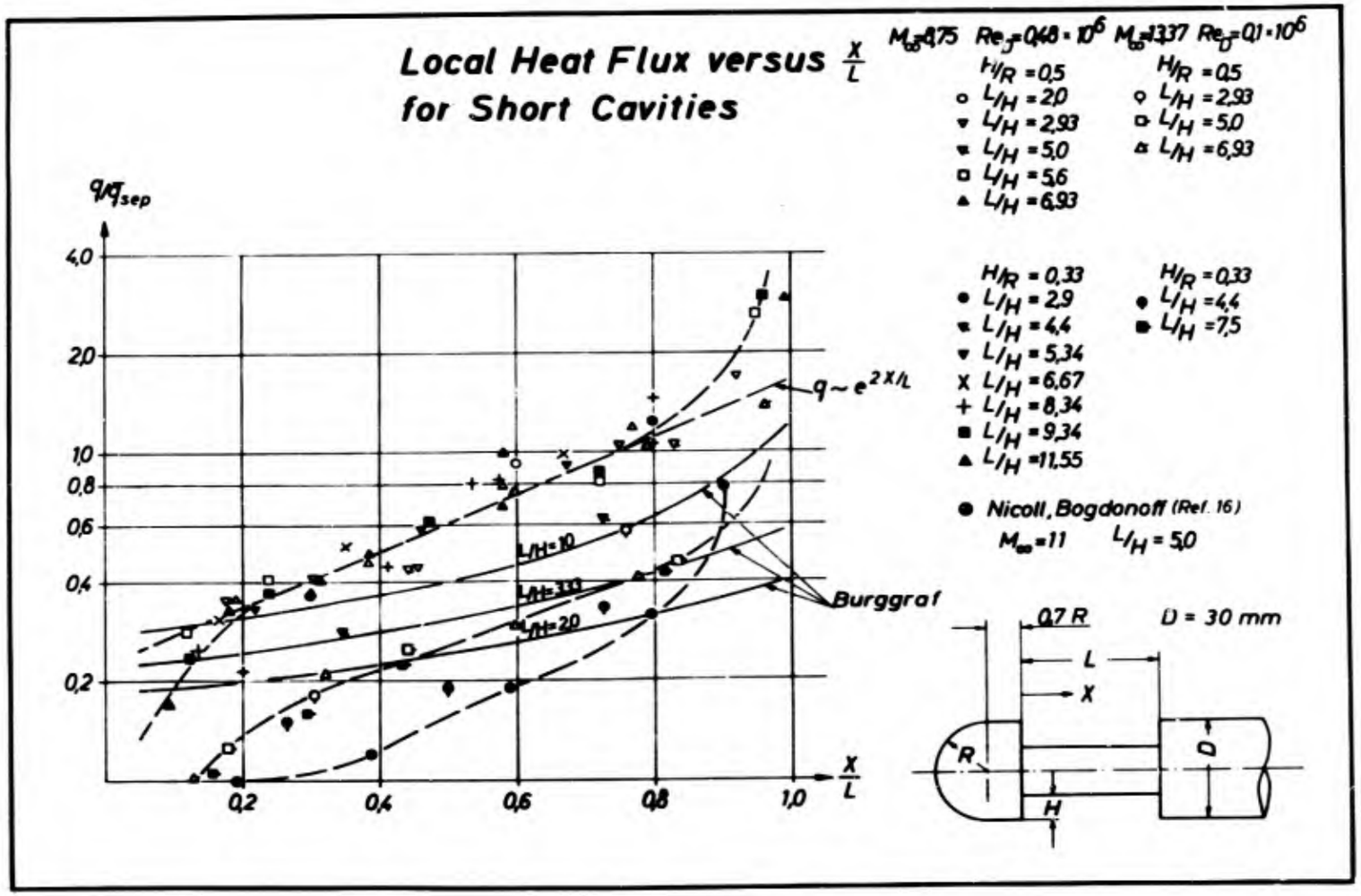

Fig. 9 Heat flux at the cavity bottom versus X/L

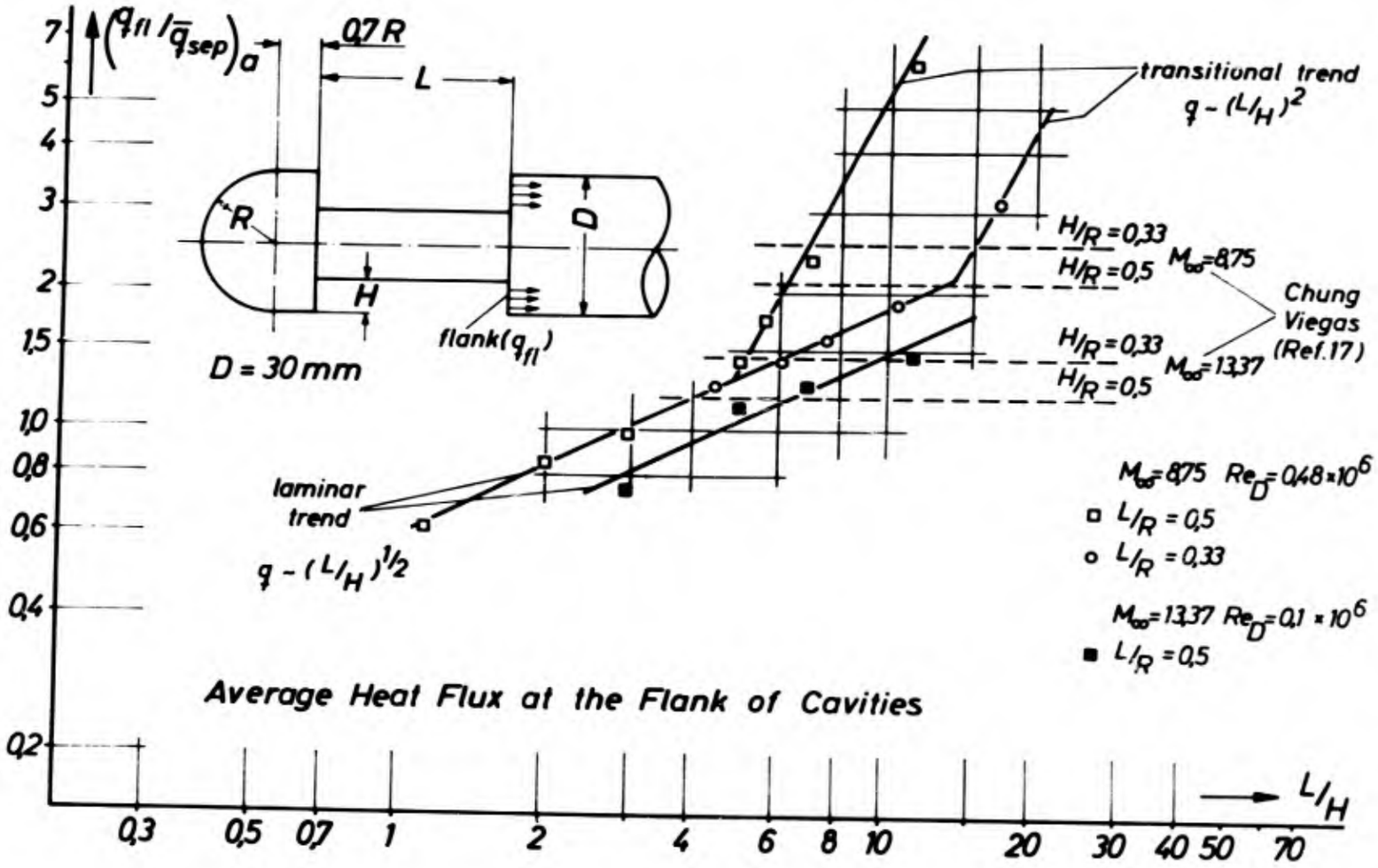

Fig. 10 Heat flux at the flank of the cavity

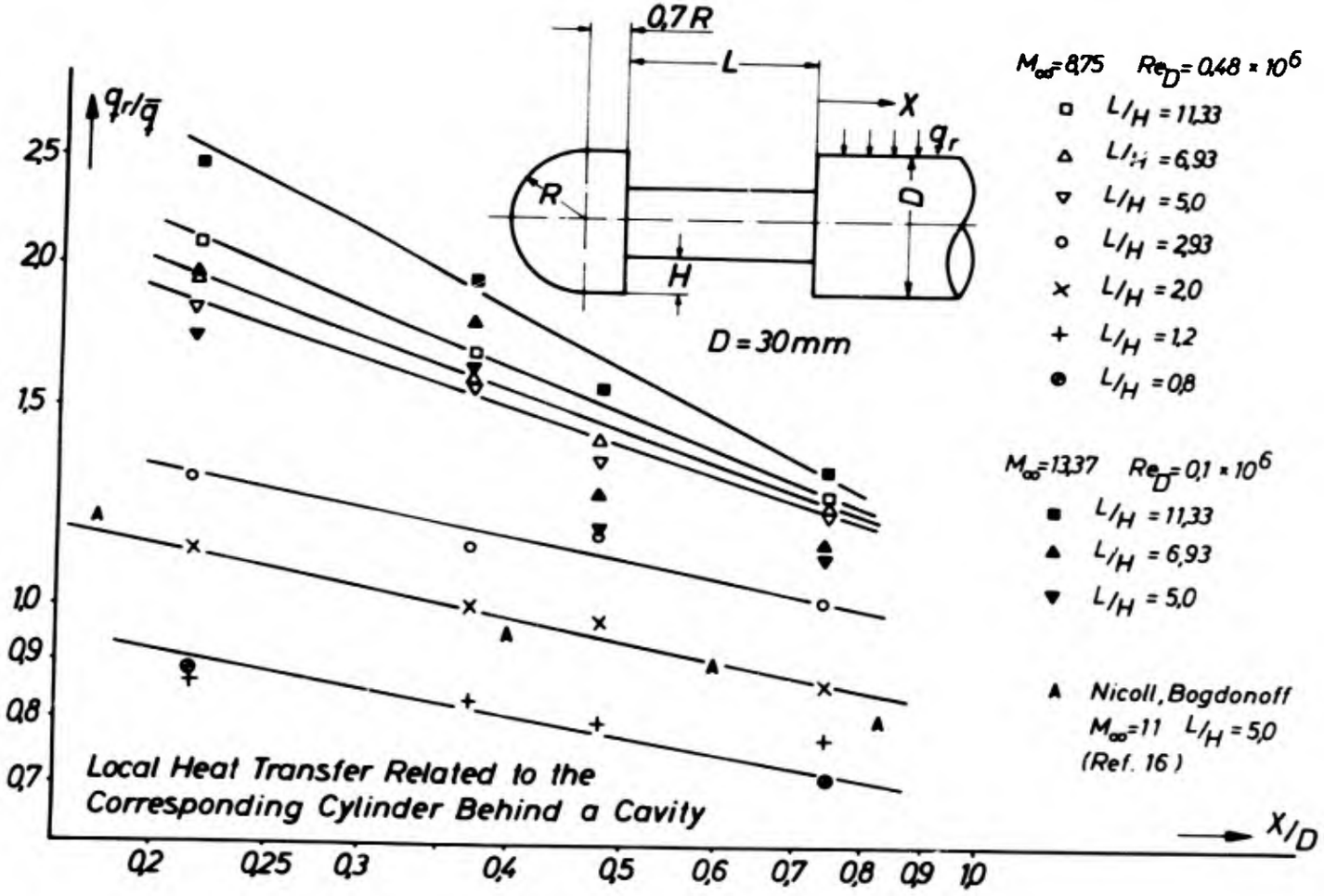

Fig. 11 Heat flux at the cylinder behind a cavity versus X/D

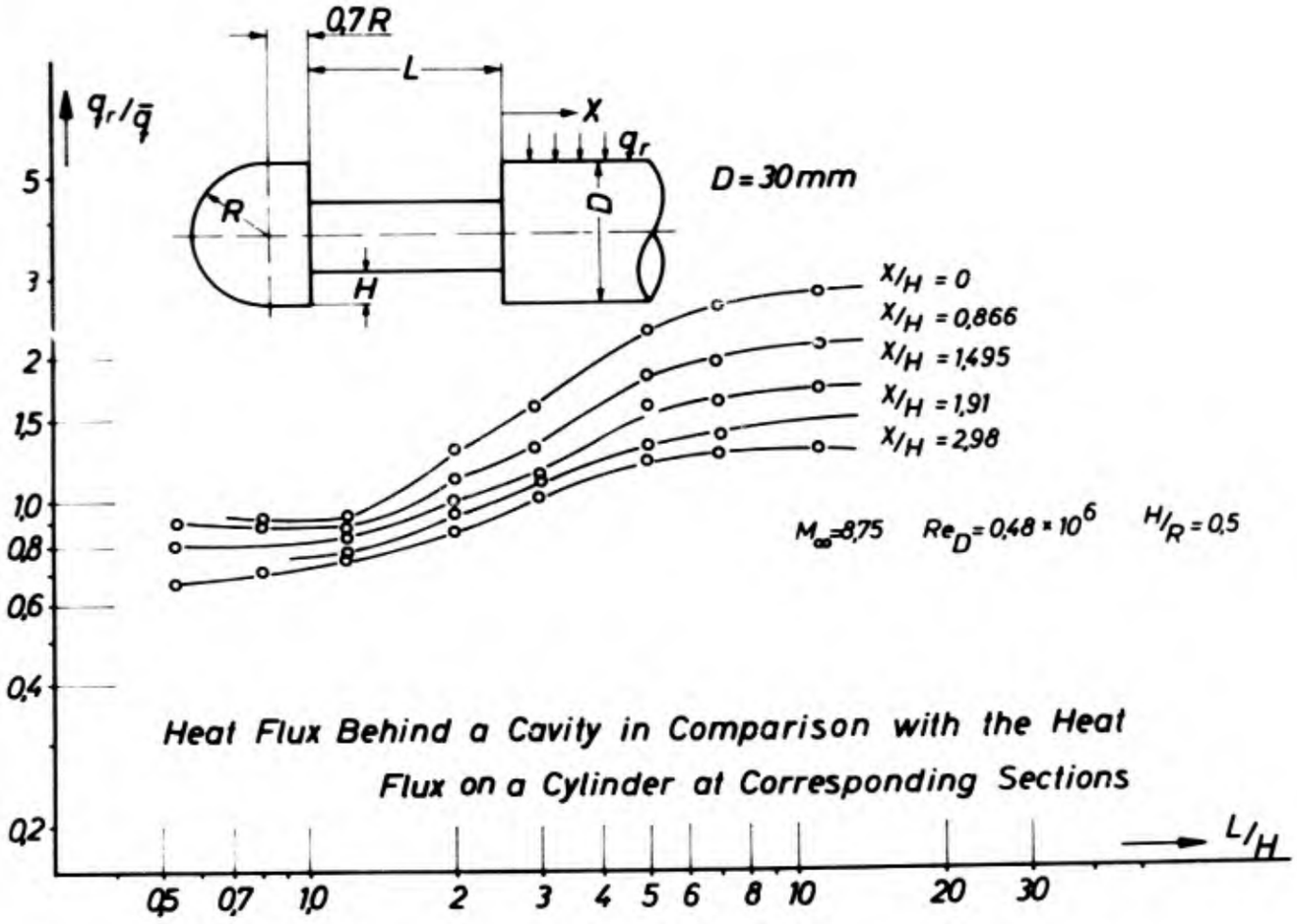

Fig. 12 Heat flux at the cylinder behind a cavity versus L/H

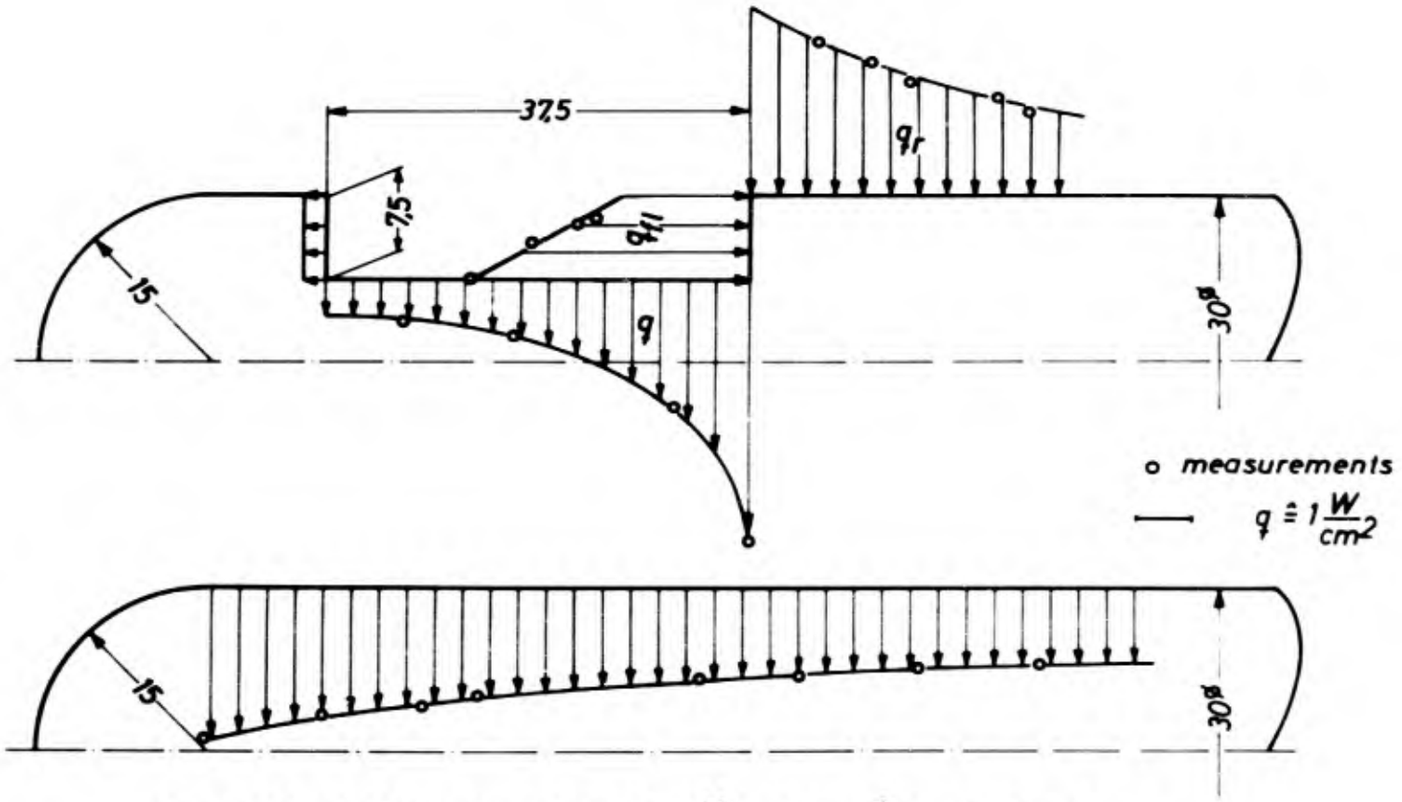

Local Heat Flux in a Cavity ($H/R = 0,5$ $L/H = 5$) and on Spherical Nosed Cylinder at $M_\infty = 8,75$ and $Re_D = 0,48 \cdot 10^6$

Fig. 13 Distribution of heat flux in a cavity and on the cylinder

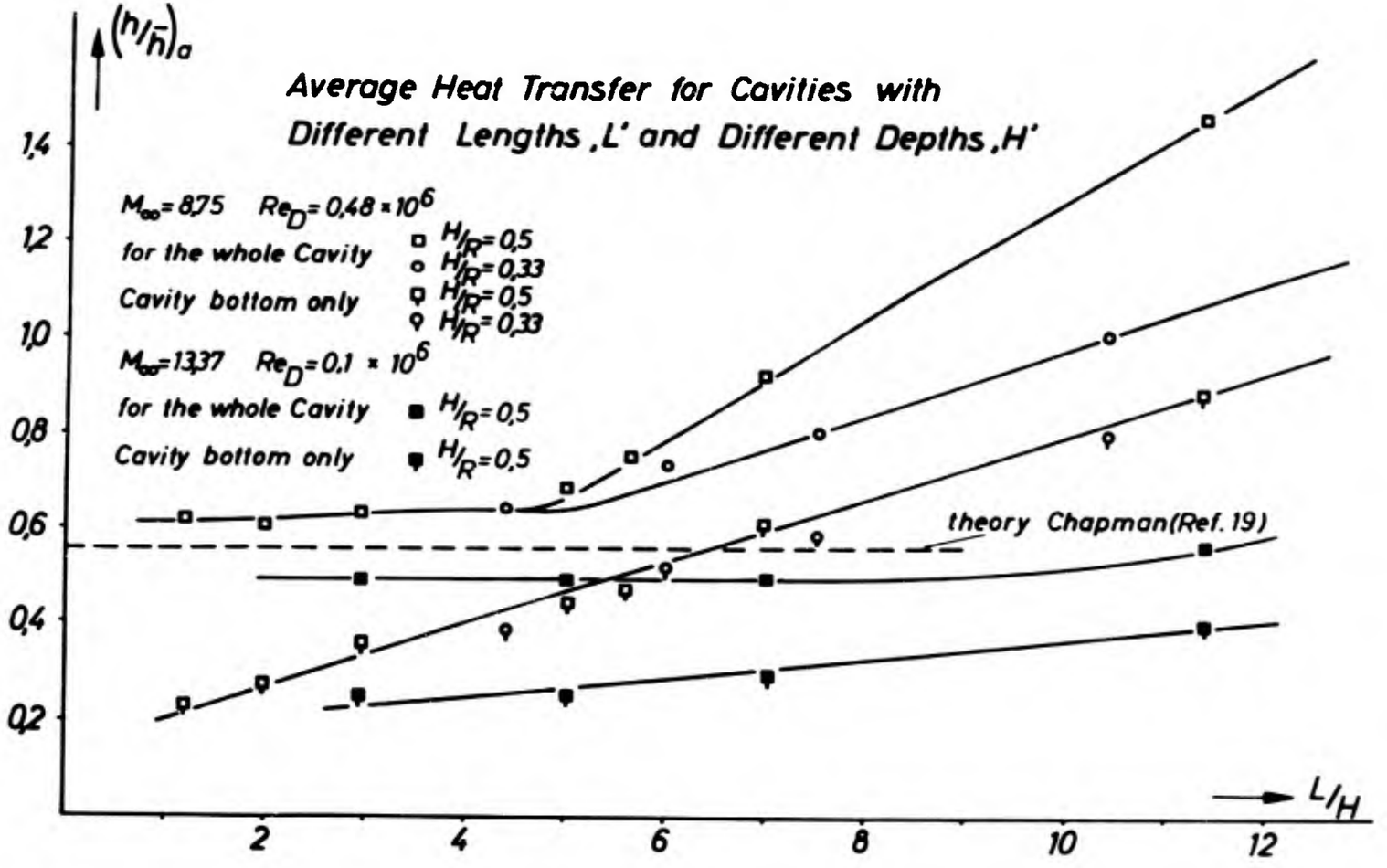

Fig. 14 Average heat transfer for cavities

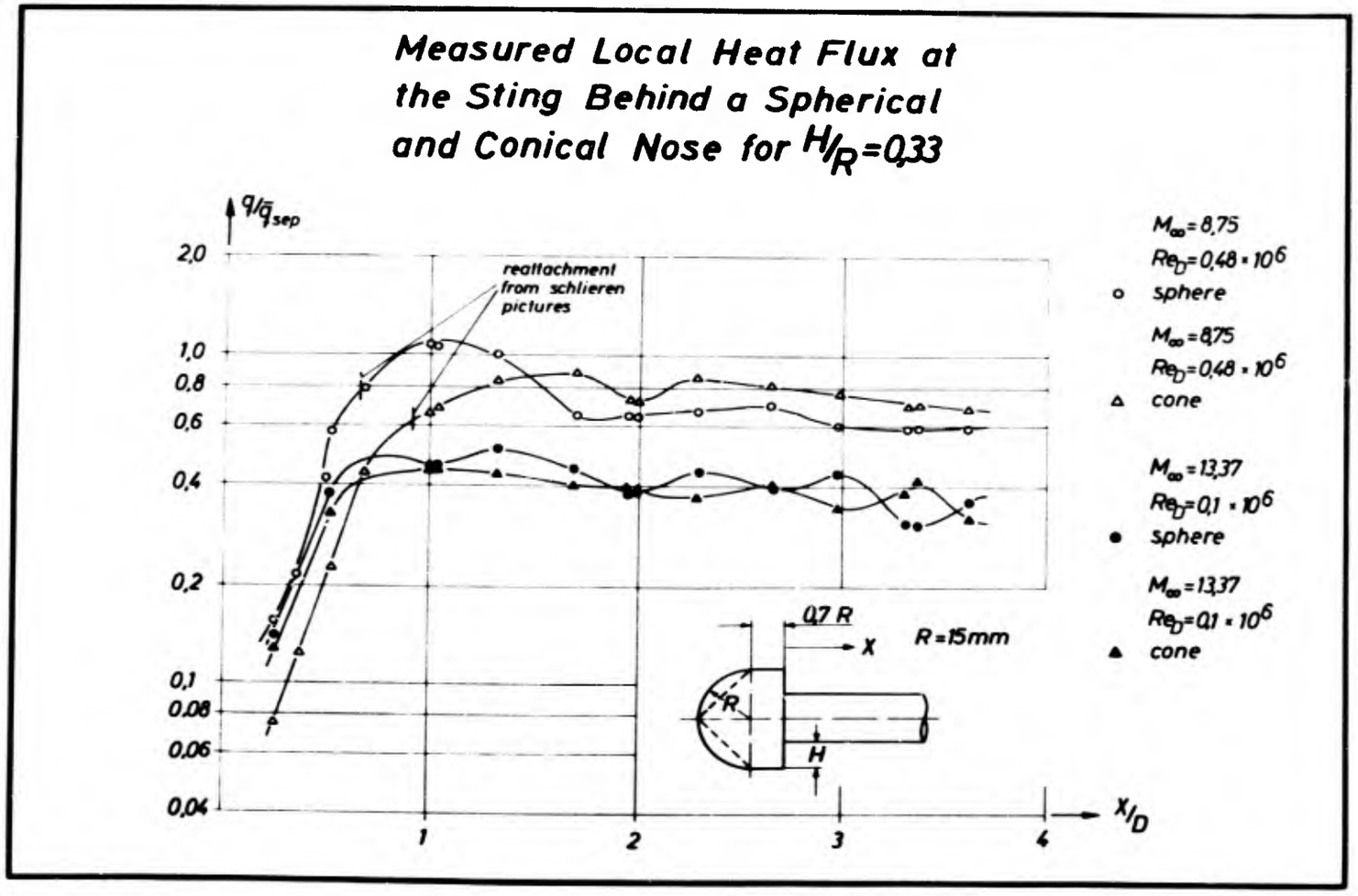

Fig. 15 Heat flux at the sting behind a rotationally symmetric step for H/R = 0,33

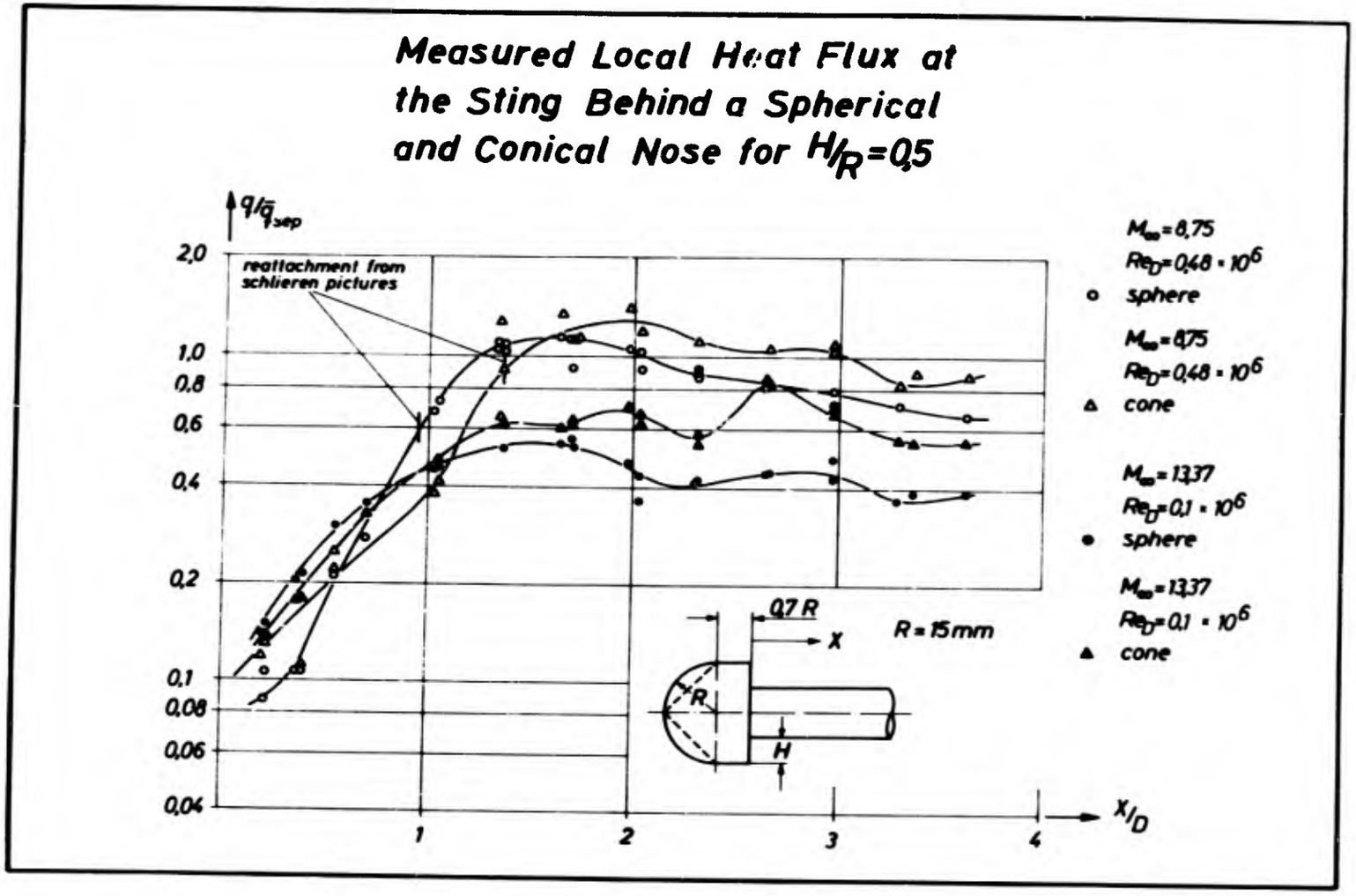

Fig. 16 Heat flux at the sting behind a rotationally symmetric step for H/R = 0,5

SOLUTION OF THE TIME-DEPENDENT NAVIER-STOKES EQUATIONS FOR THE FLOW OF DISSOCIATING GAS OVER A CIRCULAR CYLINDER

by

S. M. Scala[1] and P. Gordon[2]

General Electric Company
Space Sciences Laboratory
Philadelphia, Pennsylvania

[1] Manager, Theoretical Fluid Physics .

[2] Group Leader, Scientific Computations

SUMMARY

The authors present numerical solutions to the complete time-dependent Navier-Stokes equations for a two-dimensional flow, namely, the transient hypersonic flow around a right circular cylinder, including finite reaction rate chemistry for the dissociation of a diatomic gas. And, in particular the mathematical question of convergence is treated in detail.

The basic approach utilized here relies on the use of the time-dependent Navier-Stokes equations, since as suggested by Crocco, it is often preferable to emulate nature by solving the flow field problems as an initial value problem. The governing equations for the conservation of mass, momentum, energy and chemical species were first expressed in cylindrical coordinates. Then, a set of "explicit-implicit" finite difference equations was introduced. The resulting equations were then analyzed for stability and convergence and specific criteria were established for determining the step sizes to be used for each independent variable r, e and t.

Numerical solutions were then obtained on both IBM 7094 and CDC 6600 digital computers for the hypersonic flow around a right circular cylinder for a range of Reynolds numbers $1 < Re < 1000$. In these computations, the free stream velocity was held fixed at 20,000 ft/sec, and the Reynolds number was varied by changing the free stream density (simulated altitude) and the cylinder radius.

The new results represent the first time that our methods have been utilized for the solution of a two-dimensional flow problem, in which chemical reactions are included.

The results presented here are significant because:

1. New insight is obtained into the structure of the near wake behind a blunt object including the effects of compressibility, heat conduction, viscosity and chemical reactions.

2. The effects of Reynolds number on the wake are determined for a wide range of Reynolds number.

3. Our results can be used as a yardstick against which other approximate methods can be assessed.

4. Sufficient detail is given so that meaningful new experiments can be planned in future wake research.

RESUME

Les auteurs de cet exposé présentent des solutions numériques aux équations complètes de Navier-Stokes en instationnaire dans le cas d'un écoulement bi-dimensionnel, c'est à dire d'un écoulement hypersonique transitoire autour d'un cylindre droit circulaire, en étudiant également le processus chimique du taux de réaction fini en régissant la dissociation d'un gaz biatomique. Ils traitent particulièrement en détail la question mathématique de la convergence.

Pour aborder le problème décrit ci-dessus, les auteurs ont recours aux équations dépendantes du temps de Navier-Stokes; il est souvent préférable, en effet, ainsi que le suggère Crocco, d'imiter la nature en résolvant le problème du champ d'écoulement comme s'il s'agissait d'un problème initial de valeurs. On a d'abord exprimé les équations auxquelles obéissent la conservation de la masse, la quantité de mouvement, l'énergie, et les substances chimiques, sous forme de coordonnées cylindriques. Puis on a introduit un ensemble d'équations explicites-implicities, aux différences finies. On a analysé les équations qui en ont résulté pour obtenir la stabilité et la convergence, et l'on a établi des critères spécifiques pour déterminer la grandeur de pas à utiliser pour chacune des variables indépendantes r, e et t.

On a ensuite obtenu des solutions numériques à la fois sur l'IBM 7094 et sur la CDC 6600, dans le cas d'un écoulement hypersonique le long d'un cylindre droit circulaire, pour une gamme de nombre de Reynolds de $1 < Res < 1000$. Au cours de ces calculs, on a gardé une vitesse d'écoulement libre de 20.000 pieds par seconde, mais fait varier le nombre de Reynolds en modifiant la densité de l'écoulement libre (altitude simulée) et le rayon du cylindre.

Les nouveaux résultats sont ceux de la première application de nos méthodes à la solution d'un problème d'écoulement bi-dimensionnel comportant des réactions chimiques.

Les résultats exposés ici sont importants pour les raisons suivantes:

1. On obtient un nouvel aperçu de la structure du sillage proche à l'arrière d'un objet arrondi, y compris les effets de la compressibilité, de la conduction de la chaleur, de la viscosité et des réactions chimiques.

2. Les effets du nombre de Reynolds sur le sillage se trouvent déterminés pour une gamme étendue de nombres de Reynolds.

3. On peut utiliser nos résultats comme critère de comparaison pour l'évaluation d'autres méthodes approchées.

4. Les détails donnés sont suffisants pour permettre la mise au point d'expériences nouvelles et significatives dans les futurs travaux de recherche portant sur les sillages.

BLANK PAGE

1. INTRODUCTION

During the past several years, the authors have been engaged in the development of numerical procedures for solving the time-dependent Navier-Stokes equations [1-4] for real gas flows.[5] For the treatment of such flows, this implies that one will include in the system of equations the specific effects of compressibility, viscous dissipation, thermal conduction, diffusion and chemical reactions. The resulting system of nonlinear partial differential equations is so complex that one anticipates that a large amount of computer time will be required for the numerical solution of the finite difference representation of the system. Consequently, our rationale has been that we would begin our investigation with the simplest geometry and the simplest, but nevertheless realistic, gas model.

In our first paper,[6] in which numerical solutions were presented for the complete time-dependent Navier-Stokes equations, we treated the piston problem for a perfect non-reacting gas. The planar piston was accelerated into a quiescent gas and the development of the resulting one-dimensional shock wave and its subsequent reflection at a wall were followed in time. The gas model utilized for nitrogen specified that the molecules had a constant specific heat, but that the viscosity and thermal conductivity coefficients were variable and were taken as proportional to the square root of the local absolute temperature of the gas.

In a following investigation,[7] the one-dimensional time-dependent Navier-Stokes equations were utilized in going to the asymptotic time limit, or steady state solution. Here, it was found possible to make a direct comparison of our results with Becker's classical solution for shock wave structure.[8]

Having treated planar problems successfully, the authors also examined a spherically-symmetric flow in which the time-dependent Navier-Stokes equations were solved in spherical coordinates.[9]

In an investigation reported on earlier this year,[10] the authors extended their numerical techniques to the treatment of the supersonic flow of a non-reacting gas around a circular cylinder, and solutions were obtained for the development of the flow field as a function of time for a given Mach number and several values of the Reynolds number.

In the present paper, we will retain the cylindrical geometry utilized earlier, however, we will introduce three additional complications. At sufficiently high gas temperatures, we will allow the gas molecules to undergo dissociation and recombination processes according to the appropriate chemical kinetic equations. This results in the production of atomic species in the flow. Consequently, it becomes necessary to introduce the specific effects of diffusion and chemical reactions and it is then more realistic to utilize a variable specific heat which depends on the local gas composition and local gas temperature.

As stated in our earlier paper,[10] the authors believe that numerical work dictates that one should consider the stability, convergence and uniqueness of the results expected from a proposed computation method before one begins the computations. At the present time, methods do not exist for rigorously establishing the convergence and uniqueness of the solution of a finite difference equation to the solution of a reasonably complex nonlinear partial differential equation. In fact,

it is in general quite difficult to establish the existence of a unique solution to the partial differential equations themselves; in the case of the Navier-Stokes equations, this is still an unsolved problem.

Nevertheless, there are criteria and procedures which we think must be followed if one is to be reasonably sure of the validity of the numerical results that one obtains. Some of these are:

1) One should begin with a well-posed mathematical problem. That is, the existence of a unique solution to the mathematical system of partial differential equations should first be demonstrated. As just noted, very often this is beyond the present state of the art. However, certain mathematical concepts, such as characteristics, have been established [11] and should be applied whenever possible.

2) The stability of the difference equations should be investigated. At the present time, since the concept of stability is not yet well defined for nonlinear partial differential equations, at the very least one should study the stability for a suitably linearized system. For example, one may set the coefficients of certain terms equal to constants and hence independent of the dependent variables, and study the stability of the resulting system of equations. If these are not stable, it is unlikely that the full nonlinear set will be well behaved.

3) The consistency of the difference equations should be established. That is, one would like to demonstrate that the finite difference equations truly represent the partial differential equations. Normally, this is a truncation error type analysis, as for example the Dufort-Frankel difference equation.[12-14] However, in compiicated difference equations, where, for example, different terms are evaluated at neighboring mesh points the situation can be quite treacherous. Gordon discusses this more carefully in reference.[15] At any

rate, the possibility of converging to a solution of the wrong differential equation is not remote and should be carefully examined.

Having successfully completed this type of analytic study, one can proceed with at least a small degree of confidence to the actual computations. It is now necessary to perform an "experimental" check on the above analysis. This can be done, as discussed in reference 6, by making a sequence of computer runs for the same initial values and boundary conditions, in which the mesh size is reduced according to the criteria developed in steps 2) and 3) above. A comparison of these sequential results should clearly indicate convergence.

It is perhaps also worth mentioning that at some point it is also desirable to compare the theoretical predictions with carefully executed experiments to further verify the numerical results and conclusions which may be derived.

2. DEFINITION OF PHYSICAL PROBLEM

As discussed in reference 6, prior to 1965 the published work on viscous gas flows involving the presence of shock waves[16-25] was based on one of several approximate approaches, involving approximations to the complete Navier-Stokes equations. A major step forward was made in 1965 when Crocco[26] suggested an asymptotic method of solving the steady Navier-Stokes equations. Shortly, thereafter, the authors treated the complete time-dependent Navier-Stokes equations for the formation and reflection of a planar shock wave.[6] As noted in the introduction, the authors' success in solving the Navier-Stokes equations utilizing a new explicit-implicit finite difference scheme suggested that one might expect to attack more complex problems utilizing present generation digital computers.

In a shock tube, one establishes the supersonic flow around an object by generating a shock wave and allowing it to propagate downstream followed by a "uniform" flow which lasts for a relatively short time (usually a maximum of milliseconds). This relatively short test time is usually sufficient to establish what amounts to "steady" flow as an asymptote, depending on what physical measurements one wishes to make.

As in our most recent earlier work,[10] we have decided to imitate nature by generating a planar shock wave with a piston moving into a quiescent gas, and then permitting this planar shock wave to propagate past a right circular cylinder oriented so that the free stream flow is perpendicular to the axis of the cylinder (see Figure 1). One expects that the planar shock wave will become distorted by the cylinder, part of it being "held" by the cylinder near the axis, while those portions just off the axis

become curved and the outermost regions of the shock wave continue to propagate downstream as a planar shock wave.

In this problem, it is noted that although the free stream gas has a relatively high temperature behind the incident shock wave (i.e. $T_\infty = 8960\ ^{O}R$), it is nevertheless too low to produce a significant concentration of atomic species (i.e. $C_N < 10^{-4}$). In general, the atomic species are produced in the hotter regions of the flow field. Since we will invoke the assumption of an adiabatic wall, the region near the surface of the cylinder will be the hottest region. Hence, in this problem the atomic species will tend to be formed near the body and will be transported downstream by convection and diffusion.

3. GOVERNING EQUATIONS AND BOUNDARY CONDITIONS

In treating the two-dimensional, compressible, viscous, thermally conducting, diffusing, chemically reacting, time-dependent flow about a cylinder, it is convenient to use polar cylindrical coordinates (t, r, θ). Accordingly, the Navier-Stokes equations may be written as follows. The conservation of mass is:

$$\frac{\partial \rho}{\partial t} + \frac{1}{r}\left[\frac{\partial}{\partial r}(\rho r V_r) + \frac{\partial}{\partial \theta}(\rho V_\theta)\right] = 0 \tag{1}$$

The conservation of species i is:

$$\rho \frac{\partial C_i}{\partial t} + \rho V_r \frac{\partial C_i}{\partial r} + \rho \frac{V_\theta}{r} \frac{\partial C_i}{\partial \theta} = \frac{\partial}{\partial r}\left(\rho \mathcal{D}_{ij} \frac{\partial C_i}{\partial r}\right)$$

$$+ \frac{\rho \mathcal{D}_{ij}}{r} \frac{\partial C_i}{\partial r} + \frac{1}{r^2} \frac{\partial}{\partial \theta}\left(\rho \mathcal{D}_{ij} \frac{\partial C_i}{\partial \theta}\right) + \dot{w}_i \tag{2}$$

where thermal diffusion has been neglected.

The conservation of momentum in the r direction is:

$$\rho\left[\frac{dV_r}{dt} - \frac{V_\theta^2}{r}\right] = -\frac{\partial P}{\partial r} + \frac{\partial}{\partial r}\left[\mu\left(2\frac{\partial V_r}{\partial r} - \frac{2}{3}\nabla \cdot \vec{V}\right)\right]$$

$$+ \frac{1}{r}\frac{\partial}{\partial \theta}\left[\mu\left(\frac{1}{r}\frac{\partial V_r}{\partial \theta} + \frac{\partial V_\theta}{\partial r} - \frac{V_\theta}{r}\right)\right]$$

$$+ \frac{2\mu}{r}\left[\frac{\partial V_r}{\partial r} - \frac{1}{r}\frac{\partial V_\theta}{\partial \theta} - \frac{V_r}{r}\right] \tag{3}$$

The conservation of momentum in the θ direction is:

$$\rho\left[\frac{dV_\theta}{dt} + \frac{V_r V_\theta}{r}\right] = -\frac{1}{r}\frac{\partial P}{\partial \theta} + \frac{1}{r}\frac{\partial}{\partial \theta}\left[\mu\left(\frac{2}{r}\frac{\partial V_\theta}{\partial \theta} + \frac{2V_r}{r}\right.\right.$$

$$\left.\left. - \frac{2}{3}\nabla \cdot \vec{V}\right)\right] + \frac{\partial}{\partial r}\left[\mu\left(\frac{1}{r}\frac{\partial V_r}{\partial \theta} + \frac{\partial V_\theta}{\partial r} - \frac{V_\theta}{r}\right)\right] \tag{4}$$

$$+ \frac{2\mu}{r}\left[\frac{1}{r}\frac{\partial V_r}{\partial \theta} + \frac{\partial V_\theta}{\partial r} - \frac{V_\theta}{r}\right]$$

The conservation of energy is:

$$\rho\left[\overline{C}_V \frac{dT}{dt} + P\frac{d\left(\frac{1}{\rho}\right)}{dt}\right] = \Phi_c + \frac{1}{r}\frac{\partial}{\partial r}\left(rK\frac{\partial T}{\partial r}\right)$$

$$+\frac{1}{r^2}\frac{\partial}{\partial\theta}\left(K\frac{\partial T}{\partial\theta}\right) + \frac{\partial}{\partial r}\left[\rho \mathcal{D}_{ij}(h_i-h_j)\frac{\partial C_i}{\partial r}\right]$$

$$+\frac{1}{r^2}\frac{\partial}{\partial\theta}\left[\rho \mathcal{D}_{ij}(h_i-h_j)\frac{\partial C_i}{\partial\theta}\right] + \frac{1}{r}\rho \mathcal{D}_{ij}(h_i-h_j)\frac{\partial C_i}{\partial r}$$

$$-(e_i-e_j)\frac{\partial}{\partial r}\left(\rho \mathcal{D}_{ij}\frac{\partial C_i}{\partial r}\right) - \frac{(e_i-e_j)}{r^2}\frac{\partial}{\partial\theta}\left(\rho \mathcal{D}_{ij}\frac{\partial C_i}{\partial\theta}\right)$$

$$-(e_i-e_j)\frac{\rho \mathcal{D}_{ij}}{r}\frac{\partial C_i}{\partial r} - (e_i-e_j)\dot{w}_i \qquad (5)$$

Where again D_i^T has been taken equal to zero.

$$\nabla\cdot\underset{\rightarrow}{V} = \frac{1}{r}\left[\frac{\partial}{\partial r}(rV_r) + \frac{\partial}{\partial\theta}(V_\theta)\right] \qquad (6)$$

$$\frac{d}{dt} = \frac{\partial}{\partial t} + V_r\frac{\partial}{\partial r} + \frac{V_\theta}{r}\frac{\partial}{\partial\theta} \qquad (7)$$

and

$$\Phi_c = \mu\left\{2\left[\left(\frac{\partial V_r}{\partial r}\right)^2 + \left(\frac{1}{r}\frac{\partial V_\theta}{\partial\theta} + \frac{V_r}{r}\right)^2\right] + \left(\frac{1}{r}\frac{\partial V_r}{\partial\theta} + \frac{\partial V_\theta}{\partial r} - \frac{V_\theta}{r}\right)^2\right\} + \lambda\left[\frac{\partial V_r}{\partial r} + \frac{1}{r}\frac{\partial V_\theta}{\partial\theta} + \frac{V_r}{r}\right]^2 \qquad (8)$$

The equation of state for a chemically reacting perfect gas may be written:

$$p = \rho \bar{R} T \tag{9}$$

where

$$\bar{R} = C_i R_i + C_j R_j = \frac{\mathcal{R}}{\bar{M}}$$

$$= C_i \mathcal{R} \left[\frac{1}{M_i} + \frac{(1-C_i)}{M_j} \right] \tag{10}$$

Here $\mathcal{R}$ is the universal gas constant and M_i and M_j are the molecular weights of the atomic and molecular species, respectively. Thus, in fps units for nitrogen, one has:

$$\mathcal{R} = 1545 \frac{\text{ft.} - \text{lb.}}{\text{lb.-mole}^{\circ}\text{R}}$$

$$M_i = 14 \frac{\text{lb.}}{\text{lb.-mole}} \tag{11}$$

$$M_j = 28 \frac{\text{lb.}}{\text{lb.-mole}}$$

In the energy equation we note that

$$\bar{C}_V = C_i C_{V_i} + C_j C_{V_j} \tag{12}$$

$$e_i = \int_{T_{Ref.}}^{T} C_{V_i} \, dT + \Delta e_{f_i}^{o} \tag{13}$$

$$e_j = \int_{T_{Ref.}}^{T} C_{V_j} \, dT + \Delta e_{f_j}^{o} \tag{14}$$

$$h_i = \int_{T_{Ref.}}^{T} C_{p_i} \, dT + \Delta h_{f_i}^{o} \tag{15}$$

$$h_j = \int_{T_{Ref.}}^{T} C_{p_j}\, dT + \Delta h_{f_j}^{o} \tag{16}$$

and

$$C_{p_i} = C_{V_i} + \frac{\mathcal{R}}{JM_i} \tag{17}$$

$$C_{p_j} = C_{V_j} + \frac{\mathcal{R}}{JM_j} \tag{18}$$

where for N_2 it is noted that:

$$\Delta h_{f_j}^{o} \equiv 0. \tag{19}$$

For the atomic species, we take:

$$C_{V_i} = \frac{3}{2}\,\frac{\mathcal{R}}{JM_i} \tag{20}$$

whereas for the molecular species

$$C_{V_j} = \frac{\mathcal{R}}{JM_j}\left[\frac{5}{2} + \frac{\left(\frac{\Theta}{T}\right)^2 e^{\Theta/T}}{\left[e^{\Theta/T} - 1\right]^2}\right] \tag{21}$$

where Θ is the Debye characteristic temperature, which for N_2 is equal to $6111^{o}R$.[27]

Accordingly, upon combining eqs. (15 through (21) and integrating:

$$h_i = \frac{5}{2}\,\frac{\mathcal{R}}{JM_i}\,(T - T_{Ref.}) + \Delta h_{f_i}^{o} \tag{22}$$

$$h_j = \frac{\mathcal{R}}{JM_j}\left\{\frac{7}{2}\,(T - T_{Ref.}) + \Theta\left[\frac{1}{\left(e^{\Theta/T} - 1\right)} - \frac{1}{\left(e^{\Theta/T_{Ref.}} - 1\right)}\right]\right\} \tag{23}$$

In these equations, we will take:[27]

$$\Delta h^{o}_{f_N} = 14,527 \quad \frac{BTU}{lb.} \tag{24}$$

$$T_{Ref.} = 536.7^{o}R \tag{25}$$

As in our earlier studies[6] we will utilize the transport properties:

$$\mu = 1.28 \times 10^{-6} \left[T(^{o}R)\right]^{1/2}, \text{ lb./ft. sec.} \tag{26}$$

$$K = 4.49 \times 10^{-7} \left[T(^{o}R)\right]^{1/2}, \frac{BTU - ft.}{ft.^2 \text{ sec.} ^{o}R} \tag{27}$$

The binary diffusion coefficient may be written:

$$\mathcal{D}_{N-N_2} = \frac{1.2 \times 10^{-4} \quad T(^{o}R)^{3/2}}{P \text{ (lb./ft.}^2)}, \frac{ft.^2}{sec.} \tag{28}$$

For simplicity, we have also invoked the following relationship between the first and second viscosity coefficients (Stokes postulate):

$$\lambda + \frac{2}{3}\mu = 0 \tag{29}$$

For the dissociation or recombination of nitrogen, one may write symbolically:

$$\begin{aligned} N_2 + N_2 &\rightleftharpoons 2N + N_2 \\ N_2 + N &\rightleftharpoons 3N \end{aligned} \tag{30}$$

where the collisional efficiencies of N and N_2 are not necessarily equal either in the forward or backward directions. This leads us to write the following equation for the chemical source term which represents the net rate of formation of nitrogen atoms by chemical reactions:

$$\dot{w}_N = \frac{2M_N}{A}\left[K_{F_{N_2}} n_{N_2}^{\ 2} - K_{R_{N_2}} n_N^{\ 2} n_{N_2} + K_{F_N} n_{N_2} n_N - K_{R_N} n_N^{\ 3}\right] \tag{31}$$

where $\rho_N = \frac{n_N M_N}{A}$ and $\rho_{N_2} = \frac{n_{N_2} M_{N_2}}{A}$ and A is Avogadro's number.

The following values of the specific reaction rates were utilized:[28]

$$K_{F_{N_2}} = \frac{6.63 \times 10^{-5}\ e^{-2.034 \times 10^5/T(^oR)}}{\left[T(^oR)\right]^{1/2}}$$

$$K_{F_N} = \frac{1.046 \times 10^{1}\ e^{-2.034 \times 10^5/T(^oR)}}{\left[T\ (^oR)\right]^{3/2}} \tag{32}$$

$$K_{R_{N_2}} = \frac{1.09 \times 10^{-29}}{\left[T(^oR)\right]^{0.57}}$$

$$K_{R_N} = \frac{1.72 \times 10^{-24}}{\left[T(^oR)\right]^{1.57}}$$

It is now necessary to delimit the spatial region for which computations are to be performed. The inner boundary is simply the surface of the cylinder, R_1. Since we are working with cylindrical coordinates, it is convenient to select as an outer boundary a surface of constant radius, R_2. As in reference 10, we chose here to treat the symmetrical flow problem which occurs at low Reynolds numbers (before asymmetric vortex shedding occurs), in which a plane through the centerline of the cylinder parallel to the oncoming stream represents a plane of symmetry. Hence, we treat only the upper half-plane, $0 \leq \theta \leq \pi$. And, we can now proceed to prescribe the initial conditions and boundary

conditions for all of the dependent variables, including the two components of velocity V_r and V_θ, the temperature T, the density ρ, and the mass fraction of nitrogen atoms C_N.

The Navier-Stokes equations represent a mixed system of "hyperbolic-parabolic" partial differential equations. Mathematically, one finds that the characteristic surfaces are: 1) t = constant planes, and 2) the surface obtained by considering the continuity equation alone. Intuitively then, one expects to specify boundary conditions at all boundaries for V_r, V_θ, T and C_N. Whether or not a boundary condition for ρ is required at a particular point on the boundary is determined by the inclination of the one non-trivial characteristic surface to the boundary at the point. If one progresses in time along this characteristic surface, then at points on the boundary where one enters the region, a boundary condition on ρ must be specified; where one leaves the region, ρ must be calculated along the boundary.

As in our earlier study,[10] a cylinder of radius R_1 is assumed initially to be immersed in a stationary gas at temperature T_o and density ρ_o. Thus, throughout the annular domain defined by $R_1 \leq r \leq R_2$, $0 \leq \theta \leq \pi$, we have

$$V_r(0, r, \theta) = 0$$

$$V_\theta(0, r, \theta) = 0$$

$$T(0, r, \theta) = T_o = 400^{\circ}R$$

$$\rho(0, r, \theta) = \rho_o = 10^{-5} \text{ lb./ft.}^3$$

$$C_N(0, r, \theta) = 0$$

which corresponds to a nominal altitude of 200,000 ft. in the earth's atmosphere.

As in our earlier study, we first treated the formation of a planar shock wave which was set into motion by a piston which is accelerated to a constant velocity of 10,000 ft./sec. for this particular set of initial conditions, so that we could then utilize the planar shock solution of the Navier-Stokes equations to initiate the flow around the cylinder. Thus, this shock wave propagates unchanged in structure from upstream toward the cylinder at a velocity of 11,530 ft./sec. and the precise moment that the toe of this shock wave arrives at the cylinder will be denoted by time zero, $t = 0$. The initial shock wave structure is shown in figures 2 to 5 by those curves denoted by $t = 0$. Note that the gas properties behind the shock wave are given by:

$$\begin{aligned} V_\infty &= 10,000 \text{ ft./sec.} \\ \rho_\infty &= 7.63 \times 10^{-5} \text{ lb./ft.}^3 \\ T_\infty &= 8,960^\circ R \\ C_{N_\infty} &< 10^{-4} \end{aligned} \tag{34}$$

Having completely specified the initial conditions, let us now consider the boundary conditions. At the surface of the cylinder, both components of the velocity, V_r and V_θ, must vanish in the absence of fluid slip at the wall. Hence we have

$$V_r (t, R_1, \theta) = 0 \tag{35}$$

$$V_\theta (t, R_1, \theta) = 0 \tag{36}$$

We are also free to specify information concerning the temperature or its derivatives at the surface, by defining the heat conduction properties of the cylinder. Thus, for the case of a cylinder having an infinite heat capacity, the cylinder would remain at the isothermal temperature T_o, (since it would have become equilibrated initially with the ambient

gas temperature). Hence, for the isothermal case, the inner boundary condition on the temperature would be given by:

$$T(t, R_1, \theta) = T_o \tag{37}$$

The other limiting case would be a cylinder which is insulated in such a way that it neither removes heat nor adds heat to the flow at the surface, e.g., the adiabatic wall. This inner boundary condition is given by

$$\frac{\partial T}{\partial r}(t, R_1, \theta) = 0 \tag{38}$$

This boundary condition permits a variation of T with θ, whereas clearly eq. (37) does not.

The true physical situation which lies between these limits can only be determined by solving the transient heat conduction equation within the cylinder simultaneously with the Navier-Stokes equations for the surrounding gas. In this case, one has

$$\left[K\frac{\partial T}{\partial r} + \rho\mathcal{D}_{ij}\frac{\partial C_i}{\partial r}(h_i - h_j)\right]_{gas} = \left(K\frac{\partial T}{\partial r}\right)_{solid} \tag{39}$$

as an interface boundary condition.

In this paper we have decided to again utilize the adiabatic wall boundary condition given by eq. (38). It is noted that in an earlier work[7] we treated both the isothermal and adiabatic cases and found the latter easier to handle numerically, since it converges faster to a steady state.

Physically, one has no way of knowing either the gas density or pressure "a priori" at the surface of the cylinder. As discussed in reference 6, this is completely consistent with the mathematics. A study of the characteristics as discussed earlier indicates that ρ must be calculated at the cylinder surface.

In considering the effect of the surface on the heterogeneous chemical reactions, one notes that, as with the case of the temperature, one has freedom to specify information concerning the mass fraction or its derivatives at the surface by defining the catalytic properties of the surface of the cylinder.[29] Thus, if we assume that the surface is a perfect catalyst, ($\gamma_N = 1.0$), then the surface acts to drive the gas composition to its equilibrium value at the wall, in which case, the surface boundary condition is given by:

$$C_N(t, R_1, \theta) = C_{N_{eq.}}\left[P(t, R_1, \theta), T(t, R_1, \theta)\right] \tag{40}$$

One can readily determine $C_{N_{eq.}}$ from a knowledge of the equilibrium constant

$$K_{p_N} = \frac{C_N^2}{(1-C_N)} \frac{P\bar{M}M_{N_2}}{M_N^2} = 9.74 \times 10^5 \left[T(^oR)\right]^{1.07} e^{-(203,400/T(^oR))} \tag{41}$$

The other limiting case would be a surface which is a perfect non-catalyst, ($\gamma_N = 0$) in which case the surface does not act to alter the composition at the wall. That is, the surface acts neither as a sink nor as a source of atoms, hence, in the absence of thermal diffusion one has:

$$\left(\frac{\partial C_N}{\partial r}\right)_w (t, R_1, \theta) = 0 \tag{42}$$

The true physical situation lies between the aforementioned limits, i.e. finite catalytic efficiency ($0 < \gamma_N < 1.0$). For this case, one may write down an explicit relationship between the concentration gradients at the surface and γ_N the catalytic efficiency.[29]

Since many practical materials have a large catalytic efficiency, we have chosen to utilize the boundary condition $\gamma_N = 1.0$, namely, that the surface is a perfect catalyst so that in this work the mass fraction of nitrogen atoms at the wall will be given by eqs. (40) and (41).

As noted earlier, the mathematics indicates that at the outer boundary R_2, it is also necessary to specify a proper set of boundary conditions. Note that from a physical standpoint this should not present a problem on the upstream side of the flow field since the conditions behind the initiating shock wave are known "a priori" from the earlier solution of the one-dimensional Navier-Stokes equations. However, the requirement of specifying outer boundary conditions does present somewhat of a problem for later times on the downstream side of the cylinder. A problem with the downstream boundary conditions exists in spite of the fact that one is dealing with an initial value problem. That is, the retention of the time derivatives makes it possible to satisfy whatever downstream conditions one chooses, but lends no assistance in arriving at the choice. One should, therefore, place the outer boundary R_2 at such a large distance from the body of interest that during the physical time period of interest, the disturbance produced by the presence of the body does not reach the boundary. If one is interested in the steady state solution, one must either take R_2 at infinity (which is not computationally feasible) or one must place R_2 at a sufficiently large distance from the body such that an imprecise specification of the boundary conditions along the downstream boundary does not strongly influence the solution near the body.

In our problem, there is no difficulty in specifying the boundary conditions at R_2 for $0 \leq \theta \leq \frac{\pi}{2}$, since for sufficiently large values of R_2, we can assume that at all these points the planar shock wave propagates without being influenced by the body. For $\frac{\pi}{2} \leq \theta \leq \pi$, it is found that one cannot specify the density but rather one must calculate it. However, V_r, V_θ, T (or its normal derivative $\frac{\partial T}{\partial r}$) and C_N (or its normal derivative $\frac{\partial C_N}{\partial r}$) must be specified. We arbitrarily chose to specify that these quantities propagate along the outer boundary as if the shock wave at R_2 is not influenced by the presence of the body. This would

be precisely correct if R_2 were at infinity. Hence, imposing these same outer boundary conditions for a finite value of R_2 represents an approximation. It must be noted that this approximation becomes precisely correct if one does not continue the solution beyond that critical point in time at which any point on the outside boundary R_2 feels the presence of the non-uniform flow produced by the body.

The major question of concern in utilizing a finite value of R_2 is the extent of the upstream influence introduced by the aforementioned approximation of imposing at a finite value of R_2 the boundary conditions that are precisely correct at infinity. This question has been investigated in our earlier paper[10] by utilizing two values of R_2 in our computations, namely, $R_2/R_1 = 11$ and $R_2/R_1 = 21$. A typical result of that investigation is reproduced here as figure 8. This figure shows that the region of upstream influence tends to be confined to the immediate vicinity of R_2. Since we are dealing with a supersonic flow, in which R_2 was chosen to lie beyond the sonic surface, this desirable result was not entirely unexpected.

This question of the effect of upstream influence will always arise when R_2 is finite, and must be examined for each new class of problems investigated.

The remaining boundaries are the $\theta = 0$ and $\theta = \pi$ surfaces. The symmetry of the problem dictates that

$$V_\theta (t, r, 0) = 0 \tag{43}$$

$$V_\theta (t, r, \pi) = 0 \tag{44}$$

$$\frac{\partial V_r}{\partial \theta} (t, r, 0) = 0 \tag{45}$$

$$\frac{\partial V_r}{\partial \theta} (t, r, \pi) = 0 \tag{46}$$

$$\frac{\partial T}{\partial \theta}\,(t,\ r,\ 0) = 0 \tag{47}$$

$$\frac{\partial T}{\partial \theta}\,(t,\ r,\ \pi) = 0 \tag{48}$$

$$\frac{\partial C_N}{\partial \theta}\,(t,\ r,\ 0) = 0 \tag{49}$$

$$\frac{\partial C_N}{\partial \theta}\,(t,\ r,\ \pi) = 0 \tag{50}$$

Furthermore, along the $\theta = 0$ and $\theta = \pi$ boundaries, the density ρ must be calculated.

4. NUMERICAL APPROACH

In our earlier study [10], we mentioned that our final choice of a difference equation was strongly influenced by the following two criteria:

1) Mathematically, the equations are governed very strongly by the parabolic terms. For these terms, it is very desirable to have a difference equation which does not require stringent stability criteria. This is particular important if one desires to extend his methods to a reasonably wide range of physical problems. It is also an important factor when making a sequence of runs to obtain convergence.

2) The difference equation should be capable of handling a hyperbolic system even without the presence of the parabolic terms. In a certain sense, this is superfluous since a stability analysis is often satisfactory regardless of what is done to these low order hyperbolic terms. However, one of our major discoveries in our one-dimensional work [6] was that difference equations which remain valid as the viscous terms disappear, can be expected to produce the best results. The foregoing two points were discussed in another earlier paper. [10]

For the parabolic system, we will make use of the same explicit-implicit scheme which was used in the two-dimensional problem. [10] Stability and convergence have been established for linear cases. For the hyperbolic system, we chose to extend the scheme used in the two-dimensional case to the equation for the conservation of species. This involves reducing the system to a normal form and differencing according to the sign of the characteristics. This technique was suggested by Courant, Isaacson and Rees. [30] However, the normal form we chose (reduction to diagonal form) falls into the format discussed by Anucina [31] and Lees. [32]

As in reference 10, the convergence criterion for the difference equation is found to be: [15]

$$\lim_{\Delta r \to 0} \frac{\Delta t}{\Delta r} = 0 \quad , \quad \lim_{\Delta \theta \to 0} \frac{\Delta t}{\Delta \theta} = 0 \tag{51}$$

Also, the truncation error analysis reveals that if one desires to make a sequence of computer runs, in which the error at each step is reduced by at least a factor of one-half, then:

$$\Delta r_{i+1} = \frac{\Delta r_i}{2} \quad , \quad \Delta \theta_{i+1} = \frac{\Delta \theta_i}{2} \quad , \quad \Delta t_{i+1} = \frac{\Delta t_i}{3} \tag{52}$$

Note that in the limit, equations (52) are consistent with equations (51).

Again, one obtains the following stability and convergence criterion for the hyperbolic system:

$$\Delta t \leq \frac{1}{\frac{\lambda_1}{\Delta r} + \frac{\lambda_2}{\Delta \theta}} \quad , \quad \lambda_1 = |V_r| + C_{LS}, \; \lambda_2 = |V_\theta| + C_{LS} \tag{53}$$

where C_{LS} is the local speed of sound. Note that in the limit equations (51) require that equation (53) be automatically satisfied. However, for a particular choice of Δ's which are being used for computation, one must be sure that equation (53) is satisfied. It is perhaps interesting to note that the stability and convergence criteria are in no way changed by the presence of the diffusion and chemical reaction terms. This does not mean to imply that the Δt is unaffected by these additional terms. For example, in equation (2) the $\dot{w}$ term can certainly affect the proper step size for Δt, but it does not affect the stability and convergence criteria given in eqs. (51) to (53).

Appendix A contains the transformed Navier-Stokes equations. From these one may select the parabolic and the hyperbolic systems. The barred quantities represent the viscous terms and the unbarred quantities represent the hyperbolic subsystem. Note that a "hyperbolic subsystem" (the doubly-barred quantities) was also split off the viscous system, and difference equations for this subsystem were specified separately. This then requires a large amount of analytic effort before the final finite difference equations are arrived at. However, this expenditure of effort has in fact led to a very satisfactory set of difference equations which take on the following functional form. For the explicit scheme:

$$
\begin{aligned}
\rho_{i,j}^{n+1} &= (1 + a_9 - a_6 \Delta t)\, \rho_{i,j}^{n} - a_{10} \\
V_{i,j}^{n+1} &= V_{i,j}^{n} - \bar{b}_9 V_{i,j}^{n} + b_9 (V_{i,j}^{n})^2 + \bar{b}_8 \\
W_{i,j}^{n+1} &= W_{i,j}^{n} - \bar{c}_9 W_{i,j}^{n} + c_9 (W_{i,j}^{n})^2 + \bar{c}_8 \\
T_{i,j}^{n+1} &= (1 + d_9 - \bar{d}_{11})\, T_{i,j}^{n} + d_8 + \bar{d}_{10} \\
C_{i,j}^{n+1} &= \bar{e}_{11} + (1 - \bar{e}_{12})\, C_{i,j}^{n}
\end{aligned}
\tag{54}
$$

For the implicit scheme:

$$
\begin{aligned}
\rho_{i,j}^{n+1} &= (\rho_{i,j}^{n} - a_{10}) / (1 - a_9 + a_6 \Delta t) \\
V_{i,j}^{n+1} &= V_{i,j}^{n} - \bar{b}_9 V_{i,j}^{n+1} + b_9 (V_{i,j}^{n+1})^2 + \bar{b}_8 \\
W_{i,j}^{n+1} &= W_{i,j}^{n} - \bar{c}_9 W_{i,j}^{n+1} + c_9 (W_{i,j}^{n+1})^2 + \bar{c}_8 \\
T_{i,j}^{n+1} &= (T_{i,j}^{n} + d_8 + \bar{d}_{10}) / (1 - d_9 + \bar{d}_{11}) \\
C_{i,j}^{n+1} &= (C_{i,j}^{n} + \bar{e}_{11}) / (1 + \bar{e}_{12})
\end{aligned}
\tag{55}
$$

In the foregoing equations, we use the notation:

$$V = V_r \; ; \qquad W = V_\theta \qquad ; C = C_N$$

$$\varphi^n_{i,j} = \varphi \; (n \, \Delta t, \; i\Delta\eta, \; j \, \Delta\zeta) \tag{56}$$

The coefficients required in the two sets of eqs. (54) and (55) are discussed in Appendix B. Note that for the implicit scheme, the equations represent a system of five algebraic equations which must be solved iteratively for the five unknowns $\rho^{n+1}_{i,j}$, $V^{n+1}_{i,j}$, $W^{n+1}_{i,j}$, $T^{n+1}_{i,j}$ and $C^{n+1}_{i,j}$ whereas by definition, the explicit scheme allows direct evaluation of these five dependent variables. Note further that the alternation scheme requires that quantities at alternate points be evaluated with the explicit and implicit schemes respectively, both spatially and in time. (6) It should be noted that the criteria of equations (51) to (53) carry over to the transformed coordinate system.

5. DISCUSSION OF RESULTS

In this paper, we will present the numerical results from a set of calculations which have been performed for the supersonic flow around a circular cylinder. This flow was initiated by a planar shock wave (as shown in figure 1) travelling at M = 2.2 The cylinder has a radius of 0.005 ft. and hence the free stream Reynolds number is equal to 31.5.

The computations were carried out utilizing the following mesh size:

$$\Delta r = 0.0002777 \text{ ft.}$$

$$\Delta\theta = \frac{\pi}{18} \ (= 10^{o})$$

$$\Delta t = 1.2 \times 10^{-8} \text{ sec.}$$

This mesh resulted in 3500 spatial node points. Thus, in carrying out the computations for a physical elapsed time of 8 microseconds, over 2,275,000 individual nodal computations were made which required approximately 7 hours of CDC 6600 computer time.

A few results of the computations are shown in figures 2-14. Thus, in figures 2 to 5, we show the variation of Vr, T, ρ and C_N with r, along the forward stagnation streamline (θ= 0) for the time period of interest. Note that the curves marked t = 0 represent the initial conditions, i.e., when the toe of the shock wave encounters the cylinder. Although the qualitative behavior of Vr and T is the same as in our earlier study in which dissociation was neglected,[10] the presence of a finite number of atoms (see figure 5) not surprisingly acts to quantitatively alter the density distribution which is shown in figure 4. Also the sharp peaks in the density profiles shown in figure 4 indicate the fineness of the mesh required for the computation.

In figure 2 the shock wave is seen to first steepen up, and then to move away from the cylinder, and at the same time a long neck forms on the upstream side of the shock wave. In figure 3, it is found that just as in the case of the reflection of a planar shock wave from an adiabatically insulated plane wall,[6] the gas temperature at the wall rises rapidly from its initial value of $400^{\circ}R$, exceeds $20,000\ ^{\circ}R$, and then drops as the shock wave moves slightly forward.

Note further in figure 4 that the density variation is not monotonic as in reference 10 in which dissociation was neglected.

Since we have calculated the flow field all around the cylinder, the variation of C_N with r is shown for values of $0 \leq \theta \leq \pi$ in figures 5 through 7. It is clearly seen that steady state chemistry is essentially achieved in only 6 microseconds along the ray $\theta = 0$, whereas along the ray $\theta = \pi$, the chemistry is still approaching a steady state. Note that in figure 7, the derivative $\frac{\partial C_N}{\partial r}$ does not go asymptotically to zero with radius at later times. This implies that upstream influence is beginning to appear in the chemistry along $\theta = \pi$ when $t > 7$ microseconds.

At this point, it is certainly worth discussing the question of upstream influence. In figure 8, which appears in reference 10, it is seen how the upstream influence of the downstream boundary condition on the temperature and radial velocity of the gas are in fact confined to the immediate vicinity of the boundary, provided that R_2 lies beyond the sonic surface. Equivalent studies concerning the effect of the location of R_2 on chemistry have yet to be carried out.

In figures 9 to 12, are shown the variation of the radial velocity, angular velocity, density and temperature at selected angular positions in the flow field corresponding to

the same point in time as figure 14. Since this calculation was carried out for only one mesh size, no specific error bound was calculated. However, we expect the overall accuracy to be comparable to the earlier study.[10]

In the last two figures we show the location of the sonic line around the cylinder for two different points in time, i.e. t = 2 microseconds and t = 7.87 microseconds. Figure 13 is particularly interesting. Note that the sonic surface is not closed around the body because the initiating planar shock wave has only reached the point shown on the boundary R_2; i.e. the wave has not yet progressed beyond R_2 along the $\theta = \pi$ axis. Note that in addition to the sonic surface, shown by the dashed line, figure 14 also indicates the vector velocity flow field, along various rays emanating from the body.

It is perhaps worth repeating that since the time the authors began their investigation into the solution of the complete Navier-Stokes equations, other work has also been reported.[33-35] However, since these developments are so recent, only special cases representing particular solutions to particular physical problems have been obtained and hence it is not yet possible to draw meaningful comparisons between the methods.

For example, in the case of Brailovskaya[33], his stability condition invokes the statement that the viscosity coefficient is small. Thus, if one is concerned with shock waves where one requires a fine mesh, such that the quantity h^2/μ is small, this may present a problem. In the physical problem he chose to compute, the Reynolds number was $100 < R_e < 1000$ and the flow was subsonic, hence one has no simple way of evaluating his method for supersonic viscous flows.

Shao[34] has also treated the two-dimensional time-dependent Navier-Stokes equations, but for weak shocks so that he can neglect thermal conductivity.

Finally, Kurzrock and Mates[35] have also presented solutions for the two-dimensional time-dependent Navier-Stokes equations, based on an explicit computation scheme. Although their approach seems reasonable, we have tried to avoid difference equations having such a strong stability criterion due to the presence of the viscous terms.

Perhaps at some future time, a meaningful comparison will be made between the several methods that have now been suggested.

6. CONCLUSIONS

This investigation has shown that one can solve the complete, two-dimensional, time-dependent Navier-Stokes equations for the supersonic flow past a blunt body, where the effects of compressibility, viscosity, thermal conductivity, chemical reactions and diffusion are all explicitly treated.

In the present study, we have been able to include the effects of non-equilibrium homogeneous chemical kinetics as an extension of an earlier investigation in which gas phase chemistry was assumed frozen. The specific effects of the chemistry on the flow field variables have been determined herein.

In the future, it will be important to obtain solutions for higher Mach numbers and Reynolds numbers in order to obtain flow conditions which will produce more interesting phenomena in the region of the near wake, i.e. $\frac{3}{4}\ \pi < \theta < \pi$. In particular, in the present study for which the free stream Reynolds number was 31.5, our results indicate that the flow in the wake is steady, in that no vortex is shed, nor is a region of separated flow found behind the body. It is expected that as Re_∞ approaches 100, flow separation and vortex shedding will begin to occur and should appear in our numerical results.

7. ACKNOWLEDGMENTS

The authors wish to acknowledge the continued interest of the Advanced Research Projects Agency and the Office of Naval Research in this research, in particular, Mr. C. McLain and Mr. M. Cooper. The analytical parts of this investigation were partially supported by ARPA through Office of Naval Research Contract Nonr 4869(00). The computations were carried out at the Courant Institute of Mathematics of New York University on the CDC 6600 digital computer. Funds for these computations were made available by the General Applied Sciences Laboratory under ARPA contract No. EA-49-083-OSA-3135, through the cooperation of Mr. C. McLain of ARPA and Dr. H. Lien and Mr. S. M. Skeist of GASL.

The authors also wish to thank John Wilson for his capable assistance in programming the finite difference equations for the CDC 6600 digital computer. The figures were prepared by H. Frey and A. Tocci. The manuscript was typed by Mrs. B. Bown, Mrs. M. Riba and Miss L. Pasquale.

8. REFERENCES

1. Navier, C. L. M. H., "On the Laws of Motion of Fluids Taking into Consideration the Adhesion of the Molecules", Ann. Chim. Phys., Vol. 19, 1821, pp. 234-245.

2. Poisson, S. D., "Memoir on the General Equations of the Equilibrium and Motion of Elastic Solid Bodies and of Fluids", Journ. de l'Ecole Polytech., Cahier XX, 1831, pp. 1-174.

3. Stokes, G. G., "On the Theories of the Internal Friction of Fluids in Motion", Trans. Cambridge Phil. Soc., Vol. 8, 1845, pp. 287-319.

4. Rankine, W. J. M., "On the Thermodynamic Theory of Waves of Finite Longitudinal Disturbance", Transactions of the Royal Society of London, Vol. 160, 1870, pp. 277-288.

5. Hirschfelder, J. O., Curtiss, C. F., and Bird, R. B., Molecular Theory of Gases and Liquids, John Wiley and Sons, Inc., New York, 1954.

6. Scala, S. M. and Gordon, P., "Reflection of a Shock Wave at a Surface", G.E., M.S.D. TIS R65SD24, June 1965. Also, The Physics of Fluids, Vol. 9, No. 6, pp. 1158-1166, June 1966.

7. Scala, S. M. and Gordon, P., "Asymptotic Solutions of the Time-Dependent Navier-Stokes Equations", presented at the American Physical Society Meeting, Stanford University, November 1966, to appear.

8. Becker, R., "Stosswelle und Detonation", Zeitschrift für Physik, Vol. 8, pp. 321-363, 1922.

9. Scala, S. M. and Gordon, P., "Spherically-Symmetric Shock Formation According to the Navier-Stokes Equations", to appear.

10. Scala, S. M. and Gordon, P., "Solution of the Time-Dependent Navier-Stokes Equations for the Flow Around a Circulation Cylinder", presented at the AIAA Fifth Aerospace Sciences Meeting, N.Y., N.Y., January 1967, AIAA Paper 67-221, to appear in the AIAA Journal.

11. Courant, R. and Hilbert, D., Methods of Mathematical Physics (Vol. 2, Partial Differential Equations), Interscience Publishers, New York, 1962.

12. Dufort, E. C. and Frankel, S. P., "Stability Conditions in the Numerical Treatment of Parabolic Differential Equations", Math Tables and Other Aids to Computation, Vol. 17, 1. 135, 1953.

13. Richtmyer, R. D., Difference Methods for Initial-Value Problems, Interscience Publishers, New York, 1957.

REFERENCES (con't)

14. Forsythe, G. E. and Wasow, W. R., Finite-Difference Methods for Partial Differential Equations, John Wiley & Sons, Inc., New York, 1964.

15. Gordon, P., "Nonsymmetric Difference Equations", J. Soc., Indust. Appl. Math., Vol. 13, No. 3, 1965, pp. 667-673.

16. Courant, R. and Friedrichs, K. O., Supersonic Flow and Shock Waves, Interscience Publishers, Inc., New York, 1948.

17. Von Neumann, J. and Richtmyer, R. D., "A Method for the Numerical Calculation of Hydrodynamic Shocks", J. Appl. Phys., Vol. 21, 1950, pp. 232-237.

18. Ludford, G., Polachek, H. and Seeger, R. J., "On Unsteady Flow of Compressible Viscous Fluids", J. Appl. Physics, Vol. 24, 1953, p. 490.

19. Lighthill, M. J., "Viscosity Effects in Sound Waves of Finite Amplitude", Surveys in Mechanics (G. K. Batchelor and R. M. Davies - Eds), Cambridge University Press, 1956, pp. 250-351.

20. Kantrowitz, A. R., "One-Dimensional Treatment of Non-Steady Gas Dynamics", Fundamentals of Gas Dynamics (H. Emmons - Ed), Vol. III, High Speed Aerodynamics and Jet Propulsion, Princeton University Press, 1958, pp. 350-415.

21. Hayes, W. D., "The Basic Theory of Gas Dynamic Discontinuities", Fundamentals of Gas Dynamics (H. Emmons - Ed.), Vol. III, High Speed Aerodynamics and Jet Propulsion, Princeton University Press, 1958, pp. 417-481.

22. Sedov, L. I., Similarity and Dimensional Methods in Mechanics (Translation by M. Friedman), Academic Press, 1959.

23. Burstein, S. Z., "Numerical Calculations of Multi-dimensional Shocked Flows", Courant Institute of Mathematical Sciences, AIAA Preprint No. 64-2, January 1964, also AIAA Journal, Vol. 2, No. 12, December 1964, pp. 2111-2117.

24. Godunov, S. K., Zabrodyn, A. W. and Prokopov, G. P., "A Difference Scheme for Two-Dimensional Unsteady Problems of Gas Dynamics and Computations of Flow with a Detached Shock Wave", Zhur. Vychyslitelnoi Mat. i Mat. Fix. Vol. 1, No. 6, Nov.-Dec. 1961, p. 1020 (translated by I. O. Bochachevsky).

25. Adler, B., Fernbach, S. and Rotenberg, M., Methods in Computational Physics, Vol. 3, 1964, Academic Press, N. Y.

REFERENCES (con't)

26. Crocco, L., "A Suggestion for the Numerical Solution of the Steady Navier-Stokes Equations", AIAA Second Aerospace Sciences Meeting, AIAA Paper No. 65-1, January 1965. Also, AIAA J. Vol. 3, Oct. 1965, pp. 1824-1832.

27. Herzberg, G., Spectra of Diatomic Molecules, D. Van Nostrand, Inc., New York, 1950, pp. 553-560.

28. Bortner, M., Private communication.

29. Scala, S. M., "Hypersonic Stagnation Point Heat Transfer to Surfaces Having Finite Catalytic Efficiency", Proceedings of the Third U.S. National Congress of Applied Mechanics, pp. 799-806, December 1958.

30. Courant, R., Isaacson, E., and Rees, M., "On the Solution of Nonlinear Hyperbolic Differential Equations by Finite Differences", Communications on Pure and Applied Mathematics, Vol. V, p. 243-255, 1952.

31. Anucina, N. N., "Difference Schemes for Solving the Cauchy Problem for Symmetric Hyperbolic Systems", Sovier Math., Doklady, Vol. 5, 1964.

32. Lees, M., "The Solution of Positive-Symmetric Hyperbolic Systems by Difference Methods", Proc. of Amer. Math. Soc., Vol. 12, 1961, pp. 195-204.

33. Brailovskaya, I. Yu., "A Difference Scheme for Numerical Solution of the Two-Dimensional Nonstationary Navier-Stokes Equations for a Compressible Gas," Soviety Physics-Doklady, Vol. 10, No. 2, August 1965.

34. Shao, T. S., "Numerical Solution of Plane Viscous Shock Reflections," Report No. 190, Dept. of Computer Science, U. of Ill., Sept. 30, 1965.

35. Kurzrock, J. W. and Mates, R. E., "Exact Numerical Solutions of the Time-Dependent Compressible Navier-Stokes Equations," AIAA Paper No. 66-30, AIAA 3rd Aerospace Sciences Meeting, N.Y., N.Y., January 1966.

SYMBOLS

$a, \bar{a}, b, \bar{b}, \bar{\bar{b}}$	See Appendices A and B
$c, \bar{c}, \bar{\bar{c}}, d, \bar{d}$, etc.	
C_{LS}	local speed of sound
C_V	specific heat at constant volume
c_p	specific heat at constant pressure
$C = C_N$	mass fraction of nitrogen atoms
$\mathcal{D}_{ij}$	binary diffusion coefficient
e	internal energy
h	enthalpy
K	thermal conductivity
P	pressure
Pr	Prandtl Number
r	radius
$\bar{r}$	see Appendix A
R	gas constant
Re	Reynolds number
R_1, R_2	inner and outer radii of computation domain
t	time
T	temperature
$V = V_r$	radial component of velocity
$W = V_\theta$	tangential component of velocity
γ_i	see Appendix B

γ_N	catalytic efficiency
ζ	transformed r coordinate
η	transformed θ coordinate
θ	tangential coordinate
λ	second viscosity coefficient
μ	ordinary viscosity coefficient
ρ	density
Φ	viscous dissipation function

Superscripts

n, n + 1	adjacent time steps

Subscripts

i, j	spatial coordinates, atomic and molecular species
r	radial component, or partial derivative
t	partial derivative with respect to time
ζ	partial derivative with respect to ζ
η	partial derivative with respect to η
θ	tangential component, or partial derivative
o	initial conditions
∞	upstream conditions

APPENDIX A: TRANSFORMED NAVIER-STOKES EQUATIONS

The Navier-Stokes Equations were first transformed by means of

$$\eta = \frac{1-e^{-s_1\bar{r}}}{1-e^{-s_1}} \tag{A-1}$$

$$\zeta = \frac{1-e^{-s_2\bar{\theta}}}{1-e^{-s_2}} \tag{A-2}$$

$$\bar{r} = \frac{r-R_1}{R_2-R_1} \quad ; (R_1 \leq r \leq R_2) \tag{A-3}$$

where

$$\bar{\theta} = \frac{\theta}{\pi} \quad ; \quad (0 \leq \theta \leq \pi) \tag{A-4}$$

and s_1 and s_2 are chosen to be constants. Thus, if $s_1 > 0$ points are "squeezed" toward $r = R_1$, and if $s_1 < 0$, points are squeezed toward $r = R_2$. The same statements hold for θ.

If we introduce the notation $V = V_r$, $W = V_\theta$ and $C = C_N$ and we then let the subscripts r, θ, t, η and ζ denote partial differentiation with respect to those variables, then the governing equations take the following form. The conservation of mass becomes:

$$\rho_t = - a_1 \rho_\eta - a_2 \rho_\zeta - a_3 V_\eta - a_4 W_\zeta - a_5 \tag{A-5}$$

where

$$a_1 = V\eta_r$$

$$a_2 = \frac{W\zeta_\theta}{r}$$

$$a_3 = \rho\eta_r$$

$$a_4 = \frac{\rho\zeta_\theta}{r}$$

$$a_5 = \frac{\rho V}{r}$$

$$V_t = \bar{b}_1 V_{\eta\eta} + \bar{b}_2 V_{\zeta\zeta} + \bar{b}_3 W_{\eta\zeta} + \bar{b}_4 + \bar{b}_5 V + \bar{\bar{b}}_1 V_\eta$$

$$+ \bar{\bar{b}}_2 V_\zeta + \bar{\bar{b}}_3 W_\eta - \bar{\bar{b}}_4 W_\zeta - b_1 V_\eta - b_2 V_\zeta - b_3 \rho_\eta - b_4 T_\eta + b_5 - b_6 C_\eta$$

where

$$\bar{b}_1 = \frac{4\mu \eta_r^2}{3\rho}, \quad \bar{b}_2 = \frac{\mu \zeta_\theta^2}{\rho r^2}, \quad \bar{b}_3 = \frac{\mu \zeta_\theta \eta_r}{3\rho r}, \quad \bar{b}_4 = -\frac{\mu_\zeta \zeta_\theta W}{\rho r^2},$$

$$\bar{b}_5 = -\frac{2}{3\rho r}(\mu_\eta \eta_r + \frac{2\mu}{r}), \quad \bar{\bar{b}}_1 = \frac{4\mu}{3\rho}(\eta_{rr} + \frac{\mu_\eta \eta_r^2}{\mu} + \frac{\eta_r}{r}),$$

$$\bar{\bar{b}}_2 = \frac{\mu}{\rho r^2}(\frac{\mu_\zeta \zeta_\theta^2}{\mu} + \zeta_{\theta\theta}), \quad \bar{\bar{b}}_3 = \frac{\mu_\zeta \zeta_\theta \eta_r}{\rho r}, \quad \bar{\bar{b}}_4 = \frac{\mu \zeta_\theta}{3\rho r}(\frac{7}{r} + \frac{2\mu_\eta \eta_r}{\mu}),$$

$$b_1 = V\eta_r, \quad b_2 = \frac{W\zeta_\theta}{r}, \quad b_3 = \frac{\eta_r \bar{R} T}{\rho}, \quad b_4 = \eta_r \bar{R}, \quad b_5 = \frac{W^2}{r}, \quad b_6 = \eta_r T \frac{d\bar{R}}{dC}$$

The conservation of θ momentum becomes:

$$W_t = \bar{c}_1 W_{\eta\eta} + \bar{c}_2 W_{\zeta\zeta} + \bar{c}_3 V_{\eta\zeta} + \bar{c}_4 + \bar{c}_5 W$$

$$+ \bar{\bar{c}}_1 W_\eta + \bar{\bar{c}}_2 W_\zeta - \bar{\bar{c}}_3 V_\eta + \bar{\bar{c}}_4 V_\xi$$

$$- c_1 W_\eta - c_2 W_\zeta - c_3 \rho_\xi - c_4 T_\xi - c_5 - c_6 C_\eta$$

where

$$\bar{c}_1 = \frac{\mu \eta_r^2}{\rho}, \quad \bar{c}_2 = \frac{4\mu \zeta_\theta^2}{3\rho r^2}, \quad \bar{c}_3 = \frac{\mu \zeta_\theta \eta_r}{3\rho r}, \quad \bar{c}_4 = \frac{4\mu_\zeta \zeta_\theta V}{3\rho r^2},$$

$$\bar{c}_5 = -\frac{\mu}{\rho r}(\frac{1}{r} + \frac{\mu_\eta \eta_r}{\mu}), \quad \bar{\bar{c}}_1 = \frac{\mu}{\rho}(\eta_{rr} + \frac{\eta_r}{r} + \frac{\mu_\eta}{\mu}\eta_r^2),$$

$$\bar{\bar{c}}_2 = \frac{4\mu}{3\rho r^2}(\zeta_{\theta\theta} + \frac{\mu_\zeta}{\mu}\zeta_\theta^2), \quad \bar{\bar{c}}_3 = \frac{2\mu_\zeta \zeta_\theta \eta_r}{3\rho r},$$

$$\bar{\bar{c}}_4 = \frac{\mu \zeta_\theta}{3\rho r}(\frac{7}{r} + \frac{3\mu_\eta \eta_r}{\mu}), \quad c_1 = V\eta_r, \quad c_2 = \frac{W\zeta_\theta}{r},$$

$$c_3 = \frac{\zeta_\theta \bar{R}\, T}{\rho r}\,, \quad c_4 = \frac{\zeta_\theta \bar{R}}{r}\,, \quad c_5 = \frac{VW}{r}\,, \quad c_6 = \frac{\zeta_\theta T}{r}\,\frac{d\bar{R}}{dC}$$

The conservation of energy becomes:

$$T_t = \bar{d}_1\, T_{\eta\eta} + \bar{d}_2\, T_\eta^2 + \bar{d}_3\, T_\eta + \bar{d}_4\, T_{\zeta\zeta} + \bar{d}_5\, T_\zeta^2$$

$$+ \bar{d}_6\, T_\zeta + \bar{d}_7 - d_1\, T_\eta - d_2\, T_\zeta - d_3\, V_\eta - d_4\, W_\zeta - d_5 + \overline{\underline{X}}$$

where

$$\bar{d}_1 = \frac{K}{\rho C_v}\,\eta_r^2\,, \quad \bar{d}_2 = \frac{\bar{d}_1}{K}\left(\frac{dK}{dT}\right), \quad \bar{d}_3 = \frac{\bar{d}_1}{\eta_r}\left(\frac{1}{r} + \frac{\eta_{rr}}{\eta_r}\right),$$

$$\bar{d}_4 = \frac{K}{\rho C_v r^2}\,\zeta_\theta^2\,, \quad \bar{d}_5 = \frac{\bar{d}_4}{K}\left(\frac{dK}{dT}\right), \quad \bar{d}_6 = \bar{d}_4\,\frac{\zeta_{\theta\theta}}{\zeta_\theta^2}$$

$$\bar{d}_7 = \frac{1}{\rho C_v}\,\Phi_c\,, \quad d_1 = V\eta_r\,, \quad d_2 = \frac{W\zeta_\theta}{r}\,, \quad d_3 = \frac{\bar{R}\, T\, \eta_r}{C_v}\,,$$

$$d_4 = \frac{\bar{R}\, T\, \zeta_\theta}{r\, C_v}\,, \quad d_5 = \frac{\bar{R}\, T\, V}{r\, C_v}\,, \quad \bar{\bar{d}}_8 = (\bar{h} - \bar{\epsilon})\,\rho\,\delta_{ij} / \rho\, C_v$$

$$\Phi_c = \mu\left\{2\left[V_r^2 + \frac{1}{r^2}\,(W_\theta + V)^2\right] + \left(\frac{1}{r}\,V_\theta + W_r - \frac{W}{r}\right)^2\right\}$$

$$+ \lambda\left[V_r + \frac{1}{r}\,W_\theta + \frac{V}{r}\right]^2$$

$$\overline{\underline{X}} = \bar{\bar{d}}_8\,\eta_r^2\, C_{\eta\eta} + \bar{\bar{d}}_8\,\eta_{rr}\, C_\eta + \bar{\bar{d}}_8\left(\frac{\zeta_\theta}{r}\right)^2 C_{\zeta\zeta} + \bar{\bar{d}}_8\,\frac{\zeta_{\theta\theta}}{r^2}\, C_\zeta$$

$$+ \bar{\bar{d}}_8\,\eta_r^2\,\frac{(\rho\delta_{ij})_\eta}{\rho\delta_{ij}}\, C_\eta + \frac{\bar{\bar{d}}_8\,\zeta_\theta^2}{r^2}\,\frac{(\rho\delta_{ij})_\zeta}{\rho\delta_{ij}}\, C_\zeta$$

$$+ \frac{\bar{h}_\eta\,\rho\delta_{ij}\,\eta_r^2}{\rho\, C_v}\, C_\eta + \frac{\bar{\bar{d}}_8\,\eta_r}{r}\, C_\eta + \frac{\zeta_\theta^2\,\bar{h}_\zeta\,\rho\delta_{ij}}{\rho\, C_v\, r^2}\, C_\zeta$$

$$- \frac{\bar{e}\,\dot{W}_1}{\rho\, C_v}$$

$$\bar{h} = h_i - h_j$$

$$\bar{e} = e_i - e_j$$

The conservation of species becomes:

$$C_t = \bar{e}_1 \; C_{\eta\eta} + \bar{e}_2 \; C_\eta^2 + \bar{e}_3 \; C_\eta + \bar{e}_4 \; C_{\zeta\zeta} + \bar{e}_5 \; C_\zeta^2$$

$$+ \bar{e}_6 \; C_\zeta - e_1 \; C_\eta - e_2 \; C_\zeta + e_3$$

where

$$\bar{e}_1 = (\rho \mathcal{D}_{ij}) \; \eta_r^2 / \rho \; , \quad \bar{e}_2 = \bar{e}_1 \; f_2 \; ,$$

$$\bar{e}_3 = \frac{\bar{e}_1}{\eta_r} \left(\frac{1}{r} + \frac{\eta_{rr}}{\eta_r} \right) + \bar{e}_1 \; f_1 \; T_\eta \; , \quad \bar{e}_4 = (\rho \mathcal{D}_{ij}) \; \zeta_\theta^2 / (\rho r^2)$$

$$\bar{e}_5 = \bar{e}_4 \; f_2 \; , \quad \bar{e}_6 = \bar{e}_4 \; \frac{\zeta_{\theta\theta}}{\zeta_\theta^2} + \bar{e}_4 \; f_1 \; T_\zeta$$

$$e_1 = v \; \eta_r \; , \quad e_2 = w \; \zeta_\theta / r \; , \quad e_3 = \dot{w}_1 / \rho$$

$$f_1 = (\rho \mathcal{D}_{ij})_T / \rho \mathcal{D}_{ij} \; , \quad f_2 = (\rho \mathcal{D}_{ij})_C / (\rho \mathcal{D}_{ij})$$

APPENDIX B: COEFFICIENTS FOR FINITE DIFFERENCE FORM OF NAVIER-STOKES EQUATIONS

The coefficients appearing in the difference equations for the conservation of mass are:

$$a_6 = \left(\frac{\eta_r^2}{2C_s^2}\right)\left\{\frac{VC\bar{\alpha}_3}{\Delta\eta}(\delta_\eta^2 V) + 2C\bar{C}\left[\frac{\bar{\alpha}_2}{\Delta\eta}(\delta_\eta^2 V) + \frac{2}{\Delta\eta}\delta_\eta^- V\right] - Vb_4\frac{\bar{\alpha}_1}{\Delta\eta}(\delta_\eta^2 T)\right.$$
$$\left. + 2\bar{C}b_4\frac{\bar{\alpha}_3}{\Delta\eta}(\delta_\eta^2 T) + \frac{b_6\delta_\eta^2 C}{\Delta\eta}(2\bar{C}\bar{\alpha}_3 - v\bar{\alpha}_1)\right\}$$
$$+ \frac{\zeta_\theta\eta_r}{2rC_s^2}\left\{\frac{WC\bar{\beta}_3}{\Delta\zeta}(\delta_\zeta^2 W) + 2C_s\bar{C}\left[\frac{\bar{\beta}_2}{\Delta\zeta}(\delta_\zeta^2 W) + \frac{2}{\Delta\zeta}(\delta_\zeta^- W)\right]\right.$$
$$\left. - Wb_4\frac{\bar{\beta}_1}{\Delta\zeta}(\delta_\zeta^2 T) + 2\bar{C}b_4\frac{\bar{\beta}_3}{\Delta\zeta}(\delta_\zeta^2 T) + \frac{b_6\delta_\zeta^2 C}{\Delta\zeta}(2\bar{C}\bar{\beta}_3 - w\bar{\beta}_1)\right\}$$

$$a_7 = \left(\frac{\eta_r}{2C_s^2}\right)\left[2\alpha_1 VC_s^2 + (2\bar{C}\bar{\alpha}_3 - V\bar{\alpha}_1)a_3b_3\right] \qquad \text{(B-2)}$$

$$a_8 = \left(\frac{\zeta_\theta}{2rC_s^2}\right)\left[2\beta_1 WC_s^2 + (2\bar{C}\bar{\beta}_3 - W\bar{\beta}_1)a_3b_3\right] \qquad \text{(B-3)}$$

$$a_9 = (2a_7 - a_1)r_3 + (2a_8 - a_2)r_4 \qquad \text{(B-4)}$$

$$a_{10} = r_3a_7\rho_{i+1,j} + r_3(a_7 - a_1)\rho_{i-1,j} \qquad \text{(B-5)}$$
$$+ r_4a_8\rho_{i,j+1} + r_4(a_8 - a_2)\rho_{i,j-1} + a_5\Delta t$$

where

$$\delta_\eta^-\varphi_{i,j} = \varphi_{i,j} - \varphi_{i-1,j}$$

$$\delta_\eta^2\varphi_{i,j} = \varphi_{i+1,j} - 2\varphi_{i,j} + \varphi_{i-1,j}$$

and

$$r_1 = \frac{\Delta t}{\Delta \eta^2} \quad ; \quad r_2 = \frac{\Delta t}{\Delta \zeta^2} \quad ; \quad r_3 = \frac{\Delta t}{\Delta \eta} \quad ; \quad r_4 = \frac{\Delta t}{\Delta \zeta} \tag{B-6}$$

$$C_s = \eta_r \sqrt{\gamma g \bar{R} T} \tag{B-7}$$

$$\bar{C} = C (2 \eta_r)^{-1} \tag{B-8}$$

$$\alpha_i = \begin{cases} 1 : \lambda_i \geq 0 \\ 0 : \lambda_i < 0 \end{cases} \tag{B-9}$$

$$\beta_i = \begin{cases} 1 : \varkappa_i \geq 0 \\ 0 : \varkappa_i < 0 \end{cases} \tag{B-10}$$

where:

$$\lambda_1 = -V \; ; \; \lambda_2 = -V \; ; \; \lambda_3 = -(V+2\bar{C}) \; ; \; \lambda_4 = -(V-2\bar{C})$$

$$\varkappa_1 = -W \; ; \; \varkappa_2 = -W \; ; \; \varkappa_3 = -(W+2\bar{C}) \; ; \; \varkappa_4 = -(W-2\bar{C})$$

and

$$\bar{\alpha}_1 = 2\alpha_1 - \alpha_3 - \alpha_4 ; \quad \bar{\beta}_1 = 2\beta_1 - \beta_3 - \beta_4$$

$$\bar{\alpha}_2 = \alpha_3 + \alpha_4 \; ; \; \bar{\beta}_2 = \beta_3 + \beta_4$$

$$\bar{\alpha}_3 = \alpha_3 - \alpha_4 \; ; \; \bar{\beta}_3 = \beta_3 - \beta_4$$

Also,

$$b_6 = \frac{r_3 \eta_r}{2 C_s} \left[b_3 \bar{\alpha}_3 (\delta_\eta^2 \rho) + b_4 \bar{\alpha}_3 (\delta_\eta^2 T) + b_6 \bar{\alpha}_3 (\delta_\eta^2 C) \right]$$

$$b_7 = \frac{r_3 b_3}{2} \left[\bar{\alpha}_2 (\delta_\eta^2 \rho) + 2 (\delta_\eta^- \rho) \right] + \frac{r_3 b_4}{2} \left[\bar{\alpha}_2 (\delta_\eta^2 T) + 2 (\delta_\eta^- T) \right]$$

$$+ \frac{r_3 b_6}{2} \left[\alpha_2 (\delta_\eta^2 C) + 2 (\delta_\eta^- C) \right.$$

$$b_8 = b_6 + \frac{\eta_r \bar{\alpha}_2 r_3}{2} (V_{i+1,j} + V_{i-1,j}) - \eta_r r_3 V_{i-1,j} - C_s \bar{\alpha}_3 r_3 - b_2 r_4 (2\beta_1 - 1)$$

$$b_9 = \eta_r r_3 (\bar{\alpha}_2 - 1)$$

$$b_{10} = - \frac{C_s \bar{\alpha}_3 r_3}{2} (V_{i+1,j} + V_{i-1,j}) - b_7 \quad b_5 \Delta t$$

$$- b_2 r_4 [\beta_1 (V_{i,j+1} + V_{i,j-1}) - V_{i,j-1}]$$

$$\bar{b}_6 = \Delta t [\bar{b}_3 W_{\eta\zeta} + \bar{b}_4 + \frac{s_2}{\Delta\eta} (\delta_\eta{}^2 W) + \frac{s_4}{\Delta\zeta} (\delta_\zeta{}^2 W) + \bar{\bar{b}}_3 W_\eta^- - \bar{\bar{b}}_4 W_\zeta^*]$$

$$+ (\bar{b}_1 r_1 + s_1 r_3) (V_{i+1,j} + V_{i-1,j}) + (\bar{b}_2 r_2 + s_3 r_4) (V_{i,j+1} + V_{i,j-1})$$

$$- r_3 \bar{\bar{b}}_1 V_{i-1,j} - r_4 \bar{\bar{b}}_2 V_{i,j-1}$$

$$\bar{\bar{b}}_7 = 2 r_1 \bar{b}_1 + 2 r_2 \bar{b}_2 - \bar{b}_5 \Delta t + 2 s_1 r_3 + 2 s_3 r_4 - (r_3 \bar{\bar{b}}_1 + r_4 \bar{\bar{b}}_2)$$

$$s_1 = \gamma_1 \bar{\bar{b}}_1 + \frac{\epsilon_1}{2} (2\gamma_2 - 1), \quad s_2 = \gamma_1 \bar{\bar{b}}_3 - \frac{\epsilon_1}{2} (2\gamma_1 - 1)$$

$$s_3 = \sigma_1 \bar{\bar{b}}_2 + \frac{\epsilon_2}{2} (2\sigma_2 - 1), \quad s_4 = - \sigma_1 \bar{\bar{b}}_4 - \frac{\epsilon_2}{2} (2\sigma_1 - 1)$$

$$\epsilon_1 = \begin{cases} \frac{1}{2} [\operatorname{sgn} (\bar{\bar{b}}_3 - \bar{\bar{c}}_3)] \left[|\bar{\bar{b}}_3 - \bar{\bar{c}}_3| - \sqrt{(\bar{\bar{b}}_3 - \bar{\bar{c}}_3)^2 - B_1} \right] : B_1 < 0 \\ 0 : B_1 \geq 0 \end{cases}$$

where

$$B_1 = (\bar{\bar{b}}_1 - \bar{\bar{c}}_1)^2 - 4 \bar{\bar{b}}_3 \bar{\bar{c}}_3$$

and

$$\epsilon_2 = \begin{cases} \frac{1}{2} [\operatorname{sgn} (\bar{\bar{b}}_4 - \bar{\bar{c}}_4)] \left[|\bar{\bar{b}}_4 - \bar{\bar{c}}_4| - \sqrt{(\bar{\bar{b}}_4 - \bar{\bar{c}}_4)^2 - B_2} \right] : B_2 < 0 \\ 0 : B_2 \geq 0 \end{cases}$$

where

$$B_2 = (\bar{\bar{b}}_2 - \bar{\bar{c}}_2)^2 - 4\,\bar{\bar{b}}_4\,\bar{\bar{c}}_4$$

$$\gamma_1 = \begin{cases} 1 : \bar{\bar{b}}_1 > 0 \\ 0 : \bar{\bar{b}}_1 \le 0 \end{cases}, \quad \gamma_2 = \begin{cases} 1 : \epsilon_1 > 0 \\ 0 : \epsilon_1 \le 0 \end{cases}, \quad \gamma_3 = \begin{cases} 1 : -\epsilon_1 > 0 \\ 0 : -\epsilon_1 \le 0 \end{cases}$$

$$\sigma_1 = \begin{cases} 1 : \bar{\bar{b}}_2 > 0 \\ 0 : \bar{\bar{b}}_2 \le 0 \end{cases}, \quad \sigma_2 = \begin{cases} 1 : \epsilon_2 > 0 \\ 0 : \epsilon_2 \le 0 \end{cases}, \quad \sigma_3 = \begin{cases} 1 : -\epsilon_2 > 0 \\ 0 : -\epsilon_2 \le 0 \end{cases}$$

$$\bar{b}_8 = b_{10} + \bar{b}_6 \quad , \quad \bar{b}_9 = b_8 + \bar{b}_7$$

$$c_6 = \frac{\zeta_\theta r_4}{2 r C_s} \left[b_3 \bar{\beta}_3 (\delta_\zeta^2 \rho) + b_4 \bar{\beta}_3 (\delta_\zeta^2 T) \right] + \frac{V}{r} \Delta t + b_6 \bar{\beta}_3 (\delta_\eta^2 C)$$

$$c_7 = \frac{\zeta_\theta r_4 b_3}{2 r \eta_r} \left[\bar{\beta}_2 (\delta_\zeta^2 \rho) + 2 (\delta_\zeta^- \rho) \right] + \frac{\zeta_\theta r_4 b_4}{2 r \eta_r} \left[\bar{\beta}_2 (\delta_\zeta^2 T) \right.$$

$$\left. + 2 (\delta_\zeta^- T) \right] + \frac{\zeta_\theta r_4 b_6}{2 r \eta_r} \left[\bar{\beta}_2 (\delta_\zeta^2 C) + 2 (\delta_\zeta^- C) \right]$$

$$c_8 = a_1 r_3 (1 - 2\alpha_1) + c_6 + \frac{\zeta_\theta r_4}{2r} \left[\bar{\beta}_2 W_{i,j+1} + (\bar{\beta}_2 - 2) W_{i,j-1} \right] - \frac{2 \zeta_\theta C_s \bar{\beta}_3 r_4}{r}$$

$$c_9 = \frac{\zeta_\theta (\bar{\beta}_2 - 1) r_4}{r}$$

$$c_{10} = - a_1 r_3 \left[\alpha_1 W_{i+1,j} + (\alpha_1 - 1) W_{i-1,j} \right] - c_7$$

$$- \frac{\zeta_\theta \bar{C} \beta_3 r_4}{r} (W_{i,j+1} + W_{i,j-1})$$

$$\bar{c}_6 = \Delta t \left[\bar{c}_3 \, V_{\eta\zeta} + \bar{c}_4 - \frac{\bar{\bar{c}}_3}{\Delta\eta} (\delta_\eta^- V) + \frac{\bar{\bar{c}}_4}{\Delta\zeta} (\delta_\zeta^- V) \right]$$

$$+ \left[s_6 \, r_3 \, (\delta_\eta^2 V) + s_8 \, r_4 \, (\delta_\zeta^2 V) \right]$$

$$+ (\bar{c}_1 \, r_1 + s_5 \, r_3) (W_{i+1,j} + W_{i-1,j}) - r_3 \, \bar{\bar{c}}_1 \, W_{i-1,j}$$

$$+ (\bar{\bar{c}}_2 \, r_2 + s_7 \, r_4) (W_{i,j+1} + W_{i,j-1}) - r_4 \, \bar{\bar{c}}_2 \, W_{i,j-1}$$

$$\bar{c}_7 = 2 (\bar{c}_1 \, r_1 + \bar{c}_2 \, r_2) - \bar{c}_5 \Delta t + 2 (s_5 \, r_3 + s_7 \, r_4) - (\bar{\bar{c}}_1 \, r_3 + \bar{\bar{c}}_2 \, r_4)$$

$$s_5 = \gamma_1 \, \bar{\bar{c}}_1 + \frac{\epsilon_1}{2} (2\gamma_2 - 1)$$

$$s_6 = -\gamma_1 \, \bar{\bar{c}}_3 - \frac{\epsilon_1}{2} (2\gamma_1 - 1)$$

$$s_7 = \sigma_1 \, \bar{\bar{c}}_2 + \frac{\epsilon_2}{2} (2\sigma_2 - 1)$$

$$s_8 = \sigma_1 \, \bar{\bar{c}}_4 - \frac{\epsilon_2}{2} (2\sigma_1 - 1)$$

$$\bar{c}_8 = c_{10} + \bar{c}_6 \quad , \quad \bar{c}_9 = c_8 + \bar{c}_7$$

$$d_6 = - \frac{\eta_r V \, d_3 \, r_3 \, \bar{\alpha}_3}{2 \, C_s} (\delta_\eta^2 V) - \frac{\zeta_\theta \, W \, d_3 \, r_4 \, \bar{\beta}_3}{2 \, C_s r} (\delta_\zeta^2 W)$$

$$d_7 = \frac{\eta_r \, V \, b_3 \, d_3 \, r_3 \, \bar{\alpha}_1}{2 \, C_s^2 \, T} (\delta_\eta^2 \rho) - \frac{d_3 \, b_3 \, r_3 \, \bar{\alpha}_3}{2 \, C_s T} (\delta_\eta^2 \rho)$$

$$- \frac{d_3 \, r_3}{2 \, T} \left[\bar{\alpha}_2 \, (\delta_\eta^2 V) + 2 \, (\delta_\eta^- V) \right] - \frac{d_5 \, \Delta t}{T}$$

$$+ \frac{\eta_r V b_6 d_3 r_3 \bar{\alpha}_1}{2 C_s^2 T} (\delta_\eta^2 C) - \frac{d_3 b_6 r_3 \bar{\alpha}_3}{2 C_s T} (\delta_\eta^2 C)$$

$$+ \frac{\zeta_\theta W b_3 d_3 r_4 \bar{\beta}_1}{2 r C_s^2 T} (\delta_\zeta{}^2 \rho) - \frac{d_3 b_3 \zeta_\theta r_4 \bar{\beta}_3}{2 r \eta_r C_s T} (\delta_\zeta{}^2 \rho)$$

$$- \frac{d_3 \zeta_\theta r_4}{2 r \eta_r T} [\bar{\beta}_2 (\delta_\zeta{}^2 W) + 2(\delta_\zeta W)]$$

$$+ \frac{\zeta_\theta W b_6 d_3 r_4 \bar{\beta}_1}{2 r C_s^2 T} (\delta_\zeta^2 C) - \frac{d_3 b_6 \zeta_9 r_4 \bar{\beta}_3}{2 r C_s T \eta_r} (\delta_\zeta^2 C)$$

$$d_8 = d_6 - r_3 (T_{i+1,j} + T_{i-1,j}) \left[\frac{\eta_r V b_3 a_3 \bar{\alpha}_1}{2 C_s^2} + \frac{d_3 b_4 \bar{\alpha}_3}{2 C_s}\right]$$

$$- \frac{V \eta_r r_3}{2} [\bar{\alpha}_2 T_{i+1,j} + (\bar{\alpha}_2 - 2) T_{i-1,j}]$$

$$- \frac{\zeta_\theta W r_4}{2 r} [\bar{\beta}_2 T_{i,j+1} + (\bar{\beta}_2 - 2) T_{i,j-1}]$$

$$- r_4 (T_{i,j+1} + T_{i,j-1}) \left[\frac{\zeta_\theta W b_3 a_3 \bar{\beta}_1}{2 r C_s^2} + \frac{\zeta_\theta d_3 b_4 \bar{\beta}_3}{2 r \eta_r C_s}\right]$$

$$d_9 = d_7 + \frac{\eta_r V b_3 a_3 \bar{\alpha}_1 r_1}{C_s^2} + V \eta_r r_3 (\bar{\alpha}_2 - 1)$$

$$+ \frac{d_3 b_4 \bar{\alpha}_3 r_3}{C_s} + \frac{\zeta_\theta W b_3 a_3 r_4 \bar{\beta}_1}{r C_s^2}$$

$$+ \frac{\zeta_\theta W r_4 (\bar{\beta}_2 - 1)}{r} + \frac{\zeta_\theta d_3 b_4 \bar{\beta}_3 r_4}{r C_s \eta_r}$$

$$\bar{d}_8 = \frac{\bar{\bar{d}}_2}{2\Delta\eta}\,(T_{i+1,j} - T_{i-1,j})$$

$$\bar{d}_9 = \frac{\bar{d}_5}{2\Delta\zeta}\,(T_{i,j+1} - T_{i,j-1})$$

$$d_{10} = \bar{d}_1\, r_1\,(T_{i+1,j} + T_{i-1,j}) + \bar{d}_8\, r_3\,[\alpha_5\, T_{i+1,j} + (\alpha_5 - 1)\, T_{i-1,j}]$$

$$+ \bar{d}_3\, r_3\,[\alpha_6\, T_{i+1,j} + (\alpha_6 - 1)\, T_{i-1,j}] + \bar{d}_4\, r_2\,(T_{i,j+1} + T_{i,j-1})$$

$$+ \bar{d}_9\, r_4\,[\beta_5\, T_{i,j+1} + (\beta_5 - 1)\, T_{i,j-1}] + \bar{d}_6\, r_4\,[\beta_6\, T_{i,j+1} + (\beta_6 - 1)\, T_{i,j-1}]$$

$$+ \bar{d}_7 \Delta t + r_1\, \bar{\bar{d}}_{13}\,(\delta^2_\eta C) + r_2\, \bar{\bar{d}}_{14}\,(\delta^2_\zeta C) + r_3\, \bar{\bar{d}}_{11}\,(\delta^-_\eta C)$$

$$+ r_4\, \bar{\bar{d}}_{12}\,(\delta^-_\zeta C) - \frac{\Delta t\, \dot{W}_1\, C_s}{\rho C_v} + \bar{\bar{d}}_9\, r_3\,[\alpha_7\, T_{i+1,j} + (\alpha_7 - 1)\, T_{i-1,j}]$$

$$+ \bar{\bar{d}}_{10}\, r_4\,[\beta_7\, T_{i,j+1} + (\beta_7 - 1)\, T_{i,j-1}]$$

$$\bar{d}_{11} = 2\, r_1\, \bar{d}_1 + r_3\, \bar{d}_8\,(2\,\alpha_5 - 1) + r_3\, \bar{d}_3\,(2\,\alpha_6 - 1)$$

$$+ 2\, r_2\, \bar{d}_4 + \bar{d}_9\, r_4\,(2\,\beta_5 - 1) + \bar{d}_6\, r_4\,(2\,\beta_6 - 1)$$

$$+ \bar{\bar{d}}_9\, r_3\,(2\,\alpha_7 - 1) + \bar{\bar{d}}_{10}\, r_4\,(2\,\beta_7 - 1)$$

$$f_1 = \frac{\partial(\rho \mathcal{D}_{ij})}{\partial T} \Big/ \rho \mathcal{D}_{ij}, \quad f_2 = \frac{\partial(\rho \mathcal{D}_{ij})}{\partial C} \Big/ \rho \mathcal{D}_{ij}, \quad f_3 = \frac{\partial \bar{h}}{\partial T} \Big/ (\bar{h} - \bar{e})$$

$$\bar{\bar{d}}_9 = \eta_r^2 \, (\bar{\bar{d}}_8 \, f_1 + \bar{\bar{d}}_8 \, f_3) \left(\frac{C_{i+1,j} - C_{i-1,j}}{2 \Delta \eta} \right.$$

$$\bar{\bar{d}}_{10} = \frac{\zeta_\theta^2}{r^2} \, (\bar{\bar{d}}_8 \, f_1 + \bar{\bar{d}}_8 \, f_3) \left(\frac{C_{i,j+1} - C_{i,j-1}}{2 \Delta \zeta} \right)$$

$$\bar{\bar{d}}_{11} = \bar{\bar{d}}_8 \left[\frac{\eta_r}{r} + \eta_{rr} + \eta_r^2 \, f_2 \left(\frac{C_{i+1,j} - C_{i-1,j}}{2 \Delta \eta} \right. \right.$$

$$\bar{\bar{d}}_{12} = \frac{\bar{\bar{d}}_8}{r^2} \left[\zeta_{\theta\theta} + \zeta_\theta^2 \, f_2 \left(\frac{C_{i,j+1} - C_{i,j-1}}{2 \Delta \zeta} \right. \right) \right]$$

$$\bar{\bar{d}}_{13} = \eta_r^2 \, \bar{\bar{d}}_8 + \bar{\bar{d}}_{11} \, \alpha_8 \, \Delta\eta$$

$$\bar{\bar{d}}_{14} = \frac{\zeta_\theta^2}{r^2} \, \bar{\bar{d}}_8 + \bar{\bar{d}}_{12} \, \beta_8 \, \Delta\zeta$$

$$\alpha_5 = \begin{cases} 1 : \bar{d}_8 \geq 0 \\ 0 : \bar{d}_8 < 0 \end{cases} \qquad \alpha_6 = \begin{cases} 1 : \bar{d}_3 \geq 0 \\ 0 : \bar{d}_3 < 0 \end{cases}$$

$$\alpha_7 = \begin{cases} 1 : \bar{\bar{d}}_9 \geq 0 \\ 0 : \bar{\bar{d}}_9 < 0 \end{cases}, \qquad \alpha_8 = \begin{cases} 1 : \bar{\bar{d}}_{11} \geq 0 \\ 0 : \bar{\bar{d}}_{11} < 0 \end{cases}$$

$$\beta_5 = \begin{cases} 1 : \bar{d}_9 \geq 0 \\ 0 : \bar{d}_9 < 0 \end{cases} \qquad \beta_6 = \begin{cases} 1 : \bar{d}_6 > 0 \\ 0 : \bar{d}_6 < 0 \end{cases}$$

$$\beta_7 = \begin{cases} 1 : \bar{\bar{d}}_{10} \geq 0 \\ 0 : \bar{\bar{d}}_{10} < 0 \end{cases}, \qquad \beta_8 = \begin{cases} 1 : \bar{\bar{d}}_{12} \geq 0 \\ 0 : \bar{\bar{d}}_{12} < 0 \end{cases}$$

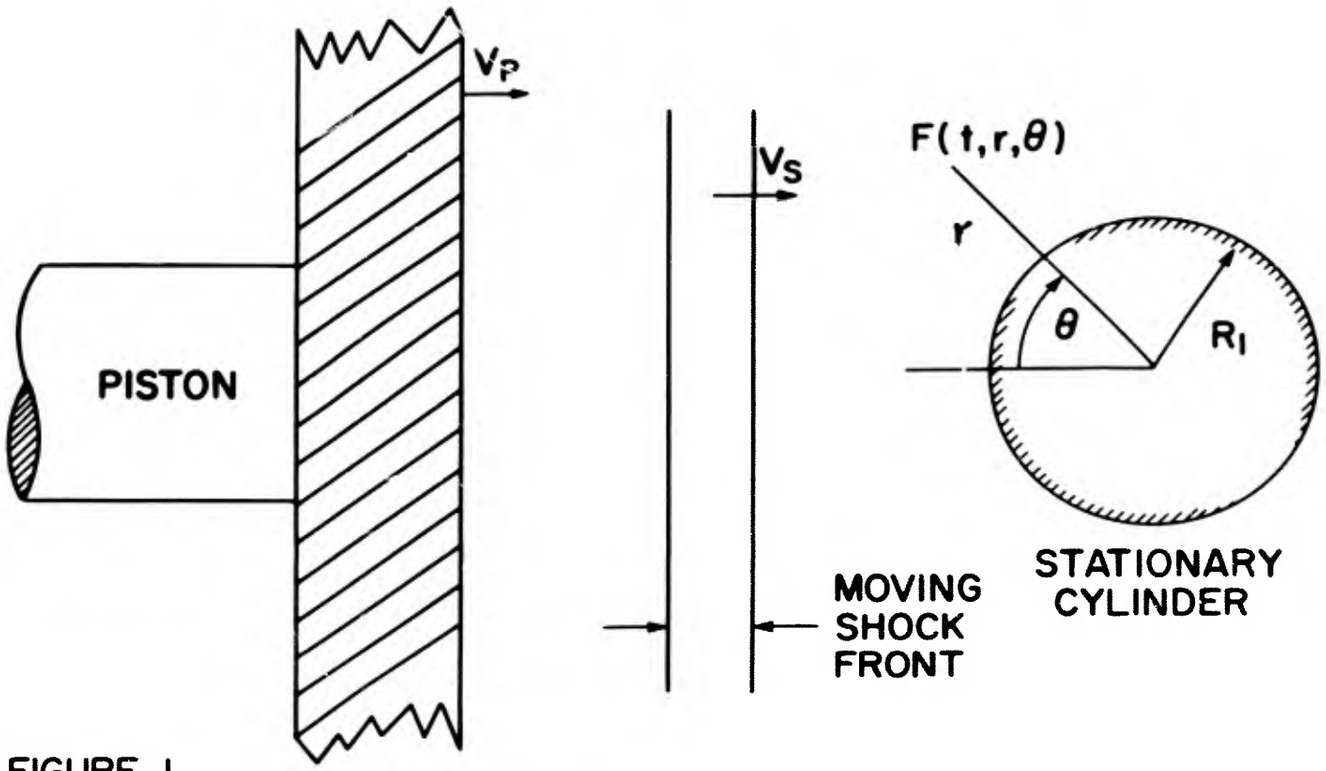
V_P
PISTON
V_S
MOVING
SHOCK
FRONT
F(t,r,θ)
r
θ
R_1
STATIONARY
CYLINDER

FIGURE 1

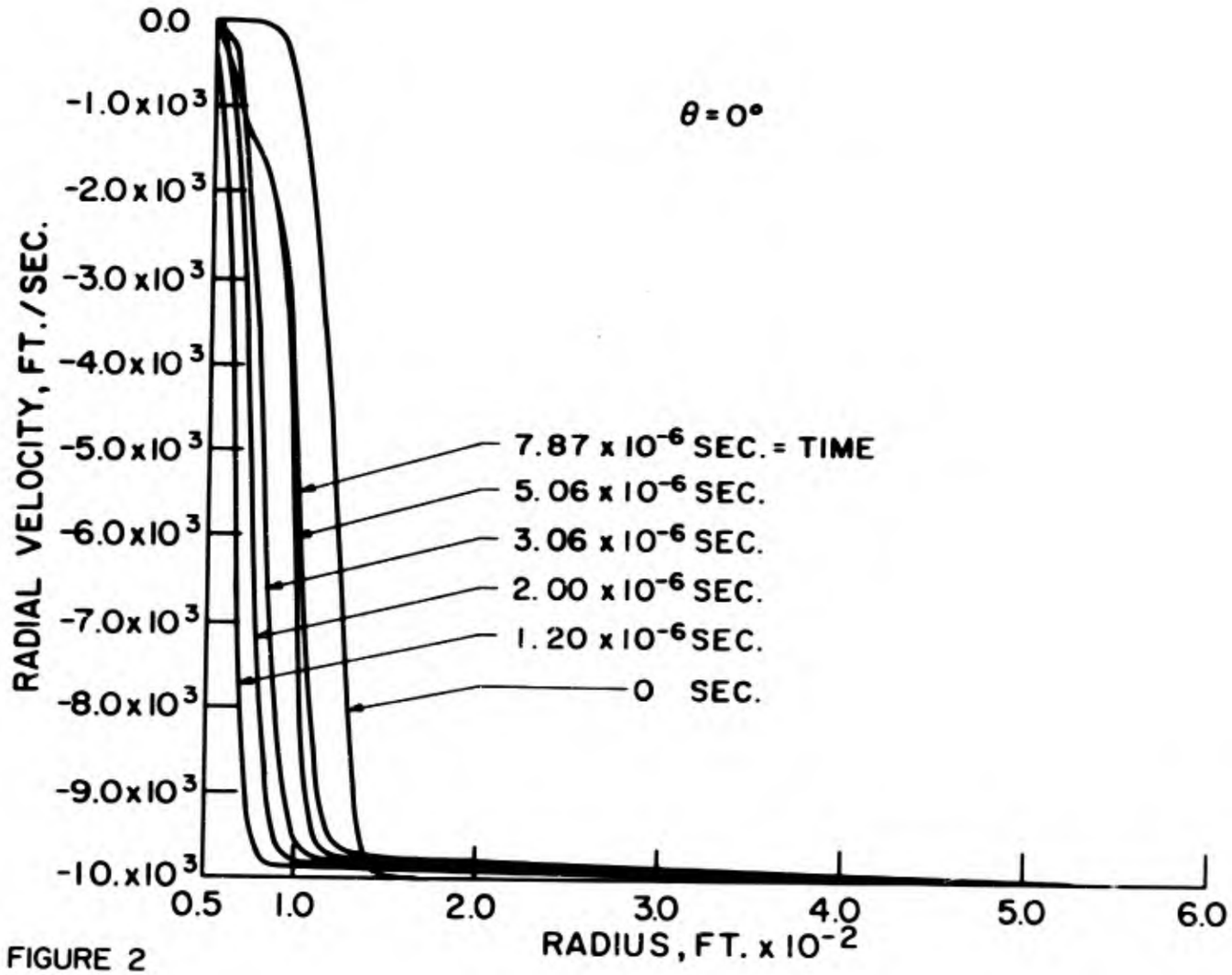
0.0
-1.0x10^3
-2.0x10^3
-3.0x10^3
-4.0x10^3
-5.0x10^3
-6.0x10^3
-7.0x10^3
-8.0x10^3
-9.0x10^3
-10.x10^3
RADIAL VELOCITY, FT./SEC.
θ = 0°
7.87 x 10^-6 SEC. = TIME
5.06 x 10^-6 SEC.
3.06 x 10^-6 SEC.
2.00 x 10^-6 SEC.
1.20 x 10^-6 SEC.
0 SEC.
0.5
1.0
2.0
3.0
4.0
5.0
6.0
RADIUS, FT. x 10^-2

FIGURE 2

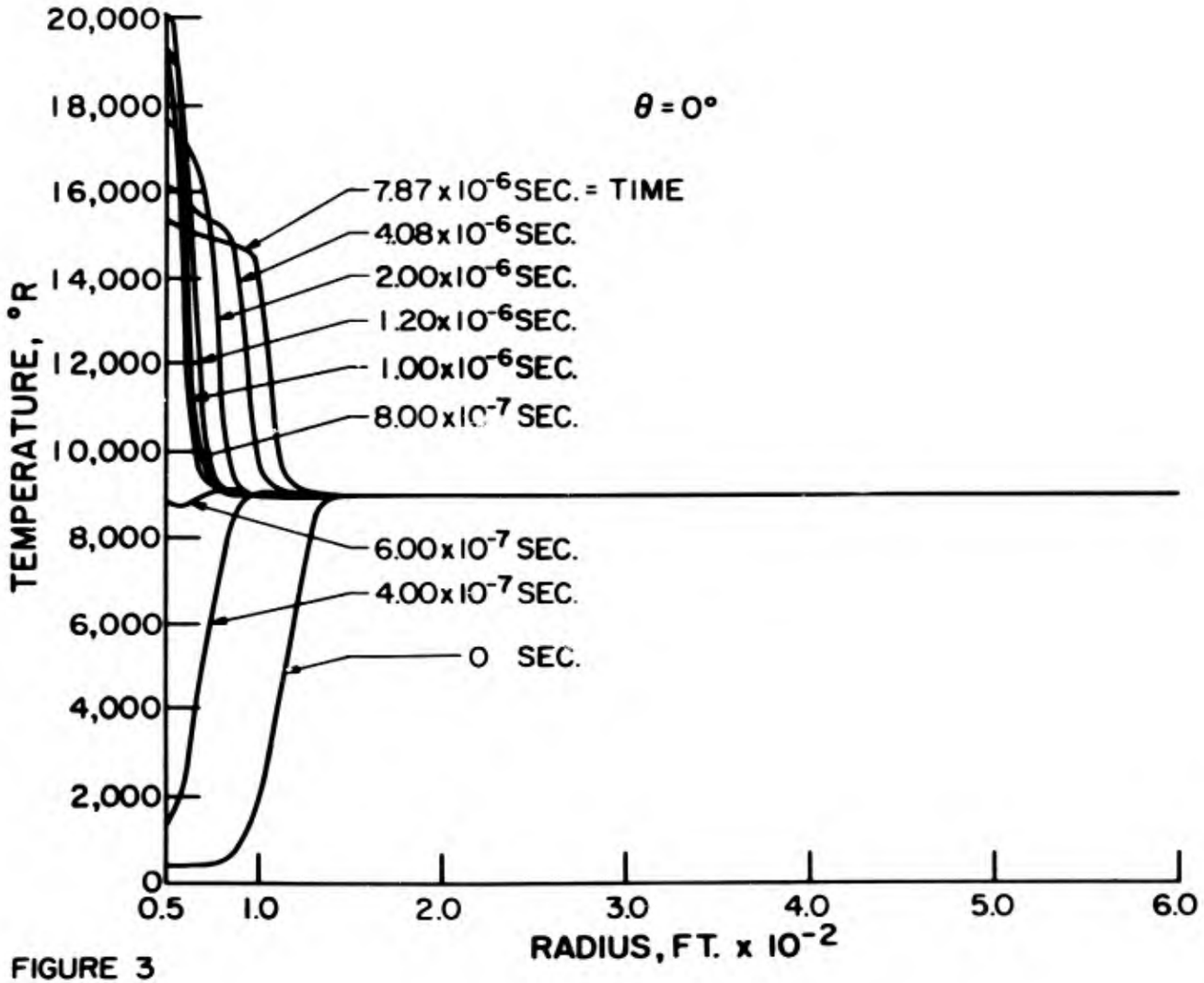
20,000
18,000
16,000
14,000
12,000
10,000
8,000
6,000
4,000
2,000
0
TEMPERATURE, °R
θ = 0°
7.87 x 10⁻⁶ SEC. = TIME
4.08 x 10⁻⁶ SEC.
2.00 x 10⁻⁶ SEC.
1.20 x 10⁻⁶ SEC.
1.00 x 10⁻⁶ SEC.
8.00 x 10⁻⁷ SEC.
6.00 x 10⁻⁷ SEC.
4.00 x 10⁻⁷ SEC.
0 SEC.
0.5
1.0
2.0
3.0
4.0
5.0
6.0
RADIUS, FT. x 10⁻²

FIGURE 3

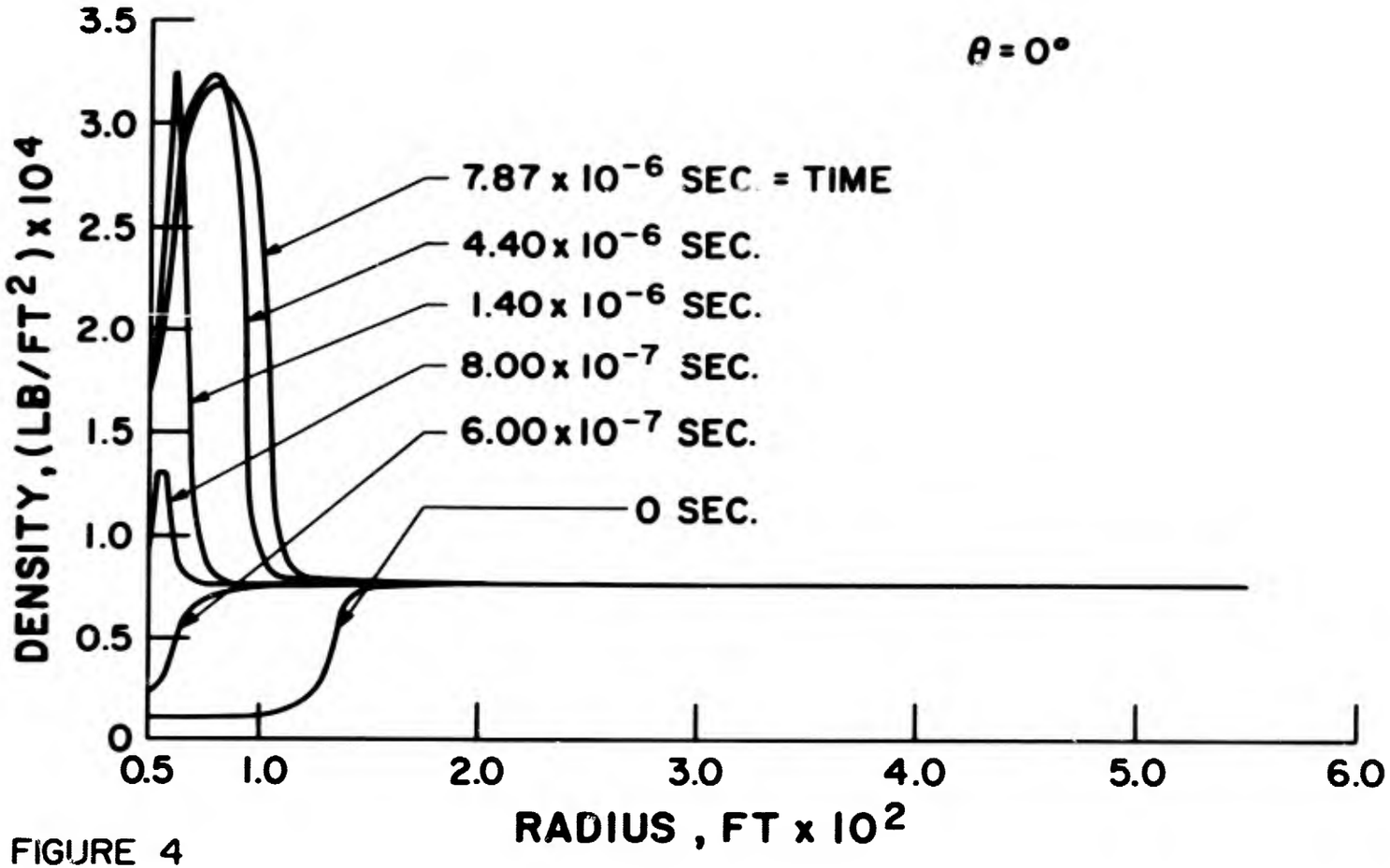
θ = 0°
7.87 x 10⁻⁶ SEC. = TIME
4.40 x 10⁻⁶ SEC.
1.40 x 10⁻⁶ SEC.
8.00 x 10⁻⁷ SEC.
6.00 x 10⁻⁷ SEC.
0 SEC.
DENSITY, (LB/FT²) x 10⁴
3.5
3.0
2.5
2.0
1.5
1.0
0.5
0
0.5
1.0
2.0
3.0
4.0
5.0
6.0
RADIUS, FT x 10²

FIGURE 4

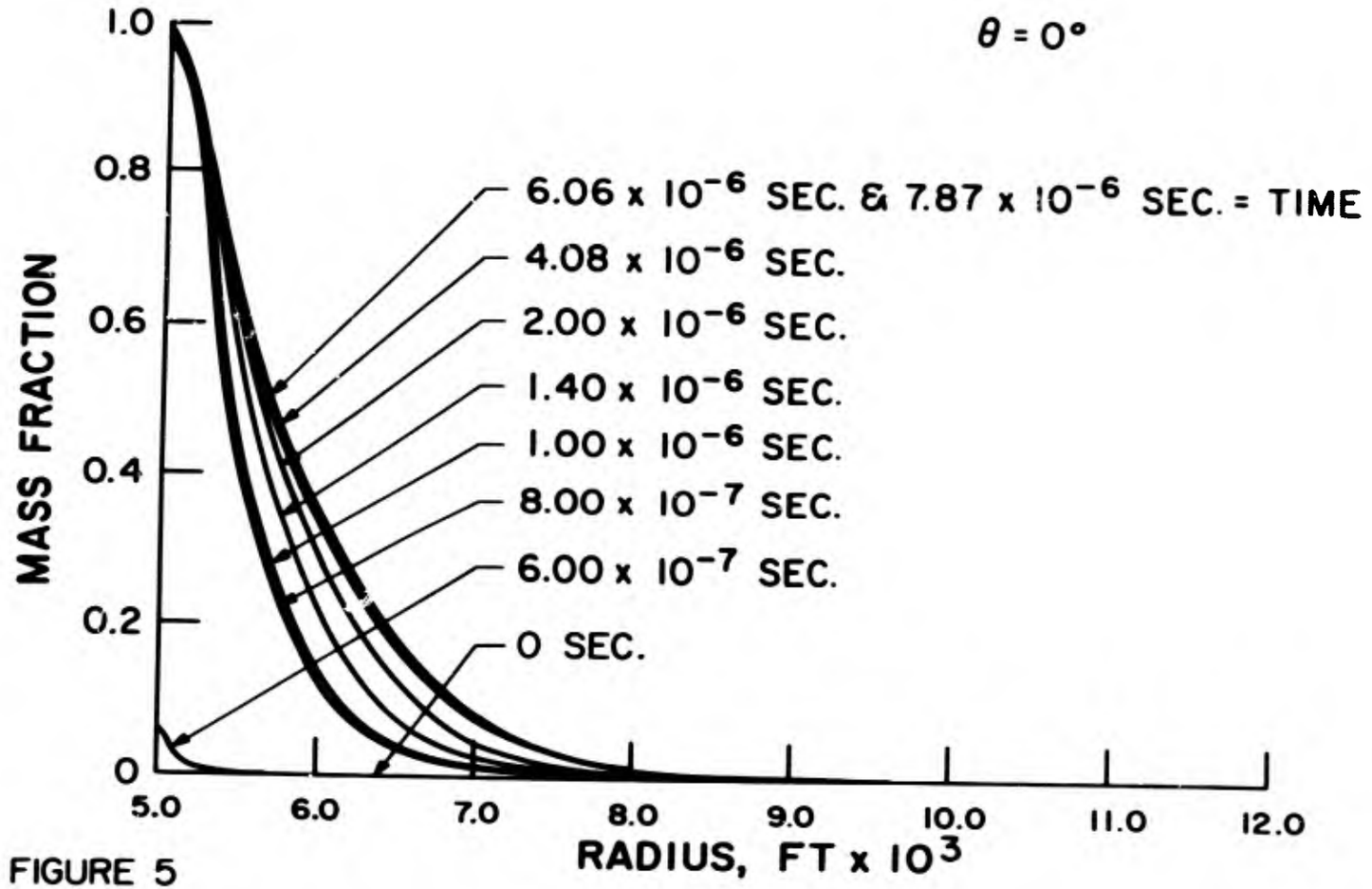
θ = 0°
6.06 x 10⁻⁶ SEC. & 7.87 x 10⁻⁶ SEC. = TIME
4.08 x 10⁻⁶ SEC.
2.00 x 10⁻⁶ SEC.
1.40 x 10⁻⁶ SEC.
1.00 x 10⁻⁶ SEC.
8.00 x 10⁻⁷ SEC.
6.00 x 10⁻⁷ SEC.
0 SEC.
MASS FRACTION
1.0
0.8
0.6
0.4
0.2
0
5.0
6.0
7.0
8.0
9.0
10.0
11.0
12.0
RADIUS, FT x 10³

FIGURE 5

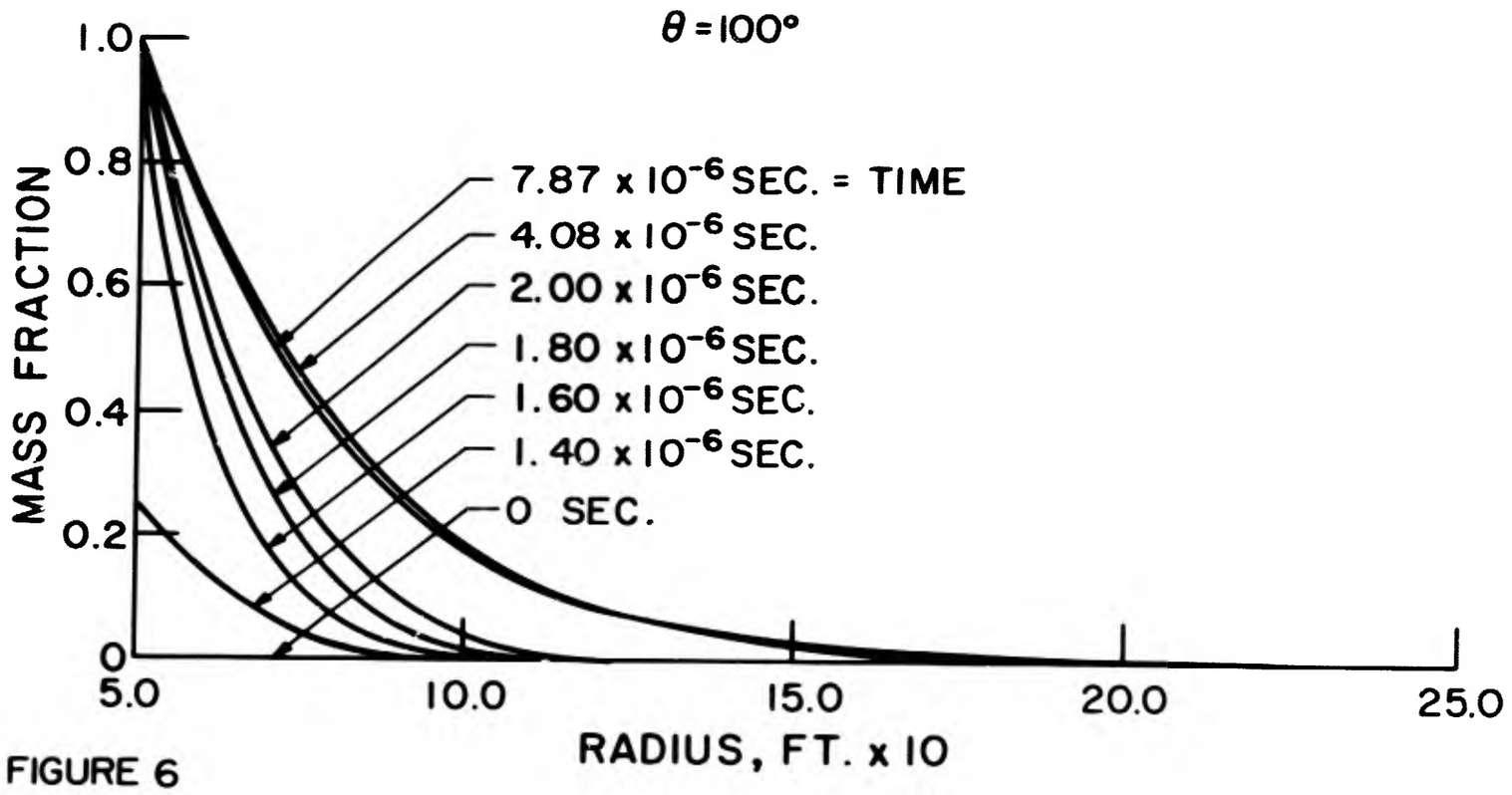
θ = 100°
1.0
0.8
0.6
0.4
0.2
0
MASS FRACTION
7.87 x 10⁻⁶ SEC. = TIME
4.08 x 10⁻⁶ SEC.
2.00 x 10⁻⁶ SEC.
1.80 x 10⁻⁶ SEC.
1.60 x 10⁻⁶ SEC.
1.40 x 10⁻⁶ SEC.
0 SEC.
5.0
10.0
15.0
20.0
25.0
RADIUS, FT. x 10

FIGURE 6

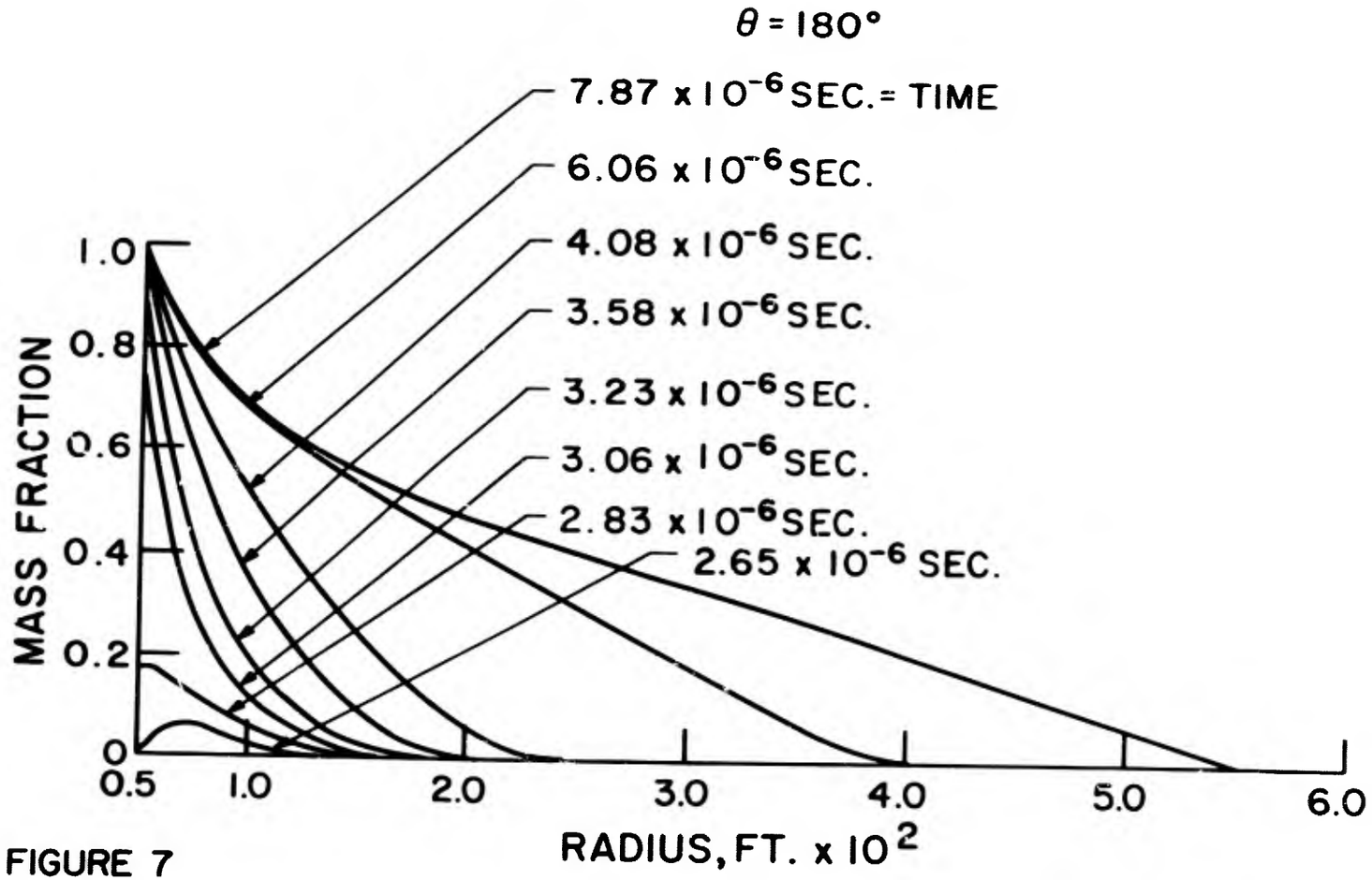
θ = 180°
7.87 x 10⁻⁶ SEC. = TIME
6.06 x 10⁻⁶ SEC.
4.08 x 10⁻⁶ SEC.
3.58 x 10⁻⁶ SEC.
3.23 x 10⁻⁶ SEC.
3.06 x 10⁻⁶ SEC.
2.83 x 10⁻⁶ SEC.
2.65 x 10⁻⁶ SEC.
MASS FRACTION
1.0
0.8
0.6
0.4
0.2
0
0.5
1.0
2.0
3.0
4.0
5.0
6.0
RADIUS, FT. x 10²

FIGURE 7

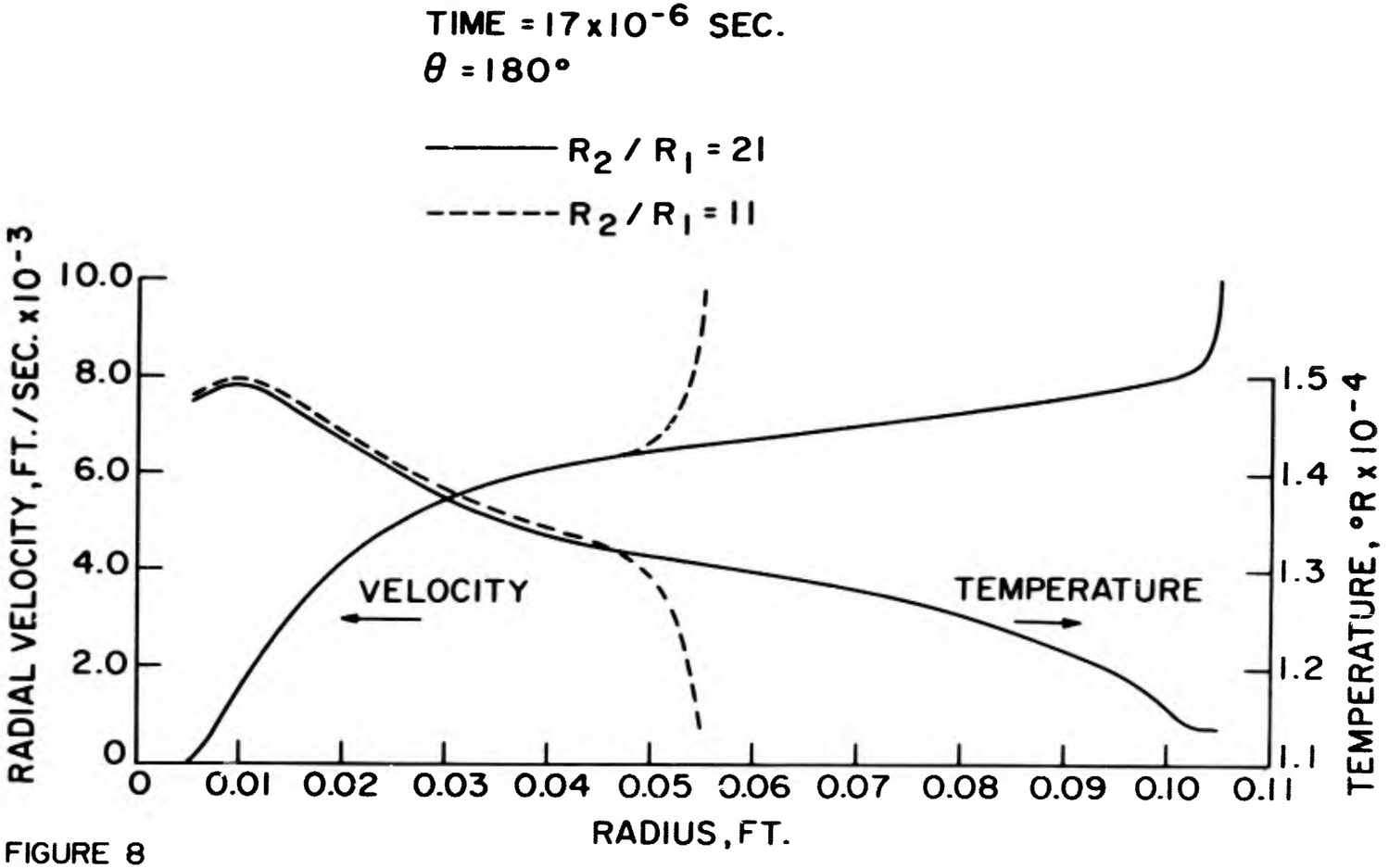
TIME = 17 x 10⁻⁶ SEC.
θ = 180°
R2 / R1 = 21
R2 / R1 = 11
RADIAL VELOCITY, FT./SEC. x10⁻³
10.0
8.0
6.0
4.0
2.0
0
VELOCITY
TEMPERATURE
1.5
1.4
1.3
1.2
1.1
TEMPERATURE, °R x 10⁻⁴
0
0.01
0.02
0.03
0.04
0.05
0.06
0.07
0.08
0.09
0.10
0.11
RADIUS, FT.

FIGURE 8

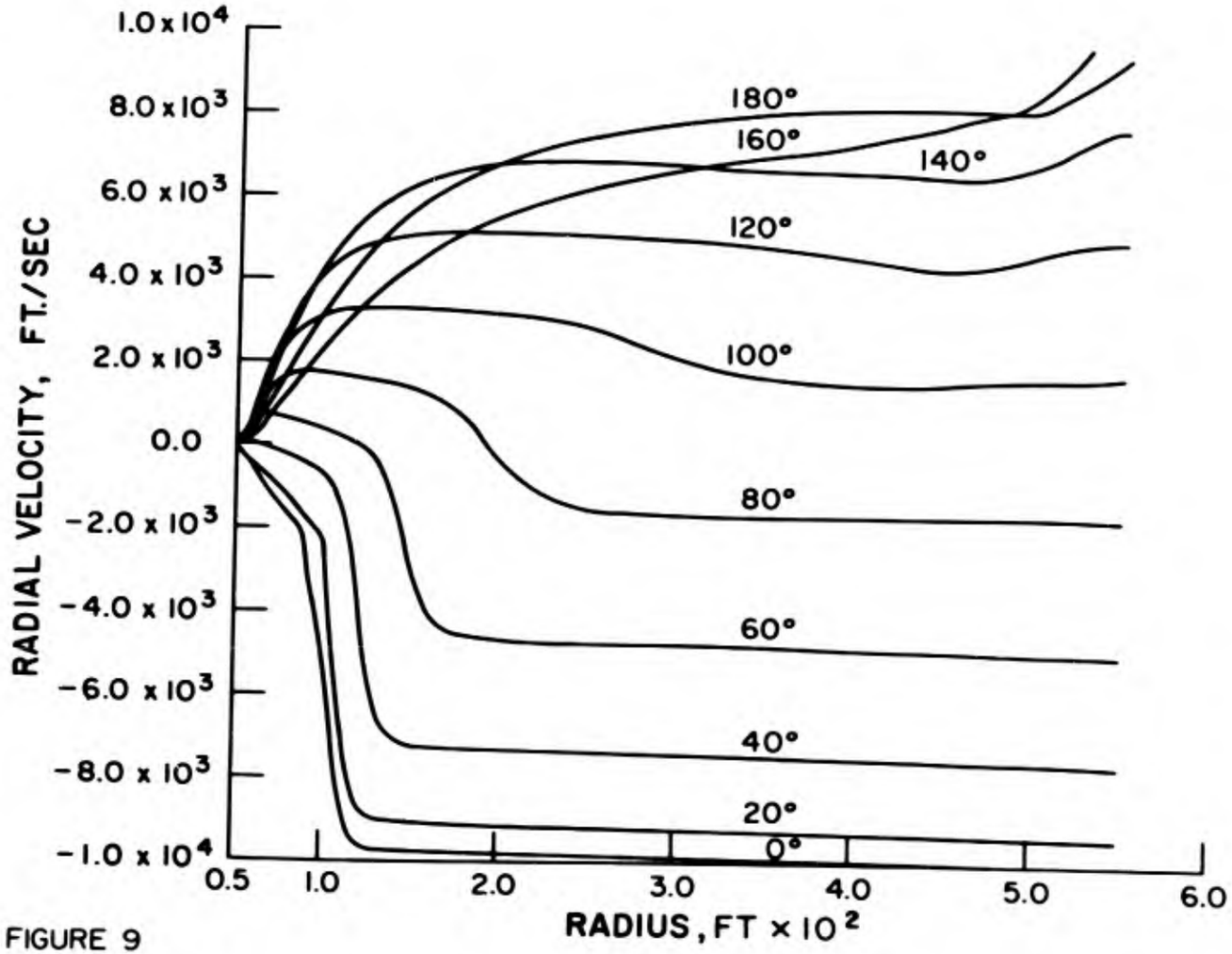
1.0 x 10^4
8.0 x 10^3
6.0 x 10^3
4.0 x 10^3
2.0 x 10^3
0.0
-2.0 x 10^3
-4.0 x 10^3
-6.0 x 10^3
-8.0 x 10^3
-1.0 x 10^4
RADIAL VELOCITY, FT./SEC
180°
160°
140°
120°
100°
80°
60°
40°
20°
0°
0.5
1.0
2.0
3.0
4.0
5.0
6.0
RADIUS, FT x 10^2

FIGURE 9

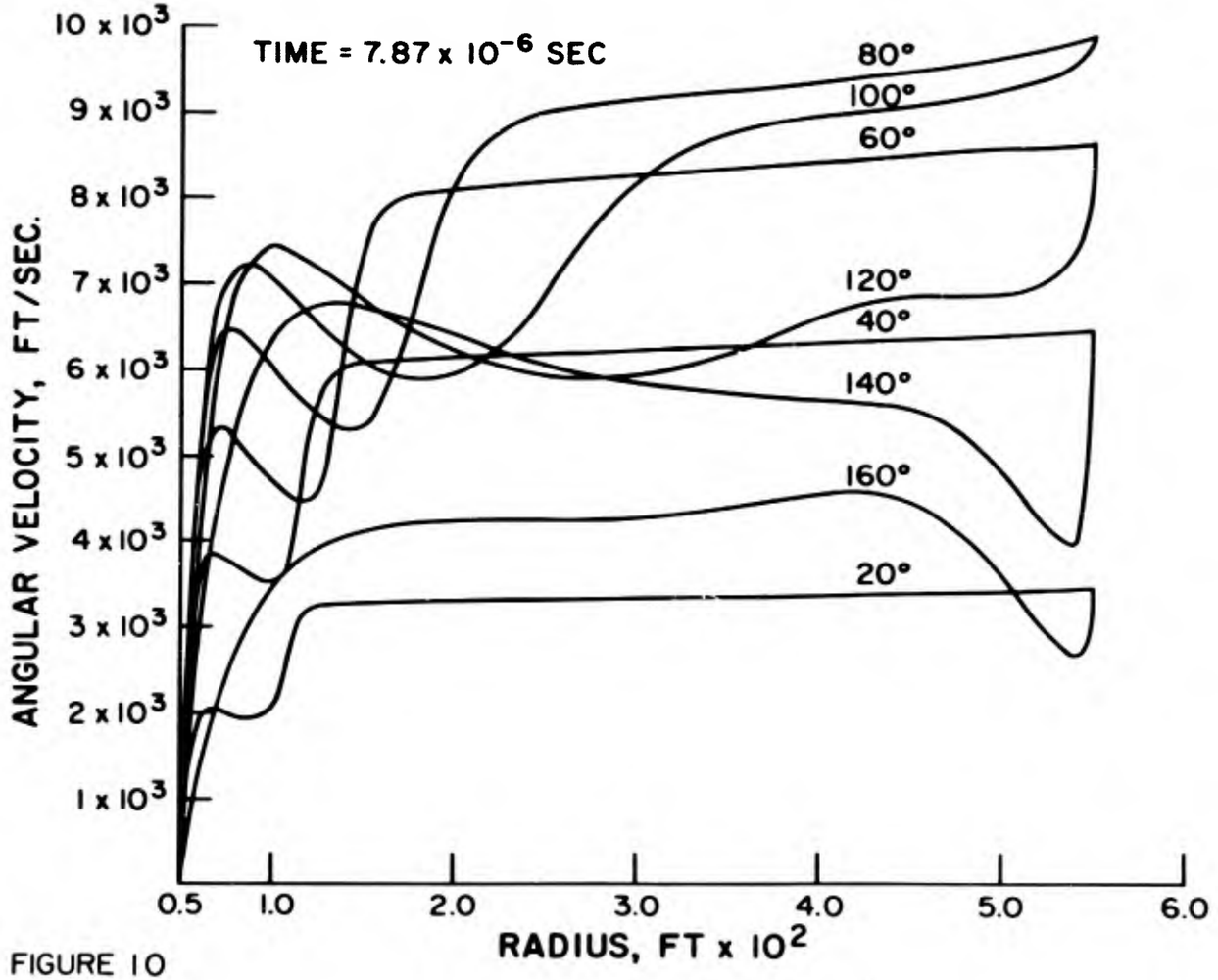
TIME = 7.87 x 10⁻⁶ SEC
80°
100°
60°
120°
40°
140°
160°
20°
10 x 10³
9 x 10³
8 x 10³
7 x 10³
6 x 10³
5 x 10³
4 x 10³
3 x 10³
2 x 10³
1 x 10³
ANGULAR VELOCITY, FT/SEC.
0.5
1.0
2.0
3.0
4.0
5.0
6.0
RADIUS, FT x 10²

FIGURE 10

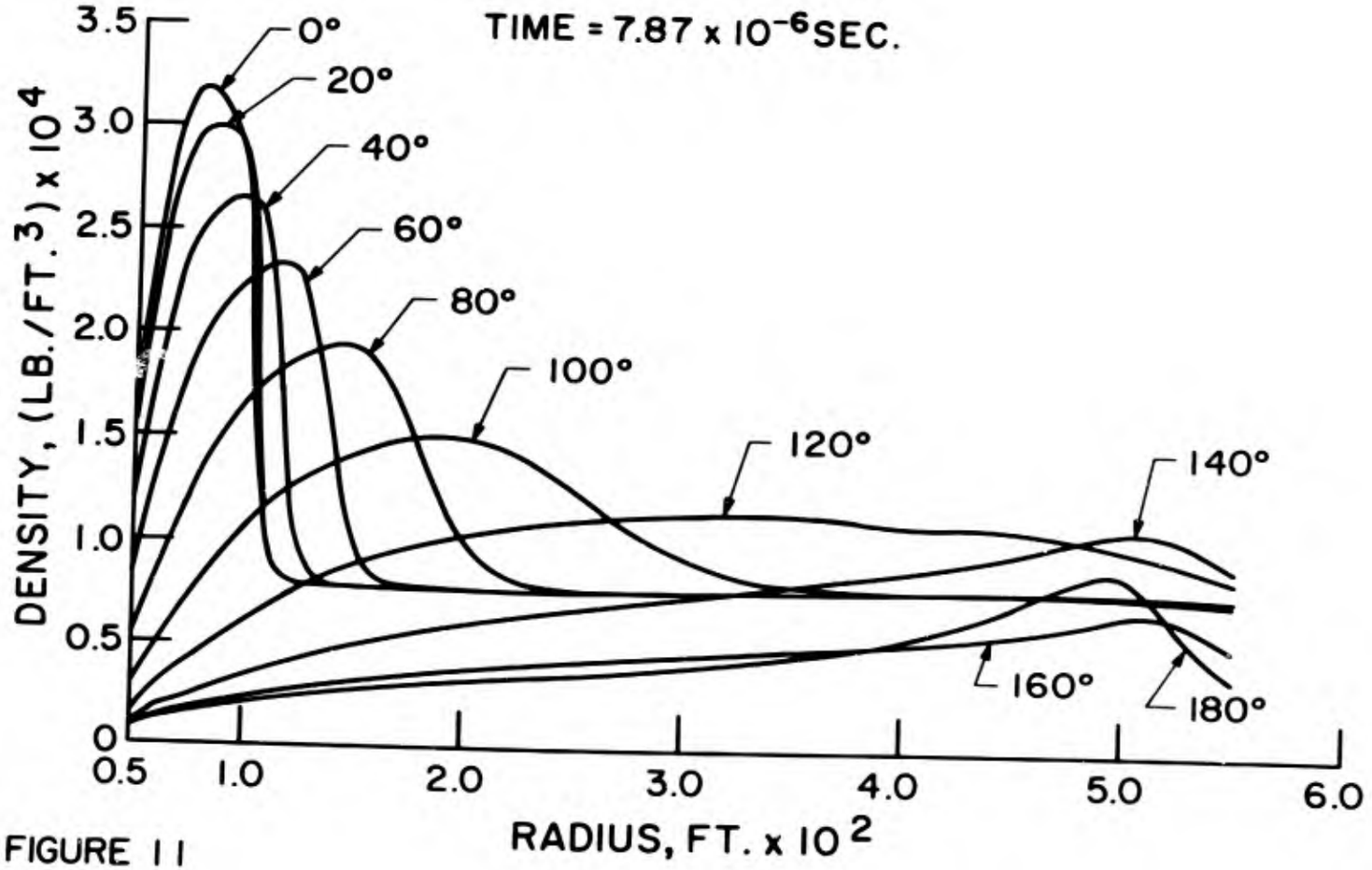
TIME = 7.87 x 10⁻⁶SEC.
0°
20°
40°
60°
80°
100°
120°
140°
160°
180°
DENSITY, (LB./FT.³) x 10⁴
3.5
3.0
2.5
2.0
1.5
1.0
0.5
0
0.5
1.0
2.0
3.0
4.0
5.0
6.0
RADIUS, FT. x 10²

FIGURE 11

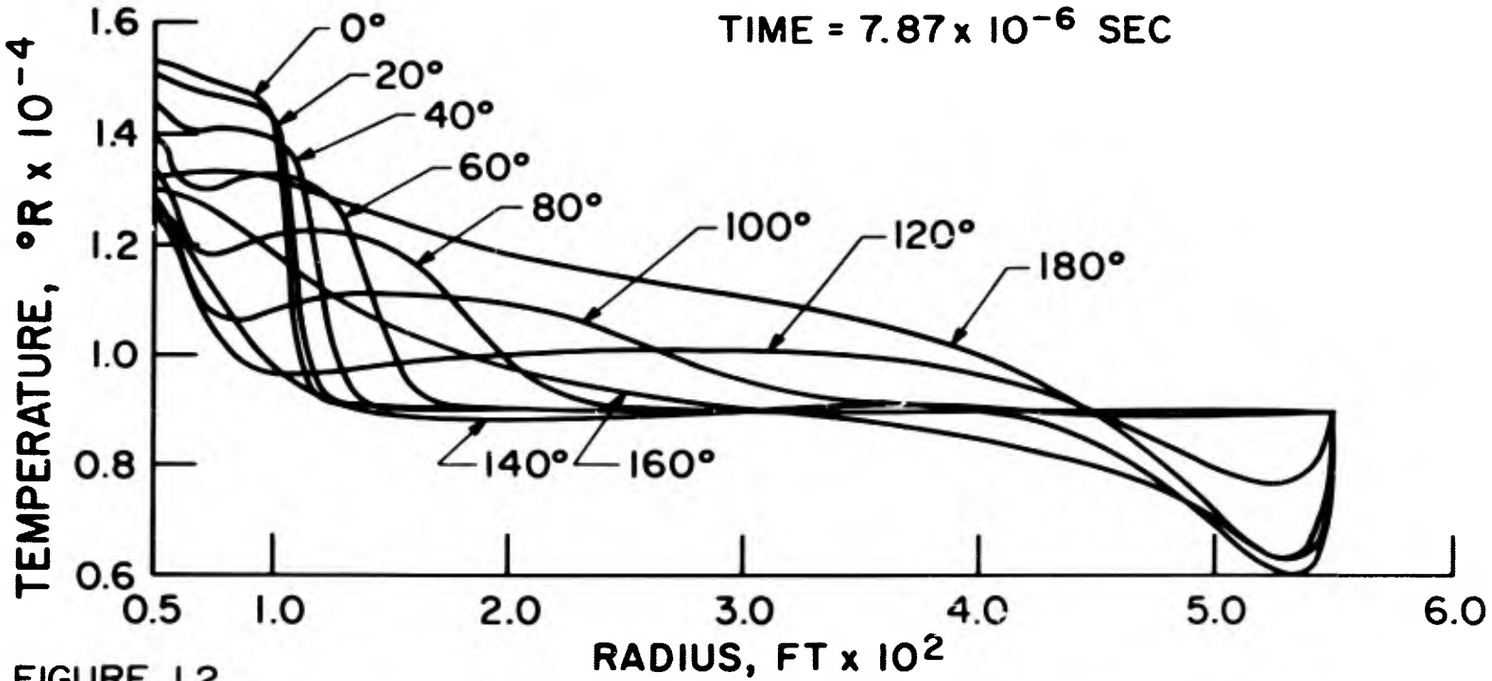
TIME = 7.87 x 10⁻⁶ SEC
0°
20°
40°
60°
80°
100°
120°
180°
140°
160°
TEMPERATURE, °R x 10⁻⁴
1.6
1.4
1.2
1.0
0.8
0.6
0.5
1.0
2.0
3.0
4.0
5.0
6.0
RADIUS, FT x 10²

FIGURE 12

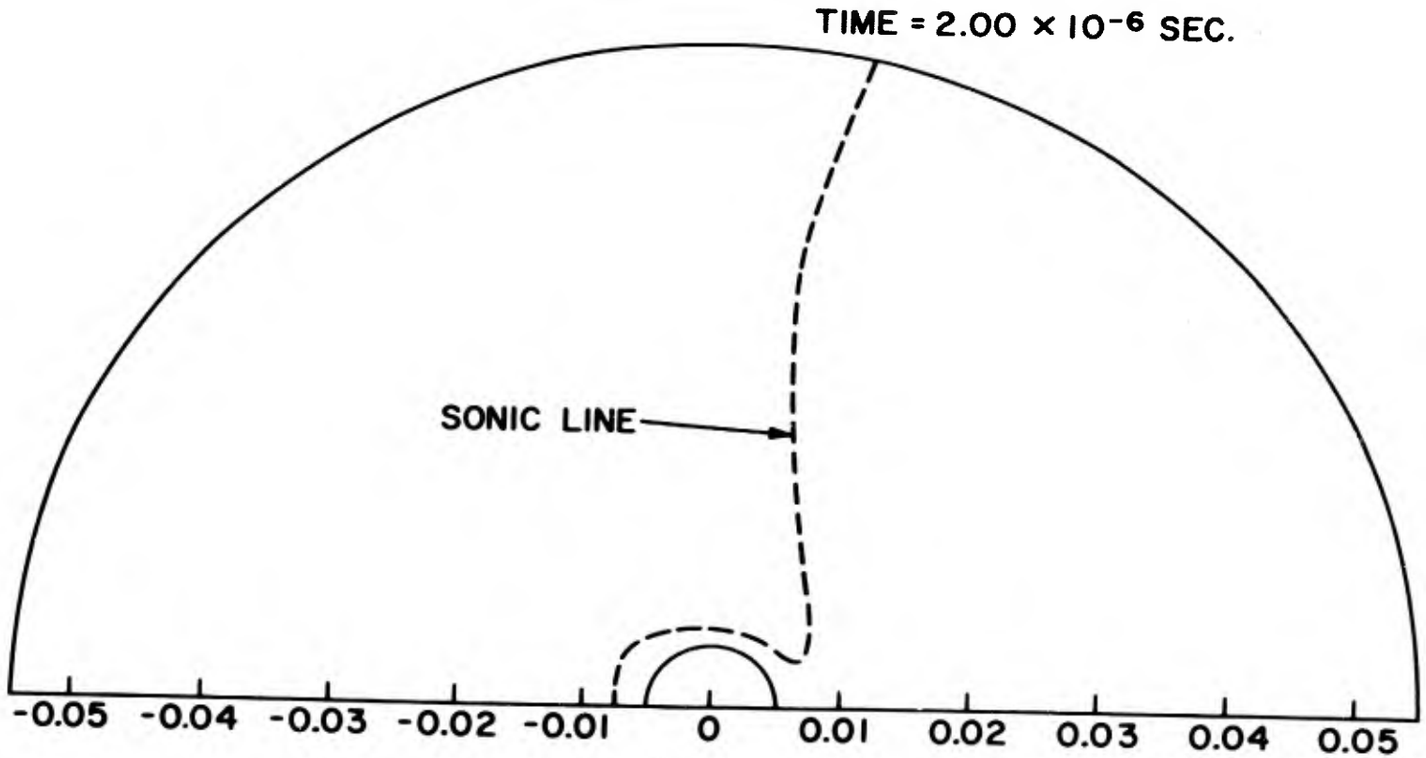
TIME = 2.00 × 10⁻⁶ SEC.
SONIC LINE
-0.05
-0.04
-0.03
-0.02
-0.01
0
0.01
0.02
0.03
0.04
0.05
RADIUS, FT. × 10²

FIGURE 13

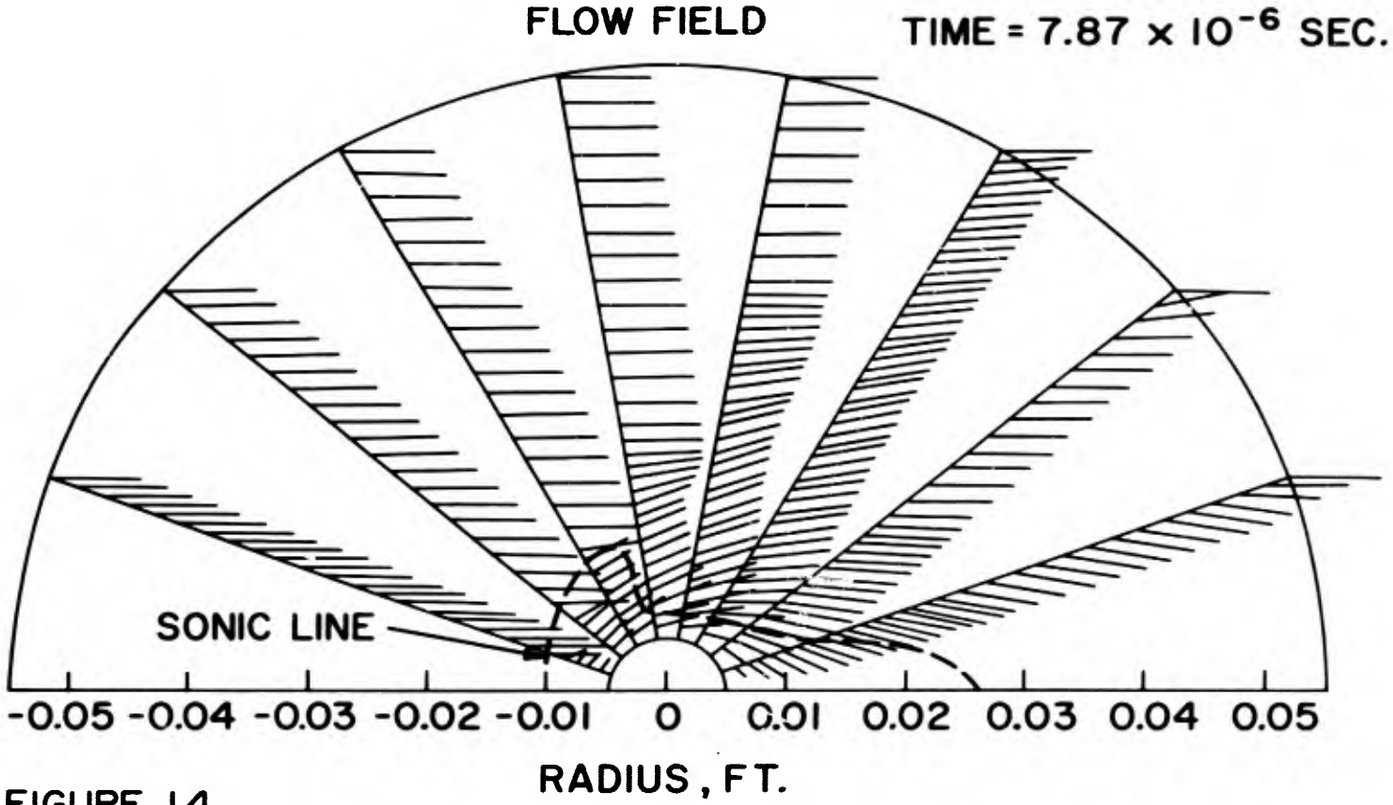
FLOW FIELD
TIME = 7.87 x 10⁻⁶ SEC.
SONIC LINE
-0.05 -0.04 -0.03 -0.02 -0.01 0 0.01 0.02 0.03 0.04 0.05
RADIUS, FT.

FIGURE 14

MASS DENSITY MEASUREMENTS IN HYPERSONIC WAKES

by

J.G.G. Dionne, C.M. Sadowski, L. Tardif, J.E.H. Vanoverschelde

This document is generated under the
CARDE-ARPA co-operative re-entry physics program
of ARPA Order 133.

CANADIAN ARMAMENT RESEARCH AND DEVELOPMENT ESTABLISHMENT
VALCARTIER, P.Q., CANADA

February, 1967

SUMMARY

Mean and fluctuating mass density measurements have been carried out in hypersonic wakes over a wide range of ambient densities. An electron beam probe was found suitable at pressures of from 1-10 torr. The mass density was related to the fluorescent intensity resulting from the collisions between the highly energetic electrons and the wake molecules. At ambient pressures above 10 torr., mean mass densities were measured using a laser probe. The intensity of the Rayleigh scattered light measured at an angle of 90^{o} to the incident beam was related in a simple way to the local wake density. Both methods were characterized by their capabilities of good spatial and temporal resolution.

This paper will present measured mean radial density distributions at several downstream positions, as well as power spectra of the fluctuations. Some discussions will also follow of the fluorescence spectra excited in air and nitrogen by electron bombardment at energies ranging from 25 to 75 kilo electron volt.

RESUME

On a procédé à des mesures de densité de masse moyenne et fluctuante dans des sillages hypersoniques, pour une gamme étendue de densités ambiantes. Une sonde à faisceau électronique s'est révélée adéquate pour des pressions allant de 1 à 10 torr. On a rapporté la densité de masse à l'intensité fluorescente résultant des collisions entre électrons à haute énergie et mollécules du sillage. Pour des pressions ambiantes supérieures à 10 torr. les densités moyennes de masse ont été mesurées à l'aide d'une sonde à laser. On a rapporté d'une manière simple, l'intensité de la lumière diffusée de Rayleigh, mesurée à un angle de 90^{o} avec le faisceau incident, à la densité locale du sillage. Les deux méthodes se sont avérées satisfaisantes à la fois du point de vue spatial et temporel.

Les auteurs présenteront des répartitions de densité radiale moyenne fournies par mesures, pour plusieurs points en aval, ainsi que des spectres de force des fluctuations. Ils étudieront également les spectres de fluorescence suscitée dans l'air et l'azote par un bombardement d'électrons à des énergies variant de 25 à 75. Kev.

NOTATION

a_ρ = an adjustable parameter used to fit equation (1) through the points on a plot of fluorescent intensity against density.

a_p = an adjustable parameter used to fit equation (2) through the points on a plot of fluorescent intensity against pressure.

F = a function defining the dependence of the Rayleigh scattered intensity on composition and wavelength.

K_p = normalizing constant relating the measured fluorescent signal voltage to the gas pressure.

K_ρ = normalizing constant relating the measured fluorescent signal voltage to the gas density.

P_s = Rayleigh scattered power falling on the light collecting lens.

P_i = incident power falling on the scattering volume under observation.

p = gas pressure.

V = fluorescent intensity signal voltage.

δ = the width of the field-of-view of a lens-slit light gathering system.

$\Delta\Omega$ = the solid angle supported by a lens of a lens-slit system at its focal plane.

ρ = gas density.

Mass Density Measurements in Hypersonic Wakes

by

J.G.G. Dionne, C.M. Sadowski, L. Tardif, J.E.H. Vanoverschelde

1.0 Introduction

Over the past several years considerable effort has been expended in obtaining a better theoretical and experimental understanding of the wakes behind hypervelocity vehicles. However, there is still a great need for experimental measurements of fundamental wake properties of theoretical interest, such as the density, velocity and temperature. The concentration of electrons is also of primary importance, since electrons are responsible for radar returns and are thus of vital interest in the design of defense systems.

The present paper discusses two techniques to measure local wake densities. The electron beam fluorescence probe, which has been very successful in the study of densities in such facilities as low density shock tubes and shock tunnels, is used in the present application to measure mass densities and mass density fluctuations in hypersonic air and nitrogen wakes. Since the electron beam is strongly attenuated by air or nitrogen, ambient range pressures were restricted to less than 10 Torr. The Rayleigh scattering probe was to be used at the higher pressures. In both techniques the detected radiant intensity was taken to be proportional to the gas density for a given incident beam intensity.

It is worth mentioning that neither of these techniques interferes mechanically with the wake flow and that both techniques are capable of high spatial and temporal resolution.

2.0 The Electron Beam Fluorescence Probe

When a beam of electrons is fired through air or nitrogen at sufficiently high energy, a small fraction of the electrons collides with the nitrogen molecules and excites them to a radiative state. The intense fluorescence released almost instantaneously by spontaneous emission is almost entirely confined within the width of the electron beam. The intensity of the fluorescence is thus a measure of the average gas density in any small volume from which the fluorescence is observed. At gas densities which are low enough to preclude non-radiative de-excitation processes, such as collisional quenching, the fluorescent intensity is a linear function of gas density and beam current.

The electron beam fluorescence probe has at least two advantages. Unlike mechanical probes, it creates no disturbances in the flow field and can be used for measurements along the flight axis. Because the electron gun can be fired continuously, measurements can be made ahead of the projectile and over the entire length of the wake.

Detailed analyses of the excitation and emission processes are given in reference 8. A complete spectrographic study of the fluorescent spectra of air and nitrogen by 50 kev electrons is reported by Davidson and O'Neill (4) at pressures from 5 to 600 Torr. The predominant radiation has been observed to be emitted by the second positive system of the neutral nitrogen molecule, N_2 (2+), and by the first negative system of the singly ionized nitrogen molecule, N_2^+ (1-). At pressures below 1 Torr the radiation from the N_2^+ (1-) system was found to be

stronger than from the N_2 (2+) system and the intensities of both systems were observed to be proportional to the density of molecular nitrogen to within the limits of experimental error (1, 8). At pressures above 3 Torr, the intensity from the N_2 (2+) system is still linearly dependent on nitrogen concentration, while the intensity from the N_2^+ (1-) system shows non-linearity and tends toward a saturation level (see Figure 2). Measurements with a S-13 photomultiplier (uncorrected for spectral response) have shown that the intensities of the two systems become equal at pressures of 3 Torr.

At ambient pressures below 1 Torr, the N_2^+ (1-) system has been previously used for wake density measurements because of its greater intensity (see reference 9). At pressures above 3 Torr, the N_2 (2+) system was preferred in view of its linear dependence of intensity on pressure or density and its higher intensity. All of the density measurements reported in this paper, which were made in the wake behind spherical projectiles fired into nitrogen or air were based on fluorescent intensity measurements of the N_2 (2+) (0,0) band at 3371 Å.

2.1 Experimental Set-Up

The proto-type of the present apparatus is illustrated in Figure 1. Originally the beam had been generated by a television electron gun. Presently, however, a more powerful unit is used, capable of delivering a one milliampere, one-hundred kilovolt electron beam. Multiple pumping in the beam collimation section together with the high beam current and energy permits operation at test section

pressures of up to 10 Torr. The present light collecting system consists of a quartz lens used in conjunction with a slit that defines a 1.2 mm field-of-view along the beam of electrons. The photodetector, a Dumont 7664 photo-multiplier, therefore observes the fluorescence originating in a cylindrical volume defined by the field-of-view and the beam diameter which is 1.5 mm at the exit aperture of the beam collimator. The spectral window is defined by an interference filter centered at 3375 Å with a 55 Å bandwidth and a 45% peak transmission. This filter permits observation of the (0,0) band of the N_2 (2+) system. An additional detector, having a similar field-of-view and looking through a 50 Å spectral window centered at 3914 Å is used to monitor the fluorescence due to the (0,0) band of the N_2^+ (1-) system. There is also a considerable contribution from the 3961 Å line of Al in this window, which cannot be ignored under any conditions.

The beam current is monitored by means of a Faraday cup assembly. Under dynamic conditions the beam monitor current and the photomultiplier output are displayed on oscilloscope screens fitted with high speed Wollensak Fastax cameras. This arrangement is capable of giving a time resolution of 4 μsec throughout the total record length of 0.3 sec. In comparison with the record length, the time of flight of the projectile within the range is about .02 sec.

2.2 Calibration and Data Reduction

The electron beam fluorescence probe was calibrated on the range under static conditions in the following manner. The photomultiplier output was measured at various pressures within the limits, 0.5 and 9.0

Torr and plotted as a function of pressure or density. Plots of this type were made for both nitrogen and air. Figure 2 is a typical example of the pressure or density dependence of the output voltage.

As can be seen, there is some departure from a straight line dependence. The points were therefore fitted with the curve

$$\frac{pM}{300R} = \rho = \frac{V a_\rho}{K_\rho a_\rho - V} \qquad \text{where} \qquad (1)$$

p = the pressure in Torr

R = universal gas constant

ρ = gas density; M = molecular weight

V = output signal from the photo-detector

a_ρ = an adjustable parameter to fit the curve shape

K_ρ = a normalizing factor to fit the un-normalized output signal

We may also write a similar expression in terms of pressure, i.e.

$$p = \frac{V a_p}{K_p a_p - V} \qquad \text{where} \qquad (2)$$

$$a_p = \frac{(300R)}{M} a_\rho \quad \text{and} \quad K_p = K_\rho (300R)^{-1} M$$

Figure 2 gives $a_\rho = 0.123$ for nitrogen and $a_\rho = 0.018$ for air. The greater departure from linearity for air is a consequence of the higher quenching cross-section for oxygen than for nitrogen.

Having obtained a_ρ, it was then possible to estimate K_ρ. However, K_ρ is dependent on various experimental parameters such as the solid angle of the light collecting system, the oscilloscope sensitivity, the position of the field-of-view along the beam, and the

particular photomultiplier used with a given optical system. Therefore K_ρ was obtained for each trial from fluorescent intensity measurements carried out under ambient conditions existing just prior to the arrival of the projectile in the field-of-view of the collecting optics. If we use the subscript ∞ to denote ambient conditions, we have

$$\frac{\rho}{\rho_\infty} = \frac{V(K_\rho a_\rho - V_\infty)}{V_\infty(K_\rho a_\rho - V)} = \frac{a_\rho V}{\rho_\infty(K_\rho a_\rho - V)} \qquad (3)$$

Equation (3) was used in all data reduction. The parameter a_ρ is related to the quenching efficiency of the gas being studied, and one should therefore expect some dependence on temperature. However, the shock tube results of Camac (1) have shown the effect of temperature to be negligible at all temperatures of interest here. Secondly, the technique estimates densities by measuring molecular nitrogen fluorescence and therefore its validity depends on the constancy of the partial density of molecular nitrogen with temperature. A glance at Gilmore's tables (6) will show that the mole fraction of nitrogen in air does not change by more than 2% under all conditions of temperature and density appropriate to the wake.

The measured density ratio, ρ/ρ_∞ was also used to estimate the relative gas fluctuation $\frac{\Delta\rho}{\rho}$ throughout the wake. The relative gas fluctuation was averaged for groups of five data points throughout the wake.

To estimate the power spectra of the fluctuations the Fastax film was reversed and passed through a data reader to

put the information in digital form on punched tape. The record was divided into sections such that the wake velocity did not change by more than 20% throughout the entire section. In this way the requirement of data stationarity was approximately fulfilled and power spectra were estimated for the density fluctuations in each section.

2.3 Results

Figure 3 shows typical experimental plots of relative wake density versus downstream distance along the axis for 2.7 in diameter spheres travelling at 15,000 fps through nitrogen or air at 8.0 Torr. All traces show densities at less than 0.5 B.D. from the flight axis and are therefore reasonably good representations of the axial density variation. Of the four traces shown, three are for nitrogen and one is for air. Also shown in Figure 3 are theoretical plots of the average density ratio versus X/d calculated by D. Ellington (5) for the conditions V_∞ = 15,000 fps and p = 76 Torr of air on the basis of the turbulent wake model of Lees and Hromas. On the whole the agreement between theory and experiment is satisfactory although the average curve through the measured densities tend to lie above the predicted densities by an approximately constant amount. The theory appears to predict the correct trend in the average density with X/d. Because of the linearity of the dependence of fluorescence output on density for nitrogen and the non-linearity of the air fluorescence, the nitrogen data were considered more reliable.

Some mention should be made of a correction that will have to be made to the measured density ratio. The reference signal was obtained under ambient conditions of temperature and pressure. The

electron beam was therefore attenuated by a certain amount in its passage from the collimator exit to the field-of-view. Under test conditions, the electron beam path consists of two segments, one characterized by ambient density and the other characterized by wake densities which are generally much lower than ambient. Therefore, under test conditions the total attenuation is less and there is consequently a higher electron flux at a given field-of-view than there would be if the entire path length had been through the gas at ambient density. Corrections for this effect would tend to lower the values of the measured density and bring closer agreement between the calculated and measured density ratios. The correction factors are expected to be less important at greater distances from the body. Attention is being given to the development of a method to make these corrections by recourse to either theoretical or measured radial profiles of the density ratio.

Figure 4 is a plot of $\frac{|\Delta\rho|}{\rho}$ versus X/d where $|\Delta\rho|$ is the r.m.s. average taken from the data of four firings. The relative density fluctuation averaged over the entire wake has a value of about 0.08. It should be pointed out that this value is a lower limit in view of corrections which have to be made with respect to the attenuation of the electron beam along its path to the field-of-view of the collecting lens (See above). Since the effect of this correction is to lower ρ , but raise $|\Delta\rho|$, $\frac{|\Delta\rho|}{\rho}$ is expected to increase.

Clay, Herrmann and Slattery (3) have measured $\frac{\Delta\rho}{\rho}$ using schlieren photodensitometry. They found a peak value of 0.15 at 400 B.D. behind 0.95 cm diameter aluminum spheres fired at 8300 fps into air. The

estimate was made at pressures ranging from 15 to 40 Torr. Figures 5 and 6 are plots of the power spectra in terms of the frequency and wave number.

The question remains as to whether or not the wake was truely turbulent. Unfortunately no corroborating evidence from schlieren photographs was available, since the schlieren technique was found to be insufficiently sensitive to the expected density changes for an ambient pressure of 7.6 Torr. There is, however, some supporting evidence from Langmuir probe measurements carried out at C.A.R.D.E. at the same ambient pressure. These showed signals which were normal for turbulent flows, although the high frequency content of the signals was not as rich as at 76 Torr, say. Moreover, turbulent wakes have often been reported for Reynold's numbers which were one-tenth of those which applied to the present experiments.

One characteristic of the density traces (see Figure 3) is the absence of high frequency fluctuations. Hot-wire and Langmuir probe measurements at C.A.R.D.E. have indicated a relative decrease in the high frequency content of the wake with decreasing ambient pressure. The electron beam signal traces, however, show even less high frequency content.

3.0 The Ruby Laser Probe

The Rayleigh scattering experiments were designed to complement the electron beam experiments. Theoretically, information concerning wake densities can be obtained with the ruby laser probe over the whole range of ambient pressures of interest. However, difficulties in reducing the background scattering of the laser beam placed a lower limit of about 10 to 30 Torr on the useable ambient pressure.

3.1 Experimental Details

The experimental arrangement is shown in Figure 7. The ruby laser head, the beam monitor cell, and a polarizing crystal were placed on an optical bench inside a large box outside the range test tank. The box rested on an adjustable table mounted rigidly on a steel platform. The beam was focussed into the centre of the range by a 30" focal length lens. A minimum beam diameter of less than 5 mm could not be achieved because of the high divergence of the beam. After passing through the wake the beam was destroyed in a light dump. The Rayleigh scattered light was collected at right angles to the incident beam by a 6" diameter lens placed about 28" from the focal point of the beam. A large Wood's Horn was used to provide a black background against which to view the scattered radiation. A RCA Victor, 7265 photomultiplier was used to measure the Rayleigh scattered intensity.

The outputs of the photomultipliers used to monitor the incident and scattered intensities were usually recorded on the same oscillograph. The oscilloscope displays were recorded either by an oscilloscope camera on Polaroid film, in which case an oscilloscope

sweep speed of 0.2 msec/cm was used, or a Fastax high speed camera on 35 mm Kodak 4X movie film, in which case a sweep speed of 1 sec/cm was used. The ratio of the amplitudes was then taken to be a measure of the wake density. The range photomultiplier was calibrated in situ against a standard source in terms of volts output as a function of the power falling on the lens. The monitor cell photomultiplier was calibrated in terms of volts output as a function of the beam power. This was effected by a simultaneous measurement of the instantaneous relative beam power by the photomultiplier and the absolute energy of the beam pulse by a calibrated laser calorimeter. The ratio of the integrated photomultiplier signal and the measured beam energy gave the desired calibration constant. It was therefore possible to make absolute measurements of the Rayleigh scattering coefficient and verify that the measured signal was indeed due to Rayleigh scattering.

The density was estimated from the following formula

$$\frac{P_s}{P_i} = (\Delta\Omega)\,\delta\,F\,\rho \qquad (4)$$

where P_s = power scattered into the lens

P_i = power incident on the scattering volume

$\Delta\Omega$ = solid angle subtended by the lens at the scattering volume

δ = width of the field-of-view

F = a function of the polarizability of the scattering gas and of the wavelength

Equation (1) was derived for an incident beam 100% plane

polarized in a direction perpendicular to the plane defined by the line of propagation of the laser beam and the axis of the collecting lens. The scattering angle was taken to be 90^{o}. The function F is dependent on the composition of the scattering gas and may change with time in a reacting mixture, especially if there is a large disparity in the polarizabilities of the reagents and the reactants. Since air can certainly be looked upon as a reacting gas at the temperatures commonly encountered in wakes, the quantity F was calculated for air in equilibrium at temperatures as high as $3000^{o}K$ and for densities ranging from 10^{-1} to 10^{-3} of that at STP to see how it varied over a wide range of conditions. The results are plotted in Figure 8 and show that P_s/P_i will be closely proportional to density at all the conditions assumed. The reason for the constancy of F is that atomic and electronic populations remain low, most of the oxygen removed from the air becomes nitric oxide and the polarizabilities of O_2, NO and N_2 are quite close to each other.

The Rayleigh scattered signal was found to be very sensitive to the dust content of the range gas. To ensure a dust free condition, the range was pumped to less than the desired pressure and the dust was allowed to settle for about 20 hrs. During this time the pressure rose due to leakage; however the air that entered the range was clean, since the range itself acted as a giant filter. The closeness of the measured to the known Rayleigh scattering cross-section and the day-to-day consistency in the ratio of the output voltage of the monitor cell and range photomultipliers confirmed that the air in the range was dust-free

after sufficient settling time had been allowed.

A more difficult problem was associated with measuring the background. One should, in principle, be able to do this by pumping the range to less than 0.1 Torr, say, and measuring the incident and scattered powers. In practice, it was found that the very act of pumping released dust from the walls of the range and within two hours the dust was within the field-of-view of the collecting lens. The dust interfered with the measurements even at pressures as low as 0.1 Torr, and so it was not possible to measure the background directly; however the following procedure was successful. The range was pumped to a desired vacuum the previous night and allowed to settle. Readings were taken on the following day. The gas was pumped out in stages during the next two hours, in which no interference from dust was expected, and readings were taken in each stage. The results were plotted on graphs in the form of the ratio of the scattered power to the incident power as a function of pressure and the best fitting line was extrapolated to zero pressure. This extrapolation gave the contribution of the background. Depending on the closeness of the alignment of the laser to the centre of the light dump, the background was found to vary from less than 1% to 6% of the Rayleigh scattered signal from one atmosphere of air.

The ruby laser head was cooled with liquid nitrogen. The output was observed to be a pulse consisting of a train of spikes of random amplitude and separation. The average separation between peaks was about 0.5μ sec. The "noisiness" of the laser output was not desirable in the measurement of density fluctuations and therefore the photomultiplier signals were filtered by a low band pass filter having a high-frequency

cut-off at 50kHz.

As mentioned above, great care had been taken to ensure that the air in the range was free from dust before each firing. Any dust shaken from the range walls by vibrations produced during the firing would not have had time to reach the field-of-view ahead of the projectile. Therefore any heterogeneous scattering observed from the wake would have had to come from particles entering the wake as the result of factors such as these listed below:

1) Ablation of material from the stagnation region of the projectile.
2) Accumulation of impurities by the projectile during its passage in its sabot through the gun barrel.
3) The release of particles that may have been ground into the surface of the projectile during the polishing.
4) The accumulation of impurities during the passage of the projectile through the two mylar diaphragms usually employed, one at the tip of the gun barrel, the other between the dump tank and the test section of the range.
5) Some sort of small scale spallation.

3.2 Results

Aluminum spheres fired at 15,000 fps consistently showed the presence of particles in the wake. On the other hand, the wakes behind steel-tipped cones have been observed to be relatively free of particulate contamination. This behaviour is illustrated in Figure 9. The spikes in the scattered signal from the wake behind aluminum spheres were taken

to be good evidence for the presence of particles. The signal amplitudes indicated particle diameters in the micron range, whereas the average base width of the spikes was consistent with the time required for the particles to move past the field-of-view at the local wake velocity.

In most firings of aluminum spheres, the dust spikes were so densely packed that it was not possible to make even average density measurements. On the other hand this difficulty was never encountered when cones were launched and density measurements were carried out. Because of the wide dispersion of cone trajectories relative to the centre of the range, it was not possible to monitor the wake at transverse distances of less than about 2 B.D. from the flight axis. Consequently the measured density was always found to be ambient at distances greater than 100 BD behind the projectile. This result is at least consistent with the finite difference calculations of Zeiberg and Bleich (10) on the turbulent wake behind a 10° half-angle cone of 1 ft. base diameter travelling at a speed of 23 kft/sec through the atmosphere at an altitude of 120 kft. They used five turbulent viscosity models to calculate the axial temperature ratio. Although there was little mutual agreement among the predicted temperatures, the axial temperature beyond 100 BD was predicted to be less than twice ambient. Assuming that the axial wake pressure has reached ambient at this distance, the density is seen to be between ambient and half ambient. In the off-axial wake regions, the density would be expected to be close to ambient as was in fact verified by the laser experiments .

One interesting feature of the density measurements was the absence of any sign of fluctuations in the signal. This was undoubtedly due to the fact that the wake was sampled outside the turbulent core.

Since particles in the wake seemed to occur when aluminum spheres were fired, but never when steel-tipped cones were fired, it was thought that ablation may have been responsible for the presence of the particles. In a search for materials less amenable to ablation, it was decided to try copper coated aluminum spheres. Of the four fired to date, two of these gave relatively particle free wakes, whereas the other two behaved very similarly to aluminum. The difference in the behaviour of the two pairs was attributed to the quality of the copper coating. The surfaces of second pair were found to be covered with pores which had very rough edges and contained small particles of some material, presumably polishing compound or bits of metal. The former pair seemed to be relatively free of pores.

Some attempt was made to test other possible sources of wake particles. Since the projectile travelled in its sabot through the gun barrel and since there was an intimate contact between the plastic sabot and the gun barrel, it was thought that perhaps some decomposition of the sabot may have occurred close to the gun barrel due to heating and that the decomposition products might then have spread over the sabot and unto the projectile. To test this hypothesis, a good experiment would have been to vary the sabot material. The experiments of Locke (7) have indicated some correlation between

sabot material and wake particle formation. For the firing conditions at CARDE, zelux seems to be the only acceptable sabot material in terms of strength and density, and thus the sabot material could not be varied. It must be pointed out that being a polycarbonate plastic of high aromatic character, zelux is prone to soot formation and charring at high temperatures. If barrel heating of the sabot were a true source of wake particles, it would be difficult to explain the differences between firings of cones and copper-plated spheres, on the one hand, and firings of aluminum spheres, on the other.

The projectiles were made to pass through mylar diaphragms in all firings. To test this as a possible source of wake particles the diaphragm was removed from between the dump tank and test section. As before, wakes behind cones were found to be clean, whereas those behind aluminum spheres were found to be contaminated. Passage of the projectile through the mylar diaphragms was not therefore a prime source of wake particles.

Wakes behind titanium spheres were found to be relatively dust free; however, radiation from TiO interfered with the signal.

Although simple in principle, the Rayleigh scattering technique is a difficult one to realize in practice. We are confident that given copper projectiles with optimum surface characteristics, useful density measurements can be made, and perhaps even power spectra can be estimated. The possibility of making local density measurements warrants a continuation of efforts to develop the laser probe. The observation of particles in the wake suggests that some careful consideration be given

to any possible effect that they may have on the measurable characteristics of the wake, such as electron density.

Concluding Remarks

The electron beam fluorescence probe has proven itself to be an effective tool for the measurement of gas densities in hypersonic air or nitrogen wakes. Some attention should be given the problem of finding a suitable method to correct the measured densities for effects arising out of the attenuation of the electron beam by the gas molecules in its path. The absence of high frequencies in the power spectrum of the measured density fluctuations is a puzzling characteristic of the electron beam probe that should be carefully examined.

The laser beam probe has proven to be somewhat of a disappointment because of the presence of particles in the wakes behind spherical projectiles. Some hope of eliminating these particles arises out of the observation of clean wakes behind two copper-coated aluminum spheres. Apparently the "cleanness" of the wake appears to be sensitive to the condition of the projectile surface, as well as to the material out of which the projectile is made.

REFERENCES

1. Camac, M., AVCO Everett Res. Lab. Private Communication. Nov 66

2. Cantin, A., Heckman, D.E., and Gouge, R., "An Autocorrelation and Power Spectral Density Analysis Computer Program for Random Signals." CARDE TR-565 (to be published). 1967.

3. Clay, W.G., Herrmann, J., and Slattery, R.E., "Statistical Properties of the Turbulent Wake Behind Hypervelocity Spheres." Phys. Fluids 8 1792-1801 1965.

4. Davidson, G., and O'Neill, R., "The Fluorescence of Air and Nitrogen Excited by 50 Kev Electrons." Air Force Cambridge Research Lab. AFCRL-64-466 May/64.

5. Ellington, D., "The Lees-Hromas Method for Wake Turbulent Diffusion at Hypersonic Speeds, Part II Numerical Solutions." CARDE TN 1744/66 January/67.

6. Gilmore, F.R., "Equilibrium Composition and Thermodynamics Properties of Air to 24,000°K." U.S. Air Force Project Rand Rept RM-1543 Aug./55 AD-84052.

7. Locke, E., "Point Measurements of Average Turbulent Wake Density by Rayleigh Scattering." AVCO Everett Research Laboratories AMP 212 November 1966.

8. Muntz, E.P., "Measurement of Rotational Temperature, Vibrational Temperature and Molecule Concentration in Non Radiating Flows of Low Density Nitrogen." UTIA Report No. 71 April/61.

9. Tardif, L., and Dionne, J.G.G., "Space Resolved Wake Density Measurements" CARDE TN-1724/66 August/66.

10. Zeiberg, S.L., and Bleich, G.D., "Finite Difference Calculation of Hypersonic Wakes." AIAA J. 2 1396-1402 1964.

Acknowledgements

Thanks are due Mr. G. Tidy, Superintendent of the Aerophysics Wing and Dr. A. Lemay, Section Leader of the Hypersonic Physics Section for their continuing support and encouragement. We acknowledge the contribution of the Range Engineering Section in the preparation and launching of the projectiles. Messrs. J.C. Pare, J.P. Poulin, and G. Labreque were responsible for all experimental measurements.

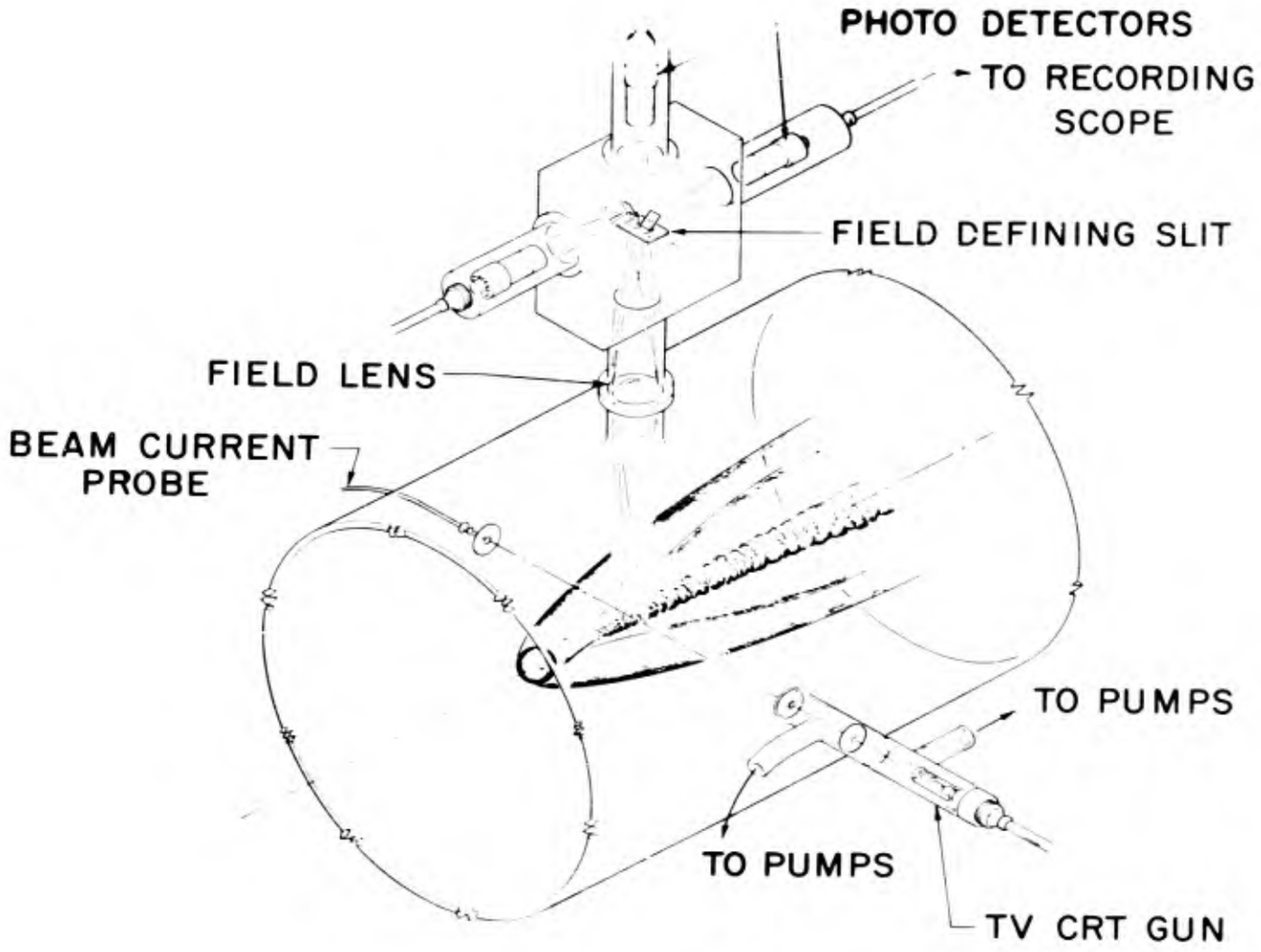

Fig. 1 Electron beam arrangement used for the measurement of mass density

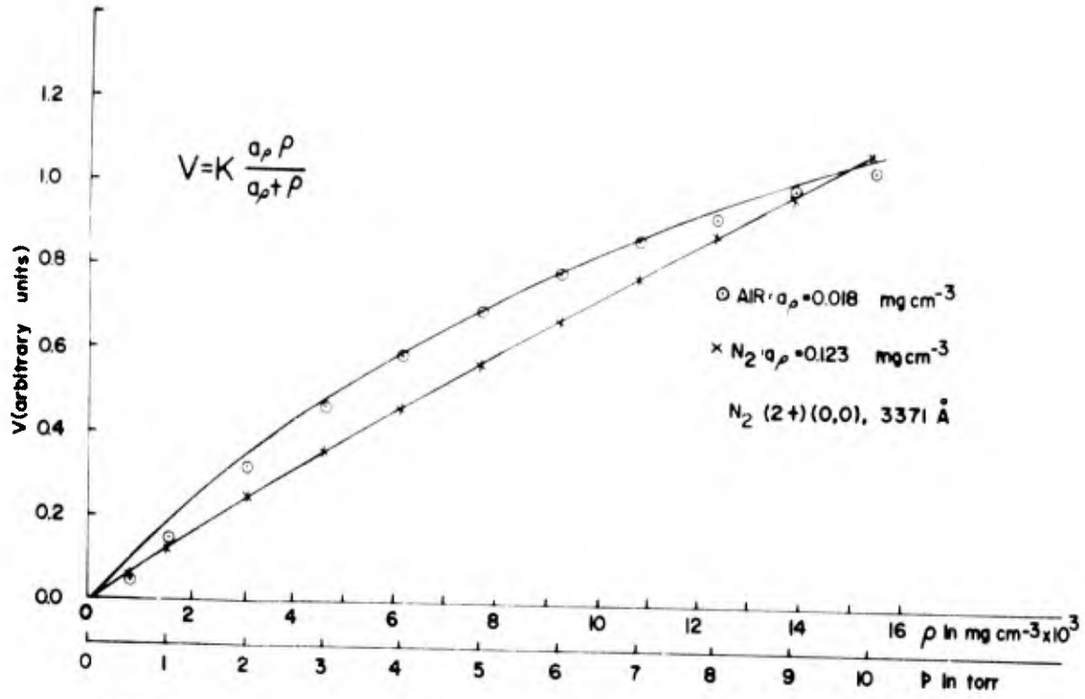

Fig. 2 Fluorescence intensity as a function of mass density

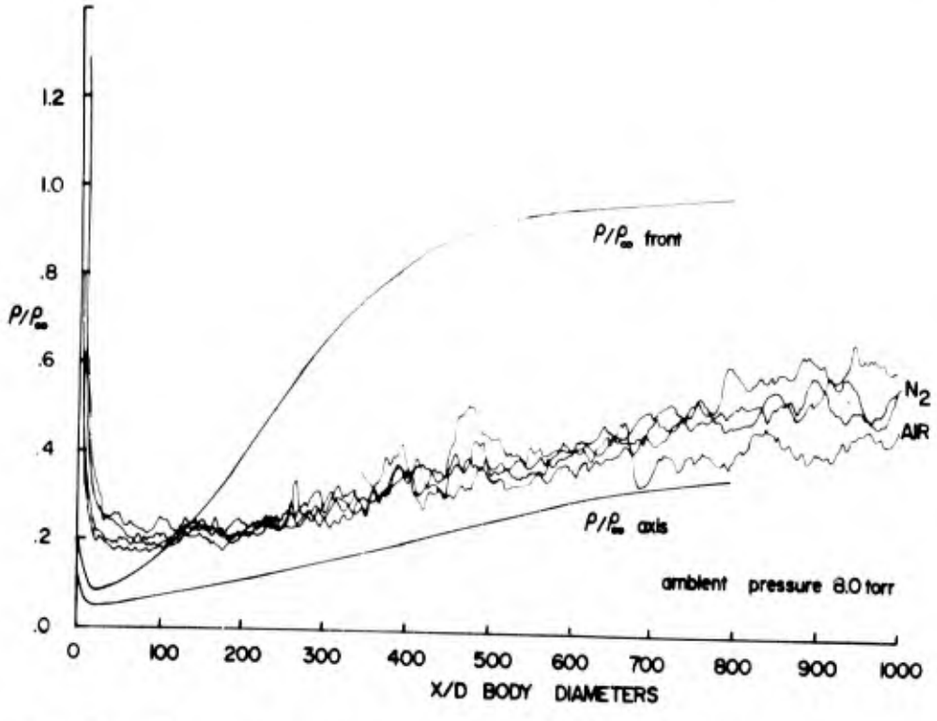

Fig. 3 Wake density ratio as a function of axial distance

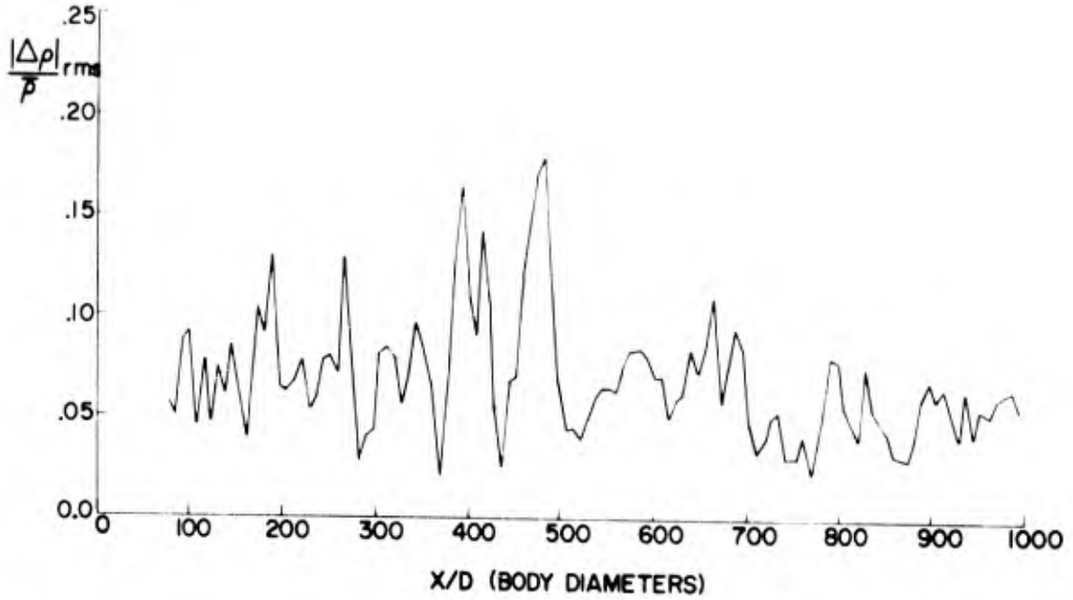

Fig. 4 R.M.S. density fluctuations as a function of axial distance

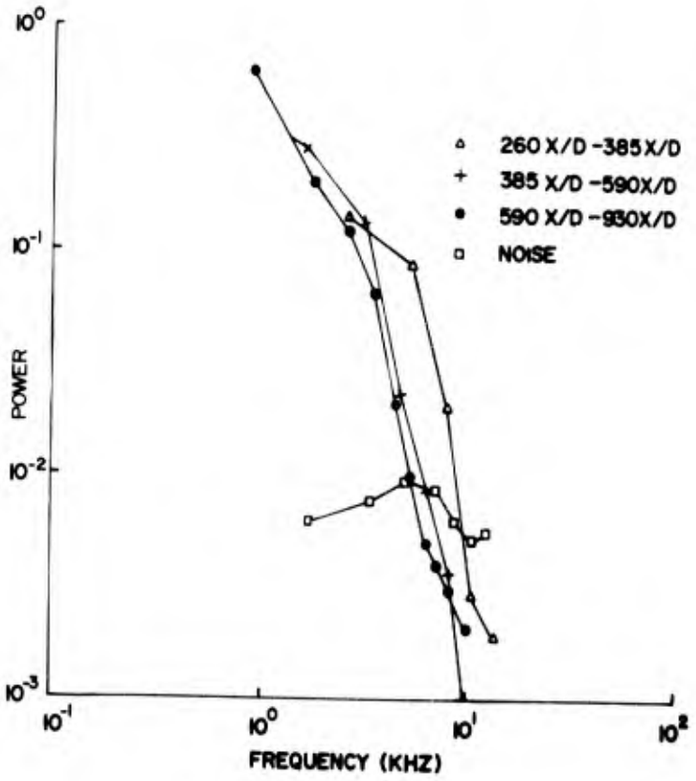

Fig. 5 Normalized power spectra of density fluctuations versus frequency

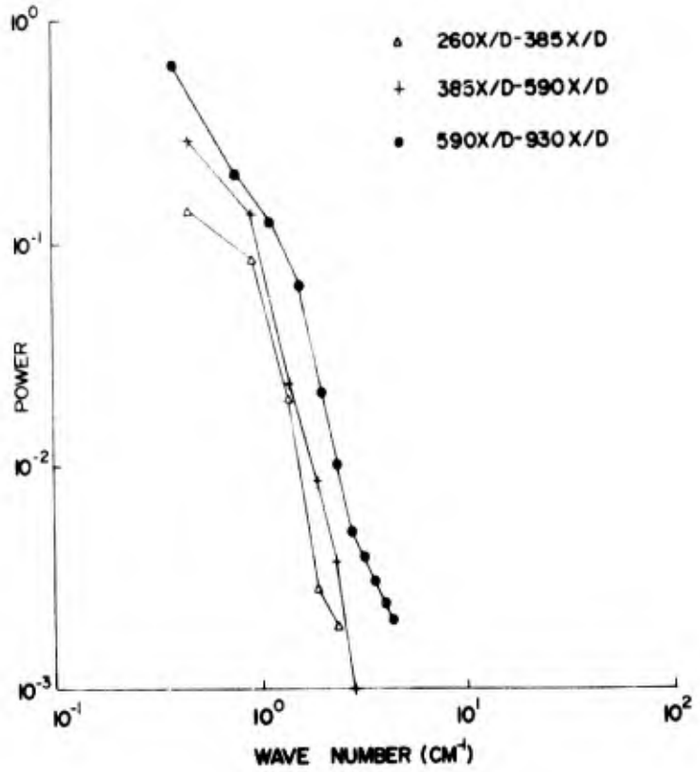

Fig.6 Normalized power spectra of density fluctuations versus wave number (cm^{-1})

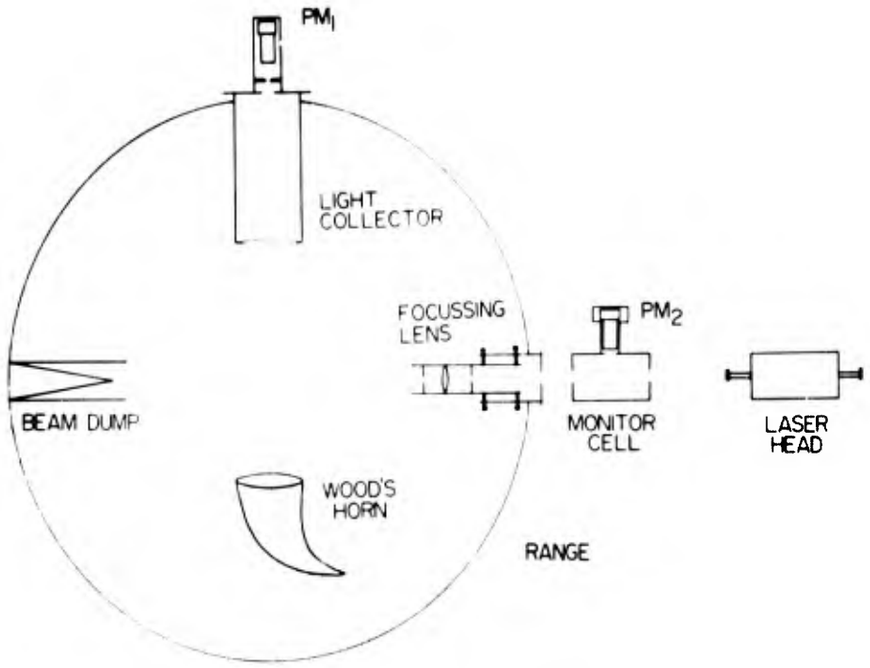

Fig.7 The Rayleigh scattering apparatus

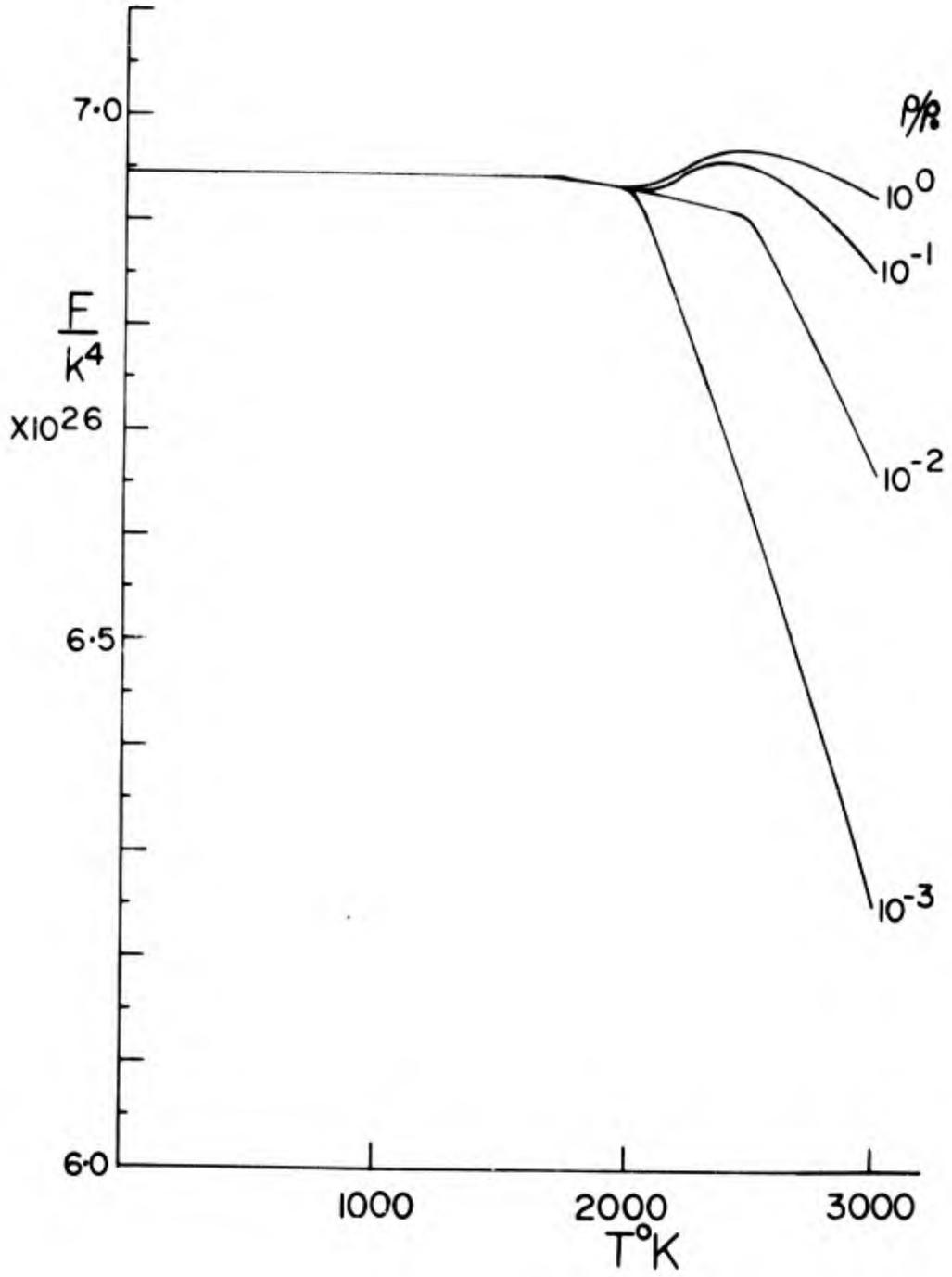

Fig.8 The dependence of the Rayleigh scattering cross-section term, F, on temperature and density

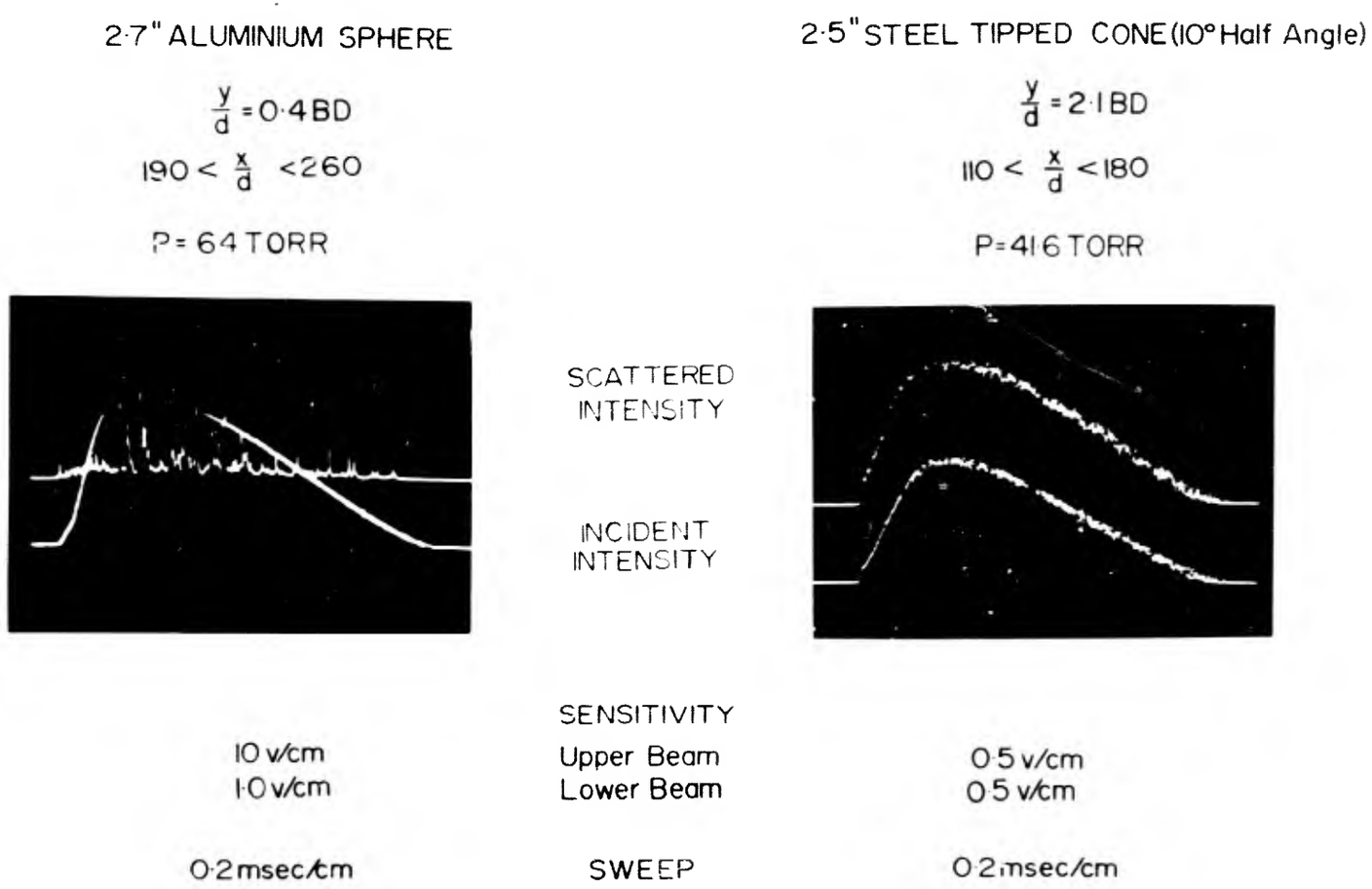

Fig. 9 Typical traces of the scattered signal from hypersonic air wakes